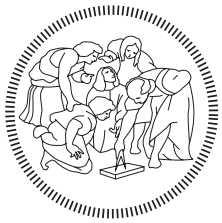

POLITECNICO
MILANO 1863

Mathematical Modeling and Machine Learning for the Numerical Simulation of Cardiac Electromechanics

Advisor:
Prof. Alfio Quarteroni

Coadvisor:
Prof. Luca Dede'

Chair of the Doctoral Program:
Prof. Irene Sabadini

Doctoral dissertation of:
Francesco Regazzoni

Politecnico di Milano
MOX – Dipartimento di Matematica
Mathematical Models and Methods in Engineering – XXXII cycle

Frustra fit per plura quod fieri
potest per pauciora.

William of Occam, c. 1287-1347

Abstract

Computer-based numerical simulations of the heart, also known as in silico cardiac models, are increasingly assuming a recognized role in the context of computational medicine and cardiology. They are based on rigorous and accurate mathematical models describing the physical phenomena determining the cardiac function. However, the intrinsic multiscale nature of the cardiac activity, for which energy is consumed at the microscale by subcellular mechanisms to produce work at the macroscale for the whole organ, risks to harm the exploitation of computational medicine for the heart, as it raises a challenging trade-off between accuracy of the models and computational efficiency of numerical simulations.

In this thesis we develop a mathematical and numerical multiscale model of cardiac electromechanics, wherein the mechanisms of active force generation are described by means of new biophysically motivated models. In these subcellular models, we explicitly represent only the most relevant interactions among the proteins involved in the force generation process, while we neglect secondary interactions, but still leading to accurate results – that we validate against experimental data – obtained with a drastic reduction of computational cost with respect to the models currently available in literature.

As it is crucial to multiscale electromechanical modeling, we establish the link between the variables describing force generation at the microscale and those describing the strain and the stress of the tissue at the macroscale. This allows to couple, in a mathematically sound manner, the subcellular models proposed in this thesis – characterized by a stochastic behavior – with models for cardiac electrophysiology and for passive and active mechanics – based on a deterministic formalism – written as systems of Ordinary Differential Equations (ODEs) and Partial Differential Equations (PDEs).

In this thesis we also combine the proposed subcellular models with a newly developed Machine Learning algorithm, in order to speedup their numerical resolution in the multiscale electromechanical model. Specifically, a reduced model based on Artificial Neural Networks (ANNs) is trained from a collection of simulations generated by means of biophysically detailed force generation models. In this manner, the computationally demanding training phase can be performed offline, with the advantage of a huge speedup when the trained ANN-based model is exploited in replacement of the high-fidelity model used to generate the training data. Overall, our multiscale model for cardiac electromechanics achieves an excellent balance between accuracy of the models, their rigorousness and computational efficiency in large-scale simulations.

Keywords: *cardiac modeling, cardiac electromechanics, numerical simulations, multiscale models, Machine Learning, Artificial Neural Networks, data-driven modeling, model order reduction.*

Sommario

I modelli cardiaci *in silico*, basati su simulazioni numeriche della funzione del cuore, stanno assumendo un ruolo sempre più riconosciuto nel contesto della medicina computazionale e della cardiologia. Tali simulazioni sono basate su rigorosi ed accurati modelli matematici che descrivono i fenomeni fisici alla base della funzione cardiaca. Tuttavia, a causa dell'intrinseca natura multiscala dell'attività cardiaca, in virtù della quale l'energia consumata da meccanismi subcellulari produce lavoro per l'intero organo, è attualmente difficile trovare un soddisfacente compromesso fra accuratezza dei modelli e efficienza computazionale delle simulazioni numeriche. Ciò rappresenta un importante limite per la concreta applicabilità degli strumenti della medicina computazionale in ambito cardiaco.

In questa tesi sviluppiamo modelli matematici e numerici, di tipo multiscala, per l'elettromeccanica cardiaca, nei quali i meccanismi di generazione di forza attiva sono descritti attraverso dei nuovi modelli, accurati dal punto di vista biofisico. In tali modelli subcellulari sono rappresentate in modo esplicito solamente le più rilevanti fra le interazioni che intercorrono fra le proteine coinvolte nel meccanismo di generazione di forza, mentre sono trascurate le interazioni di natura secondaria. Otteniamo così un'elevata accuratezza dei risultati, validati rispetto a dati sperimentali, a fronte di una drastica riduzione, rispetto ai modelli attualmente disponibili in letteratura, del costo computazionale.

Stabiliamo poi i legami intercorrenti fra le variabili che descrivono la generazione di forza a livello della microscala spaziale e quelle che descrivono le deformazioni e gli sforzi del tessuto a livello della macroscala, aspetto cruciale per la modellistica multiscala dell'elettromeccanica. Ciò permette di accoppiare, in modo matematicamente rigoroso, i modelli subcellulari proposti in questa tesi – caratterizzati da un comportamento stocastico – con modelli di elettrofisiologia cardiaca e di meccanica passiva e attiva – basati invece su un formalismo deterministico – scritti come sistemi di equazioni differenziali ordinarie e equazioni alle derivate parziali.

In questa tesi, inoltre, proponiamo un nuovo algoritmo di apprendimento automatico (*Machine Learning*), volto ad accelerare la risoluzione numerica dei modelli di forza attiva nel contesto multiscala dell'elettromeccanica cardiaca. Nello specifico, un modello ridotto basato su reti neurali artificiali (ANN) è addestrato a partire da una collezione di simulazioni ottenute attraverso modelli di generazione di forza attiva biofisicamente dettagliati (i cosiddetti modelli ad alta fedeltà). In questo modo la fase di addestramento, impegnativa sul piano computazionale, può essere effettuata *offline* (ossia una volta per tutte), con il vantaggio di una notevole accelerazione quando il

modello basato su ANN, ormai addestrato, è utilizzato in sostituzione del modello ad alta fedeltà. Nel complesso, il nostro modello multiscala di elettromeccanica cardiaca realizza un eccellente bilanciamento fra l'accuratezza dei modelli, il loro rigore e l'efficienza computazionale in simulazioni su large scala.

Parole chiave: *modellistica cardiaca, elettromeccanica cardiaca, simulazioni numeriche, modelli multiscala, apprendimento automatico, reti neurali artificiali, modellistica basata sui dati, riduzione d'ordine di modello.*

Acknowledgments

At the end of this journey, it is time to look back and to think to all the people who made it the way it was.

First of all, I gratefully thank my advisor Alfio Quarteroni and my coadvisor Luca Dede', for giving me the opportunity of working on fascinating topics and for providing me everyday with new challenges. Thank you for your support, at all levels, and for the trust you have shown towards me. In particular, I am grateful to Luca for being more than a teacher to me and for his infinite patience.

I am sincerely grateful to Dominique Chapelle and Philippe Moireau for the period I spent in the MΞDISIM team, which I believe was a precious experience of scientific growth for me. Nothing allows you to broaden your vision like experiencing an environment different from the one you grew up in. I also express my gratitude to Jinchao Xu, for the opportunity of spending a research period in his group and for the inspirational discussions about Machine Learning and approximation of PDEs.

I am grateful to Lev Truskinovsky and to François Kimmig for the insightful discussions about the intriguing function of muscle cells and the challenges related to its mathematical description.

I acknowledge the European Research Council for having partially supported this research under the EU's Horizon 2020 research and innovation programme (grant agreement 740132, iHEART, P.I. Prof. A. Quarteroni).

Besides the strictly scientific standpoint, several people contributed to the achievement of this work. It is not enough to say thanks to the Tender's crew, because each day has been different, unpredictable, enjoyable. Infinitely thanks to my (i)Heart teammates, for being more than a research group. Merci à tous les gars grâce auxquels, malgré les gilets, les grèves et les semaines sans voir le soleil, je me suis senti comme chez moi dans cette grande ville. En particulier, merci à ceux qui m'ont aidé lorsque j'ai découvert que je ne pouvais pas voler. A special thank to the Jinchao Xu's group in PSU for the special welcome, in particular to Juncai for his unexpected hospitality. 謝謝你! In fact, during this PhD path I could meet many people and tighten friendships. I feel that many of them will endure. And I am grateful for them.

Grazie ai miei amici, quelli di sempre, perchè *amicitia quae desinere potest vera numquam fuit*. Ringrazio infinitamente i miei genitori, Luigi e mia nonna Elia, per avermi sempre sostenuto, senza farmi mancare il loro incoraggiamento per un solo istante. Infine grazie a te, Giulia, che ogni giorno mi dai una ragione in più per dirtelo.

Paris, 27th January 2020 F. R.

Contents

List of Figures

List of Abbreviations

Anatomical terms

AF	Actin (thin) filament
BS	Binding site
EM	Electromechanics
LA	Left atrium
LV	Left ventricle
MF	Myosin (thick) filament
MH	Myosin head
RA	Right atrium
RU	Regulatory unit
RV	Right ventricle
Tm	Tropomyosin
Tn	Troponin
XB	Crossbridge

Mathematical models

CMC19	Model of [CMC19]
H57	Model of [Hux57b]
HS71	Model of [HS71]
R03	Model of [Ric+03]
TTP06	Model of [TTP06a]
W12	Model of [Was+12]

Others abbreviations

ANN	Artificial Neural Network
CTMC	Continuous-time Markov Chain
FEM	Finite Element method
FKE	Forward Kolmogorov equation
HF	High-fidelity
MC	Monte Carlo
MOR	Model order reduction
ODE	Ordinary differential equation
PDE	Partial differential equation
ROM	Reduced order model

Introduction

The human heart is a sophisticated machine, finely tuned by millions of years of evolution, whose functional role is pumping the blood throughout to body cells, so that organs are supplied with oxygen and nutrients, while the metabolic waste is removed. In the context of cardiovascular research and computational medicine, mathematical and numerical modeling are increasingly recognized as valuable tools, with a twofold role. On the one hand, realistic and detailed in silico models of the heart can deepen the understanding of its function, help the interpretation of experimental observations and explain the subtle links between the organ-level emergent phenomena and the underlying biophysical mechanisms. On the other hand, patient-specific numerical simulations, which are increasingly becoming available, can provide clinicians with valuable quantitative information for improving patient care and with precious tools to support decision-making [Smi+04; Cra+04; Fin+11; Cha+16; Qua+17].

The implementation of in silico models for cardiac applications requires the development of mathematical models describing the complex physical phenomena involved in the heart function. Specifically, every heartbeat is driven by the propagation of an electrical signal throughout the tissue, that breaks the delicate balance of electrical and chemical gradients across the cell membrane, thus triggering a fast succession of events, known as *action potential*. The resulting increase of calcium ions concentration inside the *cardiomyocytes* (the cardiac muscle cells) is the signal triggering the activity of *sarcomeres*, the contractile units of muscle cells, that transform into mechanical work the chemical energy stored in ATP. The macroscopic consequence of such phenomenon is the muscle contraction, that leads to a rapid increase of the internal pressure of the heart chambers, determining the opening of the heart valves and the blood injection and ejection through the ventricles and the atria [TD08; JKT07; Kat10; Ber01]. In this thesis, we focus on cardiac *electromechanics* (EM), including the electrophysiology, the mechanical activation and the passive and active mechanics of the myocardium.

To describe the different physical phenomena involved in the cardiac EM function, several mathematical models have been proposed in literature. The propagation of the electrical signal through the cell membrane is typically modeled by systems of Partial Differential Equations (PDEs), such as the monodomain and the bidomain equations [CFPS06; CFPS14], coupled with a system of Ordinary Differential Equations (ODEs) describing the dynamics of the ionic fluxes across the cell membrane [HH52a; O'H+11; TT+04; TTP06a; TTP06b; Fit61; NAY62; AP96; BOCF08]. The generation of active force at the subcellular level can be described by systems of ODEs [Zah81; BCS01;

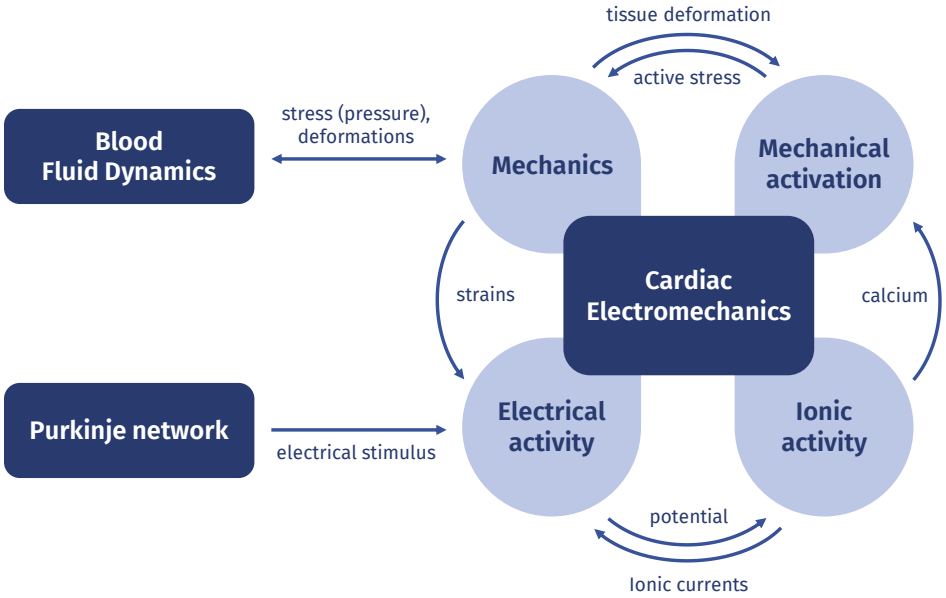

Figure 1: The building blocks of the EM activity in a ventricle and the corresponding coupling quantities. The ventricle contraction is triggered by the propagation of an electrical signal coming from the *Purkinje system* (a network of specialized conducting fibers) [TD08; JKT07] and it involves the synergic interaction between the electrical activity, ionic exchanges at the level of the cell membrane, the generation of an active force at the subcellular scale and the mechanical activity of the cardiac tissue.

Cha+12; HMTK98; NHS06; Lan+12; Lan+17; Was+12; Ros+14; RB+14; Car+14], systems of PDEs [Hux57b; CMC19; Kim+19; Kim19] or by continuous-time Markov Chains (CTMCs) [Ric+03; HTR06; Sug+12; Was+13; Was+15]. At the level of the tissue, the deformation of the cardiac muscle is modeled with the formalism of continuous mechanics [Ant95; Ogd97], by adopting a suitable hyperelastic [GMW91; GCM95; ULM02; HO09] or visco-elastic [GSH16; Zha+19] constitutive law. Such models should account for the strongly anisotropic features of the passive response of the cardiac tissue, due to the presence of oriented fibers, spanning the whole myocardium [TD08; JKT07]. As a matter of fact, these four core models are tightly coupled together to establish the so called integrated EM model, as shown in Fig. 1.

To approximate the solution of the single core models of cardiac EM, different numerical methods, based on the Finite Element method, the Finite Volume method, Isogeometric analysis or the Finite Difference method, have been devised [QSS10; Smi+04; Cra+04; Fin+11; Cha+16; Qua+17; QMV17; Pat+17; PDQ19]. Due to the interactions among the different physics involved in cardiac EM, such core models need to be coupled together to build an integrated computational model of the complete cardiac EM function. With this aim, specialized computational methods that are stable, reliable and efficient are required [Smi+04; Fin+11; Cha+16; Qua+17; GDQ18a; GDQ18b; Ger18].

The construction of an integrated mathematical and numerical model of cardiac EM is however a remarkably arduous task. This is mainly due to the *multiphysics* (due to biochemistry, electricity, solid mechanics, fluid dynamics interacting phenom-

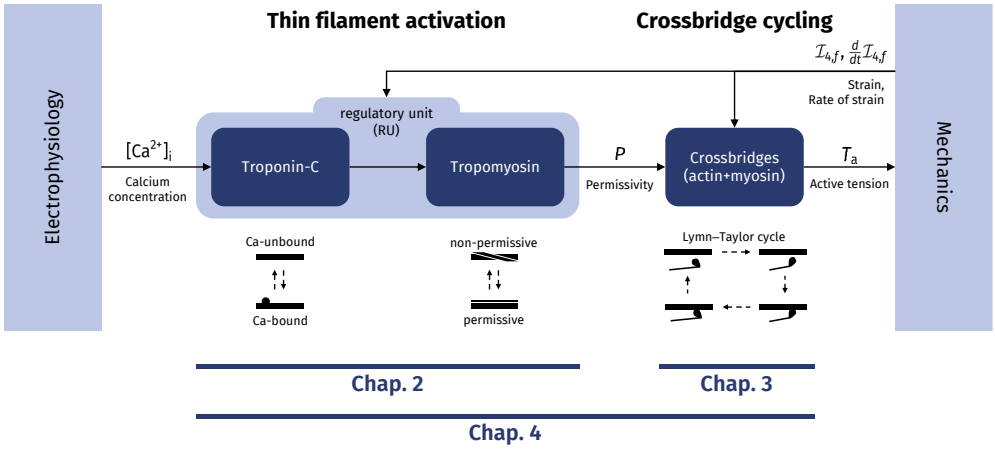

Figure 2: Representation of the different stages of the force generation mechanism and of the chapters where they are treated.

ena) and *multiscale* nature of the heart system: characteristic spatial scales range from nanometers to centimeters and the temporal ones from microseconds to seconds. This makes it difficult to combine a suitable richness and detail of the mathematical models (and thus their *reliability*) with the *computational efficiency* of their numerical approximation [Cha+16; Qua+17; QMV17].

The delicate trade-off between the need for model accuracy and for computational efficiency of numerical simulations is mainly due to the multiscale nature of the heart, for which the mechanical work responsible of the macroscopic motion of the organ is fueled by the energy consumed at the microscale by subcellular mechanisms. The phenomenon of generation of active force takes place inside sarcomeres and involves a complex chain of chemical and mechanical reactions. This mechanism is divided into two steps (Fig. 2). First, a ionic signal (specifically, an increase of calcium ions concentration) triggers the so-called *regulatory units* (protein complexes consisting of troponin and tropomyosin) that act as on-off switches for the muscle contraction. Then, when the regulatory units are activated, the *actin* and *myosin* proteins are free to interact and to form the so-called *crossbridges*, molecular motors that generate an active force by consuming the chemical energy stored in ATP [Ber01; Kat10].

The machinery of microscopic force generation features many regulatory mechanisms, forming the subcellular basis of organ-level phenomena, such as the Frank-Starling law [Kat10]. Hence, if a microscale mathematical model of force generation is used in a multiscale setting to build an integrated organ-level EM model, then it should be able to reproduce the above-mentioned mechanisms. In particular, the following experimentally observed behaviors are crucial to characterize the functioning of sarcomeres.

- The apparent calcium sensitivity of the regulatory proteins features a significant increase around the half-activating calcium concentration. This translates into a quick increase of macroscopic force when the calcium signaling reaches a given threshold [Ken+86; DKT02; TK+08].

- The shortening of sarcomeres, following the tissue contraction, has a feedback effect on the force generation mechanisms. Indeed, an increase of sarcomere

length has the twofold effect of increasing both the maximum tension that can be reached and the apparent calcium sensitivity [Ken+86; TKHK00; DKT02; TK+08]. This phenomenon is the subcellular basis of self-regulation mechanisms of the heart [NS09; Kat10].

- The functioning of sarcomeres is a multiscale phenomenon in itself. In fact, at least three different time scales can be distinguished in their response to external inputs [KS09; MT10a; MT10b; CT18; Car+16]. As the heart contraction is a dynamical phenomenon, it is crucial to accurately capture the different time scales involved in the response of sarcomeres to the external stimuli.

In the past decades, the scientific community has devoted several efforts to the construction of mathematical models describing the complex dynamics of the phenomena taking place inside sarcomeres [Hux57b; HS71; RWH99; Ric+03; NHS06; HTR06; MT10b; Car11; Cha+12; Lan+12; Was+13; Was+15; Lan+17; CT18; CMC19]. However, because of the intrinsic complexity of the phenomenon of force generation, the huge computational cost associated with the numerical approximation of such models limits their application when they are used for multiscale EM simulations. Despite several attempts to capture the fundamental mechanisms underlying the force generation phenomenon into a tractable number of equations [RWH99; SGS03; RBC99; Ric+03; Cam+10; Was+12; LN15], the existing organ-level cardiac mathematical models rely on two alternative strategies to describe the microscopic force generation phenomenon.

- **Phenomenological models** (see e.g. [HMTK98; NHS06; Ric+08; Lan+12; Lan+17]) are built by fitting the measured data with simple curves, chosen by the modeler. The models belonging to this class, however, lack of a deep understanding of the mechanisms to be modeled. As such, they do not allow for investigating the effects of the subcellular scale elements on the organ-scale behavior. Indeed, the parameters characterizing phenomenological models often lack of a clear physical interpretation. Moreover, the noisy nature and deficiency of data coming from the subcellular contractile units and the intrinsic difficulties in measuring sarcomeres under the conditions occurring during an heartbeat hamper the predictive power of such models [Fin+11].

- The alternative to phenomenological models is represented by **biophysically detailed models**, whose numerical solution, because of their complexity, is obtained by means of a **Monte Carlo approximation** (see e.g. [Was+13; Was+15; HTR06]). The Monte Carlo method is however inaccurate and inefficient, featuring a huge computational cost, both in terms of time and memory storage. Indeed, to accurately approximate the solution of a single heartbeat for a single myofilament, up to tens of hours of computational time can be required [RDQ18].

Goals and objectives

The final goal of this thesis is building a multiscale mathematical and numerical model of cardiac EM that combines biophysical models that are rigorous, detailed and accurate with computationally efficient numerical methods oriented to the large-scale simulations. Due to the intrinsic complexity of the subcellular phenomena by which sarcomeres generate active force, such goal requires the development of a detailed and, at the same time, efficient computational model for the microscopic mechanisms of force generation.

With this aim, in this thesis we analyze the different phenomena pertaining the force generation mechanisms and, for each of them, we aim at developing a mathematical description able of capturing the fundamental machinery underlying the phenomenon itself. The resulting model should be able to reproduce all the experimental characterizations of the force generation dynamics that are relevant for the organ-level behavior, with a contained computational cost.

Besides the development, calibration and validation of microscopic model of force generation models, in this thesis we aim at further reducing the computational cost associated to their numerical approximation by means of suitable *model order reduction* (MOR) techniques. Since most of the MOR techniques applicable to time-dependent problems are designed for linear models or for models whose dynamics can be well approximated by linear manifolds of reduced dimension [ASG00; BMS05; QR14; QMN15], we need techniques suitable to treat the highly nonlinear nature of the dynamics of the proteins involved in the mechanism of force generation.

Finally, the development of a multiscale model of cardiac EM requires coupling the microscale force generation models with models describing the electrophysiological and mechanical activity of the heart at the macroscopic scale. With this aim, a link between the subcellular scale and the organ scale needs to be drawn, by suitably upscaling the developed microscopic models. In this regard, we notice that the phenomena pertaining the microscale have a stochastic nature, unlike those taking place at the macroscopic level. Hence, when the two scales are coupled together, the effects on the macroscale of the stochastic fluctuations characterizing the microscale must be taken into account.

Original contributions

The original contributions of this thesis are the following.

- Concerning the **mathematical modeling of force generation** in cardiac cells, we develop several models, describing the different phenomena involved in the subcellular mechanism of cardiomyocytes contraction.
    - First, we address the calcium-driven activation of the tissue and we propose a mathematical model, that we call *activation-MH* model. The model is derived from the pre-existing model of [Was+12], under the assumption of conditional independence of specific sets of events. This physically motivated assumption allows to drastically reduce the number of degrees of freedom, thus resulting in a significantly large computational saving. Indeed, the original Markov Chain model involves a huge number of degrees of freedom (order of 10^{21}) and it is solved by means of the Monte Carlo method, which notoriously reaches statistical convergence slowly. With our reduced model, instead, numerical simulations can be carried out by solving a system of ODEs, reducing the computational time by more than 10000 times.
    - Then, we consider the whole sarcomere dynamics and we propose six different models describing both the calcium-driven activation and the cross-bridge cycling. All the models are based on a biophysically detailed description of the interactions among the sarcomere proteins and are derived under physically motivated assumptions. Such assumptions are aimed at neglecting second-order interactions among the proteins, so that the variables describing the stochastic processes associated with the states of the

proteins can be partially decoupled. This results in a drastic reduction in the size of models. Among the proposed models, based on different assumptions and modeling choices, we focus on the two that feature the best balance between model complexity, computational efficiency and availability of data to constrain the model parameters. Such models, named *spatially-explicit ODE model (SE-ODE)* and *mean-field ODE model (MF-ODE)*, are written in the form of ODEs, and allow for the simulation of 1 s of physical time in just a few seconds of computational time.

- We develop a strategy to perform the calibration of the two models SE-ODE and MF-ODE starting from the experimental measurements collected in the commonly available experiments on muscle fibers. In this manner, we calibrate the two models SE-ODE and MF-ODE for rat cardiomyocytes at room-temperature and human cardiomyocytes at body-temperature. We validate both qualitatively and quantitatively the obtained models and we show that they are capable of reproducing the main experimentally observed features of the force generation phenomenon.
- We propose a possible explanation for the so–called phenomenon of length-dependent activation (consisting in an increase of apparent calcium sensitivity when the sarcomere length increases), that is still not fully understood from a physiological perspective, and most of the explanations proposed in the past have been later rejected [TK16; AM+16]. Noticeably, the SE-ODE model correctly predicts this phenomenon, without any phenomenological length-dependent tuning of the parameters, as done in most of the existing models [NHS06; Was+12; Was+13; Was+15]. Hence, we highlight the fundamental ingredients contained in the SE-ODE by which it is able of producing the observed length-dependent activation, thus formulating a possible explanation for such phenomenon.

- In order to build an accurate but computationally efficient cardiac electromechanical model, we address the topic of **model order reduction (MOR)**. Indeed, when a model of force generation is used in a multiscale setting (such as to perform organ-scale numerical simulations), the microscale model must be solved multiple times. For instance, when a Finite Element discretization is employed, it must be solved at least in any nodal point of the computational mesh. Since capturing the complexity of realistic heart models requires as many as $10^5 - 10^6$ mesh elements [Ger18; Qua+17], the computational cost of force generation models may dramatically become an issue, both because of computing time and memory storage. Therefore, despite the models proposed in this thesis feature a significantly lower computational complexity compared with other existing models, a further reduction is desirable.

  - Motivated by the above considerations, we propose a novel data-driven MOR technique, based on *Machine Learning*, whose applicability overlooks the specific application for which it has been developed (i.e. the reduction of force generation models). Indeed, our method can be applied, in general, to dynamical systems arising from time-dependent ODEs or PDEs. Our approach, unlike model-based methods, is non-intrusive, as it just requires a collection of input-output pairs generated by the high-fidelity (HF) model, from which an Artificial Neural Network (ANN) learns the dynamics of the model. The proposed method, moreover, thanks to its non-intrusive

nature, can also be applied to the case when the input-output pairs come directly from measurements rather than from a mathematical model (in other terms, it can be employed, besides for *model reduction* purposes, for *model learning* purposes).

- The above mentioned fully black-box MOR method can be easily extended by feeding the learning process with information coming from the HF model, moving thus towards a gray-box (or semiphysical) approach. We apply such gray-box Machine Learning MOR technique to reduce our proposed activation-MH, SE-ODE and MF-ODE models. In this manner, we derive three reduced models, able of reproducing the results of the corresponding HF models with an error of the order of 1% with just two or three internal variables, thus dramatically reducing the computational cost associated with their numerical approximation.

- As the ultimate goal of this thesis consists in the construction of an **integrated electromechanical model**, we propose a multiscale formulation linking the microscopic force generation models with the macroscopic description of the tissue. We focus on the left ventricle, undoubtedly the most studied of the four cardiac chambers, because it is responsible for the systemic circulation and it features the largest stresses and strains. In this respect, we achieve the following objectives.

  - In order to couple the mechanical activation models originally proposed in this thesis with existing models of cardiac mechanics and electrophysiology, we derive relationships linking variables pertaining the microscale force generation phenomenon with the macroscopic strains and stresses of the cardiac tissue. We also show that, in the range of lengths featured by sarcomeres during the cardiac activity, the stochastic variables describing the force generated at the microscale can be replaced, when upscaling from the microscopic to the macroscopic level, by their expected value. This drastically simplifies the multiscale mathematical formulation of the electromechanical system.

  - We show that the active part of the Piola stress tensor obtained by upscaling our models is physically meaningful. Specifically, we show that it is compliant with the principle of frame-indifference and, during the normal activity of the heart, satisfies the order-preserving property between strain and stress [Ant95; Ogd97].

  - We derive an integrated EM model, where mechanical activation is described by the microscale models proposed in this thesis. In this regard, we propose a novel formulation for the boundary condition to be applied on the ventricle base for the mechanical subproblem, by accounting for the effect of the portion of the organ that is not explicitly included in the computational domain.

  - Concerning the numerical approximation of the coupled electromechanical model, we propose a novel scheme to couple the model of microscopic activation with the model of tissue mechanics, in order to avoid numerical instabilities related to the velocity-dependent feedback on the force generation phenomenon.

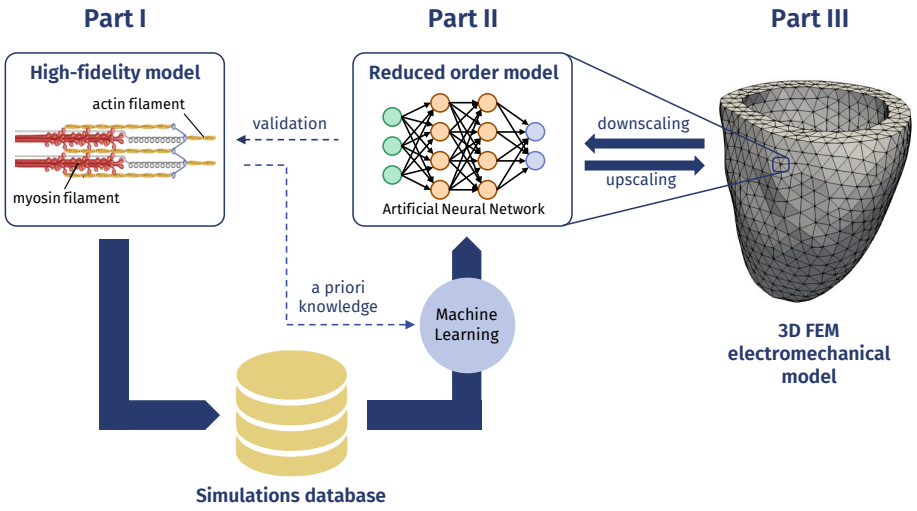

Figure 3: Conceptual map of the three parts of this thesis. Part I deals with the development of biophysically detailed mathematical models of sarcomere dynamics, that are considered, in Part II, as HF models to be reduced. With this aim, ANNs are trained from a collection of simulations, generated by means of the HF models, and by exploiting some a priori knowledge on the HF models themselves. After that the ANN-based model have been validated with respect to the HF models, in Part III we build a multiscale Finite Element model wherein the previously trained ANNs are placed at each nodal point of the computational mesh, so that they reproduce in an efficient but reliable way the results of the HF models.

  - Finally, we propose a electromechanical model, based on Machine Learning, wherein the force generation at the microscale is accounted for by means of previously trained ANNs (thanks to the above mentioned method). We show that, thanks to offline training of the ANN-based reduced model (that replaces the intrinsically complex activation subproblem) we achieve a very favorable trade-off between reliability and computational efficiency, relying on the same time on a biophysically detailed description of the microscopic force generation phenomenon.

Thesis organization

This thesis is organized along the following chapters, divided in three parts. A conceptual map illustrating the links between the three parts is shown in Fig. 3.

- **Part I** deals with the mathematical modeling of the subcellular phenomenon of force generation in the cardiac tissue. The chapters covering the different aspects of the force generation mechanism are schematically displayed in Fig. 2.

  - In **Chapter 1** we provide an overview of basic muscle anatomy and physiology. In particular, we list the main experimental characterizations of the behavior of cardiomyocytes, that serve as a basis for the understanding of the underlying mechanisms and for the development of mathematical models for their description.

- In **Chapter 2** we focus on the first stage of the force generation machinery, namely on the calcium-driven activation of regulatory units. After a literature review, we present our activation-MH model and we validate its results.
- In **Chapter 3** we focus on the second stage of force generation, that is crossbridge cycling. We analyze the different models available in literature, and we select the class of models that best reflect the level of detail required to capture the phenomena of interest in the context of cardiac electromechanics, by analyzing the time scales involved in the different phenomena.
- In **Chapter 4** we address the mathematical modeling of the whole sarcomere function (that is, considering both of the above mentioned stages). We derive and compare six models, we propose a strategy for the calibration of the SE-ODE and the MF-ODE models and, in this manner, we obtain two models for room-temperature rat and body-temperature human cardiomyocytes. Finally, we validate, both qualitatively and quantitatively, all the above mentioned models.

- **Part II** is devoted to MOR and to Machine Learning.
  - In **Chapter 5** we propose our data-driven MOR technique, based on Machine Learning. We provide a theoretical justification for its application, by showing that any differential model with Lipschitz continuous right-hand side can be approximated, within any level of accuracy, by a ANN-based model as the one built by our method. We give details on the numerical methods used to train the ANNs and we show the results obtained in different test cases, comprising large-scale ODE systems, parabolic and hyperbolic PDEs.
  - In **Chapter 6** we introduce the gray-box approach that extends the fully black-box approach presented in Chap. 5 and we apply it to the reduction of the activation-MH model (proposed in Chap. 2) and the SE-ODE and MF-ODE models (proposed in Chap. 4).

- **Part III** deals with multiscale cardiac electromechanics and its numerical approximation.
  - In **Chapter 7** we derive the links between the microscale variables of the force generation models proposed in Part I and the macroscopic quantities describing the organ-level strain and stresses. Then, we show that the active part of the Piola stress tensor is compliant with the basic theoretical requirements for its physical meaningfulness. Finally, we provide theoretical justifications of the fact that the stochastic microscopical models can be coupled with the macroscopic deterministic description of the organ-level mechanics.
  - In **Chapter 8** we present the multiscale electromechanical model and its numerical approximation. Then, we show some numerical results obtained with the cardiac contraction models proposed in this thesis and with their ANN-based reduced versions.

Finally, in **Conclusions**, we discuss some concluding remarks and perspectives for future research.

The results presented in this thesis have been partially published or submitted for publication (see [RDQ18; RDQ19b; RDQ19c; RDQ19a]) and have been obtained using the software MATLAB [Mat], PYTHON [Pyt] and FENICS [Aln+15]. Part of the software developed along with this thesis is publicly available online (see [Reg19]).

Part I

Modeling active force generation in the cardiac tissue

Chapter 1

Anatomy and physiology of the cardiac muscle tissue

In this chapter, we provide an overview on the anatomy and the physiology of the cardiac muscle tissue. Afterwards, we illustrate the experimental characterizations revealing the fundamental features of the force generation machinery, a deeper overview and insight that will serve as starting point for the construction of a mathematical model. For further information about cardiac anatomy and physiology we refer the reader to [TD08; JKT07; Kat10; Ber01].

Contents

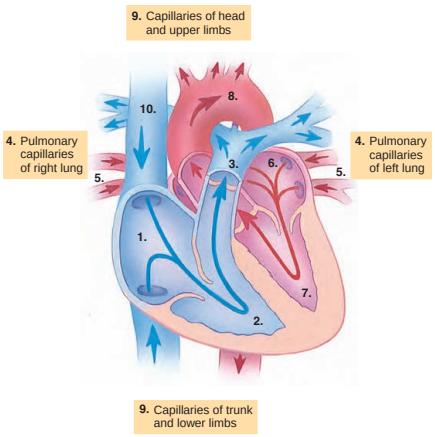

(a) Path of blood flow through the heart.

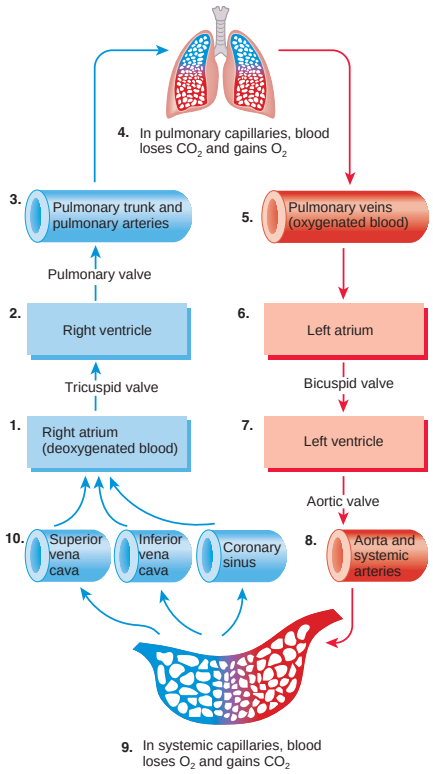

(b) Diagram of blood flow.

Figure 1.1: The blood flow through the heart and the body. Image taken from [TD08].

1.1 The cardiac function

The heart of mammalians can be seen as a pair of mechanical pumps (the left and right heart), synchronously operating in series. It is subdivided into four chambers: the *left atrium* (LA) and *left ventricle* (LV), pumping the oxygenated blood from the pulmonary veins into the systemic circulation, and the *right atrium* (RA) and the *right ventricle*, pumping the deoxygenated from the systemic veins into the pulmonary circulation (see Fig. 1.1). Each ventricle is endowed with a pair of *valves*, preventing respectively the incoming and outcoming blood from flowing backward. In particular, the LV is separated from the LA by the *mitral valve* and from the aorta (the large artery constituting the first tract of the systemic circulation) by the *aortic valve*, while the *tricuspid* and the *pulmonary valves* separate the RV from the RA and the pulmonary artery, respectively.

1.1.1 The heart contraction

Each heartbeat is triggered by an electrical signal, originating at the *sinoatrial node*, the heart natural pacemaker consisting of a cluster of self-exitable cells and located at the upper part of the RA. The electrical signal propagates from cell to cell through the two atria and it reaches to *atrioventricular node*, located between the atria and the

ventricles. The purpose of the atrioventricular note is acting as a filter between the atria and the ventricles in order to ensure the correct delay between the contraction of the former and the latter. This is crucial to guarantee that the ventricle contraction starts only when the blood has been pumped by the atria into the ventricle themselves. The electrical signal travels from the atrioventricular node through a system of specialized conducting fibers, the so-called *Purkinje network*, and it reaches the ventricles wall. Then, similarly to what happens in the atria, it travels from cell to cell through the so-called *gap junctions*.

Cardiomyocytes, the cardiac muscle cells, are excitable cells: when they are sufficiently stimulated by the application of an electrical stimulus, the chemo-electric equilibrium of the cell membrane is broken, thus originating a succession of events that make the electric potential of the cell raise and then fall. Such phenomenon, known as *action potential*, is based on the opening and closing of voltage-gated ion channels, so that the cell membrane is permeable to different ion species according to transmembrane potential, the voltage difference between the inner and outer part of the cell. The resulting fluxes of ions across the cell membrane make the transmembrane potential vary and the ionic fluxes have a feedback effect on the voltage difference itself.

Among the ionic species involved in the action potential dynamics, an important role is played by calcium ions. Calcium serves as intercellular messenger and constitutes the trigger of the muscle contraction: calcium ions induce a complex chain of reactions with the final outcome of the generation of active force inside the cardiomyocytes. Finally, the contractile force generated at the microscale causes the macroscopic contraction of the heart chambers. We will provide an extensive characterization of cardiomyocytes in Secs. 1.2 and 1.3.

1.1.2 The cardiac cycle

The heart beats about 10^5 times every day, which adds up to 2.5 billions times in an average lifetime. Each heartbeat is the result of the synchronized interplay between the four chambers, that pumps about 5 L per minute throughout the body. The cardiac cycle can be divided into the following three phases (see Fig. 1.2).

1. **Atrial systole.** At this stage, the ventricles are partially filled and the mitral and the tricuspid valves are opened, while the aortic and pulmonary valves are closed. The sinoatrial node triggers an action potential, with the effect of making the two atria contract. This forces the last 25% of blood into the ventricles.

2. **Ventricular systole.** The action potential reaches the atrioventricular node and, after a brief delay, it propagates through the ventricles, causing their contraction and the closing of the two atrio-ventricular valves. In a first and quick isochoric phase of contraction, the ventricular pressures raises, without any change of volume, as all the valves are closed. When the pressures of the LV and the RV overpass, respectively, the pressures of the aorta and of the pulmonary trunk, the aortic and pulmonary valves open and the blood is ejected from the ventricles. Ejection continues until the ventricles start to relax.

3. **Relaxation.** At this stage, the aortic and pulmonary valves close and a second isochoric phase begins, with a quick fall of the ventricular pressure. When the pressure of ventricles reaches that of atria, the mitral and the tricuspid valves open, and a slow filling phase begins. During this phase, the four chambers are in diastole (i.e. in their relaxation stage).

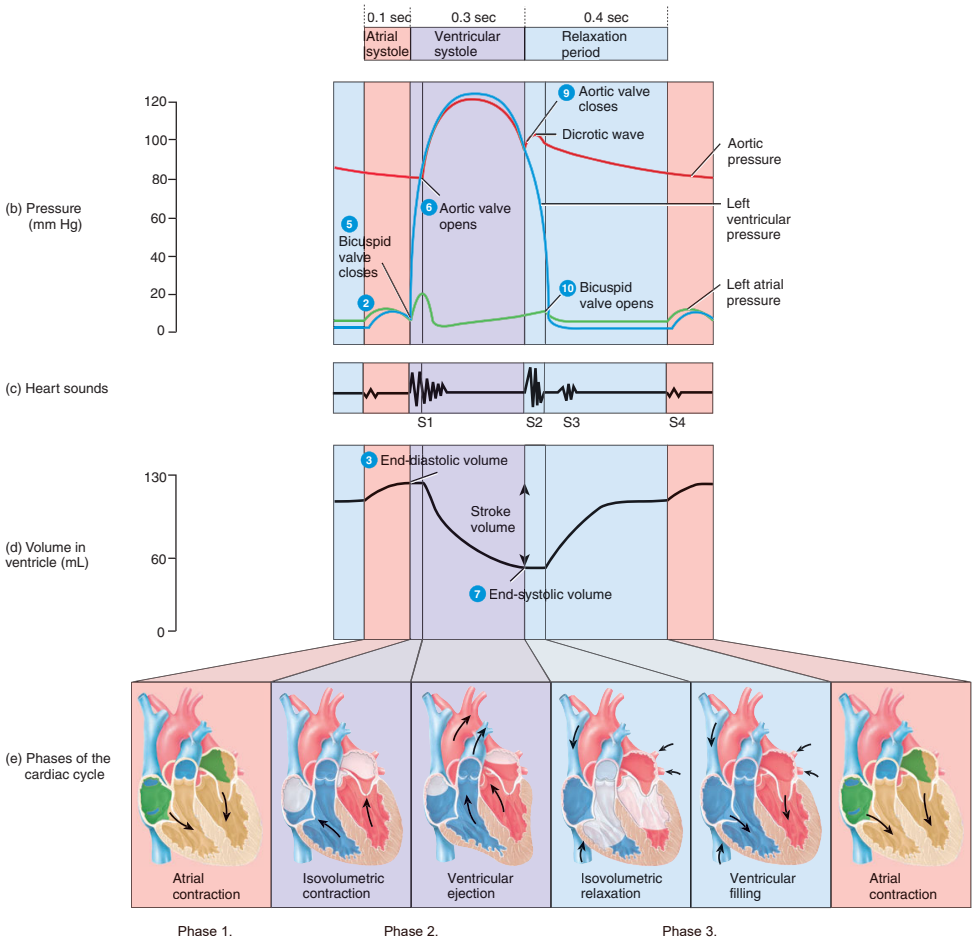

Figure 1.2: The cardiac cycle. Image adapted from [JKT07].

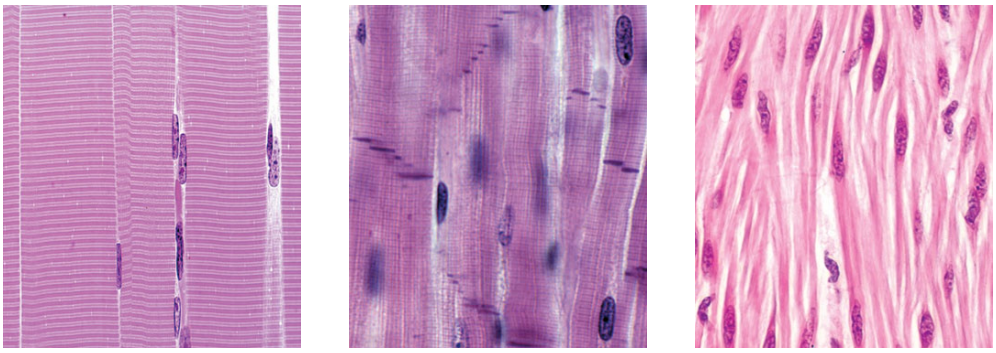

(a) Skeletal (400x) (b) Cardiac (600x) (c) Smooth (350x)

Figure 1.3: Longitudinal sections of the three different muscle tissue types. Image taken from [JKT07].

1.2 The cardiac muscle tissue

Muscles (from latin *mus* (mouse) + *-culus* (diminutive suffix), literally "little mouse", semantic loan from ancient greek μῦς) are soft tissues serving multiple purposes, including producing movement, maintaining posture and displacing substances in the organism. The main distinguishing feature of muscles is *contractility*, that is the ability of producing force in absence of an externally induced stretch, which makes them *active* materials. In other terms, unlike in passive elastic materials, in the muscle tissue stress is not uniquely determined by strain.

There exist three types of muscular tissues – skeletal, cardiac and smooth – which differ in location, microscopical anatomy and regulatory mechanism (see Fig. 1.3).

Skeletal muscles are attached to bones through tendons. Skeletal muscle tissue is *striated* (i.e. alternate dark and light striations can be observed under a microscope). This is a consequence of the microscopical arrangement of the contractile fibres in sarcomeres. Cells consists in long cylindrical unbranched fibres, with many nuclei located in the periphery, which give the tissue a clear directionality. Such fibres are 100 µm to 30cm long per 10 µm to 100 µm wide. The contraction of skeletal muscle is initiated by the central nervous system, in a *voluntary* manner.

Cardiac muscles are located in the heart and are organized in sarcomeres, as the other striated type of muscle tissue (the skeletal one). The fibres, unlike in skeletal muscles, are branched and have usually a single nucleus, located in the centre. Neighbouring fibres are joined by *intercalated disks*. Fibres are 50 µm to 100 µm long per 10 µm to 20 µm wide. Cardiac tissue is strongly anisotropic as well, thanks to the high level of organization of fibres. Cardiac muscles contraction is *involuntary*.

Smooth muscles can be found in hollow viscera, airways, blood vessels walls or ciliary body of the eye. Their name is due to the absence of striation. Smooth muscle cells are elongated ellipsoids, 30 µm to 200 µm long and 3 µm to 8 µm wide, with an almost random arrangement of contractile fibres, which endow the tissue with a nearly isotropic contractile tension. They are also subject to an involuntary nervous control.

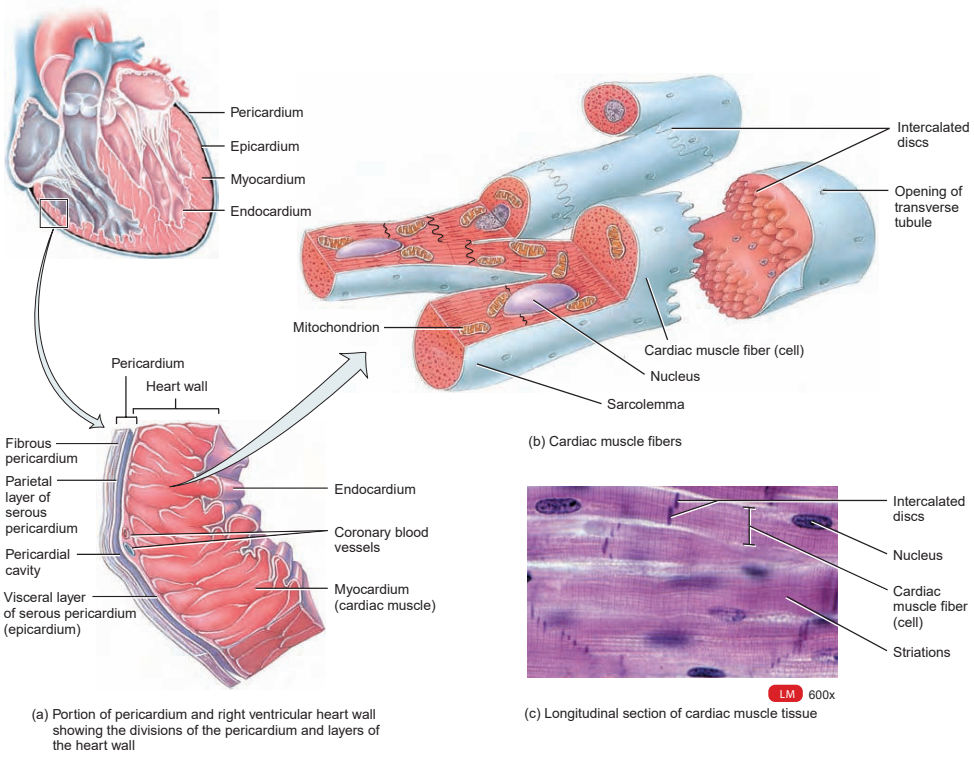

Figure 1.4: Organization of the heart wall. Image taken from [TD08].

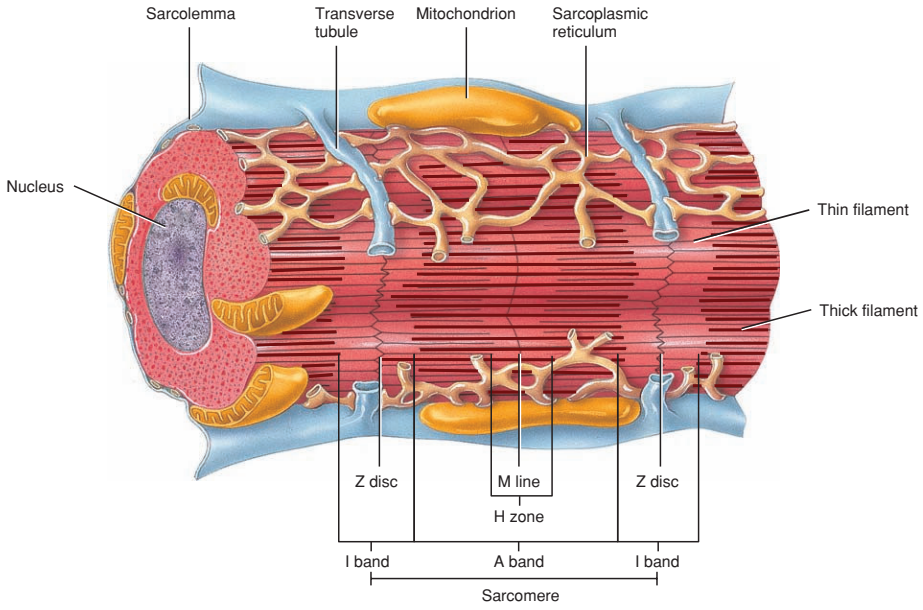

Figure 1.5: Structure of a cardiomyocyte. Image taken from [TD08].

1.2.1 Histology of the cardiac walls

The wall of the heart chambers, which is surrounded and protected by a membrane called *pericardium*, is composed of three layers (see Fig. 1.4). The *epicardium*, the thin and transparent outer layer, is composed of mesothelium and connective tissue. The *myocardium*, the middle layer, constitutes the bulk of the heart (95% in volume) and is responsible for its pumping function. It is composed of both myocytes (the muscle tissue cells) and connective tissue: vascular smooth muscle, endothelial cells and fibroblasts, which contribute to the heart's tensile stiffness. Finally, the *endocardium*, the inner thin layer, provides a smooth lining for the inner surface of the heart chambers and covers the heart valves. It is made up of a mesh of collagen and elastic fibers.

1.2.2 Hierarchical organization of the cardiac muscle tissue

The cardiac muscle tissue comprises several levels of organization, spanning different spatial scales.

The tissue level. Cardiac muscle fibres form two separate networks – the atrial and the ventricular ones. The fibres diagonally swirl around the heart in interlacing bundles.

The fibre level. Cardiac fibres, formerly believed to be a syncytium (i.e. a multinucleated cell, like skeletal fibres), are actually made of separate cells, the *myocytes* (or *cardiomyocytes*, to distinguish from the skeletal myocytes), interconnected by transverse band, orthogonal to the axis of the fibres, called *intercalated disks* (see Fig. 1.4). Such disks, consisting in thickenings of the sarcolemma (plasma membrane), provide

strong mechanical linkage within cells through *desmosomes* and, thanks to *gap junctions*, they allow the action potential to freely conduct from one cell to the other. Cardiac tissue behaves thus as a syncytium, despite being made of separate cells.

The cell level. Cardiac muscle cells, the cardiomyocytes, are primarily made of fibres called *myofibrils*, responsible of muscle contraction (see Fig. 1.5). Myofibrils are surrounded by an intracellular membrane system, the *sarcoplasmic reticulum*, consisting of the *sarcotubular network* and the *subsarcolemmal cisternae*, storing the calcium ions required for muscle contraction. The cytoplasm, called *sarcoplasm*, contains many mitochondria in charge of the production of ATP required to fuel the microscopical generation of force. Transverse tubules – called T tubules – connect the surface with the inner part of the cell.

The myofibril level. Myofibrils are long cylindrical structures extending for the full length of muscle cells. When observed under a microscope, they reveal a characteristic regular striation pattern, whence the name of striated muscle, reflecting the inner high organization of units. Dark (A-bands) and light (I-bands) stripes are observable with a regular spacing of nearly 2 µm and inside each light band a narrow dark band, called Z-line, can be observed. Such Z-lines delimit the *sarcomeres*, the fundamental contractile units of the striated muscle tissue. Each myofibril is thus a series array of sarcomeres connected by the Z-lines.

The sarcomere level. Sarcomeres are cylindrical units, of nearly 2 µm length. Sarcomeres are composed by a parallel arrangement of smaller structures, called *myofilaments*, aligned in a crystalline fashion.

The myofilament level. Two kinds of myofilaments exist: *thin filaments* (made of actin, troponin and tropomyosin) and *thick filaments* (made of myosin). Myosin heads, structures protruding from thick filaments, can bind with actin sites and pull the thin filaments towards the centre of the sarcomere. This causes the sliding between the two families of filaments and the consequent contraction of the muscle tissue.

1.2.3 Sarcomere structure

Sarcomeres (from ancient greek σάρξ (flesh) + μέρος (component), thus the basic component of flash) are the fundamental unit of striated (i.e. skeletal and cardiac) muscle tissue. Their shape is cylindrical, with a diameter of approximately 2 µm and a length ranging between 1.7 and 2.3 µm under physiological conditions.

The long-standing hypothesis that muscle contraction was led by folding of elongated protein filaments was challenged by the discovery that the filaments length is kept constant during contraction and that it is instead the mutual sliding between two families of filaments (thin and thick filaments) what makes the muscle contract [Ber01]. The latter theory, known as *sliding filaments theory*, was discovered independently by two research teams: on one hand, the British biologist Hugh Huxley and biophysicist Jean Hanson, working at MIT; on the other, the British physiologist Andrew Fielding Huxley (Nobel prize winner in 1963 for his work on the action potential) and the German physician Rolf Niedergerke, working at the University of Cambridge. The two teams decided to publish their work in two consecutive articles in the same issue of Nature [HN54; HH54].

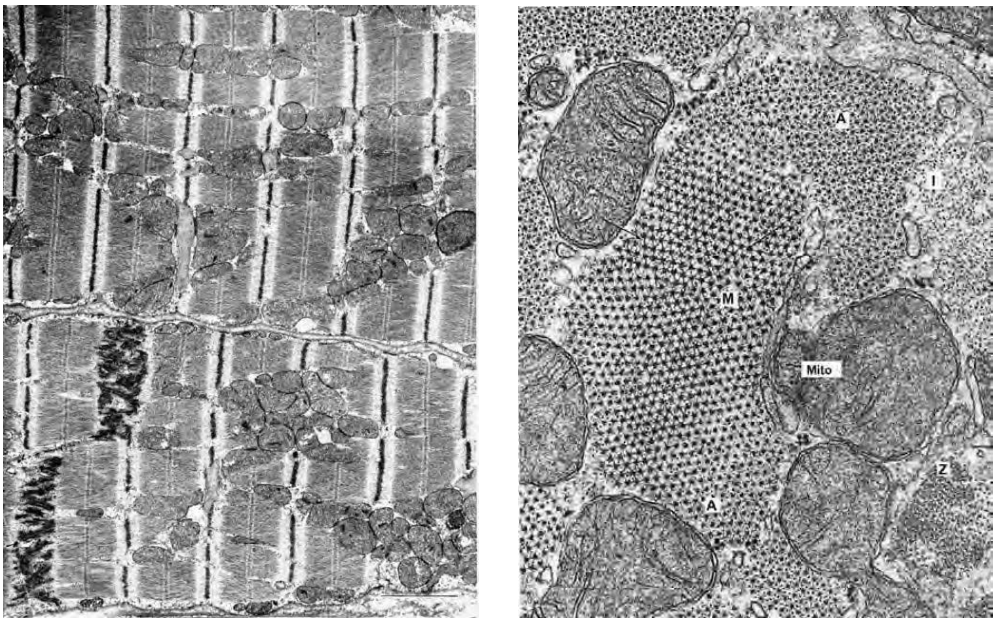

(a) Lateral section. (b) Cross section.

Figure 1.6: Electron microphotograph of cardiomyocytes. (a) Lateral section of two human left ventricular myocytes (above and below). Besides the characteristic striation and Z-lines (Z), also mitochondria (M), intercalated disc (D) and lipid droplets (L) are visible. (b) Cross section of a cat right ventricular papillary muscle. Myofilaments are cut at different levels: at the level of the A-band (A), I-band (I) or M-band (M). Mitochondria (Mito) are also visible. Image taken from [Kat10].

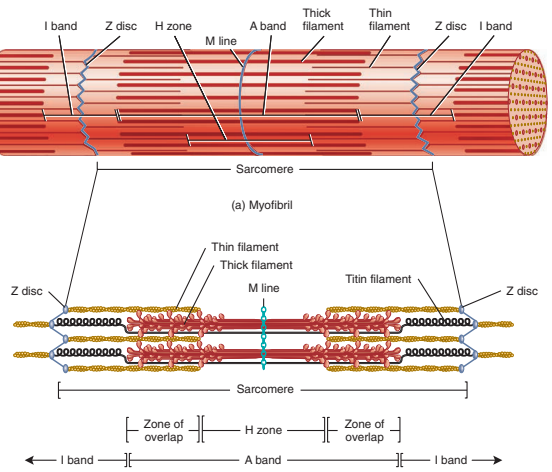

Figure 1.7: Schematic structure of a sarcomere, with the different bands observable under microscopy. Image taken from [TD08].

Observed under electron microscopy from a lateral view, sarcomeres reveal alternating bands (see Figs. 1.6a and 1.7), after which the name of striated muscle tissue:

- The dark zigzagging lines separating two neighboring sarcomeres are called **Z-discs** (from the German *Zwischenscheibe*, discs in between). Z-discs, made of a number of cytoskeletal proteins, have the function to link adjacent sarcomeres to each other and the extracellular matrix and are the anchoring points for thin filaments. Z-discs are also connected to thick filaments through a huge cytoskeletal protein named *titin*.
- Surrounding the Z-discs a light zone can be observed, where only thin filaments are present. This zone is called **I-band**, after its properties under a polarizing microscope of being little birefringent, that is highly *isotropic*.
- The darker zone following I-bands is called **A-band** (after its *anisotropic* manner of rotating polarized light). The dark color is due to the presence of thick filaments.
- In between an A-band, a brighter zone called **H-zone** (from the German *heller*, lighter) reveal the region where thick filaments do not overlap thin filaments.
- Located at the centre of H-zones, and thus at the centre of the sarcomere, **M-lines** (from the German *Mittelscheibe*, in the middle) are formed of radial cross-links connecting adjacent thick filaments, formed by cytoskeletal proteins, including myosin-binding protein C.

When observed in cross sections (see Fig. 1.6b), thick filaments are arranged in a quasi crystalline hexagonal packing, each filament being surrounded by six thin filaments (see Fig.1.8).

In accordance with the sliding filaments theory, when the muscle tissue contracts the degree of overlap between the two families of filaments changes. As a consequence, the width of I-bands decreases, as well as that of H-zones. Such mechanism is illustrated in Fig. 1.9.

(a) A-band (b) I-band (c) M-line

Figure 1.8: Schematic cross section of a sarcomere at three different levels of sarcomere length. In A bands (a), thick filaments are arranged in hexagonally packed arrays and thin filaments are located at the trigonal points. In I bands (b), where thick filaments are not present, thin filaments are less ordered. In correspondence of the M line (c), adjacent thick filaments are connected by myosin binding protein C thin radial filaments. Image elaborated from [Kat10].

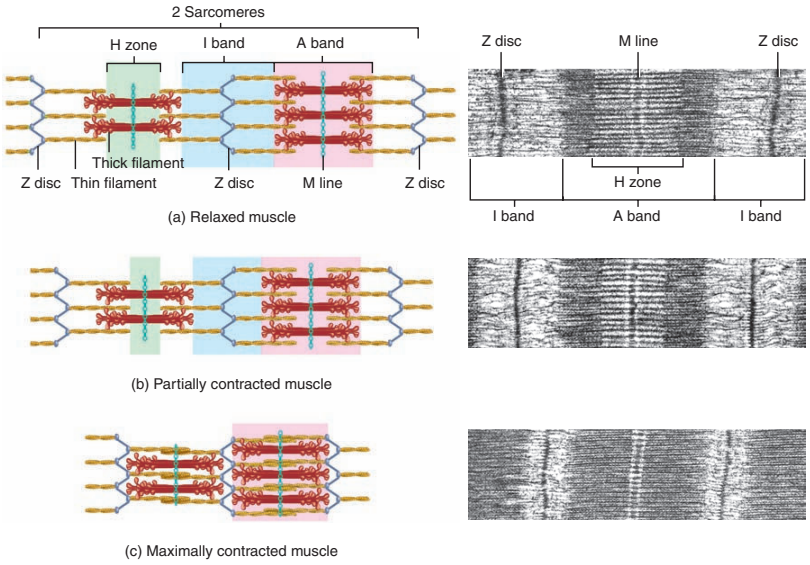

Figure 1.9: The effect of the sliding filaments on the size of the different bands. Image taken from [TD08].

(a) Thick filament and myosin molecule.

(b) Portion of thin filament.

Figure 1.10: Schematic structure of thick and thin filaments. Image taken from [TD08].

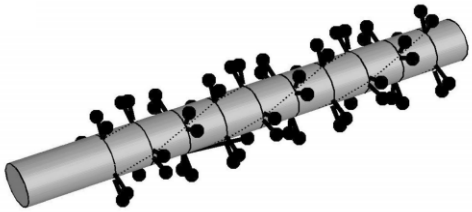

Figure 1.11: Arrangement of myosin heads in a portion of thick filament. Image taken from [Rec06].

Muscle proteins

Sarcomeres are made of three kinds of proteins:

- *Structural proteins* (titin, nebulin, α-actinin, myomesin and dystrophin), which keep the thin and thick filaments in the proper alignment, endow the tissue with elasticity and extensibility, and link sarcomeres among each other, to the sarcolemma. The largest structural protein is the gigantic titin (50 times bigger than an average-sized protein), which spans an half sarcomere, connecting a Z-disc with an M-line and helping to stabilize the position of the thick filaments. The part of titin in contact with Z-discs is highly elastic and accounts for much of the extensibility and elasticity of myofibrils.
- *Regulatory proteins* (troponin and tropomyosin), which switch the contraction process on-off in response to a calcium signal.
- *Contractile proteins* (actin and myosin), responsible of the force-generating processes.

Thin filaments

Thin filaments are about 1µm long and 8nm thick (see Fig. 1.10b). The main constituent of thin filaments is the protein *actin*. Monomeric actin is called G-actin (globular actin) and has diameter of nearly 5.5nm. Two strands of G-actin monomers, twisted into two coiled helices, form the so–called F-actin (fibrous actin), which forms the backbone of thin filaments. The internodal distance is approximatively 37.5nm.

Located in the groove of the two strands and spanning 7 actin monomers, the protein *tropomyosin* (Tm) is a rigid coiled-coil structure, with the function of regulating the contraction process by inhibiting the interactions between myosin heads

and actin. In the relaxed configuration, Tm covers the myosin binding sites located on actin, preventing the formation of the acto-myosin complex by steric hindrance. During contraction, Tm moves deeper into the groove of actin strands, thus exposing binding sites.

The *troponin* (Tn) complexes, distributed with a period of 7 actin monomers along the thin filaments, comprise three proteins, with the function of translating the calcium signal into an on-off switch of the contraction process (see Fig. 1.12):

- *Troponin C* (TnC) is a dumbbell-shaped molecule, containing two calcium-specific-sites (I and II) and two calcium-magnesium-sites (III and IV). However, as the concentration of magnesium ions is much higher than calcium in muscle cells, calcium-magnesium-sites cannot mediate signals linked to small increases in cytosolic calcium concentration. Moreover, in the cardiac TnC isoform, site I loses its ability to bind to calcium with high affinity. Therefore, in cardiac muscles, site II serves as the unique physiological calcium receptor.

- *Troponin I* (TnI) has the function of inhibiting the acto-myosin interaction. When the muscle is relaxed, TnI is tightly bound to actin in a conformation which makes Tm block the myosin binding sites located on actin. During contraction, when calcium binds to TnC, this induces an allosteric change in the thin filament that loosens the bound between TnI and actin.

- *Troponin T* (TnT) has the function of binding the Tn complex to Tm.

Thick filaments

Thick filaments, about 1.6µm long and 16nm thick, are made of the protein *myosin* (see Fig. 1.10a). Myosin is a "golf club-shaped" molecule made of a coiled-coil tail, providing rigidity to the filament, and two paired heads (S1), capable of binding to actin thus forming the so–called *crossbridges* (XBs). Myosin tails are twisted together, forming the shaft of the thick filaments (a filament is made of nearly 300 myosin II molecules). Myosin heads protrude from the centre of the thick filaments towards the surrounding thin filaments as crowns of three heads with a regular spacing of 14.3nm (see Fig. 1.11). The three heads of the crown are separated by 120° and adjacent crowns are rotated by 40° each time, so that in each plane the heads are spaced 43nm. The result is a three stranded helix, with period 43nm [Rec06].

1.2.4 Cardiac tissue contraction dynamics

Calcium ions (Ca^{2+}) have the function of intracellular messengers in muscle contraction. The signal represented by a raise of intracellular calcium concentration represents the final stage of the process by which cell depolarization triggers muscle contraction, known as *excitation-contraction coupling*. The next step is represented by the *calcium-driven activation of the thin filament*, whose outcome is that of switching on the *XB cycle*, by which force is generated.

Excitation-contraction coupling

When the muscle is relaxed, the concentration of calcium ions inside the cells is low (around 0.1µmol). During activation, the action potential propagates inside the sarcolemma through the T tubules, causing the opening of calcium release channels. The increase of calcium concentration triggers the so-called calcium-induced calcium

release, by which the huge amount of calcium ions stored inside the sarcoplasmic reticulum flows inside the cytosol, inducing a tenfold increase of calcium concentration.

The sarcoplasmic reticulum membrane also contains calcium transport pumps, which consume ATP to move calcium from the sarcoplasm into the sarcoplasmic reticulum. Active pumps constantly work, but during the propagation of the action potential, calcium flows through the calcium release channels towards the sarcoplasm is much higher than the opposite flux generated by the pumps. In turn, when the action potential terminates its effect and calcium channels close, the active pumps rapidly (fraction of second) make the calcium concentration return to its rest level. Moreover, *calsequestrin*, a calcium-binding protein located in the sarcoplasmic reticulum, enable even more calcium ions to be sequestered and stored in the sarcoplasmic reticulum, where the concentration of calcium ions is four orders of magnitude larger than in the sarcoplasm of a relaxed tissue.

Calcium-driven thin filament regulation

At low cytosolic calcium concentrations, the calcium-specific-site of TnC is unoccupied. In this configuration, the interaction between TnC and TnI is weak, so that the bound between TnI and actin is stronger and, consequently, the peripheral position of the Tn-Tm complex is favoured (see Fig. 1.12, left). Such non-permissive conformation sterically hinders the binding between myosin heads and actin.

When calcium ions concentration increases in the region surrounding the myofilaments, calcium binds to site II of TnC. This strengthen the TnC-TnI interaction, destabilizing in turn the TnI-actin interaction. The configuration of the Tn-Tm complex deeper into the actin groove is thus favoured, and the steric hindrance to the actin-myosin interaction is removed (see Fig. 1.12, right). When Tm is in such permissive configuration, contraction is switched on.

In this way a series of 7 actin molecules are activated by a single Tn-Tm complex. Moreover, the head to tail overlap of Tm molecules allows for the movement of the Tn-Tm complex to take place in a cooperative manner, by spreading the signal to neighbouring Tn-Tm units.

Crossbridge cycle

Myosin is a molecular motor, which translates the chemical energy stored inside ATP into mechanical energy. This is allowed by XBs, bounds between myosin heads and actin and the so–called *power-stroke*, that is a rotation of the attached myosin heads which pulls the actin filament towards the centre of the sarcomere. After power-stroke, the myosin head detaches and binds to actin in a different position and the cycle is repeated. The joint work of several thousands of pulling myosin heads makes the sarcomere contract.

Such attachment-detachment process takes place along a cyclical path, described by the so–called *Lymn-Taylor cycle* [LT71]. The Lymn-Taylor cycle comprises four steps (Fig. 1.13):

1. **ATP hydrolisis.** Myosin, in the stage of the cycle that is traditionally considered as the starting point, is bound to ATP and detached from actin. The catalytic site of myosin hydrolyses ATP into ADP and a phosphate group (which remains attached to myosin), transferring to myosin the energy stored in ATP. The myosin head is still detached from actin, but reoriented and in a higher energetic state.

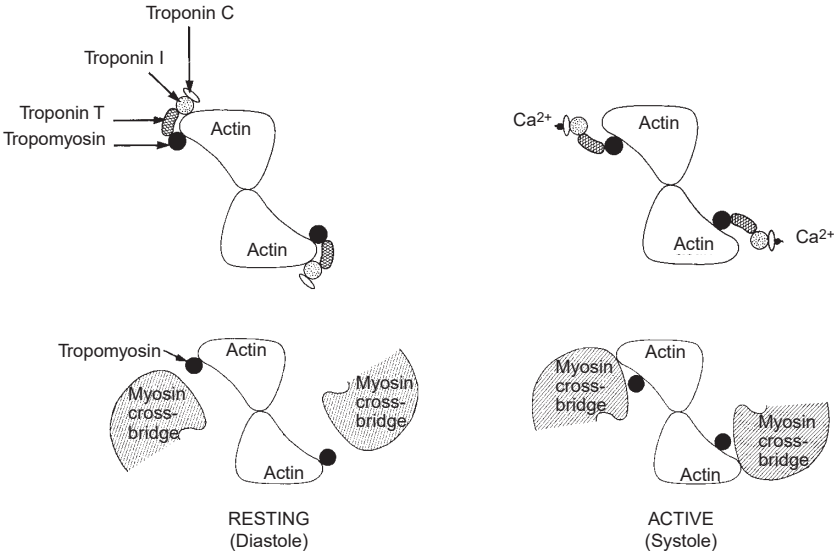

Figure 1.12: Cross section of thin filament, showing the configuration of the troponin-tropomyosin complex (top) and of myosin heads (bottom) in a relaxed (left) and contracted (right) configuration. Adapted from [Kat10].

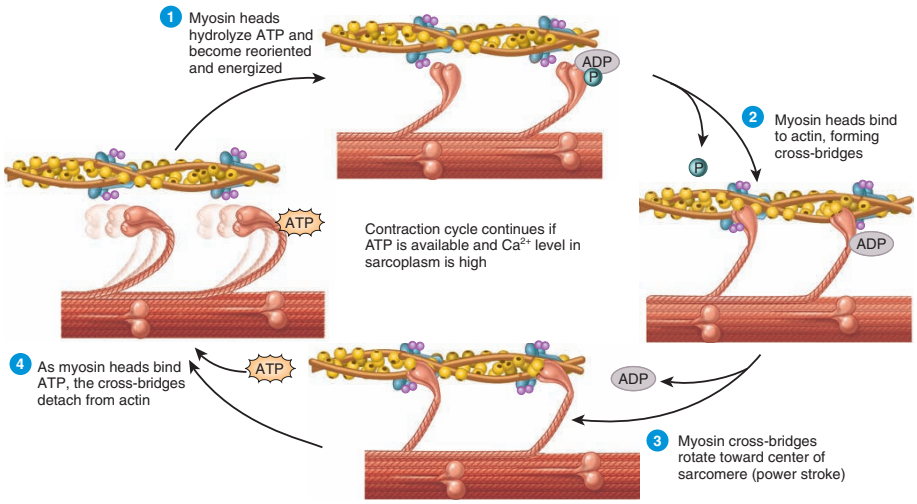

Figure 1.13: The Lymn-Taylor cycle. Image taken from [TD08].

2. **XB attachment.** The energized myosin head binds to actin and the phosphate group is released.

3. **Power stroke.** The myosin head rotates towards the centre of the sarcomere (less energetic state), thus pulling the actin filament in the same direction. ADP is released from myosin. The force developed by a single power stroke is nearly 0.5–1.0 pN, and the head rotation is nearly 5–10 nm.

4. **XB detachment.** At the end of the power stroke, myosin is tightly bound to actin in a *rigor* configuration, until an ATP molecule binds to myosin, making it detach from actin.

The Lymn-Taylor cycle is repeated, with a pace of nearly 5 times per second, as long as two conditions are satisfied: enough ATP to fuel the process is available; calcium ions level is high enough to keep Tm in the permissive configuration. When ATP is depleted, the cycle stops in the phase between step 3 and step 4, where all XBs are firmly attached (leading, for skeletal muscle, to the *rigor* state observed in cadavers). When calcium concentration returns to its rest concentration, instead, the cycle is stopped in the phase between step 1 and step 2.

1.3 Experimental characterizations and modeling issues

The fundamental properties of the muscular force generation machinery have been assessed by the scientific community by a series of experiments. The different experimental setups (including steady-state conditions, isometric and isotonic responses, constant shortening regimes, etc.) allow to isolate the phenomena pertaining different regimes of behavior and different time scales. To build a mathematical model for the microscopic force generation in the muscle tissue, it is mandatory to address first such experimental characterizations and to understand the mechanisms at their basis.

In this section we review the main experimental characterizations of the muscle tissue, by providing, when available, the interpretation commonly given to the observed results. Such experiments will be also used, in the following chapters, to validate, both at the qualitative and the quantitative level, mathematical models describing the mechanisms by which the muscle tissue is activated by a calcium signal and it produces an active force.

1.3.1 Passive muscle properties

Besides their distinguishing active properties, muscle fibers have also a passive behavior, mainly due to titin, but also to other components of the cytoskeleton. The resting length of sarcomeres (also called slack length) is around 1.9 µm and it is not significantly affected by variables such as temperature and species [TK+80; JH95; Pir+07; TK16; Lan+17]. The passive response around the slack length is approximately symmetric, until SL reaches a value of nearly 2.3 µm, where the muscle features a strong passive response, preventing the sarcomere to elongate further [Ken+86; Ber01; Kat10; TK16]. This prevents the muscle to enter a regime of behavior where the force-length relationship is inverted with respect to the range of length where the sarcomere is designed to work, as we will see in Sec. 1.3.2.

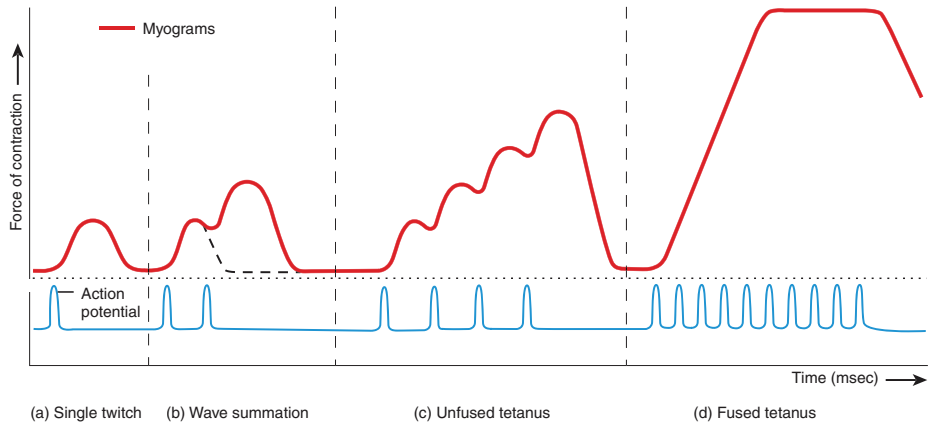

Figure 1.14: Effect of different frequencies of stimulation in skeletal muscle. Image taken from [JKT07].

When experimental measurements of tension are taken from muscle fibers, the passive force should be previously evaluated and then removed from the measured force, to get the active force (see e.g. [Ken+86]).

1.3.2 Steady-state conditions

A sarcomere is said to be in steady-state conditions when its geometry (i.e. its length SL) and its chemical environment (i.e. intracellular ions concentration, in particular $[Ca^{2+}]_i$) are stationary and the force generation process reaches an equilibrium state. We notice that such state is in fact a *dynamic equilibrium*, inasmuch as XBs keep cycling and calcium binding-unbinding takes place: the microscopic state is not in equilibrium, but macroscopic observable quantities are in a steady-state. Steady-state tension (measured as force per unit area), denoted by T_a^{iso}, is thus a function of SL and $[Ca^{2+}]_i$, but also of temperature (see e.g. [HB89; JSM02]), pH (see e.g. [Ber01]) and other factors.

The main characterization of the state-state condition lies in the steady-state force-calcium and force-length relationships, obtained by varying $[Ca^{2+}]_i$ and SL respectively, while keeping constant all the other factors. The effect of SL on the force-calcium relationship and, vice versa, of $[Ca^{2+}]_i$ on the force-length relationship are of primary importance since those are the factors periodically changing during the heart beat and they are linked, as we will se, to the regulation of the heart pumping strength.

While in skeletal muscle the steady-state represents a physiological condition, known as *tetanus*, and it can be easily reproduced in experiments, in the cardiac muscle tissue tetanic contractions cannot occur. This represents a serious limitation for the experimental characterization of steady-state condition; however, as we will see in the next section, this limitation has been overcome by advances in the experimental setups.

Tetanic contractions

When striated muscles are stimulated by an action potential (i.e. the electrical activity of excitable cells), a *twitch* (i.e. an isolated contraction) occurs (see Fig. 1.14). In the first moments of the twitch, called *latent (or refractory) period*, the action potential is still taking place; this means that another stimulus would not be able to achieve any effect. In skeletal muscle, however, the latent period is much shorter than the twitch duration and, if a second stimulus is applied before the end of the twitch, the recorder force is larger than that of a single twitch. This phenomenon is known as *wave summation*, and it is linked to higher calcium levels reached inside the cells. If the muscle is stimulated with a frequency of nearly 20Hz, a sustained contraction, known as *unfused tetanus*, occurs, where the single twitches are still distinguishable. If skeletal muscle is stimulated with a frequency of order of 100Hz, the muscle does not relax at all, and a sustained state of contraction is observed (see Fig. 1.14).

In the cardiac tissue, instead, cells contraction is more than 10 times longer than in skeletal muscles and the rarefactory period lasts longer as well. This means that another contraction cannot occur before the muscle is fully relaxed. For this reason, *tetanus* (i.e. maintained contraction) cannot take place in the cardiac muscle, unlike in skeletal muscle. Therefore, to characterize the force-calcium relationship, early studies considered peak force in twitches versus $[Ca^{2+}]_o$, i.e. calcium concentration outside the cell membrane [Ken+86]. However, it has been shown that the two relationships are significantly different since calcium waves dynamics is faster than the activation of the thin filament, which does not reach a steady-state at the time of calcium peak [Bac+95].

A muscle preparation widely used to experimentally study the cardiac tissue, named *skinning*, consists in permeabilizing (by saponin) or removing (by superfusing the muscle in a *relaxing solution*, typically 1% of Triton X-100 or Lubrol WZ) the sarcolemma. This allows to precisely control the level of activator $[Ca^{2+}]$ by EGTA buffers [Ken+86; Bac+95]. Because of the deactivation of the sarcoplasmic reticulum, which uptakes calcium, tetanic contractions are possible for skinned preparations and the steady-state can be reached. However, skinning has been reported to alter the properties of sarcomeres, in particular its calcium sensitivity, as we will see later.

Despite the significant biases introduced by skinning, this preparation has been employed for the vast majority of experimental data available in the literature [Ken+86; DKT02; AW94]. More recently, steady-state measurements in intact (i.e. non skinned) muscles have been obtained thanks to the action of cyclopiazonic acid, which inhibits the sarcoplasmic reticulum calcium uptake, without affecting calcium sensitivity [TKHK00; TK+08]. In this way summation can occur, by stimulating the muscle with a frequency of 12Hz (first reference) or 4-6Hz (second reference), and tetanus is elicited. Intracellular calcium concentration $[Ca^{2+}]_i$ and sarcomere length SL are measured through flura-2 fluorescence and laser diffraction respectively.

Force-calcium relationship

The force-calcium relationship in striated muscle is well approximated by the Hill equation [Ken+86; DKT02; TK+08], originally formulated by A. V. Hill to describe binding of oxygen to haemoglobin [Hil10]. The Hill equation models the binding of a ligand to a macromolecule under the hypothesis that the binding affinity changes when other ligands are already bound to the same macromolecule (*cooperative binding*). In

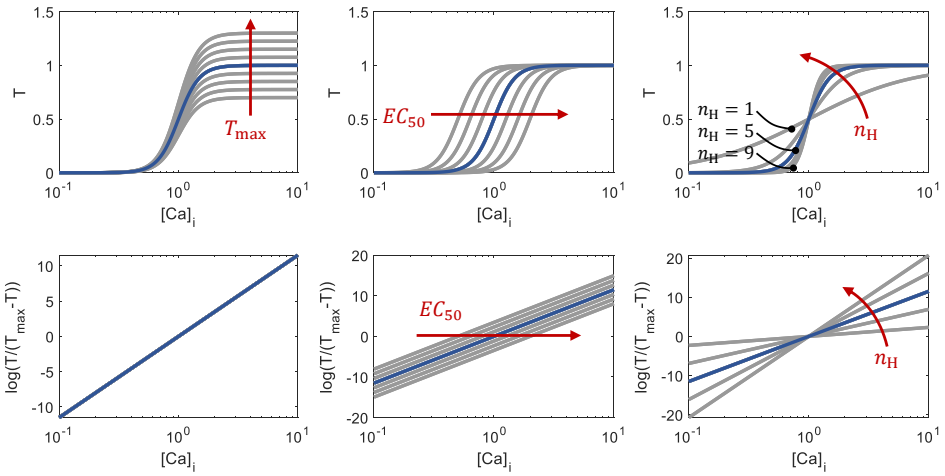

Figure 1.15: Effect of $T_{\mathrm{a}}^{\max}$ (first column), EC_{50} (second column) and n_H (third column) in the Hill equation (1.1). First row: $T_{\mathrm{a}}^{\mathrm{iso}}$ versus logarithmic $[\mathrm{Ca}^{2+}]_{\mathrm{i}}$; second row: $\log\left(\frac{T_{\mathrm{a}}^{\mathrm{iso}}}{T_{\mathrm{a}}^{\max}-T_{\mathrm{a}}^{\mathrm{iso}}}\right)$ versus logarithmic $[\mathrm{Ca}^{2+}]_{\mathrm{i}}$ (Hill plot). Increasing of $T_{\mathrm{a}}^{\max}$ vertically stretches the sigmoidal curves. An increase of EC_{50} translates is a right-ward shift of the tension curve with respect logarithmic $[\mathrm{Ca}^{2+}]_{\mathrm{i}}$. The Hill coefficient n_H controls the steepness of sigmoidal curves, and corresponds to the linear slope of in the Hill plot.

our context, the Hill equation reads as:

$$T_{\mathrm{a}}^{\mathrm{iso}} = \frac{T_{\mathrm{a}}^{\max}}{1+\left(\frac{\mathrm{EC}_{50}}{[\mathrm{Ca}^{2+}]_{\mathrm{i}}}\right)^{n_H}}, \tag{1.1}$$

where $T_{\mathrm{a}}^{\max}$ is the maximum tension (tension at saturating calcium levels), EC_{50} is the *half maximal effective concentration* (i.e. the calcium concentration producing half maximal force) and n_H is the *Hill coefficient*, a measure of cooperativity (see Fig. 1.15). An Hill coefficient larger than one means positive cooperativity (i.e. already bound ligands increase affinity for other ligands); lower than one means negative cooperativity; equal to one means no cooperativity.

The sigmoidal curve predicted by the Hill equation has been observed in the force-calcium relationship (see Figs. 1.17, 1.16 and 1.18) either by considering peak force during a twitch versus $[\mathrm{Ca}^{2+}]_{\mathrm{o}}$ or by considering steady-state force versus $[\mathrm{Ca}^{2+}]_{\mathrm{i}}$ and $[\mathrm{Ca}^{2+}]_{\mathrm{o}}$ (either in skinned or in intact preparations). In intact preparations, the level of calcium producing half-maximal tension is of the order of $0.5-1\,\mu\mathrm{mol}$ for intracellular concentration $[\mathrm{Ca}^{2+}]_{\mathrm{i}}$, of the order of 1 mmol for intercellular concentration $[\mathrm{Ca}^{2+}]_{\mathrm{o}}$; in skinned preparations, it is of order $5-10\,\mu\mathrm{mol}$ [Bac+95; DKT02; TK+08].

In all the cases a Hill coefficient significantly greater than one (range 3-8) has been recorded, revealing a positive apparent cooperativity. This is of fundamental importance, since it means that a small increment in calcium concentration leads to a significant increment of force. Without cooperativity, an increase of force from 10% to 90% of maximal force would require an 81-fold increase of $[\mathrm{Ca}^{2+}]_{\mathrm{i}}$; with an Hill coefficient of $n_H = 5$, to obtain the same force increment, just a factor 2.4 in calcium concentration is enough.

Manipulations of the above relationship reveal a linear relationship in the plane $\log(T_{\mathrm{a}}^{\mathrm{iso}}/(T_{\mathrm{a}}^{\mathrm{max}} - T_{\mathrm{a}}^{\mathrm{iso}}))$ versus logarithmic calcium concentration (known as *Hill plot*, see second row of Fig. 1.15), where the slope coincides with the Hill coefficient:

$$\log\left(\frac{T_{\mathrm{a}}^{\mathrm{iso}}}{T_{\mathrm{a}}^{\mathrm{max}} - T_{\mathrm{a}}^{\mathrm{iso}}}\right) = n_H \left(\log\left[\mathrm{Ca}^{2+}\right]_{\mathrm{i}} - \log \mathrm{EC}_{50}\right). \tag{1.2}$$

However, experimental data reveal two distinct segments in the force-calcium relationship, with a larger n_H for lower $[\mathrm{Ca}^{2+}]_{\mathrm{i}}$ (Fig. 1.17). This is referred in the literature as *asymmetry in the force-calcium relationship*, which reveals higher apparent cooperativity al lower calcium levels [DKT02]. The crossing point of the two segments lies slightly above the EC_{50} level and the associated relative force is nearly independent of SL, corresponding approximately to 60% of maximum force [DKT02].

The force-calcium relationship depends on the stretch of the muscle (i.e. on SL). This is of primary importance, since it is on this dependence that one of the autonomous regulatory mechanisms of the heart, known af Frank-Startling law, is based (we will return on this later in this section). In the physiological range of SL (i.e. 1.7–2.3µm), the effect of sarcomere length are summarized below.

- **Influence on plateau force ($T_{\mathbf{a}}^{\mathbf{max}}$).** The plateau force $T_{\mathrm{a}}^{\mathrm{max}}$ increases with SL, as observed in the force-length relationship for saturating calcium concentration (see below). The reason for this phenomenon is discussed later in this section, together with the force-length relationship.

- **Influence on calcium sensitivity ($\mathbf{EC}_{50}$).** Stretch enhances calcium sensitivity, that is an increase of SL induces a decrease of EC_{50}, which translates in a leftward shift of the force-calcium curves [Ken+86; TKHK00; DKT02; TK+08]. In skinned preparations the relationship is approximatively linear, as shown in Fig. 1.17 [DKT02]. The hypotheses explaining such phenomenon, known as *length-dependent activation* (LDA) [RT04; TK+80; FM98; Far+10; Pea+07], are treated in detail later in this section.

- **Influence on apparent cooperativity (n_H).** It has been debated for long whether SL has an impact on the apparent cooperativity or not. We remark an intrinsic difficulty in the estimation of the Hill coefficient when few data are available (the estimation of n_H is much more sensitive to noise than the one of $T_{\mathrm{a}}^{\mathrm{max}}$ and EC_{50}). Moreover, experimental curves does not follow exactly the Hill law (1.1), thus making the estimation of n_H strongly dependent on the regression technique. In [Ken+86] an increase of n_H has been reported; however such study has been carried out at a concentration of Mg^{2+} much higher than the physiological one [JG91; DKT02]. Experiments at physiological Mg^{2+} concentrations on skinned rat trabeculae shown that there is not statistical evidence for a dependence of n_H on SL (p-value 0.2, see[DKT02]). Experiments on intact cells also reported just little dependence of n_H on SL [TKHK00; TK+08].

Force-length relationship

As anticipated, the tension developed by muscles depends on their length. The force-length relationship has been fully characterized and interpreted for skeletal muscle in [GHJ66] (see Fig. 1.19). Force is generated in an interval of SL, comprised between nearly 1.25µm and 3.65µm. Inside this range, three main stages (*ascending limb*,

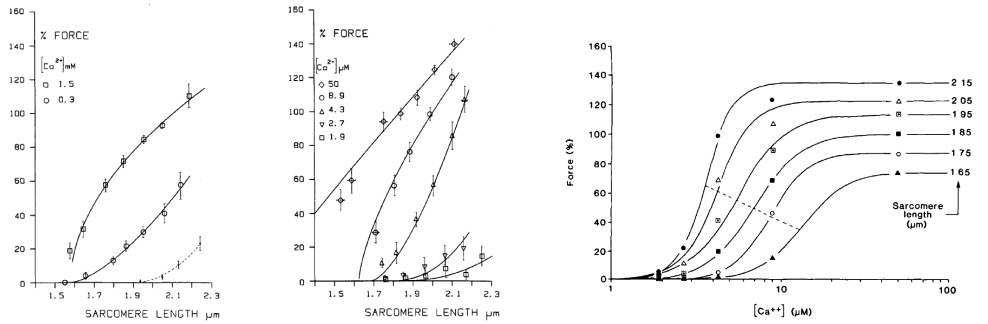

(a) Intact: peak force versus SL for different $[Ca^{2+}]_o$.

(b) Skinned: steady-state force versus SL for different $[Ca^{2+}]$.

(c) Skinned: steady-state force versus $[Ca^{2+}]$ for different SL.

Figure 1.16: Force-length relationship averaged over six rat trabeculae before and after skinning. Data are fitted with a polynomial law ($T_a = a(SL - SL_0)^c$). The obtained curves for skinned are replotted for different values of SL in the last image and then fitted with the Hill equation. Image taken from [Ken+86].

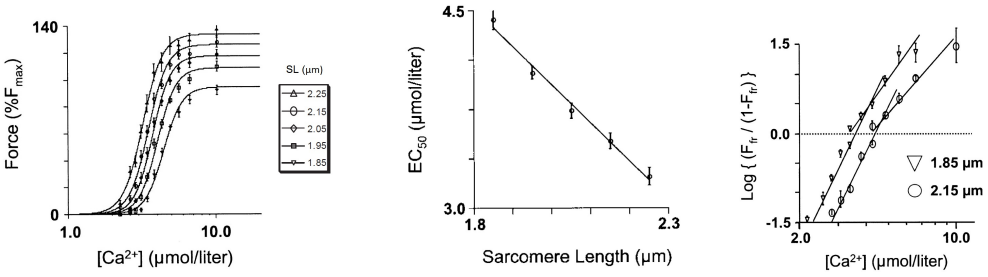

(a) T_a^{iso} versus logarithmic $[Ca^{2+}]$

(b) EC_{50} versus SL

(c) Hill plots showing asymmetry

Figure 1.17: Steady-state force-calcium relationship at different SL in skinned rat trabeculae (image from [DKT02]). We remark that in (c) the triangle and circle bullets are incorrectly indicated and should be switched.

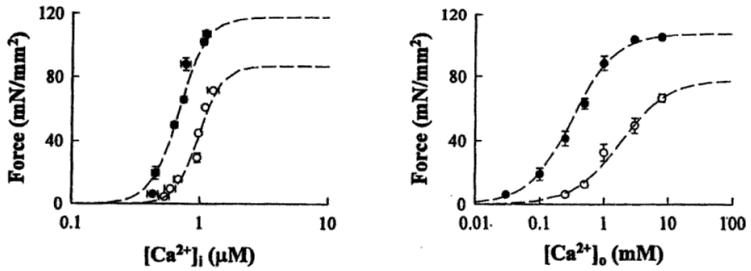

(a) T_a^{iso} versus logarithmic $[Ca^{2+}]_i$ (b) T_a^{iso} versus logarithmic $[Ca^{2+}]_o$

Figure 1.18: Steady-state force-calcium relationship at different SL (open symbols: $SL = 1.85\,\mu m$; filled symbols: $SL = 2.15\,\mu m$) in intact rat trabeculae. Left: T_a^{iso} versus $[Ca^{2+}]_i$; Right: T_a^{iso} versus $[Ca^{2+}]_o$. Image taken from [TKHK00].

plateau, *descending limb*) can be identified. A classical interpretation – well accepted for the plateau and the descending limb, less satisfactory for the ascending limb – of the three regimes is purely geometric and it is based on the mutual overlap between filaments.

- **Plateau** (2.0-2.25µm). In this range, the region of thick filaments containing force generating myosin that overlaps the corresponding thin filament is maximal (optimal overlapping). The generated tension is constant and equal to its maximal value.

- **Descending limb** (2.25-3.65µm). By increasing SL, the overlap between thick and thin filaments decreases in the centre of the sarcomere, until it reaches a condition of zero overlap. In this range, force decreases linearly. The very good agreement of the experimentally measured extrema of this interval with the length values where overlap starts to decrease and reaches zero (respectively), strongly suggests that a fixed amount of force is generated for each XB that can be formed in the overlap region, in agreement with the sliding filaments theory.

- **Ascending limb** (1.25-2.0µm). In this range, force increase monotonically, with a steeper slope in the range 1.25-1.65µm. The interpretation of this regime is less clear, and still today a full understanding has not been reached (see e.g. [Ric+08]). Force starts first to decrease nearly 2.0µm, that is close to the SL value for which thin filaments meets in the centre of the sarcomere. A common interpretation of force decrease is linked to *double overlap*, that is the condition when the thick filament faces two thin filaments. At nearly 1.65µm, that is when thick filaments end meet Z-discs, tension reports a quick drop and it reaches zero nearly at 1.25µm. This is reasonable, because this could cause resistance to shortening and crumpling of thick filaments is likely to reduce the number of recruitable XBs.

The force-length relationship has been first measured for cardiac muscles in [AJM74], by recording peak forces in isometric twitches of right ventricle papillary muscles of kittens. The most striking difference between skeletal and cardiac muscles reported by the authors is a steeper ascending limb, reaching zero nearly at 1.6µm (see [Ber01]).

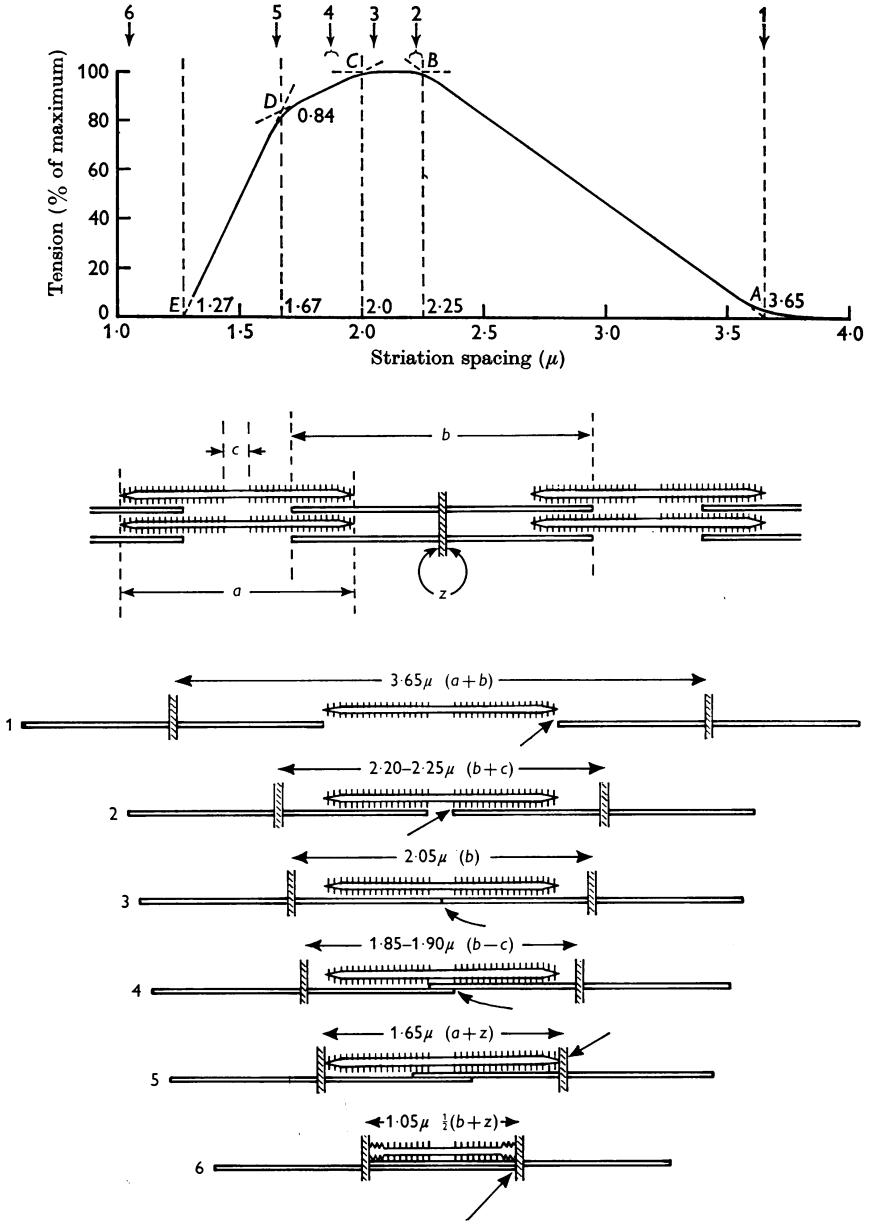

Figure 1.19: Scheme of steady-state force-length relationship for skeletal muscle (top). The arrows along the top denotes the SL values corresponding to stages of overlap represented below (bottom). The notation for sarcomere geometry is also represented (middle). Adapted from [GHJ66].

By repeating the experiment for decreasing values of $[Ca^{2+}]_o$, the ascending limb showed a more and more convex shape and an increase in the intercept.

The change of convexity in the force-length curves at different calcium concentrations has been characterized in [Ken+86] (see Figs. 1.16a and 1.16b), where rat trabeculae were studied before and after skinning. In both the cases, the force-length curves were convex at low calcium concentrations, they became concave at higher concentration, to get linear (in intact preparations), at maximal activating calcium, like in skeletal. However, unlike skeletal muscle, where the plateau starts approximately at 2.0µm, in this set of measurements the ascending limb extends up to 2.3µm. Like in the measurements of [AJM74], the intercept for intact muscles is at nearly 1.5µm (see Fig.1.16a).

The above mentioned experiments and the observed steeper ascending limb may lead to the misleading conclusion that the mechanism by which SL affects the generated force is significantly different in skeletal and cardiac muscles [Ber01; KTKA88; KN12]. However, force-length curves should be compared at maximal activating calcium concentrations. At lower calcium concentrations, indeed, LDA (that is the lower calcium sensitivity at lower SL) enhances the decrease of force, making the slope steeper (see 1.16b). This also explains the convexity of force-length curves. As a matter of fact, the values of $[Ca^{2+}]_o$ employed in [Ken+86] were far from saturating levels, as later highlighted in [TKHK00] thanks to the use of cyclopiazonic acid (see Fig. 1.18b). On the other hand, in skinned preparations, where the maximum level of calcium is sufficiently high, the linear relationship observed in skeletal muscles is recovered, with a similar slope (the intercept is nearly at 1.2-1.3µm).

The force-length experiments were repeated in [TKHK00] and [TK+08] for intact cells (tetanized thanks to calcium uptake inhibition by cyclopiazonic acid), confirming the conclusion that there is no significant difference in the mechanisms dictating maximal force at saturating $[Ca^{2+}]$ for skeletal and cardiac muscles (see also [RT04] and [Ric+08]). For completeness, we report the resulting curves in Fig. 1.20, even if there is a quantitative mismatch between the text of the article and the figure, probably due to a mistake in the labels on the horizontal axis (the article text reports a plateau located between 2.25-2.45µm, a change of slope located at 1.65µm and an intercept located at 1.25µm).

As mentioned before, the transition between the ascending limb and the plateau in cardiac muscle appears at larger SL than in skeletal muscle (nearly 2.3µm instead of 2.0µm). This is probably due to slightly different sizes of myofilaments in cardiac with respect to skeletal muscles [RT04]. We also notice that a larger variability in thin filament sizes has been observed in cardiac muscle [RW77].

Thanks to very stiff parallel passive elasticity, cardiac muscle is never stretched over 2.3µm (see e.g. [Ber01; Kat10]). The physiological working range of cardiac tissue is approximately 1.7-2.3µm, which lays in the ascending limb. This is considered, together with LDA, as the microscopical source of the Frank-Starling law, by which increased end diastolic volume (that is sarcomere stretching) leads to increased systolic contraction (that is microscopically developed force), see e.g. [Kat10]. Preventing the tissue from reaching the descending limbs is undoubtedly advantageous since a progressive decrease of force would lead to heart failure [Ber01]. We notice that in cardiac muscle, force-length relationship is of greater importance than for skeletal, which tends to work in the optimal overlap region.

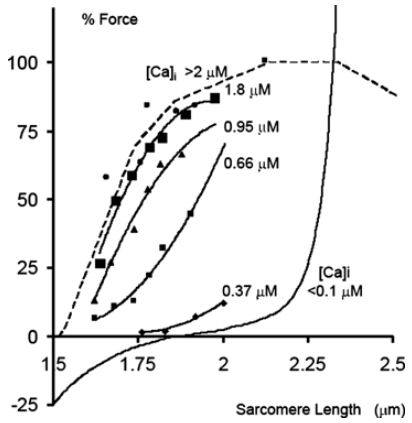

Figure 1.20: Steady-state force-length relationship at different $[Ca^{2+}]_i$ in intact rat trabeculae. Image taken from [TK+08].

Sources of cooperativity

A prominent feature of the cardiac tissue is the anomalously high (with respect to the skeletal muscle) sensitivity of the developed force to calcium concentration. The steeply nonlinear response to activator calcium ions can be explained by the cooperative interactions inside sarcomeres, even if the exact cooperativity mechanism has been debated for long (see e.g. [RWH99; RT04; Dup+16]).

The theories proposed in the literature can be collected into three groups. The first hypothesis (RU-RU) is that the transition of a Tm unit to the permissive state facilitates the same transition for neighboring RUs by means of end-to-end interactions [Bra+87; GRH01]. In such a manner, when the number of permissive RUs reaches a critical threshold, the activation spreads along the filament and a little increase of calcium leads to a steep increase of activation. The theories belonging to the second group (XB-XB) state that attached XBs increase the rate of formation of nearby XBs [FPM01]. An hypothesis is that formed XBs hold the RUs in a permissive configuration, thus facilitating the formation of nearby XBs. This could be either a secondary effect of RU-RU cooperative interactions, or caused by more that one XB forming under the same RU [CL01]. Finally, the XB-RU hypothesis is that the attachment of a XB increases the affinity of TnC to calcium ions [SM92].

More recent studies showed that XB-induced thin filament activation occurs just in rigor conditions (the motivation by which this phenomenon had been previously observed), but it does not occur in physiological conditions. Hence, the phenomenon of regulation of calcium sensitivity must be intrinsic to the thin filament [SLI09]. Moreover, in [Far+10], skinned rat trabeculae treated with blebbistatin to inhibit XB attachment showed virtually no effect on EC_{50} and Hill coefficient. In conclusion, the source of cooperativity should be found in RU-RU interactions, in particular in the end-to-end interaction of Tm [SV17]. Indeed, the removal of the overlap of Tm among adjacent RUs reduced the apparent cooperativity of activation [HSLV89; PGL89].

Length-dependent activation (LDA)

LDA is the phenomenon by which, when SL increases, the apparent calcium sensitivity of thin filaments increases as well. As mentioned before, this is of fundamental

importance, due to its link with the Frank-Starling mechanism. Several explanations for the LDA have been proposed in the past, but most of them have been later rejected and a definitive explanation is still lacking [TK16; NCC19].

The hypothesis that the increase of sensitivity to $[Ca^{2+}]_o$ was linked to a higher $[Ca^{2+}]_i$ at higher SL [Ken+86], was rejected by the finding that stretch does not affect peak $[Ca^{2+}]_i$ [AK82]. Increases in the amount of the released calcium can be observed only after several minutes of stretching, while the observed LDA instantaneously takes place when SL varies [MH06]. Thus, the thin filament must feature a higher sensitivity to $[Ca^{2+}]_i$ at larger SL.

The remaining putative reasons are a feedback from either SL or force [Ken+86]. Earlier studies were in favour of the presence of force-feedback on calcium sensitivity [SM92; TKHK00; TK+08], mainly because of experimental evidence of the so-called XB-RU cooperativity hypothesis (i.e. increase of TnC affinity to $[Ca^{2+}]$ in presence of attached XBs) [Bra+87; FM98]. However, as we mentioned above, more recent studies denied the hypothesis of a feedback from XBs to the RUs, proving that the LDA originates upstream of XB attachment [SLI09; SLI09; SV17].

A further hypothesis is that SL might modulate interfilament spacing, thus reducing the distance between actin and myosin and increasing the binding probability [TK+08; Pea+07]. Indeed, X-ray diffraction reveals an inverse relationship between interfilament lattice spacing and SL in both skeletal and cardiac muscles [Irv+00]. However, in a multitude of experimental models, a consistent correlation between lattice spacing and EC_{50} sensitivity seems to be absent [AM+16].

At the best of our knowledge, the most recent results suggest that the LDA is linked to "stretch-induced structural rearrangements in both the thin and thick filaments that is likely directly mediated by titin strain" [AM+16].

1.3.3 Activation and relaxation kinetics

The heart is an organ finely tuned to work at the right rhythm, which is adapted according to the needs of the body. The main driving factor of the microscale muscle contraction, calcium, periodically raises and falls at each heartbeat, and the generated active tension follows such periodic signal. Thus, besides the steady-state relationships considered in Sec. 1.3.2, also the kinetics of activation and relaxation (that is to say, how fast the muscle is activated and relaxes) are crucial to characterize the muscle functionality.

Indeed, the activation and relaxation transients are not rate-limited by the calcium release and by the calcium uptake, respectively, as it is evident from the experimentally obtained curves in the calcium-force plane (see Fig. 1.21). If the force generation machinery was much faster than the calcium dynamics, then the curves would follow, in a quasi-static manner, the steady-state force-calcium curve. Conversely, the experimental curves lie below the curve in the activation phase, then cross the steady-state curve with horizontal tangent in proximity of the force peak and stay above the curve during the relaxation phase. In [Bac+95], the authors showed that if the calcium uptake is slowed down by adding Ca-ATPase inhibitor cyclopiazonic acid (CPA), then the relaxation phase follows the steady-state curve, while in control conditions the relaxation kinetics is slower than the calcium one.

The typical experimental setups to quantitatively evaluate the kinetics of force generation are the following ones.

- Activation after step-wise increase of $[Ca^{2+}]_i$. Thanks to the light-induced release of caged $[Ca^{2+}]$ compounds such as nitrophenyl-EGTA and DM-nitrophen,

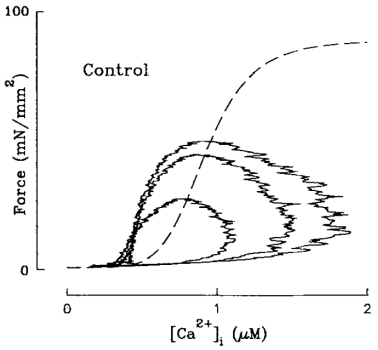

Figure 1.21: Phase plot of three different twitches (for three different levels of $[Ca^{2+}]_o$) from rat intact trabeculae at temperature of $20 - 22\,°C$. Image taken from [Bac+95].

the intracellular calcium concentration is suddenly increased. This allows to study the kinetics of activation and force generation, without any artifact linked to the kinetics of calcium release that takes place during the physiological behavior of the muscle. In this manner, the inverse time constant k_{act} associated with activation can be estimated [FPM98; Sae+01; Sae+04; PTS05; Pir+07].

- Relaxation after step-wise reduction of $[Ca^{2+}]_i$. Similarly to the above experimental setup, a light-activated caged calcium chelator (such as chelator diazo-2) almost instantaneously reduces $[Ca^{2+}]_i$ to the pre-systolic value and the fiber consequently relaxes, with rate k_{rel} [FPM98; Sae+01; Sae+04; PTS05; Pir+07].

- Tension regeneration after a step in SL. In this experimental setup, a muscle fiber is kept in isometric conditions until it reaches the tetanic force T_a^{iso}. Then, a sudden step-change in SL is applied, which is thought to detach all XBs, so that the force abruptly falls to zero and then recovers the pre-existing level with an exponential-like recovery. The inverse time constant associated with the tension redevelopment k_{tr}, unlike k_{act}, is thought to be related only to the XB cycling phenomenon, and not to the thin filament activation [FHS77; WMM95; TS97; AW94; PTS05; TS07; Pir+07].

The possible determinants of the activation and relaxation kinetics are (1) the calcium raise and uptake, (2) the thin filament regulation and (3) the XB formation mechanism. While the calcium kinetics has for sure an influence on the force transients, as we mentioned before, it cannot be its major determinant. However, there is not common agreement on whether activation and relaxation are rate-limited by the RUs or the XBs kinetics [NHS06; PTS05]. The hypothesis that the activation kinetics is determined by XB cycling is supported by the fact that the measurements of k_{act} and k_{tr} are very similar under the same experimental conditions and by Tn replacements studies that leave the kinetics unaffected [PTS05]. In [Pir+07] the addition of bepibril (a drug increasing affinity of TnC to calcium) does not induce any significant change in the relaxation kinetics, supporting the hypothesis that relaxation is not rate-limited by calcium binding to TnC. Conversely, in [NHS06] the authors notice that the relaxation rate is very similar accross species featuring different myosin isoforms, which makes unlikely the hypothesis that relaxation is determined by XB kinetics; since the relaxation rate is slower than the measured calcium binding rate to TnC, the authors conclude that the main determinant should be the kinetics of Tm.

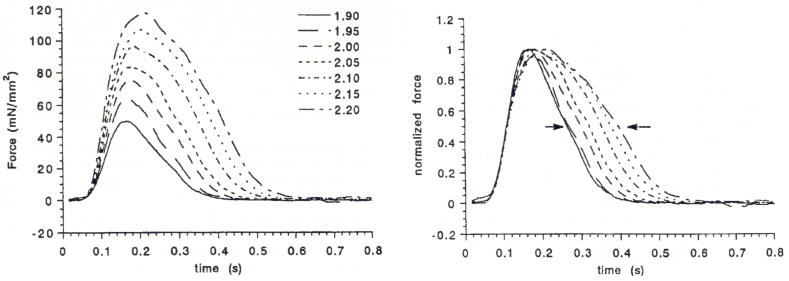

(a) Absolute tension (b) Normalized tension

Figure 1.22: Isometric twitches at different SL from intact rat trabeculae at temperature $T = 23 - 24\,°\mathrm{C}$ and with $[Ca^{2+}]_o = 2.0\,\mathrm{mM}$. Left: absolute traces; Right: normalized traces. Image taken from [JH95].

The measurements of the activation rates k_{act} and k_{tr} show a positive correlation between the rapidity of force generation and the amount of active force T_a^{iso} [WMM95; PTS05; Pir+07]. A similar trend for relaxation is shown in [PTS05].

An experimental characterization of activation and relaxation kinetics closer to the dynamics that takes place during each heartbeat consists in the force transients during isometric twitches [Bac+95; JH95; JT97]. A muscle fiber is kept in isometric conditions and stimulated while the generated active force is measured. The experiment is repeated for different values of $[Ca^{2+}]_o$ and SL, with different effects on the force transient. The same effects can be recorded either with fixed SL and increasing $[Ca^{2+}]_o$, or by keeping $[Ca^{2+}]_o$ constant and increasing SL (see Fig. 1.22 and [JH95; DBY95]).

- The peak force increases.
- The relaxation time increases.
- The activation time is virtually not affected. This means that the velocity of force increase is approximately proportional to peak force.

The last two effects become mostly evident from the normalized transient curves (see Fig. 1.22b)

1.3.4 Force-velocity relationship

One of the earliest experimental characterizations of muscle functionality is the force-velocity relationship, dating back to Archibald V. Hill, Nobel Prize winner for his work on the heat production and mechanical work in muscles [Hil38]. In the Hill's experimental setup, a muscle fiber is stimulated under isometric conditions until it reaches the tetanic force T_a^{iso}. Then, a negative (or positive) force step is applied. After a transient phase (which is discussed in Sec. 1.3.5), the fiber reaches a steady-state with a constant shortening (or lengthening) velocity. The measured force-velocity relationship is a convex curve for positive shortening velocities (see Fig. 1.23), connecting the so-called *stall force*, namely the force in isometric conditions, with the *maximum shortening velocity*, in correspondence of which the generated tension is zero.

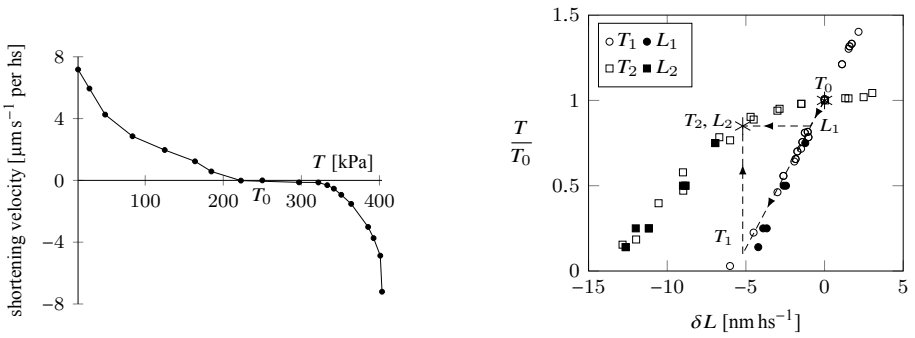

(a) (b)

Figure 1.23: Force-velocity (a) and tension-elongation (b) relationships in the skeletal muscle. The images are reproduced from [CT18] and collect data coming from different sources (see [CT18] and references therein.)

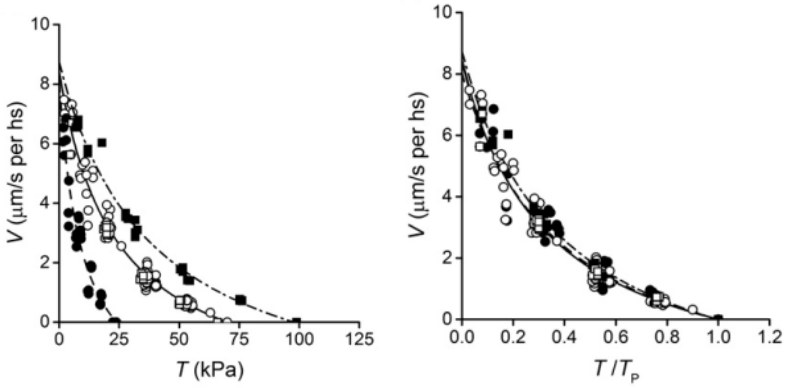

(a) Absolute force (b) Normalized force

Figure 1.24: Force-velocity relationship in intact rat trabeculae at 27 °C. Different symbols refer to the following isometric conditions: $[Ca^{2+}]_o = 1.0\,mM$ and $SL = 1.9\,\mu m$ (filled circles); $[Ca^{2+}]_o = 1.0\,mM$ and $SL = 2.2\,\mu m$ (open circles and open squares); $[Ca^{2+}]_o = 2.5\,mM$ and $SL = 2.2\,\mu m$ (filled squares). Image taken from [Car+16].

In Fig. 1.24, we report the force-velocity relationship in intact cardiac cells obtained starting from different values of $[Ca^{2+}]_o$ and SL. When the tension is normalized with respect to the isometric values, the curves virtually superimpose. The maximum shortening velocity for half-sarcomere is independent on the $[Ca^{2+}]_i$ and SL and it is about $v_{hs}^{max} = 8\,\mu m\,s^{-1}$ (significantly larger than for skeletal muscle). This observation suggests that the mechanism underlying the force-velocity relationship is largely independent of the calcium-driven regulation and, therefore, it is linked to the cycling of XBs [KS09; CT18; Car+16].

1.3.5 Fast isometric and isotonic transients

Fast isometric and isotonic experiments help shedding light on the fastest time scales involved in the dynamics of force generation in the muscle tissue. The two experimental setups are briefly described in the following.

- **Force clamp** (soft device or isotonic transient). It consists in the same setup employed to obtain the force-velocity relationship. After the isometric force is reached, a step in tension is applied. After a fast transient, the fiber reaches a constant velocity.

- **Length clamp** (hard device or isometric transient). In this case, after that the steady-state is reached while keeping constant the length of the fibers (typically in the plateau region of the force-length curve, see Sec. 1.3.2), a step in length is applied (without exiting the plateau region). The measured force undergoes a fast transient, before going back to the original level.

In both the cases, the observed transient can be split into 4 different phases (in the cardiac muscle we have only 3 phases, as the third is absent), associated with different time scales [KS09; MT10a; MT10b; CT18; Car+16].

- **Phase 1** ($\sim 200\,\mu s$). In a first phase the tension T (respectively, the length of the fiber L) changes simultaneously with the step in L (respectively, in T), until it reaches a level called T_1 (respectively, L_1). Interestingly, by plotting the values of T_1 and L_1 in the T-L plane, the curves obtained with the soft and hard devices superimpose (Fig. 1.23b) and show a linear relationship between tension and elongation. This first phase of the transient is indeed linked to the instantaneous elastic response of XBs. Measurements of the stiffness of this relationship under *rigor* conditions (when the number of attached XBs can be estimated) allow to estimate the stiffness of a single XB [Pia+07].

- **Phase 2** ($\sim 2 - 3\,ms$). After the instantaneous response, tension (respectively, length) quickly reaches a second level, denoted by T_2 (respectively, L_2). Also in this case, the curves of T_2-L_2 obtained with the soft and hard devices superimpose (Fig. 1.23b). For length close to the rest length, the T_2 tension is very similar to the isometric tension T_a^{iso}, but for larger length steps it is approximately linear in L, with a lower stiffness than the elastic stiffness (related to T_1). The time scale associated with this phase coincides with the time scale of the power stroke: in this phase, MHs rearrange from the non-equilibrium condition due to the fast step in length until a new equilibrium is reached. Indeed, for small length steps, the power stroke is sufficient for the fibers to almost recover the initial tension level T_a^{iso}.

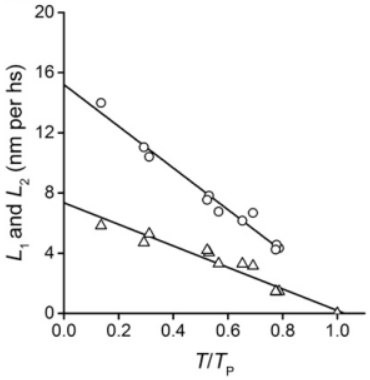

Figure 1.25: T_1-L_1 and T_2-L_2 tension-elongation curves from intact rat trabeculae at temperature 27 °C. Image taken from [Car+16].

- **Phase 3 and 4** ($\sim$ 500 ms). After the rapid second phase, in length clamp experiments tension slowly recovers its original level T_a^{iso} (if the step in length is such that the sarcomeres are still in the plateau region of the force-length relationship). In force clamp experiments, as described in Sec. 1.3.4, the filament reaches a steady-state with a constant shortening (or lengthening) velocity. Such velocity, plotted against the isotonic tension, gives the force-velocity curve. This final phase is associated with the XBs attachment and detachment, the slower step of the Lymn-Taylor cycle (see Sec. 1.2.4).

Fast transient experiments have been carried out in [Car+16] for intact cardiac cells (only with the force clamp setup). The obtained T_1-L_1 and T_2-L_2 tension-elongation curves are reported in Fig. 1.25.

In Fig. 1.24, we report the force-velocity relationship in intact cardiac cells obtained starting from different values of $[Ca^{2+}]_o$ and SL. When the tension is normalized with respect to the isometric values, the curves virtually superimpose. As for the force-velocity curve (see Sec. 1.3.4), this fact supports the hypothesis that the phenomena associated with the fast time scales observed through this experimental setup are linked to the XB dynamics, and not to the RU dynamics.

1.3.6 The influence of temperature and cellular preparation

As we mentioned before (Sec. 1.3.2), the main variables that drive the muscle function are the calcium concentration and the tissue elongation (together with its time derivative), but other variables can affect the force generation mechanism, such as temperature, pH and the concentration of chemical species other than calcium. However, such variables do not change significantly during the heartbeat and thus are not involved in the regulation machinery of force generation. Nonetheless, the experimental measurements in laboratories may be carried out under different conditions than the physiological ones and, thus, an understanding of the effects of such secondary factors is mandatory in order to interpret the results. In the following we recap the effects of two of the main variables varying among the experiments, namely temperature and the cellular treatment.

The effect of temperature

Temperature has a significant impact on muscle tension generation, both in steady-state and in dynamical conditions. Nonetheless, the vast majority of muscle experiments are carried out, for evident practical reasons, at room temperature.

As far as steady-state relationships are concerned, in [HB89] has been reported, by increasing the temperature from room (22°C) to body (36°C) levels, a 18% increase of T_a^{max} and a 35% decrease of EC_{50} in skinned rabbit ventricular muscle.

In [JSM02], twitches have been measured at different temperatures in intact rat cardiac trabeculae. Peak force is just slightly affected between 22.5°C and 30°C, but reports a 66% decrease between 30°C and 37.5°C. This is linked to a decrease in $[Ca^{2+}]_i$ peak associated with the temperature raise. In the same range of temperature, the time of relaxation decreases by 80%.

The effect of skinning

Aiming to support the reader in interpreting experimental data of the literature, we summarize here the features of skinned preparation compared to intact ones.

- Nearly five-fold decrease of $[Ca^{2+}]$ sensitivity with respect to intact preparations (more precisely with respect to the sensitivity to $[Ca^{2+}]_i$) [Bac+95; TK+08].
- In [Gao+94] a reduce in Hill coefficient with skinning has been reported. However, the experiment was performed without a proper control of SL. As a matter of fact, an uncontrolled shortening of sarcomeres in the inner part of the sample, due to the compliace of the damaged ends, leads to an underestimation of the Hill coefficient [DKT02]. A more detailed analysis revealed that the level of cooperativity in skinned myocardium is comparable to intact one [DKT02].
- Swelling of the myofilament lattice in skinned preparations [RT04].
- Increase of passive compliance [Ken+86].
- Saturating force is not affected [Bac+95; Gao+94; Ken+86].

Chapter 2

Modeling the thin filament regulation

Muscle contraction is driven by a chemical signal, consisting in the intracellular concentration of calcium ions. The mechanism by which such intracellular messenger triggers the contraction of the muscle is known as *thin filament regulation*, or *calcium-driven activation*, and it is achieved by conformational changes of the proteins Tn and Tm, forming the so-called RUs. Each RU acts as an on-off switch for the cycling of XBs (the microscopical motors of muscles) that are located in the portion of the myofilament regulated by the RU itself. In this chapter, we review the mathematical models that have been developed to describe the calcium-driven activation of RUs. One of the main modeling issues concerning this topic is related to the steep response of force near the half-activating calcium concentration, that is thought to be linked to a cooperative activation of RUs (see Sec. 1.3.2).

The need of explicitly representing the physical arrangement of the RUs along the thin filament (in order to capture such cooperative behavior) makes it hard to derive a computationally affordable mathematical model that is able of predicting the observed steep response to calcium. The number of variables required to explicitly represent the interactions among RUs is indeed exponential in the number of units. In this chapter, after a presentation of the main classes of models available in literature and of the different attempts to capture the cooperative phenomena with models featuring a low number of variables, we propose a model that is capable of accurately reproducing cooperative activation of RUs, with a number of variables that is linear in the number of units, thus significantly reducing the computational cost.

Our model, that we denote as *activation-MH* model (since it is centered on MHs) is derived from the model proposed in [Was+12] (W12 model) under suitable assumptions. In the final part of this chapter, we propose two alternative models (that we denote as *activation-RUa* and *activation-RUb* models), aimed at overcoming a criticality in the definition of the W12 model. Part of the results presented in this chapter have been published in [RDQ18].

Contents

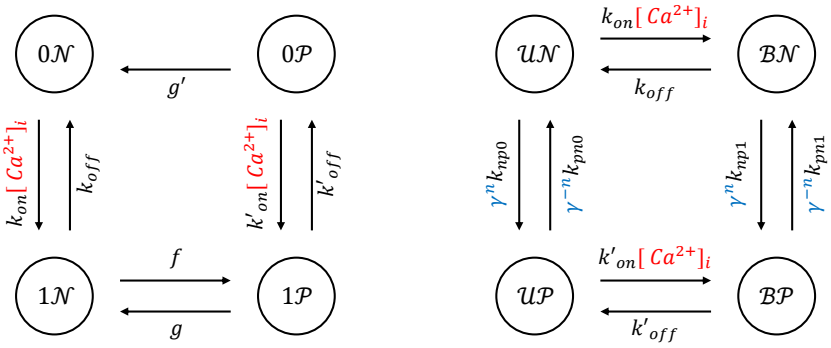

(a) Model of [RWH99].

(b) R03 model [Ric+03].

Figure 2.1: Markov chains describing the dynamics of a RUs in (a) the first of the the 4 models presented in [RWH99] and (b) the R03 model [Ric+03].

2.1 Mathematical models of regulatory units dynamics

The first mathematical models of muscle force generations incorporated only the description of XB dynamics, without including the calcium-driven regulation of the thin filaments [HS71; KS09; NCC19]. This is a consequence of the fact that the role of Tn and Tm in the force generation mechanisms has been discovered later than that of acto-myosin interactions. In this thesis, however, we revert this order to consider first the calcium-driven regulation and later (in Chapter 3) the XB dynamics, as the latter is driven by the former.

2.1.1 CTMC description of RUs

The earliest attempts to model the calcium-driven regulation of the muscular contractile system date back to the 1990s-2000s [LS94; ZPJ94; DBY95; RBC99; RWH99; SGS03]. Those models rely on the formalism of continuous-time Markov Chains (CTMC), also known as Markov Jump processes (see e.g. [Nor98]), to model the transitions between the different configurations assumed by the proteins involved in the force regulation process.

To illustrate the features of such models, we present here the first of the four models considered in [RWH99], which is a slightly simplified version of the model proposed in [LS94]. The model considers a single RU, whose state is determined by two conditions: first, it can be either in non-permissive ($\mathcal{N}$) or permissive ($\mathcal{P}$) configuration (the latter situation is verified when a calcium ion binds to the regulatory unit, as the transition of Tm is assumed to be instantaneous); additionally, the actin site regulated by the RU can undergo the formation of a XB. We consider therefore four states: $\mathcal{N}0$ (non-permissive state with no XB), $\mathcal{P}0$ (permissive state with no XB), $\mathcal{N}1$ (non-permissive state with a formed XB) and $\mathcal{P}1$ (permissive state with a formed XB).

We consider a stochastic process $R^t \in \mathcal{S} := \{\mathcal{N}0, \mathcal{P}0, \mathcal{N}1, \mathcal{P}1\}$, for $t > 0$, and we associate a rate to every possible transition within the states. The transition rate from the state $\alpha \in \mathcal{S}$ to the state $\beta \in \mathcal{S}$ is denoted by $k_{\alpha\beta}$ and is defined through the

following relationship:

$$\mathbb{P}\left[R^{t+\Delta t}=\beta|R^t=\alpha\right]=k_{\alpha\beta}\,\Delta t+o\left(\Delta t\right),$$

where $\mathbb{P}\left[Z|W\right]=\mathbb{P}\left[Z\cap W\right]/\mathbb{P}\left[W\right]$ denotes the conditional probability of the event Z given W (we set by convention $\mathbb{P}\left[Z|W\right]=0$ is $\mathbb{P}\left[W\right]=0$) and where $o\left(\Delta t\right)$ denotes a higher order term in Δt. The transition rates for the first model of [RWH99] are represented in Fig. 2.1a. The transition rate from the $\mathcal{N}$ to the $\mathcal{P}$ state is assumed to be proportional to the calcium concentration $[\mathrm{Ca}^{2+}]_\mathrm{i}$. To model the effect of the calcium-driven regulation on the formation of XBs, the XBs attachment and detachment rates depend on the state of the RU: in the configuration $\mathcal{N}$, the detachment rate g' is much larger than g (associated in turn to the $\mathcal{P}$ state), whereas the attachment rate is set to zero.

In order to derive an equation for the evolution of the probabilities associated with the possible configurations of the considered RU, we write:

$$\begin{aligned}\mathbb{P}\left[R^{t+\Delta t}=\beta\right]&=\sum_{\alpha\in\mathcal{S}}\mathbb{P}\left[R^{t+\Delta t}=\beta,R^t=\alpha\right]\\&=\sum_{\alpha\in\mathcal{S}}\mathbb{P}\left[R^{t+\Delta t}=\beta|R^t=\alpha\right]\mathbb{P}\left[R^t=\alpha\right]\\&=\sum_{\alpha\in\mathcal{S},\alpha\neq\beta}\mathbb{P}\left[R^{t+\Delta t}=\beta|R^t=\alpha\right]\mathbb{P}\left[R^t=\alpha\right]\\&+\left(1-\sum_{\alpha\in\mathcal{S},\alpha\neq\beta}\mathbb{P}\left[R^{t+\Delta t}=\alpha|R^t=\beta\right]\right)\mathbb{P}\left[R^t=\beta\right].\end{aligned}$$

By the definition of transition rate, it follows:

$$\begin{aligned}&\mathbb{P}\left[R^{t+\Delta t}=\beta\right]\\&=\sum_{\alpha\in\mathcal{S},\alpha\neq\beta}k_{\alpha\beta}\mathbb{P}\left[R^t=\alpha\right]\,\Delta t+\left(1-\sum_{\alpha\in\mathcal{S},\alpha\neq\beta}k_{\beta\alpha}\right)\mathbb{P}\left[R^t=\beta\right]\,\Delta t+o\left(\Delta t\right).\end{aligned}$$

The time derivative of $\mathbb{P}\left[R^t=\beta\right]$ is then given by:

$$\begin{aligned}\frac{d}{dt}\mathbb{P}\left[R^t=\beta\right]&=\lim_{\Delta t\to0}\frac{\mathbb{P}\left[R^{t+\Delta t}=\beta\right]-\mathbb{P}\left[R^t=\beta\right]}{\Delta t}\\&=\sum_{\alpha\in\mathcal{S},\alpha\neq\beta}k_{\alpha\beta}\mathbb{P}\left[R^t=\alpha\right]-\sum_{\alpha\in\mathcal{S},\alpha\neq\beta}k_{\beta\alpha}\mathbb{P}\left[R^t=\beta\right].\end{aligned}\tag{2.1}$$

Equation (2.1), valid for any $\beta\in\mathcal{S}$, can be written as the following system of linear ODEs:

$$\frac{d}{dt}\mathbf{p}(t)=\mathbf{A}(t)\,\mathbf{p}(t)\qquad t\geq0,\tag{2.2}$$

where the state vector is defined as

$$\mathbf{p}(t)=(\mathbb{P}\left[R^t=\mathcal{N}0\right],\mathbb{P}\left[R^t=\mathcal{P}0\right],\mathbb{P}\left[R^t=\mathcal{N}1\right],\mathbb{P}\left[R^t=\mathcal{P}1\right])^T,$$

and the *transition matrix* $\mathbf{A}$ collects the transition rates. Specifically, the transition matrix of the first model of [RWH99] reads as follows (see Fig. 2.1a):

$$\mathbf{A}(t)=\begin{pmatrix}-k_\mathrm{on}[\mathrm{Ca}^{2+}]_\mathrm{i}(t)&k_\mathrm{off}&g'&0\\k_\mathrm{on}[\mathrm{Ca}^{2+}]_\mathrm{i}(t)&-k_\mathrm{off}-f&0&g\\0&0&-k'_\mathrm{on}[\mathrm{Ca}^{2+}]_\mathrm{i}(t)-g'&k'_\mathrm{off}\\0&f&k'_\mathrm{on}[\mathrm{Ca}^{2+}]_\mathrm{i}(t)&-k'_\mathrm{off}-g\end{pmatrix},$$

where the transition matrix depends on time as it depends on the current calcium concentration $[Ca^{2+}]_i(t)$. The transition matrix has by construction zero-sum columns, which ensures the conservation of probability. Indeed, if the probabilities vector $\mathbf{p}$ has sum one at time $t = 0$, the property is preserved as time goes by since we have

$$\frac{d}{dt}\mathbf{1}^T\mathbf{p}(t) = \mathbf{1}^T\mathbf{A}(t)\mathbf{p}(t) = \mathbf{0}, \qquad \forall\, t \geq 0,$$

where $\mathbf{1}$ is the vector containing 1 in each of its entries.

Equation (2.2) is known as the *forward Kolmogorov equation* (FKE), or *master equation*, associated with the CTMC. It is a linear system of ODEs, ruling the time evolution of the probability associated with each of the elementary state of the Markov Chain.

The force predicted by the model is given by:

$$T_a(t) = T_a^{\max}\, \chi_{so}(SL(t)) \left(\mathbb{P}\left[R^t = \mathcal{N}1\right] + \mathbb{P}\left[R^t = \mathcal{P}1\right]\right),$$

which is proportional to the fraction of RUs in the force generating states ($\mathcal{N}1$ and $\mathcal{P}1$), to the single-overlap ratio $\chi_{so}(SL)$, that measures the fraction of RUs recruitable for tension generation, and a constant $T_a^{\max}$, that quantifies the maximal force.

2.1.2 Accounting for cooperative interactions: the mean-field hypothesis

The model presented in the previous section provides a simple and easy way to describe the calcium-driven regulation of the muscle tissue. However, the results are far from being satisfactory when compared with experimental measurements, as the predicted steady-state force-calcium relationship does not show the observed steep response near the half-activating calcium concentration, resulting in an Hill coefficient n_H significantly grater than one [RWH99]. The reason is that in this model RUs act independently of each other. Whereas this hypothesis allows to model a single RU, it does not account for cooperative interactions within the sarcomere, that are crucial for its functioning (see Sec. 1.3.2).

In order to account for cooperative mechanisms, different strategies have been proposed [LS94; RWH99; SGS03; Sac04; RBC99]. For instance, the model proposed in [LS94] considers a description similar to the first model of [RWH99], but the transition rate k_{off} is defined as a decreasing function of the fraction of units in the force-generating states ($\mathbb{P}[R^t = \mathcal{N}1] + \mathbb{P}[R^t = \mathcal{P}1]$). This model belongs to the family of *mean-field* models, as it considers a single representative unit with the assumption that the interactions with the remaining units can be well approximated by quantities that are averaged over the whole population.

In the previously cited models [LS94; RWH99; SGS03; Sac04; RBC99], different strategies to incorporate the postulated cooperative mechanisms within a mean-field framework have been proposed. However, despite the many efforts, no model managed to accurately reproduce the experimentally measured steady-state force-calcium curves [RT04]. The model of [LS94], for instance, predicts a low apparent cooperativity at low and high activating calcium concentration and very high cooperativity near EC_{50}. In the seminal paper [RT04], the authors made the following key observation:

> *Because the multitude of models have been developed assuming different cooperative mechanisms and/or parameters, one can postulate that some*

> *fundamental "ingredient" must be missing or alternatively some fundamental assumption is wrong. We will argue that the missing ingredient is explicit spatial consideration of nearest-neighbor cooperativity and the fundamental wrong assumption is that the spatial cooperativity can be well represented using a mean-field approach.*

Indeed, in the mean-field framework, the state of *all* units affects the transition rates of *all* units (a spatially-detailed description is missing).

2.1.3 Spatially-explicit models

In [Ric+03], the authors proposed a spatially-explicit model (in the following, we will call it R03 model), consisting in a filament of $N_A = 26$ RUs, each one described by a 4-states CTMC. To account for end-to-end interactions, the transition rates between the permissive and the non-permissive states were assumed to depend on the state of nearest-neighbouring RUs. The results of the numerical simulations performed with this model showed a great improvement, with respect to mean-field models, in the agreement with experimental observed behaviors, both under steady and dynamic conditions.

In the R03 model, the 4-states CTMC describing each RU is similar to that of the first model of [RWH99]. In this case, however, the XB binding state is not tracked, but instead the state of TnC (bound or unbound to calcium) is explicitly represented. We have thus the following states: $\mathcal{UN}$ (Tn unbound, Tm non-permissive), $\mathcal{BN}$ (Tn bound, Tm non-permissive), $\mathcal{UP}$ (Tn unbound, Tm permissive) and $\mathcal{BP}$ (Tn bound, Tm permissive). As in the models of [RWH99], the transition rates within the states depend on $[Ca^{2+}]_i$. The prominent feature of this model, compared to mean-fields models, is that the transition rates associated with each unit depend on the nearest-neighbouring RUs.

More precisely, the model assumes that the end-to-end interactions between adjacent units are such that two consecutive units in the same permissivity state (either $\mathcal{N}$-$\mathcal{N}$ or $\mathcal{P}$-$\mathcal{P}$) are energetically more favorable than the case of different state (either $\mathcal{N}$-$\mathcal{P}$ or $\mathcal{P}$-$\mathcal{N}$). If we denote by ΔE the difference in internal energy between the former and the latter case, by k_B the Boltzmann constant and by T the absolute temperature, basic thermodynamics entails that the rate of the $\mathcal{N} \to \mathcal{P}$ transition is $\exp(2\frac{\Delta E}{k_B T})$ larger if the two neighboring units are in $\mathcal{P}$ state (this transition would lead to a gain of $2\Delta E$ in energetic terms) than the case when one neighboring unit is in state $\mathcal{N}$ and the other one is in $\mathcal{P}$ (this transition would leave unaffected the number of consecutive units in the same state) and $\exp(4\frac{\Delta E}{RT})$ times larger than the case when both neighboring units are in state $\mathcal{N}$ (which would lead to a loss of $2\Delta E$).

Therefore, by denoting by $R_i^t \in \mathcal{S} := \{\mathcal{UN}, \mathcal{BN}, \mathcal{UP}, \mathcal{BP}\}$ the stochastic process associated with the i-th RU (where $i = 1, \ldots, N_A$), we define:

$$k^{\beta,\eta|\alpha,\delta} = \lim_{\Delta t \to 0} \frac{1}{\Delta t} \mathbb{P}\left[R_i^{t+\Delta t} = \eta \,|\, (R_{i-1}, R_i, R_{i+1})^t = (\alpha, \beta, \delta)\right];$$

then, we set the transition rates between the nonpermissive to the permissive states as follows:

$$k^{\mathcal{UN},\mathcal{UP}|\alpha,\delta} = \gamma^{n(\alpha,\delta)} k_{np0}, \qquad k^{\mathcal{UP},\mathcal{UN}|\alpha,\delta} = \gamma^{-n(\alpha,\delta)} k_{pn0},$$
$$k^{\mathcal{BN},\mathcal{BP}|\alpha,\delta} = \gamma^{n(\alpha,\delta)} k_{np1}, \qquad k^{\mathcal{BP},\mathcal{BN}|\alpha,\delta} = \gamma^{-n(\alpha,\delta)} k_{pn1},$$

where we define $\gamma := \exp(2\frac{\Delta E}{k_B T})$ and we denote by $n(\alpha, \delta)$ the number of permissive states among α and δ (we have $n = 0, 1, 2$). In this manner, the cooperative interactions by which a RU in $\mathcal{P}$ state facilitates the adjacent units to switch to the same state are included in the model. The CTMC representing each RU is represented in Fig. 2.1b.

As anticipated, thanks to the explicit description of nearest-neighbor interactions within RUs, this models showed a great improvement in the ability of capturing the experimental steady-state curves with respect to mean-field models. Moreover, the spatial description of the filament allows to model the SL-dependence in a more rigorous way than in mean-field models since the overlap of MFs and AFs can be explicitly incorporated, as done in the model proposed in [Was+12] (that we denote by W12 model), a modification of the R03 model.

The drawback of spatially-explicit models is their overwhelming computational complexity. Because of the explicit description of the interactions within the units, when writing the FKE associated with this class of models, the state of all the units needs to be simultaneously taken into account. Since a model comprising N_A units, each one modeled by a Markov Chain with s states, has s^{N_A} total possible states, it follows that the FKE associated, e.g., to the W12 model is a system of nearly $5 \cdot 10^{21}$ ODEs. Hence, if the variables are represented with 8-bytes precision, more than 37 millions of petabytes would be required just to store the state vector in the computer memory, corresponding to more than 100000 times the storage capacity of the largest supercomputer in the world (June 2019) [Top]. This clearly hinders the possibility of numerically solving the FKE associated with such models.

For this reason, numerical simulations of spatially-explicit models are typically carried out by means of a Monte Carlo (MC) approximation [RT04; HTR06; Was+13; Was+15]. The MC method consists in generating a number of realizations n_{MC} of the stochastic process and to approximate its expected value by means of the sample average. However, the order of convergence of the MC method is $n_{\mathrm{MC}}^{-1/2}$, thus requiring a very large number of samples to reach statistical convergence, with a huge computational cost, both in terms of time and memory storage.

2.1.4 Phenomenological modeling of cooperative interactions

To avoid an explicit representation of end-to-end interactions, [Ric+08] proposed a mean-field model whose transition rates were phenomenologically modified to reproduce the steeply nonlinear response of the tissue to calcium concentration. This approach is similar to the one employed in [HMTK98] and in [NHS06], where the rate of activation is set as a nonlinear function of calcium concentration, such that the steady state solution coincides with the Hill's function (see Eq. (1.1)). A similar phenomenological model, based on measurements on human cardiomyocytes, is proposed in [Lan+17].

2.1.5 Capturing nearest-neighbor interactions by means of systems of ODEs

To overcome the large computational cost induced by the MC method without renouncing to represent the spatial activity within the sarcomeres (unlike in phenomenological models), several attempts to capture nearest-neighbor interactions by means of numerically tractable ODE systems have been done in literature in the past two decades.

In [Ric+03], periodic boundary conditions are considered, so that the model formally reduces to a two-spins Ising model, whose analytical solution is known [Cip87]. However, this approach is restricted only to the steady-state.

In [Cam+10], the authors assume periodic boundary conditions for the filament, so that a large number of states can be identified, being defined but for a translation of the filament. This reduces by an order of magnitude the number of states; however, this approach can still be applied to a limited number of units, due to its large computational cost.

In [Was+12], the authors developed a novel method to derive an approximate ODE model starting from a modification of the R03 model, comprising $N_A = 36$ CTMCs with 4 states each. They considered the FKE associated with each one of the N_A units, amounting to a total of $4N_A$ ODEs. Since the units are mutually coupled, at right-hand side they came across the joint probabilities of consecutive units, which have to be modelled for model closure. The joint probabilities were approximated by a function of the probabilities of single units assumed in the past times, ending up with an integro-differential system with memory. This model requires the determination of a number of coefficients, which were estimated with a least-squares fitting on the results of a collection of MC simulations, obtained with different calcium transients. In spite of the remarkable reduction of complexity, this approach features some drawbacks. It requires a long off-line phase for the estimation of coefficients, to be repeated any time the parameters of the underlying MC model are modified. Moreover, since the coefficients are fitted for very specific calcium transients, they are not guaranteed to be meaningful under different conditions.

In [LN15], a spatially detailed model incorporating both thin filaments kinetics and XB dynamics is proposed. The model includes $n = 26$ RUs, with allowed "unblocked" and "blocked" states, and $m = 69$ XBs, with allowed "unbound" and "bound" states. To reduce the complexity of the model, the authors identified the state of the model by the number of unblocked RUs and of bound XBs, lowering the number of states down to $(n + 1)(m + 1)$ in place of the original 2^{n+m}. To compute the free energy associated with a given state they had to sum over all possible configurations belonging to that state, for which they combined two reduction techniques. First, they grouped the 2^n thin filament states into 3 010 classes, according to the number and length of adjacent stretches of unblocked RUs, and they considered a single representative state for each class. Then, they computed the sum over all XBs configurations by using a MC approximation by random sampling.

2.2 Proposed model (activation-MH model)

In [RDQ18], we proposed a new model for the calcium-driven regulation of the cardiac muscle tissue, based on the spatially-explicit W12 model. Under physically motivated assumptions, the nearest-neighbor interactions within the units are described in our model by a tractable number (less than 2200) of ODEs. We notice that similar reduced models can be derived from other spatially-explicit models. Before showing the derivation of our model (in Sec. 2.2.2), we present, in Sec. 2.2.1, the W12 model, on which our model is based.

2.2.1 Description of the full order model: the W12 model

In this section we illustrate the model of sarcomere dynamics that was firstly proposed in [Ric+03] (R03 model) and later modified in [Was+12] (W12 model) to account for

the dependence of the dynamics on the elongation of the sarcomere. In order to avoid possible confusion, we recall that in [Was+12] two different models are actually proposed. The first one (that we denote as W12 model) is a CTMC model that requires the MC method for its numerical approximation. The second one is the reduced ODE model mentioned in Sec. 2.1.5. The model considered in this section is the first of the two.

We point out that in the W12 model of the calcium-driven regulatory mechanism is associated with the thick filament, rather than with the thin filament, the latter being actually responsible for such mechanism [Ber01]. In the original paper [Was+12] this association is motivated by the fact that the spacing between two consecutive MHs is similar to the one between two consecutive RUs (about 43 nm and 38 nm respectively, see e.g. [Ber01; KS09]). Moreover, the model does not encode the description of the states of both filaments, but just of a single one; therefore, there is no need to track which unit on the one filament faces which unit on the other. The unique effect of filaments sliding which directly affects the model is the modification of the overlap region. Nevertheless, when the filaments mutually slide, the length of the overlap region is the same either if viewed from one filament or from the other.

The above considerations suggest that the modeling choice made in [Was+12] should yield just a small modeling error. Nevertheless, this modeling choice is not formally correct, thus a careful validation of the experimental results is needed. However, an extensive validation of the original model, because of the large computational cost of the MC method (more than three days to simulate a single heart beat on a single core Intel i7-65000U laptop), would be unaffordable. Therefore, by exploiting the large reduction of computational cost of our reduced model, which allows to reduce the computational time by more than 10 000 times, we compare experimental data with the results of our model by repeating the tests made in [Was+12] and by exploring additional experimental settings (see Sec.2.3).

In Section 2.4 we propose a modification of the W12 model to better account for more realistic hypotheses according to which the calcium-driven regulatory mechanism is associated with the thin filament, instead of the thick one. We will show that, coherently with the above observations, the results of the model are not significantly affected by this modification. Therefore, in the following we will keep using the original W12 model, so that a direct comparison of the results obtained by means of the reduced model with those reported in the original paper can be carried out.

The sarcomere representation is depicted in Fig. 2.2. The model considers a single thick filament (MF) and two thin filaments (AFs). Thanks to the symmetry of the model, we consider just half sarcomere. The current sarcomere length (SL), which is an input parameter of our model, determines the mutual superimposition between the AFs and the MF. Along the MF, at each side of the H-zone, N_M MHs are placed at regular intervals. Depending on SL, each MH can face either no AFs, or a single AF (which is the most favourable condition for XBs to formate), or two AFs. As anticipated, following [Was+12] we here make a RU coincide with each MH.

As in the R03 model, the state of each RU is determined by the calcium binding state ($\mathcal{U}$ stands for *unbound*, while $\mathcal{B}$ for *bound*) and XB permissivity ($\mathcal{N}$ stands for *non-permissive*, $\mathcal{P}$ for *permissive*). The transition rates between the 4 possible states, whose set will be denoted by $\mathcal{S} = \{\mathcal{UN}, \mathcal{BN}, \mathcal{UP}, \mathcal{BP}\}$, are summarized in Fig. 2.3 and depend on the free calcium concentration (high concentrations favour the transition $\mathcal{U} \to \mathcal{B}$), the number of opposite AFs (through the RU index i and the variable SL), and $n \in \{0, 1, 2\}$, namely the number of adjacent heads in permissive state. The last dependence is responsible for the cooperative mechanism: a large value of n favours

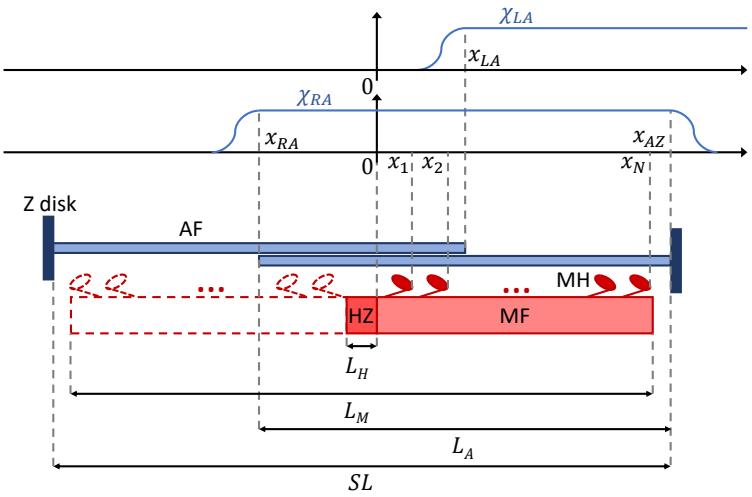

Figure 2.2: Sketch of the sarcomere model described in Sec. 2.2.1. The thick filament (MF) is represented in red and two thin filaments (AF) are represented in blue (mid). A reference system is placed with the origin at the right-hand side of the H-zone (HZ). The functions χ_{LA} and χ_{RA}, indicating respectively the region at the right of the left AF, and the region covered by the right AF, are represented (top). The length of the H-zone (L_H), of the thick filament (L_M), of a thin filament (L_A), and of the sarcomere (SL) are also depicted (bottom).

the transition $\mathcal{N} \to \mathcal{P}$ and hinders the opposite transition. The RUs located at the end of the filament, that have only one neighboring unit, behave as the missing neighbor is in state $\mathcal{N}$.

Henceforth, we will denote by $n(\xi, \eta)$ the number of permissive states among $\xi \in \mathcal{S}$ and $\eta \in \mathcal{S}$. The transition rate of the i-th RU from a generic state $\beta \in \mathcal{S}$ to the state $\alpha \in \mathcal{S} \setminus \{\beta\}$, knowing that the two adjacent heads are in the states $\xi \in \mathcal{S}$ and $\eta \in \mathcal{S}$ respectively, is denoted by:

$$k_i^{\beta\alpha|\xi\eta}([\mathrm{Ca}^{2+}]_\mathrm{i}, SL). \tag{2.3}$$

To avoid possible confusion to the reader, we recall that, while the subscript i of k_i refers to the unit index, the subscript i of $[\mathrm{Ca}^{2+}]_\mathrm{i}$ stands for "intracellular". By identifying the states $\mathcal{UN}$, $\mathcal{BN}$, $\mathcal{BP}$, $\mathcal{UP}$ with the indexes 1,2,3 and 4, respectively, the transition rates, illustrated in Fig. 2.3, are given by:

$$k_i^{\beta\alpha|\xi\eta}([\mathrm{Ca}^{2+}]_\mathrm{i}, SL) = \mathbf{A}_{\alpha\beta}([\mathrm{Ca}^{2+}]_\mathrm{i}, SL, i, n(\xi, \eta)),$$

for $1 \le \alpha, \beta \le 4$ and $\alpha \neq \beta$, where the matrix $\mathbf{A}$ is defined as:

$$\mathbf{A}\left([\mathrm{Ca}^{2+}]_\mathrm{i}, SL, i, n\right) = \begin{bmatrix} 0 & k_\mathrm{off} & 0 & \gamma^{-n} k_\mathrm{pn0} \\ \overline{k}_\mathrm{on}(SL, i)[\mathrm{Ca}^{2+}]_\mathrm{i} & 0 & \gamma^{-n} k_\mathrm{pn1} & 0 \\ 0 & \gamma^{n} \overline{k}_\mathrm{np1}(SL, i) & 0 & \overline{k}'_\mathrm{on}(SL, i)[\mathrm{Ca}^{2+}]_\mathrm{i} \\ \gamma^{n} \overline{k}_\mathrm{np0}(SL, i) & 0 & k'_\mathrm{off} & 0 \end{bmatrix}.$$

In the following, we provide formulae for the involved quantities. The values of the constants are reported in Table 2.1.

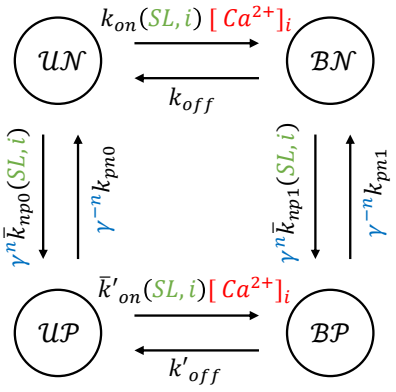

Figure 2.3: The cooperative four states CTMC of the W12 model. The terms depending on the intracellular calcium concentration $[\mathrm{Ca}^{2+}]_\mathrm{i}$ are highlighted in red; terms depending on the state of neighbouring RUs (i.e. depending on n) are highlighted in blue; terms depending on the position of the RU and the current sarcomere elongation are highlighted in green.

$$
\begin{aligned}
\overline{k}_{\mathrm{np0}}(SL,i) &= \chi_{LA}(SL,i)\chi_{RA}(SL,i)k_{\mathrm{np0}},\\
\overline{k}_{\mathrm{on}}(SL,i) &= \chi_{RA}(SL,i)k_{\mathrm{on}},\\
\overline{k}_{\mathrm{np1}}(SL,i) &= \chi_{LA}(SL,i)\chi_{RA}(SL,i)k_{\mathrm{np1}},\\
\overline{k}'_{\mathrm{on}}(SL,i) &= \chi_{RA}(SL,i)k'_{\mathrm{on}};
\end{aligned}
\tag{2.4}
$$

$$
x_{AZ} = (SL - L_H)/2, \qquad x_{LA} = L_A - x_{AZ} - L_H,
$$
$$
x_{RA} = x_{AZ} - L_A, \qquad x_i = \frac{(L_M - L_H)}{2\,N_M} i;
$$

$$
\chi_{RA}(SL,i) = \begin{cases} \exp\left(-\frac{(x_{RA}-x_i)^2}{\varepsilon_{SL}^2}\right) & x_i \le x_{RA} \\ 1 & x_{RA} < x_i < x_{AZ} \\ \exp\left(-\frac{(x_i-x_{AZ})^2}{\varepsilon_{SL}^2}\right) & x_i \ge x_{AZ}, \end{cases}
$$
$$
\chi_{LA}(SL,i) = \begin{cases} \exp\left(-\frac{(x_{LA}-x_i)^2}{\varepsilon_{SL}^2}\right) & x_i \le x_{LA} \\ 1 & x_i > x_{LA}, \end{cases}
$$
$$
Q(SL) = \begin{cases} Q_0 & SL \ge SL_Q \\ Q_0 - \alpha_Q(SL_Q - SL) & SL < SL_Q; \end{cases}
$$

$$
k_{\mathrm{np0}} = Qk_{\mathrm{basic}}/\mu, \qquad k_{\mathrm{np1}} = Qk_{\mathrm{basic}},
$$
$$
k_{\mathrm{pn0}} = k_{\mathrm{basic}}\gamma^2, \qquad k_{\mathrm{pn1}} = k_{\mathrm{basic}}\gamma^2,
$$
$$
k'_{\mathrm{on}} = k_{\mathrm{on}}, \qquad k'_{\mathrm{off}} = k_{\mathrm{off}}/\mu\,.
$$

Parameter	Value	Units	Parameter	Value	Units
Sarcomere geometry			**Transition rates permissivity**		
L_A (length of AF)	1.2	µm	Q_0	3	–
L_M (length of MF)	1.65	µm	SL_Q	2.2	µm
L_H (length of H-zone)	0.1	µm	α_Q	1.4	μm^{-1}
N_M (number of MHs)	36	–	k_{basic}	10	s^{-1}
Transition rates Ca binding			μ	10	–
k_{on}	80	$\mu\text{M}^{-1}\,\text{s}^{-1}$	γ	40	–
k_{off}	80	s^{-1}	SL **dependence**		
k'_{on}	80	$\mu\text{M}^{-1}\,\text{s}^{-1}$	ε_{SL}	0.1	µm
k'_{off}	8	s^{-1}			

Table 2.1: Model parameters; values taken from [Was+12].

Following [Ric+03] we assume that, when the fraction of RUs in permissive state is equal to one, all XBs can cycle, leading to the maximum amount of generated force (the normalized force equals one). On the other hand, when none of the RUs is in a permissive state (i.e. all RUs are in state $\mathcal{N}$), the active force cannot be generated, since XBs cannot cycle. For the intermediate levels of permissivity the amount of generated force is assumed to be proportional to the fraction of permissive heads, since each cycling XB is assumed to produce a fixed amount of force. Therefore, denoting by $P(t)$ the permissivity (i.e. fraction of RUs in permissive state) at time t and by $T_{\text{a}}(t)$ the active force, we have a law of the following type:

$$T_{\text{a}}(t) = T_{\text{a}}^{\max} P(t), \tag{2.5}$$

where $T_{\text{a}}^{\max}$ is the maximal exerted force.

2.2.2 A reduced ODE model for sarcomere dynamics

The FKE provides a way to compute the exact evolution of the probability of each of the 4^{N_M} states of this model. However, the practical resolution of this equation is infeasible because of the huge number of degrees of freedom: for $N_M = 36$ units we have $4^{N_M} \simeq 5 \cdot 10^{21}$ degrees of freedom. However, we are not interested in the joint probability of the states of the N_M units, but rather in the expected value of the number of RUs in permissive states (see Eq. (2.5)). Therefore, instead of studying the evolution of the probabilities of each elementary event in the state space, we look for a smaller set of events, still able of providing an expression for the permissivity $P(t)$. Then, we look for an equation for the evolution of the probabilities associated with such events.

We consider a collection of stochastic processes $R_i^t \in \mathcal{S}$ and we define the following notation to denote events at a given time in a compact way:

$$(\alpha, \overset{i}{\beta}, \delta)^t := \{R_{i-1}^t = \alpha, R_i^t = \beta, R_{i+1}^t = \delta\},$$
$$(\alpha, \overset{i}{\beta})^t := \{R_{i-1}^t = \alpha, R_i^t = \beta\},$$
$$(\alpha, \beta, \overset{i}{\delta}, \eta)^t := \{R_{i-2}^t = \alpha, R_{i-1}^t = \beta, R_i^t = \delta, R_{i+1}^t = \eta\}.$$

Since the transition rates of the i-th unit are fully determined by the states of the triplet centred in i, it is reasonable to assume that the set of all the joint probabilities of triplets of consecutive RUs provides an effective portrait of the state of the whole system. Therefore, we consider events of the kind:

$$(\alpha, \overset{i}{\beta}, \delta)^t \quad \text{with } i = 2, \dots, N_M - 1 \text{ and } \alpha, \beta, \delta \in \mathcal{S}. \tag{2.6}$$

We notice that this set of events allows to compute the permissivity (i.e. the fraction of RUs in permissive state) as follows:

$$\begin{aligned} P(t) &= \frac{1}{N_M} \sum_{i=1}^{N_M} \mathbb{P}\left(R_i^t \in \{\mathcal{UP}, \mathcal{BP}\}\right) \\ &= \frac{1}{N_M} \sum_{\substack{\alpha,\delta \in \mathcal{S} \\ \beta \in \{\mathcal{UP},\mathcal{BP}\}}} \left[\mathbb{P}((\beta, \overset{2}{\alpha}, \delta)^t) + \sum_{i=2}^{N_M-1} \mathbb{P}((\alpha, \overset{i}{\beta}, \delta)^t) + \mathbb{P}((\alpha, \overset{N_M-1}{\delta}, \beta)^t) \right]. \end{aligned} \tag{2.7}$$

The time evolution of the probability of such events is given, thanks to the Bayes formula [Nor98], by the following relation, holding for all $i = 2, \dots, N_M - 1$:

$$\begin{aligned} \mathbb{P}((\alpha, \overset{i}{\beta}, \delta)^{t+\Delta t}) &= \mathbb{P}((\alpha, \overset{i}{\beta}, \delta)^{t+\Delta t} | (\alpha, \overset{i}{\beta}, \delta)^t)\, \mathbb{P}((\alpha, \overset{i}{\beta}, \delta)^t) \\ &+ \sum_{\eta \in \mathcal{S}\setminus\{\alpha\}} \mathbb{P}((\alpha, \overset{i}{\beta}, \delta)^{t+\Delta t} | (\eta, \overset{i}{\beta}, \delta)^t)\, \mathbb{P}((\eta, \overset{i}{\beta}, \delta)^t) \\ &+ \sum_{\eta \in \mathcal{S}\setminus\{\beta\}} \mathbb{P}((\alpha, \overset{i}{\beta}, \delta)^{t+\Delta t} | (\alpha, \overset{i}{\eta}, \delta)^t)\, \mathbb{P}((\alpha, \overset{i}{\eta}, \delta)^t) \\ &+ \sum_{\eta \in \mathcal{S}\setminus\{\delta\}} \mathbb{P}((\alpha, \overset{i}{\beta}, \delta)^{t+\Delta t} | (\alpha, \overset{i}{\beta}, \eta)^t)\, \mathbb{P}((\alpha, \overset{i}{\beta}, \eta)^t) + o(\Delta t)\ . \end{aligned} \tag{2.8}$$

In the following, we show how the conditional probabilities in Eq. (2.8) can be evaluated. The probability of transition of the central RU of the triplet is given, by definition of transition rate, by the following formula, where $i = 2, \dots, N_M - 1$ and $\eta \neq \beta$:

$$\mathbb{P}((\alpha, \overset{i}{\beta}, \delta)^{t+\Delta t} | (\alpha, \overset{i}{\eta}, \delta)^t) = k_i^{\eta\beta|\alpha\delta}\, \Delta t + o(\Delta t)\ .$$

On the other hand, the probability of transition of the outer RUs of the triplet cannot be computed as a function of probabilities of events in the form of (2.6). However,

this can be approximated as follows ($i = 3, \ldots, N_M - 1$ and $\eta \neq \alpha$):

$$
\begin{aligned}
&\mathbb{P}((\alpha, \overset{i}{\beta}, \delta)^{t+\Delta t} | (\eta, \overset{i}{\beta}, \delta)^t) \\
&= \frac{\mathbb{P}((\alpha, \overset{i}{\beta}, \delta)^{t+\Delta t} \cap (\eta, \overset{i}{\beta}, \delta)^t)}{\mathbb{P}((\eta, \overset{i}{\beta}, \delta)^t)} \\
&= \frac{\sum_{\xi \in \mathcal{S}} \mathbb{P}((\xi, \alpha, \overset{i}{\beta}, \delta)^{t+\Delta t} \cap (\xi, \eta, \overset{i}{\beta}, \delta)^t)}{\mathbb{P}((\eta, \overset{i}{\beta}, \delta)^t)} + o(\Delta t) \\
&= \frac{\sum_{\xi \in \mathcal{S}} \mathbb{P}((\xi, \alpha, \overset{i}{\beta}, \delta)^{t+\Delta t} | (\xi, \eta, \overset{i}{\beta}, \delta)^t) \, \mathbb{P}((\xi, \eta, \overset{i}{\beta}, \delta)^t)}{\mathbb{P}((\eta, \overset{i}{\beta}, \delta)^t)} + o(\Delta t) \\
&= \sum_{\xi \in \mathcal{S}} \left[\mathbb{P}((\xi, \alpha, \overset{i}{\beta})^{t+\Delta t} | (\xi, \eta, \overset{i}{\beta})^t) \, \mathbb{P}((\overset{i+1}{\delta})^t | (\xi, \eta, \overset{i}{\beta})^t) \frac{\mathbb{P}((\xi, \eta, \overset{i}{\beta})^t)}{\mathbb{P}((\eta, \overset{i}{\beta}, \delta)^t)} \right] + o(\Delta t) \, .
\end{aligned}
$$

At this stage, we make the following assumption:

$$
\mathbb{P}((\overset{i}{\delta})^t | (\xi, \eta, \overset{i-1}{\beta})^t) \simeq \mathbb{P}((\overset{i}{\delta})^t | (\eta, \overset{i-1}{\beta})^t) \, . \tag{2.9}
$$

This is equivalent to assume that the knowledge of the $(i-3)$-th RU does not provide any additional information about the probability distribution of the i-th head beyond the knowledge of the state of the $(i-1)$-th and the $(i-2)$-th head. We will return again to this concept later in Sec. 2.2.5.

Using assumption (2.9), the calculation leads to the following result:

$$
\begin{aligned}
&\mathbb{P}((\alpha, \overset{i}{\beta}, \delta)^{t+\Delta t} | (\eta, \overset{i}{\beta}, \delta)^t) \\
&\simeq \sum_{\xi \in \mathcal{S}} \left[\mathbb{P}((\xi, \alpha, \overset{i}{\beta})^{t+\Delta t} | (\xi, \eta, \overset{i}{\beta})^t) \, \mathbb{P}((\overset{i+1}{\delta})^t | (\eta, \overset{i}{\beta})^t) \frac{\mathbb{P}((\xi, \eta, \overset{i}{\beta})^t)}{\mathbb{P}((\eta, \overset{i}{\beta}, \delta)^t)} \right] + o(\Delta t) \\
&= \frac{\sum_{\xi \in \mathcal{S}} \mathbb{P}((\xi, \alpha, \overset{i}{\beta})^{t+\Delta t} | (\xi, \eta, \overset{i}{\beta})^t) \, \mathbb{P}((\xi, \eta, \overset{i}{\beta})^t)}{\mathbb{P}((\eta, \overset{i}{\beta})^t)} + o(\Delta t) \\
&= \frac{\sum_{\xi \in \mathcal{S}} k_{i-1}^{\eta\alpha|\xi\beta} \, \mathbb{P}((\xi, \overset{i-1}{\eta}, \beta)^t)}{\sum_{\xi \in \mathcal{S}} \mathbb{P}((\xi, \overset{i-1}{\eta}, \beta)^t)} \Delta t + o(\Delta t) \, .
\end{aligned}
$$

Remark 2.1. The same result can be equivalently obtained by proceeding as follows:

$$\begin{aligned}
\mathbb{P}((\alpha,\overset{i}{\beta},\delta)^{t+\Delta t}|(\eta,\overset{i}{\beta},\delta)^t) &= \mathbb{P}((\alpha,\overset{i}{\beta})^{t+\Delta t}|(\eta,\overset{i}{\beta},\delta)^t) + o(\Delta t)\\
&\simeq \mathbb{P}((\alpha,\overset{i}{\beta})^{t+\Delta t}|(\eta,\overset{i}{\beta})^t) + o(\Delta t)\\
&= \frac{\mathbb{P}((\alpha,\overset{i}{\beta})^{t+\Delta t}\cap(\eta,\overset{i}{\beta})^t)}{\mathbb{P}((\eta,\overset{i}{\beta})^t)} + o(\Delta t)\\
&= \frac{\sum_{\xi\in\mathcal{S}}\mathbb{P}((\xi,\alpha,\overset{i}{\beta})^{t+\Delta t}\cap(\xi,\eta,\overset{i}{\beta})^t)}{\sum_{\xi\in\mathcal{S}}\mathbb{P}((\xi,\eta,\overset{i}{\beta})^t)} + o(\Delta t)\\
&= \frac{\sum_{\xi\in\mathcal{S}}\mathbb{P}((\xi,\overset{i-1}{\alpha},\beta)^{t+\Delta t}|(\xi,\overset{i-1}{\eta},\beta)^t)\,\mathbb{P}((\xi,\overset{i-1}{\eta},\beta)^t)}{\sum_{\xi\in\mathcal{S}}\mathbb{P}((\xi,\overset{i-1}{\eta},\beta)^t)} + o(\Delta t)\,.
\end{aligned}$$

Here we made the approximation that the transition rate of the $(i-1)$-th head does not depend on the state of the $(i+1)$-th one. Nonetheless, we are neglecting the fact that the knowledge of the $(i+1)$-th head may provide information about the state of the $(i-2)$-th head, and in turn on the transition rate of the $(i-1)$-th head. This approximation is coherent with assumption (2.9).

With similar arguments, the following formula for the transition probability of the right RU of the triplet is recovered for $i=2,\dots,N_M-2$ and $\eta\neq\delta$:

$$\mathbb{P}((\alpha,\overset{i}{\beta},\delta)^{t+\Delta t}|(\alpha,\overset{i}{\beta},\eta)^t) \simeq \frac{\sum_{\xi\in\mathcal{S}}k_{i+1}^{\eta\delta|\beta\xi}\mathbb{P}((\beta,\overset{i+1}{\eta},\xi)^t)}{\sum_{\xi\in\mathcal{S}}\mathbb{P}((\beta,\overset{i+1}{\eta},\xi)^t)}\Delta t + o(\Delta t)\,.$$

The probabilities of transition of the outer RUs of the first and last triplets, on the other hand, are exactly determined as:

$$\begin{aligned}
\mathbb{P}((\overset{1}{\alpha},\beta,\delta)^{t+\Delta t}|(\overset{1}{\eta},\beta,\delta)^t) &= \Delta t\,k_1^{\eta\alpha|(\mathcal{UN})\beta} + o(\Delta t)\,,\\
\mathbb{P}((\alpha,\beta,\overset{N_M}{\delta})^{t+\Delta t}|(\alpha,\beta,\overset{N_M}{\eta})^t) &= \Delta t\,k_{N_M}^{\eta\delta|\beta(\mathcal{UN})} + o(\Delta t)\,.
\end{aligned}$$

Finally, we calculate the probability that a triplet does not change state in the time interval $(t,t+\Delta t)$. We have for $i=2,\dots,N_M-1$:

$$\begin{aligned}
\mathbb{P}((\alpha,\overset{i}{\beta},\delta)^{t+\Delta t}|(\alpha,\overset{i}{\beta},\delta)^t) = 1 &- \sum_{\eta\in\mathcal{S}\setminus\{\alpha\}}\mathbb{P}((\eta,\overset{i}{\beta},\delta)^{t+\Delta t}|(\alpha,\overset{i}{\beta},\delta)^t)\\
&- \sum_{\eta\in\mathcal{S}\setminus\{\beta\}}\mathbb{P}((\alpha,\overset{i}{\eta},\delta)^{t+\Delta t}|(\alpha,\overset{i}{\beta},\delta)^t)\\
&- \sum_{\eta\in\mathcal{S}\setminus\{\delta\}}\mathbb{P}((\alpha,\overset{i}{\beta},\eta)^{t+\Delta t}|(\alpha,\overset{i}{\beta},\delta)^t) + o(\Delta t)\,,
\end{aligned}$$

where each term have been previously calculated.

To sum up, by dividing Eq. (2.8) by Δt and taking the limit $\Delta t\to 0$, we obtain the following nonlinear system of ODEs, for $i=2,\dots,N_M-1$ (notice that $i=1$ and

$i = N_M$ are not comprised since no triplet is centred in the outer RUs):

$$\begin{aligned}\frac{d}{dt}\mathbb{P}((\alpha,\overset{i}{\beta},\delta)^t) = &\sum_{\eta\in\mathcal{S}\setminus\{\alpha\}} \left[\Phi_L^i(\eta,\beta,\delta;\alpha;t) - \Phi_L^i(\alpha,\beta,\delta;\eta;t)\right] \\ &+ \sum_{\eta\in\mathcal{S}\setminus\{\beta\}} \left[\Phi_C^i(\alpha,\eta,\delta;\beta;t) - \Phi_C^i(\alpha,\beta,\delta;\eta;t)\right] \\ &+ \sum_{\eta\in\mathcal{S}\setminus\{\delta\}} \left[\Phi_R^i(\alpha,\beta,\eta;\delta;t) - \Phi_R^i(\alpha,\beta,\delta;\eta;t)\right] ,\end{aligned} \tag{2.10}$$

endowed with initial conditions, where we defined the following probability fluxes, for $i = 2,\dots,N_M-1$:

$$\begin{aligned}&\Phi_C^i(\alpha,\beta,\delta;\eta;t) = k_i^{\beta\eta|\alpha\delta}\mathbb{P}((\alpha,\overset{i}{\beta},\delta)^t)\,; \\ &\Phi_L^i(\alpha,\beta,\delta;\eta;t) = \begin{cases} \dfrac{\sum_{\xi\in\mathcal{S}} k_{i-1}^{\alpha\eta|\xi\beta}\mathbb{P}((\xi,\overset{i-1}{\alpha},\beta)^t)\,\mathbb{P}((\alpha,\overset{i}{\beta},\delta)^t)}{\sum_{\xi\in\mathcal{S}}\mathbb{P}((\xi,\overset{i-1}{\alpha},\beta)^t)} & \text{for } i = 3,\dots,N_M-1, \\ k_1^{\alpha\eta|(\mathcal{UN})\beta}\mathbb{P}((\alpha,\overset{i}{\beta},\delta)^t) & \text{for } i = 2; \end{cases} \\ &\Phi_R^i(\alpha,\beta,\delta;\eta;t) = \begin{cases} \dfrac{\sum_{\xi\in\mathcal{S}} k_{i+1}^{\delta\eta|\beta\xi}\mathbb{P}((\beta,\overset{i+1}{\delta},\xi)^t)\,\mathbb{P}((\alpha,\overset{i}{\beta},\delta)^t)}{\sum_{\xi\in\mathcal{S}}\mathbb{P}((\beta,\overset{i+1}{\delta},\xi)^t)} & \text{for } i = 2,\dots,N_M-2, \\ k_{N_M}^{\delta\eta|\beta(\mathcal{UN})}\mathbb{P}((\alpha,\overset{i}{\beta},\delta)^t) & \text{for } i = N_M-1. \end{cases}\end{aligned} \tag{2.11}$$

When the rates in the definitions of Φ_L and Φ_R turn out to be $\frac{0}{0}$, these are set by convention equal to 0, coherently with the definition of conditional probability. We notice that Eq. (2.10), henceforth referred to as *reduced ODE model* (or *activation-MH model*, to distinguish it from the alternative formulations that we will present in Sec. 2.4), is a system of nonlinear ODEs, while the FKE is a system of linear ODEs. The pay-off is that the size of the system is dramatically reduced, as we switch from the $4^{N_M} \simeq 5\cdot 10^{21}$ dofs of the full FKE to the $N = (N_M-2)\cdot 4^3 = 2176$ dofs of the reduced model (2.10).

We notice that, thanks to the fact that, for any $i = 2,\dots,N_M$ and for any $\alpha,\beta\in\mathcal{S}$ we have:

$$\sum_{\xi\in\mathcal{S}}\mathbb{P}((\xi,\overset{i-1}{\alpha},\beta)^t) = \sum_{\xi\in\mathcal{S}}\mathbb{P}((\alpha,\overset{i}{\beta},\xi)^t), \tag{2.12}$$

Eq. (2.10) can be equivalently rewritten as:

$$\begin{aligned}\frac{d}{dt}\mathbb{P}((\alpha,\overset{i}{\beta},\delta)^t) = &\sum_{\eta\in\mathcal{S}\setminus\{\alpha\}} \left[\widetilde{\Phi}_L^i(\eta,\beta,\delta;\alpha;t) - \widetilde{\Phi}_L^i(\alpha,\beta,\delta;\eta;t)\right] \\ &+ \sum_{\eta\in\mathcal{S}\setminus\{\beta\}} \left[\Phi_C^i(\alpha,\eta,\delta;\beta;t) - \Phi_C^i(\alpha,\beta,\delta;\eta;t)\right] \\ &+ \sum_{\eta\in\mathcal{S}\setminus\{\delta\}} \left[\widetilde{\Phi}_R^i(\alpha,\beta,\eta;\delta;t) - \widetilde{\Phi}_R^i(\alpha,\beta,\delta;\eta;t)\right] ,\end{aligned} \tag{2.13}$$

where

$$\widetilde{\Phi}_L^i(\alpha,\beta,\delta;\eta;t) = \begin{cases} \dfrac{\sum_{\xi\in\mathcal{S}} k_{i-1}^{\alpha\eta|\xi\beta}\mathbb{P}((\xi,\overset{i-1}{\alpha},\beta)^t)\,\mathbb{P}((\alpha,\overset{i}{\beta},\delta)^t)}{\sum_{\xi\in\mathcal{S}}\mathbb{P}((\alpha,\overset{i}{\beta},\xi)^t)} & \text{for } i=3,\dots,N_M-1, \\ k_1^{\alpha\eta|(\mathcal{UN})\beta}\mathbb{P}((\alpha,\overset{i}{\beta},\delta)^t) & \text{for } i=2; \end{cases}$$

$$\widetilde{\Phi}_R^i(\alpha,\beta,\delta;\eta;t) = \begin{cases} \dfrac{\sum_{\xi\in\mathcal{S}} k_{i+1}^{\delta\eta|\beta\xi}\mathbb{P}((\beta,\overset{i+1}{\delta},\xi)^t)\,\mathbb{P}((\alpha,\overset{i}{\beta},\delta)^t)}{\sum_{\xi\in\mathcal{S}}\mathbb{P}((\xi,\overset{i}{\beta},\delta)^t)} & \text{for } i=2,\dots,N_M-2, \\ k_{N_M}^{\delta\eta|\beta(\mathcal{UN})}\mathbb{P}((\alpha,\overset{i}{\beta},\delta)^t) & \text{for } i=N_M-1. \end{cases} \tag{2.14}$$

2.2.3 Analysis of the continuous model

Both Eqs. (2.10) and (2.13) can be written in the following form:

$$\begin{cases} \dfrac{d\mathbf{z}(t)}{dt} = \mathbf{\Phi}(\mathbf{z}(t),t) & t\in[0,T], \\ \mathbf{z}(0)=\mathbf{z}_0, \end{cases} \tag{2.15}$$

where the state vector $\mathbf{z}(t)\in\mathbb{R}^N$ is defined as:

$$\mathbf{z}(t) = \left\{ \mathbb{P}((\alpha,\overset{i}{\beta},\delta)^t)\colon i=2,\dots,N_M-1, \quad \alpha,\beta,\delta\in\mathcal{S} \right\}. \tag{2.16}$$

We notice that the right-hand side of Eq. (2.15) depends on time since the transition rates are function of the two time-dependent inputs $[\mathrm{Ca}^{2+}]_\mathrm{i}(t)$ and $SL(t)$.

The elements of the state vector $\mathbf{z}(t)$ represent probabilities and, thus, they are physically meaningful only if $\mathbf{z}(t)\in[0,1]^N$. Moreover, the events associated to the different elements of the vector $\mathbf{z}(t)$ are mutually related. Therefore, in order for $\mathbf{z}(t)$ to be consistent, the two conditions defined in the following (Defs. 2.1 and 2.2) should hold.

Definition 2.1. *We say that the collection of probabilities* $\mathbf{z}(t)$*, defined in Eq.* (2.16)*, satisfies the conservation of probability if, for all* $=2,\dots,N_M-1$ *it holds true:*

$$\sum_{\alpha,\beta,\delta\in\mathcal{S}} \mathbb{P}((\alpha,\overset{i}{\beta},\delta)^t) = 1. \tag{2.17}$$

Thanks to the linearity of Eq. (2.17)*, we introduce a matrix* $\mathbf{U}$ *and a vector* $\mathbf{b}$ *such that* $\mathbf{z}$ *satifies the conservation of probabilities if and only if:*

$$\mathbf{U}\mathbf{z} = \mathbf{b}. \tag{2.18}$$

Definition 2.2. *We say that the collection of probabilities* $\mathbf{z}(t)$*, defined in Eq.* (2.16)*, is self-consistent if it fulfils the following conditions:*

(a) $$\sum_{\beta,\delta\in\mathcal{S}} \mathbb{P}((\alpha,\overset{i}{\beta},\delta)^t) = \sum_{\xi,\beta\in\mathcal{S}} \mathbb{P}((\xi,\overset{i-1}{\alpha},\beta)^t) \qquad \textit{for all } i=3,\dots,N_M-1, \quad \alpha\in\mathcal{S}$$

$$(b)\ \sum_{\alpha,\beta\in\mathcal{S}} \mathbb{P}((\alpha,\overset{i}{\beta},\delta)^t) = \sum_{\beta,\xi\in\mathcal{S}} \mathbb{P}((\beta,\overset{i+1}{\delta},\xi)^t) \qquad \text{for all } i=2,\dots,N_M-2, \quad \delta\in\mathcal{S}$$

$$(c)\ \sum_{\delta\in\mathcal{S}} \mathbb{P}((\alpha,\overset{i}{\beta},\delta)^t) = \sum_{\xi\in\mathcal{S}} \mathbb{P}((\xi,\overset{i-1}{\alpha},\beta)^t) \qquad \text{for all } i=3,\dots,N_M-1, \quad \alpha,\beta\in\mathcal{S}$$

Thanks to the linearity of the conditions (a)–(c), we introduce a matrix $\mathbf{W}$ *such that* $\mathbf{z}$ *is self consistent if and only if:*

$$\mathbf{z}\in\mathrm{Ker}(\mathbf{W}). \tag{2.19}$$

Conditions (a)–(b) state that the marginal probabilities of single MHs, when computed in different ways by means of the joint probabilities of triplets, should lead to the same result. On the other hand, condition (c) states the same property about the joint probability of pairs of consecutive MHs. Therefore, we expect that, provided that the conservation of probability and self-consistency are satisfied at the initial time, those properties are maintained by the solution as time goes by.

In order to prove such property, we provide the following results (Props. 2.1 and 2.1), whose proof is reported in App. A.

Proposition 2.1. *The right-hand side* $\mathbf{\Phi}\colon \mathbb{R}^N\times\mathbb{R}\to\mathbb{R}^N$ *defined in Eq.* (2.10) *satisfies, for any* $t\geq 0$*:*

$$\begin{aligned}&\mathbf{\Phi}(\mathbf{z},t)\in\mathrm{Ker}(\mathbf{U}) \quad \forall\,\mathbf{z}\in\mathbb{R}^N,\\ &\mathbf{\Phi}(\mathbf{z},t)\in\mathrm{Ker}(\mathbf{W}) \quad \forall\,\mathbf{z}\in\mathrm{Ker}(\mathbf{W}).\end{aligned}$$

Proposition 2.2. *The right-hand side* $\mathbf{\Phi}\colon \mathbb{R}^N\times\mathbb{R}\to\mathbb{R}^N$ *defined in Eq.* (2.13) *satisfies, for any* $t\geq 0$*:*

$$\begin{aligned}&\mathbf{\Phi}(\mathbf{z},t)\in\mathrm{Ker}(\mathbf{U}) \quad \forall\,\mathbf{z}\in\mathbb{R}^N,\\ &\mathbf{\Phi}(\mathbf{z},t)\in\mathrm{Ker}(\mathbf{W}) \quad \forall\,\mathbf{z}\in\mathbb{R}^N.\end{aligned}$$

Moreover, the right-hand sides of both Eqs. (2.10) and (2.13) satisfy the following regularity property, on a set where the state $\mathbf{z}(t)$ is physically meaningful (we report its proof in App. A).

Proposition 2.3. *In the inputs* $[Ca^{2+}]_i(t)$ *and* $SL(t)$ *are uniformly bounded in* $[0,T]$*, then the right-hand sides* $\mathbf{\Phi}\colon \mathbb{R}^N\times\mathbb{R}\to\mathbb{R}^N$ *defined in Eqs.* (2.10) *and* (2.13) *are Lipschitz continuous is their first argument, uniformly in* t*, on the set* $\mathbf{z}\in\mathrm{Ker}(\mathbf{W})\cap[0,+\infty)^N$*. That is, there exists a constant* $L>0$ *such that:*

$$|\mathbf{\Phi}(\mathbf{z}_1,t)-\mathbf{\Phi}(\mathbf{z}_2,t)|\leq L\,|\mathbf{z}_1-\mathbf{z}_2| \qquad \forall\,\mathbf{z}_1,\mathbf{z}_1\in\mathrm{Ker}(\mathbf{W})\cap[0,+\infty)^N, \quad \forall\,t\in[0,T].$$

Finally, thanks to Props. 2.1, 2.2 and 2.3, it is possible to prove the following result, whose proof is provided in App. A.

Proposition 2.4. *Let us consider two functions* $[Ca^{2+}]_i(t)$ *and* $SL(t)$*, bounded in* $[0,T]$*, and an initial state* $\mathbf{z}_0\in\mathrm{Ker}(\mathbf{W})\cap[0,1]^N$*, satisfying* $\mathbf{U}\mathbf{z}_0=\mathbf{b}$*. Then, there exists a unique solution to Eqs.* (2.10) *and* (2.13) *such that* $\mathbf{z}(t)\in\mathrm{Ker}(\mathbf{W})\cap[0,1]^N$ *for any* $t\in[0,T]$*. Moreover, the solutions of Eqs.* (2.10) *and* (2.13) *coincide and they satisfy the conservation of probability (i.e.* $\mathbf{U}\mathbf{z}(t)=\mathbf{b}$ *for any* $t\in[0,T]$*).*

Therefore, we conclude that if the initial state $\mathbf{z}_0$ is physically meaningful (i.e. with probabilities contained in the interval $[0, T]$ and satisfying the conservation of probability and self-consistent), then there exists a unique physically meaningful solution of the model proposed in Sec. 2.2.2. Moreover, the solutions of Eqs. (2.10) and (2.13) coincide. Hence, in the following, we will indifferently refer to the two formulations of Eqs. (2.10) and (2.13).

2.2.4 Numerical approximation

To derive a numerical approximation of the model defined in Eqs. (2.10) and (2.13), we consider a uniform subdivision $0 = t_0 < t_1 < \cdots < t_M = T$ of the time interval $[0, T]$ with time step size Δt. We denote by $\mathbf{z}^{(k)} \approx \mathbf{z}(t_k)$ an approximation of the solution at the k-th time step. Let us consider a generic multistep scheme [QSS10]:

$$\begin{cases} \mathbf{z}^{(k)} = \mathbf{z}_k & \text{for } k = 0, \dots, p-1, \\ \mathbf{z}^{(k)} = \displaystyle\sum_{s=1}^{p} \alpha_s \mathbf{z}^{(k-s)} + \Delta t \sum_{s=0}^{p} \beta_s \mathbf{\Phi}(\mathbf{z}^{(k-s)}, t_{k-s}) & \text{for } k \geq pm. \end{cases} \tag{2.20}$$

The method is explicit if $\beta_0 = 0$, implicit otherwise. Clearly, if the method is consistent (in the sense of [QSS10]), then $\sum_{s=1}^{p} \alpha_s = 1$. We notice that the family of numerical schemes of Eq. (2.20) contains the explicit Euler method ($p = 1$, $\beta_0 = 0$, $\alpha_1 = \beta_1 = 1$), the implicit Euler method ($p = 1$, $\beta_1 = 0$, $\alpha_1 = \beta_0 = 1$), BDF (backward differentiation formulas) schemes and Adams-Bashforth methods [QSS10].

The numerical approximation of the model proposed in Sec. 2.2.2 should satisfy the following properties, in order to provide physically meaningful solutions.

Definition 2.3. *We say that a numerical scheme conserves probability if, in case the initial states satify the conservation of probabilities (i.e.* $\mathbf{U}\mathbf{z}_k = \mathbf{b}$ *for* $k = 0, \dots, p-1$*), then:*

$$\mathbf{U}\mathbf{z}^{(k)} = \mathbf{b} \qquad \text{for } k \geq p.$$

Furthermore, we say that a numerical scheme preserves self-consistency if, in case the initial states are self-consistent (i.e. $\mathbf{z}_k \in \mathrm{Ker}(\mathbf{W})$ *for* $k = 0, \dots, p-1$*), then:*

$$\mathbf{z}^{(k)} \in \mathrm{Ker}(\mathbf{W}) \qquad \text{for } k \geq p.$$

Even if the two formulations of Eqs. (2.10) and (2.13) are equivalent in the continuous setting (see Prop. 2.4), they could possibly lead to different results when their numerical approximations are considered. Nonetheless, we notice that, if a method preserves self-consistency, then the formulations (2.10) and (2.20) are equivalent, as the right-hand sides defined in the two cases coincide on the set $\mathrm{Ker}\,\mathbf{W}$.

Concerning the conservation of probability, the following result holds.

Proposition 2.5. *For both Eqs.* (2.10) *and* (2.13)*, any consistent method of the family of Eq.* (2.20) *(implicit or explicit) conserves probability.*

Proof. Let us suppose that, for some $r \geq 0$, we have $\mathbf{U}\mathbf{z}^{(r+k)} = \mathbf{b}$ for any $k = 0, \dots, p-1$. Then, by left-multiplying both sides of Eq. (2.20) by $\mathbf{U}$, we get:

$$\begin{aligned} \mathbf{U}\mathbf{z}^{(r+p)} &= \sum_{s=1}^{p} \alpha_s \mathbf{U}\mathbf{z}^{(r+p-s)} + \Delta t \sum_{s=0}^{p} \beta_s \mathbf{U}\mathbf{\Phi}(\mathbf{z}^{(r+p-s)}, t_{r+p-s}) \\ &= \sum_{s=1}^{p} \alpha_s \mathbf{b} = \mathbf{b}. \end{aligned}$$

where we have used the fact that, by Props. 2.1 and 2.2, $\mathbf{\Phi}(\mathbf{z}, t) \in \mathrm{Ker}(\mathbf{U})$ for any $\mathbf{z} \in \mathbb{R}^N$ and the fact that, since the method is consistent, $\sum_{s=1}^{p} \alpha_s = 1$. Then, by induction, we have that $\mathbf{U}\mathbf{z}^{(k)} = \mathbf{b}$ for any $k \geq p$. □

On the other hand, the conservation of self-consistency, for the methods of the family of Eq. (2.20), depend on the specific choice of the formulation (either Eq. (2.10) or Eq. (2.13)). Indeed, while the latter preserves self-consistency with both explicit and implicit methods, the former preserves self-consistency only with explicit schemes, as stated in the following result.

Proposition 2.6. *For Eq.* (2.10)*, any explicit method of the family of Eq.* (2.20) *preserves self-consistency. For Eq.* (2.13)*, any method of the family of Eq.* (2.20) *(implicit or explicit) preserves self-consistency.*

Proof. Let us suppose that, for some $r \geq 0$, we have $\mathbf{z}^{(r+k)} \in \mathrm{Ker}(\mathbf{W})$ for any $k = 0, \ldots, p-1$. Then, by left-multiplying both sides of Eq. (2.20) by $\mathbf{W}$, we have:

$$\begin{aligned}\mathbf{W}\mathbf{z}^{(r+p)} &= \sum_{s=1}^{p} \alpha_s \mathbf{W}\mathbf{z}^{(r+p-s)} + \Delta t \sum_{s=0}^{p} \beta_s \mathbf{W}\mathbf{\Phi}(\mathbf{z}^{(r+p-s)}, t_{r+p-s}) \\ &= \Delta t \sum_{s=0}^{p} \beta_s \mathbf{W}\mathbf{\Phi}(\mathbf{z}^{(r+p-s)}, t_{r+p-s}).\end{aligned}$$

Hence, in the case of Eq. (2.10), if the method is explicit (i.e. $\beta_0 = 0$), by Prop. 2.1 we get $\mathbf{W}\mathbf{z}^{(r+p)} = \mathbf{0}$. Similarly, in the case of Eq. (2.13), by Prop. 2.2 we get $\mathbf{W}\mathbf{z}^{(r+p)} = \mathbf{0}$ (both for explicit and for implicit schemes). Therefore, by induction, we have that $\mathbf{z}^{(k)} \in \mathrm{Ker}(\mathbf{W})$ for any $k \geq p$. □

An advantage of implicit methods lies in their better stability properties, compared to explicit methods, for which severe restrictions on the time step size may occur [QSS10]. However, the implicit schemes of the family of Eq. (2.20) require to solve a system of N nonlinear equations at each time iteration. Our tests showed that for this model, due to the high computational cost associated to the solution of such nonlinear systems, explicit schemes accomplish a better balance between accuracy and computationally efficiency than implicit schemes.

2.2.5 Model accuracy

In the derivation of Eq. (2.10), the following assumptions were made:

$$\begin{aligned}&\mathbb{P}(\overset{i}{(\delta)}^t | (\alpha, \beta, \overset{i-1}{\gamma})^t) \simeq \mathbb{P}(\overset{i}{(\delta)}^t | (\beta, \overset{i-1}{\gamma})^t), \\ &\mathbb{P}(\overset{i}{(\alpha)}^t | (\overset{i+1}{\beta}, \gamma, \delta)^t) \simeq \mathbb{P}(\overset{i}{(\alpha)}^t | (\overset{i+1}{\beta}, \gamma)^t).\end{aligned} \tag{2.21}$$

As we already mentioned (Sec. 2.2.2), hypotheses (2.21) can be interpreted as follows: if one is interested in the probability distribution of a single RU, the knowledge of the state of a RU at distance of three heads does not provide any information beyond that provided by the knowledge of the two intermediate RUs. A compact way to express this notion is to say that, at each time instant t, the states of RUs at distance of three heads are *conditionally independent* given the states of the two intermediate RUs, which reads in symbols (see [Daw79]):

$$X_t^i \perp\!\!\!\perp X_t^{i+3} | (X_t^{i+1}, X_t^{i+2}), \qquad \forall\, t > 0, \text{ for } i = 1, \ldots, N_M - 3. \tag{2.22}$$

Variable	Value	Units	Variable	Value	Units
Dynamics of $[Ca^{2+}]_i$			**Dynamics of SL**		
c_0	0.1	μM	SL_0	2.2	μm
$c_{\max}$	1.1	μM	γ_f^{max}	-0.07	$-$
t_0^c	0.1	s	t_0^{SL}	0.15	s
τ_1^c	0.02	s	t_1^{SL}	0.55	s
τ_2^c	0.11	s	τ_0^{SL}	0.05	s
			τ_1^{SL}	0.02	s

Table 2.2: Constants associated with the dynamics of $[Ca^{2+}]_i$ and SL; values of the constants for $[Ca^{2+}]_i$ taken from [Was+12]; values for SL set to reproduce a realistic SL transient.

We notice that the assumption of conditional independence is different than that of pure independence: RUs at distance of three heads are not independent in fact; on the contrary these are strongly correlated (by observing MC simulations it is evident that the typical correlation length is much larger than 3). The assumption we are making is that the i-th head is correlated to the $i+3$-th head because these are correlated with the $(i+1)$-th and to the $(i+2)$-th respectively, which are correlated to each other. In other words, we are supposing that the correlation of distant RUs is mediated by the states of the RUs located in-between. This is coherent with the physics of the model, as we are assuming that the transition rates of RUs are affected only by adjacent units.

In order to assess the accuracy of this approximation, we consider a short filament (with $N_M = 6$ heads instead of 36), so that the solution of the full FKE can be numerically approximated. We impose the following $[Ca^{2+}]_i$ and SL transients (the former taken from [Was+12]):

$$[Ca^{2+}]_i(t) = \begin{cases} c_0 & t < t_0^c, \\ c_0 + \frac{c_{\max}-c_0}{\beta}\left[e^{-\frac{t-t_0^c}{\tau_1^c}} - e^{-\frac{t-t_0^c}{\tau_2^c}}\right] & t \geq t_0^c\,, \end{cases} \tag{2.23}$$

where

$$\beta = \left(\frac{\tau_1^c}{\tau_2^c}\right)^{-\left(\frac{\tau_1^c}{\tau_2^c}-1\right)^{-1}} - \left(\frac{\tau_1^c}{\tau_2^c}\right)^{-\left(1-\frac{\tau_2^c}{\tau_1^c}\right)^{-1}}$$

and

$$SL(t) = SL_0\left[1 + \gamma_f^{max}\left(\max\left(0, 1 - e^{-\frac{t-t_0^{SL}}{\tau_0^{SL}}}\right) - \max\left(0, 1 - e^{-\frac{t-t_1^{SL}}{\tau_1^{SL}}}\right)\right)\right]. \tag{2.24}$$

Physiological values for the constants involved in the dynamics of $[Ca^{2+}]_i$ and SL are reported in Table 2.2. Here we employ such values for the constants, with the modification $c_{\max} = 5.1\,\mu M$, otherwise such shortened filament would lead to negligible levels of activation.

The numerical solutions of the full FKE and the reduced ODE system (2.10) are obtained by means of the Forward Euler method, and we run a very large set of MC simulations (10^4 for each value of Δt), according to the algorithm presented in [Was+12]. As suggested in the same reference, the transition rates (2.3) are updated at 0.25 ms intervals.

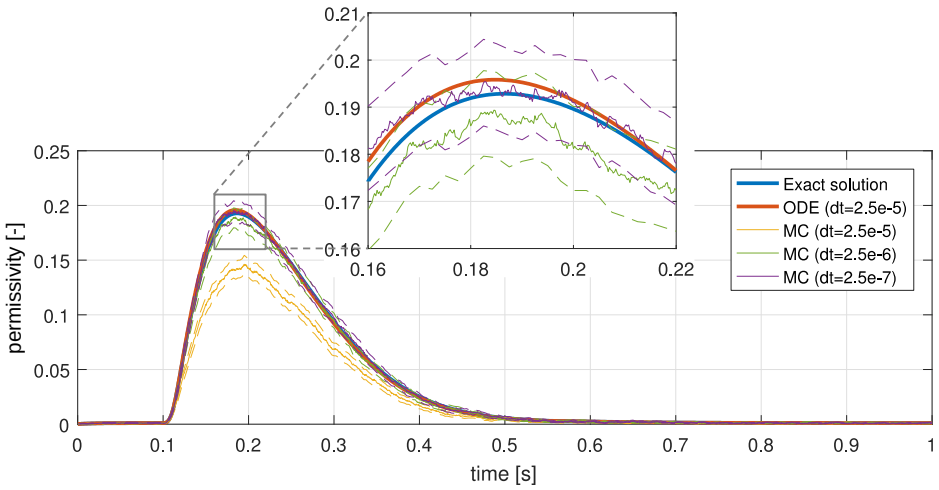

Figure 2.4: Comparison of the solutions for $N_M = 6$ of the full FKE, the reduced ODE model (2.10) and MC simulations with different values of Δt (expressed in s). For the MC simulations the mean (solid line) and the 95% confidence intervals for the mean (dotted line) are shown. Bottom: full time interval. Top: zoom of the activation-peak.

Figure 2.4 reports a comparison of the results. For our reduced ODE model a time step of $\Delta t = 2.5 \cdot 10^{-5}$ s is employed, since with larger time steps the numerical scheme may become unstable, while smaller time steps do not provide any appreciable improvement in accuracy. On the other hand, MC simulations require a much smaller time step, since the numerical solution changes significantly reducing the value of Δt.

Figure 2.5 compares the relative error obtained with the two methods, defined as follows. We consider a collection of time instants $\{t_1, \dots, t_{N_T}\}$, common to any time discretization of the simulations under comparison (here we consider an uniform partition of the interval $[0, 1\,\text{s}]$ with time step 2.5 ms). We denote by P_*^n (where $*$ stands either for ODE or MC) the numerical approximation of the exact permissivity $P(t_n)$ (which we assume to be equal to that obtained with the full FKE with $\Delta t = 1 \cdot 10^{-6}$ s). The relative error in euclidean norm is defined as:

$$\varepsilon_r = \frac{\sqrt{\sum_{n=1}^{N_T} \left(P_*^n - P(t_n)\right)^2}}{\sqrt{\sum_{n=1}^{N_T} P(t_n)^2}}.$$

For the MC simulations, we consider n_{MC} random realizations of the Markov Chain, and we denote by $P_{MC,j}^n$ the random variables associated with the j-th realization. The random variables are independent and identically distributed (i.i.d.), so we can write their expected values as the sum of the exact solution and an error due to the time discretization:

$$\mathbb{E}\left[P_{MC,j}^n\right] = P(t_n) + \varepsilon^n(\Delta t), \quad \text{Var}\left[P_{MC,j}^n\right] = \sigma^n(\Delta t)^2.$$

The expected value and the variance of the MC average $P_{MC}^n = \frac{1}{n_{\text{MC}}} \sum_{j=1}^{n_{\text{MC}}} P_{MC,j}^n$ is given by:

$$\mathbb{E}\left[P_{MC}^n\right] = P(t_n) + \varepsilon^n(\Delta t), \quad \text{Var}\left[P_{MC}^n\right] = \frac{\sigma^n(\Delta t)^2}{n_{\text{MC}}}.$$

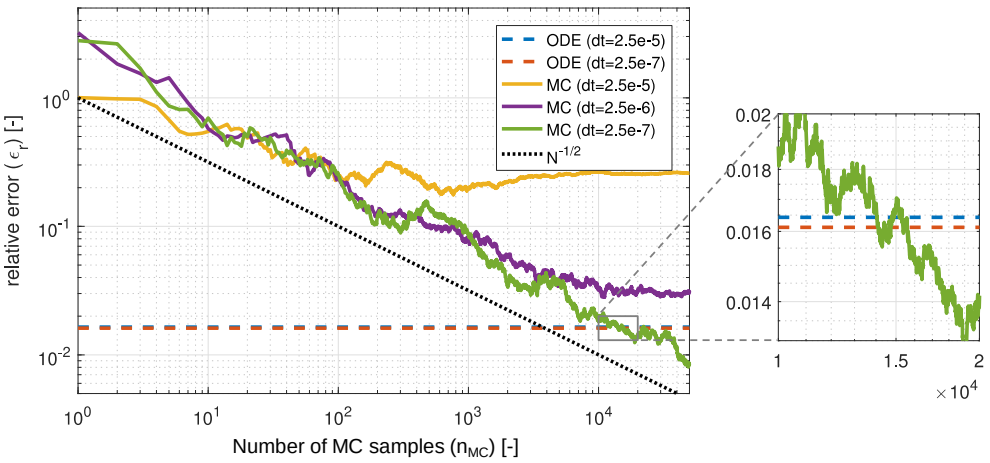

Figure 2.5: Relative errors in euclidean norm with respect to the results obtained through the full ODE model with $N_M = 6$. Right: zoom on the values of n_{MC} for which the errors obtained through MC method and the reduced ODE model are comparable.

Therefore, the expected value of the mean square of the errors is given by:

$$\mathbb{E}\left[\sum_{n=1}^{N_T}\left(P^n_{MC} - P(t_n)\right)^2\right] = \sum_{n=1}^{N_T}\varepsilon^n(\Delta t)^2 + \frac{\sum_{n=1}^{N_T}\sigma^n(\Delta t)^2}{n_{\text{MC}}}.$$

Thus, for relatively small values of n_{MC}, the error ε_r associated with the MC approximation is dominated by the second term and scales as $\varepsilon_r = \mathcal{O}(n_{\text{MC}}^{-1/2})$, while for high n_{MC} the error is dominated by the term associated with the time discretization ($\varepsilon_r = \mathcal{O}(1)$ as $n_{\text{MC}} \to +\infty$).

Since the reduced ODE model (2.10) represents an approximation of the W12 model, we split the error as $\varepsilon_r = \varepsilon_r^{mod} + \varepsilon_r^{\Delta t}$, where the first term accounts for the error introduced by the model (the model error) while the second term is the contribution of the time discretization (the discretization error). For sufficiently small Δt the first term dominates over the second.

Numerical simulations were performed in Matlab and on a single core Intel i7-65000U (2.50 GHz, RAM 12 GB) laptop. We notice that, in order to reach an accuracy comparable to that of the reduced ODE model, which takes 4.5 seconds for one second of physical time, at least 10^4 MC samples with $\Delta t = 2.5 \cdot 10^{-7}$ s are required, which takes more than 11 hours to simulate the same range of physical time. We notice that with the physiological value of RUs (i.e. $N_M = 36$) the gap is even more pronounced, as we switch from 15.9 seconds required by our reduced ODE model to more than 72 hours for the MC method.

2.3 Numerical results

In this section, we show some numerical results obtained by the solution of the reduced ODE model (2.10). For the time discretization, a Forward Euler scheme with a time step size of $2.5 \cdot 10^{-5}$ s is employed. For computational convenience, we update the

transition rates (2.3) at 0.25 ms intervals, since they depend on quantities (SL and $[Ca^{2+}]_i$) that change slowly in time. At time $t = 0$ the sarcomere is assumed to be fully deactivated, namely all MHs are in state $\mathcal{UN}$. Hence the following initial condition is applied:

$$\mathbb{P}((\alpha, \overset{i}{\beta}, \delta)^0) = \begin{cases} 1 & \text{if } \alpha = \beta = \delta = \mathcal{UN}, \\ 0 & \text{otherwise.} \end{cases}$$

In some cases, we perform the same numerical tests also with the original W12 model by means of the MC method, and we compare the results with those of our reduced model. For all the simulations we show the results obtained with $n_{\text{MC}} = 10^4$ samples, since as shown Sec. 2.2.5 this amount of samples is required to keep fluctuations below a reasonable level. In the time-dependent case, we employ a time step of $\Delta t = 2.5 \cdot 10^{-7}$ s (required to keep the discretization error under control, see Sec. 2.2.5); for the steady-state simulations instead, since we are interested just in the equilibrium configuration, we employ a time step of $\Delta t = 2.5 \cdot 10^{-5}$ s.

We validate the numerical results against the experimental data. With this aim, since we assume that the developed force is proportional to the level of permissivity (see Eq. (2.5)), we compare the experimentally measured force with the numerical permissivity, obtained by evaluating Eq. (2.7) on the numerical solution of the reduced ODE model (2.10). Since we do not have a closure law between force and permissivity, and these are assumed to be just mutually proportional, we remark that one should always compare their normalized values.

The goal of the numerical tests is twofold. First, we validate our model against the original one [Was+12] to assess the validity of the reduction procedure shown in Sec. 2.2.2. Then, thanks to the large complexity reduction and negligible computational cost allowed by our model, we use it to explore additional experimental settings. The aim is to verify that the modeling choice made in [Was+12] and discussed in Sec. 2.2.1 does not affect the validity of the model. Whenever experimental measurements are available, we compare our numerical results against these ones.

2.3.1 Steady-state conditions

By fixing the calcium level $[Ca^{2+}]_i$ and the sarcomere length SL, letting the system reach the steady-state and considering the level of activation at the equilibrium, one gets the steady-state relationships between calcium and force and between length and force. The capability of reproducing the physiological steady-state curves is a distinguishing feature of activation models (see Sec. 1.3.2).

In this section, we consider the steady-state curves obtained by solving the reduced ODE model (2.10) and the full W12 model and we compare them with the experimental measurements of [Ken+86] and [DKT02]. Both data sets refer to skinned rat cardiac trabeculae.

Force-calcium relationship

Figure 2.6 shows the steady-state force-calcium relationship for different values of SL obtained with the proposed model. The comparison with the experimental curves (see Figs. 1.17a, 1.16c and 1.18) highlights the following points:

- We obtain the experimentally observed sigmoidal curves, well fitted by the Hill equation (1.1).

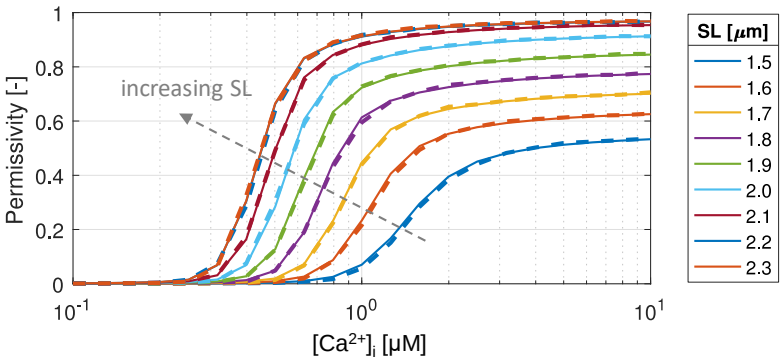

Figure 2.6: Steady-state force-calcium relationship for different SL: comparison of the results of the reduced ODE model (solid lines) with the results of the full W12 model (dashed lines).

- The maximal force $T_{\mathrm{a}}^{\max}$ increases as SL grows.

- As SL increases, in the physiological range (approximately $1.7 - 2.3\,\mu\mathrm{m}$), the sarcomere becomes more sensitive to $[\mathrm{Ca}^{2+}]_{\mathrm{i}}$. This translates into a leftward shift of the curve, or equivalently in a reduction of EC_{50}. In Fig. 2.7b we compare the dependence of EC_{50} on SL obtained by solving the reduced ODE model with experimental data (see also Fig. 1.17b). Since there is evidence that the skinning procedure (i.e. the removal of the cell membrane), employed in both sets of measurement, lower the sarcomere sensisivity to calcium [Ken+86; RWH99; Gao+94], it is not meaningful to compare the absolute values of EC_{50}; for this reason calcium concentrations are normalized.

- The Hill coefficient n_H is significantly larger than 1, revealing a high cooperativity level, and approximately constant for all values of SL.

- The Hill plots of Fig. 2.8 (see Eq. (1.2)) show the experimentally observed asymmetry in the force-calcium relationship (see Sec. 1.3.2). Specifically the curves obtained with the model are shown, with the best-fit lines in the least-squares sense, to be compared with experimental measurements (see Fig. 1.17c). We notice that the model is capable of reproducing physiological features such as: (i) force-calcium relationship, which is fitted by two distinct lines, with decreasing slope as $[\mathrm{Ca}^{2+}]_{\mathrm{i}}$ increases, thus showing a higher cooperativity at lower calcium levels; (ii) the intersection between these lines, which lies above the level of half activation (i.e. $\log(T_{\mathrm{a}}^{\mathrm{iso}}/(T_{\mathrm{a}}^{\max} - T_{\mathrm{a}}^{\mathrm{iso}})) = 0$, which corresponds to $T_{\mathrm{a}}^{\mathrm{iso}} = T_{\mathrm{a}}^{\max}/2$); (iii) the slopes of both lines, which are nearly independent of SL; (iv) the normalized force corresponding to the intersection between these lines, which is nearly independent of SL; (v) the calcium level corresponding to half activation, which decreases as SL increases.

In Figs. 2.6 and 2.8 we compare the results of our reduced model with those obtained by simulating the full model of [Was+12] by means of the MC method. This comparison shows a very good qualitative and quantitative agreement between the two, and thus supports the validity of assumption (2.21).

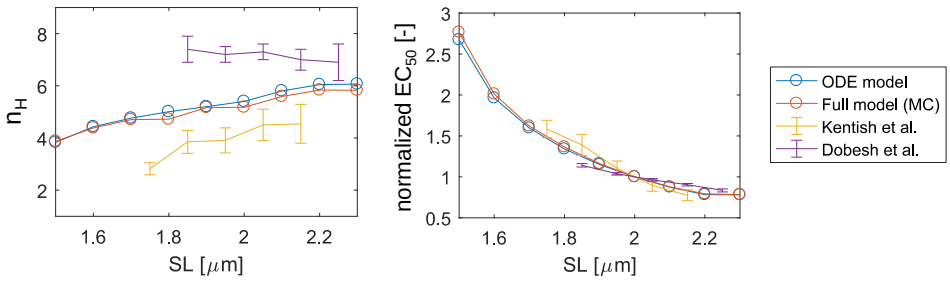

(a) n_H versus SL (b) Normalized EC_{50} versus SL

Figure 2.7: Dependence of the Hill coefficient n_H (a) and the calcium level corresponding to half activation EC_{50} (b) on the sarcomere length SL, compared with experimental data. The Hill coefficients obtained with the proposed model and the full W12 model are comprised between the two experimental sets, and have a similar trend to those on [Ken+86]. Also EC_{50} report a similar trend to experimental measurements. Notice that, since the skinning procedure employed in the experiments alters significantly the calcium level which triggers activation, the values of EC_{50} are normalized to the value assumed at $SL = 2.0\,\mu\text{m}$.

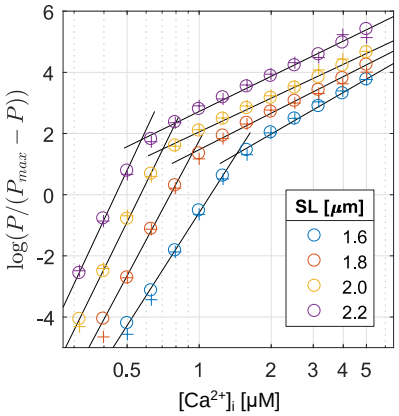

Figure 2.8: Steady-state force-calcium relationship in the plane $\log(P/(P_{\max} - P))$ versus $\log[Ca^{2+}]_i$, for different SL: comparison of the results of the reduced ODE model ($\circ$) with the results of the full W12 mode ($+$).

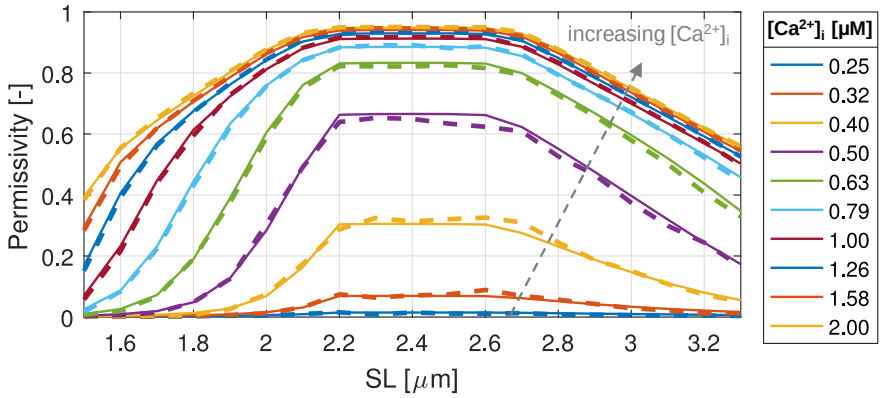

Figure 2.9: Steady-state force-length relationship for different calcium concentrations: comparison of the results of the reduced ODE model (solid lines) with the results of the full W12 model (dashed lines). We notice that the curves report the observed change in convexity (see text for details).

Force-Length relationship

In Fig. 2.9 the force-length curves of the proposed model for different calcium levels are reported. Because of the overlapping between the AFs near the H-zone, which lowers the number of interacting actin and myosin units, the force exerted by a shortened sarcomere is smaller than the force of a relaxed sarcomere (corresponding to $SL \simeq 2.2\,\mu\text{m}$). In the range $2.2\,\mu\text{m} \leq SL \leq 2.6\,\mu\text{m}$ the whole MF faces a single AF, which is the most favourable condition for muscle activation, and the permissivity is constant. For $SL > 2.6\,\mu\text{m}$ the central region of the MF faces no AF, and the width of the region increases as SL increases, making the permissivity reduce (see Sec. 1.3.2).

We notice that the curves of Fig. 2.9 resemble these of the *sarcomere overlap function* employed in mean-field models to account for the effect of SL [Sac04; TR11]; however, whereas in those models the force-length dependency is assumed to be invariant with respect to $[Ca^{2+}]_i$, this model is capable of capturing the calcium dependency of the force-length relationship. Indeed, force-length curves obtained with our model exhibit the change in curvature observed experimentally (see Sec. 1.3.2): in the physiological range ($1.6\,\mu\text{m} \leq SL \leq 2.2\,\mu\text{m}$), the curves are convex at low calcium levels, concave at intermediate calcium levels, while at maximally activating $[Ca^{2+}]_i$ the relation is approximately linear (see Fig. 1.16). We notice that also in this case the reduced ODE model accurately reproduces the results of the full W12 model obtained by means of the MC method.

2.3.2 Isometric versus shortening twitches

We showed in Sec. 2.2.5 that our reduced model, with $N_M = 6$ MHs, reproduces with a good qualitative and quantitative correspondence the results of the full W12 model. In this section we investigate whether this is still valid when we consider the physiological number of MHs (i.e. $N_M = 36$). Since the numerical solution of the full FKE cannot be achieved because of the gigantic number of dofs ($4^{N_M} \simeq 5 \cdot 10^{21}$), we compare the results of our reduced model with those obtained by means of the MC method.

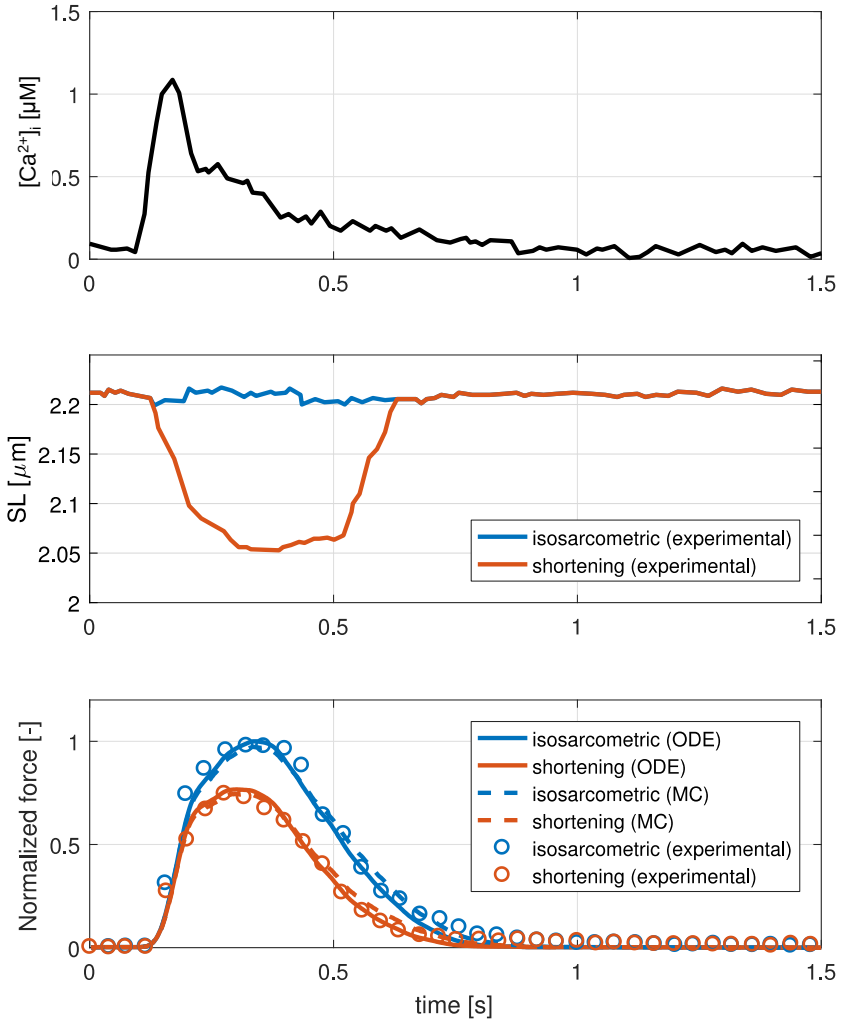

Figure 2.10: Time transients of calcium concentration $[Ca^{2+}]_i$ (top) and sarcomere length SL (middle) taken from [Was+12]; normalized force (bottom) obtained with the reduced ODE model (solid lines), with the full W12 model (dashed lines) and experimentally observed (circles, taken from [Was+12]).

With this aim, we perform the following test, also reported in [Was+12]. The calcium concentration and the sarcomere length time transients taken from [JT97] are applied, and the resulting force obtained with the reduced ODE model and with the full W12 model are compared with the experimental measurements, both under isometric conditions and during a shortening twitch (see Fig. 2.10).

As mentioned before, since the generated force is taken proportional to permissivity (see Sec. 2.2.1), we compare the experimentally observed force, normalized with respect to its peak during isometric contraction, with the permissivity P normalized with respect to its peak under the same conditions.

Figure 2.10 shows a very good qualitative and quantitative agreement between the results of the reduced ODE model and those obtained with the MC method, thus supporting the validity of our reduced model with respect to the full one.

2.3.3 Isometric twitch contractions

In Sec. 2.3.1 we have considered the stationary solutions of the proposed model. In order to test the capability of the reduced ODE model of reproducing the dynamics of the sarcomere, we simulate twitches by imposing the calcium transient of Eq. (2.23), while keeping the value of SL constant. We run several simulations by changing the sarcomere length SL and the calcium concentration peak $c_{\max}$. In Fig. 2.11 the obtained results are compared with the experimental observations on rat trabeculae reported in [JH95].

The numerical simulations of the reduced ODE model reproduce the main features of the force transients of isometric twitches when either SL or $c_{\max}$ increases, namely: (1) peak force increases; (2) activation time is not affected; (3) relaxation time increases (see Sec. 1.3.3).

It has been experimentally observed that the third effect, namely the slowing down of the relaxation phase, is more influenced by changes in SL than by changes in $c_{\max}$ [JH95; Ric+08]. This feature too can be observed in the results of the proposed model. Indeed, in Fig. 2.12, two force transients associated with two different couples $(SL, c_{\max})$, but exhibiting a similar peak force, are compared: the relaxation time is slower in the curve associated with the larger SL.

In Fig. 2.13 isometric twitches are plotted as phase loops and compared with experimental measurements on intact rat cardiac trabeculae [Bac+95]. The figure highlights the delayed response of force with respect to calcium: in the early stages of the twitches, loops are placed below the steady-state curve (dashed line), meaning that calcium has peaked while force is still low; then the trajectories cross the steady-state curve with nearly null derivative (this corresponds to the force peak), and eventually they return to their initial configuration staying above the steady-state curve (see Sec. 1.3.3).

2.4 Alternative formulations

As discussed in Sec. 2.2.1, in the original W12 model a modeling choice not consistent with the experimental evidence is made, namely the association of the calcium-driven regulatory mechanism to the MHs instead of to the RUs. In this section, we show how the W12 model can be modified to better reflect the physical arrangement of proteins inside the sarcomere.

First, instead of tracking the states of the $N_M = 36$ MHs of half thick filament, we focus on the state of the $N_A = 32$ RUs on a thin filament (also in this case the

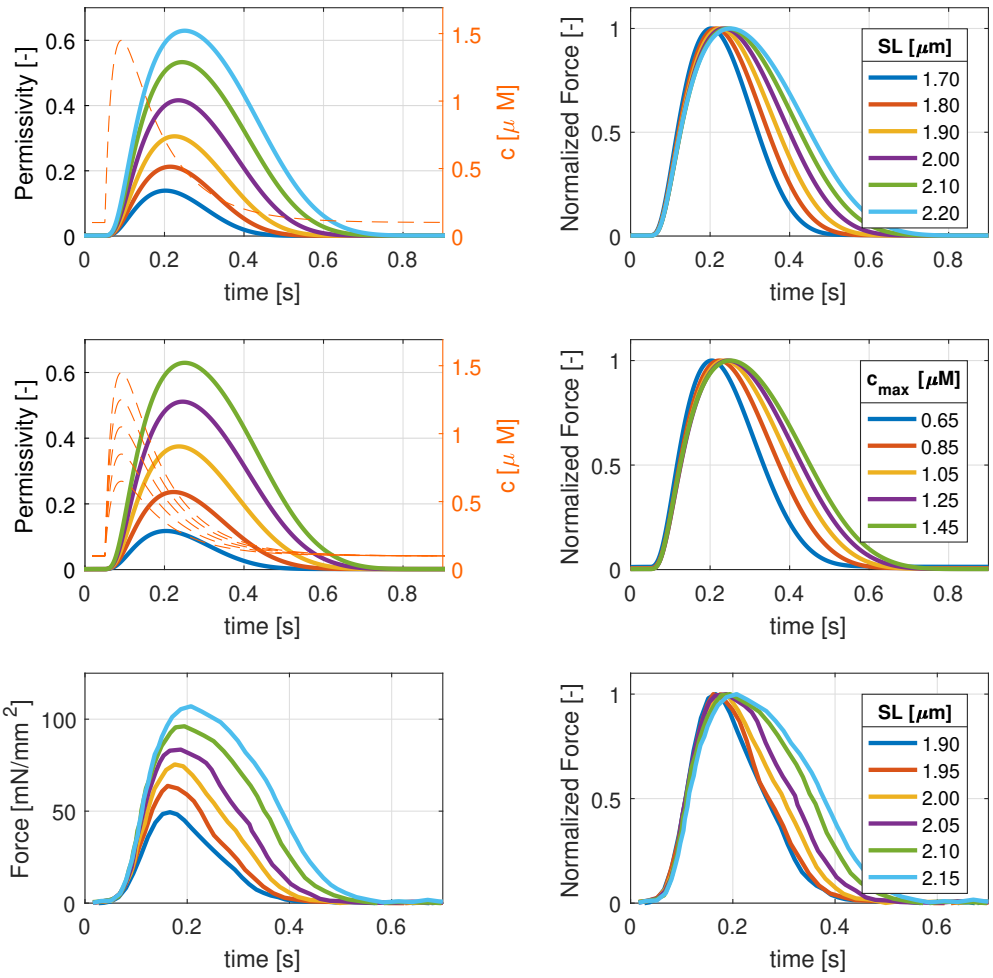

Figure 2.11: Force transients in isometric twitch contractions, without (first column) and with (second column) normalization. First row: reduced ODE model results for $c_{\max} = 1.45\,\mu\text{M}$ and different values of SL. Second row: reduced ODE model results for $SL = 2.2\,\mu\text{m}$ and different values of $c_{\max}$. Third row: experimental measurements with fixed maximum calcium level and different SL (data from [JH95]). In the first two rows, solid lines refer to permissivity (axis on the left), while dashed lines refer to calcium concentration (axis on the right). In both experimental and numerical cases activation starts at 0.05 s.

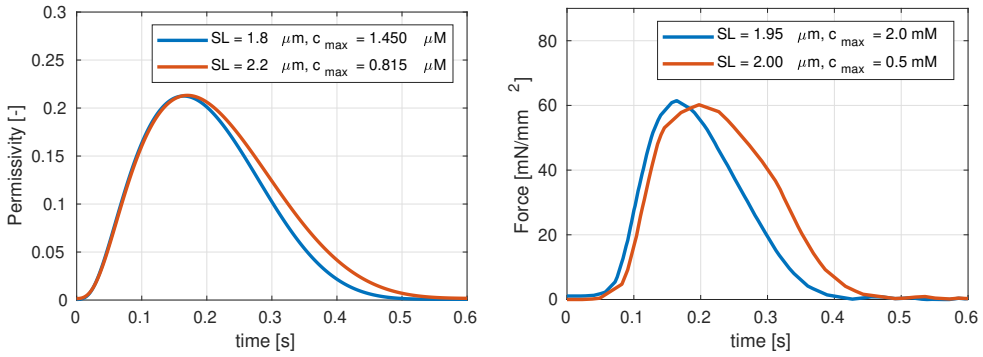

(a) Reduced ODE model (b) Experimental data from [JH95]

Figure 2.12: Comparison of force transients of twitches with similar peak force and different SL and $c_{\max}$: simulations results (a) and experimental measurements (b). In both cases, the larger SL the longer the relaxation phase.

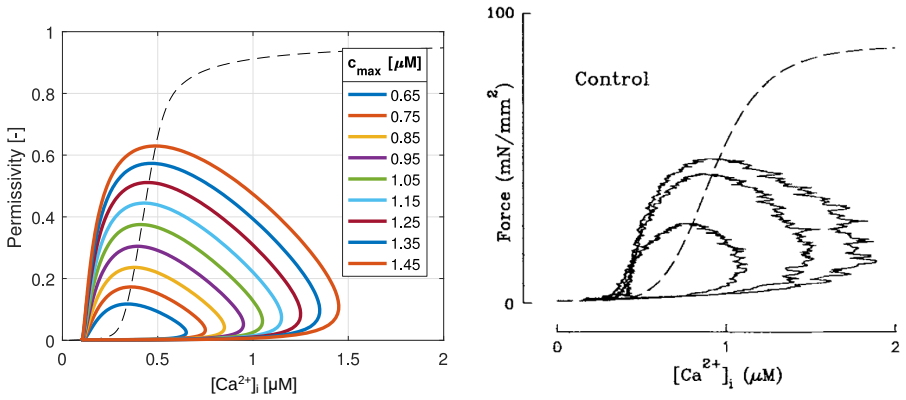

(a) Reduced ODE model (b) Experimental data from [Bac+95]

Figure 2.13: Loops in phase diagram of twitch responses (solid lines) and steady-state force-calcium relationship (dashed line): comparison of the reduced ODE model results (a) with experimental data (b). Experimental data, taken from [Bac+95] refer to intact rat cardiac trabeculae at SL in the range $2.1 - 2.3\,\mu$m.

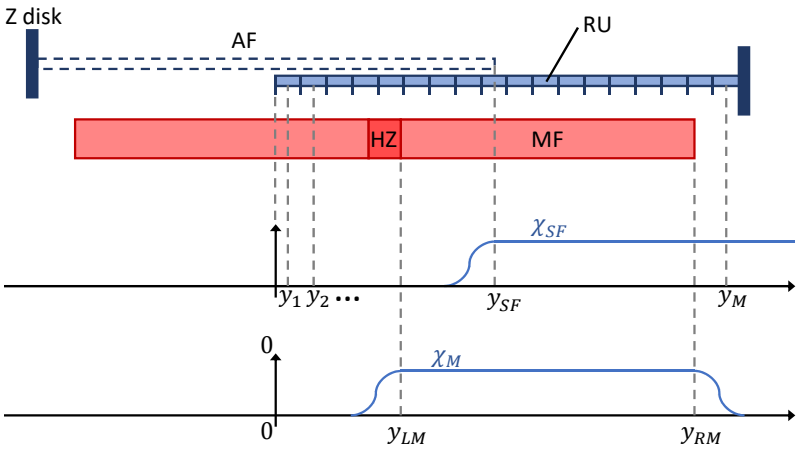

Figure 2.14: Sketch of the sarcomere models described in Sec. 2.4 (to be compared with Fig. 2.2). The thick filament (MF) is represented in red and two thin filaments (AF) are represented in blue (top). The origin of the frame of reference is the left side of the reference AF. The functions χ_{SF} and χ_M are also represented (bottom).

other one can be recovered by symmetry). Thus, we change the frame of reference by placing the origin at the left side of the reference thin filament (see Fig. 2.14), and we denote the mid-point of the i-th RU by y_i. Moreover, we introduce the geometrical factors χ_{SF} and χ_M, which indicate the single-filament (or non-overlap) region and the region faced by the myosin filament, respectively:

$$y_{LM} = (2\,L_A - SL + L_H)/2, \qquad y_{SF} = 2\,L_A - SL,$$
$$y_{RM} = (2\,L_A - SL + L_M)/2, \qquad y_i = \frac{L_A}{N_A}(i - 0.5);$$

$$\chi_M(SL, i) = \begin{cases} \exp\left(-\frac{(y_{LM}-y_i)^2}{\varepsilon_{SL}^2}\right) & y_i \le y_{LM}, \\ 1 & y_{LM} < y_i < y_{RM}, \\ \exp\left(-\frac{(y_i-y_{RM})^2}{\varepsilon_{SL}^2}\right) & y_i \ge y_{RM}; \end{cases}$$
$$\chi_{SF}(SL, i) = \begin{cases} \exp\left(-\frac{(y_{SF}-y_i)^2}{\varepsilon_{SL}^2}\right) & y_i \le y_{SF}, \\ 1 & y_i > y_{SF}. \end{cases}$$

Then, we model each RU with the CTMC of Fig. 2.3 and we adapt the dependence of the transition rates on the location w.r.t. the filament according to the new physical arrangement of units. In the next sections we propose two different ways of taking into account the position of the RU along the filament, that we we denote by activation-RUa model and activation-RUa model, in contrast to the activation-MH model, considered in the rest of the chapter.

We remark that, in the activation-RUa and activation-RUb models, the permissivity computed with Eq. (2.7) measures the fraction of RUs in permissive state, instead of the fraction of MHs which can undergo XB formation, like in the activation-MH model. Therefore, we denote by $P_{RU}(t)$ the permissivity computed in the activation-RUa and activation-RUb models. Since $P(t) = 1$ corresponds to the condition of

maximum exerted force, which occurs when the half MF faces a fully permissive non-overlapped region of AF, $P(t)$ and $P_{RU}(t)$ are linked by the relation

$$P(t) = \frac{N_A}{N_A^{\max}} P_{RU}(t),$$

where

$$N_A^{\max} = \max_{SL} \sum_{i=1}^{N_A} \chi_M(SL,i)\chi_{SF}(SL,i).$$

We also remark that in this way we get a model with the same mathematical structure of the W12 model since the only differences are: (a) the number of units switches from $N_M = 36$ to $N_A = 32$; (b) the transition rates (2.4) are adapted to the new configuration. Thus, the reduced ODE system (2.10) is valid also in the activation-RUa and activation-RUb models.

2.4.1 Accounting for SL dependence: activation-RUa model

In this setting, we consider similar assumptions to these made for the activation-MH model: the transition $\mathcal{N} \to \mathcal{P}$ is allowed just in the region where the MF faces a single AF, while the transition $\mathcal{U} \to \mathcal{B}$ is forbidden where the thin and the thick filaments do not face each other. Thus, the transition rates (2.4) are replaced by:

$$\begin{aligned}
\overline{k}_{\mathrm{np0}}(SL,i) &= \chi_{SF}(SL,i)\chi_M(SL,i)k_{\mathrm{np0}},\\
\overline{k}_{\mathrm{on}}(SL,i) &= \chi_M(SL,i)k_{\mathrm{on}},\\
\overline{k}_{\mathrm{np1}}(SL,i) &= \chi_{SF}(SL,i)\chi_M(SL,i)k_{\mathrm{np1}},\\
\overline{k}'_{\mathrm{on}}(SL,i) &= \chi_M(SL,i)k'_{\mathrm{on}}.
\end{aligned} \tag{2.25}$$

Since in the original paper the value of the RU affinity to calcium k_{on} was set to fit experimental data [Was+12], in this setting we have to re-calibrate its value from 80 to $100\,\mu\mathrm{M}^{-1}\,\mathrm{s}^{-1}$ so that we get a comparable permissivity for a given calcium level.

2.4.2 Accounting for SL dependence: activation-RUb model

With this model, we propose a different way to account for length-dependent effects. First, since the influence of XBs on calcium binding to troponin is already modelled through the factor μ which reduces the transition rate of $\mathcal{B} \to \mathcal{U}$ in the permissive case, we do not make the transition rates $\mathcal{U} \to \mathcal{B}$ further depend on the mutual position of the filaments (see cooperativity mechanism (RU-XB), Sec. 1.3.2). On the other hand, we modify the transition rates $\mathcal{N} \to \mathcal{P}$, in such a way that this transition becomes more favourable when a XB is present on the opposite filament (see again Sec. 1.3.2). However, unlike in the activation-RUb model, in which the transition is forbidden where XB cannot form, here we just reduce the transition rate by a factor $\gamma_2 = 1/2$:

$$\begin{aligned}
\overline{k}_{\mathrm{np0}}(SL,i) &= \gamma_2^{1-\chi_{SF}(SL,i)\chi_M(SL,i)}k_{\mathrm{np0}},\\
\overline{k}_{\mathrm{on}}(SL,i) &= k_{\mathrm{on}},\\
\overline{k}_{\mathrm{np1}}(SL,i) &= \gamma_2^{1-\chi_{SF}(SL,i)\chi_M(SL,i)}k_{\mathrm{np1}},\\
\overline{k}'_{\mathrm{on}}(SL,i) &= k'_{\mathrm{on}}.
\end{aligned} \tag{2.26}$$

We notice that, in this setting, a RU may be in permissive state also in the thin filaments overlap region and even in absence of a MH in front. Therefore, we have to adapt the definition of permissivity, so that it measures the fraction of RUs which can actually form a XB. Thus, we replace Eq. (2.7) by

$$P_{RU}(t) = \frac{1}{N_A} \sum_{i=1}^{N_A} \mathbb{P}\left(X_t^i \in \{\mathcal{UP}, \mathcal{BP}\}\right) \chi_{SF}(SL, i)\chi_M(SL, i). \tag{2.27}$$

In this setting the re-calibration of the parameter k_{on} is not needed.

2.4.3 Comparison of the results

In Figs. 2.15 and 2.16 we show the steady-state force-calcium and force-length relationships and the simulations of isometric twitches, for different values of SL and maximum $[\text{Ca}^{2+}]_{\text{i}}$, obtained with the activation-RUa and activation-RUb models. The comparison of the results with those obtained with the activation-MH model (see Sec. 2.3) shows that all the experimentally observed features mentioned in Sec. 2.3 are not affected by the performed modifications. This validates the fact that the modeling choice made in [Was+12], despite it does not fully reflect the physical arrangement of units in the sarcomere, does not harm the ability of the model to capture the fundamental behaviors of the calcium-driven regulation of active force.

2.5 Final remarks

We have developed a mathematical model (activation-MH model) based on an ODE system suitable to approximate the FKE (forward Kolmogorov equation) associated with the CTCM (continuous-time Markov Chain) model for sarcomere contraction presented in [Was+12] (W12 model). Our proposed model reduces the $5 \cdot 10^{21}$ variables of the original system to less than 2200 variables. Moreover, the proposed model produces very accurate results with a much lower computational effort than the original model, whose complexity dictates the use of the MC method: the simulation of one second of physical time takes about 15.9 seconds with our reduced ODE model, against more than 72 hours required on the same computer platform by the original model.

Our numerical tests highlight that the model is able to reproduce physiological behaviors observed under various experimental settings, including the steady-state relationships between calcium, length and force and isometric and shortening twitches. This supports the hypotheses on which also the original W12 model is based, as discussed in Sec. 2.2.1.

Compared with previously proposed reduction strategies, the concept proposed in this chapter presents significant advantages. First, it does not require the so-called "ring" approximation employed both in [Ric+03] and in [Cam+10], making the model able to capture the effects related to the spatial distribution of filaments. Moreover, as highlighted in Section 2.1.5, the strategy proposed in [Ric+03] is limited to steady conditions, while the complexity of the reduced model of [Cam+10] is still too high to allow that more than 9 RUs are simulated. The approach proposed in [Was+12] produces a larger complexity reduction, compared to the present chapter, since it ends up with a system of 144 ODEs, but it still requires a time consuming off-line phase to tune the model by fitting the registered data. Moreover, the error introduced by the approximation is larger than in the present chapter and the validity of the parameters

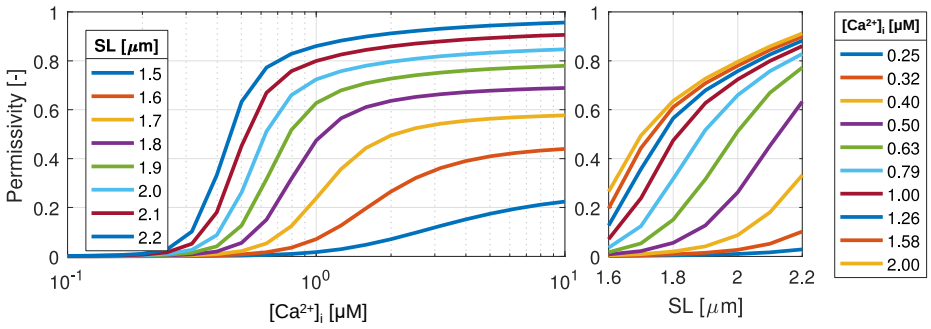

(a) Activation-RUa model.

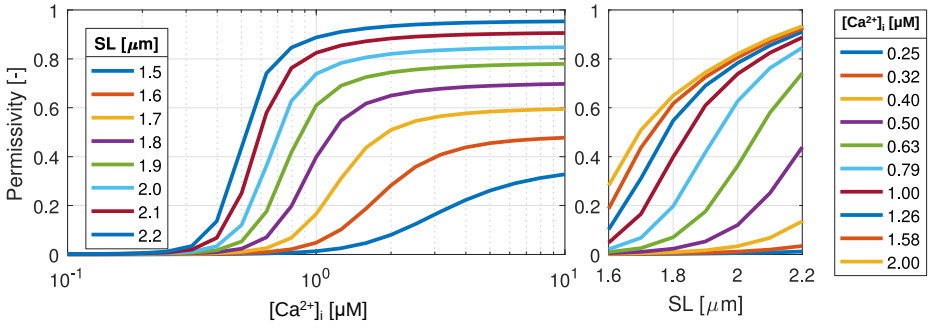

(b) Activation-RUb model.

Figure 2.15: Steady-state force-calcium (first column) and force-length (second column) relationships in the physiological range of SL obtained with the activation-RUa (a) and activation-RUb (a) models. The results should be compared with Fig. 2.6 and Fig. 2.9.

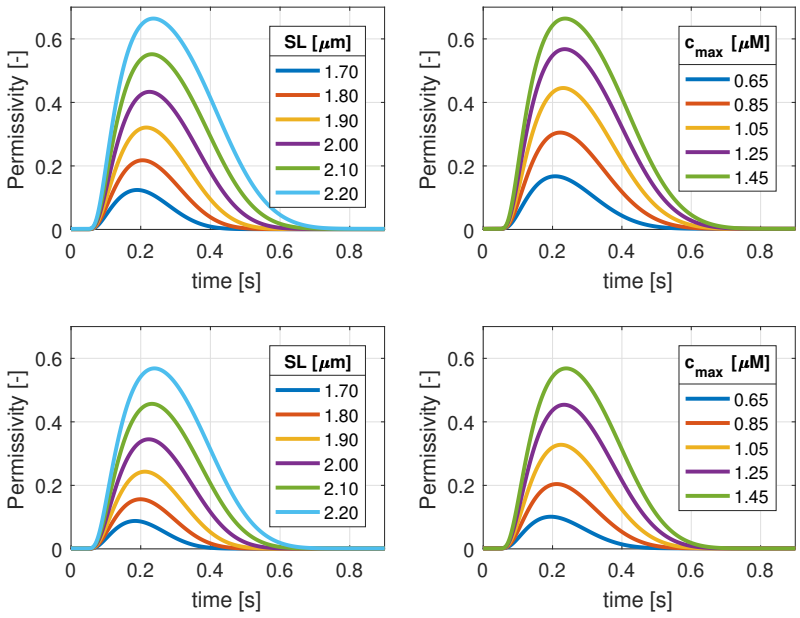

Figure 2.16: Force transients in isometric twitch contractions with fixed $c_{\max} = 1.45\,\mu M$ (first column) and fixed $SL = 2.2\,\mu m$ (second column) obtained with the activation-RUa and activation-RUb models (first and second row respectively). The results should be compared with Fig. 2.11.

is not guaranteed beyond the settings used to tune them. The technique proposed in [LN15] yields a system of 750 ODEs, but still requiring a long off-line phase to compute transition rates. Finally, having characterized each state by the number of unblocked RUs and bound XBs, the explicit spatial description is lost during the reduction procedure. Therefore, length-dependent effects on tension are neglected and their inclusion would require modifications to the employed strategy.

We remark that our approach to complexity reduction is not limited to the current model, but it can be applied to any spatially explicit Markov Chain model with end-to-end cooperative interactions. In general, given a model comprising N units, each described by a CTMC with S states, assumption (2.21) yields to an ODE system whose size depends linearly in the number of units ($(N-2)\cdot S^3$ variables), in place of the exponential dependence on N of the original model (S^N variables).

As previously mentioned, unlike most previously proposed techniques [Was+12; LN15], our approach does not require an off-line phase to calibrate model parameters, given sub-cellular properties. The advantage is that this property speeds up the investigation of the influence of those microscopic properties, such as changes in individual channels or proteins, on the tissue contractile properties. Moreover, it opens to the possibility of investigating dynamic changes of sub-cellular properties.

Chapter 3

Modeling the crossbridge dynamics

In Chap. 2 we dealt with the mathematical modeling of the dynamics of the RUs. When a RU is in permissive state, the associated Tm exposes the actin BSs, so that MHs can bind and form the so called XBs. In this chapter we deal with the mathematical modeling of the XB dynamics. As we have seen in Chap. 1, the dynamics of XBs is responsible for the observed decrease of tension when a muscle fiber shortens at a constant velocity (force-velocity relationship) and for the tension transients following an isometric or isotonic step in either tension or length. The two above mentioned experimental setups will be used in this chapter to assess the capability of different mathematical models to reproduce, both qualitatively and quantitatively, the related experimentally observed characterization.

In this chapter we do not propose a new model, but rather we review the mathematical models available in literature and we highlight their strengths and limitations, in light of their application in the context of cardiac EM. In particular, we try to assess the level of biophysical detail that is best suited when the considered temporal scales are those characterizing cardiac EM. Part of this chapter can be found in the submitted paper [RDQ19a].

Contents

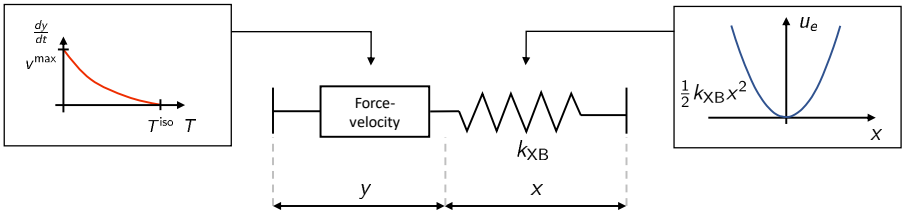

Figure 3.1: Scheme of the phenomenological model of [Hil38]. A contractile element, following the law (3.2), is coupled in series with an elastic element, to which a quadratic energy $u_e(x) = \frac{1}{2} k\, x^2$ is associated.

3.1 Mathematical models of crossbridges cycling

In this section, we review the main contributions available in literature to the definition of mathematical models describing the dynamics of XBs. The historical development of such models reflects the progresses in the understanding by the physiologists community of the mechanisms underlying the microscopic force generation.

3.1.1 Hill '38 model

One of the earliest mathematical descriptions of muscles dates back to [Hil38]. By studying the release of heat when a muscle contracts against a constant load (isotonic contraction), A. V. Hill discovered that the relationship between the tension T_a and the shortening velocity v_fiber is well described by the hyperbolic law:

$$(T_\mathrm{a} + a)\, v_\mathrm{fiber} = b_\mathrm{fiber}\, (T_\mathrm{a}^\mathrm{iso} - T_\mathrm{a}), \tag{3.1}$$

where $T_\mathrm{a}^\mathrm{iso}$ is the isometric tension (i.e. the tension for $v_\mathrm{fiber} = 0$), a and b_fiber are positive constants. In the following, it will be helpful to write relationships that are independent of the length of the muscle fiber used to perform the experiment. With this aim, by dividing Eq. (3.1) by the length of the fiber L_fiber, we get the following relationship:

$$(T_\mathrm{a} + a)\, v = b\, (T_\mathrm{a}^\mathrm{iso} - T_\mathrm{a}). \tag{3.2}$$

where we call $v = v_\mathrm{fiber}/L_\mathrm{fiber}$ the *normalized velocity* (dimensionally, v is the inverse of time units). The maximum shortening velocity, that is the maximum speed at which the muscle is able to shorten (see Sec. 1.3.4), can be computed as $v^\mathrm{max} = b\, T_\mathrm{a}^\mathrm{iso}/a$. In the original paper [Hil38], Hill obtained $\frac{a}{T_\mathrm{a}^\mathrm{iso}} = 0.22$, $b_\mathrm{fiber} = 1.03\,\mathrm{cm\,s^{-1}}$ for a fiber of length $L_\mathrm{fiber} = 38\,\mathrm{mm}$, thus $b = 0.27\,\mathrm{s^{-1}}$ and $v^\mathrm{max} = 1.23\,\mathrm{s^{-1}}$.

On the basis of the relationship (3.2), Hill proposed a phenomenological model where an elastic element is in series with a contractile element governed by the law (3.2) itself. This model, however, does not provide any insight into the muscle functioning, as it is not based on a microscopical description of the tissue (this is not surprising since the muscle anatomy was not known at that time).

3.1.2 Huxley '57 model

In 1957, A. F. Huxley proposed a model (H57 model) to link the force-velocity relationship observed by A. V. Hill with the subcellular attachment-detachment process

of MHs [Hux57b]. This model considers two states (bound and unbound) and assumes that the transition rates depend on the distance between the myosin arm rest position and the BS, denoted by x. We have $x > 0$ when the attachment leads to a positive tension, $x \leq 0$ otherwise (see Fig. 3.2).

Let us consider a population of MHs and BSs, and assume that the probability density of finding a couple with a given displacement x is constant in a an interval sufficiently close to $x = 0$ (more precisely, the number of couples with displacement $x \in (a, b)$ for each half filament is $\rho_{\mathrm{AM}}|b - a|$, if a and b are sufficiently close to 0). This is well motivated, assuming the effect of the units located at the border of the filaments negligible.

Let $n(x, t) \in [0, 1]$ denote the probability that a couple MH-BS with elongation x is attached. Then, the expected value of the number of attached XBs with elongation between a and b at time t is given by:

$$\rho_{\mathrm{AM}} \int_a^b n(x, t)dx.$$

Let us consider a small time interval Δt. The variation of the population of attached MHs from t to $t+\Delta t$ with displacement in the interval (a, b) is given (at the first order in Δt) by:

$$\begin{aligned}\int_a^b n(x, t + \Delta t)dx \simeq \int_a^b n(x, t)dx + n(b, t)v_{\mathrm{hs}}(t)\Delta t - n(a, t)v_{\mathrm{hs}}(t)\Delta t \\ + \int_a^b (1 - n(x, t))f(x)\Delta t\, dx - \int_a^b n(x, t)g(x)\Delta t\, dx,\end{aligned} \tag{3.3}$$

where $v_{\mathrm{hs}}(t) = -\frac{dSL(t)/2}{dt}$, the shortening velocity of half sarcomere (that is the relative velocity between the MF and the AF), convects the MH distribution and $f(x)$ and $g(x)$ are the attachment and detachment rates, respectively. By dividing the above equation by $\Delta t\,(b - a)$ and letting both intervals go to zero, we get the H57 model:

$$\frac{\partial n(x, t)}{\partial t} - v_{\mathrm{hs}}(t)\frac{\partial n(x, t)}{\partial x} = (1 - n(x, t))f(x) - n(x, t)g(x), \qquad x \in \mathbb{R},\, t \geq 0, \tag{3.4}$$

with suitable initial conditions. Finally, assuming that each attached XB acts as a linear spring with stiffness k_{XB}, the total force exerted by the pair of interacting half thick filament and thin filament is equal to:

$$F_{\mathrm{hf}}(t) = \rho_{\mathrm{AM}}\, k_{\mathrm{XB}} \int_{-\infty}^{+\infty} x\, n(x, t)dx. \tag{3.5}$$

In [Hux57b], the transition rates are phenomenologically set as:

$$f(x) = f_1 \frac{x}{h} \mathbb{1}_{[0,h]}(x), \qquad g(x) = g_2 \mathbb{1}_{x\leq 0} + g_1 \frac{x}{h} \mathbb{1}_{x>0}, \tag{3.6}$$

where f_1, g_1 and g_2 are positive constants. Attachment can occur only in the interval $x \in [0, h]$, that is for positive displacement: such symmetry-breaking feature is what makes the muscle contract. For $x < 0$ the detachment rate is very high, in order to prevent the XBs to generate force in the opposite direction.

The H57 model provides a microscopical explanation of the force-velocity relationship. When the shortening velocity is high, the attached XBs are convected towards

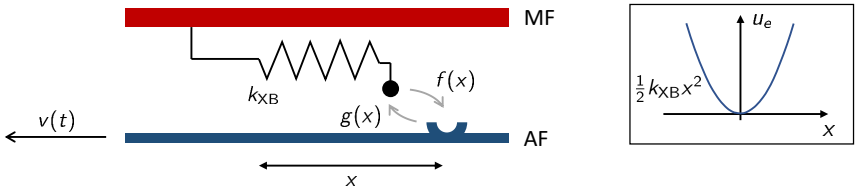

Figure 3.2: Scheme of the H57 model. The attachment-detachment rates of MHs (denoted respectively by f and g) depend on the XB distortion x. The myosin arm is modeled as a linear elastic element with stiffness k_{XB}.

lower values of x, thus leading to a reduction of force. This mechanism is often compared to a "tug-of-war" game. If the rod is quickly pulled, the players need to detach their hands and reattach them further on the rod, otherwise they are not able to pull any more. Thus, when the rod is sliding towards to players, their action is less efficient than in the steady regime, when they can firmly hold the rod. It is all about how fast the rod slides and how are the players fast in detaching and reattaching their hands. We will see later a quantitative description of the competition between the two phenomena.

With the choice (3.6), Huxley derived a steady-state solution (with a constant shortening velocity) for (3.4):

$$n(x) = \begin{cases} F_1 \left(1 - e^{-\varphi/v_{\mathrm{hs}}}\right) e^{\frac{x}{2h} G_2 \frac{\varphi}{v_{\mathrm{hs}}}} & x < 0, \\ F_1 \left(1 - e^{\left(\frac{x^2}{h^2} - 1\right) \frac{\varphi}{v_{\mathrm{hs}}}}\right) & 0 \le x < h, \\ 0 & x \ge h, \end{cases} \tag{3.7}$$

where $\varphi = (f_1 + g_1)h/2$, $F_2 = \frac{f_1}{f_1+g_1}$, $G_2 = \frac{g_2}{f_1+g_1}$. This gives the following force-velocity relationship:

$$F_{\mathrm{hf}} = \rho_{\mathrm{AM}} k_{\mathrm{XB}} F_1 \frac{h^2}{2} \left(1 - \frac{v_{\mathrm{hs}}}{\varphi}\left(1 - e^{-\varphi/v_{\mathrm{hs}}}\right)\left(1 + \frac{1}{2G_2^2}\frac{v_{\mathrm{hs}}}{\varphi}\right)\right). \tag{3.8}$$

Huxley, proceeding by trial and error, obtained a good fit of experimental data with $F_1 = 13/16$ and $G_2 = 3.919$. For this parameters, by setting $F_{\mathrm{hf}} = 0$ we have $v_{\mathrm{hs}}^{\max} \simeq 4\varphi$. For instance, in [Bro76], with the choice $f_1 = 65\,\mathrm{s}^{-1}$, $g_1 = 15\,\mathrm{s}^{-1}$, $g_1 = 313.5\,\mathrm{s}^{-1}$, $h = 10\,\mathrm{nm}$, one gets $v_{\mathrm{hs}}^{\max} \simeq 1600\,\mathrm{nm\,s}^{-1}$, which gives $v^{\max} = v_{\mathrm{hs}}^{\max}/(SL_0/2) \simeq 1.45\,\mathrm{s}^{-1}$. All the above mentioned constants are calibrated for the skeletal muscle.

The distribution-moment equations

To avoid the solution of a PDE, in [Zah81] an approximation of the model (3.4) by means of ODEs was proposed. By applying a general strategy of statistical physics, the author computed the equations for the evolution of the distribution-moments of $n(x,t)$, defined as:

$$\mu^p(t) := \int_{-\infty}^{+\infty} x^p n(x,t) dx.$$

Indeed, thanks to the linear spring hypothesis for the myosin arm, the full distribution $n(x,t)$ is not needed to compute the force, but rather its first moment is enough, as

we have, from Eq. (3.5):

$$F_{\mathrm{hf}}(t) = \rho_{\mathrm{AM}}\, k_{\mathrm{XB}}\, \mu^1(t). \tag{3.9}$$

By multiplying Eq. (3.4) by x^p and integrating over $(-\infty, +\infty)$ one gets, for $p = 0, 1, \ldots$:

$$\frac{d}{dt}\mu^p(t) - p\, v_{\mathrm{hs}}(t)\, \mu^{p-1}(t) = \mu_f^p - \int_{-\infty}^{+\infty} x^p (f(x) + g(x)) n(x,t) dx, \tag{3.10}$$

where we have integrated by parts the term

$$\int_{-\infty}^{+\infty} x^p \frac{\partial n(x,t)}{\partial x} dx = \left[x^p\, n(x,t)\right]_{-\infty}^{+\infty} - p \int_{-\infty}^{+\infty} x^{p-1} n(x,t) dx = -p\, \mu^{p-1}(t),$$

and we have used the fact that, for $x \to \pm\infty$, n is definitely equal to zero. The last term of (3.10) needs to be modeled for model closure. In [Zah81] the authors proposed to assume a specific distribution (a gaussian distribution) for $n(\cdot, t)$, so that that term can be computed. Specifically, by assuming that:

$$n(x,t) = \frac{\mu^0(t)}{\sqrt{2\pi}\sigma(t)} \exp\left(-\frac{(x - \bar{x}(t))^2}{2\sigma^2(t)}\right),$$

where

$$\bar{x}(t) = \frac{\mu^1(t)}{\mu^0(t)}, \quad \sigma^2(t) = \frac{\mu^2(t)}{\mu^0(t)} - \left(\frac{\mu^1(t)}{\mu^0(t)}\right)^2,$$

the distribution $n(\cdot, t)$ is fully characterized by its first three moments, and thus the first three equations of (3.10) are completely equivalent to the PDE model (3.4). However, we have here to pay the price of a strong assumption of gaussianity for $n(\cdot, t)$. Still, the analytical solution of Eq. (3.7) shows that even in the steady-state case the distribution may be very skewed and thus significantly differ from a gaussian one.

When the transition rates $f(x)$ and $g(x)$ take special forms, the distribution-moments strategy can be used to derive exact equivalents of the PDE model (3.4) [BCS01; Cha+12]. In fact, if the total transition rate is independent of the displacement (i.e. $f(x) + g(x) = r$), the last term in (3.10) can be computed as:

$$\int_{-\infty}^{+\infty} x^p (f(x) + g(x)) n(x,t) dx = r\mu^p(t),$$

and the hierarchy of equations (3.10) can be truncated by considering only the first two moments:

$$\begin{cases} \dfrac{d}{dt}\mu^0(t) = \mu_f^0 - r\, \mu^0(t) & t \geq 0, \\ \dfrac{d}{dt}\mu^1(t) = \mu_f^1 - r\, \mu^1(t) + v_{\mathrm{hs}}(t)\, \mu^0(t) & t \geq 0. \end{cases} \tag{3.11}$$

Extensions of the H57 model

To account for the fact that not all XBs can be recruitable for attachment (e.g. because they do not lie in the overlap region, see 1.3.2), in [Cha+12] the authors modified the source term $(1 - n(x,t))f(x)$ of (3.4) into $(n_0(t) - n(x,t))f(x)$, where the reduction factor $0 \leq n_0(t) \leq 1$ denotes the fraction of recruitable XBs.

In [BCS01; Cha+12] the authors introduced a chemical input, affecting the transition rates $f(x)$ and $g(x)$ (that are in this case functions of time), to model the effect of the calcium-driven regulation. Moreover, by assuming that high relative velocities between the two filaments can lead to destruction of XBs, they introduced a further sink term, linearly proportional to $|v(t)|$. Specifically, the following transition rates were chosen:

$$f(x,t) = k_{\text{ATP}}\,\mathbb{1}_{x\in[0,1]}\,\mathbb{1}_{[\text{Ca}^{2+}]_\text{i}(t)>C},$$
$$g(x,t) = k_{\text{ATP}}\,\mathbb{1}_{x\notin[0,1]}\,\mathbb{1}_{[\text{Ca}^{2+}]_\text{i}(t)>C} + k_{\text{RS}}\,\mathbb{1}_{[\text{Ca}^{2+}]_\text{i}(t)\leq C} + \alpha|v(t)|,$$

where k_{ATP} is the ATP turnover rate, C is the activation threshold for $[\text{Ca}^{2+}]_\text{i}$ and α is a positive constant. Despite the introduction of the dependence on $[\text{Ca}^{2+}]_\text{i}(t)$ and $v(t)$, the sum $f(x,t) + g(x,t)$ is still independent of x. Hence, distribution-moment equations analogous to (3.11) can be derived for this model.

In [Kim+19; Kim19] the authors proposed a model, based on the H57 formalism, where the population of MHs is split into two pools: the first one contains the MHs located in the single-overlap zone, while the other one (for which $f = 0$) contains the remaining MHs. Each pool is characterized by its own density function $n(x,t)$, whose evolution is described by an equation similar to Eq. (3.4), supplemented with a source and a sink term accounting for fluxes across the two pools. Moreover, a variable representing the fraction of permissive BSs multiplies to attachment rate term.

Limitations of the H57 model

The models belonging to the family of the H57 model, however, are not able to explain some of the experimentally observed phenomena. In particular, they fail to reproduce the phenomena related to time scales that are faster than the time scale of the power-stroke (~ 1 ms). The reason is that this class of models does not incorporate a description of the power-stroke, but rather assumes that MHs attach in a stretched configuration. This cannot explain the fast force recovery following a sudden change in the sarcomere length (see Sec. 1.3.5) since, in the H57 model, force is recovered with a time scale that is compatible with the ATP turnover (order of 100 ms). These limitations were recognized by A. F. Huxley himself, who proposed, in 1971, a model incorporating an explicit description of the power-stroke.

3.1.3 Power-stroke models

In [HS71] the authors proposed a new model (HS71 model), by interpreting the pre-power-stroke and the post-power-stroke configurations as discrete states. Thus, they introduced a degree of freedom, y, that can be interpreted as the angular position of the rotating MH. The variable y is associated with a discrete energy potential, with two minima in 0 and a (where a is the power-stroke length), separated by an energy barrier. This newly introduced degree of freedom supplements the linear elastic element of the H57, with potential energy $u_e(x) = k_{\text{XB}}/2\,(x+y)^2$.

This *hard-spin* model provided a first quantitative description of the power-stroke, with the assumption that the fast force recovery (see Sec. 1.3.5) is a passive mechanisms, interpretable as a mechanical conformational change. This is coherent with the observation that the fast force recovery is not rate limited by the chemical stages, supporting the hypothesis that the power-stroke is a mechanical phenomenon.

The main drawback of the hard-spin HS71 model is that the transition between the two configurations requires the linear spring to be stretched by the effect of thermal

fluctuation in order to overcome the energy barrier. As a consequence, this model predicts a slower time-constant for the power-stroke than what is measured in experiments [Car11; CT18]. This led researchers to assume the existence of intermediate configurations, by the introduction of a number of additional states [HS71; Smi+08].

Soft-spin models

In contrast, in [MT10b; MT10a] the authors proposed to replace the rigid bistable device (or multi-stable) of hard-spin models by a bistable element, parametrized by a continuous variable. The transition from hard-spin to soft-spin removed the contradictions concerning the time scale of the power-stroke [CT18].

This model was extended with the inclusion of the attachment-detachement ATP-driven mechanism by adding a coloured noise (mimicking the out-of-equilibrium ATP reactions) to the Langevin dynamics within the energy landscape [MT10b].

In [CMC19] the authors proposed a mechano-chemical model (that we denote by CMC19 model), with a soft-spin model for MHs coupled with a chemical state describing the ATP-driven attachment-detachment process, obtaining a unified framework capable of matching both the phenomena related to the power-stroke (such as the fast velocity recovery) and those related to the attachment-detachment of XBs (such as the force-velocity curve). Moreover, the authors showed that the H57 model can be derived from the CMC19 model under simplifying assumptions, thus giving an interpretation to the H57 model in terms of Langevin dynamics. Remarkably, the authors also showed that a lumped version of the CMC19 model in which the power-stroke variable is assumed to be in equilibrium formally reduces to a H57-like model, thus allowing to interpret the transition rates of the H57 model as *effective* rates, in light of the CMC19 model. We illustrate in what follows the construction of the CMC19 model.

Caruel-Moireau-Chapelle 2019 model

Model setup. We consider a single MH, described by a discrete degree of freedom, namely ω^t ($\omega^t = 1$ when the MH is attached, $\omega^t = 0$ when it is detached), and two continuous degrees of freedom, namely Z^t (measuring the distance of the MH tip from the rest-position of the myosin harm) and Y^t (associated with the angular orientation of the MH), as it is shown in Fig. 3.3. In the pre-power-stroke configuration, we typically have $Y^t = 0$, and thus the elongation of the myosin arm coincides with Z^t. When power-stroke occurs, Y^t becomes positive, making the total myosin arm elogation increase. The myosin arm elogation is thus given by $X^t + Y^t$ (see Fig. 3.3). When the MH is attached ($\omega^t = 1$) the tip of the MH is attached to the BS. Therefore, we have by definition $Z^t \equiv x$ (where we denote by x, as in the previous sections, the distance between to myosin arm rest position and the BS).

The elastic element is associated with a quadratic energy u_e, while the internal degree of freedom Y^t is associated with a bistable energy u_ω, that takes different expression when the XB is attached and when instead is not. Specifically, in the attached (respectively, detached) configuration, the minimum corresponding to the post-power-stroke configuration ($Y^t > 0$) is endowed with a lower (respectively, higher) energy than the pre-power-stroke configuration ($Y^t = 0$). The resulting energy landscape for the mechanical variables (Z^t, Y^t) is thus associated with the energy $w_\omega(z, y) = u_\omega(y) + u_e(z + y)$.

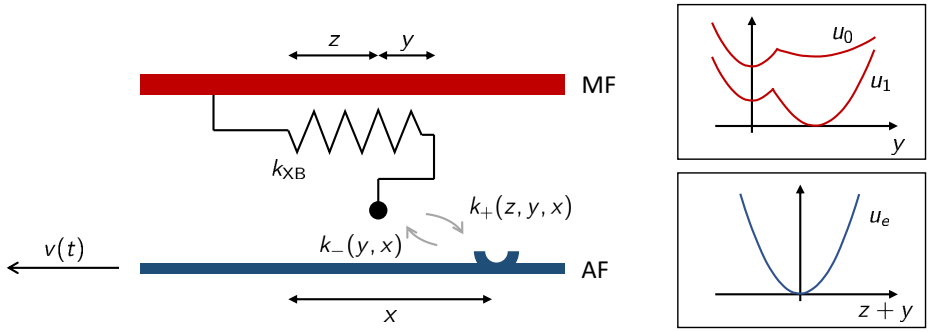

Figure 3.3: Scheme of the CMC19 model. The MH is described by two degrees of freedom (z and y). When the MH is attached, the degree of freedom z coincides with the variable x. The attachment-detachment rates of MHs (f and g) depend on the XB distortion x. The myosin arm is modeled as a linear elastic element with stiffness k_{XB}, while the degree of freedom y is associated with a bistable energy, which depends on the XB attachment state.

The Langevin dynamics [KS98] associated with the energy $w_\omega(z,y)$ gives the following stochastic differential equation:

$$\begin{cases} \eta\, dZ^t = \left(-\omega^t \eta\, v_{\text{hs}} - (1-\omega^t)\dfrac{\partial w_\omega}{\partial z}(Z^t, Y^t)\right) dt \\ \qquad\quad + \eta \delta_{t_s}(t)\left(x - Z^t\right) dt + (1-\omega^t)\sqrt{2\eta k_B T}\, dB_z^t \qquad t \geq 0, \\ \eta\, dY^t = -\dfrac{\partial w_\omega}{\partial y}(Z^t, Y^t) dt + \sqrt{2\eta k_B T}\, dB_y^t \qquad t \geq 0, \end{cases} \tag{3.12}$$

where dB_z^t and dB_y^t are the increments of a two-dimensional Brownian motion, η is the viscous damping coefficient associated with the surrounding fluid, k_B denotes the Boltzmann constant, T the absolute temperature, and t_s denotes the time of any switch from $\omega^t = 0$ to $\omega^t = 1$. We notice that, far from $t = t_s$, when the XB is detached (i.e. $\omega^t = 0$), the first equation reduces to:

$$\eta dZ^t = -\frac{\partial w_\omega}{\partial z}(Z^t, Y^t) dt + \sqrt{2\eta k_B T}\, dB_z^t,$$

while when the XB is attached (i.e. $\omega^t = 1$), it reduces to:

$$dZ^t = -v_{\text{hs}}\, dt,$$

coherently with the fact that $Z^t \equiv x$ (remember that v_{hs} denotes the *shortening* velocity, thus $\dot{x} = -v_{\text{hs}}$). Finally, at time $t = t_s$ the Dirac delta term makes the variable Z^t instantaneously jump to $Z^t = x$.

The kinetics of the chemical degree of freedom ω^t is determined by the following transition rates:

$$\begin{aligned} \mathbb{P}\left[\omega^{t+\Delta t} = 1 | \omega^t = 0\right] &= k_+(Z^t, Y^t, x, t)\Delta t + o(\Delta t), \\ \mathbb{P}\left[\omega^{t+\Delta t} = 0 | \omega^t = 1\right] &= k_-(Y^t, x, t)\Delta t + o(\Delta t), \end{aligned} \tag{3.13}$$

where the detachment transition rate is independent of Z^t since when the MH is attached we have $Z^t = x$.

Fokker-Plank equation. To write the Fokker-Plank equation (i.e. the equivalent of the FKE for continuous variables) associated with Eq. (3.12), we denote by $p(z, y, \omega; x, t)$ the probability density for a MH (at time t and located at distance x) of being in state (z, y, ω) (we notice that x and t are regarded as deterministic variables). Since for attached heads we have $Z^t = x$, the probability density for $\omega = 1$ can be written as:

$$p(z, y, 1; x, t) = \delta_x(z)\bar{p}(y; x, t).$$

With this notation, the Fokker-Plank equation reads:

$$\begin{cases} \dfrac{\partial}{\partial t}p(z,y,0;x,t) = v_{\text{hs}}\dfrac{\partial}{\partial x}p(z,y,0;x,t) \\ \qquad + \eta^{-1}\dfrac{\partial}{\partial z}\left(\dfrac{\partial}{\partial z}w_0(z,y)\,p(z,y,0;x,t)\right) \\ \qquad + \eta^{-1}\dfrac{\partial}{\partial y}\left(\dfrac{\partial}{\partial y}w_0(z,y)\,p(z,y,0;x,t)\right) \\ \qquad + \dfrac{k_BT}{\eta}\left(\dfrac{\partial^2}{\partial z^2}p(z,y,0;x,t) + \dfrac{\partial^2}{\partial y^2}p(z,y,0;x,t)\right) \\ \qquad + k_-(y,x)\delta_x(z)\bar{p}(y;x,t) \\ \qquad - k_+(z,y,x)p(z,y,0;x,t) \qquad\qquad x,y,z \in \mathbb{R},\ t \geq 0, \\ \dfrac{\partial}{\partial t}\bar{p}(y;x,t) = v_{\text{hs}}\dfrac{\partial}{\partial x}\bar{p}(y;x,t) \\ \qquad + \eta^{-1}\dfrac{\partial}{\partial y}\left(\dfrac{\partial}{\partial y}w_1(x,y)\,\bar{p}(y;x,t)\right) \\ \qquad + \dfrac{k_BT}{\eta}\dfrac{\partial^2}{\partial y^2}\bar{p}(y;x,t) \\ \qquad + \displaystyle\int_{-\infty}^{+\infty} k_+(z,y,x)p(z,y,0;x,t)dz \\ \qquad - k_-(y,x)\bar{p}(y;x,t) \qquad\qquad x,y \in \mathbb{R},\ t \geq 0. \end{cases} \tag{3.14}$$

To link this model with the H57 formalism, we notice that the fraction of attached MHs with displacement x at time t is given by:

$$n(x,t) = \int\int p(z,y,1;x,t)\,dz\,dy = \int \bar{p}(y;x,t)\,dy.$$

By integrating the equations of (3.14) with respct to z and y, we obtain the following H57 like equation:

$$\frac{\partial n(x,t)}{\partial t} - v_{\text{hs}}(t)\frac{\partial n(x,t)}{\partial x} = (1 - n(x,t))f(x,t) - n(x,t)g(x,t),$$

where the transition rates are given by:

$$\begin{aligned} f(x,t) &= \int\int k_+(z,y,x)\frac{p(z,y,0;x,t)}{1-n(x,t)}dz\,dy, \\ g(x,t) &= \int k_-(y,x)\frac{\bar{p}(y;x,t)}{n(x,t)}dy. \end{aligned} \tag{3.15}$$

We notice that this H57 version of Eq. (3.14) is not written in closed form, as $f(x,t)$ and $g(x,t)$ depend on the specific distribution of the degrees of freedom z and y and not only on the averaged quantity $n(x,t)$.

Recovering the H57 model. This analogy with the H57 model allows for a more direct comparison when hypotheses closer to those of the H57 model are assumed. Indeed, by canceling the degree of freedom associated with the power-stroke (i.e. $Y^t \equiv 0$), we have:

$$p(z, y, 0; x, t) = \hat{p}(z; x, t)\delta(y),$$
$$\bar{p}(y; x, t) = n(x, t)\delta(y),$$

which gives, thanks to (3.15), $g(x,t) = k_-(0,x) = \hat{g}(x)$. Moreover, coherently with H57, let us assume that the binding rate is independent of Z^t, that is $k_+(z, 0, x) = \hat{f}(x)$, which gives, thanks to (3.15), $f(x,t) = \hat{f}(x)$. In this way, we recover the original H57 model.

Thermal equilibrium model. More interestingly, the authors recovered an analogy with the H57 model under the hypothesis that the time scale of the macroscopic behavior is large enough for the internal degrees of freedom to be at thermal equilibrium. The equilibrium distributions can be multiplicatively decomposed as:

$$p(z, y, 0; x, t) = p_0^{th}(z, y)(1 - n(x, t)),$$
$$\bar{p}(y; x, t) = p_1^{th}(y; x)n(x, t),$$

where

$$p_0^{th}(z, y) = \frac{\exp\left(-\frac{w_0(z,y)}{k_B T}\right)}{\int\int \exp\left(-\frac{w_0(z,y)}{k_B T}\right) dz\, dy},$$
$$p_1^{th}(y; x) = \frac{\exp\left(-\frac{w_1(x,y)}{k_B T}\right)}{\int \exp\left(-\frac{w_1(x,y)}{k_B T}\right) dy}.$$

When the probability distribution takes this form, Eq. (3.15) reduces to:

$$\begin{aligned} f(x,t) = f^{th}(x) &= \int\int k_+(z, y, x)p_0^{th}(z, y)dz\, dy, \\ g(x,t) = g^{th}(x) &= \int k_-(y, x)p_1^{th}(y; x)dy, \end{aligned} \tag{3.16}$$

which gives a model, equivalent to the H57 one, in closed form. This conclusion is more than a mere analogy and it allows to shed a new light on the H57 model. The H57 model, which does not explicitly represent the power-stroke, can indeed be interpreted as a model where the variable describing the degree of freedom associated with the power-stroke is considered at equilibrium. Unlike in the H57 original formulation, where the power-stroke is simply neglected, here it is accounted for in the definition of the transition rates given by (3.16). This allows to relate a microscopic description of the contractile mechanism with macroscopic effective quantities.

3.2 A generalized Huxley '57 model

In light of the interpretation of the H57 model given in [CMC19], in this section we consider a (generalized) version of the H57 model, to investigate to which extent this model can explain the experimentally observed behaviors linked to the XB dynamics.

First, we make some comments on the hypotheses underlying the H57 model.

- When writing the source term $(1-n(x,t))f(x)$, we are assuming that, for all x in the support of f, the number of recruitable MH-BS pairs is $1-n(x,t)$. However, we are not considering the possibility that a MH-BS pair with such displacement is not recruitable for XB formation, since either the MH is attached with a BS with displacement $x + kD_A$ or the BS is attached to a MH with displacement $x+kD_M$, with $k \in \mathbb{Z}\setminus\{0\}$ (where D_A and D_M denote, respectively, the distance between two consecutive MHs and BSs). This cannot be excluded a priori, in particular when the muscle is stretched or elongated in a very fast manner, unless g is chosen in such a way to exclude this possibility (e.g. by assuming an infinite detachment rate for x out of a given interval). We will return to this issue in Sec. 4.2.2.

- Up to now we have considered the condition of full activation. To take into account, in a simple way, the fact that not all binding sites may be in permissive state, we consider two options. The first one is to multiply, in the computation of force, the number of XBs by the fraction of permissive BSs, P. The second is to replace in (3.4) the term $(1-n(x,t))$ by $(P-n(x,t))$, similarly to what proposed, to account for the filaments overlapping, in [Cha+12]. Notice that, thanks to the linearity of the equation, both approaches lead to the same result. Even if this approach is approximate, as it does not take into account the possible time dependence of $P(t)$, for the moment we restrict ourselves to the condition of constant activation.

- As the support of f is clearly compact and close to $x = 0$ and g is positive elsewhere, solutions of the H57 model are such that n is zero (or very small) far from $x = 0$. Therefore, to compute average quantities for the XB population one can integrate n over the whole real line (even if the assumption that ρ_{AM} represents the density of MH-BS couples is valid only close to $x = 0$).

On the basis of the above considerations and being aware of the limitations of the H57 model, we consider the following modified H57 model, where we allow (as in [BCS01; Cha+12]) for a dependency of the transition rate on the shortening velocity $v_{\mathrm{hs}}(t)$, and we introduce the dependence on the permissivity P:

$$\frac{\partial n(x,t)}{\partial t} - v_{\mathrm{hs}}(t)\frac{\partial n(x,t)}{\partial x} = (P - n(x,t))f(x,v(t)) - n(x,t)g(x,v(t)), \quad x \in \mathbb{R},\, t \geq 0, \tag{3.17}$$

where we prefer to express the transition rates in function of the normalized shortening velocity $v(t) = v_{\mathrm{hs}}(t)/(SL_0/2)$. In (3.17), the quantities to be modeled are $f(x,v)$ and $g(x,v)$.

The force generated by half filament, by assuming that a XB attached with displacement x exerts a force of $F_{\mathrm{XB}}(x)$, is given by:

$$F_{\mathrm{hf}}(t) = \rho_{\mathrm{AM}} \int_{-\infty}^{+\infty} F_{\mathrm{XB}}(x) n(x,t) dx. \tag{3.18}$$

In particular, with a linear spring XB model (i.e. $F_{\mathrm{XB}}(x) = k_{\mathrm{XB}}\, x$), we have:

$$F_{\mathrm{hf}}(t) = \rho_{\mathrm{AM}} k_{\mathrm{XB}} \int_{-\infty}^{+\infty} x\, n(x,t) dx. \tag{3.19}$$

The macroscopic tension, in turn, is proportional to the force generated by half filament.

3.2.1 Distribution-moments equation

Under the hypothesis that the total transition rate is independent of x (i.e. there exists a function $r(v) = f(x,v) + g(x,v)$), it is possible to write the distribution-moments equations (see Sec. 3.1.2). With this aim, we introduce the moments for $p = 0, 1, \ldots$ (we notice that, differently from the notation used in Sec. 3.1.2, μ^p are dimensionless, while μ_f^p are inverse of time units):

$$\begin{aligned} \mu^p(t) &:= \int_{-\infty}^{+\infty} \left(\frac{x}{SL_0/2}\right)^p n(x,t)\frac{dx}{D_M}, \\ \mu_f^p(v) &:= \int_{-\infty}^{+\infty} \left(\frac{x}{SL_0/2}\right)^p f(x,v)\frac{dx}{D_M}. \end{aligned} \tag{3.20}$$

Thanks to this definition, $\mu^0(t)$ can be interpreted as the fraction of BSs involved in a XB. Moreover, $\mu^1(t)/\mu^0(t)$ corresponds to the average distortion of attached XBs, normalized with respect to $SL_0/2$. We notice that, under the linear spring hypothesis, thanks to Eq. (3.19), the total active force is proportional to $\mu^1(t)$. Therefore, we can write $T_{\mathrm{a}}(t) = a_{\mathrm{XB}}\mu^1(t)$, where a_{XB} has the dimension of a pressure. In Chap. 7 we will extensively deal with the issue of upscaling from the miscoscopic level to the macroscopic one and we will give an explicit expression for the factor a_{XB}. Moreover, we will show that the active stiffness at the tissue level is given by $K_{\mathrm{a}}(t) = a_{\mathrm{XB}}\mu^0(t)$.

By multiplying by $(x/(SL_0/2))^p$, integrating over $x \in (-\infty, +\infty)$ and using the fact that $n(-\infty,t) = n(+\infty,t) = 0$, we get the following distribution-moments equations:

$$\begin{cases} \dfrac{d}{dt}\mu^0(t) = -r(v(t))\mu^0(t) + P\,\mu_f^0(v(t)) & t \geq 0, \\ \dfrac{d}{dt}\mu^1(t) = -r(v(t))\mu^1(t) + P\,\mu_f^1(v(t)) - \mu^0(t)v(t) & t \geq 0. \end{cases} \tag{3.21}$$

By assuming that $f + g$ is independent of x, the freedom in the choice of the functions describing the model has been reduced, as we have to model $\mu_f^0(v)$, $\mu_f^1(v)$ and $r(v)$, that are only functions of v.

3.2.2 Steady-state solution

By assuming a constant shortening $v(t) \equiv \bar{v}$, and solving (3.20) for $\frac{d}{dt} = 0$, we get the following steady-state solution:

$$\begin{aligned} \bar{\mu}^0 &= P\frac{\mu_f^0(\bar{v})}{r(\bar{v})}, \\ \bar{\mu}^1 &= P\frac{\mu_f^1(\bar{v}) - \mu^0(t)\bar{v}}{r(\bar{v})} = P\left(\frac{\mu_f^1(\bar{v})}{r(\bar{v})} - \frac{\mu_f^0(\bar{v})}{r(\bar{v})^2}\bar{v}\right). \end{aligned} \tag{3.22}$$

Since the force is proportional to μ^1, the last equation gives the force-velocity relationship. Moreover, the steady-state solution allows to compute some quantities of interest. The force in isometric conditions is given by $T_{\mathrm{a}}^{\mathrm{iso}} = a_{\mathrm{XB}}(\bar{\mu}^1)_{\bar{v}=0} = a_{\mathrm{XB}}P\frac{\mu_f^1(0)}{r(0)}$. The fraction of attached XBs, in turn, is given by $(\bar{\mu}^0)_{\bar{v}=0} = P\frac{\mu_f^0(0)}{r(0)}$. Finally, the maximum shortening velocity $v^{\max}$ can be computed as the positive solution of the equation $\mu_f^1(v^{\max})r(v^{\max}) = \mu_f^0(v^{\max})v^{\max}$.

We now show how the above mentioned quantities can be expressed under more restrictive hypotheses for f and g. For instance, it is reasonable to assume that the sliding velocity only affects the detachment rate, so that $f(x,v) = \bar{f}(x)$. In this case, assuming again that the sum $f+g$ is independent of x, we can write $g(x,v) = r_0 - \bar{f}(x) + q(v)$, for some $q(v)$ such that $q(0) = 0$ and where $r_0 = r(0)$. The term $q(v)$ models the rate of XB destruction due to rapid length changes. Under this additional hypothesis, the objects to be modeled are just $\mu^0_{\bar{f}}$, $\mu^1_{\bar{f}}$, r_0 and $q(v)$ (three scalar values and a function). If we set, as in [Cha+12], $q(v) = \alpha|v|$ (which reduces the quantities to be modeled to 4 scalars), the maximum shortening velocity takes the form:

$$v^{\max} = r_0 \left(\frac{\mu^0_{\bar{f}}}{\mu^1_{\bar{f}}} - \alpha \right)^{-1}.$$

Let us consider now the particular case of constant attachment rate within the interval $x \in [s_0, s_0 + h]$ (as in [BCS01]):

$$f(x,v) = k_{\text{ATP}} \mathbb{1}_{[s_0, s_0+h]}(x), \qquad g(x,v) = k_{\text{ATP}}(1 - \mathbb{1}_{[s_0,s_0+h]}(x)) + q(v). \tag{3.23}$$

This choice falls within the above mentioned case. The quantities to be modeled, in this case, are k_{ATP}, h, s_0, $q(v)$, which are linked to the previous ones by:

$$\mu^0_{\bar{f}} = k_{\text{ATP}} \frac{h}{D_M}, \qquad \mu^1_{\bar{f}} = k_{\text{ATP}} \frac{h(h+2\,s_0)}{SL_0\, D_M}, \qquad r_0 = k_{\text{ATP}}, \tag{3.24}$$

and, conversely:

$$h = \frac{k_{\text{ATP}}}{\mu^0_{\bar{f}} D_M}, \qquad s_0 = \frac{1}{2}\left(\frac{SL_0\, D_M \mu^1_{\bar{f}}}{k_{\text{ATP}} h} - h \right), \qquad k_{\text{ATP}} = r_0, \tag{3.25}$$

which allows to give a microscopical interpretation to the constants. In this case, the steady-state solution reads:

$$\begin{aligned} \bar{\mu}^0 &= P \frac{h}{D_M} \left(1 + \frac{q(\bar{v})}{k_{\text{ATP}}} \right)^{-1}, \\ \bar{\mu}^1 &= P \frac{h}{2\, D_M} \left(1 + \frac{q(\bar{v})}{k_{\text{ATP}}} \right)^{-2} \left(\frac{h + 2s_0}{SL_0/2} \left(1 + \frac{q(\bar{v})}{k_{\text{ATP}}} \right) - 2 \frac{\bar{v}}{k_{\text{ATP}}} \right). \end{aligned} \tag{3.26}$$

Moreover, the isometric tension is given by $T_{\text{a}}^{\text{iso}} = a_{\text{XB}} P \frac{h(h+2\,s_0)}{SL_0\, D_M}$ and the fraction of attached XBs in isometric conditions is $(\bar{\mu}^0)_{\bar{v}=0} = P \frac{h}{D_M}$. With the choice $q(v) = \alpha|v|$, the maximum shortening velocity, if $\alpha < \frac{SL_0}{h+2s_0}$, is given by:

$$v^{\max} = k_{\text{ATP}} \left(\frac{SL_0}{h + 2s_0} - \alpha \right)^{-1}.$$

Conversely, if $\alpha \geq \frac{SL_0}{h+2s_0}$, $v^{\max}$ is not defined, as the force-velocity relationship never intercepts the $T_{\text{a}} = 0$ axis.

3.2.3 Fast transients solution

Because of the lack of explicit representation of the power-stroke, the generalized H57 model (3.20) fails to reproduce the three phases after a fast step, either in length or in

tension (see Sec. 1.3.5). Indeed, in place of the two fast steps (the elastic response and the fast force recovery, due to the power-stroke), we have only one fast step, followed by the slow force recovery (or by the constant shortening, in the case of the soft device experiment). In this section, we study the predictions of the model concerning such fast phase.

In order to study the behavior predicted by the model when a fast transient experiment is performed (here we focus on steps in length), we suppose that at $t = 0$ the muscle is in steady-state isometric conditions (i.e. $\mu^0(0) = P\mu_f^0(0)/r(0)$, $\mu^1(0) = P\mu_f^1(0)/r(0)$). We then consider a sudden change in length ΔL (the relative shortening w.r.t. half sarcomere, thus a dimensionless quantity), accomplished in a small amount of time δ (i.e. $v(t) = \frac{\Delta L}{\delta}\mathbb{1}_{[0,\delta]}(t)$). We study the solution at $t = \delta$, for $\delta \to 0^+$.

The solution of (3.21) when $v(t) = \bar{v}$ is constant is given by:

$$\begin{cases} \mu^0(t) = \mu^0(0) + \left(P\dfrac{\mu_f^0(\bar{v})}{r(\bar{v})} - \mu^0(0)\right)\left(1 - e^{-r(\bar{v})t}\right) & t \geq 0, \\ \mu^1(t) = \mu^1(0) + \left(P\left(\dfrac{\mu_f^1(\bar{v})}{r(\bar{v})} - \dfrac{\mu_f^0(\bar{v})}{r(\bar{v})^2}\bar{v}\right) - \mu^1(0)\right)\left(1 - e^{-r(\bar{v})t}\right) & \\ \qquad + \left(P\dfrac{\mu_f^0(\bar{v})}{r(\bar{v})} - \mu^0(0)\right)\bar{v}\,t\,e^{-r(\bar{v})t} & t \geq 0. \end{cases} \tag{3.27}$$

By setting $\bar{v} = \frac{\Delta L}{\delta}$, the tension at the end of the length step reads:

$$\begin{aligned} T_{\mathrm{a}}(\delta) = a_{\mathrm{XB}}\mu^1(\delta) = a_{\mathrm{XB}}P\Bigg[\frac{\mu_f^1}{r(0)} + \left(\mu_f^1\left(\frac{1}{r(\bar{v})} - \frac{1}{r(0)}\right) - \frac{\mu_f^0}{r(\bar{v})^2}\frac{\Delta L}{\delta}\right)\left(1 - e^{-r(\bar{v})\delta}\right) \\ + \mu_f^0\left(\frac{1}{r(\bar{v})} - \frac{1}{r(0)}\right)\Delta L\,e^{-r(\bar{v})\delta}\Bigg]. \end{aligned} \tag{3.28}$$

For time $t > \delta$, the solution is given by (3.27), shifted by δ, with $\bar{v} = 0$ and with initial state given by (3.28). However, to characterize the fast phase, we are here only interested in studying the asymptotic behavior of (3.28) for $\delta \to 0^+$. The solution depends on the behavior of $r(v)$ for $v \to +\infty$. We distinguish between four possible cases: bounded or with sublinear, linear or superlinear growth.

- **Saturating behavior.** Suppose that for $v \to +\infty$, $r(v) \to r_{\max}$. Then, we have:

$$\begin{aligned} T_{\mathrm{a}}(\delta) &\sim a_{\mathrm{XB}}P\left[\frac{\mu_f^1}{r(0)} + \frac{\mu_f^0}{r_{\max}}\Delta L - \mu_f^0\left(\frac{1}{r_{\max}} - \frac{1}{r(0)}\right)\Delta L\right] \\ &= \frac{a_{\mathrm{XB}}P\mu_f^1}{r(0)} - \frac{a_{\mathrm{XB}}P\mu_f^0}{r(0)}\Delta L, \end{aligned} \tag{3.29}$$

  which is a linear response, with slope $\frac{a_{\mathrm{XB}}P\mu_f^0}{r(0)}$. In this case, therefore, the fast response is that of a linear elastic spring (like the T_1/L_1 curve), with stiffness given by $\frac{a_{\mathrm{XB}}P\mu_f^0}{r(0)}$.

- **Sublinear growth.** Suppose that $r(v) \to +\infty$, but $r(v)/v \to 0$. Then we have $r(\bar{v})\delta = r(\frac{\Delta L}{\delta})\delta \to 0$, and thus:

$$T_{\mathrm{a}}(\delta) \sim \frac{a_{\mathrm{XB}} P \mu_f^1}{r(0)} - \frac{a_{\mathrm{XB}} P \mu_f^0}{r(0)} \Delta L, \tag{3.30}$$

  which is the same behavior as the previous case. For this reason, from now on, we will include both cases in the sublinear growth one.

- **Linear growth.** Suppose now that $r(v) \sim \alpha v$. In this case, we have $r(\bar{v})\delta = r(\frac{\Delta L}{\delta})\delta \sim \alpha \Delta L$ and thus:

$$T_{\mathrm{a}}(\delta) \sim \frac{a_{\mathrm{XB}} P \mu_f^1}{r(0)} e^{-\alpha \Delta L} - \frac{a_{\mathrm{XB}} P \mu_f^0}{r(0)} e^{-\alpha \Delta L} \Delta L. \tag{3.31}$$

  Hence, in this case the response is different from a linearly elastic element. In order to compare the stiffness for small step lengths with the stiffness predicted in the sublinear growth case, we linearize around $\Delta L = 0$, getting:

$$T_{\mathrm{a}}(\delta) \sim \frac{a_{\mathrm{XB}} P \mu_f^1}{r(0)} - a_{\mathrm{XB}} P \frac{\mu_f^0 + \alpha \mu_f^1}{r(0)} \Delta L. \tag{3.32}$$

  In conclusion, the stiffness associated with small steps is increased by a term $\alpha\, a_{\mathrm{XB}}\, P\, \mu_f^1 / r(0)$.

- **Superlinear growth.** Suppose that $r(v) \to +\infty$ and $r(v)/v \to +\infty$. Then we have $r(\bar{v})\delta = r(\frac{\Delta L}{\delta})\delta \to +\infty$, which gives:

$$T_{\mathrm{a}}(\delta) \to 0. \tag{3.33}$$

  This means that if the destruction rate grows more than linearly in the velocity, then, in the limit of an instantaneous length step, the velocity is such that all the XB are destructed.

3.2.4 Model calibration

As noticed in Sec. 3.2, the calibration of the generalized H57 model (3.20) requires the definition of the functions $f(x, v)$ and $g(x, v)$. However, such functions, without a detailed microscopical model, are difficult to be constrained solely based on experimental results. By assuming that the sum $f + g$ is independent of x and that v only affects detachment, instead, the objects to be constrained reduce to the four scalars μ_f^0, μ_f^1, r_0, a_{XB} and the function $q(v)$. In addition, as shown in Sec. 3.2.3, the response to fast transients is only affected by the asymptotic behavior of $q(v)$ for $|v| \to +\infty$, while the force-velocity relationship is only affected by the values of $q(v)$ for $0 \le v \le v^{\max}$. Therefore, in the following, we will restrict ourselves to the following two cases:

- **Sublinear growth**: we consider $q(v)$ such that $q(v) = \alpha|v|$ for small velocities, while for $|v| \to +\infty$ we have $q(v)/|v| \to 0$.

- **Linear growth**: we consider for simplicity the case $q(v) = \alpha|v|$.

We do not consider the case of superlinear growth since in the limit of instantaneous response it predicts the detachment of all the XBs, which hinders the possibility of fitting any fast response curve.

The behavior of the model is thus determined by five scalar parameters ($\mu_{\bar{f}}^0$, $\mu_{\bar{f}}^1$, r_0, a_{XB}, α) and by the asymptotic of behavior $q(v)$ (linear or sublinear). From the previous sections, it follows that by acting on the above mentioned parameters, the generalized H57 model can match the following experimentally measured quantities.

- Under **isometric conditions**, the solution allows to compute the following quantities.
  - The isometric tension:
$$T_{\mathrm{a}}^{\mathrm{iso}} = a_{\mathrm{XB}}(\bar{\mu}^1)_{\bar{v}=0} = a_{\mathrm{XB}} P \frac{\mu_{\bar{f}}^1}{r_0}.$$
  - The fraction of attached XBs:
$$\mu_{\mathrm{iso}}^0 := (\bar{\mu}^0)_{\bar{v}=0} = P \frac{\mu_{\bar{f}}^0}{r_0}.$$
- The **force-velocity** is invariant after normalization with respect to the isometric tension (see 1.3.4). The generalized H57 model correctly predicts this fact. If we suppose, for instance, to vary the calcium concentration and consequently the value of P, the normalized force-length relationship would be unaffected. Indeed, the normalized force-length relationship is given by:
$$T_{\mathrm{a}}/T_{\mathrm{a}}^{\mathrm{iso}} = \frac{1}{1+\alpha\frac{|v|}{r_0}} - \frac{\mu_{\bar{f}}^0/\mu_{\bar{f}}^1}{\left(1+\alpha\frac{|v|}{r_0}\right)^2}\frac{v}{r_0}.$$
  Unlike the original H57 model, that predicts a linear force-velocity relationship (corresponding to the case $\alpha = 0$), by allowing for a dependence of the detachment rate on the velocity, the experimentally observed convex shape can be obtained. Indeed, by properly choosing the parameters of the model, one can fit the following two quantities, characterizing the relationship for large and for small velocities, respectively.
  - The maximum shortening velocity:
$$v^{\max} = r_0 \left(\frac{\mu_{\bar{f}}^0}{\mu_{\bar{f}}^1} - \alpha\right)^{-1}.$$
  - The inverse of the sensitivity of the normalized force w.r.t. velocity changes in isometric conditions (see Fig. 3.4a):
$$v^0 := -\left(\frac{\partial \bar{T}_{\mathrm{a}}/T_{\mathrm{a}}^{\mathrm{iso}}}{\partial v}\bigg|_{v=0}\right)^{-1} = r_0\left(\frac{\mu_{\bar{f}}^0}{\mu_{\bar{f}}^1} + \alpha\right)^{-1}.$$
  With the original H57 model, having $\alpha = 0$, we have $v^{\max} = v^0$ and the behaviors at small and large velocities cannot be decoupled.
- The **fast transients** response is characterized by two distinct curves, associated with different time scales (see Sec. 1.3.5). As previously noticed, models belonging to the H57 class do not incorporate a description of the power-stroke and are

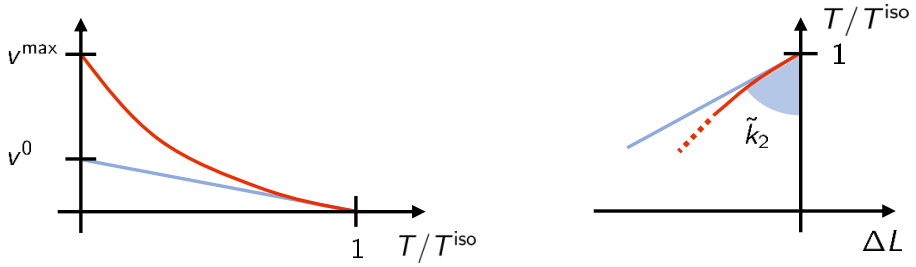

(a) Force-velocity relatioship

(b) Fast transient response

Figure 3.4: The force-velocity relationship (a) is characterized by the maximum shortening velocity $v^{\max}$ (the intercept of the curve with the axis $T_a = 0$) and by the inverse sensitivity of the force to velocity in isometric conditions v^0, which can be interpreted as the intercept with the axis $T_a = 0$ of the tangent to the curve in isometric conditions. On the other hand, the response to fast transients is characterized by the normalized stiffness $\tilde{k}_2$, where the subscript 2 reflects the fact that this value characterizes the T_2-L_2 response.

thus only capable of reproducing the instantaneous linear response. However, if we interpret the H57 model as the limit of a more detailed model where the power-stroke is considered at equilibrium (see Sec. 3.1.3), the fast response is only characterized by a single time constant, corresponding to the slowest of the two time constants observed experimentally. Such time constant, therefore, corresponds to the second of the phases considered in 1.3.5. For this reason, we interpret the stiffness associated with fast steps in the generalized H57 model of Eq. (3.20) as the stiffness associated with the $T_2 - L_2$ curve. In particular, the parameters can be chosen so that to fit the following value.

- The tangent normalized stiffness in isometric conditions (see Fig. 3.4b):

$$\tilde{k}_2 := -\left.\frac{\partial T_a(0^+)/T_a^{iso}}{\partial \Delta L}\right|_{\Delta L=0} = \begin{cases} \mu_{\bar{f}}^0/\mu_{\bar{f}}^1 & \text{sublinear q,} \\ \mu_{\bar{f}}^0/\mu_{\bar{f}}^1 + \alpha & \text{linear q.} \end{cases}$$

Moreover, we notice that, if one is interested in macroscopic regimes characterized by sufficiently large time scales, only the region of the T_2-L_2 curve associated with small steps is of interest. Indeed, the larger the length step, the higher shortening velocities are needed to appreciate the distinction between phase 2 and phases 3-4 of the response (we will quantitatively support this point in Sec. 4.4.6). In conclusion, since in the region associated with small steps a linear fit provides a good approximation of the curve, the quantity $\tilde{k}_2$ alone provides a sufficiently complete characterization of the fast step response.

The five parameters characterizing the generalized H57 model (3.20) can be assigned to match the five measured quantities T_a^{iso}, μ_{iso}^0, $v^{\max}$, v^0 and $\tilde{k}_2$. This provides a practical way of calibrating the model parameters from experimental measurements. Specifically, in the linear growth case, the parameters of the model can be constrained

by the following relationships:

$$\begin{aligned} r_0 &= \tilde{k}_2\, v^0, \\ \alpha &= \frac{r_0}{2}((v^0)^{-1} - (v^{\max})^{-1}) = \frac{\tilde{k}_2}{2}\left(1 - \frac{v^0}{v^{\max}}\right), \\ \mu^0_{\bar{f}} &= \frac{\mu^0_{\text{iso}} r_0}{P} = \frac{\mu^0_{\text{iso}} \tilde{k}_2 v^0}{P}, \\ \mu^1_{\bar{f}} &= \left(\tilde{k}_2 - \alpha\right)^{-1} \mu^0_{\bar{f}}, \\ a_{\text{XB}} &= \frac{T^{\text{iso}}_{\text{a}} r_0}{\mu^1_{\bar{f}} P} = \frac{T^{\text{iso}}_{\text{a}} \tilde{k}_2 (1 + \frac{v^0}{v^{\max}})}{2\mu^0_{\text{iso}}}. \end{aligned} \tag{3.34}$$

Conversely, in the sublinear growth case we have:

$$\begin{aligned} r_0 &= \frac{2\,\tilde{k}_2 v^{\max}}{1 + v^{\max}/v^0}, \\ \alpha &= \frac{v^{\max} - v^0}{v^{\max} + v^0}\tilde{k}_2, \\ \mu^0_{\bar{f}} &= \frac{\mu^0_{\text{iso}} r_0}{P}, \\ \mu^1_{\bar{f}} &= \mu^0_{\bar{f}}/\tilde{k}_2, \\ a_{\text{XB}} &= \frac{T^{\text{iso}}_{\text{a}} r_0}{\mu^1_{\bar{f}} P}. \end{aligned} \tag{3.35}$$

In both the cases of linear and sublinear growth, P denotes the permissivity associated with the condition in which $T^{\text{iso}}_{\text{a}}$ and μ^0_{iso} are measured.

Remark 3.1. Among the five quantities used to calibrate the model parameters, only one (namely μ^0_{iso}) is related to the microscopic scale, while the others are related to the macroscale. The measurement of μ^0_{iso} may be hard to be accomplished, indeed. However, if one is interested only in the prediction of the generated tension and not in the moments μ^0 and μ^1, the calibration can be accomplished regardless of μ^0_{iso}, by considering only the macroscopic scale. As a matter of fact, the three parameters a_{XB}, $\mu^0_{\bar{f}}$ and $\mu^1_{\bar{f}}$ appear always in the two combinations $a_{\text{XB}}\mu^1_{\bar{f}}$ and $\mu^0_{\bar{f}}/\mu^1_{\bar{f}}$, apart from in the expression of μ^0_{iso}. Therefore, one could calibrate the two combined terms $a_{\text{XB}}\mu^1_{\bar{f}}$ and $\mu^0_{\bar{f}}/\mu^1_{\bar{f}}$ rather than the three parameters.

In other terms, thanks to the linearity of the equations, the value of μ^0_{iso} used in the calibration of the model only affects the prediction of the quantities related to the microscale (i.e. μ^0 and μ^1), but not the tension T_{a} (and the active stiffness K_{a}). Therefore, as far as the modeling of T_{a} and K_{a} is concerned, the model is fully characterized by the four quantities $T^{\text{iso}}_{\text{a}}$, $v^{\max}$, v^0 and $\tilde{k}_2$.

3.3 Final remarks

The dynamics of XBs is characterized by different time scales. In [CMC19], the authors have shown that if the degrees of freedom associated to the fastest dynamics are considered in equilibrium, the CMC19 model formally reduces to the H57 model. Therefore, the H57 model, despite it does not explicitly represent the power-stroke,

can still be considered as a good description of the muscle behavior under regimes characterized by time-scales slower than that of the power-stroke.

Motivated by this observation, we have considered a generalized version of the H57 model (where the dependence of the transition rates from the shortening velocity is allowed and where the amount of recruitable XBs depends on the RUs permissivity P). We have shown that the model possesses enough flexibility to match the main features of the experimental characterizations associated with the XB dynamics, namely the force-velocity relationship and the response to fast transients. Coherently with the interpretation of the H57 model (as if the power-stroke is considered at equilibrium), we here interpret the tension predicted by the model as the tension measured after that the power-stroke has reached a new equilibrium (i.e. the T_2-L_2 curve of Sec. 1.3.5). In fact, to distinguish the T_1-L_1 curve from the T_2-L_2 one, the tissue must undergo a very large shortening/lengthening velocity; however, if we consider only regimes associated to relatively slow time-scales (or, equivalently, small shortening/lengthening velocities), this cannot occur and, hence, one can only observe the T_2-L_2 curve. More precisely, one can observe only the part of the T_2-L_2 curve associated with small time steps, as to decouple the time-scales of the phase 2 from that of the phase 4 of force recovery (see Sec. 1.3.5) for large length steps a large shortening velocity is needed as we will quantitatively show in Sec. 4.4.6.

Finally, we have shown that under the hypothesis that the total transition rate is independent of x and that, as it is reasonable, v only affects the detachment rate, the distribution-moments equations can be written for the generalized H57. Such equations depend on 5 parameters (or 4, if one is not interested in predicting the microscopical quantities μ^0 and μ^1, but only the generated tension). We have shown that the parameters can be easily constrained from 5 (respectively, 4) experimentally measurable quantities. This provides an effective way of calibrating the model parameters. This model, therefore, strikes a good balance between number of parameters and model flexibility.

Chapter 4

Modeling the full-sarcomere dynamics

After having considered, in Chap. 2, the RU dynamics and, in Chap. 3, the XB dynamics, in this chapter we deal with the mathematical modeling of the overall sarcomere dynamics. Besides the issues already encountered in the modeling of the RUs and the XB dynamics alone, the coupling of the two makes further complications arise. A major issue is related to the fact that, when the muscle contracts, the thin and the thick filaments mutually slide. Therefore, the XBs faced by each RUs change as time goes by. The consequent necessity of tracking which XB faces which BS is typically addressed in literature by explicitly representing the physical arrangement of filaments and by approximating the average behavior of the sarcomere by the MC method.

After a review of the literature, we present our strategies to deal with the above mentioned issues. Hence, we derive several microscale force generation models, under different assumptions. We present our strategy for the calibration of the parameters of the models and, finally, we show the results obtained under different experimental conditions.

Contents

4.1 Full-sarcomere mathematical models

In the past two decades, several models describing the generation of active force in the cardiac tissue, including both the calcium-driven regulation and the XB cycling, have been proposed. The main challenge faced in the development of such models is well summarized by J. J. Rice and coauthors in [Ric+08]:

> *[...] [The] difficulty lies in trying to compress the spatial aspects of myofilaments at the molecular level into a tractable system of equations. Moreover, if computational speed is desired, then the system must be fairly simple and implemented with ordinary differential equations (ODEs) instead of partial differential equations or Monte Carlo approaches typically required for explicit consideration of the spatial aspects.*

Indeed, the spatial dependence of the cooperativity phenomenon, crucial to reproduce the calcium dependence of muscle activation (see Sec. 2.1), dramatically increases the computational complexity of activation models, even more so when such models are coupled with models described XB cycling. When the interactions between BSs and MHs is considered, indeed, one must face the further difficulty of tracking which BS faces which MH when the filaments mutually slide. The attempt of capturing such spatially dependent phenomena in a compact system of ODEs is the *fil rouge* of most of the literature on sarcomere modeling (see e.g. [Zah81; BCS01; Ric+03; Sac04; Ric+08; Cam+10; Cha+12; Was+12; LN15; RDQ18]).

Computationally efficiency is a major issue when the sarcomere model is employed in multiscale simulation, such as cardiac electromechanics. For instance, as we will see in Chap. 8, when a Finite Element discretization is employed at the macroscale, the microscale model needs to be solved at least at each nodal point of the computational mesh, that may feature millions of points. Hence, if the sarcomere model is not enough computationally efficient, it represents the bottleneck of the whole simulation, making the overall computational cost dramatically increase. Moreover, a multiscale simulation also requires to store the state of the microscale contraction model in each nodal point of the computational mesh. Therefore, if the model features a large number of variables, the resulting total number of variables to be stored can pose serious memory issues.

4.1.1 Phenomenological models

Most of the available full-sarcomere models, linking the calcium-driven tissue activation with the generation of force, are based on phenomenological considerations. The model proposed in [HMTK98] and later modified in [NHS06] consists in system of a few ODEs, describing the time evolution of the fraction of permissive RUs, the concentration of bound calcium ions and the variables of the so-called fading-memory model, a phenomenological description of the tension development phenomenon accounting for the shortening velocity. The cooperativity mechanism is phenomenologically represented by assuming a steeply nonlinear response, with respect to calcium dynamics, for the fraction of permissive RUs. A similar model have been proposed in [Lan+12] and, in [Tøn+15], the two models of [Lan+12] and [NHS06] have been re-calibrated to fit data from human cardiomyocytes. In [Lan+17] a model with similar features has been proposed, based on measurements from human cardiomyocytes.

In the model proposed in [Ric+08], cooperativity is captured again by a phenomenological modification of the transition rates of the variables describing the RUs

permissivity. On the other hand, XB cycling is modeled by a four states CTMC (detached XB with RU in non permissive or permissive state, attached XB in pre and post power-stroke configuration). The attachment and detachment transition rates of the CTMC depend on two continuous variables representing the mean distortion of attached XBs in pre and post power-stroke configuration respectively, adapted from the stiffness-distortion model of [RBC99]. This model goes along with the approximation that the distance of attached MHs from the nearest BS is well approximated by its average value.

In [Ros+14; RB+14] an active strain model is proposed, where the sarcomere dynamics is modeled by a phenomenological instantaneous relationship linking $[Ca^{2+}]_i$ and SL to the generated tension. The model neglects time-dependent effects of force generation and assumes a multiplicative decomposition between the dependence on $[Ca^{2+}]_i$ and SL, thus neglecting length-dependent effect on activation (see Sec. 1.3.2).

4.1.2 Monte Carlo models

The alternative to phenomenological models is given by CTMC models based on a detailed description of the sucellular mechanisms, with variables describing the calcium-driven activation of the thin filament and the XB cycling. However, the huge number of possible states of the system makes the solution of the FKE associated with the CTMC unaffordable. This dictates the usage of the unefficient MC method.

The University of Tokio heart simulator (UT-Heart, see [Was+13; Was+15]) employs a CTMC model describing half MF with N_M MHs and an AF with N_A RUs. The CTMCs describing the RUs are coupled together by means of nearest-neighboring interactions, as in the R03 model, to capture the cooperativity phenomenon. Each MH, in turn, is modeled by a CTMC where the power-stroke is described within the HS71 formalism, that is to say as transitions between discrete states. A continuous variable describing the myosin arm stretch is associated with each MH, so that the transition rates are made dependent on the XB distortion. Moreover, the state of each RU affects the transition rate of the facing MH and also a feedback from XBs to RUs is included into the model. Finally, the SL dependence is accounted for by making the transition rates dependent on the overlap between the filaments, as in the model of [Was+12]. Because of the difficulties in capturing the spatial interactions between units by means of an ODE system, the solution of the CTMC model is approximated by means of the MC method.

A similar CTMC model, where the cooperative R03 model for RUs is coupled with a HS71-like model for XBs is proposed in [HTR06]. This model assumes that when a XB is attached, the transition of the corresponding RU from the non permissive state to the permissive one is prevented. Also in this case, the model is solved by the MC method.

The drawback of the MC method is its huge computational complexity, an issue that is made even more important by the very small time steps dictated by the fast power-stroke dynamics (in [HTR06] a time step of $\Delta t = 0.1\,\mu s$ is used, while in [Was+13] the authors use $\Delta t = 5\,\mu s$). Indeed, the number of MC samples (n_{MC}) required to reach statistical convergence for a cooperative CTMC belonging to the class of the R03 model may be very large. In [Sug+12], the authors write that "MC simulation required more than 1000 repeats to obtain reasonable mean values". In our experience (see Sec. 2.2.5), more that $n_{MC} = 10000$ is needed to obtain an error of the order of 10^{-2}. Moreover, because of the very slow convergence of the MC method ($\mathcal{O}(n_{MC}^{-1/2})$), to reduce the error of one order of magnitude, the number of MC samples

need to be increased by two orders of magnitude.

4.2 Proposed full-sarcomere models

In this chapter we propose different models of the full-sarcomere function, featuring a description of both the RU and the XB dynamics. All the models are based on a common formalism to describe the physical arrangement and the interactions among the regulatory and contractile proteins, that is described in Sec. 4.2.1. In Sec. 4.2.2 we present and discuss different assumptions that we use to derive, in Secs. 4.2.3 and 4.2.6, our models. Finally, in Sec. 4.2.7 we provide an overview on the proposed models and on the different assumptions they are based on.

In the definition of such models and in their selection we follow the epistemological principle of parsimony, known as *Occam's razor principle* [GJGGJ03; MMK03] after William of Occam (1287–1347, English Franciscan friar, scholastic philosopher and theologian), by which *entia non sunt multiplicanda praeter necessitatem* (entities are not to be multiplied beyond necessity). This means that the simplest description for the phenomenon to be modeled should be preferable and, at the same time, the irrelevant aspects should be neglected. This principle is the basis of the construction af mathematical models, that are by definition idealized descriptions of more complicated phenomena ("all models are wrong, but some are useful", to use the words of the statistician George Box). The application of the Occam's razor principle to the development of mathematical models reduces the number of the parameters to be fitted from experimental data, thus enhancing the predictive power of models [Kno90; GJGGJ03; MMK03; RG01].

As in most of RUs models (see Sec. 2.1), we describe Tn and Tm by discrete states. Moreover, based on the experimental evidence that cooperativity is due to RUs end-to-end interactions (see Sec. 1.3.2 and, e.g., [SV17]), we include nearest-neighbor interactions among RUs with the R03 formalism.

Concerning the modeling of XBs, we recall that we are here interested in developing a model of cardiomyocytes contraction in a beating heart. Moreover, we notice that the time-scales characterizing cardiac EM are slower than the fast time-scale of the power-stroke (as we will quantitatively assess later on). This suggests that, coherently with the Occam's razor principle, the level of detail that best suits the application to cardiac EM does not require to explicitly represent the power-stroke. In [CMC19], indeed, the authors showed that if the considered time-scales are slower than the time-scale of the power-stroke, a detailed model including the power-stroke reduces to a H57-like model, where only the attachment-detachment process of XBs is explicitly represented (see Sec. 3.1.3). Therefore, we model the XB dynamics as a two-states process, within the H57 formalism, where the attachment-detachment rates depend on the myosin arm distortion. Moreover, we allow the transition rate to depend also on the sliding velocity of the myofilaments.

4.2.1 Models setup

We consider half MF, where N_M MHs are located, and one AF, regulated by N_A RUs. As we did in Sec. 2.4, we place a reference system at the end of the AF closer to the center of the sarcomere (see Fig. 2.14) and we consider the following smoothed geometrical factors (similar to the ones presented in Sec. 2.4, but where the smoothing

function is centered to the threshold), for $i \in \mathcal{I}_A$:

$$\chi_M(SL,i) = \frac{1}{2}\tanh\left(\frac{y_i - y_{LM}}{\varepsilon_{SL}}\right) + \frac{1}{2}\tanh\left(-\frac{y_i - y_{RM}}{\varepsilon_{SL}}\right),$$
$$\chi_{SF}(SL,i) = \frac{1}{2}\left(1 + \tanh\left(\frac{y_i - y_{SF}}{\varepsilon_{SL}}\right)\right),$$

where

$$y_{LM} = (2\,L_A - SL + L_H)/2, \qquad y_{SF} = 2\,L_A - SL,$$
$$y_{RM} = (2\,L_A - SL + L_M)/2, \qquad y_i = \frac{L_A}{N_A}(i - 0.5).$$

We notice that we have $\chi_M(SL,i) \simeq 1$ if the i-th RU faces the considered half MF and $\chi_{SF}(SL,i) \simeq 1$ if the i-th RU is in the single filament region (no overlap with other AFs occurs). Let $d_{ij}(t)$ be the distance between the i-th actin BS and the j-th MH at time t, defined as:

$$\begin{aligned} d_{ij}(t) &= \frac{L_A}{N_A}i - \frac{L_M - L_H}{2N_M}j + \frac{SL(t)}{2} - \frac{(1+2N_A)L_A + N_A L_H}{2N_A} \\ &= D_A i - D_M j + \frac{SL(t)}{2} - d_0. \end{aligned} \tag{4.1}$$

In the model that we propose, each RU is characterized by the state of Tn (bound to calcium or not) and Tm (permissive or not). Moreover, each RU corresponds to a BS to which the MHs can bind. Obviously, each MH can bind to a single BS at a time and, conversely, each BS can have at most a single MH attached. We consider therefore the following stochastic processes, for $i \in \mathcal{I}_A := \{1,\dots,N_A\}$, $j \in \mathcal{I}_M := \{1,\dots,N_M\}$ and $t \geq 0$:

$$C_i^t = \begin{cases} \mathcal{B} & \text{if the } i\text{-th Tn is bound to calcium,} \\ \mathcal{U} & \text{else;} \end{cases}$$
$$T_i^t = \begin{cases} \mathcal{P} & \text{if the } i\text{-th Tm is permissive,} \\ \mathcal{N} & \text{else;} \end{cases}$$
$$A_i^t = \begin{cases} j & \text{if the } i\text{-th actin BS is attached to the } j\text{-th MH,} \\ 0 & \text{if the } i\text{-th actin BS is not attached to any MH;} \end{cases} \tag{4.2}$$
$$M_j^t = \begin{cases} i & \text{if the } j\text{-th MH is attached to the } i\text{-th actin BS,} \\ 0 & \text{if the } j\text{-th MH is not attached to any actin BS;,} \end{cases}$$
$$Z_i^t = \begin{cases} x & \text{if the } i\text{-th actin BS is attached to a MH with displacement x,} \\ \emptyset & \text{if the } i\text{-th actin BS is not attached to any MH.} \end{cases}$$

We notice that the last three processes are redundant, as we have:

$$(A_i^t = j) \iff (M_j^t = i) \iff (Z_i^t = d_{ij}(t)).$$

In the following we will use the notation $\overline{\mathcal{N}} = \mathcal{P}$, $\overline{\mathcal{P}} = \mathcal{N}$, $\overline{\mathcal{U}} = \mathcal{B}$ and $\overline{\mathcal{B}} = \mathcal{U}$ to denote opposite states.

We assume, coherently with the hypotheses of the R03 model, that the dynamics of TnC is affected by the state of the corresponding Tm, and that the dynamics of

Tm is affected by the TnC belonging to the same RUs and by the state of Tm in the nearest neighboring RUs, by a cooperativity mechanism. We exclude any feedback from XBs on the dynamics of the RUs, as recent experimental evidence supports that this kind of feedback is not present (see [SLI09; Far+10] and Sec. 1.3.2). Conversely, the attachment-detachment rates of the XBs may depend on the distance between the MH and the BS, the relative velocity between the filaments and the permissivity state of the RU. Moreover, transition rates can be affected by the mutual arrangements between the filaments: we allow thus for a dependence of the transition rates on the index corresponding to each unit. We consider therefore the following transition rates for the stochastic processes defined in (4.2), where $\delta \in \{\mathcal{B},\mathcal{U}\}$, $\alpha,\beta,\eta \in \{\mathcal{P},\mathcal{N}\}$:

$$\begin{aligned}
k_{C,i}^{\delta\overline{\delta}|\beta} &= \lim_{\Delta t\to 0}\frac{1}{\Delta t}\mathbb{P}\left[C_i^{t+\Delta t} = \overline{\delta}\,|\,(C_i,T_i)^t = (\delta,\beta)\right],\\
k_{T,i}^{\beta\overline{\beta}|\alpha\,\cdot\,\eta,\delta} &= \lim_{\Delta t\to 0}\frac{1}{\Delta t}\mathbb{P}\left[T_i^{t+\Delta t} = \overline{\beta}\,|\,(T_{i-1},T_i,T_{i+1},C_i)^t = (\alpha,\beta,\eta,\delta)\right],\\
f_\alpha^i(x,v(t)) &= \lim_{\Delta t\to 0}\frac{1}{\Delta t}\mathbb{P}\left[Z_i^{t+\Delta t} = x\,|\,Z_i^t = \emptyset, T_i^t = \alpha,\right.\\
&\qquad\qquad \left.\exists\, j\in\mathcal{I}_M\, d_{ij}^t = x + v_{\mathrm{hs}}\Delta t, M_j^t = 0\right],\\
g_\alpha^i(x,v(t)) &= \lim_{\Delta t\to 0}\frac{1}{\Delta t}\mathbb{P}\left[Z_i^{t+\Delta t} = \emptyset\,|\,Z_i^t = x, T_i^t = \alpha\right],
\end{aligned} \tag{4.3}$$

where $v(t)$ plays the role of independent variable. In the definition of f_α^i, the events conditioning the probability ensure that, at time t, the i-th BS is not attached and that there exists a non-attached MH at distance $x + v_{\mathrm{hs}}\Delta t$ (so that at time $t+\Delta t$ the distance is reduced to x).

As mentioned before, the transition rates may be affected by the mutual arrangement of the filaments. Specifically, we assume that binding is possible only in the single-overlap region and that it may be characterized by different rates inside and outside the single-overlap region. Hence, we have, for $\alpha \in \{\mathcal{N},\mathcal{P}\}$ and $i \in \mathcal{I}_A$:

$$\begin{aligned}
f_\alpha^i(x,v) &= f_\alpha(x,v)\,\chi_M(SL,i)\,\chi_{SF}(SL,i),\\
g_\alpha^i(x,v) &= g_\alpha(x,v)\,\chi_M(SL,i)\,\chi_{SF}(SL,i) + \tilde{g}_\alpha(x,v)\,(1-\chi_M(SL,i)\,\chi_{SF}(SL,i)).
\end{aligned} \tag{4.4}$$

Moreover, we assume that XBs can form only when the RU regulating the BS is in permissive configuration (i.e. $f_{\mathcal{N}} \equiv 0$). For the sake of simplicity, we shorten the notations as:

$$\begin{aligned}
f_{\mathcal{P}}^{ij} &= f_{\mathcal{P}}^i(d_{ij}(t),v(t)), \qquad & f_{\mathcal{N}}^{ij} &= f_{\mathcal{N}}^i(d_{ij}(t),v(t)),\\
g_{\mathcal{P}}^{ij} &= g_{\mathcal{P}}^i(d_{ij}(t),v(t)), \qquad & g_{\mathcal{N}}^{ij} &= g_{\mathcal{N}}^i(d_{ij}(t),v(t)).
\end{aligned} \tag{4.5}$$

Finally, the expected value of the force exerted by the considered pair of interacting half MF and AF is given by:

$$F_{\mathrm{hf}}(t) = \sum_{i\in\mathcal{I}_A}\mathbb{E}\left[F_{\mathrm{XB}}(Z_i^t)\right],$$

where we set by convention $F_{\mathrm{XB}}(\emptyset) = 0$.

4.2.2 Models assumptions

The stochastic processes (4.2) and the transition rates (4.3) define a CTMC, whose evolution is driven by the associated FKE. However, as for the models considered in

Chap.2, the size of the FKE model is huge. Indeed, each RU is characterized by four possible states and the corresponding actin BS can be either unbound or bound to one of the N_M MHs, leading to a system of ODEs with $(4(N_M+1))^{N_A}$ variables. Therefore, if we set, for instance, $N_M = 18$ and $N_A = 32$, we would have more than 10^{60} variables!

To derived a compact equation describing the evolution of the system, we introduce some assumptions by following a similar strategy to the one we used to derive the model of Sec. 2.2.2. These assumptions allow to neglect second-order interactions among the stochastic processes, so that the variables can be partially decoupled, thus leading to drastic reductions in the size of model. Such strategy is illustrated in the following proposition.

Proposition 4.1. *Let $(\Omega, \mathcal{A}, \mathbb{P})$ be a probability space. Let $A, B, C \subset \Omega$ and let $\mathcal{D}$ be a finite partition of Ω, such that:*

(H1) $A \perp\!\!\!\perp B \,|\, C, D \quad \forall\, D \in \mathcal{D}$;

(H2) $B \perp\!\!\!\perp D \,|\, C \quad \forall\, D \in \mathcal{D}$.

Then, we have:

$$\mathbb{P}\left[A|B,C\right] = \frac{\sum_{D\in\mathcal{D}} \mathbb{P}\left[A|C,D\right]\mathbb{P}\left[C,D\right]}{\mathbb{P}\left[C\right]} = \mathbb{P}\left[A|C\right]. \tag{4.6}$$

Proof. We have:

$$\begin{aligned}\mathbb{P}\left[A|B,C\right] &= \frac{\mathbb{P}\left[A,B,C\right]}{\mathbb{P}\left[B,C\right]} = \frac{\sum_{D\in\mathcal{D}} \mathbb{P}\left[A,B,C,D\right]}{\mathbb{P}\left[B,C\right]} = \frac{\sum_{D\in\mathcal{D}} \mathbb{P}\left[A|B,C,D\right]\mathbb{P}\left[B,C,D\right]}{\mathbb{P}\left[B,C\right]} \\ &= \frac{\sum_{D\in\mathcal{D}} \mathbb{P}\left[A|B,C,D\right]\mathbb{P}\left[B|C,D\right]\mathbb{P}\left[C,D\right]}{\mathbb{P}\left[B,C\right]}.\end{aligned} \tag{4.7}$$

Tanks to (H1), we have:

$$\mathbb{P}\left[A|B,C,D\right] = \mathbb{P}\left[A|C,D\right]. \tag{4.8}$$

Moreover, thanks to (H2), we have:

$$\mathbb{P}\left[B|C,D\right] = \mathbb{P}\left[B|C\right] = \mathbb{P}\left[B,C\right]/\mathbb{P}\left[C\right]. \tag{4.9}$$

By substituting into the above equation, the thesis follows. □

In the following, we will use several times the result of Prop. 4.1, where (H1) is a modeling choice on the dynamics of the system and (H2) is a simplifying assumption. Specifically, A is the target event, whose probability is the aim of the computation. In many situations, we know the joint probability of C and B, whereas the probability of A can be obtained by the joint probability of C and a different event D. Proposition 4.1 allows to pass from B to D, by assuming that the knowledge of B does not provide any further information when C and D are known.

In the following we will consider the following conditional independence assumptions:

(Ii) $(T_{i+1}, C_i)^t \perp\!\!\!\perp (T_{i-2}, C_{i-1})^t | (T_{i-1}, T_i)^t$ for $i = 3, \ldots, N_A - 1$,
$(T_{i-1}, C_i)^t \perp\!\!\!\perp (T_{i+2}, C_{i+1})^t | (T_{i+1}, T_i)^t$ for $i = 2, \ldots, N_A - 2$.

(Iii) $(T_{i+1}, C_{i+1})^t \perp\!\!\!\perp T^t_{i-2} | (T_{i-1}, T_i, C_{i-1}, C_i)^t$ for $i = 3, \dots, N_A - 1$,
$(T_{i-1}, C_{i-1})^t \perp\!\!\!\perp T^t_{i+2} | (T_{i+1}, T_i, C_{i+1}, C_i)^t$ for $i = 2, \dots, N_A - 2$.

(Iiii) $A^t_i \perp\!\!\!\perp (T_{i-1}, T_{i+1}, C_i)^t | T^t_i$ for $i = 2, \dots, N_A - 1$.

(Iiv) $A^t_h \perp\!\!\!\perp (T_i, A_i)^t$ for $i, h = 1, \dots, N_A$ s.t. $i \neq h$.

Assumptions (Ii) and (Iii) are similar to assumption (2.22) and state that far RUs along the filament are conditionally independent given the states of the intermediate RUs. As we noticed in Sec. 2.2.5, this is coherent with the modeling assumptions, as the dynamics of RUs is affected by the state of nearest-neighboring units and long-range interactions are always mediated by the intermediate units. In the following we will assume either (Ii) or (Iii).

Assumption (Iiii), on the other hand, entails that the state of a BS is conditionally independent of the state of surrounding RUs, given the permissivity state of the associated RU. This is also coherent with the assumptions underlying the model, as the only feature of the RUs that directly affects the XBs binding rates is the permissivity state of Tm.

Finally, assumption (Iiv) states that the attachment state of far units can be considered as independent. We will see that assumption (Iiv) can be replaced by the following dual assumptions:

(Ai) $f^{ij}_{\mathcal{P}} \neq 0 \implies A_h \neq j \quad \forall\, h \neq i$;

(Aii) $f^{ij}_{\mathcal{P}} \neq 0 \implies M_k \neq i \quad \forall\, k \neq j$.

Assumption (Ai) states that, whenever a XB can form, the MH cannot be involved in a XB with a farther BS. Suppose that the support of f is contained in the interval $[x_1, x_1 + h]$. Then, this is equivalent to say that, if $d_{ij} \in [x_1, x_1 + h]$, the XBs between the couples $(i-1, j)$ and $(i+1, j)$, which feature displacements $d_{ij} - D_A$ and $d_{ij} + D_A$ respectively, cannot exist. This condition is automatically fulfilled if XBs are present only for displacements in the interval $(-D_A + x_1 + h, D_A + x_1)$, which has width $2D_A - h$. The interval consists in the support of f, with width h, surrounded by two bands of width $D_A - h$.

On the other hand, assumption (Aii) accounts to say that, whenever a XB can form, the BS cannot be involved in a XB with a farther MH. By similar considerations, it turns out that this hypothesis is satisfied if XBs are present only in the range $(-D_M + x_1 + h, D_M + x_1)$. Since $D_M > D_A$, assumption (Ai) is stronger than (Aii).

Assumptions (Ai)-(Aii) allow to decouple the dynamics of the different units. Their validity is justified when the shortening velocity is relatively small, whereas, for large velocities, the XB displacements may be convected outside the region $(-D_A + x_1 + h, D_A + x_1)$. Figure 4.1 provides a visual representation of assumptions (Ai)-(Aii). We notice that all the models belonging to the family of the H57 model are based on these assumptions, without which, as we mentioned in Sec. 3.2, the H57 equation cannot be derived.

4.2.3 Thin filament regulation

Due to the lack of feedback from XBs to RUs, it is possible to write an equation describing the evolution of the stochastic processes C^t_i and T^t_i independently of the stochastic processes associated with XBs. Moreover, we notice that by introducing the stochastic processes $R^t_i := (C^t_i, T^t_i) \in \{\mathcal{U}, \mathcal{B}\} \times \{\mathcal{N}, \mathcal{P}\}$, their evolution is driven by

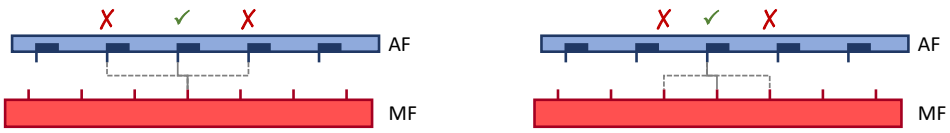

(a) Assumption (Ai). (b) Assumption (Aii).

Figure 4.1: Representation of assumptions (Ai)-(Aii). According to assumption (Ai) (respectively, assumption (Aii)) when a BS-MH pair is within the XB formation range, then the adjacent BSs (respectively, MHs) cannot be bound to the considered MH (respectively, BS).

a CTMC formally equivalent to the model considered in Sec. 2.2. Hence, we consider probabilities written in the form of:

$$\pi_i^{\alpha\beta\delta,\vartheta\eta\lambda}(t) := \mathbb{P}\left[(T_{i-1},T_i,T_{i+1})^t=(\alpha,\beta,\delta),(C_{i-1},C_i,C_{i+1})^t=(\vartheta,\eta,\lambda)\right], \quad (4.10)$$

where $i=2,\dots,N_A-1$, $\vartheta,\eta,\lambda\in\{\mathcal{U},\mathcal{B}\}$ and $\alpha,\beta,\delta\in\{\mathcal{N},\mathcal{P}\}$. We notice that this notation is related to the notation used in Chap. 2 by the following relationship:

$$\pi_i^{\alpha\beta\delta,\vartheta\eta\lambda}(t)\equiv(\vartheta\alpha,\overset{i}{\eta}\beta,\lambda\delta)^t.$$

In this chapter, however, for the sake of clearness we will follow the newly introduced notation.

By proceeding as in Sec. 2.2, we consider the time increment Δt and we compute the probability $\pi_i^{\alpha\beta\delta,\vartheta\eta\lambda}(t+\Delta t)$. By adopting assumption (Iii), we approximate the terms in the following form as:

$$\begin{aligned}
&\mathbb{P}\left[T_{i-1}^{t+\Delta t}=\alpha|(T_{i-1},T_i,T_{i+1})^t=(\overline{\alpha},\beta,\delta),(C_{i-1},C_i,C_{i+1})^t=(\vartheta,\eta,\lambda)\right]\\
&\quad=\left(\sum_{\xi,\zeta}\pi_{i-1}^{\xi\overline{\alpha}\beta,\zeta\vartheta\eta}(t)\right)^{-1}\sum_{\xi,\zeta}\mathbb{P}\left[T_{i-1}^{t+\Delta t}=\alpha|(T_{i-2},T_{i-1},T_i)^t=(\xi,\overline{\alpha},\beta),\right.\\
&\qquad\qquad\left.(C_{i-2},C_{i-1},C_i)^t=(\zeta,\vartheta,\eta)\right]\pi_{i-1}^{\xi\overline{\alpha}\beta,\zeta\vartheta\eta}(t)\\
&\quad=\frac{\sum_{\xi,\zeta}k_{T,i}^{\overline{\alpha}\alpha|\xi\,\cdot\,\beta,\vartheta}\pi_{i-1}^{\xi\overline{\alpha}\beta,\zeta\vartheta\eta}(t)}{\sum_{\xi,\zeta}\pi_{i-1}^{\xi\overline{\alpha}\beta,\zeta\vartheta\eta}(t)}\Delta t+o\left(\Delta t\right),
\end{aligned}$$

where we have applied Prop. 4.1 for $A=(T_{i-1}^{t+\Delta t}=\overline{\alpha})$, $B=(T_{i+1}^t=\delta,C_{i+1}^t=\lambda)$, $C=((T_{i-1},T_i)^t=(\alpha,\beta),(C_{i-1},C_i)^t=(\vartheta,\eta))$ and $\mathcal{D}=\{(T_{i-2}^t=\xi,C_{i-2}^t=\zeta)\}_{\xi,\zeta}$.

By taking the limit $\Delta t\to 0$, we get the following system of nonlinear ODEs, for

$t \geq 0$ and for any $i = 2, \dots, N_A - 1$, $\vartheta, \eta, \lambda \in \{\mathcal{U}, \mathcal{B}\}$ and $\alpha, \beta, \delta \in \{\mathcal{N}, \mathcal{P}\}$:

$$\begin{aligned}\frac{d}{dt}\pi_i^{\alpha\beta\delta,\vartheta\eta\lambda} = &\widetilde{k}_{T,i-1}^{\overline{\alpha}\alpha|\circ\,\cdot\,\beta,\circ\vartheta\eta} \quad \pi_i^{\overline{\alpha}\beta\delta,\vartheta\eta\lambda} \quad - \widetilde{k}_{T,i-1}^{\alpha\overline{\alpha}|\circ\,\cdot\,\beta,\circ\vartheta\eta} \quad \pi_i^{\alpha\beta\delta,\vartheta\eta\lambda} \\ &+ k_{T,i}^{\overline{\beta}\beta|\alpha\,\cdot\,\delta,\eta} \quad \pi_i^{\alpha\overline{\beta}\delta,\vartheta\eta\lambda} \quad - k_{T,i}^{\beta\overline{\beta}|\alpha\,\cdot\,\delta,\eta} \quad \pi_i^{\alpha\beta\delta,\vartheta\eta\lambda} \\ &+ \widetilde{k}_{T,i+1}^{\overline{\delta}\delta|\beta\,\cdot\,\circ,\eta\lambda\circ} \quad \pi_i^{\alpha\beta\overline{\delta},\vartheta\eta\lambda} \quad - \widetilde{k}_{T,i+1}^{\delta\overline{\delta}|\beta\,\cdot\,\circ,\eta\lambda\circ} \quad \pi_i^{\alpha\beta\delta,\vartheta\eta\lambda} \\ &+ k_{C,i-1}^{\overline{\vartheta}\vartheta|\alpha} \quad \pi_i^{\alpha\beta\delta,\overline{\vartheta}\eta\lambda} \quad - k_{C,i-1}^{\vartheta\overline{\vartheta}|\alpha} \quad \pi_i^{\alpha\beta\delta,\vartheta\eta\lambda} \\ &+ k_{C,i}^{\overline{\eta}\eta|\beta} \quad \pi_i^{\alpha\beta\delta,\vartheta\overline{\eta}\lambda} \quad - k_{C,i}^{\eta\overline{\eta}|\beta} \quad \pi_i^{\alpha\beta\delta,\vartheta\eta\lambda} \\ &+ k_{C,i+1}^{\overline{\lambda}\lambda|\delta} \quad \pi_i^{\alpha\beta\delta,\vartheta\eta\overline{\lambda}} \quad - k_{C,i+1}^{\lambda\overline{\lambda}|\delta} \quad \pi_i^{\alpha\beta\delta,\vartheta\eta\lambda},\end{aligned} \tag{4.11}$$

endowed with suitable initial conditions and where we have defined the transition rates with missing information as follows (the symbol $\circ$ denotes the lack of information regarding the corresponding state):

$$\begin{aligned}\widetilde{k}_{T,i}^{\overline{\alpha}\alpha|\circ\,\cdot\,\beta,\circ\vartheta\eta} &:= \begin{cases} \dfrac{\sum_{\xi,\zeta} k_{T,i}^{\overline{\alpha}\alpha|\xi\,\cdot\,\beta,\vartheta} \pi_i^{\xi\overline{\alpha}\beta,\zeta\vartheta\eta}}{\sum_{\xi,\zeta} \pi_i^{\xi\overline{\alpha}\beta,\zeta\vartheta\eta}} & \text{for } i = 2, \dots, N_A - 1, \\ k_{T,i}^{\overline{\alpha}\alpha|\mathcal{N}\,\cdot\,\beta,\vartheta} & \text{for } i = 1; \end{cases} \\ \widetilde{k}_{T,i}^{\overline{\delta}\delta|\beta\,\cdot\,\circ,\eta\lambda\circ} &:= \begin{cases} \dfrac{\sum_{\xi,\zeta} k_{T,i}^{\overline{\delta}\delta|\beta\,\cdot\,\xi,\lambda} \pi_i^{\beta\overline{\delta}\xi,\eta\lambda\zeta}}{\sum_{\xi,\zeta} \pi_i^{\beta\overline{\delta}\xi,\eta\lambda\zeta}} & \text{for } i = 2, \dots, N_A - 1, \\ k_{T,i}^{\overline{\delta}\delta|\beta\,\cdot\,\mathcal{N},\lambda} & \text{for } i = N_A. \end{cases}\end{aligned} \tag{4.12}$$

The permissivity of the i-th regulatory unit, defined as $P_i(t) = \mathbb{P}\left[T_i^t = \mathcal{P}\right]$, can be obtained as:

$$P_i(t) = \begin{cases} \displaystyle\sum_{\beta,\delta\in\{\mathcal{N},\mathcal{P}\}} \sum_{\vartheta,\eta,\lambda\in\{\mathcal{U},\mathcal{B}\}} \pi_2^{\mathcal{P}\beta\delta,\vartheta\eta\lambda}(t) & \text{for } i = 1, \\ \displaystyle\sum_{\alpha,\delta\in\{\mathcal{N},\mathcal{P}\}} \sum_{\vartheta,\eta,\lambda\in\{\mathcal{U},\mathcal{B}\}} \pi_i^{\alpha\mathcal{P}\delta,\vartheta\eta\lambda}(t) & \text{for } i = 2, \dots, N_A - 1, \\ \displaystyle\sum_{\alpha,\beta\in\{\mathcal{N},\mathcal{P}\}} \sum_{\vartheta,\eta,\lambda\in\{\mathcal{U},\mathcal{B}\}} \pi_{N_A-1}^{\alpha\beta\mathcal{P},\vartheta\eta\lambda}(t) & \text{for } i = N_A. \end{cases}$$

4.2.4 Crossbridge dynamics: discrete setting

Equation 4.11 drives the evolution of the probabilities associated with the stochastic processes describing the state of the RUs. In order to derive an equation for the evolution of the stochastic processes describing the attachment and detachment of XBs, we proceed in a similar manner. Specifically, we consider the following probabilities, for $i \in \mathcal{I}_A$, $j \in \mathcal{I}_M$:

$$n_{ij,\mathcal{P}}(t) = \mathbb{P}\left[(A_i, T_i)^t = (j, \mathcal{P})\right], \quad n_{ij,\mathcal{N}}(t) = \mathbb{P}\left[(A_i, T_i)^t = (j, \mathcal{N})\right], \tag{4.13}$$

and we look for an equation for the evolution of $n_{ij,\mathcal{P}}(t)$ and $n_{ij,\mathcal{N}}(t)$ written in closed form. Thanks to the Bayes formula [KS98] we have:

$$\begin{aligned}\mathbb{P}\left[(A_i,T_i)^{t+\Delta t}=(j,\mathcal{P})\right] &\overset{\Delta t\to 0}{\sim}\\ &\mathbb{P}\left[(A_i,T_i)^{t+\Delta t}=(j,\mathcal{P})|(A_i,T_i)^t=(0,\mathcal{P})\right]\mathbb{P}\left[(A_i,T_i)^t=(0,\mathcal{P})\right]\\ &+\mathbb{P}\left[(A_i,T_i)^{t+\Delta t}=(j,\mathcal{P})|(A_i,T_i)^t=(j,\mathcal{N})\right]\mathbb{P}\left[(A_i,T_i)^t=(j,\mathcal{N})\right]\\ &+\mathbb{P}\left[(A_i,T_i)^{t+\Delta t}=(j,\mathcal{P})|(A_i,T_i)^t=(j,\mathcal{P})\right]\mathbb{P}\left[(A_i,T_i)^t=(j,\mathcal{P})\right].\end{aligned}$$

Thanks to Prop. 4.1, by taking $A=((A_i,T_i)^{t+\Delta t}=(j,\mathcal{P}))$, $B=(A_i^t=j)$, $C=(T_i^t=\mathcal{N})$ and $\mathcal{D}=\{(T_{i-1},T_{i+1},C_i)^t=(\alpha,\eta,\delta)\}_{\alpha,\eta,\delta}$, assumption (Iiii) leads to

$$\mathbb{P}\left[(A_i,T_i)^{t+\Delta t}=(j,\mathcal{P})|(A_i,T_i)^t=(j,\mathcal{N})\right]\overset{\Delta t\to 0}{\sim}\widetilde{k}_{T,i}^{\mathcal{NP}}\Delta t,$$

where we have defined:

$$\begin{aligned}\widetilde{k}_{T,i}^{\mathcal{NP}}&:=\frac{\sum_{\alpha,\eta,\delta}k_{T,i}^{\mathcal{NP}|\alpha\,\cdot\,\eta,\delta}\mathbb{P}\left[(T_{i-1},T_i,T_{i+1},C_i)^t=(\alpha,\mathcal{N},\eta,\delta)\right]}{\mathbb{P}\left[T_i^t=\mathcal{N}\right]},\\ \widetilde{k}_{T,i}^{\mathcal{PN}}&:=\frac{\sum_{\alpha,\eta,\delta}k_{T,i}^{\mathcal{PN}|\alpha\,\cdot\,\eta,\delta}\mathbb{P}\left[(T_{i-1},T_i,T_{i+1},C_i)^t=(\alpha,\mathcal{P},\eta,\delta)\right]}{\mathbb{P}\left[T_i^t=\mathcal{P}\right]}.\end{aligned}\tag{4.14}$$

We notice that the transition rates $\widetilde{k}_{T,i}^{\mathcal{NP}}$ and $\widetilde{k}_{T,i}^{\mathcal{PN}}$ can be obtained from the variables $\pi_i^{\alpha\beta\delta,\vartheta\eta\lambda}$ as:

$$\begin{aligned}\widetilde{k}_{T,i}^{\mathcal{NP}}&:=\frac{\sum_{\alpha,\delta,\vartheta,\eta,\lambda}k_{T,i}^{\mathcal{NP}|\alpha\,\cdot\,\delta,\eta}\,\pi_i^{\alpha\mathcal{N}\delta,\vartheta\eta\lambda}}{1-P_i},\\ \widetilde{k}_{T,i}^{\mathcal{PN}}&:=\frac{\sum_{\alpha,\delta,\vartheta,\eta,\lambda}k_{T,i}^{\mathcal{PN}|\alpha\,\cdot\,\delta,\eta}\,\pi_i^{\alpha\mathcal{P}\delta,\vartheta\eta\lambda}}{P_i}.\end{aligned}\tag{4.15}$$

Moreover, we have:

$$\begin{aligned}&\mathbb{P}\left[(A_i,T_i)^{t+\Delta t}=(j,\mathcal{P})|(A_i,T_i)^t=(j,\mathcal{P})\right]\\ &\overset{\Delta t\to 0}{\sim}1-\mathbb{P}\left[A_i^{t+\Delta t}=0|(A_i,T_i)^t=(j,\mathcal{P})\right]-\mathbb{P}\left[T_i^{t+\Delta t}=\mathcal{N}|(A_i,T_i)^t=(j,\mathcal{P})\right]\\ &\overset{\Delta t\to 0}{\sim}1-\Delta t\left(g_{\mathcal{P}}^{ij}-\widetilde{k}_{T,i}^{\mathcal{PN}}\right).\end{aligned}\tag{4.16}$$

Concerning the XB formation term, we have:

$$\begin{aligned}(F)&:=\mathbb{P}\left[A_i^{t+\Delta t}=j,T_i^{t+\Delta t}=\mathcal{P},A_i^t=0,T_i^t=\mathcal{P}\right]\mathbb{P}\left[A_i^t=0,T_i^t=\mathcal{P}\right]\\ &=\mathbb{P}\left[(A_i,T_i)^{t+\Delta t}=(j,\mathcal{P}),(A_i,T_i)^t=(0,\mathcal{P})\right]\\ &=\mathbb{P}\left[(A_i,T_i)^{t+\Delta t}=(j,\mathcal{P}),(A_i,T_i)^t=(0,\mathcal{P}),M_j^t=0\right]\\ &+\mathbb{P}\left[(A_i,T_i)^{t+\Delta t}=(j,\mathcal{P}),(A_i,T_i)^t=(0,\mathcal{P}),M_j^t\neq 0\right].\end{aligned}$$

The first term can be obtained as:

$$\begin{aligned}&\mathbb{P}\left[(A_i,T_i)^{t+\Delta t}=(j,\mathcal{P}),(A_i,T_i)^t=(0,\mathcal{P}),M_j^t=0\right]\\ &=\mathbb{P}\left[(A_i,T_i)^{t+\Delta t}=(j,\mathcal{P})|(A_i,T_i)^t=(0,\mathcal{P}),M_j^t=0\right]\mathbb{P}\left[(A_i,M_j,T_i)^t=(0,0,\mathcal{P})\right]\\ &\overset{\Delta t\to 0}{\sim}f_{\mathcal{P}}^{ij}\,\mathbb{P}\left[(A_i,M_j,T_i)^t=(0,0,\mathcal{P})\right]\Delta t,\end{aligned}$$

while the second one vanishes for $\Delta t \to 0$:

$$\begin{aligned}
&\mathbb{P}\left[(A_i,T_i)^{t+\Delta t}=(j,\mathcal{P}),(A_i,T_i)^t=(0,\mathcal{P}),M_j^t\neq 0\right]\\
&=\mathbb{P}\left[(A_i,T_i)^{t+\Delta t}=(j,\mathcal{P})|(A_i,T_i)^t=(0,\mathcal{P}),M_j^t\neq 0\right]\mathbb{P}\left[(A_i,T_i)^t=(0,\mathcal{P}),M_j^t\neq 0\right]\\
&=o\left(\Delta t\right).
\end{aligned}$$

Therefore, the XB formation term (F) is given by:

$$(F)\overset{\Delta t\to 0}{\sim} f_{\mathcal{P}}^{ij}\,\mathbb{P}\left[(A_i,M_j,T_i)^t=(0,0,\mathcal{P})\right]\Delta t. \tag{4.17}$$

Such term can be obtained in different ways, by undertaking different assumptions.

- If assumption (Iiv) holds, we have:

  $$\begin{aligned}
  &\mathbb{P}\left[(A_i,M_j,T_i)^t=(0,0,\mathcal{P})\right]\\
  &=\mathbb{P}\left[(A_i,T_i)^t=(0,\mathcal{P}),\forall\, h\neq i\; A_h^t\neq j\right]\\
  &\simeq\mathbb{P}\left[(A_i,T_i)^t=(0,\mathcal{P})\right]\prod_{h\neq i}\mathbb{P}\left[A_h^t\neq j\right]\\
  &\simeq\mathbb{P}\left[(A_i,T_i)^t=(0,\mathcal{P})\right]\prod_{h\neq i}(1-\mathbb{P}\left[(A_h,T_h)^t=(j,\mathcal{P})\right]-\mathbb{P}\left[(A_h,T_h)^t=(j,\mathcal{N})\right]),
  \end{aligned}$$

  where:

  $$\mathbb{P}\left[(A_i,T_i)^t=(0,\mathcal{P})\right]=(\mathbb{P}\left[T_i^t=\mathcal{P}\right]-\sum_{k=1}^{N_M}\mathbb{P}\left[(A_i,T_i)^t=(k,\mathcal{P})\right]).$$

- Otherwise, as alternative to the former, if we assume (Ai), it follows that for the values i,j such that $f_{\mathcal{P}}^{ij}\neq 0$, the event $(A_i^t=0)$ implies $(M_j^t=0)$ and thus:

  $$\begin{aligned}
  (F)&\sim f_{\mathcal{P}}^{ij}\Delta t\mathbb{P}\left[(A_i,T_i)^t=(0,\mathcal{P})\right]\\
  &=f_{\mathcal{P}}^{ij}\Delta t(\mathbb{P}\left[T_i^t=\mathcal{P}\right]-\sum_{k=1}^{N_M}\mathbb{P}\left[(A_i,T_i)^t=(k,\mathcal{P})\right]).
  \end{aligned}$$

  Moreover, thanks to (Aii) (which is implied by assuming (Ai)) the unique nonzero term of the summation is $k=j$, thus leading to:

  $$(F)\sim f_{\mathcal{P}}^{ij}\Delta t(\mathbb{P}\left[T_i^t=\mathcal{P}\right]-\mathbb{P}\left[(A_i,T_i)^t=(j,\mathcal{P})\right]).$$

To sum up, with assumptions (Iiii) and (Iiv) we have:

$$\begin{cases}
\dfrac{d}{dt}n_{ij,\mathcal{P}}=(P_i-\sum_{k=1}^{N_M}n_{ik,\mathcal{P}})\prod_{h\neq i}(1-n_{hj,\mathcal{P}}-n_{hj,\mathcal{N}})f_{\mathcal{P}}^{ij}\\
\qquad\qquad -g_{\mathcal{P}}^{ij}n_{ij,\mathcal{P}}-\widetilde{k}_{T,i}^{\mathcal{P}\mathcal{N}}n_{ij,\mathcal{P}}+\widetilde{k}_{T,i}^{\mathcal{N}\mathcal{P}}n_{ij,\mathcal{N}} & t\geq 0, i\in\mathcal{I}_A, j\in\mathcal{I}_M,\\
\dfrac{d}{dt}n_{ij,\mathcal{N}}=((1-P_i)-\sum_{k=1}^{N_M}n_{ik,\mathcal{N}})\prod_{h\neq i}(1-n_{hj,\mathcal{P}}-n_{hj,\mathcal{N}})f_{\mathcal{N}}^{ij}\\
\qquad\qquad -g_{\mathcal{N}}^{ij}n_{ij,\mathcal{N}}-\widetilde{k}_{T,i}^{\mathcal{N}\mathcal{P}}n_{ij,\mathcal{N}}+\widetilde{k}_{T,i}^{\mathcal{P}\mathcal{N}}n_{ij,\mathcal{P}} & t\geq 0, i\in\mathcal{I}_A, j\in\mathcal{I}_M.
\end{cases} \tag{4.18}$$

By combining Eq. (4.11) (describing the dynamics of RUs) with Eq. (4.18) (describing the dynamics of XBs), we obtain a model for the whole sarcomere function. In the following, we will refer to it as the *SE-disc-I model* (the first spatially-explicit model with discrete description on XBs).

On the other hand, with assumptions (Iiii) and (Ai) we have:

$$\begin{cases} \dfrac{d}{dt}n_{ij,\mathcal{P}} = (P_i - n_{ij,\mathcal{P}})f_{\mathcal{P}}^{ij} - g_{\mathcal{P}}^{ij}n_{ij,\mathcal{P}} \\ \qquad\qquad - \widetilde{k}_{T,i}^{\mathcal{P}\mathcal{N}}n_{ij,\mathcal{P}} + \widetilde{k}_{T,i}^{\mathcal{N}\mathcal{P}}n_{ij,\mathcal{N}} & t \geq 0, i \in \mathcal{I}_A, j \in \mathcal{I}_M, \\ \dfrac{d}{dt}n_{ij,\mathcal{N}} = ((1 - P_i) - n_{ij,\mathcal{N}})f_{\mathcal{N}}^{ij} - g_{\mathcal{N}}^{ij}n_{ij,\mathcal{N}} \\ \qquad\qquad - \widetilde{k}_{T,i}^{\mathcal{N}\mathcal{P}}n_{ij,\mathcal{N}} + \widetilde{k}_{T,i}^{\mathcal{P}\mathcal{N}}n_{ij,\mathcal{P}} & t \geq 0, i \in \mathcal{I}_A, j \in \mathcal{I}_M. \end{cases} \tag{4.19}$$

By combining Eq. (4.11) with Eq. (4.19) we obtain an alternative model, that we denote as the *SE-disc-II model*.

In both the cases of the SE-disc-I and the SE-disc-II models, the expected value of the force exerted by the whole half filament can be obtained as:

$$F_{\mathrm{hf}}(t) = \sum_{i,j} F_{\mathrm{XB}}(d_{ij}(t))(n_{ij,\mathcal{P}}(t) + n_{ij,\mathcal{N}}(t)). \tag{4.20}$$

4.2.5 Crossbridge dynamics: continuous setting

A set of equations describing the XB dynamics presented in Sec. 4.2.1, alternative to the ones of Sec. 4.2.4, can be derived if we consider that the filaments of different sarcomeres may feature heterogeneities in their dimension, so that the value of d_0 itself in Eq. (4.1) should be regarded as a random variable rather than a constant. We assume therefore that, given a BS facing the MF, the probability that the closest MH is located at distance x is uniform for $x \in [0, D_M)$. We denote by $\rho_M := \mathbb{f}\left[\exists\, j \in \mathbb{Z}\, d_{ij}^t = x\right] = {D_M}^{-1}$ the MH linear density, where the symbol $\mathbb{f}$ denotes the probability density function, that is:

$$\mathbb{P}\left[\exists\, j \in \mathbb{Z}\, d_{ij}^t = x \in (a,b)\right] = \int_a^b \mathbb{f}\left[\exists\, j \in \mathbb{Z}\, d_{ij}^t = x\right]dx.$$

We define the following variables, for $i \in \mathcal{I}_A$, corresponding to the probability density that the i-th BS is attached to a MH with displacement x and that the associated RU is in a given permissivity state:

$$\begin{aligned} n_{i,\mathcal{P}}(x,t) &= \mathbb{f}\left[Z_i^t = x, T_i^t = \mathcal{P}\right], \\ n_{i,\mathcal{N}}(x,t) &= \mathbb{f}\left[Z_i^t = x, T_i^t = \mathcal{N}\right]. \end{aligned} \tag{4.21}$$

We notice that we make here the choice of tracking the XBs from the point of view of the BSs, rather than of the MHs, as it is traditionally done in literature [Hux57a; HS71; Smi+08; CMC19]. This change of perspective has the significant advantage of preventing us from the need of tracking which RU faces which MH, from time to time. Indeed, each BS and each RU, being located on the same filament, rigidly move with respect of each others and, thus, each BS is always associated with the same RU.

Considering for instance the variable $n_{i,\mathcal{P}}(x,t)$ (similar calculations can be carried

out for $n_{i,\mathcal{N}}(x,t)$), we have:

$$\begin{aligned}
&\mathbb{f}\left[(Z_i,T_i)^{t+\Delta t}=(x-v_{\mathrm{hs}}(t)\Delta t,\mathcal{P})\right]\overset{\Delta t\to 0}{\sim}\\
&\quad\mathbb{f}\left[(Z_i,T_i)^{t+\Delta t}=(x-v_{\mathrm{hs}}(t)\Delta t,\mathcal{P})|(Z_i,T_i)^t=(\emptyset,\mathcal{P})\right]\mathbb{P}\left[(Z_i,T_i)^t=(\emptyset,\mathcal{P})\right]\\
&\quad+\mathbb{f}\left[(Z_i,T_i)^{t+\Delta t}=(x-v_{\mathrm{hs}}(t)\Delta t,\mathcal{P})|(Z_i,T_i)^t=(x,\mathcal{N})\right]\mathbb{f}\left[(Z_i,T_i)^t=(x,\mathcal{N})\right]\\
&\quad+\mathbb{f}\left[(Z_i,T_i)^{t+\Delta t}=(x-v_{\mathrm{hs}}(t)\Delta t,\mathcal{P})|(Z_i,T_i)^t=(x,\mathcal{P})\right]\mathbb{f}\left[(Z_i,T_i)^t=(x,\mathcal{P})\right].
\end{aligned}$$

Thanks to assumption (Iiii), we have (by applying Prop. 4.1 as in Sec. 4.2.4):

$$\mathbb{f}\left[(Z_i,T_i)^{t+\Delta t}=(x-v_{\mathrm{hs}}(t)\Delta t,\mathcal{P})|(Z_i,T_i)^t=(x,\mathcal{N})\right]\overset{\Delta t\to 0}{\sim}\widetilde{k}_{T,i}^{\mathcal{N}\mathcal{P}}\,\Delta t.$$

Moreover, we have:

$$\begin{aligned}
&\mathbb{P}\left[(Z_i,T_i)^{t+\Delta t}=(x-v_{\mathrm{hs}}(t)\Delta t,\mathcal{P})|(Z_i,T_i)^t=(x,\mathcal{P})\right]\\
&\overset{\Delta t\to 0}{\sim}1-\mathbb{P}\left[(Z_i,T_i)^{t+\Delta t}=(\emptyset,\mathcal{P})|(Z_i,T_i)^t=(x,\mathcal{P})\right]\\
&\qquad-\mathbb{P}\left[(Z_i,T_i)^{t+\Delta t}=(x-v_{\mathrm{hs}}(t)\Delta t,\mathcal{N})|(Z_i,T_i)^t=(x,\mathcal{P})\right]\\
&\overset{\Delta t\to 0}{\sim}1-\Delta t\left(g_{\mathcal{P}}^i(x,v(t))-\widetilde{k}_{T,i}^{\mathcal{P}\mathcal{N}}\right),
\end{aligned}$$

where we have applied once again assumption (Iiii). Concerning the XB formation term, we have:

$$\begin{aligned}
(F)&:=\mathbb{f}\left[(Z_i,T_i)^{t+\Delta t}=(x-v_{\mathrm{hs}}(t)\Delta t,\mathcal{P})|(Z_i,T_i)^t=(\emptyset,\mathcal{P})\right]\mathbb{P}\left[(Z_i,T_i)^t=(\emptyset,\mathcal{P})\right]\\
&=\mathbb{f}\left[(Z_i,T_i)^{t+\Delta t}=(x-v_{\mathrm{hs}}(t)\Delta t,\mathcal{P}),(Z_i,T_i)^t=(\emptyset,\mathcal{P})\right]\\
&=\mathbb{f}\left[(Z_i,T_i)^{t+\Delta t}=(x-v_{\mathrm{hs}}(t)\Delta t,\mathcal{P}),(Z_i,T_i)^t=(\emptyset,\mathcal{P}),\exists\, j\in\mathcal{I}_M\, d_{ij}^t=x,M_j^t=0\right]\\
&+\mathbb{f}\left[(Z_i,T_i)^{t+\Delta t}=(x-v_{\mathrm{hs}}(t)\Delta t,\mathcal{P}),(Z_i,T_i)^t=(\emptyset,\mathcal{P}),\exists\, j\in\mathcal{I}_M\, d_{ij}^t=x,M_j^t\neq 0\right]\\
&+\mathbb{f}\left[(Z_i,T_i)^{t+\Delta t}=(x-v_{\mathrm{hs}}(t)\Delta t,\mathcal{P}),(Z_i,T_i)^t=(\emptyset,\mathcal{P}),\exists\, j\in\mathbb{Z}\setminus\mathcal{I}_M\, d_{ij}^t=x\right].
\end{aligned}$$

The last two terms are of order higher than one in Δt for $\Delta t\to 0$, while the first term gives:

$$\begin{aligned}
&\mathbb{f}\left[(Z_i,T_i)^{t+\Delta t}=(x-v_{\mathrm{hs}}(t)\Delta t,\mathcal{P}),(Z_i,T_i)^t=(\emptyset,\mathcal{P}),\exists\, j\in\mathcal{I}_M\, d_{ij}^t=x,M_j^t=0\right]\\
&=\mathbb{P}\left[(Z_i,T_i)^{t+\Delta t}=(x-v_{\mathrm{hs}}(t)\Delta t,\mathcal{P})|(Z_i,T_i)^t=(\emptyset,\mathcal{P}),\exists\, j\in\mathcal{I}_M\, d_{ij}^t=x,M_j^t=0\right]\\
&\quad\mathbb{f}\left[(Z_i,T_i)^t=(\emptyset,\mathcal{P}),\exists\, j\in\mathbb{Z}\, d_{ij}^t=x,M_j^t=0\right]\\
&\overset{\Delta t\to 0}{\sim}f_{\mathcal{P}}^i(x,v_{\mathrm{hs}}(t))\,\mathbb{f}\left[(Z_i,T_i)^t=(\emptyset,\mathcal{P}),\exists\, j\in\mathbb{Z}\, d_{ij}^t=x,M_j^t=0\right]\Delta t;
\end{aligned}\tag{4.22}$$

the remaining two terms are null. Thus:

$$(F)\sim f_{\mathcal{P}}^i(x,v(t))\,\Delta t\,\mathbb{f}\left[(Z_i,T_i)^t=(\emptyset,\mathcal{P}),\exists\, j\in\mathcal{I}_M\, d_{ij}^t=x,M_j^t=0\right].\tag{4.23}$$

By assumption (Ai), for any i and x such that $f_{\mathcal{P}}^i(x,v(t))\neq 0$, the event $(M_j^t=0)$ for j s.t. $d_{ij}^t=x$ implies the event $(Z_i^t=\emptyset)$, thus:

$$\begin{aligned}
&\mathbb{f}\left[(Z_i,T_i)^t=(\emptyset,\mathcal{P}),\exists\, j\in\mathcal{I}_M\, d_{ij}^t=x,M_j^t=0\right]\\
&\quad=\mathbb{f}\left[(Z_i,T_i)^t=(\emptyset,\mathcal{P}),\exists\, j\in\mathcal{I}_M\, d_{ij}^t=x\right]\\
&\quad=(\mathbb{f}\left[T_i^t=\mathcal{P},\exists\, j\in\mathcal{I}_M\, d_{ij}^t=x\right]\\
&\qquad-\sum_k\mathbb{f}\left[(Z_i,T_i)^t=(x+kD_M,\mathcal{P}),\exists\, j\in\mathcal{I}_M\, d_{ij}^t=x\right]),
\end{aligned}$$

since the BS can be only attached with displacements that are multiple of D_M. Moreover, we recall that the RU dynamics is independent of the interaction with XBs and thus of d_0 (see Sec. 4.2.3) and that for i and x such that $f^i_{\mathcal{P}}(x, v(t)) \neq 0$ the events $(\exists\, j \in \mathcal{I}_M\, d^t_{ij} = x)$ and $(\exists\, j \in \mathbb{Z}\, d^t_{ij} = x)$ coincide. Therefore, we have (on the support of $f^i_{\mathcal{P}}$):

$$\mathbb{f}\left[T^t_i = \mathcal{P}, \exists\, j \in \mathcal{I}_M\, d^t_{ij} = x\right] = \mathbb{P}\left[T^t_i = \mathcal{P}\right]\mathbb{f}\left[\exists\, j \in \mathbb{Z}\, d^t_{ij} = x\right].$$

In addition, since $(Z_i = x + kD_M)$ implies $(\exists\, j \in \mathbb{Z}\, d^t_{ij} = x)$, on the support of $f^i_{\mathcal{P}}$ it holds true:

$$\mathbb{f}\left[(Z_i, T_i)^t = (x + kD_M, \mathcal{P}), \exists\, j \in \mathcal{I}_M\, d^t_{ij} = x\right] = \mathbb{f}\left[(Z_i, T_i)^t = (x + kD_M, \mathcal{P})\right].$$

Since assumption (Ai) implies (Aii), the unique nonzero term of the sum is $k = 0$ and thus:

$$(F) \sim= f^i_{\mathcal{P}}(x, v(t))\Delta t(\mathbb{P}\left[T^t_i = \mathcal{P}\right]\mathbb{f}\left[\exists\, j \in \mathbb{Z}\, d^t_{ij} = x\right] - \mathbb{f}\left[(Z_i, T_i)^t = (x, \mathcal{P})\right]). \quad (4.24)$$

Finally, we divide everything by Δt we let $\Delta t \to 0$ and we observe that:

$$\begin{aligned}
&\frac{n_{i,\mathcal{P}}(x - v_{\mathrm{hs}}(t)\Delta t, t + \Delta t) - n_{i,\mathcal{P}}(x, t)}{\Delta t} \\
&\quad = \frac{n_{i,\mathcal{P}}(x - v_{\mathrm{hs}}(t)\Delta t, t + \Delta t) - n_{i,\mathcal{P}}(x - v_{\mathrm{hs}}(t)\Delta t, t)}{\Delta t} \\
&\quad + \frac{n_{i,\mathcal{P}}(x - v_{\mathrm{hs}}(t)\Delta t, t) - n_{i,\mathcal{P}}(x, t)}{\Delta t\, v_{\mathrm{hs}}(t)} v_{\mathrm{hs}}(t) \\
&\quad \to \frac{\partial n_{i,\mathcal{P}}}{\partial t}(x, t) - v_{\mathrm{hs}}(t)\frac{\partial n_{i,\mathcal{P}}}{\partial x}(x, t).
\end{aligned} \quad (4.25)$$

We get in such a way the following PDE model, derived under assumptions (Iiii) and (Ai):

$$\begin{cases}
\dfrac{\partial n_{i,\mathcal{P}}}{\partial t} - v_{\mathrm{hs}}\dfrac{\partial n_{i,\mathcal{P}}}{\partial x} = (\rho_M P_i - n_{i,\mathcal{P}})f^i_{\mathcal{P}} - g^i_{\mathcal{P}} n_{i,\mathcal{P}} \\
\qquad\qquad - \widetilde{k}^{\mathcal{P}\mathcal{N}}_{T,i} n_{i,\mathcal{P}} + \widetilde{k}^{\mathcal{N}\mathcal{P}}_{T,i} n_{i,\mathcal{N}} \qquad x \in \mathbb{R},\, t \geq 0,\, i \in \mathcal{I}_A, \\
\dfrac{\partial n_{i,\mathcal{N}}}{\partial t} - v_{\mathrm{hs}}\dfrac{\partial n_{i,\mathcal{N}}}{\partial x} = (\rho_M(1 - P_i) - n_{i,\mathcal{P}})f^i_{\mathcal{N}} - g^i_{\mathcal{N}} n_{i,\mathcal{N}} \\
\qquad\qquad - \widetilde{k}^{\mathcal{N}\mathcal{P}}_{T,i} n_{i,\mathcal{N}} + \widetilde{k}^{\mathcal{P}\mathcal{N}}_{T,i} n_{i,\mathcal{P}} \qquad x \in \mathbb{R},\, t \geq 0,\, i \in \mathcal{I}_A,
\end{cases} \quad (4.26)$$

endowed with suitable initial conditions. By combining Eq. (4.11) with Eq. (4.26), respectively describing the dynamics of RUs and XBs, we obtain a model that we denote as the *SE-PDE model* (spatially explicit model written in the form of a PDEs system).

The expected value of the force exerted by the whole half filament can be determined as follows:

$$\begin{aligned}
F_{\mathrm{hf}}(t) &= \sum_i \int_{-\infty}^{+\infty} F_{\mathrm{XB}}(x)\mathbb{f}\left[Z^t_i = x\right]dx \\
&= \sum_i \int_{-\infty}^{+\infty} F_{\mathrm{XB}}(x)\left(\mathbb{f}\left[Z^t_i = x, T^t_i = \mathcal{P}\right] + \mathbb{f}\left[Z^t_i = x, T^t_i = \mathcal{N}\right]\right)dx \\
&= \sum_i \int_{-\infty}^{+\infty} F_{\mathrm{XB}}(x)\left(n_{i,\mathcal{P}}(x, t) + n_{i,\mathcal{N}}(x, t)\right)dx.
\end{aligned} \quad (4.27)$$

We notice that Eq. (4.26), for each $i \in \mathcal{I}_A$, is formally similar to the H57 model. The main difference is that the population of BSs is here split into two groups (permissive ones and non-permissive ones). This is the reason of the appearance of the terms $\widetilde{k}_{T,i}^{\mathcal{PN}} n_{i,\mathcal{P}}$ and $\widetilde{k}_{T,i}^{\mathcal{NP}} n_{i,\mathcal{N}}$, that account for the fluxes of probability from one population to the other. The terms P_i and $(1-P_i)$ represent the maximum possible proportion of attached BSs in each group. Finally, the term ρ_M appears because in this setting $n_{i,\mathcal{P}}$ and $n_{i,\mathcal{N}}$ are, from a dimensional point of view, the inverse of length units (they are probability densities), whereas the variables of the H57 model are dimensionless.

Distribution-moments equations

Like for the H57 model, distribution-moments equations can be derived for the model of Eq. (4.26), under suitable assumptions. Specifically, let us assume that the total attachment-detachment rate is independent of the XB distortion (i.e. there exist functions $r_{\mathcal{P}}^i(v)$ and $r_{\mathcal{N}}^i(v)$, for $i \in \mathcal{I}_A$, such that $r_{\mathcal{P}}^i(v) = f_{\mathcal{P}}^i(x,v) + g_{\mathcal{P}}^i(x,v)$ and $r_{\mathcal{N}}^i(v) = f_{\mathcal{N}}^i(x,v) + g_{\mathcal{N}}^i(x,v)$ for any $x \in \mathbb{R}$). Then, we define, for $\alpha \in \{\mathcal{N}, \mathcal{P}\}$, and for $\psi \in \{f_{\mathcal{P}}^i, f_{\mathcal{N}}^i, g_{\mathcal{P}}^i, g_{\mathcal{N}}^i\}$:

$$\begin{aligned} \mu_{i,\alpha}^p(t) &:= \int_{-\infty}^{+\infty} \left(\frac{x}{SL_0/2}\right)^p n_{i,\alpha}(x,t)dx, \\ \mu_{\psi}^p(v) &:= \int_{-\infty}^{+\infty} \left(\frac{x}{SL_0/2}\right)^p \psi(x,v)\frac{dx}{D_M}. \end{aligned} \tag{4.28}$$

We notice that $\mu_{i,\mathcal{N}}^0(t)$ (respectively, $\mu_{i,\mathcal{P}}^0(t)$) can be interpreted as the probability that the i-th BS is attached and associated to a non-permissive (respectively, permissive) RU. Moreover, $\mu_{i,\mathcal{N}}^1(t)/\mu_{i,\mathcal{N}}^0(t)$ (respectively, $\mu_{i,\mathcal{P}}^1(t)/\mu_{i,\mathcal{P}}^0(t)$) corresponds to the expected value of the distortion (normalized with respect to $SL_0/2$) of the XB attached to the i-th RU, provided that the corresponding RU is in non-permissive (respectively, permissive) state.

By proceeding as in Sec. 3.1.2, we get the following distribution-moments equations:

$$\begin{cases} \dfrac{d}{dt}\mu_{i,\mathcal{P}}^0 = -\left(r_{\mathcal{P}}^i + \widetilde{k}_{T,i}^{\mathcal{PN}}\right)\mu_{i,\mathcal{P}}^0 + \widetilde{k}_{T,i}^{\mathcal{NP}}\mu_{i,\mathcal{N}}^0 + P_i\mu_{f_{\mathcal{P}}^i}^0 & t \geq 0,\ i \in \mathcal{I}_A, \\ \dfrac{d}{dt}\mu_{i,\mathcal{N}}^0 = -\left(r_{\mathcal{N}}^i + \widetilde{k}_{T,i}^{\mathcal{NP}}\right)\mu_{i,\mathcal{N}}^0 + \widetilde{k}_{T,i}^{\mathcal{PN}}\mu_{i,\mathcal{P}}^0 + (1-P_i)\mu_{f_{\mathcal{N}}^i}^0 & t \geq 0,\ i \in \mathcal{I}_A, \\ \dfrac{d}{dt}\mu_{i,\mathcal{P}}^1 + v\,\mu_{i,\mathcal{P}}^0 = -\left(r_{\mathcal{P}}^i + \widetilde{k}_{T,i}^{\mathcal{PN}}\right)\mu_{i,\mathcal{P}}^1 + \widetilde{k}_{T,i}^{\mathcal{NP}}\mu_{i,\mathcal{N}}^1 + P_i\mu_{f_{\mathcal{P}}^i}^1 & t \geq 0,\ i \in \mathcal{I}_A, \\ \dfrac{d}{dt}\mu_{i,\mathcal{N}}^1 + v\,\mu_{i,\mathcal{N}}^0 = -\left(r_{\mathcal{N}}^i + \widetilde{k}_{T,i}^{\mathcal{NP}}\right)\mu_{i,\mathcal{N}}^1 + \widetilde{k}_{T,i}^{\mathcal{PN}}\mu_{i,\mathcal{P}}^1 + (1-P_i)\mu_{f_{\mathcal{N}}^i}^1 & t \geq 0,\ i \in \mathcal{I}_A. \end{cases} \tag{4.29}$$

We notice that, thanks to (4.4), we have:

$$\begin{aligned} \mu_{f_\alpha^i}^p &= \mu_{f_\alpha}^p\,\chi_M(SL,i)\,\chi_{SF}(SL,i), \\ \mu_{g_\alpha^i}^p &= \mu_{g_\alpha}^p\,\chi_M(SL,i)\,\chi_{SF}(SL,i) + \mu_{\bar{g}_\alpha}^p\,(1-\chi_M(SL,i)\,\chi_{SF}(SL,i)). \end{aligned} \tag{4.30}$$

By assuming a linear spring hypothesis, the expected value of the force of half filament is given by:

$$F_{\mathrm{hf}}(t) = k_{\mathrm{XB}}\frac{SL_0}{2}N_A\mu^1(t), \tag{4.31}$$

where we have defined:

$$\mu^p(t) = \frac{1}{N_A} \sum_{i=1}^{N_A} \left(\mu^p_{i,\mathcal{P}} + \mu^p_{i,\mathcal{N}} \right). \tag{4.32}$$

Moreover, the active tension and active stiffness at the tissue level are given by:

$$\begin{aligned} T_{\mathrm{a}}(t) &= a_{\mathrm{XB}}\, \mu^1(t), \\ K_{\mathrm{a}}(t) &= a_{\mathrm{XB}}\, \mu^0(t). \end{aligned} \tag{4.33}$$

In the following, we denote by *SE-ODE model* the one that is obtained by combining Eq. (4.11) with Eq. (4.29).

4.2.6 Mean-field approximation

In the previous sections we proposed a model of tension generation in the muscle tissue based on an explicit spatial description of the physical arrangements of proteins along the myofilaments. The spatial description allows to model the cooperativity mechanism (linked to the nearest-neighbor interactions within RUs) and the SL related effects on the force generation machinery (linked to the filament overlapping). However, the first phenomenon, despite being spatial dependent, is based on interactions of local type; the effect of the second phenomenon, in turn, largely depends on the size of the single-overlap zone, that is a scalar quantity non dependent on the spatial variable. Based on the above considerations, in this section, we propose a mean-field approximation of the spatially dependent CTMC presented in 4.2.1, where the nearest-neighboring interaction are captured as a local effect, and the effect of SL is modeled in function of the size of the single-overlap zone.

The mean-field model is based on the assumption that the single-overlap zone can be considered as infinitely long. Such approximation is reasonable as far as the effect of the edges can be neglected (the validity of such approximation will be discussed in Sec. 4.3). A direct consequence of this assumption is the invariance by translation of the joint distribution of RUs. This means that for any set of indices $\mathcal{I}_1 \subset \mathbb{Z}$ and $\mathcal{I}_2 \subset \mathbb{Z}$ and for any collection of states $\alpha_i \in \{\mathcal{N}, \mathcal{P}\}$ (for $i \in \mathcal{I}_1$) and $\beta_i \in \{\mathcal{U}, \mathcal{B}\}$ (for $i \in \mathcal{I}_2$), the joint distribution of the states of the corresponding RUs is not affected if the RUs are translated by a count of $k \in \mathbb{Z}$ units:

$$\mathbb{P}\left[\left(\bigcap_{i\in\mathcal{I}_1} T_i^t = \alpha_i \right) \cap \left(\bigcap_{i\in\mathcal{I}_2} C_i^t = \beta_i \right) \right] = \mathbb{P}\left[\left(\bigcap_{i\in\mathcal{I}_1} T_{i+k}^t = \alpha_i \right) \cap \left(\bigcap_{i\in\mathcal{I}_2} C_{i+k}^t = \beta_i \right) \right].$$

It follows that the variables $\pi_i^{\alpha\beta\delta,\vartheta\eta\lambda}(t)$ defined in (4.10) coincide for each i. In addition, we further reduce the number of variables by tracking only the state of the TnC of the central RU of the triplet (this further reduction is made possible by the fact that we never have to track the behavior at the boundaries of the filaments, as we will see in what follows). We define thus the following variables, for $\alpha, \beta, \delta \in \{\mathcal{N}, \mathcal{P}\}$ and $\eta \in \{\mathcal{U}, \mathcal{B}\}$:

$$\pi^{\alpha\beta\delta,\eta}(t) := \mathbb{P}\left[(T_{i-1}, T_i, T_{i+1})^t = (\alpha, \beta, \delta), C_i^t = \eta \right]. \tag{4.34}$$

We notice that the variables $\pi^{\alpha\beta\delta,\eta}(t)$ are well-defined thanks to the translational invariance of the distribution of RUs. Moreover, the transition rates $k_{C,i}^{\delta\bar{\delta}|\beta}$ and $k_{T,i}^{\beta\bar{\beta}|\alpha\,\cdot\,\eta,\delta}$ for the units in the single-overlap region do not depend on i. Hence, we will denote them simply as $k_C^{\delta\bar{\delta}|\beta}$ and $k_T^{\beta\bar{\beta}|\alpha\,\cdot\,\eta,\delta}$.

The time evolution of the variables can be determined, with a similar strategy to that adopted in Sec. 4.2.3, by proceeding as follows:

$$\begin{aligned}\pi^{\alpha\beta\delta,\eta}(t+\Delta t) \overset{\Delta t\to 0}{\sim} &\mathbb{P}\left[T_{i-1}^{t+\Delta t}=\alpha|(T_{i-1},T_i,T_{i+1})^t=(\overline{\alpha},\beta,\delta),C_i^t=\eta\right]\pi^{\overline{\alpha}\beta\delta,\eta}(t)\\ &+\mathbb{P}\left[T_{i}^{t+\Delta t}=\beta|(T_{i-1},T_i,T_{i+1})^t=(\alpha,\overline{\beta},\delta),C_i^t=\eta\right]\pi^{\alpha\overline{\beta}\delta,\eta}(t)\\ &+\mathbb{P}\left[T_{i+1}^{t+\Delta t}=\delta|(T_{i-1},T_i,T_{i+1})^t=(\alpha,\beta,\overline{\delta}),C_i^t=\eta\right]\pi^{\alpha\beta\overline{\delta},\eta}(t)\\ &+\mathbb{P}\left[C_{i}^{t+\Delta t}=\eta|(T_{i-1},T_i,T_{i+1})^t=(\alpha,\beta,\delta),C_i^t=\overline{\eta}\right]\pi^{\alpha\beta\delta,\overline{\eta}}(t)\\ &+\mathbb{P}\left[(T_{i-1},T_i,T_{i+1})^{t+\Delta t}=(\alpha,\beta,\delta),C_i^{t+\Delta t}=\eta|\right.\\ &\qquad\left.(T_{i-1},T_i,T_{i+1})^t=(\alpha,\beta,\delta),C_i^t=\eta\right]\pi^{\alpha\beta\delta,\eta}(t),\end{aligned} \tag{4.35}$$

where, by definition, we have:

$$\mathbb{P}\left[T_{i}^{t+\Delta t}=\beta|(T_{i-1},T_i,T_{i+1})^t=(\alpha,\overline{\beta},\delta),C_i^t=\eta\right]\overset{\Delta t\to 0}{\sim} k_T^{\overline{\beta}\beta|\alpha\,\cdot\,\delta,\eta}\Delta t,$$

and

$$\mathbb{P}\left[C_{i}^{t+\Delta t}=\eta|(T_{i-1},T_i,T_{i+1})^t=(\alpha,\beta,\delta),C_i^t=\overline{\eta}\right]\overset{\Delta t\to 0}{\sim} k_C^{\overline{\eta}\eta|\beta}\Delta t.$$

By adopting assumption (Ii), Prop. 4.1 for $A=(T_{i-1}^{t+\Delta t}=\eta)$, $B=(T_{i+1}^t=\delta,C_i^t=\eta)$, $C=((T_{i-1},T_i)^t=(\alpha,\beta))$ and $\mathcal{D}=\{(T_{i-2}^t=\xi,C_{i-1}^t=\zeta)\}_{\xi,\zeta}$ leads to:

$$\begin{aligned}&\mathbb{P}\left[T_{i-1}^{t+\Delta t}=\alpha|(T_{i-1},T_i,T_{i+1})^t=(\overline{\alpha},\beta,\delta),C_i^t=\eta\right]\\ &\quad=\frac{\sum_{\xi,\zeta}\mathbb{P}\left[T_{i-1}^{t+\Delta t}=\alpha|(T_{i-2},T_{i-1},T_i)^t=(\xi,\overline{\alpha},\beta),C_{i-1}^t=\zeta\right]\pi_{i-1}^{\xi\overline{\alpha}\beta,\zeta}(t)}{\sum_{\xi,\zeta}\pi_{i-1}^{\xi\overline{\alpha}\beta,\zeta}(t)}\\ &\quad\overset{\Delta t\to 0}{\sim}\widetilde{k}_T^{\overline{\alpha}\alpha|\circ\,\cdot\,\beta,\circ}\,\Delta t,\end{aligned}$$

where we have defined:

$$\widetilde{k}_T^{\overline{\alpha}\alpha|\circ\,\cdot\,\beta,\circ}:=\frac{\sum_{\xi,\zeta}k_T^{\overline{\alpha}\alpha|\xi\,\cdot\,\beta,\zeta}\pi^{\xi\overline{\alpha}\beta,\zeta}(t)}{\sum_{\xi,\zeta}\pi^{\xi\overline{\alpha}\beta,\zeta}(t)},$$

$$\widetilde{k}_T^{\overline{\delta}\delta|\beta\,\cdot\,\circ,\circ}:=\frac{\sum_{\xi,\zeta}k_T^{\overline{\delta}\delta|\beta\,\cdot\,\xi,\zeta}\pi^{\beta\overline{\delta}\xi,\zeta}(t)}{\sum_{\xi,\zeta}\pi^{\beta\overline{\delta}\xi,\zeta}(t)}.$$

In conclusion, we get the following ODE model, valid for $t\geq 0$ and for any $\alpha,\beta,\delta\in\{\mathcal{N},\mathcal{P}\}$ and $\eta\in\{\mathcal{U},\mathcal{B}\}$:

$$\begin{aligned}\frac{d}{dt}\pi^{\alpha\beta\delta,\eta}=&\ \widetilde{k}_T^{\overline{\alpha}\alpha|\circ\,\cdot\,\beta,\circ}\ \pi^{\overline{\alpha}\beta\delta,\eta}\ -\widetilde{k}_T^{\alpha\overline{\alpha}|\circ\,\cdot\,\beta,\circ}\ \pi^{\alpha\beta\delta,\eta}\\ &+k_T^{\overline{\beta}\beta|\alpha\,\cdot\,\delta,\eta}\ \pi^{\alpha\overline{\beta}\delta,\eta}\ -k_T^{\beta\overline{\beta}|\alpha\,\cdot\,\delta,\eta}\ \pi^{\alpha\beta\delta,\eta}\\ &+\widetilde{k}_T^{\overline{\delta}\delta|\beta\,\cdot\,\circ,\circ}\ \pi^{\alpha\beta\overline{\delta},\eta}\ -\widetilde{k}_T^{\delta\overline{\delta}|\beta\,\cdot\,\circ,\circ}\ \pi^{\alpha\beta\delta,\eta}\\ &+k_C^{\overline{\eta}\eta|\beta}\ \pi^{\alpha\beta\delta,\overline{\eta}}\ -k_C^{\eta\overline{\eta}|\beta}\ \pi^{\alpha\beta\delta,\eta}.\end{aligned} \tag{4.36}$$

The permissivity of a RU in the single-overlap zone, defined as $P(t)=\mathbb{P}\left[T_i^t=\mathcal{P}\right]$ (such that the i-th RU belongs to the single-overlap zone), can be obtained as:

$$P(t)=\sum_{\alpha,\delta\in\{\mathcal{N},\mathcal{P}\}}\ \sum_{\eta\in\{\mathcal{U},\mathcal{B}\}}\pi^{\alpha\mathcal{P}\delta,\eta}(t).$$

By similar arguments, it follows that also the joint distribution of the stochastic processes associated with XB formation enjoy the translational invariance property and, consequently, the following variables are well defined, as the right-hand sides are independent of the index i (for i belonging to the single-overlap zone):

$$\begin{aligned} n_{\mathcal{P}}(x,t) &= \mathbb{f}\left[Z_i^t = x, T_i^t = \mathcal{P}\right], \\ n_{\mathcal{N}}(x,t) &= \mathbb{f}\left[Z_i^t = x, T_i^t = \mathcal{N}\right]. \end{aligned} \tag{4.37}$$

By proceeding as in Sec. 4.2.5 we get the following model:

$$\begin{cases} \dfrac{\partial n_{\mathcal{P}}}{\partial t} - v_{\text{hs}}\dfrac{\partial n_{\mathcal{P}}}{\partial x} = (\rho_M P - n_{\mathcal{P}})f_{\mathcal{P}} - g_{\mathcal{P}} n_{\mathcal{P}} \\ \qquad\qquad - \widetilde{k}_T^{\mathcal{P}\mathcal{N}} n_{\mathcal{P}} + \widetilde{k}_T^{\mathcal{N}\mathcal{P}} n_{\mathcal{N}} \qquad\qquad x \in \mathbb{R},\, t \geq 0, \\ \dfrac{\partial n_{\mathcal{N}}}{\partial t} - v_{\text{hs}}\dfrac{\partial n_{\mathcal{N}}}{\partial x} = (\rho_M (1-P) - n_{\mathcal{P}})f_{\mathcal{N}} - g_{\mathcal{N}} n_{\mathcal{N}} \\ \qquad\qquad - \widetilde{k}_T^{\mathcal{N}\mathcal{P}} n_{\mathcal{N}} + \widetilde{k}_T^{\mathcal{P}\mathcal{N}} n_{\mathcal{P}} \qquad\qquad x \in \mathbb{R},\, t \geq 0, \end{cases} \tag{4.38}$$

where we have defined:

$$\begin{aligned} \widetilde{k}_T^{\mathcal{N}\mathcal{P}} &:= \frac{\sum_{\alpha,\eta,\delta} k_T^{\mathcal{N}\mathcal{P}|\alpha\,\cdot\,\eta,\delta}\mathbb{P}\left[(T_{i-1}, T_i, T_{i+1}, C_i)^t = (\alpha, \mathcal{N}, \eta, \delta)\right]}{\mathbb{P}\left[T_i^t = \mathcal{N}\right]}, \\ \widetilde{k}_T^{\mathcal{P}\mathcal{N}} &:= \frac{\sum_{\alpha,\eta,\delta} k_T^{\mathcal{P}\mathcal{N}|\alpha\,\cdot\,\eta,\delta}\mathbb{P}\left[(T_{i-1}, T_i, T_{i+1}, C_i)^t = (\alpha, \mathcal{P}, \eta, \delta)\right]}{\mathbb{P}\left[T_i^t = \mathcal{P}\right]}. \end{aligned} \tag{4.39}$$

We notice that the transition rates $\widetilde{k}_T^{\mathcal{N}\mathcal{P}}$ and $\widetilde{k}_T^{\mathcal{P}\mathcal{N}}$ can be obtained from the variables $\pi^{\alpha\beta\delta,\eta}$ as:

$$\begin{aligned} \widetilde{k}_T^{\mathcal{N}\mathcal{P}}(t) &:= \frac{\sum_{\alpha,\delta,\eta} k_T^{\mathcal{N}\mathcal{P}|\alpha\,\cdot\,\delta,\eta}\,\pi^{\alpha\mathcal{N}\delta,\eta}(t)}{1 - P(t)}, \\ \widetilde{k}_T^{\mathcal{P}\mathcal{N}}(t) &:= \frac{\sum_{\alpha,\delta,\eta} k_T^{\mathcal{P}\mathcal{N}|\alpha\,\cdot\,\delta,\eta}\,\pi^{\alpha\mathcal{P}\delta,\eta}(t)}{P(t)}. \end{aligned} \tag{4.40}$$

The expected value of the force exerted by the whole half filament can be obtained as follows:

$$F_{\text{hf}}(t) = N_A\,\chi_{\text{so}}(SL(t))\int_{-\infty}^{+\infty} F_{\text{XB}}(x)\,(n_{\mathcal{P}}(x,t) + n_{\mathcal{N}}(x,t))\,dx, \tag{4.41}$$

where the single-overlap ratio χ_{so} denotes the fraction of the AF filament in the single-overlap zone:

$$\chi_{\text{so}}(SL) := \frac{L_{\text{so}}(SL(t))}{L_A} = \begin{cases} 0 & \text{if } SL \leq L_A, \\ \dfrac{2(SL - L_A)}{L_M - L_H} & \text{if } L_A < SL \leq L_M, \\ \dfrac{SL + L_M - 2L_A}{L_M - L_H} & \text{if } L_M < SL \leq 2L_A - L_H, \\ 1 & \text{if } 2L_A - L_H < SL \leq 2L_A + L_H, \\ \dfrac{L_M + 2L_A - SL}{L_M - L_H} & \text{if } 2L_A + L_H < SL \leq 2L_A + L_M, \\ 0 & \text{if } SL > 2L_A + L_M. \end{cases} \tag{4.42}$$

We notice that we are here assuming that the relative sliding between the filaments is such that $\chi_{\rm so}$ slowly varies, so that we can neglect the effects linked to the state transitions taking place at the border of the single-overlap zone.

The combination of Eq. (4.36) with Eq. (4.38) gives a model for the full-sarcomere function, that we denote as the *MF-PDE model* (mean-field model written in the form of a PDEs system).

Moreover, under the assumption that the total attachment-detachment rate does not depend on the XB elongation (i.e. there exist two functions $r_{\mathcal{P}}(v)$ and $r_{\mathcal{N}}(v)$ such that $r_{\mathcal{P}}(v) = f_{\mathcal{P}}(x,v) + g_{\mathcal{P}}(x,v)$ and $r_{\mathcal{N}}(v) = f_{\mathcal{N}}(x,v) + g_{\mathcal{N}}(x,v)$ for any $x \in \mathbb{R}$), we can derive the following distribution-moment equation:

$$\begin{cases} \dfrac{d}{dt}\mu^0_{\mathcal{P}} = -\left(r_{\mathcal{P}}(v) + \widetilde{k}_T^{\mathcal{P}\mathcal{N}}\right)\mu^0_{\mathcal{P}} + \widetilde{k}_T^{\mathcal{N}\mathcal{P}}\mu^0_{\mathcal{N}} + P\,\mu^0_{f_{\mathcal{P}}} & t \geq 0, \\ \dfrac{d}{dt}\mu^0_{\mathcal{N}} = -\left(r_{\mathcal{N}}(v) + \widetilde{k}_T^{\mathcal{N}\mathcal{P}}\right)\mu^0_{\mathcal{N}} + \widetilde{k}_T^{\mathcal{P}\mathcal{N}}\mu^0_{\mathcal{P}} + (1-P)\,\mu^0_{f_{\mathcal{N}}} & t \geq 0, \\ \dfrac{d}{dt}\mu^1_{\mathcal{P}} + v\,\mu^0_{\mathcal{P}} = -\left(r_{\mathcal{P}}(v) + \widetilde{k}_T^{\mathcal{P}\mathcal{N}}\right)\mu^1_{\mathcal{P}} + \widetilde{k}_T^{\mathcal{N}\mathcal{P}}\mu^1_{\mathcal{N}} + P\,\mu^1_{f_{\mathcal{P}}} & t \geq 0, \\ \dfrac{d}{dt}\mu^1_{\mathcal{N}} + v\,\mu^0_{\mathcal{N}} = -\left(r_{\mathcal{N}}(v) + \widetilde{k}_T^{\mathcal{N}\mathcal{P}}\right)\mu^1_{\mathcal{N}} + \widetilde{k}_T^{\mathcal{P}\mathcal{N}}\mu^1_{\mathcal{P}} + (1-P)\,\mu^1_{f_{\mathcal{N}}} & t \geq 0, \end{cases} \tag{4.43}$$

where we have defined, for $\alpha \in \{\mathcal{N}, \mathcal{P}\}$:

$$\mu^p_\alpha(t) := \int_{-\infty}^{+\infty} \left(\frac{x}{SL_0/2}\right)^p n_\alpha(x,t)dx. \tag{4.44}$$

The force exerted by half thick filament is then given by:

$$F_{\rm hf}(t) = k_{\rm XB}\frac{SL_0}{2}N_A\,\mu^1(t), \tag{4.45}$$

where

$$\mu^p(t) := \chi_{\rm so}(SL(t))\left[\mu^p_{\mathcal{P}}(t) + \mu^p_{\mathcal{N}}(t)\right], \tag{4.46}$$

for $p = 0, 1$ and, hence, the tissue level active tension and stiffness are:

$$\begin{aligned} T_{\rm a}(t) &= a_{\rm XB}\,\mu^1(t), \\ K_{\rm a}(t) &= a_{\rm XB}\,\mu^0(t). \end{aligned} \tag{4.47}$$

Finally, by combining Eq. (4.36) with Eq. (4.43) we obtain a model that we denote as *MF-ODE model*.

4.2.7 Overview of the models

Table 4.1 provides a list of the different models proposed in this chapter, with the assumptions under which the models are derived. The two models derived by the distribution-moments (SE-ODE and MF-ODE) also require that the sum of the attachment and detachment rates is independent of x (we write $f + g \perp\!\!\!\perp x$). We notice that this is not a simplificatory assumption, but rather a specific modeling choice that allows to write the model with the distribution-moments formalism.

Model name (Equations)	Number of ODEs Number of PDEs	Assumptions	Modeling choices
SE-disc-I	$(N_A-2)2^6+2N_AN_M = 2432$	(Iii),(Iiii),(Iiv)	
(4.11)-(4.18)	-		
SE-disc-II	$(N_A-2)2^6+2N_AN_M = 2432$	(Iii),(Iiii),(Ai)	
(4.11)-(4.19)	-		
SE-PDE	$(N_A-2)2^6 = 1280$	(Iii),(Iiii),(Ai)	
(4.11)-(4.26)	$2N_A = 64$		
SE-ODE	$(N_A-2)2^6+4N_A = 1408$	(Iii),(Iiii),(Ai)	$f+g \perp\!\!\!\perp x$
(4.11)-(4.29)	-		
MF-PDE	$2^4 = 16$	(Ii),(Iiii),(Ai), m.f.	
(4.36)-(4.38)	$2 = 2$		
MF-ODE	$2^4+4 = 20$	(Ii),(Iiii),(Ai), m.f.	$f+g \perp\!\!\!\perp x$
(4.36)-(4.43)	-		

Table 4.1: List of the models proposed in Sec. 4.2. For future reference, we assign a name to each model (*SE* stands for spatially-explicit, *MF* stands for mean-field, *disc* stands for discrete). In the second column we report the number of ODEs and PDEs included in each model as a function of N_A and N_M and we specify the resulting values in the case $N_A = 32$, $N_M = 18$. In the "Assumptions" column, *m.f.* stands for *mean-field assumption*.

4.3 Models calibration

In Sec. 4.2.1 we have presented a description of a pair of interacting myofilaments, where the dynamics of the proteins located on the myofilaments is ruled by a collection of transition rates. Then, in the rest of Sec. 4.2 we have shown that under some assumptions and, in some cases, for specific choices of the transition rates, the dynamics of the stochastic processes associated with the proteins located on the myofilaments can be described by different systems of ODEs and/or PDEs. The models listed in Sec. 4.2.7 are thus valid independently of the specific choice of the transition rates (with the only exception of the models SE-ODE and MF-ODE that require that the sum of the detachment and attachment rate is independent of the XB distorsion). In this section, we present and motivate the specific choice of transition rates that we will adopt in this thesis and the strategy that we follow for the calibration of the associated parameters.

Available experimental data that can be used to calibrate the model parameters differ by various factors, including:

- the tissue type: skeletal or cardiac (see Sec. 1.2);
- the animal species;
- the temperature (see Sec. 1.3.6 for its influence on the sarcomere dynamics);
- the cellular treatment: intact or skinned cells (see Sec. 1.3.2);
- the chemical environment of the experimental setup, which is typically kept as faithful as possible to the physiological environment, unless it is intentionally altered to achieve specific conditions.

Parameter	Value	Units
SL_0	2.2	µm
L_A	1.25	µm
L_M	1.65	µm
L_H	0.18	µm
ε_{SL}	0.05	µm
N_M	18	-
N_A	32	-

Table 4.2: List of geometrical constants.

To calibrate the model, we will restrict ourselves to experimental measurements from the literature coming from intact cardiac cells since the skinning procedure alters in a significant (and not yet fully understood) manner the machinery of activation and force generation (see Sec. 1.3.2). Moreover, thanks to the technique of flura-2 fluorescence, it is noways possible to measure the intracellular calcium concentration without depriving the cell of its membrane, and it is also possible to inhibit the sarcoplasmic reticulum calcium uptake by cyclopiazonic acid, so that the calcium level can be controlled without the need of skinning the cells.

However, only few data are available from human cells, compared to animal cells, and most of experiments are performed at room temperature, whereas the most interesting application of a mathematical model is that of replicating in vivo conditions, thus at body temperature. Since the available data for human cells at body temperature are not sufficient to adequately constrain the parameters of our models, we proceed as follows. First, we calibrate the model parameters from rat experiments at room temperature since for this species many experimental data are available, and than we adjust the parameters that are reasonably affected by the two varying factors (i.e. inter-species variability and temperature) to fit the available data from human cells as body temperature. We compensate in this way for the data deficiency. We notice that we work under the hypothesis that inter-species variability does not affect the fundamental machinery of tissue activation and force generation, but, since different species express different isoforms of the same protein, it can be encompassed by changing the parameters of the same mathematical model (see [Tøn+15] for a detailed discussion on this topic).

We report in Table 4.2 the geometrical constants describing the size of the myofilament components that we use in the following.

4.3.1 RUs transition rates

The RU dynamics is determined by the 8 rates ruling the forward and backward transitions $\mathcal{UN} \rightleftharpoons \mathcal{BN}$, $\mathcal{UP} \rightleftharpoons \mathcal{BP}$, $\mathcal{UN} \rightleftharpoons \mathcal{UP}$ and $\mathcal{BN} \rightleftharpoons \mathcal{BP}$. The transition rates are affected by $[Ca^{2+}]_i$ (that enhances in a multiplicative way the transition $\mathcal{U} \to \mathcal{B}$), the filament overlap and the state of the nearest-neighboring Tm units (for the latter interaction we adopt the cooperative interactions proposed in the R03 model). We start by considering the single-overlap zone, where we adopt the transition rates of the R03 model. We show below that the transition rates of R03 are, however, rather general, as they are based on just a couple of assumptions. In any case, we keep the notation consistent with the R03 model to allow for comparisons.

We call $k_C^{\mathcal{BU}|\mathcal{N}} := k_{\text{off}}$ and, without loss of generality, we set $k_C^{\mathcal{BU}|\mathcal{P}} := k_{\text{off}}/\mu$,

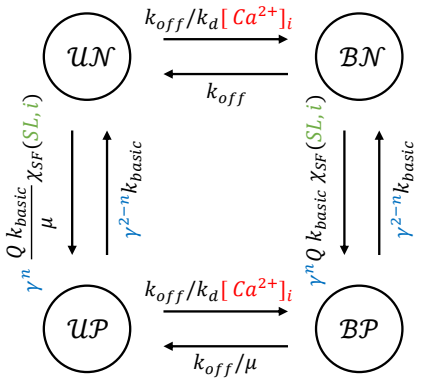

Figure 4.2: The proposed four states Markov model describing each RU. The terms depending on the intracellular calcium concentration $[\mathrm{Ca}^{2+}]_\mathrm{i}$ are highlighted in red; terms depending on the state of neighbouring RUs (i.e. depending on n) are highlighted in blue; terms depending on the position of the RU and the current sarcomere elongation are highlighted in green.

where the constant μ allows to differentiate the two rates. Experiments carried out with protein isoforms from different species highlight that there is no apparent variation in the transition $\mathcal{U} \to \mathcal{B}$ in different combinations of Tn subunits and Tm. We assume thus that the transition rates for $\mathcal{UN} \to \mathcal{BN}$ and for $\mathcal{UP} \to \mathcal{BP}$ coincide, and we set $k_C^{\mathcal{UB}|\mathcal{N}} = k_C^{\mathcal{UB}|\mathcal{P}} := k_\mathrm{off}/k_\mathrm{d}[\mathrm{Ca}^{2+}]_\mathrm{i}$. Conversely, we allow the reverse transition rates to depend on the state of the associated Tm. Concerning the transitions involving Tm, we assume that the calcium binding state of Tn affects the transition rate of $\mathcal{N} \to \mathcal{P}$ for the associated Tm (see Sec. 1.2.4), but not the reverse rate. Therefore, we set $k_T^{\mathcal{PN}|\alpha\,\cdot\,\delta,\mathcal{U}} = k_T^{\mathcal{PN}|\alpha\,\cdot\,\delta,\mathcal{B}} = k_\mathrm{basic}\gamma^{2-n(\alpha,\delta)}$, where $n(\alpha,\delta)$ denotes the number of permissive states among α and δ, as in Sec. 2.2.1. Then, without loss of generality we denote $k_T^{\mathcal{NP}|\alpha\,\cdot\,\delta,\mathcal{B}} = Q\,k_\mathrm{basic}\gamma^{n(\alpha,\delta)}$, where the constant Q allows to differentiate the forward and backward transition rates. The only transition rate left is given, to satisfy the detailed-balance consistency with the other rates, by $k_T^{\mathcal{NP}|\alpha\,\cdot\,\delta,\mathcal{U}} = Q/\mu\,k_\mathrm{basic}\gamma^{n(\alpha,\delta)}$.

In conclusion, the transition rates are determined by the five parameters Q, μ, k_d, k_off, k_basic (plus the parameter γ that regulates the amount of cooperativity), resulting from the eight free parameters constrained by the two assumptions ($\mathcal{U} \to \mathcal{B}$ not affected by Tm, $\mathcal{P} \to \mathcal{N}$ not affected by Tn) and by the detailed-balance consistency.

Concerning the dependence on the filament overlap, we assume that the only transition affected by filament overlap is $\mathcal{N} \to \mathcal{P}$, that is prevented in the central zone of the sarcomere, where the two AFs meet (see Sec. 1.3.2). Specifically, we set, for $\eta \in \{\mathcal{U},\mathcal{B}\}$ and for $\alpha,\delta \in \{\mathcal{N},\mathcal{P}\}$:

$$k_{T,i}^{\mathcal{NP}|\alpha\,\cdot\,\delta,\eta} = \chi_{SF}(SL,i)\,k_T^{\mathcal{NP}|\alpha\,\cdot\,\delta,\eta}. \tag{4.48}$$

The resulting 4-states CTMC associated with each RU is represented in Fig. 4.2.

4.3.2 Calibration of the XBs rates

Even if the thin-filament activation comes before the XB cycling from a logical viewpoint, we start to illustrate the calibration procedure for the latter part. The reason will be clarified later.

Concerning the transition rates associated with the XB dynamics, in this thesis we work under the hypothesis that the total attachment-detachment rate is independent of the XB elongation since this assumption allows to reduce the number of free parameters without depriving the model of the capability of reproducing a wide range of experimental characterizations. In this case, the models SE-ODE and MF-ODE can be used in place of the more computationally expansive counterparts SE-PDE and MF-PDE, which involve the solution of a PDE system. Moreover, we also make the reasonable assumption that the sliding velocity only affects the detachment rate (see Sec. 3.2).

As we mentioned before, XB attachment is only possible when the corresponding Tm is in the state $\mathcal{P}$ (thus $f_{\mathcal{N}} \equiv 0$). Moreover, it is well motivated that out of the single-overlap zone, the detachment rates are not affected by the state of Tm (i.e. $\tilde{g}_{\mathcal{N}} \equiv \tilde{g}_{\mathcal{P}}$) and that the detachment rate when Tm is in state $\mathcal{N}$ is not affected by the filament overlap (i.e. $\tilde{g}_{\mathcal{N}} \equiv g_{\mathcal{N}}$). In summary, if we assume that the total transition rate in the single-overlap zone does not depend on the Tm state, we have:

$$f_{\mathcal{P}}(x,v) + g_{\mathcal{P}}(x,v) = g_{\mathcal{N}}(x,v) = \tilde{g}_{\mathcal{N}}(x,v) = \tilde{g}_{\mathcal{P}}(x,v) = r_0 + q(v),$$

for some constant r_0 and function q, such that $q(0) = 0$. Therefore, Eq. (4.29) reduces to:

$$\begin{cases} \dfrac{d}{dt}\mu^0_{i,\mathcal{P}} = -\left(r_0 + q(v) + \widetilde{k}^{\mathcal{P}\mathcal{N}}_{T,i}\right)\mu^0_{i,\mathcal{P}} + \widetilde{k}^{\mathcal{N}\mathcal{P}}_{T,i}\,\mu^0_{i,\mathcal{N}} + P_i\,\mu^0_{f_{\mathcal{P}}} & t \geq 0,\ i \in \mathcal{I}_A, \\ \dfrac{d}{dt}\mu^0_{i,\mathcal{N}} = -\left(r_0 + q(v) + \widetilde{k}^{\mathcal{N}\mathcal{P}}_{T,i}\right)\mu^0_{i,\mathcal{N}} + \widetilde{k}^{\mathcal{P}\mathcal{N}}_{T,i}\,\mu^0_{i,\mathcal{P}} & t \geq 0,\ i \in \mathcal{I}_A, \\ \dfrac{d}{dt}\mu^1_{i,\mathcal{P}} + v\,\mu^0_{i,\mathcal{P}} = -\left(r_0 + q(v) + \widetilde{k}^{\mathcal{P}\mathcal{N}}_{T,i}\right)\mu^1_{i,\mathcal{P}} + \widetilde{k}^{\mathcal{N}\mathcal{P}}_{T,i}\,\mu^1_{i,\mathcal{N}} + P_i\,\mu^1_{f_{\mathcal{P}}} & t \geq 0,\ i \in \mathcal{I}_A, \\ \dfrac{d}{dt}\mu^1_{i,\mathcal{N}} + v\,\mu^0_{i,\mathcal{N}} = -\left(r_0 + q(v) + \widetilde{k}^{\mathcal{N}\mathcal{P}}_{T,i}\right)\mu^1_{i,\mathcal{N}} + \widetilde{k}^{\mathcal{P}\mathcal{N}}_{T,i}\,\mu^1_{i,\mathcal{P}} & t \geq 0,\ i \in \mathcal{I}_A, \end{cases} \tag{4.49}$$

and similarly for Eq. (4.43), where we only drop the index i from Eq. (4.49). Hence, the objects to calibrate are $\mu^0_{f_{\mathcal{P}}}$, $\mu^1_{f_{\mathcal{P}}}$, r_0, $q(v)$ and a_{XB}, to link the microscopic force with the macroscopic active tension.

We have shown in Sec. 3.2.4 that by acting on the four mentioned parameters plus the parameter α, that determines the slope of q for small velocities, the generalized H57 model (3.20) can fit experimentally measured data concerning the isometric solution ($T_{\mathrm{a}}^{\mathrm{iso}}$ and μ^0_{iso}), the force-velocity relationship ($v^{\max}$ and v^0) and the fast transients response ($\tilde{k}_2$). All the above mentioned experimental setups are such that the thin filament activation machinery can be considered in steady-state. Indeed, $[\mathrm{Ca}^{2+}]_{\mathrm{i}}$ is constant in all the cases and, concerning SL: it is also constant under isometric conditions; constant shortening experiments are typically performed in the plateau region of the force-length relationship, and thus the effect of changes in SL is irrelevant; fast transient experiments are carried out at a time-scale such that the activation variables can be considered constant, since they are characterized by a much slower dynamics (see Sec. 1.2). Therefore, in these cases, the values of P_i, $\widetilde{k}^{\mathcal{P}\mathcal{N}}_{T,i}$ and $\widetilde{k}^{\mathcal{N}\mathcal{P}}_{T,i}$ can be considered as fixed in Eq. (4.29) (and similarly in Eq. (4.29)). This observation is crucial since it allows to decouple the calibration of the parameters involved in the thin

Parameter	Value	Units	Reference
$T_{\mathrm{a}}^{\mathrm{iso}}$	120	kPa	[TKHK00]
μ_{iso}^{0}	0.22	-	[Bru+14]
$v^{\max}$	8	s^{-1}	[Car+16]
v^{0}	2	s^{-1}	[Car+16]
$\tilde{k}_2$	66	-	[Car+16]

Table 4.3: List of the experimental data used for model calibration.

filament activation from the calibration of the parameters involved in XBs cycling. In fact, the five parameters of the XBs cycling model can be calibrated from the five above mentioned experimental values.

We notice that, while for the generalized H57 model of Sec. 3.2 the relationship between the five parameters and the five experimentally measured values can be inverted analytically (see Eqs. (3.34)-(3.35)), in this case we find the values of the parameters with a numerical strategy. Specifically, to find the steady-state solution we solve Eq. (4.29) by setting to zero the time derivative terms; we find the solution after the fast transient by solving exactly the linear ODE system (4.29); we approximate the derivative appearing in the definition of v^0 and $\tilde{k}_2$ by finite differences. Finally, we solve, for the five parameters, the nonlinear system of equations linking the five measured values with the parameters themselves. With this aim we employ the Newton-Raphson method, by approximating the Jacobian matrix by means of finite differences.

Therefore, once the thin filament activation model (4.11) (or (4.36)) has been calibrated, we have at our disposal an automatic procedure to calibrate the remaining model parameters. For this reason, we first setup such calibration procedure for the model parameters associated with the XBs cycling (i.e. Eq. (4.29) or (4.43)) and, successively, we calibrate the model parameters associated with the RUs activation (i.e. Eq. (4.11) or (4.36)), so that we can directly see the effect of changes of such parameters on the resulting force since the remaining parameters are automatically adjusted.

The experimental data used to calibrate the model are reported in Table 4.3, together with a reference to the source in literature. As we mentioned at the beginning of Sec. 4.3, we consider data coming from intact cardiac rat cell at room temperature. The unique datum not satisfying these condition is μ_{iso}^{0} (which is acquired from skeletal frog muscle). However, as we mentioned in Sec. 3.2.4, the value of such parameter only affects the value of the microscopic variables (i.e. $\mu_{i,\alpha}^{p}$), but not the macroscopic ones (i.e. T_{a} and K_{a}). We notice that the constants $v^{\max}$, v^0 and $\tilde{k}_2$ are normalized with respect to $T_{\mathrm{a}}^{\mathrm{iso}}$ and are thus valid for a wide range of activation levels (see Sec. 1.3). Conversely, the value of $T_{\mathrm{a}}^{\mathrm{iso}}$ is associated with a SL in the plateau region and to saturating calcium concentration. Therefore, when we calibrate the parameters we set $[\mathrm{Ca}^{2+}]_{\mathrm{i}} = 10\,\mu\mathrm{M}$ and $SL = 2.2\,\mu\mathrm{m}$.

4.3.3 Calibration of the RUs rates

The steady-state solution of the activation models (4.11) and (4.36) only depends on the ratio between the pairs of opposite transition rates (e.g. $k_T^{\mathcal{NP}|\alpha\cdot\delta,\mathcal{B}}/k_T^{\mathcal{PN}|\alpha\cdot\delta,\mathcal{B}} = Q\,\gamma^{2n(\alpha,\delta)-2}$). Therefore, the 6 parameters can be split into two groups: the first group (Q, μ, k_{d} and γ) determines the steady-state solution, while the second group (k_{off},

k_{basic}) only affects the kinetics of the model (that is to say how fast the transients are). This allows to calibrate first the parameters of the first group, and, only successively, those of the second group.

Calibration at the steady-state

The steady-state characterization of the muscle tissue activation is represented by the force-calcium and force-length relationships (see Sec. 1.3.2), whose main features are the behavior for SL in the plateau region (characterized by the tension for saturating calcium $T_{\text{a}}^{\text{iso}}$, the calcium sensitivity EC_{50} and the cooperativity degree n_H) and the effect of SL (on the saturating tension $T_{\text{a}}^{\text{iso}}$ and on the calcium sensitivity EC_{50}).

The tension for saturating calcium concentrations $T_{\text{a}}^{\text{iso}}$ in the plateau region of SL is automatically fitted, thanks to Sec. 4.3.2. The effect of k_{d} is that of shifting the force-calcium curves with respect to the $\log [\text{Ca}^{2+}]_{\text{i}}$ axes, since it only appears in combination with $[\text{Ca}^{2+}]_{\text{i}}$ in the model equations. Therefore, the value of k_{d} can be easily calibrated to match the experimental data since it only affects EC_{50}. The effect of γ, on the other hand, is that of tuning the amount of cooperativity and in fact it acts on n_H. The role of the remaining parameters (Q and μ) is more involved and cannot be easily decoupled, as they affect the cooperativity, calcium sensitivity, and the asymmetry of the force-calcium relationship below and above EC_{50} (see Sec. 1.3.2 and [Ric+03]). Moreover, in the SE-ODE case, they also act on the SL regulation on calcium sensitivity.

In the following we set $\mu = 10$, coherently with the fact that the experimentally measured dissociation rate of Tn from calcium varies of about one order of magnitude in different combinations [NHS06]. For the SE-ODE model, we set $\gamma = 20$, $Q = 3$ and $k_{\text{d}} = 1.347$, to fit the steady-state force-calcium measurements of [TKHK00] (referred to the two different values of SL of 1.85 and 2.15 µm) from intact rat cardiac cells at room temperature. The resulting steady-state curves are reported in Fig. 4.3. We are able to well fit the main features of the curves, including the characteristic S-shape, the plateau forces at both SL, the significant cooperativity typical of the cardiac tissue and the SL-induced change in calcium sensitivity (LDA, see Sec. 1.3.2).

We remark that we are here able to reproduce the LDA without any phenomenological SL-dependent tuning of the parameter, as done, e.g. in [NHS06; Was+12; Was+13; Was+15]. Conversely, the LDA emerges from this model in a spontaneous way. We will examine in Sec. 4.4.3 how this model is capable of reproducing this phenomenon, providing thus a possible microscopical explanation for the LDA.

Conversely, with the MF-ODE model it is not possible to reproduce the LDA by simply acting on the model parameters. Indeed, the only effect of SL in the model is to multiplicatively tune the generated force by the factor $\chi_{\text{so}}(SL(t))$. Therefore, no SL induced effect on the calcium sensitivity can be achieved. The mechanism reproducing LDA in the SE-ODE model is indeed intrinsically linked, as we will see in Sec. 4.4.3, to the explicit spatial representation of the myofilaments. Therefore, in the mean-field model MF-ODE, without an explicit spatial representation, we phenomenologically tune the calcium sensitivity k_{d} in function of SL, by setting

$$k_{\text{d}}(t) = \overline{k}_{\text{d}} + \alpha_{k_{\text{d}}}(SL(t) - SL_{k_{\text{d}}}), \tag{4.50}$$

where $SL_{k_{\text{d}}} = 2.15\,\mu\text{m}$. In Fig. 4.3, where we have set $\gamma = 12$, $Q = 2$, $\overline{k}_{\text{d}} = 0.775$ and $\alpha_{k_{\text{d}}} = -1.667$, we show that, with this modification, we can fit the experimental data also with the MF-ODE model.

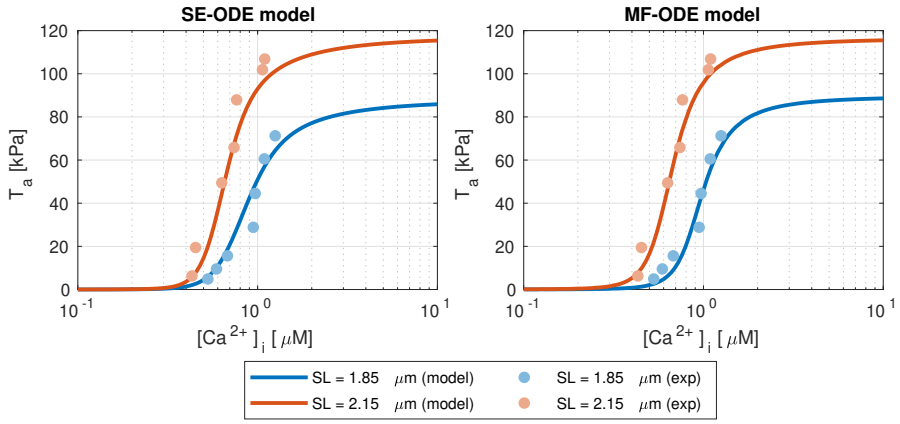

Figure 4.3: Steady-state force-calcium curves obtained with the SE-ODE (left) and MF-ODE (right) models with the optimal parameters values reported in Tab. 4.6 for $SL = 1.85\,\mu\text{m}$ and $SL = 2.15\,\mu\text{m}$, compared to experimental data from intact rat cardiac cells at room temperature, from [TKHK00].

Calibration in dynamic conditions (kinetics)

To complete the calibration of the SE-ODE and MF-ODE models, we only need to set the parameters k_{basic} and k_{off}, ruling the rapidity at which the transitions $\mathcal{N} \rightleftharpoons \mathcal{P}$ and $\mathcal{U} \rightleftharpoons \mathcal{B}$ take place, respectively. Despite the fact that, at this stage, only two parameters need to be addressed, their calibration reveals some difficulties, mainly related to two aspects. First, the interplay between the two parameters is tight and their roles cannot be easily decoupled (moreover, it is still under debate which is the rate limiting stage in the activation and relaxation dynamics, see Sec. 1.3.3). This results is a poor identifiability of the parameters: different combinations of parameters give similar results in terms of force transients. This issue has been reported also by [Tøn+15], while calibrating the models of [Lan+12] and [NHS06]. Additionally, the force transients predicted by the model are very sensitive to the calcium transient given in input (this is a typical feature of activation models, see e.g. [Tøn+15]). Therefore, since the experimentally measured calcium transients are much affected by noise (see e.g. [Bac+95; JT97; Tøn+15], a calibration based on the best fit of the model response to experimentally measure calcium transients should be performed with care.

Based on the former remarks, we calibrate the parameters k_{basic} and k_{off} by the following procedure. We consider the isometric twitches of intact rat cardiac muscle fibers reported in [JH95] for different values of SL, and with $[\text{Ca}^{2+}]_{\text{o}} = 1.0\,\text{mM}$. Since the corresponding calcium transients are not reported, we consider the calcium transient reported by the same author in [JT97], for the same muscle preparation. As the reported trace is much affected by noise, we fit it with the idealized transient of Eq. (2.23), obtaining $c_{\max} = 1.35\,\mu\text{M}$, $t_0^c = 0.05\,\text{s}$, $\tau_1^c = 0.02\,\text{s}$, $\tau_2^c = 0.19\,\text{s}$.

Then we sample the candidate parameters space, that we set to $(k_{\text{basic}}, k_{\text{off}}) \in [0, 80\,\text{s}^{-1}] \times [0, 300\,\text{s}^{-1}]$, by a MC strategy, for each parameters value we compute the tension transients corresponding to $SL = 1.90$, 2.05 and $2.20\,\mu\text{m}$ and we compare them with the experimental measurements from [JH95]. We consider the following discrepancy metrics, where $T_{\text{a}}^{i,\text{mod}}(t)$ denotes the tension predicted by the model for

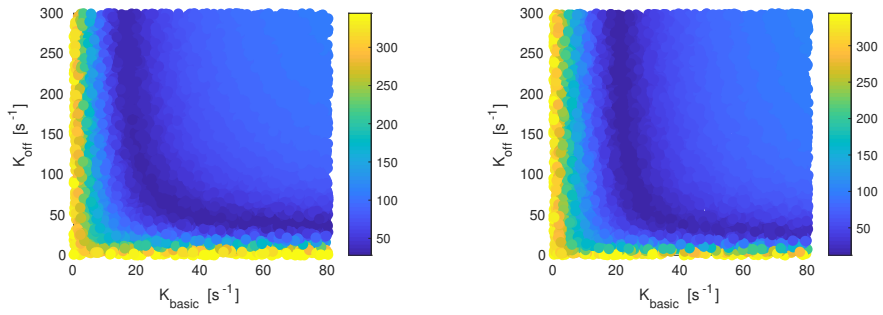

(a) SE-ODE model (b) MF-ODE model

Figure 4.4: Discrepancy metric E_{tot} in the parameters space $(k_{\text{basic}}, k_{\text{off}})$ for intact room-temperature rat cells, obtained with the SE-ODE model (a) and with the MF-ODE model (b).

the i-th value of SL and $T_{\text{a}}^{i,\text{exp}}(t)$ denotes the measured one:

$$E_{L^2} := \sqrt{\sum_{i=1}^{3} \int_0^T \left| T_{\text{a}}^{i,\text{mod}}(t) - T_{\text{a}}^{i,\text{exp}}(t) \right|^2 dt},$$

$$E_{\text{peak}} := \sqrt{\sum_{i=1}^{3} \left| \sup_{t\in[0,T]} T_{\text{a}}^{i,\text{mod}}(t) - \sup_{t\in[0,T]} T_{\text{a}}^{i,\text{exp}}(t) \right|^2}.$$

The first metric coincides with the L^2 error over time, while the second one evaluates the error of the predicted force peak. We notice indeed that the parameters k_{basic} and k_{off} also determine the force peak attained during a sarcomere twitch: the most rapid the tissue activation is, the more the force-calcium curve stays close to the steady-state curve (see Sec. 1.3.3) and thus reaches higher force values before the relaxation begins. As criterion to select the best parameters values, we consider as overall metric a weighted combination between the two, given by $E_{\text{tot}} = (E_{L^2}^2 + w_{\text{peak}}^2 E_{\text{peak}}^2)^{1/2}$, where we set $w_{\text{peak}} = 5$.

The obtained values of the discrepancy metric E_{tot} in the parameters space for both the SE-ODE and the MF-ODE models are reported in Fig. 4.4. We notice that the level curves do not clearly identify an optimal pair $(k_{\text{basic}}, k_{\text{off}})$, but, conversely, these exhibit a wide region in the parameters space producing very similar results. Given the uncertainty in the measurements of both force and, mostly, calcium, it makes few sense to select the best parameters by blindly selecting the pair that realizes the smaller discrepancy from experimental results. Therefore, we supplement the results of Fig. 4.4 with direct measurements of calcium binding rates to TnC, showing that $k_{\text{on}} = k_{\text{off}}/k_{\text{d}}$ lies between 50 and 200 $\mu\text{M}^{-1}\,\text{s}^{-1}$ [NHS06]. On this basis, we restrict the region of candidate values and we select the parameters reported in Tab. 4.6.

The predicted isometric twitches obtained with the selected values of the parameters are compared with the experimental data in Fig. 4.5. We notice here that the MF-ODE model accomplishes a better fit of experimental data than the SE-ODE model. This is an effect of the phenomenological tuning of k_{d} of Eq. (4.50), that allows for a significant increase of calcium sensitivity and, consequently, of twitch duration, for higher values of SL. Nonetheless, also the SE-ODE model predicts, even if

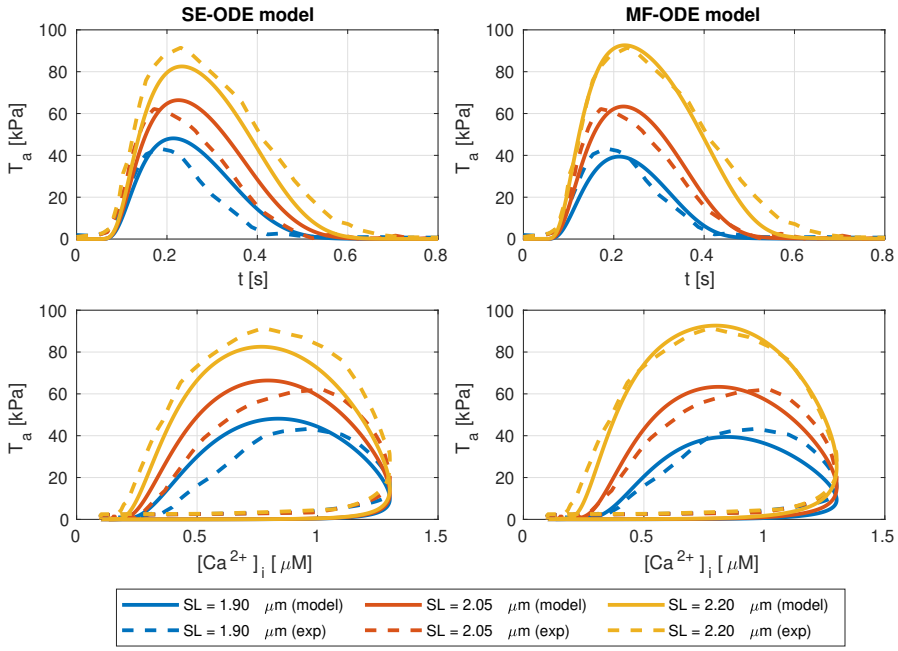

Figure 4.5: Force transients (top line) and phase-loops (bottom line) in isometric twitches, for different values of SL, predicted by the SE-ODE model (left column) and MF-ODE model (right column), in comparison with the experimental measurements from intact rat cardiac cells taken from [JH95].

to a fewer extent, the experimentally observed prolongation of twitches at higher SL, without any phenomenological tuning of the calcium sensitivity.

We notice that there is room for improvement in the calibration of the kinetic parameters k_{basic} and k_{off}, which could be better constrained in presence of more abundant and more reliable experimental data and when a deeper understanding on the determinants of the kinetics of activation and relaxation will be available. Nevertheless, a bad calibration of k_{basic} and k_{off} for the rat model does not affect the quality of the human model, since those two parameters are the only ones to be completely re-calibrated for the human model.

The full list of the parameters, including those associated with the XB cycling, calibrated by the procedure presented in Sec. 4.3.2, is provided in Tab. 4.6.

4.3.4 Human model at body temperature

Due to the lack of a sufficiently large set of measurements from human cells at body temperature [Lan+17] to constrain all the model parameters, as we anticipated at the beginning of Sec. 4.3, to calibrate the SE-ODE and MF-ODE models for body-temperature human cardiomyocytes we start from the corresponding sets of parameters for room-temperature rat cells and we adapt those parameters that are reasonably affected by the change in species and temperature. Specifically, different species mainly differ in their calcium-sensitivity (i.e. k_{d}) and in the kinetics (different species feature highly different heart rates), while temperature mainly affects the kinetics.

By exploiting the decoupling of the parameters of the RUs model ruling the steady-

Species	Temperature	Preparation	SL(µm)	EC_{50}(µM)	Reference
Rat	Room	Skinned	2.15	3.51	[DKT02]
Rat	Room	Intact	2.15	0.68	[TKHK00]
Human	Body	Skinned	2.00	1.72	[Lan+17]
Human	Body	Skinned	2.20	1.56	[Lan+17]

Table 4.4: List of the experimental values used to calibrate the calcium sensitivity for the human models at body temperature.

Parameter	Lower bound	Upper bound	Units
$T_{\mathrm{a}}^{\mathrm{peak}}$	40	45	kPa
TTP	147	172	s
RT_{50}	109	125	s
RT_{95}	291	377	s

Table 4.5: Output metrics used to calibrate the kinetics of the body-temperature human models. Data are taken from [Tøn+15]. The range of values of $T_{\mathrm{a}}^{\mathrm{peak}}$ has been reduced with the aim of more strongly forcing the models to match the desired output.

state relationships from those ruling the kinetics (see Sec. 4.3.3), we first focus on the steady-state, and we adjust k_{d} to reflect the higher calcium sensitivity of human cells compared to rat [NHS06; Tøn+15; Lan+17]. For this purpose, we employ the data reported in [Lan+17], which, however, refer to skinned cells. In order to estimate the effect of skinning on k_{d}, we compare the calcium sensitivity measured for room-temperature rat cardiac cells in skinned [DKT02] and intact preparations [TKHK00] at $SL = 2.15\,\mu\mathrm{m}$ and we assume that the same relationship holds for skinned versus intact body-temperature human cells. Finally, we rescale the values of k_{d} to reflect the estimated change in calcium sensitivity between intact body-temperature human cells and intact room-temperature rat cells, obtaining the values reported in Tab. 4.6. The experimental data used in such procedure are listed in Tab. 4.4.

Since the RUs kinetics may depend on both the species and the temperature, we re-calibrate the parameters k_{off} and k_{basic} on the base of the output metrics reported in Tab. 4.5 (taken from [Tøn+15]), referred to body-temperature human cells. The output metric comprise the peak tension $T_{\mathrm{a}}^{\mathrm{peak}}$, the time-to-peak TTP (defined as the time separating the beginning of the stimulus and the tension peak) and the relaxation times RT_{50} and RT_{95} (defined as the time needed to accomplish 50% and 95% of relaxation, respectively). Since, at the best of our knowledge, detailed calcium transients measurements for intact human cells at body temperature are not available, we employ the synthetic calcium transient predicted by the ten Tusscher-Panfilov 2006 ionic model [TTP06a], that we denote as the TTP06 model. In Fig. 4.6 we show the landscape, in the parameters space $(k_{\mathrm{basic}}, k_{\mathrm{off}})$ of the overall distance of the output metrics from the ranges reported in Tab. 4.5. Similarly as for the rat models, large parameters regions feature similar values. Therefore, we proceed as for the calibration of rat cells, by reducing the parameters space based on direct experimental measurements (see Sec. 4.3.3). In this case, we manage to select a unique couple of values suitable for both the SE-ODE and the MF-ODE model (see Tab. 4.6).

Finally, for the calibration of the parameters ruling the XBs cycling, we use the same values of Tab. 4.3. Therefore, since the calibration depends on the parameters

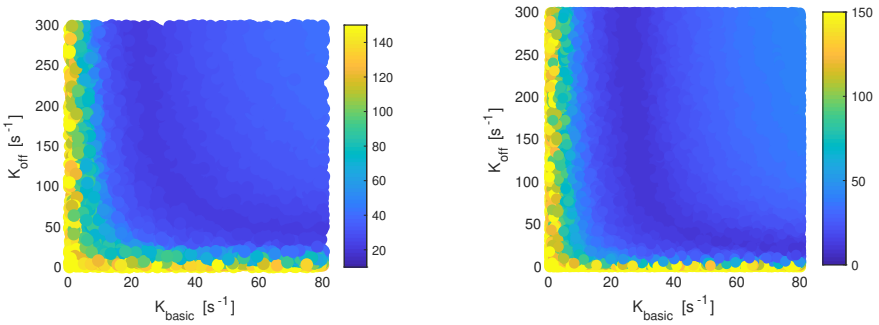

(a) SE-ODE model (b) MF-ODE model

Figure 4.6: Overall distance, in the parameters space, of the output metrics from the target values ranges indicated in Tab. 4.5 for intact body-temperature human cells, obtained with the SE-ODE model (left) and with the MF-ODE model (right).

previously set for the RUs activation, the resulting values of the parameters are slightly different. We provide in Tab. 4.6 the full list of parameters for both species (room-temperature rat and body-temperature human) and for both models (SE-ODE and MF-ODE).

4.4 Numerical results

In this section, we show the results of numerical simulations obtained with the models presented in Sec. 4.2.7. First, in Sec. 4.4.1 we present the numerical schemes used to approximate the solution of such models. Then, in Sec. 4.4.2 we make a comparison between the results obtained with the models based on a discrete representation of BSs (i.e. the SE-disc-I and the SE-disc-II models) and the remaining models, based on a continuous description of BSs. Finally, we consider different experimental settings and we test the capabilities of the proposed models to reproduce the main experimental characterization that we have listed in Sec. 1.3.

4.4.1 Numerical approximation

Since the equations describing the evolution of the RUs are independent of the variables describing the XB states, their solution can be approximated by adopting the same numerical schemes considered in Sec. 2.2.4. Specifically, we adopt a Forward Euler scheme with a time step size of $2.5 \cdot 10^{-5}$ s.

Concerning the equations describing the XB dynamics, we notice that Eqs. (4.19), (4.29) and (4.43) can be written in the following form:

$$\begin{cases} \dot{\mathbf{x}}(t) = \mathbf{A}(t)\mathbf{x}(t) + \mathbf{r}(t) & t \in (0, T], \\ \mathbf{x}(0) = \mathbf{x}_0, \end{cases} \tag{4.51}$$

where $\mathbf{x}(t)$ is the vector of the variables describing the states of XBs, while $\mathbf{A}(t)$ and $\mathbf{r}(t)$ are respectively a time-dependent matrix and vector, determined by the input $v(t)$ and by the RUs states $\pi_i^{\alpha\beta\delta,\vartheta\eta\lambda}(t)$ (or, for mean-field models, $\pi^{\alpha\beta\delta,\eta}(t)$).

In order to approximate the solution of Eq. (4.51), we consider a subdivision $0 = t_0 < t_1 < \cdots < t_M = T$ of the time interval $[0, T]$ with time step size Δt and we

Parameter	Units	SE-ODE Rat, room temp.	SE-ODE Human, body temp.	MF-ODE Rat, room temp.	MF-ODE Human, body temp.
RU steady-state					
μ	-	10	10	10	10
γ	-	20	20	12	12
Q	-	3	3	2	2
$\overline{k}_{\mathrm{d}}$	µM	1.347	0.615	0.775	0.35
$\alpha_{k_{\mathrm{d}}}$	$\mu\mathrm{M}\,\mu\mathrm{m}^{-1}$	0	0	−1.667	−0.542
RU kinetics					
k_{off}	s^{-1}	110	121	135	121
k_{basic}	s^{-1}	20.7	28.8	22.5	28.8
XB cycling					
$\mu^0_{f_{\mathcal{P}}}$	s^{-1}	58.421	58.192	33.161	33.082
$\mu^1_{f_{\mathcal{P}}}$	s^{-1}	1.390	1.384	0.789	0.788
r_0	s^{-1}	133.958	134.075	134.182	134.230
α	-	25.113	25.129	25.149	25.160
Micro-macro upscaling					
a_{XB}	MPa	22.941	22.931	22.919	22.913

Table 4.6: Parameters of the SE-ODE and MF-ODE models calibrated for room-temperature rat and body-temperature human cells.

denote by $\mathbf{x}^{(k)} \approx \mathbf{x}(t_k)$ the approximated solution at time t_k. Due to the linearity of Eq. (4.51), we consider the following exponential scheme [HO10]:

$$\begin{cases} \mathbf{x}^{(0)} = \mathbf{x}_0, & \\ \mathbf{x}^{(k)}_{\infty} = -\mathbf{A}^{-1}(t_k)\mathbf{r}(t_k) & \text{for } k \geq 1, \\ \mathbf{x}^{(k)} = \mathbf{x}^{(k)}_{\infty} + e^{\Delta t \mathbf{A}(t_k)}(\mathbf{x}^{(k-1)} - \mathbf{x}^{(k)}_{\infty}) & \text{for } k \geq 1. \end{cases} \tag{4.52}$$

Due to the implicit nature of the scheme of Eq. (4.52), that entails better stability properties than the explicit scheme used for the RUs equations [QSS10], we solve it with a larger time step size than the one used for the RUs model ($\Delta t = 1 \cdot 10^{-3}\,\mathrm{s}$).

4.4.2 Discrete vs. continuous representation of binding sites

While the SE-disc-I and the SE-disc-II models are derived under the assumption that all the sarcomere are identical, the other models presented in Sec. 4.2 allow for some variability in the inner alignment of proteins in the sarcomeres, by assuming that the value of the offset d_0 in Eq. (4.1) is a random variable, rather than a constant. To investigate the implications of the assumption made by the discrete models (SE-disc-I and SE-disc-II), we perform the following test. We simulate an isometric twitch by applying the calcium transient of Eq. (2.23), with $c_{\max} = 0.9\,\mu\mathrm{M}$ and with $SL = 2.2\,\mu\mathrm{m}$. Then, we repeat the simulation after having incremented by a small amount D_d the offset d_0. The results, shown in Fig. 4.7, where the same twitch is simulated multiple times with different values of D_d, reveal that the solution of the discrete models is highly sensitive on the value of the offset d_0.

In Fig. 4.7a the tension transients obtained with the SE-disc-II model 8with different values of D_d) are compared with the one predicted by the SE-ODE model. The

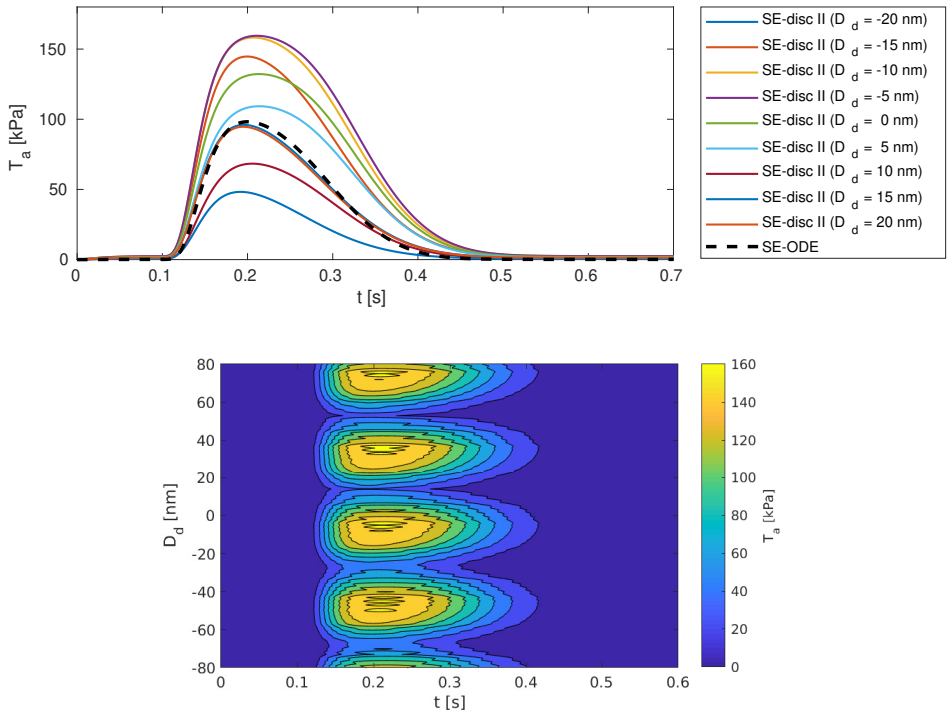

Figure 4.7: Isometric twitches simulated with the SE-disc-II model for different values of D_d. In (a), the force transients obtained with the SE-disc-II model are compared with the force transient predicted by the SE-ODE model. In (b), the force transients are represented in function of time and of D_d. The results are reproduced almost periodically in D_d, with a period similar to D_A. Both models are calibrated for intact body-temperature human cells.

latter assumes that the value of d_0 is a uniformly distributed random variable. Hence, continuous models can be considered as the average of the discrete models for the different possible values of d_0.

Therefore, in the following, we will only consider the continuous models, as the discrete ones are not able to account for the heterogeneities featured by the sarcomeres and produce results that are too sensitive on the value of the sarcomere elongation. In particular, we focus on the SE-ODE and MF-ODE models, that feature the best trade-off between model complexity, computational efficiency and availability of experimental data needed to constraint the model parameters.

4.4.3 Steady-state results

First, we consider steady-state solutions. To numerically obtain the steady-state curves, we fix a level of $[Ca^{2+}]_i$ and SL and we let the model reach the equilibrium solution.

Force-calcium relationship

We show in Figs. 4.8 and 4.9 the force-calcium curves predicted by the SE-ODE and MF-ODE models for rat and human cells, respectively. In all the cases, the

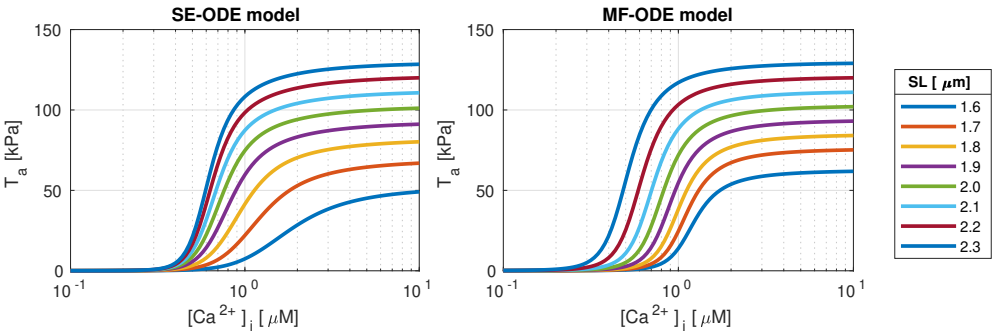

Figure 4.8: Steady-state force-calcium relationship at different SL obtained with the SE-ODE (left) and the MF-ODE (right) models for intact room-temperature rat cardiomyocytes.

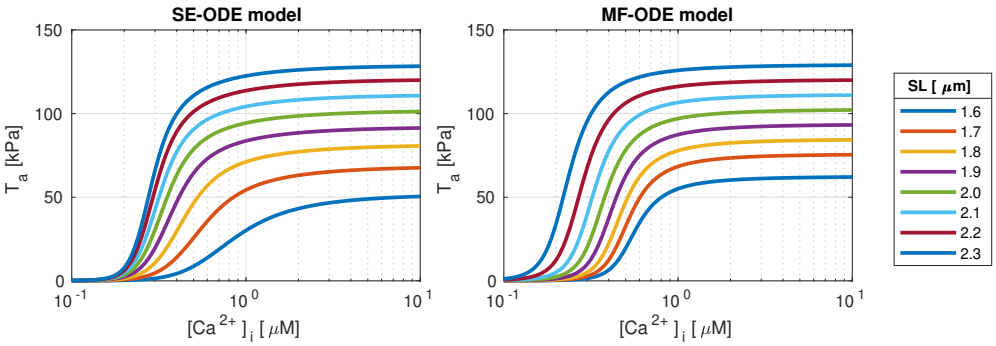

Figure 4.9: Steady-state force-calcium relationship at different SL obtained with the SE-ODE (left) and the MF-ODE (right) models for intact body-temperature human cardiomyocytes.

curves reproduce the main experimentally observed features reported in Sec. 1.3.2. Figure 4.10 shows the dependence of the Hill coefficient n_H and of the half-activating calcium concentration EC_{50} on the sarcomere length SL. We notice that, while the MF-ODE model produces an Hill coefficient that is independent of SL (the reason is that the role of SL on activation is just that of shifting and rescaling the curves, thus leaving n_H unaffected), the SE-ODE model predicts a small increase of n_H with SL. Both the results are equally acceptable since there is no common agreement on whether the Hill coefficient depend on SL or not (see Sec. 1.3.2). Both the models correctly predict for both the species an increase of EC_{50} as SL decreases. The relationship is approximately linear in the typical working range of SL (as experimentally observed, e.g., in [DKT02]), while, for small values of SL, the SE-ODE model produces a faster decrease of sensitivity.

Force-length relationship

Figures 4.11 and 4.12 show the ascending limb of the steady-state force-length relationships. For both the SE-ODE and MF-ODE models we observe a change of slope for saturating calcium concentration around 1.65 µm, coherently with the experimental observations (see Sec. 1.3.2). Moreover, both models predict the change of convexity

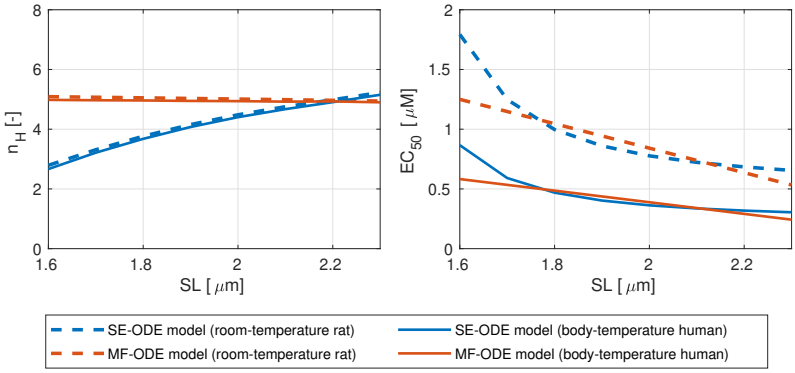

Figure 4.10: Dependence of the Hill coefficient n_H and of the half-activating calcium concentration EC_{50} on the sarcomere length SL, for the SE-ODE (blue lines) and MF-ODE (red lines) model, calibrated for intact room-temperature rat cardiomyocytes (dashed lines) and for intact body-temperature human cardiomyocytes (solid lines).

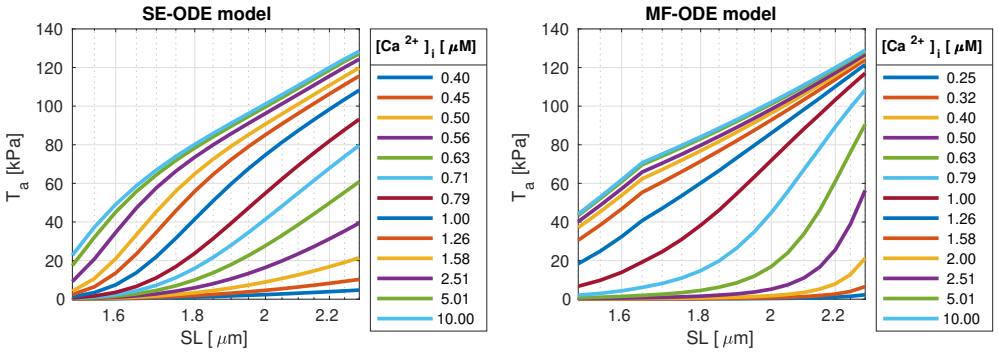

Figure 4.11: Steady-state force-length relationship at different $[\mathrm{Ca}^{2+}]_\mathrm{i}$ obtained with the SE-ODE (left) and the MF-ODE (right) models for intact room-temperature rat cardiomyocytes.

of the force-length curves at different calcium levels.

A possible explanation for LDA

The phenomenon of LDA, by which the calcium sensitivity increases with SL (at least in the working regime of sarcomeres), is one of the main regulatory mechanisms of the cardiac contractile system, being responsible, at the microscopic level, of the Frank-Starling effect (see Sec. 1.3.2). However, a commonly agreed explanation for this phenomenon still lacks to be reached by the scientific community (see e.g. [TK16; NCC19]). Remarkably, the numerical results obtained with the SE-ODE model reproduce the phenomenon LDA, without any phenomenological SL-dependent tuning of the calcium sensitivity, as it is typically done in activation models (see e.g. [NHS06; Was+12; Was+13; Was+15] or even the MF-ODE model). Therefore, the model setup presented in Sec. 4.2.1 must contain the fundamental ingredients that form the basis for the LDA phenomenon, or, at least one of its possible explanations.

The LDA is mirrored in both the steady-state force-calcium curves (as a leftward shift of the curves when SL increases) and in the steady-state force-length curves (as

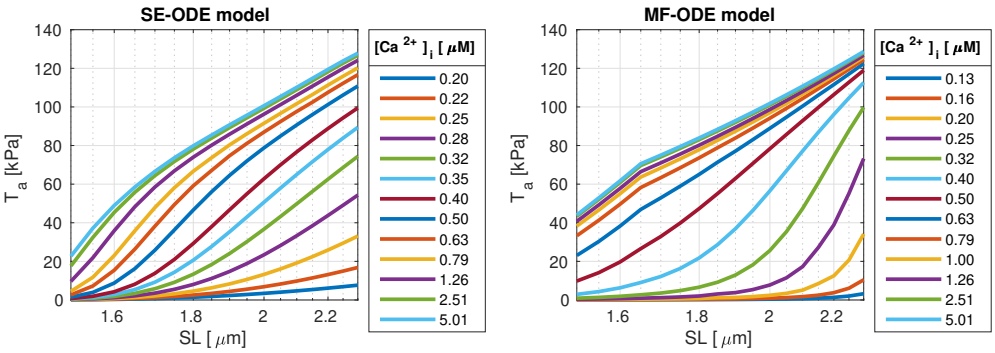

Figure 4.12: Steady-state force-length relationship at different $[Ca^{2+}]_i$ obtained with the SE-ODE (left) and the MF-ODE (right) models for intact body-temperature human cardiomyocytes.

a convex shape of the curves near EC_{50}). The two effects are two sides of the same coin. In the following we show the basis by which the SE-ODE model reproduces the LDA by resorting to its interpretation from the force-length curves.

The mechanism by which the SE-ODE model reproduces the LDA is based on the edge-effect, due to the fact that RUs located at the borders of the single-overlap zone are biased towards the non-permissive states by the cooperative nearest-neighboring interactions. This is due, on one side, by the fact that the RUs located at the borders of the filaments behave as the missing neighbor is in $\mathcal{N}$ state; on the other side, by the fact that the transition $\mathcal{N} \rightarrow \mathcal{P}$ is prevented in the double-overlap region (see Eq. (4.48)). Hence, by means of the nearest-neighbor interactions, the edge-effect is propagated towards the center of the single-overlap zone, as we can see by Fig. 4.13a, that shows the typical profile of the permissivity P_i along the filament. The highest the calcium concentration, the more the C_i variables are biased towards the $\mathcal{B}$ state and, consequently, the corresponding T_i are biased towards the $\mathcal{P}$ state, softening the influence of the low-permissive borders. Therefore, for large values of $[Ca^{2+}]_i$, the curve connecting the two ends of the single-overlap zone features large gradients and thus a large overall permissivity P (given by the average of the permissivities P_i) is reached and, consequently, a large tension T_a (see Fig. 4.13a).

Interestingly, the curvature of the permissivity profile is determined by $[Ca^{2+}]_i$ (by the competition between nearest-neighbor interactions and the calcium-driven activation presented above) and it is virtually independent of SL, as we show in Fig. 4.13b. Indeed, if we translate the permissivity profiles obtained with the same $[Ca^{2+}]_i$ for different SL so that the maximum points coincide (see Fig. 4.13b), the curves virtually overlay. This observation has two important consequences in the relationship between SL and P, for fixed $[Ca^{2+}]_i$: first, when SL increases, P (which is proportional to the area below the permissivity profile) increases as well, since the two end points of the single-overlap zone can be connected by a longer section of the curve; moreover, the larger SL is, the faster P increases with SL is (see Fig. 4.14). In other terms, P is an increasing and convex function of SL and this explains the LDA phenomenon.

Moreover, also the experimentally observed change of convexity for large calcium levels (see Sec. 1.3.2) can be explained by similar arguments. Indeed, if $[Ca^{2+}]_i$ and SL are large enough, the central part of the single-overlap zone reaches $P_i \simeq 1$, and thus the permissivity cannot increase further. Therefore, if SL further increases, the

permissivity profile starts to widen, leading to a linear growth of P (see Fig. 4.13c). Such change in the mechanism by which P increases also leads to a sudden decrease of the rate of growth of P, thus leading to a concave curve in correspondence of the transition (see Fig. 4.15). This explains why the force-length curves are convex for low $[Ca^{2+}]_i$, concave for intermediate $[Ca^{2+}]_i$ and finally linear for saturating $[Ca^{2+}]_i$: the curves are just different segments of the curve shown in Fig. 4.15. The different regimes show up at different values of SL according to $[Ca^{2+}]_i$: for low $[Ca^{2+}]_i$, only the convex regime can be observed, due to the limited extension of SL; for medium $[Ca^{2+}]_i$, the working range of sarcomeres is located in correspondence of the transition point, so we observe a concave curve; finally, at saturating $[Ca^{2+}]_i$ we only observe the final and linear part of the curve.

We notice that the above described machinery is made possible by two ingredients: the first is the nearest-neighboring interactions among RUs, the second is the hypothesis that the RUs located at the end of the single-overlap zone behave as the neighboring outer units are in $\mathcal{N}$ state. While there is experimental evidence for the former (see Sec. 1.3.2 and [Bra+87; GRH01; SV17]), to the best of our knowledge there are no experimental results either in favour or against of the latter. Hence, the results presented above show that:

- In the case that the latter hypothesis is accepted, it could provide an explanation for the LDA and for the change of convexity in the force-length curves.
- Conversely, without this hypothesis, the permissivity profile along the single-overlap region appears to be less significant. Hence, in this case, the dynamics of activation is well captured by the mean-field model MF-ODE. As a matter of fact, in absence of a theory about the mechanisms underlying the LDA, the only possibility is that of incorporating it in a phenomenological way, by making the calcium sensitivity dependent on SL, as done in the MF-ODE model (see Eq. (4.50)).

In conclusion, the SE-ODE and MF-ODE models provide different descriptions of the thin filament dynamics according to which hypothesis on the behavior of the units located at the end-points of the single-overlap zone is accepted.

4.4.4 Isometric twitches

We show in Fig. 4.16 the tension transients obtained by simulating isometric twitches giving as input to the rat models the calcium transient of Eq. (2.23). On the other hand, to obtain the isometric twitch transients for human cells shown in Fig. 4.17, we employ the synthetic calcium transient of the TTP06 model.

We notice that both models predict the tension-dependent prolongation of the relaxation time (see Sec. 1.3.3), as it can be seen from the normalized traces reported in the bottom lines of the figures. Moreover, we report in Figs. 4.18 and 4.19 the dependence of the time indicators TTP, RT_{50} and RT_{95} on SL, for the rat and the human models, respectively. Coherently with the experimental measurement, the TTP is nearly independent of SL, while RT_{95} shows an increasing trend with SL.

4.4.5 Force-velocity relationship

Figures 4.20 and 4.21 show the force-velocity relationship predicted with the rat and the human models, respectively. In both the cases, and for both the SE-ODE and the

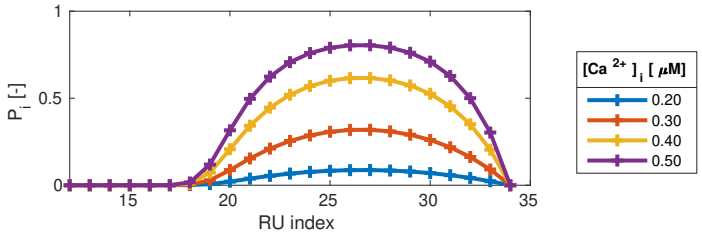

(a) Effect of $[Ca^{2+}]_i$ at fixed SL

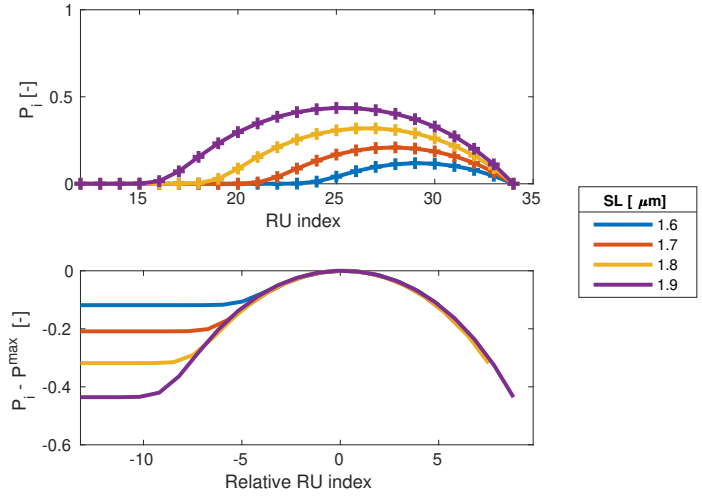

(b) Effect of SL at low activation levels.

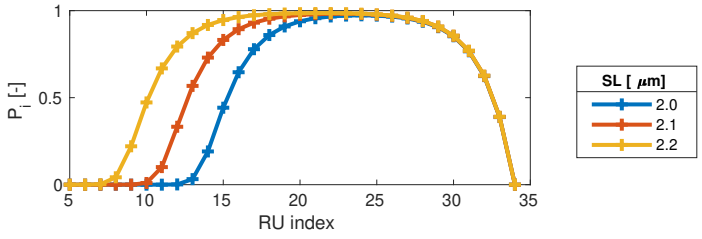

(c) Effect of SL at high activation levels.

Figure 4.13: Interpretation of the LDA as consequence of the edge effect, with the SE-ODE model.

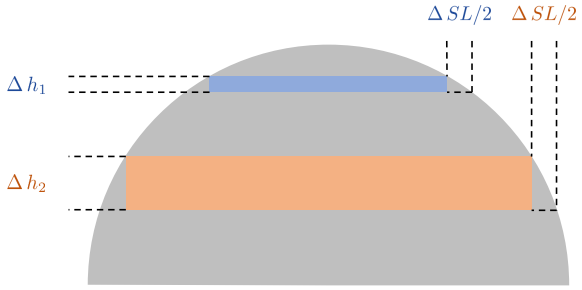

Figure 4.14: Scheme of the edge-effect as the underlying mechanism for the LDA. The figure shows that the same increment of SL leads to a larger increment of P when the sarcomere is more stretched. Indeed, the increment of P associated with an increment ΔSL can be approximated, at the first order in ΔSL, by a rectangle whose base corresponds to the single-overlap length (that increases with SL), and whose height is larger when the sarcomere is more stretched, due to the larger steepness of the permissivity profile.

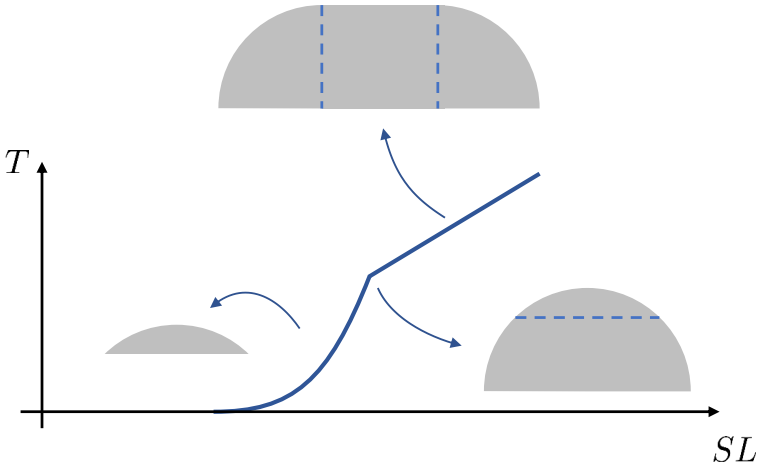

Figure 4.15: Scheme of the two regimes in the $SL \rightarrow P$ relationship, for fixed $[Ca^{2+}]_i$. When SL increases, the relationship is first convex, as explained in Fig. 4.14. Then, when the permissivity hits $P_i \simeq 1$ in the center of the single-overlap zone, we have a transition point and a linear growth regime starts, where P increases only by the enlargement of the region where $P_i \simeq 1$.

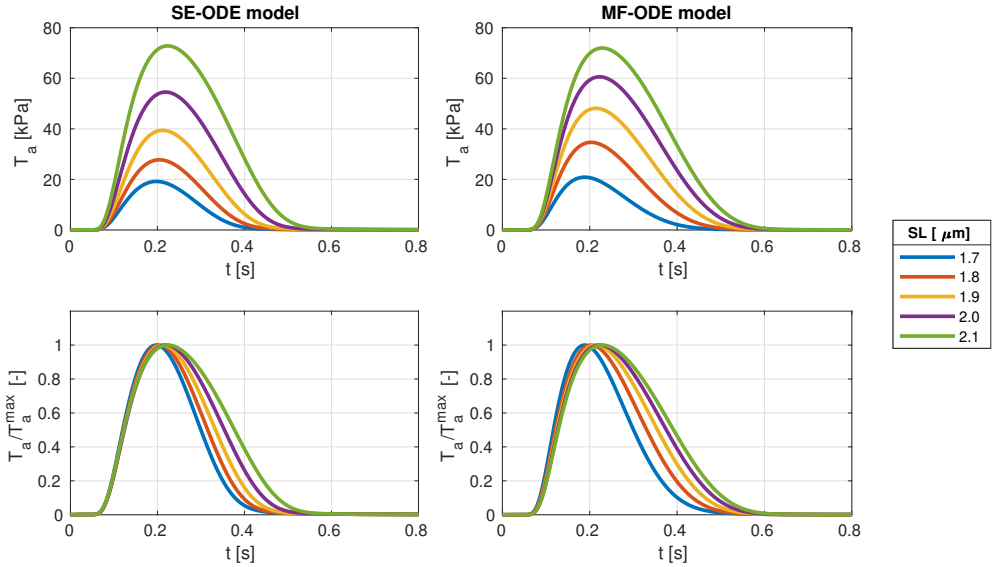

Figure 4.16: Tension transients during isometric twitches at different SL obtained with the SE-ODE (left) and the MF-ODE (right) models for intact room-temperature rat cardiomyocytes.

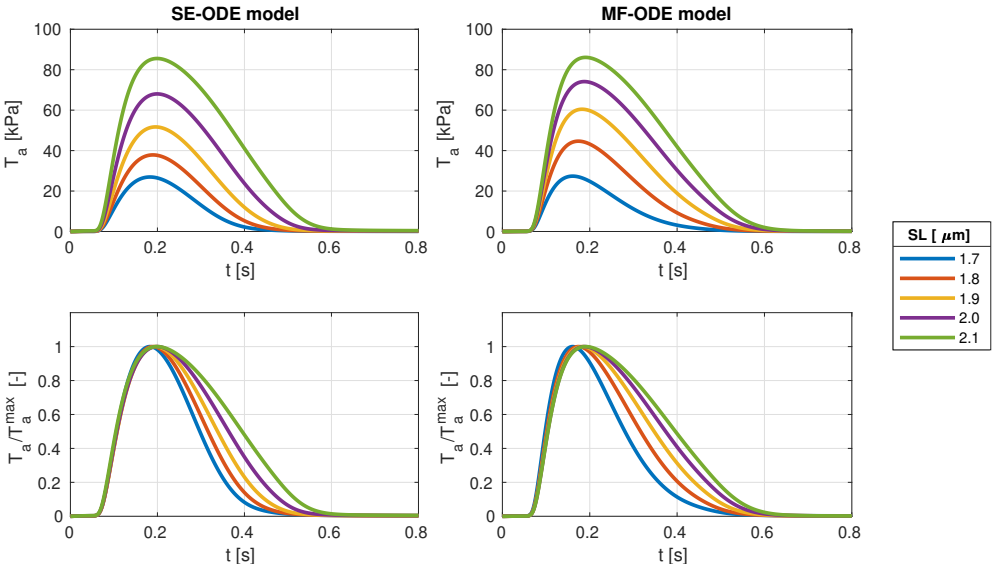

Figure 4.17: Tension transients during isometric twitches at different SL obtained with the SE-ODE (left) and the MF-ODE (right) models for intact body-temperature human cardiomyocytes.

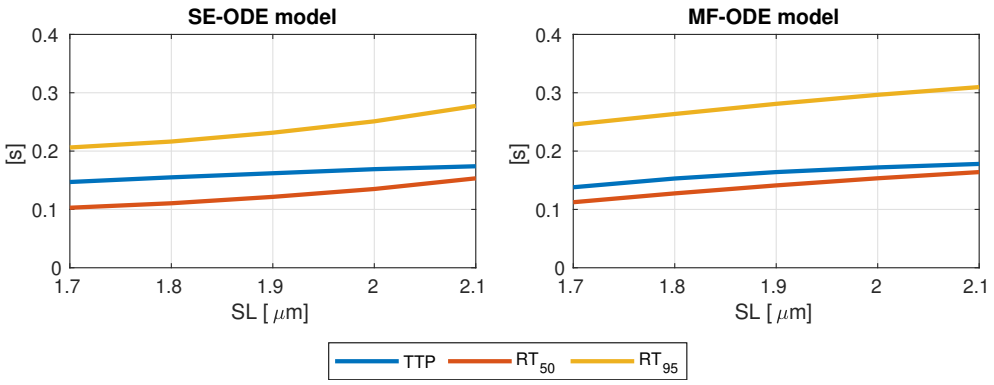

Figure 4.18: Metrics of activation and relaxation kinetics as function of SL during isometric twitches obtained with the SE-ODE (left) and the MF-ODE (right) models for intact room-temperature rat cardiomyocytes.

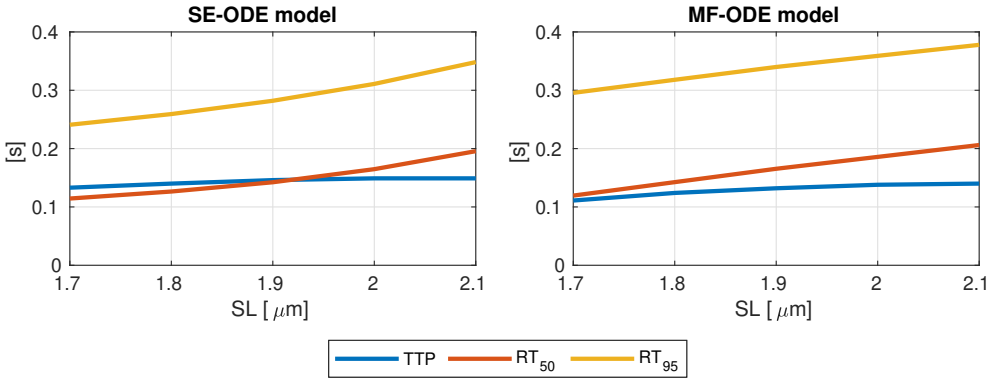

Figure 4.19: Metrics of activation and relaxation kinetics as function of SL during isometric twitches obtained with the SE-ODE (left) and the MF-ODE (right) models for intact body-temperature human cardiomyocytes.

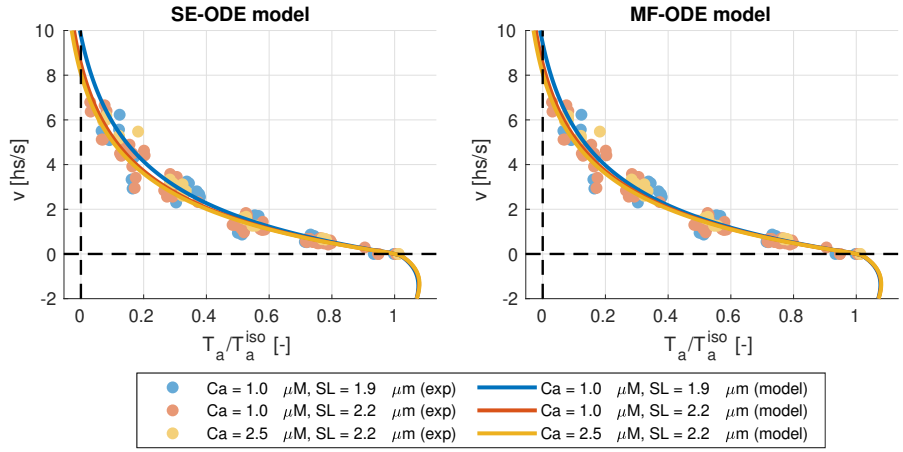

Figure 4.20: Normalized force-velocity relationships for different combinations of $[Ca^{2+}]_i$ and SL obtained with the SE-ODE (left) and the MF-ODE (right) models for intact room-temperature rat cardiomyocytes in comparison with experimental measurements from [Car+16].

MF-ODE model, the experimentally observed convex profile is obtained, with the force reaching zero in correspondence of a finite value of velocity, the so-called maximum shortening velocity (see Sec. 1.3.4). Moreover, the value of v_{hs}^{max} is not significantly affected by the level of activation (that is to say, by the values of $[Ca^{2+}]_i$ and SL), as well as the curvature of the curve. This is also coherent with the experimental observations [Car+16]. We have seen that the generalized H57 model considered in Sec. 3.2 satisfies this property, thanks to the fact that the permissivity P has just a multiplicative effect on the generated active tension. We have now shown, at least through numerical tests, that the effect of the terms $\widetilde{k}_{T,i}^{\mathcal{PN}}$ and $\widetilde{k}_{T,i}^{\mathcal{NP}}$ is secondary and thus the property is largely preserved by the XB models of Eqs. (4.29) and (4.43).

In Fig. 4.20 we also compare the force-velocity curves obtained by the models with the experimental data used to calibrate the rat models (from [Car+16]), thus validating that the automatic calibration procedure presented in Sec. 4.3.2 has been successful.

4.4.6 Fast force transients

Finally, we consider the response to fast steps predicted by the SE-ODE and the MF-ODE models. With this aim, we set a fixed value for the calcium concentration and sarcomere length (we set $[Ca^{2+}]_i = 1.2\,\mu M$ and $SL = 2.2\,\mu m$, but the results are not significantly affected by this choice) and we let the system reach the steady-state. Then, we apply a length step, by applying a constant shortening velocity in a small time interval Δt, and we plot the tension at the end of the step as a function of the step length ΔL (see Sec. 3.2.3). We repeat this protocol twice: first, by reproducing the same conditions employed in laboratory, that is by applying the length step in a very small time interval ($\Delta t = 200\,\mu s$, see [Car+16] and Sec. 1.3.5); then, we repeat the simulation, this time by applying the step with a lower shortening velocity, compatible with the typical velocity by which the cardiac tissue shortens during an heartbeat (we set $v = 0.5\,s^{-1}$).

We show in Figs. 4.22 and 4.23 the results obtained for the rat and the human mod-

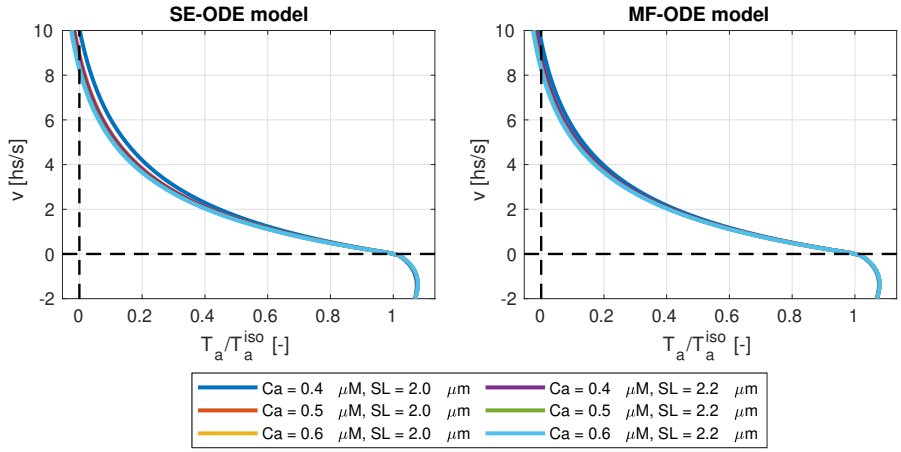

Figure 4.21: Normalized force-velocity relationships for different combinations of $[Ca^{2+}]_i$ and SL obtained with the SE-ODE (left) and the MF-ODE (right) models for intact body-temperature human cardiomyocytes.

els, respectively. The models here considered do not explicitly represent the power-stroke, which is instead lumped inside the definition of the attachment-detachment rates (see Sec. 3.2.4). Therefore, we compare the tension after the 200 µs fast-transient with the experimentally measured T_2-L_2 data, measured by applying a fast step within the same time interval (see again Sec. 3.2.4). The good match between the simulation results and the experimental measurements provide a further validation of the calibration procedure.

The curves obtained by letting the tissue shorten with a velocity similar to that observed during an heartbeat are close to those obtain with an almost instantaneous step, for small values of ΔL; conversely, for larger ΔL, the former curves saturate and a smaller force drop is observed. The reason is that a large length step takes a longer time to be accomplished, and, consequently, the time interval is large enough for the attachment-detachment process to partially recover the original tension. In other terms, when we consider the typical time scales of an heartbeat, the dynamics of the length changes is not sufficiently fast to appreciate the scale separation between the different phases following a fast transient (see Sec. 1.3.5). This provides a further justification for the fact that a lumped description of the power-stroke is an acceptable approximation if the model is used for organ-level simulations and for the fact that, in the model calibration, fitting the T_2-L_2 curve for small values of ΔL is enough (see Sec. 3.2.4).

4.5 Final remarks

In this chapter we have shown that, thanks to the introduction of suitable assumptions, the dynamics of a microscopically detailed sarcomere model can be described by a drastically reduced number of equations than those of the associated FKE equation. We have thus derived, by following this strategy, several models, corresponding to different assumptions (see Tab. 4.1).

The main difficulties to be addressed in the derivation of models concern the spatial correlation of the states of the RUs due to the nearest-neighbor interactions, which

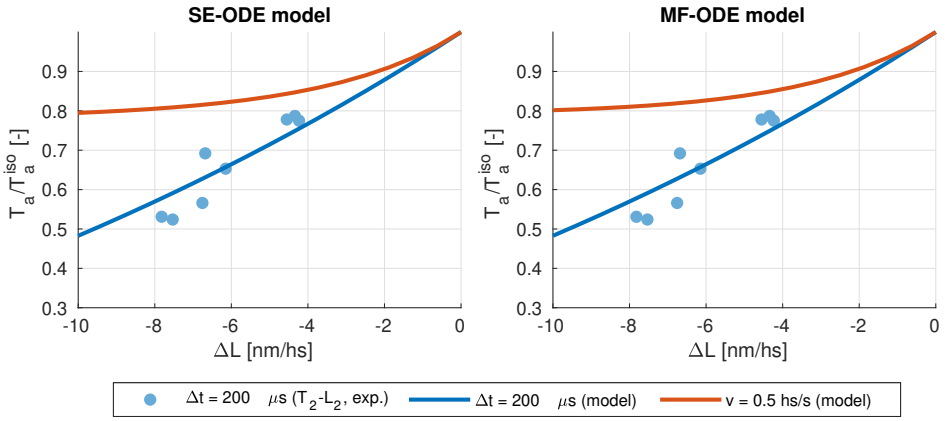

Figure 4.22: Normalized force after the application of a fast length step ΔL for intact room-temperature rat cardiomyocytes. The fast steps reported by the blue line (model result) and the blue circles (T_2-L_2 experimental data from [Car+16]) are applied within a time interval of $\Delta t = 200\,\mu s$, while the red line refers to fast steps applied with a shortening velocity of $v = 0.5\,s^{-1}$.

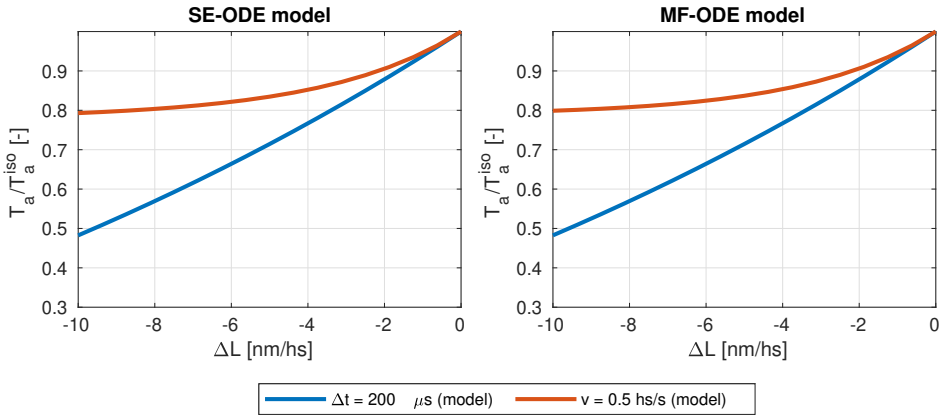

Figure 4.23: Normalized force after the application of a fast length step ΔL for intact body-temperature human cardiomyocytes. The fast steps reported by the blue line are applied within a time interval of $\Delta t = 200\,\mu s$, while the red line refers to fast steps applied with a shortening velocity of $v = 0.5\,s^{-1}$.

hinders a straightforward decoupling of the adjacent RUs, and the mutual filament sliding, that changes which RU regulates which XB from time to time. As done in Chap. 2 we address the first problem by introducing a conditional independence assumption for far RUs, given the state of intermediate RUs (this is coherent with the local nature of nearest-neighboring interactions). As we have shown in Sec. 2.2.5 this kind of assumption dramatically reduces, with the introduction of just a small approximation, the number of equations needed to describe the evolution of the stochastic processes. Moreover, thanks to the absence of feedback from the XBs to the RUs, the dynamics of the latter can be considered independently of the former.

Remarkably, in the derivation of the equations describing the dynamics of XBs, we never encountered the need of tracking which RU faces which XB at each time. This is a consequence of the fact that we departed from the traditional MHs-centered representation of XBs, in favour of a BSs-centered point of view. Thanks to this change of perspective, we derived a set of equations describing the XB dynamics without the need to track the mutual position of the RUs and the MHs.

Under the hypothesis that the total attachment-detachment rate is independent of the myosin arm stretch (as done in [BCS01; Cha+12]), the PDE system describing the XBs can be replaced by a system of ODEs. We remark that this is not a simplificatory assumption, like the conditional independence assumptions mentioned before, but rather a feature of the specific modeling choice for the transition rates describing the attachment-detachment process.

We have also presented a class of models (MF-PDE and MF-ODE), such that the myofilaments overlap is not explicitly described, but it is replaced by a mean-field description of a single representative RUs triplet. We remark that such mean-field models differ from the mean-field models presented in Sec. 2.1.2 (such as [LS94; RWH99; SGS03; Sac04; RBC99]). The latter, indeed, considers a single RU, instead of a triplet. In this manner, the short-range spatial correlation, responsible of cooperativity, cannot be captured. Conversely, the mean-field triplet framework here proposed, thanks to the local nature of cooperativity, allows to capture the effect of nearest-neighbor interactions, as testified by the remarkably good agreement between model predictions as experimental measurements, in particular in the reproduction of the highly cooperative steady-state force-calcium curves (see Sec. 4.4.3).

We have then calibrated the SE-ODE and the MF-ODE models in the case of room-temperature rat intact cardiomyocytes and, later, of body-temperature human intact cardiomyocytes. The results of the numerical simulations showed that the models are capable of reproducing the main features of the experimental characterizations of muscle contraction associated with the time scales of interest (that is to say, the time scales longer that that of the power-stroke), including the steady-state force-calcium and force-length relationships, the kinetics of activation of relaxation, the force-dependent twitches prolongation, and the force-velocity relationship.

The SE-ODE model predicts the so-called LDA (the increment of calcium sensitivity when the sarcomere stretches in the physiological range, see Sec. 1.3.2) and the observed change of convexity of the steady-state force-length curves when the calcium concentration increases (see Sec. 1.3.2). We remark that there is not a common agreement in the scientific community about the microscopical phenomena producing the above mentioned effect and most of the hypotheses proposed in the past have been later rejected (see Sec. 1.3.2). Therefore, we believe that our results are remarkable in this sense, because the phenomena of LDA and of the change of convexity of the force-length curves spontaneously emerge without the need of phenomenologically tune the parameters in dependence of SL. The model here proposed, thus, should contain

some fundamental ingredients capable of producing such phenomena. We have shown in Sec. 4.4.3 that this is due to the fact that the RUs located at the end-points of the single-overlap zone have a low probability of being in the $\mathcal{P}$ state and, because of the nearest-neighbor interactions, such bias towards the $\mathcal{N}$ state spreads along the filament. When the muscle shortens and, consequently, the single-overlap zone reduces its extension, this effect is enhanced, thus reducing the overall permissivity in a nonlinear manner.

Therefore, if the hypothesis that the RUs located at the end-point of the single-overlap zone behave as if the outer neighboring units are in state $\mathcal{N}$ is accepted, then the SE-ODE model provides an explanation for LDA and for the change of convexity of force-length curves. Conversely, if this hypothesis in not accepted, the best that one can do is to model the length-dependent regulation of calcium sensitivity in a phenomenological way. In this case, the MF-ODE model provides a reliable description of the thin filament dynamics since the role of the permissivity profile along the single-overlap is not significant any more to capture the LDA.

In conclusion, according to the hypothesis made on the behavior of the RUs near the end-points of the single-overlap zone, the SE-ODE and the MF-ODE models represent two alternative descriptions of the sarcomere dynamics based on a microscopically detailed representation of the regulatory and contractile proteins, where phenomenological modeling choices are only introduced for phenomena whose underlying mechanisms is not clear to the physiologists scientific community.

Part II

Model order reduction and Machine Learning

Chapter 5

Machine Learning for fast and reliable solution of time-dependent models

In Part I we proposed several mathematical models to describe the microscopic cardiac mechanical activation. These models have a dimension that is significantly reduced with respect to that of the FKE associated to the CTMC describing the dynamics of the contractile proteins from which they are derived (Sec. 2.2.2). Moreover, the computational cost associated with the numerical approximation of such models is much lower than that of MC models. Still, some of the proposed models feature order of 10^3 variables and the numerical simulation of 1 s of physical time requires few seconds of computational time. Therefore, when such activation models are used for three-dimensional numerical simulations at the tissue scale (such as cardiac EM), they need to be solved simultaneously in many points of the computational domain, thus likely becoming the bottleneck of the simulation so that the overall consumption of computational resources dramatically increases, both in terms of memory storage and computational time. A further significant reduction of the dimensionality of the proposed force generation models is thus desirable, if not necessary, in view of cardiac EM simulations. This is precisely our goal in Part II of this thesis.

With this aim, we consider the topic of model order reduction (MOR) of time-dependent models. In this chapter, we deal with such topic in general terms, due to the generality of the results here presented. Then, in Chap. 6, we we will apply the method proposed in this chapter to the mechanical activation models presented in Part I.

Specifically, in this chapter, we propose a data-driven MOR techniques based on Machine Learning. The proposed method is non-intrusive, as it only needs a collection of input-output pairs generated through the model to be reduced. Most of the results presented in this chapter have been published in [RDQ19b].

Contents

5.1 Model order reduction for time-dependent models

The numerical simulation of time-dependent mathematical models is often needed in applied sciences. The increasing demand of more complex and reliable mathematical models may lead to an unbearable demand for computational resources, either in terms of computational power or memory storage. Very often, in several applications, numerical simulations of a given model need to be performed multiple times (many-query) and for many different inputs, either for sensitivity-analysis, optimization, control or uncertainty-quantification purposes, or to deal with multiscale problems, such as cardiac EM, as we will see in Part III. In computational medicine and meteorology e.g., complex mathematical models, although precise and reliable, may be useless for predictive purposes if these cannot be solved nearly in real-time.

This strongly motivates the development of *reduced models*, that is computationally tractable, lower dimensional mathematical models that can be solved with a smaller effort (both in terms of time and computational resources), yet reproducing with a good approximation the results of the *high-fidelity* (HF) model [ASG00; BMS05; QR14; QMN15].

In this chapter, we focus on time-invariant dynamical systems, whose behavior is determined by a time-dependent input $\mathbf{u}(t) \in \mathbb{R}^{N_u}$ and endowed with an output $\mathbf{y}(t) \in \mathbb{R}^{N_y}$. Let us consider the following general[1] form for our HF model:

$$\begin{aligned} &\begin{cases} \dot{\mathbf{X}}(t) &= \mathbf{F}(\mathbf{X}(t), \mathbf{u}(t)) \qquad t \in (0,T], \\ \mathbf{X}(0) &= \mathbf{X}_0, \end{cases} \\ &\mathbf{y}(t) = \mathbf{G}(\mathbf{X}(t)) \qquad t \in (0,T], \end{aligned} \tag{5.1}$$

with $\mathbf{F}\colon \mathbb{R}^N \times \mathbb{R}^{N_u} \to \mathbb{R}^N$, $\mathbf{G}\colon \mathbb{R}^N \to \mathbb{R}^{N_y}$, where $\mathbf{X}(t)$ represents the HF state of the system and can be either finite-dimensional, for ODE models (i.e. $\mathbf{X}(t) \in \mathbb{R}^N$), or infinite-dimensional, e.g. for PDE models. We notice that (5.1) is not the most general form that we can face: indeed the equation can be stated in implicit form. However we stick to form (5.1) just to illustrate the concept.

Moreover, we notice that the cardiac mechanical models presented in Part I can be written in form (5.1), where the input $\mathbf{u}(t)$ is given by the calcium concentration, the sarcomere length and, possibly, the tissue shortening velocity and the output is given by the permissivity or the generated active tension.

Most of MOR methods for time-dependent problems provide a reduced order model (ROM) in the following form:

$$\begin{aligned} &\begin{cases} \dot{\mathbf{x}}(t) &= \mathbf{f}(\mathbf{x}(t), \mathbf{u}(t)) \qquad t \in (0,T], \\ \mathbf{x}(0) &= \mathbf{x}_0, \end{cases} \\ &\widetilde{\mathbf{y}}(t) = \mathbf{g}(\mathbf{x}(t)) \qquad t \in (0,T], \end{aligned} \tag{5.2}$$

where the reduced-order state $\mathbf{x}(t)$ belongs to a lower dimensional space $\mathbb{R}^n$ (typically with $n \ll N$) and the functions $\mathbf{f}\colon \mathbb{R}^n \times \mathbb{R}^{N_u} \to \mathbb{R}^n$ and $\mathbf{g}\colon \mathbb{R}^n \to \mathbb{R}^{N_y}$ can be evaluated with a smaller computational effort than $\mathbf{F}$ and $\mathbf{G}$ in Eq. (5.1). Notice that, in several

[1] The non time-invariant case (i.e. $\dot{\mathbf{X}}(t) = \mathbf{F}(\mathbf{X}(t), \mathbf{u}(t), t)$) can be written in the form (5.1) by introducing a further dependent variable X_{N+1}, representing time, with equation $\dot{X}_{N+1}(t) = 1$ and $X_{N+1}(0) = 0$. Moreover, Eq. (5.1) also includes parametric differential equations, that is the case when $\mathbf{u}(t)$ is constant in time and is regarded as a parameter.

cases, the knowledge of the evolution of the full-order state $\mathbf{X}(t)$ is not essential since the user may be interested in just one or a few output quantities, represented by $\mathbf{y}(t)$. Should the ROM (5.2) be able to reliably reproduce the input-output map $\mathbf{u} \mapsto \mathbf{y}$, it could replace the HF model (5.1), hopefully with a considerable gain in terms of computational resources and simulation time. We here denote by $\widetilde{\mathbf{y}}(t)$ the output of the ROM, which generally differs from that of the HF model $\mathbf{y}(t)$.

MOR methods can be categorized as *model-based* or *data-driven* [BGW15; Ant05; PW15a; PW15b; PGW17]. In model-based MOR, Eq. (5.1) is the starting point to derive its reduced version (5.2). With data-driven approaches instead, the ROM is built upon a collection of input-output pairs, through which the dynamics of the system is inferred. The advantages of model-based approaches are that, often, the ROM inherits structural properties (e.g. stability) from the HF model; moreover, the underlying HF system structure provides the base for deriving error estimates, hence error certification. Unfortunately, an equation in the form of (5.1) is not always available to express the dynamics of the HF model, which may be accessible only through input-output data. This is the case, for instance, when the system dynamics is available only through experimental measurements, either in the time domain or in the frequency domain (i.e. through samples of the transfer function, in the case of a linear system), or when the HF system is accessible through the simulations of a black-box software library. On the other hand, even when the HF model is available, the implementation of model-based MOR into existing codes may not be straightforward. Data-driven MOR, instead, thanks to its black-box approach, is intrinsically non-intrusive and can thus be applied even when the HF model is not directly accessible.

5.1.1 Model-based MOR

The most popular approach to model-based MOR for dynamical systems consists in *projection-based* methods [BGW15; BMS05; ASG00; Ant05]. In this framework, the full-order state space $\mathbb{R}^N$ is approximated by a lower-dimensional subspace span($\mathbf{V}$), where $\mathbf{V} \in \mathbb{R}^{N \times n}$ is the matrix whose columns are the basis of the subspace. The full-order state is approximated as $\mathbf{X}(t) \simeq \mathbf{V}\mathbf{x}(t)$ and the HF model equation is projected in the Galerkin (or Petrov-Galerkin) sense, by left multiplying it by $\mathbf{V}^T$ (or by another matrix $\mathbf{W}^T$, respectively):

$$\begin{aligned} &\begin{cases} \dot{\mathbf{x}}(t) &= \mathbf{W}^T\mathbf{F}(\mathbf{V}\mathbf{x}(t), \mathbf{u}(t)) \qquad t \in (0, T] \\ \mathbf{x}(0) &= \mathbf{W}^T\mathbf{X}_0, \end{cases} \\ &\widetilde{\mathbf{y}}(t) = \mathbf{G}(\mathbf{V}\mathbf{x}(t)) \qquad t \in (0, T], \end{aligned} \tag{5.3}$$

This is equivalent to imposing orthogonality of the HF residual to span($\mathbf{V}$) (or, respectively, to span($\mathbf{W}$)). Various projection-based methods differ on the selection procedure of the bases for $\mathbf{V}$ and $\mathbf{W}$.

When the HF model (5.1) is linear in the state $\mathbf{X}$, the Moment-Matching approach (or Padé approximation) consists in building $\mathbf{V}$ and $\mathbf{W}$ in such a way that the associated transfer function interpolates, up to a desired order, the first few moments of the full-order transfer function for a given frequency [Bai02; Bau+11; Fre03]. The Balanced-Truncation approach applies in the linear case too: it neglects the states corresponding to the smallest Hankel singular values, which measure the relevance of each state in terms of both reachability and observability [Moo81; Ant05]. Proper Orthogonal Decomposition (POD), originally dating back to [Pea01] and developed by Sirovich in 1987 (see [Sir87]), is tightly related to Principal Component Analysis

(PCA, see [Hot33]) and to Karhunen-Loève expansion, also known as Hotelling transform in stochastic process theory [Loe78]. The POD approach consists in collecting a set of *snapshots* of the full-order state $\mathbf{X}$ (i.e. solutions computed at different times for different input values) and in building a basis by selecting the left singular vectors of the snapshot matrix corresponding to the largest singular values, computed through Singular Value Decomposition (SVD) of this snapshot matrix. Such basis is optimal as it minimizes the least-squares error of snapshot reconstruction [Ant05]. POD gained a huge popularity in the PDE framework: the POD Galerkin projection-based approach represents one of the two classical forms of the Reduced Basis (RB) method, the other one being based on the greedy algorithm to generate the snapshots (see e.g. [FR83; Pet89; QMN15; Pru+02; HRS16]).

The effectiveness of projection-based MOR relies on the offline/online decomposition. Such decoupling is straightforward in the case of linear models with affine dependence of $\mathbf{F}$ on the input $\mathbf{u}$ since the algebraic structures (matrices and vectors) of the ROM can be precomputed *offline* (i.e. during the construction of the ROM) by projection of the full-order algebraic structures [QMN15; BMS05]; the latter do not need to be accessible in the *online* phase (i.e. during the numerical simulation of the ROM). In the nonlinear case and/or with non-affine input dependence the offline and online phases cannot be decoupled in principle, and the full-order right-hand side $\mathbf{F}$ should be evaluated at each time step of the online phase, thus preventing the reduction of the HF model complexity. To overcome this issue, the nonlinear dependence on the state and the input is replaced by affine approximations by employing techniques such as the empirical interpolation method, EIM [Bar+04; Mad+07], the discrete empirical interpolation method, DEIM [CS10; DHO12], its matrix version MDEIM [NMA15] or the gappy POD reconstruction [ES95]. In [LC18] the authors proposed a projection-based MOR technique, where the system is projected into a nonlinear manifold, determined by convolutional autoencoders from deep learning.

Another class of model-based MOR techniques is that of hierarchical surrogates, that is to say models derived from the HF one under simplified physical assumptions, simplified geometries or coarser computational grids. While this approach is ubiquitous, we limit to mention a few applications, e.g. [Ale+01; QV03; Hac79]. Most methods in this category are dependent on the class of differential problems describing the phenomenon or are tailored to a specific model.

5.1.2 Data-driven MOR

In the Loewner framework [Löw34] a linear reduced model is derived from transfer function measurements at a collection of *interpolation points*, either in left or right *tangential directions* (i.e. by left or right multiplying the transfer function matrix by the vector corresponding to the tangential direction). The ROM matrices and arrays are computed in such a way that the ROM transfer function interpolates the full-order one at the interpolation points and in the tangential directions (see [MA07; LA10]). In [PGW17] the Loewner framework has been extended to derive ROMs from time-domain data, instead of frequency-domain data. Although the Loewner framework only applies to linear models, it has recently been extended to bilinear (i.e. linear independently in the state and the input) models [AGI16], quadratic-bilinear models [GA15] and to analytic nonlinear models with affine input dependence, by rewriting models with analytic state nonlinearities as quadratic-bilinear models (however increasing the size of the original model, see [Gu11]). The orthonormal vector fitting (OVF) method, suitable for linear systems, is another frequency-domain approach.

Starting from transfer function data samples, OVF approximates the transfer function through orthonormal rational functions [DD05; DHD07].

Kriging, originally developed in geosciences [Kri51] and also known as Gaussian Process (GP) regression, is widely used to perform MOR for nonlinear models in the steady-state case [Ras04; MSDR13]. It is a regression method that employs, as prior for the outcome of a function, a GP whose covariance function depends on so–called hyperparameters, tuned according to a maximum likelihood principle. This technique has been extended to the dynamical case in [HG08] under the name of dynamic mapping kriging (DMK); here, by considering the discrete time version of the evolution equation (5.2) (i.e. $\mathbf{x}^{k+1} = \mathbf{f}(\mathbf{x}^k, \mathbf{u}^k)$), DMK performs kriging on the function $\mathbf{f}$ starting from sample data for several $(\mathbf{x}, \mathbf{u})$ pairs. In [BPK16] the authors propose, under the name of Sparse Identification of Nonlinear Dynamics (SINDy), a technique to infer a model for a dynamical system starting from measurements of $(\mathbf{x}(t), \mathbf{u}(t), \dot{\mathbf{x}}(t))$ tuples. This technique, under the assumption that $\mathbf{f}$ depends on few combinations of the inputs (such as linear combinations, products, and trigonometric functions), seeks a sparse solution for the coefficients of a predetermined collection of linear and nonlinear terms. Despite DMK and SINDy can be applied to nonlinear systems, both these techniques require access to the full-order state of the model and do not perform any reduction in the state dimension.

The method proposed in [GH19] stands at the interplay between model-based and data-driven MOR, by combining the RB method with GP regression. In particular the authors build a reduced basis by POD of a collection of snapshots collected by the HF solution of time-dependent parametric differential equations; then, by GP regression, they approximate the map from the parameters and the time instant to the reduced basis coefficients of the solution. This method, however, is restricted to parametric differential equations (i.e. when $\mathbf{u}(t)$ is constant in time) and cannot be easily extended to the case of models with time-dependent inputs.

5.1.3 Learning models from data

Data-driven MOR, due to its black-box nature, can also be applied when the HF model for the state $\mathbf{X}$ is not accessible, or may not fit in known families of mathematical models: that is, when one is unable or may not be interested in explicitly building a model. This is the case when a physical system is accessible through measurements and one tries to *identify* the underlying law generating the input-output pairs. This task is commonly known in the field of control theory as *System Identification*, SI (see e.g. [Lju98; Kee11]). Models in the form (5.2) are known in the SI field as internal-dynamics or state-space models, whereas the most commonly treated form in the SI field is that of external-dynamics models (see NARX/NARMAX models, [Nel13]), i.e. discrete time models in the form

$$\widehat{\mathbf{y}}^{k+1} = \boldsymbol{\eta}(\mathbf{y}^k, \mathbf{y}^{k-1}, \dots, \mathbf{y}^{k-p}, \mathbf{u}^k, \mathbf{u}^{k-1}, \dots, \mathbf{u}^{k-q}),$$

where the prediction for the next output $\widehat{\mathbf{y}}^{k+1}$ depend on the value of the previous $p+1$ output measurements $\{\widehat{\mathbf{y}}^j\}_{j=k-p}^{k}$ and the previous $q+1$ inputs $\{\widehat{\mathbf{u}}^j\}_{j=k-q}^{k}$. However, models in this family are designed for online identification and, most of all, for online predictions: the model must be fed with the output measured at previous steps, so that the *true* output should be available not only at the identification (or training/offline) stage, but also at the prediction (online) stage. Instead, we are looking here for a model that can be used in a stand-alone way in the online phase, once an offline training phase has been carried out. The use of ANNs in the context of nonlinear SI

is quite popular [NP90; NP92; Nel13], even if their application is limited, up to our knowledge, to online identification and prediction of discrete time systems.

In some recent works the authors have developed learning machines, either based on GP [RPK17a; RK18] or ANNs [RPK17b; RPK17c; RPK19], for data-driven solution and *data-driven discovery* of PDEs. However, the learning machine must have knowledge of the form of the equations that generated the observed data. This technique can be applied to linear or nonlinear parametric PDEs, where the parameters of the PDE (e.g. diffusion, reaction coefficients, etc.) are unknown.

In [RPK18] the authors make use of ANNs to perform data-driven discovery of nonlinear dynamical systems. In particular, they train the ANN to minimize the residuals of a given multi-step time-stepping scheme (such as Adams-Bashforth or BDF schemes) on a collection of available snapshots of the full-order state $\{\mathbf{X}(t^k)\}_{k=1}^M$. However, this approach, like DMK and SINDy techniques, requires $\mathbf{X}$ to be accessible and, moreover, does not perform any dimensionality reduction of the state space.

In [SM18] the authors use ANNs in combination with projection-based MOR for time-dependent models, to approximate the effect of the discarded modes on the retained ones. In [TCD17; FC18] the authors use machine-learning techniques to model the error of projection-based ROM of parametrized nonlinear dynamical systems.

5.1.4 Original contributions

In this chapter, we address the problem of data-driven MOR for nonlinear dynamical systems (which can be interpreted as a nonlinear SI problem), where we suppose to have no direct access either to the HF model (that is $\mathbf{F}$ and $\mathbf{G}$ in Eq. (5.1)), nor to full-order state observations $\mathbf{X}(t)$, but only to input-output pairs $(\mathbf{u}(t), \mathbf{y}(t))$. This task is remarkably hard since we aim at the same time at (i) reconstructing the internal state of the system through its reduced description $\mathbf{x}(t)$ without the possibility of observing the true internal state of the system $\mathbf{X}(t)$ and (ii) finding a model for the dynamics of $\mathbf{x}(t)$ itself. We notice that the reconstruction of the system state through $\mathbf{x}(t)$ is not the final goal, but it is just instrumental to reconstruction the input-output map $\mathbf{u} \mapsto \mathbf{y}$.

In [RDQ19b] we have proposed a data-driven MOR technique (that we present in this chapter), based on Artificial Neural Networks (ANNs), applicable to dynamical systems arising from Ordinary Differential Equations (ODEs) or time-dependent Partial Differential Equations (PDEs). Unlike model-based approaches, the proposed approach is non-intrusive since it just requires a collection of input-output pairs generated through the high-fidelity (HF) ODE or PDE model. We proceed by setting the problem in an abstract form, where we look for the best-approximation of the HF model into a class of simpler models (i.e. the class of ROMs with a prescribed level of complexity). This is an optimization problem, where the unknown is the model itself. Noticeably, we need to carefully select the class of candidate models and to find a suitable representation for the models to define an optimization algorithm for solving the best-approximation problem. Because of their ability to approximate any continuous function with a desired level of accuracy (see [Cyb89; SX19; He+18]) and to learn from data, we represent the right-hand side $\mathbf{f}$ in (5.2) through an ANN, that we train to learn the underlying physics from input-output pairs. We prove that ANN models are able to approximate every time-dependent model described by ODEs with any desired level of accuracy. We test the proposed technique on different problems, including the model reduction of two large-scale models. Two of the HF systems of ODEs here considered stem from the spatial discretization of a parabolic and an hy-

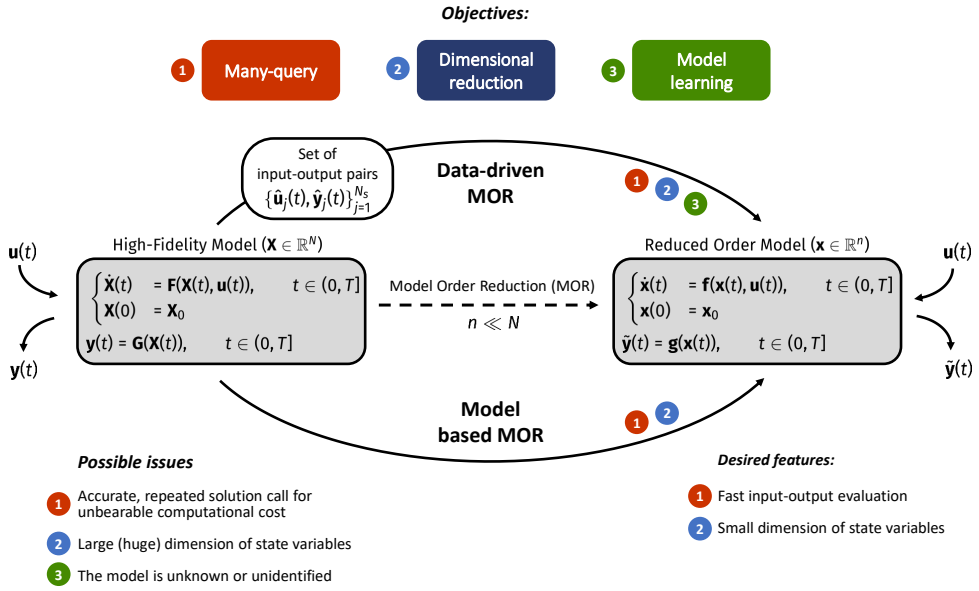

Figure 5.1: Model-based and data-driven MOR. The HF model can have three undesired features: ① it may be computationally demanding, ② it can have a high state dimension, ③ it may not be accessible. A ROM can be derived either directly from the HF model (model-based MOR), or from input-output pairs generated by the HF model (data-driven MOR). The latter approach allows to learn a model, in the case when the HF model is not accessible (see ③). In both the cases, the ROM represents a surrogate of the HF model allowing for fast evaluations, lowering the computational burden in multi-query applications (see ①), and features a low dimensional state (see ②).

perbolic PDE respectively, which sheds light on a promising field of application of the proposed technique.

In this chapter we introduce a general framework which serves multiple purposes (see Fig. 5.1):

- Building surrogates of time-dependent differential models, which allow for fast evaluations and are suitable for multi-query problems.
- Reducing the dimensionality of the state variables of time-dependent differential models (e.g. when a mathematical model needs to be solved virtually in each point of a computational domain and the overall memory storage must be contained).
- Learning mathematical models from available input-output pairs.

This chapter is structured as follows. In Sec. 5.2 we present our strategy, by rephrasing the model reduction problem in terms of an optimization problem, for which we define the objective functional. Then, in Sec. 5.3, we present the strategy employed to numerically find a solution of the optimization problem. In particular, we show: (i) how the unknowns of the problem are discretized; (ii) how the time discretization is performed; (iii) the optimization algorithm employed. Finally, in Sec. 5.4, we show the obtained results and we analyse and critically discuss them.

5.2 Model order reduction strategy

We start by giving a definition of *model* (in the way this is meant in this chapter): an object which maps time-dependent inputs into time-dependent outputs.

5.2.1 The dynamical model

A *model* for us is a general framework including either a physical model (like a natural phenomenon or an engineering process) or a mathematical or numerical model, which associates a time-dependent output to a time-dependent input. We consider a limited time interval $[0, T]$ and we denote by $U \subset \mathbb{R}^{N_u}$ and by $Y \subset \mathbb{R}^{N_y}$ the sets where the input $\mathbf{u} : [0, T] \to U$ and the output $\mathbf{y} : [0, T] \to Y$ take values, respectively. We name as *experiment* the action of inputing $\mathbf{u}(t)$ to the model and recording the corresponding output $\mathbf{y}(t)$ and by *sample* we refer to the couple $(\mathbf{u}, \mathbf{y})$. For the sake of abstraction, we make the following minimal assumptions on the model:

(A1) **Time invariance**: by denoting with $\mathbf{y}(t)$ the output obtained by starting at time t_0 an experiment with input $\mathbf{u}(t)$, the output of another experiment started at time $t_1 \geq t_0$ with input $\mathbf{u}(t-(t_1-t_0))$ is $\mathbf{y}(t-(t_1-t_0))$. Hence in the following we will consider, without loss of generality, each experiment starting from the initial time $t = t_0 = 0$.

(A2) **Existence of an initial state**: at time $t = 0$, for each experiment, the model is in the same initial state, that is it always responds in the same way to a prescribed input. Otherwise, the map $\mathbf{u} \mapsto \mathbf{y}$ would not be well defined.

(A3) **Causality principle**: The input-output relationship must be consistent with the arrow of time, that is the output of the model is allowed to depend only on previous values of the input and not on future values: given two inputs $\mathbf{u}_1$

and $\mathbf{u}_2$, such that, for some t^*, $\mathbf{u}_1(t) = \mathbf{u}_2(t)$ for $t \in [0, t^*]$, the corresponding outputs $\mathbf{y}_1$ and $\mathbf{y}_2$ must satisfy $\mathbf{y}_1(t) = \mathbf{y}_2(t)$ for $t \in [0, t^*]$.

(A4) **No input-output direct dependence**: the output at time t depends just on the state of the system at the same time, but not (directly) on the input at time t. As a consequence, thanks to (A2), the output at time $t = 0$ will be the same for each experiment. Notice that this assumption could be removed, by allowing $\mathbf{g}$ in (5.2) to depend also on $\mathbf{u}(t)$. However, for the sake of simplicity, we will not consider the latter case in this thesis.

For simplicity, we consider the case when both the input and output are continuous functions in time. Therefore, the model can be seen as a map $\boldsymbol{\varphi}\colon \mathcal{U} \to \mathcal{Y}$ from the space of input signals $\mathcal{U} = \mathcal{C}^0([0,T]; U)$ to the space of output signals $\mathcal{Y} = \mathcal{C}^0([0,T]; Y)$. Thanks to assumptions (A1) and (A2) the map $\boldsymbol{\varphi}$ is well defined. Moreover, assumption (A3) can be written as

$$\forall\, \mathbf{u}_1, \mathbf{u}_2 \in \mathcal{U} \quad \forall\, t^* \in [0,T] \qquad \mathbf{u}_1|_{[0,t^*]} = \mathbf{u}_2|_{[0,t^*]} \implies (\boldsymbol{\varphi}\mathbf{u}_1)|_{[0,t^*]} = (\boldsymbol{\varphi}\mathbf{u}_2)|_{[0,t^*]}, \tag{5.4}$$

where $\boldsymbol{\varphi}\mathbf{u}_1$ denotes the output $\mathbf{y}_1 \in \mathcal{Y}$ of the model when the input is $\mathbf{u}_1 \in \mathcal{U}$ (thus both $\mathbf{u}_1$ and $\boldsymbol{\varphi}\mathbf{u}_1$ are functions of time) and $(\boldsymbol{\varphi}\mathbf{u}_1)|_{[0,s]}$ denotes the restriction of the output $\mathbf{y}_1$ to the time interval $[0, s]$. On the other hand, assumption (A4) entails

$$\exists\, \mathbf{y}_0 \in Y \quad \text{s.t.} \quad \forall\, \mathbf{u} \in \mathcal{U} \quad (\boldsymbol{\varphi}\mathbf{u})(0) = \mathbf{y}_0, \tag{5.5}$$

where $(\boldsymbol{\varphi}\mathbf{u})(0)$ denotes the output $\mathbf{y} \in \mathcal{Y}$ of the model – corresponding to the time-dependent input $\mathbf{u} \in \mathcal{U}$ – evaluated at time $t = 0$ (i.e. $\mathbf{y}(0)$). Thus, we define the set of all the models associated with the input and output sets $\mathcal{U}$ and $\mathcal{Y}$ as

$$\Phi = \{\boldsymbol{\varphi}\colon \mathcal{U} \to \mathcal{Y} \quad \text{s.t. (5.4) and (5.5) hold}\},$$

endowed with the norm of the supremum:

$$|\boldsymbol{\varphi}|_\Phi = \sup_{\mathbf{u}\in\mathcal{U}} |\boldsymbol{\varphi}\mathbf{u}|_{\mathcal{Y}} = \sup_{\mathbf{u}\in\mathcal{U}} \sup_{t\in[0,T]} |(\boldsymbol{\varphi}\mathbf{u})(t)|_Y.$$

5.2.2 Building a reduced model

We perform N_s experiments with the HF model and we collect a set of N_s input-output pairs:

$$\{(\widehat{\mathbf{u}}_j, \widehat{\mathbf{y}}_j)\}_{j=1,\dots,N_s} \subset \mathcal{U} \times \mathcal{Y}. \tag{5.6}$$

Then we select a subset of candidate models, which we denote by $\widehat{\Phi} \subseteq \Phi$, and we consider the problem of finding the best-approximation of the HF model, in the least-squares sense, in the subset $\widehat{\Phi}$:

$$\boldsymbol{\varphi}^* = \operatorname*{argmin}_{\boldsymbol{\varphi}\in\widehat{\Phi}} J(\boldsymbol{\varphi}), \tag{5.7}$$

where the objective functional is given by

$$J(\boldsymbol{\varphi}) = \frac{1}{2} \sum_{j=1}^{N_s} \int_0^T |\widehat{\mathbf{y}}_j(t) - (\boldsymbol{\varphi}\widehat{\mathbf{u}}_j)(t)|^2 dt. \tag{5.8}$$

When the measurements of the output $\widehat{\mathbf{y}}_j$ are affected by Gaussian noise, the least-squares best-approximation corresponds to the maximum-likelihood estimation (see e.g. [CB02]).

The next step is the choice of the subset of candidate models $\widehat{\Phi} \subseteq \Phi$. A possible approach is that of directly approximating the input-output map $\mathbf{u} \mapsto \mathbf{y}$ in the time domain (i.e. from $\mathcal{U}$ to $\mathcal{Y}$), e.g. by means of an ANN which takes as an input a set $\{\mathbf{u}(t_0), \mathbf{u}(t_1), \dots, \mathbf{u}(t_M)\}$ of values associated to a collection of time instants and returns the corresponding output values $\{\mathbf{y}(t_0), \mathbf{y}(t_1), \dots, \mathbf{y}(t_M)\}$. However, working on input and outputs as signals (i.e. in the spaces $\mathcal{U}$ and $\mathcal{Y}$) would clearly lead to a remarkably large-size problem, potentially making the learning process unaffordable because of its computational complexity. Thus, we pursue a different approach: by exploiting the structure of the elements in Φ, which is based on assumptions (A1)–(A4), we restrict the investigation to input-output maps described by systems of ODEs. This dramatically reduces the size of the problem, as we show in the following.

5.2.3 Models described by systems of ODEs

We refer now to the specific class of models, in the framework of Sec 5.2.1, which are governed by a system of ODEs in the form of (5.2). Such class represents a subset of Φ, as we will show. First, we notice that, given two functions $\mathbf{f} \in \mathcal{F}_n := \{\mathbf{f} \in \mathcal{C}^0(\mathbb{R}^n \times U; \mathbb{R}^n)$, which are Lipschitz continuous in $\mathbf{x}$ uniformly in $\mathbf{u}\}$ and $\mathbf{g} \in \mathcal{G}_n := \mathcal{C}^0(\mathbb{R}^n; Y)$ and a vector $\mathbf{x}_0 \in \mathcal{X}_n \equiv \mathbb{R}^n$ (where the subscript n stands for the number of internal reduced states), the system (5.2) identifies a unique map from $\mathcal{U}$ to $\mathcal{Y}$. We denote by $\boldsymbol{\varphi}_{\mathbf{f},\mathbf{g},\mathbf{x}_0}$ such map.

Proposition 5.1. *For each $\mathbf{f} \in \mathcal{F}_n$, $\mathbf{g} \in \mathcal{G}_n$ and $\mathbf{x}_0 \in \mathcal{X}_n$, we have $\boldsymbol{\varphi}_{\mathbf{f},\mathbf{g},\mathbf{x}_0} \in \Phi$, that is the input-output map represented by* (5.2) *is a model according to the definition of Sec. 5.2.1.*

Proof. Thanks to the Picard-Lindelöf theorem, Eq. (5.2) has a unique solution. Thus, the map $\boldsymbol{\varphi}_{\mathbf{f},\mathbf{g},\mathbf{x}_0}$ is well defined. Moreover, it is continuous from $\mathcal{U}$ to $\mathcal{Y}$, thus the norm in Φ is finite. Property (5.4) is easy to be checked, while (5.5) holds by setting $\mathbf{y}_0 = \mathbf{g}(\mathbf{x}_0)$. □

Moreover, given the triplet $\widehat{\mathcal{F}} \subseteq \mathcal{F}_n$, $\widehat{\mathcal{G}} \subseteq \mathcal{G}_n$ and $\widehat{\mathcal{X}} \subseteq \mathcal{X}_n$, we define the following subset of models:

$$\Phi^{\widehat{\mathcal{F}},\widehat{\mathcal{G}},\widehat{\mathcal{X}}} = \left\{\boldsymbol{\varphi}_{\mathbf{f},\mathbf{g},\mathbf{x}_0} \in \Phi \text{ s.t. } \mathbf{f} \in \widehat{\mathcal{F}}, \mathbf{g} \in \widehat{\mathcal{G}}, \mathbf{x}_0 \in \widehat{\mathcal{X}}\right\} \subset \Phi. \tag{5.9}$$

We have the following result, which states that the expressive power of the class of models with n state variables grows as n increases.

Proposition 5.2. *The classes of models with n internal states are nested, that is:*

$$\Phi^{\mathcal{F}_n,\mathcal{G}_n,\mathcal{X}_n} \subseteq \Phi^{\mathcal{F}_m,\mathcal{G}_m,\mathcal{X}_m} \qquad \forall\, n \leq m.$$

Proof. Given a model in the form Eq. (5.2) with n state variables, by adding $m - n$ further variables which affect neither the dynamics of the other variables, nor the output, we obtain a model with m state variables, still representing the same input-output map of the previous model. □

Moreover, we have the following result.

Proposition 5.3. *Let U be compact. Suppose that the subsets $\widehat{\mathcal{F}} \subseteq \mathcal{F}_n$ and $\widehat{\mathcal{G}} \subseteq \mathcal{G}_n$ are such that the restrictions of their functions to compact sets are dense in the full spaces, that is for each compact set $E \subset \mathbb{R}^n$ we have:*

$$\forall\, \varepsilon > 0 \quad \forall\, \mathbf{f} \in \mathcal{F}_n \quad \exists\, \widehat{\mathbf{f}} \in \widehat{\mathcal{F}} \quad \forall\, \mathbf{x} \in E, \mathbf{u} \in U \quad \left|\mathbf{f}(\mathbf{x},\mathbf{u}) - \widehat{\mathbf{f}}(\mathbf{x},\mathbf{u})\right| \leq \varepsilon, \tag{5.10}$$

$$\forall\, \varepsilon > 0 \quad \forall\, \mathbf{g} \in \mathcal{G}_n \quad \exists\, \widehat{\mathbf{g}} \in \widehat{\mathcal{G}} \quad \forall\, \mathbf{x} \in E \quad |\mathbf{g}(\mathbf{x}) - \widehat{\mathbf{g}}(\mathbf{x})| \leq \varepsilon. \tag{5.11}$$

Then, the subset of models $\Phi^{\widehat{\mathcal{F}},\widehat{\mathcal{G}},\mathcal{X}_n}$ is dense in the model space $\Phi^{\mathcal{F}_n,\mathcal{G}_n,\mathcal{X}_n}$, that is:

$$\forall\, \varepsilon > 0 \quad \forall\, \boldsymbol{\varphi} \in \Phi^{\mathcal{F}_n,\mathcal{G}_n,\mathcal{X}_n} \quad \exists\, \widehat{\boldsymbol{\varphi}} \in \Phi^{\widehat{\mathcal{F}},\widehat{\mathcal{G}},\mathcal{X}_n} \quad s.t. \quad |\boldsymbol{\varphi} - \widehat{\boldsymbol{\varphi}}|_\Phi \leq \varepsilon. \tag{5.12}$$

Proof. By definition, there exists $\mathbf{f} \in \mathcal{F}_n$, $\mathbf{g} \in \mathcal{G}_n$ and $\mathbf{x}_0 \in \mathcal{X}_n$ such that $\boldsymbol{\varphi} = \boldsymbol{\varphi}_{\mathbf{f},\mathbf{g},\mathbf{x}_0}$. First, we show that the state $\mathbf{x}$ of the HF model $\boldsymbol{\varphi}$ is bounded. We have:

$$\begin{aligned}\frac{d}{dt}\left(\frac{1}{2}\left|\mathbf{x}(t)\right|^2\right) = \dot{\mathbf{x}}(t)\cdot\mathbf{x}(t) = \mathbf{f}(\mathbf{x}(t),\mathbf{u}(t))\cdot\mathbf{x}(t) &\leq \left|\mathbf{f}(\mathbf{x}(t),\mathbf{u}(t))\right|\left|\mathbf{x}(t)\right| \\ &\leq \left(\left|\mathbf{f}(\mathbf{x}(t),\mathbf{u}(t)) - \mathbf{f}(\mathbf{x}_0,\mathbf{u}(t))\right| + \left|\mathbf{f}(\mathbf{x}_0,\mathbf{u}(t))\right|\right)\left|\mathbf{x}(t)\right|.\end{aligned}$$

By denoting by $L_{\mathbf{f}}$ the Lipschitz constant of $\mathbf{f}$, we have $|\mathbf{f}(\mathbf{x}(t),\mathbf{u}(t)) - \mathbf{f}(\mathbf{x}_0,\mathbf{u}(t))| \leq L_{\mathbf{f}}\left|\mathbf{x}(t) - \mathbf{x}_0\right| \leq L_{\mathbf{f}}\left(|\mathbf{x}(t)| + |\mathbf{x}_0|\right)$. Moreover, as U is compact, we have $|\mathbf{f}(\mathbf{x}_0,\mathbf{u}(t))| \leq M$ for some finite $M \in \mathbb{R}$. Therefore, we have:

$$\begin{aligned}\frac{d}{dt}\left(\frac{1}{2}\left|\mathbf{x}(t)\right|^2\right) &\leq L_{\mathbf{f}}\left|\mathbf{x}(t)\right|^2 + \left(L_{\mathbf{f}}\left|\mathbf{x}_0\right| + M\right)\left|\mathbf{x}(t)\right| \\ &\leq \left(L_{\mathbf{f}} + \frac{1}{2}\right)\left|\mathbf{x}(t)\right|^2 + \frac{1}{2}\left(L_{\mathbf{f}}\left|\mathbf{x}_0\right| + M\right)^2.\end{aligned}$$

Using the Gronwall lemma [QSS10] we get:

$$|\mathbf{x}(t)| \leq \sqrt{\left(|\mathbf{x}_0|^2 + \left(L_{\mathbf{f}}\left|\mathbf{x}_0\right| + M\right)^2 T\right) e^{(2L_{\mathbf{f}}+1)T}} =: R \quad \forall t \in [0,T].$$

Thanks to (5.11), there exists $\widehat{\mathbf{g}} \in \widehat{\mathcal{G}}$ such that $|\mathbf{g}(\mathbf{x}) - \widehat{\mathbf{g}}(\mathbf{x})| \leq \frac{1}{2}\varepsilon$ for $\mathbf{x} \in \overline{B_{2R}}$, the closed ball of radius $2R$.

Moreover, being $\mathbf{g}$ continuous, by the Heine-Cantor theorem, it is also uniformly continuous on the compact ball $\overline{B_{2R}}$, thus there exists some ε' such that for any $\mathbf{x}_1, \mathbf{x}_2 \in \overline{B_{2R}}$, if $|\mathbf{x}_1 - \mathbf{x}_2| \leq \varepsilon'$; this implies that $|\mathbf{g}(\mathbf{x}_1) - \mathbf{g}(\mathbf{x}_2)| \leq \frac{1}{2}\varepsilon$.

We define the positive number:

$$\varepsilon'' = \min\left\{\varepsilon', \frac{1}{2}R\right\}\left(Te^{(2L_{\mathbf{f}}+1)T}\right)^{-1/2}.$$

Thanks to (5.10), there exists $\widehat{\mathbf{f}} \in \widehat{\mathcal{F}}$ such that $\left|\mathbf{f}(\mathbf{x},\mathbf{u}) - \widehat{\mathbf{f}}(\mathbf{x},\mathbf{u})\right| \leq \varepsilon''$ for $\mathbf{x} \in \overline{B_{2R}}, \mathbf{u} \in U$.

Consider the model $\widehat{\boldsymbol{\varphi}} = \boldsymbol{\varphi}_{\widehat{\mathbf{f}},\widehat{\mathbf{g}},\mathbf{x}_0}$, whose state is denoted by $\widehat{\mathbf{x}}(t)$. Let $\mathbf{u} \in \mathcal{U}$ be a generic input signal. Now, we show that the trajectory of the state $\widehat{\mathbf{x}}(t)$ is contained in B_{2R}. Suppose by contradiction that $\widehat{\mathbf{x}}(s) = 2R$ for some $s \in [0,T]$, $\widehat{\mathbf{x}}(t) < 2R$ for $t < s$. Then, in the interval $[0,s)$ the discrepancy between the two states $\mathbf{z}(t) := \mathbf{x}(t) - \widehat{\mathbf{x}}(t)$

satisfies:

$$\begin{aligned}\frac{d}{dt}\left(\frac{1}{2}\left|\mathbf{z}(t)\right|^2\right) &= \dot{\mathbf{z}}(t)\cdot\mathbf{z}(t) = \Big[\mathbf{f}(\mathbf{x}(t),\mathbf{u}(t)) - \widehat{\mathbf{f}}(\widehat{\mathbf{x}}(t),\mathbf{u}(t))\Big]\cdot\mathbf{z}(t)\\ &= \left|\mathbf{f}(\mathbf{x}(t),\mathbf{u}(t)) - \mathbf{f}(\widehat{\mathbf{x}}(t),\mathbf{u}(t))\right|\,\left|\mathbf{z}(t)\right|\\ &+ \Big|\mathbf{f}(\widehat{\mathbf{x}}(t),\mathbf{u}(t)) - \widehat{\mathbf{f}}(\widehat{\mathbf{x}}(t),\mathbf{u}(t))\Big|\,\left|\mathbf{z}(t)\right|\\ &\le L_{\mathbf{f}}\left|\mathbf{z}(t)\right|^2 + \varepsilon''\left|\mathbf{z}(t)\right| \le \left(L_{\mathbf{f}}+\frac{1}{2}\right)\left|\mathbf{z}(t)\right|^2 + \frac{1}{2}(\varepsilon'')^2.\end{aligned} \tag{5.13}$$

By Gronwall inequality we get

$$\left|\mathbf{x}(t)-\widehat{\mathbf{x}}(t)\right| \le \varepsilon''\sqrt{Te^{(2L_{\mathbf{f}}+1)T}} \le \frac{1}{2}R,$$

where the second inequality follows from the definition of ε''. The, we have $|\widehat{\mathbf{x}}(t)| \le |\mathbf{x}(t)-\widehat{\mathbf{x}}(t)| + |\mathbf{x}(t)| \le \frac{3}{2}R$ for $t\in[0,s)$. Since $|\widehat{\mathbf{x}}(s)| = 2R$, we reach a contradiction and we have proved that the trajectory of $\widehat{\mathbf{x}}(t)$ is contained into B_{2R}. Therefore, inequality (5.13) holds on the whole time interval $[0,T]$ and we conclude:

$$\left|\mathbf{x}(t)-\widehat{\mathbf{x}}(t)\right| \le \varepsilon''\sqrt{Te^{(2L_{\mathbf{f}}+1)T}} \le \varepsilon' \qquad t\in[0,T],$$

which entails $|\mathbf{g}(\mathbf{x}(t)) - \mathbf{g}(\widehat{\mathbf{x}}(t))| \le \frac{1}{2}\varepsilon$ for $t\in[0,T]$. Finally, we have

$$\begin{aligned}|(\boldsymbol{\varphi}\mathbf{u})(t) - (\widehat{\boldsymbol{\varphi}}\mathbf{u})(t)| &= |\mathbf{g}(\mathbf{x}(t)) - \widehat{\mathbf{g}}(\widehat{\mathbf{x}}(t))|\\ &\le |\mathbf{g}(\mathbf{x}(t)) - \mathbf{g}(\widehat{\mathbf{x}}(t))| + |\mathbf{g}(\widehat{\mathbf{x}}(t)) - \widehat{\mathbf{g}}(\widehat{\mathbf{x}}(t))| \le \frac{\varepsilon}{2}+\frac{\varepsilon}{2} = \varepsilon.\end{aligned}$$

□

Proposition 5.3 states that if the subsets $\widehat{\mathcal{F}}$ and $\widehat{\mathcal{G}}$ approximate in a suitable sense (see Eqs. (5.10)–(5.11)) the spaces $\mathcal{F}_n$ and $\mathcal{G}_n$ respectively, the class of candidate models $\Phi^{\widehat{\mathcal{F}},\widehat{\mathcal{G}},\mathcal{X}_n}$ approximate the space of models $\Phi^{\mathcal{F}_n,\mathcal{G}_n,\mathcal{X}_n}$ with arbitrary accuracy.

We notice that by setting $\widehat{\Phi} = \Phi^{\widehat{\mathcal{F}},\widehat{\mathcal{G}},\widehat{\mathcal{X}}}$, the abstract problem (5.7) reads:

$$\begin{cases}\min\limits_{\mathbf{f}\in\widehat{\mathcal{F}},\mathbf{g}\in\widehat{\mathcal{G}},\mathbf{x}_0\in\widehat{\mathcal{X}}} & \frac{1}{2}\sum_{j=1}^{N_s}\int_0^T |\widehat{\mathbf{y}}_j(t) - \mathbf{g}(\mathbf{x}_j(t))|^2 dt\\ \text{s.t.} & \dot{\mathbf{x}}_j(t) = \mathbf{f}(\mathbf{x}_j(t),\widehat{\mathbf{u}}_j(t)), \quad t\in(0,T], \quad j=1,\dots,N_s,\\ & \mathbf{x}_j(0) = \mathbf{x}_0, \quad j=1,\dots,N_s,\end{cases} \tag{5.14}$$

We are thus addressing a least-squares minimization problem where the design variables are the two functions $\mathbf{f}\in\widehat{\mathcal{F}}$ and $\mathbf{g}\in\widehat{\mathcal{G}}$ and the vector $\mathbf{x}_0\in\widehat{\mathcal{X}}$.

5.2.4 Non-uniqueness of the representation

Remark 5.1. Given a model $\boldsymbol{\varphi}_{\mathbf{f},\mathbf{g},\mathbf{x}_0} \in \Phi^{\mathcal{F}_n,\mathcal{G}_n,\mathcal{X}_n}$, its representation in terms of the triplet $(\mathbf{f},\mathbf{g},\mathbf{x}_0)$ may not be unique. Indeed, by taking any invertible and sufficiently regular map $\mathbf{h}\colon \mathbb{R}^n\to\mathbb{R}^n$, let us consider the change of variables $\widetilde{\mathbf{x}} = \mathbf{h}(\mathbf{x})$ and define

$$\widetilde{\mathbf{f}}(\widetilde{\mathbf{x}},\mathbf{u}) = (\nabla\mathbf{h}\circ\mathbf{h}^{-1})(\widetilde{\mathbf{x}})\,\mathbf{f}(\mathbf{h}^{-1}(\widetilde{\mathbf{x}}),\mathbf{u}), \quad \widetilde{\mathbf{g}}(\widetilde{\mathbf{x}}) = \mathbf{g}(\mathbf{h}^{-1}(\widetilde{\mathbf{x}})), \quad \widetilde{\mathbf{x}}_0 = \mathbf{h}(\mathbf{x}_0). \tag{5.15}$$

We have $\boldsymbol{\varphi}_{\mathbf{f},\mathbf{g},\mathbf{x}_0} = \boldsymbol{\varphi}_{\widetilde{\mathbf{f}},\widetilde{\mathbf{g}},\widetilde{\mathbf{x}}_0}$ (i.e. the input-output map represented by the two models is equivalent). As a particular case, for any $\alpha\in\mathbb{R}\setminus\{0\}$, we have that, with the transformation $\widetilde{\mathbf{f}}(\widetilde{\mathbf{x}},\mathbf{u}) = \alpha\,\mathbf{f}(\widetilde{\mathbf{x}}/\alpha,\mathbf{u})$, $\widetilde{\mathbf{g}}(\widetilde{\mathbf{x}}) = \mathbf{g}(\widetilde{\mathbf{x}}/\alpha)$, $\widetilde{\mathbf{x}}_0 = \alpha\,\mathbf{x}_0$, the triplets $(\mathbf{f},\mathbf{g},\mathbf{x}_0)$ and $(\widetilde{\mathbf{f}},\widetilde{\mathbf{g}},\widetilde{\mathbf{x}}_0)$ identify the same model.

Because of Remark 5.1, the best-approximation problem (5.7) might be ill-posed. Indeed, if the spaces $\widehat{\mathcal{F}}$, $\widehat{\mathcal{G}}$ and $\widehat{\mathcal{X}}$ are wide enough to contain both $(\mathbf{f}, \mathbf{g}, \mathbf{x}_0)$ and – according to (5.15) – their equivalent counterparts $(\widetilde{\mathbf{f}}, \widetilde{\mathbf{g}}, \widetilde{\mathbf{x}}_0)$, the solution of problem (5.7) may lose uniqueness in terms of its $(\mathbf{f}, \mathbf{g}, \mathbf{x}_0)$ representation. This is certainly an issue since non-uniqueness can deteriorate the performance of the optimization algorithm. Nevertheless, we can reduce the size of the spaces $\widehat{\mathcal{F}}$, $\widehat{\mathcal{G}}$ and $\widehat{\mathcal{X}}$ by imposing specific constraints on the solution to choose a priori a representative solution for a given class of equivalent solutions. In such a way we can restrict the design space for the optimization problem without ruling out possible solutions, thus reducing its complexity. We now show two possible ways of performing this task.

Partial disambiguation by constraining $\mathbf{x}_0$

Consider a model $\boldsymbol{\varphi}_{\mathbf{f},\mathbf{g},\mathbf{x}_0} \in \Phi$. Consider then the (invertible) state transformation $\widetilde{\mathbf{x}} = \mathbf{h}_1(\mathbf{x}) = \mathbf{x} - \mathbf{x}_0$. By applying the transformation (5.15), we get an equivalent model $\boldsymbol{\varphi}_{\widetilde{\mathbf{f}},\widetilde{\mathbf{g}},\widetilde{\mathbf{x}}_0}$, where $\widetilde{\mathbf{f}}(\widetilde{\mathbf{x}}, \mathbf{u}) = \mathbf{f}(\widetilde{\mathbf{x}} + \mathbf{x}_0, \mathbf{u})$, $\widetilde{\mathbf{g}}(\widetilde{\mathbf{x}}) = \mathbf{g}(\widetilde{\mathbf{x}} + \mathbf{x}_0)$ and $\widetilde{\mathbf{x}}_0 = \mathbf{0}$. Thanks to this property, when we look for the solution of the best-approximation problem (5.7) we suppose, without loss of generality that $\mathbf{x}_0 = \mathbf{0}$. This is equivalent to reducing the set of possible initial states to the singleton $\widehat{\mathcal{X}} = \{\mathbf{0}\}$, or equivalently, to minimize the cost functional J under the constraint $\mathbf{x}_0 = \mathbf{0}$. The statement of the best-approximation problem improves since the number of design variables decreases (the design variables are now just $\mathbf{f}$ and $\mathbf{g}$) and we have disambiguated among a number of equivalent solutions, without ruling out possible solutions.

Partial disambiguation by constraining $\mathbf{g}$ and $\mathbf{x}_0$

Consequence of Remark 5.1 is that the state variables $\mathbf{x}$ are just auxiliary variables to track the time evolution of the internal state of the model, not necessarily inferring a clear physical interpretation. There is thus large freedom in their choice. Consider the case when $n \geq N_y$: one could possibly decide a priori to force the first N_y state variables $x_1, \ldots, x_{N_y}$ to coincide with the outputs $y_1, \ldots, y_{N_y}$. A natural question is then the following: given a model $\boldsymbol{\varphi}_{\mathbf{f},\mathbf{g},\mathbf{x}_0}$, is it always possible to rewrite it in an equivalent form such that the first N_y state variables coincide with the output itself? If the answer is affirmative, then we can restrict ourselves to models such that $\mathbf{g}(\mathbf{x})$ is the function extracting the first N_y component of a vector, which we denote by $\boldsymbol{\pi}^{N_y}(\mathbf{x}) = (x_1\,, x_2\,, \ldots\,, x_{N_y})^T$.

To answer this question, consider a model $\boldsymbol{\varphi}_{\mathbf{f},\mathbf{g},\mathbf{x}_0} \in \Phi$ and suppose that there exists a smooth function $\mathbf{q}\colon \mathbb{R}^n \to \mathbb{R}^{n-N_y}$ – we will address later the existence issue – such that $\mathbf{h}_2(\mathbf{x}) = (\mathbf{g}^T(\mathbf{x}), \mathbf{q}^T(\mathbf{x}))^T$ is invertible (where $\mathbf{g}(\mathbf{x}) \in \mathbb{R}^{N_y}$, $\mathbf{q}(\mathbf{x}) \in \mathbb{R}^{n-N_y}$ and thus $\mathbf{h}_2(\mathbf{x}) \in \mathbb{R}^n$). In such a case, by applying the transformation (5.15) with $\mathbf{h}_2$, we get the equivalent model $\boldsymbol{\varphi}_{\widetilde{\mathbf{f}},\widetilde{\mathbf{g}},\widetilde{\mathbf{x}}_0}$ where:

$$\begin{aligned} \widetilde{\mathbf{f}}(\widetilde{\mathbf{x}}, \mathbf{u}) &= (\nabla \mathbf{h}_2 \circ \mathbf{h}_2^{-1})(\widetilde{\mathbf{x}})\ \mathbf{f}(\mathbf{h}_2^{-1}(\widetilde{\mathbf{x}}), \mathbf{u}), \\ \widetilde{\mathbf{g}}(\widetilde{\mathbf{x}}) &= \boldsymbol{\pi}^{N_y}(\widetilde{\mathbf{x}}), \\ \widetilde{\mathbf{x}}_0 &= (\mathbf{g}^T(\mathbf{x}_0), \mathbf{q}^T(\mathbf{x}_0))^T, \end{aligned} \tag{5.16}$$

for which the desired property, that the output is given by the first N_y state variables, holds. We notice that, in the expression of the initial condition $\widetilde{\mathbf{x}}_0$, we can substitute $\mathbf{g}(\mathbf{x}_0) = \mathbf{y}_0$, which is available from the measurements. Moreover, as in the previous case, we may set, without loss of generality, $\mathbf{q}(\mathbf{x}_0) = \mathbf{0}$ (this can be obtained by

applying once again (5.15) with the transformation $\mathbf{h}_3(\mathbf{x}) = \mathbf{h}_2(\mathbf{x}) - (\mathbf{0}^T, \mathbf{q}^T(\mathbf{x}_0))^T)$. To summarize, we get a model in the form:

$$\begin{cases} \dot{\mathbf{x}}(t) &= \mathbf{f}(\mathbf{x}(t), \mathbf{u}(t)) \qquad t \in (0, T], \\ \mathbf{x}(0) &= (\mathbf{y}_0^T, \mathbf{0}^T)^T, \end{cases} \tag{5.17}$$

where the state is written in the form $\mathbf{x} = (\mathbf{y}^T, \mathbf{z}^T)^T$, where $\mathbf{z}(t)$ are the other auxiliary variables. We have not ruled out yet all the ambiguity since, being the output transparent to such auxiliary variables, the latter can be still subject to invertible transformations which does not affect the input-output map of the model; nonetheless, the size of design space has been dramatically reduced since the unique design variable left is $\mathbf{f}$. We notice that this reduction is afforded by setting $\widehat{\mathcal{G}} = \{\boldsymbol{\pi}^{N_y}\}$ and $\widehat{\mathcal{X}} = \{(\mathbf{y}_0^T, \mathbf{0}^T)^T\}$. We have thus shown that all the models admitting the existence of a function $\mathbf{q}\colon \mathbb{R}^n \to \mathbb{R}^{n-N_y}$ such that $\mathbf{h}_2(\mathbf{x}) = (\mathbf{g}^T(\mathbf{x}), \mathbf{q}^T(\mathbf{x}))^T$ is invertible are in fact equivalent to a model in the form of (5.17).

Clearly, this hypothesis is not fulfilled by every model $\boldsymbol{\varphi}_{\mathbf{f},\mathbf{g},\mathbf{x}_0}$. If, for instance, the outputs $y_1, \ldots, y_{N_y}$ are linearly dependent, then $\mathbf{h}_2$ cannot be invertible. However, this case does not have any practical interest since in such case the dimension of the output can be reduced. Conversely, let us consider a point $\mathbf{x}^*$, and suppose that $\nabla\mathbf{g}(\mathbf{x}^*)$ has full rank. Then, let $\{\mathbf{v}_i\}_{i=1}^{n-N_y}$ be an orthonormal basis of $\mathrm{Col}(\nabla\mathbf{g}(\mathbf{x}^*)^T)^\perp$. By defining $q_i(\mathbf{x}) := (\mathbf{x} - \mathbf{x}^*) \cdot \mathbf{v}_i$ for $i = 1, \ldots, n - N_y$, the Jacobian of $\mathbf{h}_2(\mathbf{x}) = (\mathbf{g}^T(\mathbf{x}), \mathbf{q}^T(\mathbf{x}))^T$ has full-rank and $\mathbf{h}_2(\mathbf{x})$ is thus locally invertible. Even if this property holds just locally, the message is that the constraint $\mathbf{g} = \boldsymbol{\pi}^{N_y}$ keeps virtually intact the capacity of the class of models to approximate a given HF model. In Sec. 5.4.2 we will address numerically this issue.

5.2.5 The best-approximation problem

We will address both the cases considered in Sec. 5.2.4, namely:

1. $\widehat{\mathcal{X}} = \{\mathbf{0}\}$, which we refer to as *output-outside-the-state* (the output is a function of the state, but it is not part of the state);
2. $\widehat{\mathcal{G}} = \{\boldsymbol{\pi}^{N_y}\}$ and $\widehat{\mathcal{X}} = \{(\mathbf{y}_0^T, \mathbf{0}^T)^T\}$, which we refer to as *output-inside-the-state* (the first N_y state variables coincide with the output variables).

We notice that the second approach is available only for $n \geq N_y$. In both the cases, $\mathbf{x}_0$ is given and thus it is not counted as a design variable. Therefore, the best-approximation problem, in the most general case, consists of:

- Collecting the input-output observations (5.6) of the HF model to be approximated (i.e. to be reduced or to be identified).
- Selecting a suitable state dimension $n \geq 1$ for the ROM, the subset $\widehat{\mathcal{F}}$ and, in the output-outside-the-state case, the subset $\widehat{\mathcal{G}}$.
- Solving the abstract problem (5.7); this reads, in the output-outside-the-state case:

$$\begin{cases} \min\limits_{\mathbf{f}\in\widehat{\mathcal{F}},\mathbf{g}\in\widehat{\mathcal{G}}} & \frac{1}{2}\sum_{j=1}^{N_s}\int_0^T |\widehat{\mathbf{y}}_j(t) - \mathbf{g}(\mathbf{x}_j(t))|^2 dt \\ \text{s.t.} & \dot{\mathbf{x}}_j(t) = \mathbf{f}(\mathbf{x}_j(t), \widehat{\mathbf{u}}_j(t)), \quad t \in (0, T], \quad j = 1, \ldots, N_s, \\ & \mathbf{x}_j(0) = \mathbf{x}_0, \quad j = 1, \ldots, N_s, \end{cases} \tag{5.18}$$

where $\mathbf{x}_0 = \mathbf{0}$, while in the output-inside-the-state case:

$$\begin{cases} \min\limits_{\mathbf{f}\in\widehat{\mathcal{F}}} & \frac{1}{2}\sum_{j=1}^{N_s}\int_0^T |\widehat{\mathbf{y}}_j(t) - \boldsymbol{\pi}^{N_y}(\mathbf{x}_j(t))|^2 dt \\ \text{s.t.} & \dot{\mathbf{x}}_j(t) = \mathbf{f}(\mathbf{x}_j(t), \widehat{\mathbf{u}}_j(t)), \quad t \in (0,T], \quad j = 1,\dots,N_s, \\ & \mathbf{x}_j(0) = \mathbf{x}_0, \quad j = 1,\dots,N_s, \end{cases} \tag{5.19}$$

where $\mathbf{x}_0 = (\mathbf{y}_0^T, \mathbf{0}^T)^T$. We notice that (5.19) can be seen as a particular case of (5.18) (by setting $\widehat{\mathcal{G}} = \{\boldsymbol{\pi}^{N_y}\}$); therefore, in the following we will confine ourselves, without loss of generality, to (5.18).

5.2.6 On the choice of the sets $\widehat{\mathcal{F}}$ and $\widehat{\mathcal{G}}$

The richness of the spaces $\widehat{\mathcal{F}}$ (and, in the output-outside-the-state case, $\widehat{\mathcal{G}}$) should be chosen according to the Occam's razor principle of parsimony [GJGGJ03; MMK03] (see also Sec. 4.2). Indeed, one should avoid the two opposite situations: when too poor spaces are considered, the expressive power of the model class $\Phi^{\widehat{\mathcal{F}},\widehat{\mathcal{G}},\widehat{\mathcal{X}}}$ is too small to capture the complexity of the HF model, thus resulting in underfitting of the training data; on the other hand, if $\widehat{\mathcal{F}}$ (and $\widehat{\mathcal{G}}$) are too rich (in the extreme, $\widehat{\mathcal{F}} = \mathcal{F}_n$ and $\widehat{\mathcal{G}} = \mathcal{G}_n$), we expect a very good match on the training set (5.6), but this typically leads to overfitting (see e.g. [RG01]). The compromise stays in the middle, where the so-called Occam's hill is located [RG01], i.e. where the richness of the spaces $\widehat{\mathcal{F}}$ and $\widehat{\mathcal{G}}$ is enough to satisfactorily reproduce the observations (5.6), but not beyond.

5.2.7 Solution strategy

The unknowns of problem (5.19) and, more in general, (5.18) are the functions $\mathbf{f}$ and, in the output-outside-the-state case, also $\mathbf{g}$. We are thus performing optimization in function spaces. One should look at the first-order optimality conditions for this optimization problem, when $\widehat{\mathcal{F}} = \mathcal{F}_n$ and $\widehat{\mathcal{G}} = \mathcal{G}_n$. With this aim, we write the Lagrangian functional associated to problem (5.18). Thus, we introduce a family of Lagrange multipliers $\mathbf{w}_j \in \mathcal{C}^0([0,T];\mathbb{R}^n)$, for $j = 1,\dots,N_s$, associated to the constraints given by the state equations:

$$\begin{aligned} \mathcal{L}(\mathbf{f},\mathbf{g},\{\mathbf{x}_j\}_j,\{\mathbf{w}_j\}_j) = {} & \frac{1}{2}\sum_{j=1}^{N_s}\int_0^T |\widehat{\mathbf{y}}_j(t) - \mathbf{g}(\mathbf{x}_j(t))|^2 dt \\ & - \sum_{j=1}^{N_s}\int_0^T \mathbf{w}_j(t)\cdot(\dot{\mathbf{x}}_j(t) - \mathbf{f}(\mathbf{x}_j(t),\widehat{\mathbf{u}}_j(t)))\,dt \\ & - \sum_{j=1}^{N_s}\mathbf{w}_j(0)\cdot(\mathbf{x}_j(0) - \mathbf{x}_0). \end{aligned} \tag{5.20}$$

The adjoint equations are recovered by setting to zero the variation of the Lagrangian with respect to the state variables, for any $j = 1,\dots,N_s$:

$$\begin{cases} -\dot{\mathbf{w}}_j(t) = \nabla_{\mathbf{x}}\mathbf{g}(\mathbf{x}_j(t))^T\,(\mathbf{g}(\mathbf{x}_j(t)) - \widehat{\mathbf{y}}_j(t)) + \nabla_{\mathbf{x}}\mathbf{f}(\mathbf{x}_j(t),\widehat{\mathbf{u}}_j(t))^T\,\mathbf{w}_j(t) & t \in [0,T), \\ \mathbf{w}_j(T) = \mathbf{0}. \end{cases} \tag{5.21}$$

The first-order optimality conditions are obtained by setting equal to zero the Gâteaux derivative of the objective functional J with respect to the two unknowns $\mathbf{f} \in \mathcal{F}_n$ and $\mathbf{g} \in \mathcal{G}_n$, for any possible variations $\delta\mathbf{f} \in \mathcal{F}_n$ and $\delta\mathbf{g} \in \mathcal{G}_n$:

$$\begin{cases} \langle \dfrac{\partial J}{\partial \mathbf{f}}, \delta\mathbf{f} \rangle = \displaystyle\sum_{j=1}^{k} \int_0^T \delta\mathbf{f}(\mathbf{x}_j(t), \widehat{\mathbf{u}}_j(t)) \cdot \mathbf{w}_j(t) dt = 0 & \forall\, \delta\mathbf{f} \in \mathcal{F}_n, \\ \langle \dfrac{\partial J}{\partial \mathbf{g}}, \delta\mathbf{g} \rangle = \displaystyle\sum_{j=1}^{k} \int_0^T \delta\mathbf{g}(\mathbf{x}_j(t)) \cdot (\mathbf{g}(\mathbf{x}_j(t)) - \widehat{\mathbf{y}}_j(t))\, dt = 0 & \forall\, \delta\mathbf{g} \in \mathcal{G}_n. \end{cases} \tag{5.22}$$

In Eqs. (5.21)–(5.22), which state the conditions that the unknowns $\mathbf{f}$ and $\mathbf{g}$ must fulfil to yield a (local) minimum of the cost functional J, $\mathbf{f}$ and $\mathbf{g}$ are evaluated just in $\mathbf{x}_j(t)$ and $\widehat{\mathbf{u}}_j(t)$ for $j = 1, \ldots, N_s$ and $t \in [0, T]$. However, the trajectories of $\mathbf{x}_j(t)$ and $\widehat{\mathbf{u}}_j(t)$ do not fill the whole spaces $\mathbb{R}^n$ and U. Therefore, the problem of fullfilling Eqs. (5.21)–(5.22) is ill–posed, being underdetermined. This has to be compensated for by proper regularization of the unknown themselves. Hence, the differentials in (5.22) cannot be written in gradient form and thus gradient descent strategies cannot be applied for an iterative optimization procedure.

Our strategy is that of parametrizing both the functions $\mathbf{f}$ and $\mathbf{g}$ by a finite set of real parameters, which we denote respectively $\boldsymbol{\mu} \in \mathbb{R}^{N_f}$ and $\boldsymbol{\nu} \in \mathbb{R}^{N_g}$, and then tackling problem (5.18) by optimizing with respect to $\boldsymbol{\mu}$, $\boldsymbol{\nu}$ (to stress the parametrization, we write $\mathbf{f}(\mathbf{x}, \mathbf{u}; \boldsymbol{\mu})$ and $\mathbf{g}(\mathbf{x}; \boldsymbol{\nu})$). In this way the desired regularization is obtained by controlling the size of N_f and N_g since the complexity of candidate models is controlled by N_f and N_g. Indeed, by writing the variation of the functions as $\delta\mathbf{f} = \nabla_{\boldsymbol{\mu}}\mathbf{f}\, \delta\boldsymbol{\mu}$ and $\delta\mathbf{g} = \nabla_{\boldsymbol{\nu}}\mathbf{g}\, \delta\boldsymbol{\nu}$, the sensitivity of the objective functional can now be written in gradient form:

$$\begin{cases} \nabla_{\boldsymbol{\mu}} J = \displaystyle\sum_{j=1}^{k} \int_0^T \nabla_{\boldsymbol{\mu}}\mathbf{f}(\mathbf{x}_j(t), \widehat{\mathbf{u}}_j(t); \boldsymbol{\mu})^T\, \mathbf{w}_j(t) dt, \\ \nabla_{\boldsymbol{\nu}} J = \displaystyle\sum_{j=1}^{k} \int_0^T \nabla_{\boldsymbol{\nu}}\mathbf{g}(\mathbf{x}_j(t); \boldsymbol{\nu})^T\, (\mathbf{g}(\mathbf{x}_j(t); \boldsymbol{\nu}) - \widehat{\mathbf{y}}_j(t))\, dt. \end{cases} \tag{5.23}$$

We notice that the same result can be obtained by differentiating the Lagrangian functional (5.20) with respect to $\boldsymbol{\mu}$ and $\boldsymbol{\nu}$. In Sec. 5.3 we will derive the discrete counterpart of (5.21) and (5.23), employed to numerically solve problem (5.18).

The parametrization of $\mathbf{f}$ and $\mathbf{g}$ can be obtained in different manners, such as by polynomials, piecewise polynomials, truncated Fourier series, splines, NURBS, etc. Here we choose to represent them by means of ANNs, that can be seen as nonlinear maps parametrized by a finite number of real parameters (see Sec. 5.3.1). Our choice is driven by the universal approximation properties of ANNs (see [Cyb89; SX19; He+18]) and their recognized properties of learning from data.

5.3 Optimization strategy

We address the solution of the model reduction problem, formulated as the constrained optimization problem (5.18). We briefly recall ANNs and their universal approximation properties and, then, we show how ANNs can be employed to approximate time-dependent models.

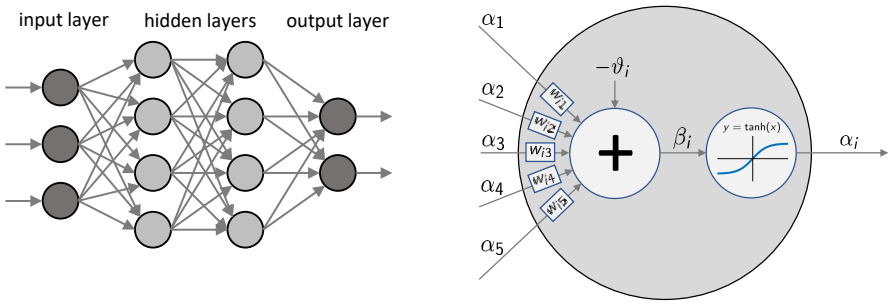

(a) Feed-forward ANN

(b) Action of the i-th neuron

Figure 5.2: Scheme of a feed-forward ANN with two hidden layers (a) and of a general neuron (b).

5.3.1 Artificial Neural Networks

An ANN consists of a number of simple processing units (the *neurons*), each one incorporating a linear and a nonlinear application, interconnected to form a complex network (see e.g. [Yeg09]). We consider feed-forward ANNs (known as multilayer perceptrons), consisting of n_L layers of neurons (the input layer, $n_L - 2$ hidden layers, and the output layer), where each neuron of a given layer has a connection (or synapse) towards each neuron of the next layer (see Fig. 5.2). A feed-forward ANN represents a class of functions written as:

$$\mathbf{f}(\mathbf{p}; \boldsymbol{\mu}) = \mathbf{W}_{n_L-1}\, f_{\text{act}}\left(\dots \mathbf{W}_2\, f_{\text{act}}\left(\mathbf{W}_1\, \mathbf{p} - \boldsymbol{\vartheta}_1\right) - \boldsymbol{\vartheta}_2 \dots\right) - \boldsymbol{\vartheta}_{n_L-1}, \tag{5.24}$$

where $\mathbf{p} \in \mathbb{R}^{n_I}$ is the input vector and $\boldsymbol{\mu} \in \mathbb{R}^{N_f}$ is the parameters vector, collecting the entries of the weights matrices $\mathbf{W}_i$ and of the bias vectors $\boldsymbol{\vartheta}_i$. The action of the nonlinear activation function f_{act} must be interpreted component-wise. In this thesis, we use the sigmoidal activation function $f_{\text{act}}(s) = \tanh(s)$.

The calculation by means of the chain rule of the sensitivity of the ANN output with respect to the input $\mathbf{p}$ or to the parameters $\boldsymbol{\mu}$ (which we denote respectively by $\nabla_{\mathbf{p}}\mathbf{f}$ and $\nabla_{\boldsymbol{\mu}}\mathbf{f}$) gives rise to the so-called *back-propagation* [Yeg09].

In virtue of the *universal approximation theorem* [Cyb89], ANNs with a single hidden layer can approximate with arbitrarily small error any continuous function on a compact set, provided that a sufficient number of hidden neurons are employed.

Normalization

Even if ANNs can work with data values spanning different order of magnitudes, their performance is optimal when both input and output data are normalized. Therefore, before training the network, we normalize both the input $\mathbf{u}$ and the output $\mathbf{y}$ so that their components take values in the interval $[-1, 1]$. Moreover, since the output of the ANN representing $\mathbf{f}$ are time derivatives, we also normalize time with respect to the fastest time scale associated with the HF model (5.1), which can be inferred from the training set.

Normalizing inputs, outputs and time scales do not ensure that the state variables (or just the hidden variables in the output-inside-the-state case) lay in the range $[-1, 1]$, because of their hidden nature (see Sec. 5.2.4). Therefore, at each optimization

epoch, if the mean square value of a component of the state exceeds a lower or an upper bound (that we set to 0.1 and 2 respectively), we renormalize it. To perform this task, we exploit the fact that the parameters of the ANN arising from another ANN after an invertible and affine change of variables can be derived as follows. Consider the following affine transformation of both the input and the output of the ANN $\mathbf{q} = \mathbf{f}(\mathbf{p}; \boldsymbol{\mu})$, i.e. $\widetilde{\mathbf{p}} = \mathbf{A}\mathbf{p} + \mathbf{b}$, $\widetilde{\mathbf{q}} = \mathbf{C}\mathbf{q} + \mathbf{d}$. By simple calculations it turns out that the weights $\widetilde{\boldsymbol{\mu}}$ such that $\widetilde{\mathbf{q}} = \mathbf{f}(\widetilde{\mathbf{p}}; \widetilde{\boldsymbol{\mu}})$ are obtained by substituting the weights and the biases associated to the first and last layers of synapses as follows:

$$\widetilde{\mathbf{W}}_1 = \mathbf{W}_1\mathbf{A}^{-1}, \qquad \widetilde{\boldsymbol{\vartheta}}_1 = \boldsymbol{\vartheta}_1 - \mathbf{W}_1\mathbf{A}^{-1}\mathbf{b},$$
$$\widetilde{\mathbf{W}}_{n_L-1} = \mathbf{C}\mathbf{W}_{n_L-1}, \qquad \widetilde{\boldsymbol{\vartheta}}_{n_L-1} = \mathbf{C}\boldsymbol{\vartheta}_{n_L-1} - \mathbf{d}.$$

5.3.2 Representation of the unknowns in terms of ANN

Motivated by the universal approximation property of ANNs, we choose the spaces of candidate functions $\widehat{\mathcal{F}}$ and $\widehat{\mathcal{G}}$ as subsets of the space of functions represented by ANNs. We denote by $\mathcal{F}_n^{\text{ANN}}$ the space of ANNs with $n + N_u$ input neurons and n output neurons and by $\mathcal{G}_n^{\text{ANN}}$ the space of ANNs with n and N_y input and output neurons, respectively. We have the following result:

Proposition 5.4. *If U is compact, the space of ANN models $\Phi^{\mathcal{F}_n^{ANN},\mathcal{G}_n^{ANN},\mathcal{X}_n}$ is dense in the model space $\Phi^{\mathcal{F}_n,\mathcal{G}_n,\mathcal{X}_n}$.*

Proof. ANNs are by construction Lipschitz continuous, being the composition of Lipschitz continuous functions; thus, we have $\mathcal{F}_n^{\text{ANN}} \subset \mathcal{F}_n$ and $\mathcal{G}_n^{\text{ANN}} \subset \mathcal{G}_n$. Properties (5.10) and (5.11) hold by the universal approximation theorem [Cyb89]. Hence, the thesis follows from Prop. 5.3. □

We conclude that models represented by ANNs are universal approximators of the class of models described by systems of ODEs.

5.3.3 Discretization of the state equation and of the objective functional

In order to numerically approximate problem (5.18), we discretize both the state equation (5.2) and the objective functional J (Eq. (5.8)). We split the time domain $[0, T]$ into a collection of time instants $0 = t_0 < t_1 < \cdots < t_M = T$. For simplicity, we consider the case of constant time step Δt (i.e. $t_k = k\Delta t$ for $k = 0, \ldots, M$) as the generalization to the varying time step case is straightforward. On the other hand, it is convenient to consider the case when the experiments have different durations. Therefore, we suppose that the j-th experiment takes place in the interval $[0, T_j]$, where $T_j = M_j\Delta t$ and we denote $\mathbf{u}_j^k = \widehat{\mathbf{u}}_j(t_k) \in U$ and $\mathbf{y}_j^k = \widehat{\mathbf{y}}_j(t_k) \in Y$ the input and the output at discrete times. The discretized version of the objective functional J thus reads

$$\mathcal{J} = \frac{1}{2}\Delta t \sum_{j=1}^{N_s} \sum_{k=0}^{M_j-1} |\mathbf{y}_j^k - \mathbf{g}(\mathbf{x}_j^k; \boldsymbol{\nu})|^2. \tag{5.25}$$

To simplify as much as possible the computational burden of the numerical solution of the state equation, which has to be performed many times in the optimization loop,

we choose to discretize it by means of the forward Euler scheme. Thus, the discrete counterpart of problem (5.18) reads:

$$\begin{cases} \min\limits_{(\boldsymbol{\mu},\boldsymbol{\nu})\in\mathbb{R}^{N_f+N_g}} & \frac{1}{2}\Delta t \sum_{j=1}^{N_s}\sum_{k=0}^{M_j-1} |\mathbf{y}_j^k - \mathbf{g}(\mathbf{x}_j^k;\boldsymbol{\nu})|^2 \\ \text{s.t.} & \mathbf{x}_j^{k+1} = \mathbf{x}_j^k + \Delta t\, \mathbf{f}(\mathbf{x}_j^k, \mathbf{u}_j^k;\boldsymbol{\mu}), \quad k=0,\dots,M_j-1, \quad j=1,\dots,N_s, \\ & \mathbf{x}_j^0 = \mathbf{x}_0, \quad j=1,\dots,N_s. \end{cases} \tag{5.26}$$

We notice that, after time discretization, the ANN model of Eq. (5.26) has a structure resembling that of a *recurrent neural network* (RNN), that is an ANN whose internal state is fed back to the input after each evaluation of the network (see e.g. [Hay09]). RNNs are widely used for Machine Learning tasks involving sequential inputs, such as handwriting recognition, speech recognition and natural language processing, and also for time series prediction [Gra13; Hin+12; CMA94]. However, the approach presented in the present work is more general since it allows to recast the MOR problem within the setting of a best-approximation problem of a differential equation. Moreover, by addressing the problem at the continuous level and thanks to the setting of (5.14), the ROM that we obtain by solving the best-approximation problem is independent of the RNN structure used in the training stage. In other words, once the optimization problem in the discrete setting (5.26) has been solved (i.e. the ANN has been trained), the ROM is available in the form of Eq. (5.2). This allows more flexibility in the choice of the time discretization scheme and time step size than with RNN, wherein the forward Euler scheme is exclusively used with fixed Δt. A further advantage is the possibility of coupling the ROM problem with other mathematical models.

Finally, we notice that the RNN structure resulting by the time discretization is not restricted to this specific choice of time stepping scheme; therefore, it is preserved by employing higher-order methods, such as Runge-Kutta schemes.

5.3.4 Training the ANN: optimization algorithm

Problem (5.26) can be written in the form of the following nonlinear least-squares problem:

$$\min_{\boldsymbol{\xi}} \frac{1}{2}|\mathbf{r}(\boldsymbol{\xi})|^2, \tag{5.27}$$

where $\boldsymbol{\xi} = (\boldsymbol{\mu}^T, \boldsymbol{\nu}^T)^T$ is the vector collecting all the design variables and $\mathbf{r}$ is the vector of residuals, containing all the terms in the following form, for $j = 1,\dots,N_s$, $k = 0,\dots,M_j-1$, $h = 1,\dots,N_y$:

$$r^{j,k,h} = \sqrt{\Delta t}\,(\mathbf{g}(\mathbf{x}_j^k;\boldsymbol{\nu}) - \mathbf{y}_j^k)\cdot\mathbf{e}_h,$$

where $\mathbf{e}_h$ denotes the h-th element of the canonical basis of $\mathbb{R}^{N_y}$. To numerically find an approximate solution of this minimization problem we employ the Levenberg-Marquardt method, which is designed for least-squares problems in the form (5.27) (see e.g. [NW06]). At each iteration k of the optimization loop, one finds the descent direction $\mathbf{d}^{(k)}$ by solving the following problem:

$$\left(\left(\nabla\mathbf{r}^{(k)}\right)^T\nabla\mathbf{r}^{(k)} + \lambda^{(k)}\mathbf{I}\right)\mathbf{d}^{(k)} = -\left(\nabla\mathbf{r}^{(k)}\right)^T\mathbf{r}^{(k)},$$

where $\lambda^{(k)} \geq 0$ is a weight and $\mathbf{r}^{(k)}$ denotes $\mathbf{r}(\boldsymbol{\xi}^{(k)})$. The update of the solution follows the rule $\boldsymbol{\xi}^{(k+1)} = \boldsymbol{\xi}^{(k)} + \gamma^{(k)}\mathbf{d}^{(k)}$, where the step length $\gamma^{(k)}$ is selected by means of line-search in such a way that the Wolfe conditions are fulfilled (see [NW06] for details). Specifically, in this thesis we employ the line-search Algorithm 3.5 in [NW06].

The Levenberg-Marquardt descent direction can be seen as a combination of the steepest-descent direction (which is recovered for $\lambda^{(k)} \gg 1$) with the Gauss-Newton direction ($\lambda^{(k)} = 0$), which is an approximation of the Newton direction obtained by neglecting the quadratic term in the computation of the Hessian. We choose $\lambda^{(k)} = \min\left\{|\mathbf{r}^{(0)}|^2, |(\nabla \mathbf{r}^{(k)})^T \mathbf{r}^{(k)}|\right\}$, which ensures superlinear convergence for the method, provided that the objective functional is twice continuously differentiable (see [GS11]).

We adopt a random initialization of the design variables $\boldsymbol{\xi}^{(0)}$, by taking independent samples within the standard normal distribution.

5.3.5 Computation of sensitivities

The Levenberg-Marquardt method requires the computation of the sensitivities of the residuals $r^{j,k,h}$ with respect to the unknown parameters $\boldsymbol{\mu}$ and $\boldsymbol{\nu}$. Since the map from $\boldsymbol{\mu}$ to the variables $\mathbf{x}_j^k$ is implicitly given by the state equation in (5.26), we employ the Lagrange multipliers method to compute the sensitivities. If one aims at computing the sensitivity of a quantity $Q = Q(\{\mathbf{x}_j^k\}_{j,k})$ with respect to $\boldsymbol{\mu}$, then, by introducing a family of Lagrange multipliers $\mathbf{w}_j^k$, the Lagrangian associated to the problem reads:

$$\begin{aligned}&\mathcal{L}(\boldsymbol{\mu}, \boldsymbol{\nu}, \{\mathbf{x}_j^k\}_{j,k}, \{\mathbf{w}_j^k\}_{j,k}) = Q(\{\mathbf{x}_j^k\}_{j,k}) \\ &- \sum_{j=1}^{N_s} \left[\sum_{k=1}^{M_j} \mathbf{w}_j^k \cdot \left(\mathbf{x}_j^k - \mathbf{x}_j^{k-1} - \Delta t\, \mathbf{f}(\mathbf{x}_j^{k-1}, \mathbf{u}_j^{k-1}; \boldsymbol{\mu})\right) + \mathbf{w}_j^0 \cdot \left(\mathbf{x}_j^0 - \mathbf{x}_0\right) \right].\end{aligned}$$

By setting the derivative of $\mathcal{L}$ with respect to the variables $\mathbf{x}_j^k$ equal to zero, it turns out that the dual variables $\mathbf{w}_j^k$ solve the following backward difference equations, for $j = 1, \ldots, N_s$:

$$\begin{cases} \mathbf{w}_j^{M_j} = \dfrac{\partial Q}{\partial \mathbf{x}_j^{M_j}}, \\ \mathbf{w}_j^k = \mathbf{w}_j^{k+1} + \Delta t\, \nabla_{\mathbf{x}} \mathbf{f}(\mathbf{x}_j^k, \mathbf{u}_j^k; \boldsymbol{\mu})^T\, \mathbf{w}_j^{k+1} + \dfrac{\partial Q}{\partial \mathbf{x}_j^k}, \qquad \text{for } k = 0, \ldots, M_j - 1. \end{cases} \tag{5.28}$$

Once the dual variables $\mathbf{w}_j^k$ are available, the gradient of Q with respect to $\boldsymbol{\mu}$ reads:

$$\nabla_{\boldsymbol{\mu}} Q = \frac{\partial Q}{\partial \boldsymbol{\mu}} + \Delta t \sum_{j=1}^{N_s} \sum_{k=1}^{M_j} \nabla_{\boldsymbol{\mu}} \mathbf{f}(\mathbf{x}_j^{k-1}, \mathbf{u}_j^{k-1}; \boldsymbol{\mu})^T\, \mathbf{w}_j^k.$$

By setting $Q = r^{j,m,h}$, we have, for $j = 1, \ldots, N_s$, $m = 0, \ldots, M_j - 1$:

$$\nabla_{\boldsymbol{\mu}} r^{j,m,h} = \Delta t \sum_{k=1}^{m} \nabla_{\boldsymbol{\mu}} \mathbf{f}(\mathbf{x}_j^{k-1}, \mathbf{u}_j^{k-1}; \boldsymbol{\mu})^T\, \mathbf{w}^k, \quad \nabla_{\boldsymbol{\nu}} r^{j,m,h} = \sqrt{\Delta t}\, \nabla_{\boldsymbol{\nu}} \mathbf{g}(\mathbf{x}_j^m; \boldsymbol{\nu})^T\, \mathbf{e}_h,$$

where

$$\begin{cases} \mathbf{w}^k = \mathbf{w}^{k+1} + \Delta t\, \nabla_{\mathbf{x}} \mathbf{f}(\mathbf{x}_j^k, \mathbf{u}_j^k; \boldsymbol{\mu})^T\, \mathbf{w}^{k+1}, \qquad \text{for } k = 0, \ldots, m-1, \\ \mathbf{w}^m = \sqrt{\Delta t}\, \nabla_{\mathbf{x}} \mathbf{g}(\mathbf{x}_j^k; \boldsymbol{\nu})^T\, \mathbf{e}_h. \end{cases} \tag{5.29}$$

Test case	Name	Source of HF model	N	N_u	N_y
1	Nonlinear pendulum	System of ODEs	2	2	1
2	Nonlinear transmission line circuit	System of ODEs	1000	1	1
3	Heat equation	Parabolic PDE	3721	9	3
4	Wave equation	Hyperbolic PDE	202	2	1

Table 5.1: Test cases list.

The line-search algorithm for determining the step length $\gamma^{(k)}$ also requires the computation of the gradient with respect to $\boldsymbol{\mu}$ and $\boldsymbol{\nu}$ of the discretized objective functional $\mathcal{J} = \frac{1}{2}\mathbf{r}^T\,\mathbf{r}$. If the residuals $\mathbf{r}$ and their gradient $\nabla\mathbf{r}$ has been already computed, the gradient of $\mathcal{J}$ can be recovered as $\nabla\mathbf{r}^T\mathbf{r}$. However, if it is not the case, it is more efficient to compute it by applying the above procedure with $Q = \mathcal{J}$, thus getting:

$$\nabla_{\boldsymbol{\mu}}\mathcal{J} = \Delta t \sum_{j=1}^{N_s}\sum_{k=1}^{M_j} \nabla_{\boldsymbol{\mu}}\mathbf{f}(\mathbf{x}_j^{k-1}, \mathbf{u}_j^{k-1}; \boldsymbol{\mu})^T\,\mathbf{w}_j^k,$$
$$\nabla_{\boldsymbol{\nu}}\mathcal{J} = \Delta t \sum_{j=1}^{N_s}\sum_{k=0}^{M_j-1} \nabla_{\mathbf{x}}\mathbf{g}(\mathbf{x}_j^k; \boldsymbol{\nu})^T\,(\mathbf{g}(\mathbf{x}_j^k; \boldsymbol{\nu}) - \mathbf{y}_j^k),$$

where

$$\begin{cases} \mathbf{w}_j^k = \mathbf{w}_j^{k+1} + \Delta t\,\nabla_{\mathbf{x}}\mathbf{f}(\mathbf{x}_j^k, \mathbf{u}_j^k; \boldsymbol{\mu})^T\,\mathbf{w}_j^{k+1} \\ \qquad\quad + \Delta t\,\nabla_{\mathbf{x}}\mathbf{g}(\mathbf{x}_j^k; \boldsymbol{\nu})^T\,(\mathbf{g}(\mathbf{x}_j^k; \boldsymbol{\nu}) - \mathbf{y}_j^k), \qquad \text{for } k = 0, \ldots, M_j - 1, \\ \mathbf{w}_j^{M_j} = \mathbf{0}, \end{cases} \tag{5.30}$$

which are the discrete counterparts of (5.21) and (5.23).

5.4 Numerical Results

In this section we assess the capability of the proposed approach through four test cases, summarized in Table 5.1. First, in Sec. 5.4.1, we consider the nonlinear pendulum problem. In virtue of the modest complexity of this test case ($N = 2$), we perform a sensitivity analysis on the network architecture, highlighting the Occam's hill (Sec. 5.2.6). Moreover, we can directly compare the internal dynamics of the ROMs with that of the HF model.

Next, to test the proposed reduction approach on large-scale problems, we consider an electric circuit with nonlinear elements, described by a nonlinear system of 1000 ODEs (Sec. 5.4.2). Finally, we consider a parabolic PDE, whose HF model is given by its Finite Element (FE) approximation, featuring about 4000 state variables (Sec.5.4.3), and an hyperbolic PDE (Sec.5.4.4).

All the results shown in this chapter are produced with the internally developed MATLAB library `model-learning`, publicly available in the online repository [Reg19]. In the same repository, also the datasets accompanying this chapter are available.

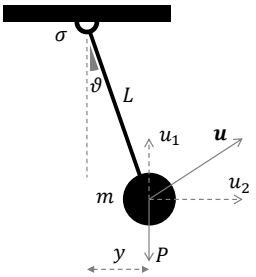

Figure 5.3: Nonlinear pendulum problem considered in Sec. 5.4.1

5.4.1 *Test case 1*: Nonlinear pendulum

Consider a mass m, subject to its weight P, suspended by a weightless inextensible string of length L and connected to a fixed support through a hinge subject to viscous damping with constant σ. The pendulum, starting from its resting condition, is subject to an external force $\mathbf{u}(t) = u_1(t)\mathbf{e}_1 + u_2(t)\mathbf{e}_2$. By denoting the angle formed with the vertical direction by $\vartheta(t)$, we have that the motion of the pendulum is described by the following ODE:

$$\begin{cases} \ddot{\vartheta}(t) = \frac{1}{Lm}\left(u_2(t)\cos\vartheta(t) + (u_1(t) - P)\sin\vartheta(t)\right) - \sigma\,\dot{\vartheta}(t) & t \in (0, T], \\ \vartheta(0) = 0,\ \dot{\vartheta}(0) = 0. \end{cases} \tag{5.31}$$

We set the constants values to $m = L = 1$, $P = 2$, $\sigma = 3$. Moreover, we set the external force $\mathbf{u} \in [-1, 1]^2$. Suppose that we are interested in predicting the horizontal displacement of the mass $y(t) = L\sin\vartheta(t)$ (in this case we drop the bold notation being the output a scalar), given the input $\mathbf{u}(t)$. The input-output map given by (5.31) fall within the concept of model introduced in Sec. 5.2.1, where $N_u = 2$, $N_y = 1$, $U = [-1, 1]^2$, $Y = [-1, 1]$. Moreover, this model can be written in the form (5.1), by setting $\mathbf{X} = (\vartheta, \dot{\vartheta})^T$ and thus we have $N = 2$.

For the discretization of the state equation (see Sec. 5.3.3), we set $\Delta t = 5 \cdot 10^{-2}$. Moreover, to mitigate the computational cost of the evaluation of the objective functional and its derivatives, we evaluate the error every 10 time steps. For this test, we consider the output-inside-the-state case.

Training, validation and test sets

The optimization of the ANN described in Sec. 5.3.4 is led by the set of experiments (5.6) collected from the HF model. The choice of such *training set* is crucial since it is expected to be representative of all the possible working regimes of the system. Moreover, it should be large enough to avoid overfitting of the ROM on the training set itself.

In this first example, we intentionally consider a poor training set, such that overfitting is likely to occur in order to better investigate the sensitivity of the proposed reduction approach with respect to n (i.e. the number of states) and to the complexity of the network. The training set is represented in Fig. 5.4. It comprises the step responses associated to different stationary values of the input, in the form $\mathbf{u}(t) = \bar{\mathbf{u}}\mathbb{1}_{[t_1,t_2]}(t)$ (notice that $\bar{\mathbf{u}}$ span all the set $U = [-1, 1]^2$) and four samples with oscillating input, obtained by sinusoids with different frequency, amplitude and mean

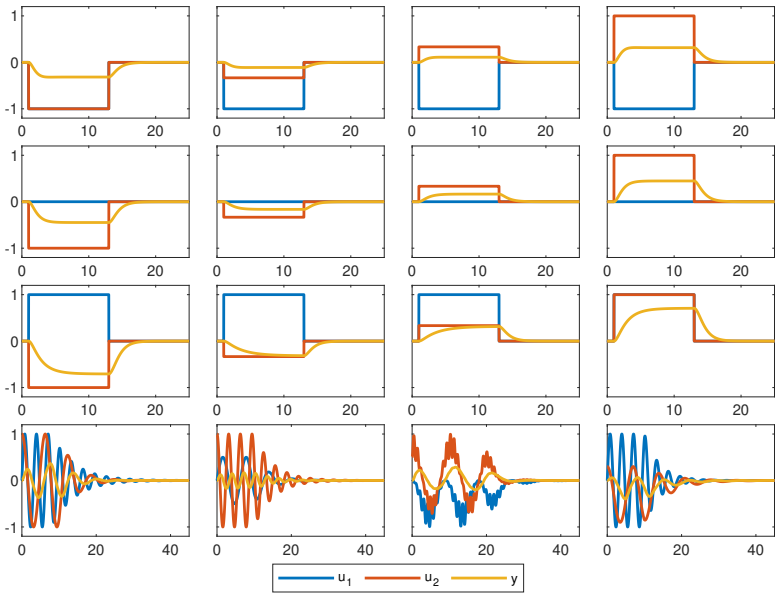

Figure 5.4: *Test case 1*: Training set.

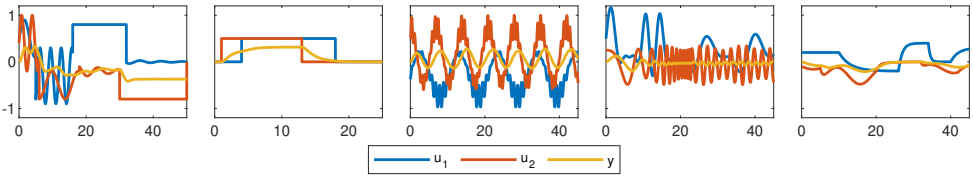

Figure 5.5: *Test case 1*: Validation set.

value. The frequency range of the signals is chosen in such a way that it covers several characteristic time scales of the considered HF model.

To monitor the ANN learning process, at each optimization epoch, we evaluate the performance of the ANN on a further set, that we call *validation set*. The comparison between the relative L^2 error on the training set (which we denote by $\mathcal{E}_{\text{train}}$) and the error on the validation set (which we denote by $\mathcal{E}_{\text{val}}$) allows to perform *regularization by early stopping* (see e.g. [Yeg09]): as long as the error on the validation set start increasing, we stop the optimization loop since this is an indication that overfitting occurs. In the validation set we place 5 samples, comprising several working regimes of the system (see Fig. 5.5). Notice that in this set we also switch from a regime to another inside the same sample, to monitor the capability of the model to cope with it.

Finally, when the optimization loop is completed, we test the performance of the ROM on a large-size *test set*, comprising step responses, oscillatory inputs and randomly generated ones. The test set amounts to 126 samples.

Sensitivity analysis of the network complexity

The objective functional $\mathcal{J}$ is non-convex and features several many local minima. As a consequence, the optimized ANN obtained by means of the strategy of Sec. 5.3.4 may

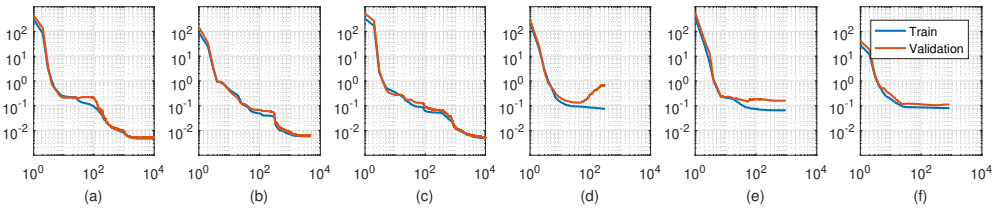

Figure 5.6: *Test case 1*: examples of evolution of the error on the training ($\mathcal{E}_{\text{train}}$) and validation sets ($\mathcal{E}_{\text{val}}$).

depend on the initialization of the ANN itself. Since we adopt a random initialization for the ANN, by running the proposed strategy several times with the same ANN architecture, we actually end up with very different results. This is intimately linked to the non-uniqueness of representation of a given model (see Remark 5.1): very different ANNs may represent the same model. We will go back to this issue in Sec. 5.4.1.

Fig. 5.6 shows the evolution, through the optimization process, of the error on the test ($\mathcal{E}_{\text{train}}$) and validation sets ($\mathcal{E}_{\text{val}}$) for different random initializations of the ANN . Cases (a)-(c) show "good" outcomes of the optimization process: both errors decrease until a minimum of the functional is reached; a very good correlation between the two errors is observed during the optimization process, thus indicating good performances of the learning process; the final levels of error for the test and validation set are comparable, thus we are not in the presence of overfitting. The remaining cases, in turn, show "bad" outcomes:

- In (d) the optimization proceeds well, until $\mathcal{E}_{\text{val}}$ starts increasing, which is a typical sign a overfitting. Notice that the online evaluation of $\mathcal{E}_{\text{val}}$ allows to detect this phenomenon and to perform early stop the optimization process.
- In (e), instead, a more subtle case of overfitting occurs since it originates in the early stages of the optimization and we do not observe an increase of $\mathcal{E}_{\text{val}}$.
- In (f) finally, even if we are not in presence of significant overfitting, the ANN is not performing well since the final levels of $\mathcal{E}_{\text{train}}$ and $\mathcal{E}_{\text{val}}$ are much higher than the usual values obtained with the same ANN architecture. In this case the optimization problem got stuck into a "bad" local minimum. Globalization strategies, such as Simulated Annealing (see e.g. [Pre+86]), can be selected to handle with this issue, even if this is beyond the scope of the present work.

In the following we perform a sensitivity analysis of the performance of the proposed reduction approach w.r.t. the complexity of the network, i.e. the number of hidden neurons, which we denote by N_{neurons}. For simplicity, we consider only the case of ANNs with a single hidden layer. Figure 5.7 shows the dependency of the performance of the proposed reduction approach on the number of hidden neurons, in the cases $n = 1$ and $n = 2$. Each cross is associated to a single test, while the coloured regions highlight the areas spanned by the test which did not get stuck into a "bad" local minimum (we tag a local minimum as "bad" if the error $\mathcal{E}_{\text{train}}$ is more than 10 times the best error obtained with the same ANN architecture).

Let us consider first the case $n = 1$. By switching form $N_{\text{neurons}} = 2$ to $N_{\text{neurons}} = 3$, thanks to the enhanced representative capacity of the ANN, the errors associated with the three sets significantly decrease (see Fig. 5.7a). However, by further increasing N_{neurons}, we are in presence of overfitting: even if $\mathcal{E}_{\text{train}}$ keeps decreasing, $\mathcal{E}_{\text{test}}$ and $\mathcal{E}_{\text{val}}$

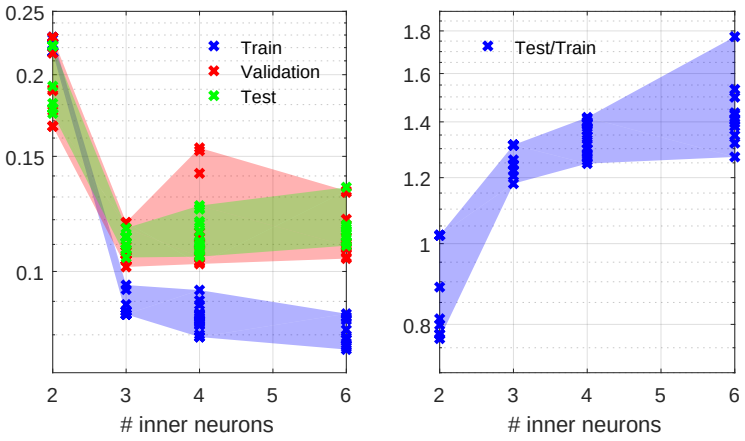

(a) $n = 1$

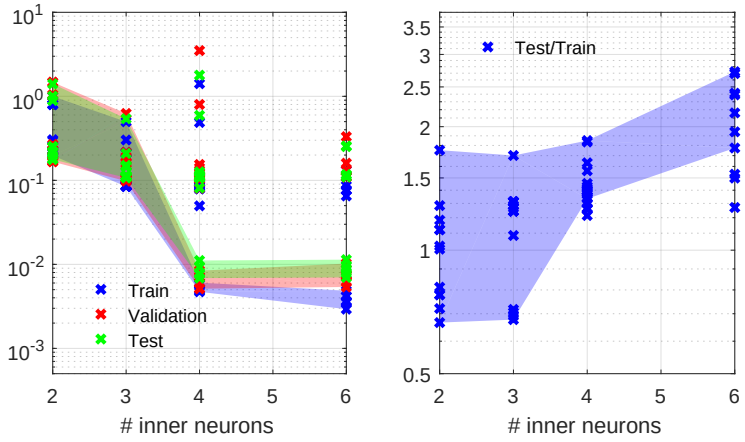

(b) $n = 2$

Figure 5.7: *Test case 1*: errors vs number of hidden neurons N_{neurons}, in the cases (a) $n = 1$ and (b) $n = 2$. For both the cases, the left plot shows the errors $\mathcal{E}_{\text{train}}$, $\mathcal{E}_{\text{val}}$ and $\mathcal{E}_{\text{test}}$, while the right plot shows the ratio $\mathcal{E}_{\text{test}}/\mathcal{E}_{\text{train}}$. Each cross represents the final result of a test (including when the tests gets stuck into a "bad" local minimum). Coloured regions represent the areas spanned by the tests, excluding the tests which got stuck into a "bad" local minimum.

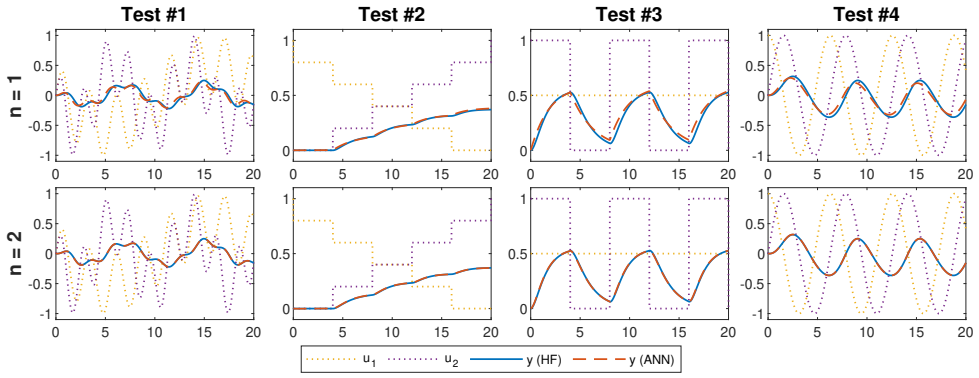

Figure 5.8: *Test case 1*: comparison of the exact solution (blue line) and the solution obtained with the ANN model (red line) in four different test cases. First row: one-variable model; Second column: two-variables model.

start increasing. This phenomenon is also evident from the right figure, showing the ratio $\mathcal{E}_{\text{test}}/\mathcal{E}_{\text{train}}$ increasing with the network complexity. Even if the issue of designing the training set falls beyond the purposes of the present work, we notice that with a richer training set the optimal number of neurons would probably increase, thus allowing to reach a better performance of the ROM.

We then consider the case $n = 2$ (see Fig. 5.7b). The introduction of a further state variable in the system, w.r.t. the case $n = 1$, translates in a significant increment of the model ability to faithfully reproduce the input-output map given by the HF model, as expected according to Prop. 5.2. Indeed, even if for $N_{\text{neurons}} \leq 3$ the errors are similar to the case $n = 1$, by increasing the network complexity the errors drop by one order of magnitude for $N_{\text{neurons}} = 4$, before slowly diverging (the training error $\mathcal{E}_{\text{train}}$ decreases, while the validation $\mathcal{E}_{\text{val}}$ and test error $\mathcal{E}_{\text{test}}$ slightly increase). We also notice the occurrence of tests which got stuck in "bad" local minima (highlighted in Fig. 5.7b by the presence of crosses outside the coloured areas) for $N_{\text{neurons}} \geq 4$, due to the raising of complexity of the landscape of $\mathcal{E}_{\text{train}}$ when the dimensionality of the design space increases.

To sum up, we select as best networks the ones minimizing the error on the test set for $N_{\text{neurons}} = 3$ in the case $n = 1$ and for $N_{\text{neurons}} = 4$ in the case $n = 2$, namely where the top of the Occam's hill is located in the two cases. Figure 5.8 shows the comparison of the results obtained in four test cases with the HF and the two selected ROMs (the first row refers to the model with $n = 1$, the second to the model obtained with $n = 2$).

What did the ANN actually learn?

The feasibility of the reduction approach proposed in this chapter is strictly related to the possibility of faithfully representing the state of the HF model (which we denote by $\mathbf{X}(t) \in \mathbb{R}^N$) by means of a lower-dimensional state $\mathbf{x}(t) \in \mathbb{R}^n$. If this is the case, then the knowledge of $\mathbf{x}(t)$ and $\mathbf{u}(t)$ provides enough information to compute, with just a little approximation, both the output $\mathbf{y}(t)$ and the evolution of the state of the system (that is to say the value of $\frac{d}{dt}\mathbf{x}(t)$).

We may thus interpret the learning process as that of implicitly building a map from the reduced-order state $\mathbf{x}$ to the full-order state $\mathbf{X}$, which is not directly observed,

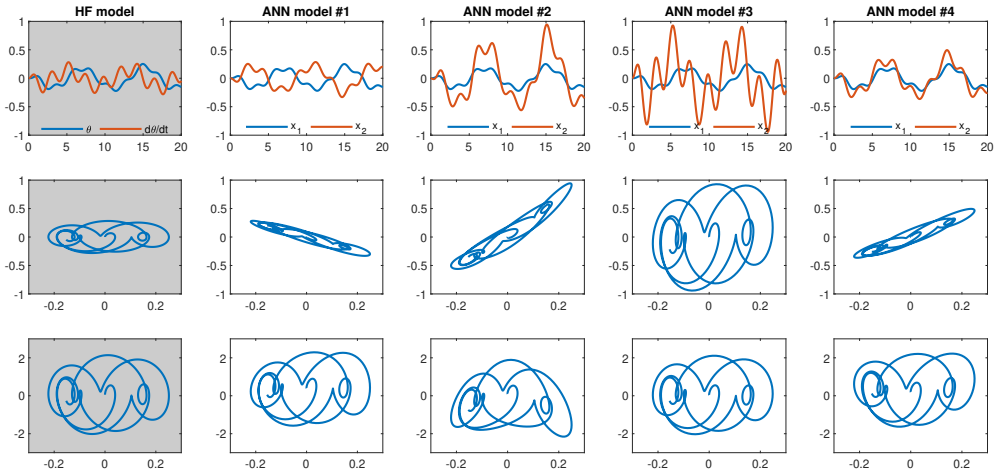

Figure 5.9: *Test case 1*: results of the test case considered in Sec. 5.4.1. Each column refers to a different model (first column: HF model; other columns: four different ANN models). First line: time evolution of the two state variables of the system (first column: ϑ and $\dot{\vartheta}$; other columns: x_1 and x_2). Second line: trajectories in the phase space (first column: $(\vartheta, \dot{\vartheta})$; other columns: (x_1, x_2)). Third line: trajectories in the $(\vartheta, \dot{\vartheta}''')$ phase space (first column) and (x_1, x_2''') phase space (other columns).

but it is observed only through its effects to the time evolution of $\mathbf{y}(t)$. This is somehow similar to projection-based MOR strategies (see Sec. 5.1.1), with the important differences that: (i) in this case the map is not explicitly built and thus is not available; (ii) while in projection-based methods the map is linear, here nonlinear mappings can be exploited; (iii) since the effects of the internal state $\mathbf{X}$ are seen just through $\mathbf{y}$, only the features which are relevant for the input-output map are exploited, whereas POD for example may extract features from the snapshots which do not provide a significant contribution to the input-output map.

As mentioned before, the ROM implicitly defines a map from the HF model state $\mathbf{X}(t)$ to the ROM state $\mathbf{x}(t)$. This map is not explicitly built. Moreover, as noticed in Remark 5.1, a model described by an ODE is invariant with respect to change of variables for its internal state $\widetilde{\mathbf{x}} = \mathbf{h}(\mathbf{x})$. For these reasons, it is usually troublesome to give a physical interpretation to the state variables of the ROM.

Let us consider the example addressed in this Section, for $n = N = 2$. This case may not be interesting in a MOR perspective, but it helps to shed light on the machinery behind the proposed reduction approach. Indeed, thanks to the choice $\mathbf{g}(\mathbf{x}) = \boldsymbol{\pi}^{N_y}$, we have, in principle, $x_1(t) = L \sin \vartheta(t)$. Consequently, we may speculate that the knowledge of the first variable of the ROM x_1 provides all the information needed to reconstruct the first variable of the HF model ϑ. Therefore, we expect that the second variable of the ROM x_2 provides the missing information to reconstruct $\dot{\vartheta}$. This does not necessarily entail that $\dot{\vartheta}$ is a function of x_2, but in general we have that $\dot{\vartheta}$ is a function of *both* x_1 and x_2. If this is true, then when a trajectory in the $(\vartheta, \dot{\vartheta})$ plane crosses, then the same should happen for the trajectory in the (x_1, x_2) plane. In other words, all the trajectories of the ROMs, corresponding to the a given input $\mathbf{u}$, should be homotopic to the corresponding trajectory of the HF model (i.e. they can be obtained by a continuous deformation of the HF trajectory).

To verify these conjectures, we consider the oscillating input also employed in

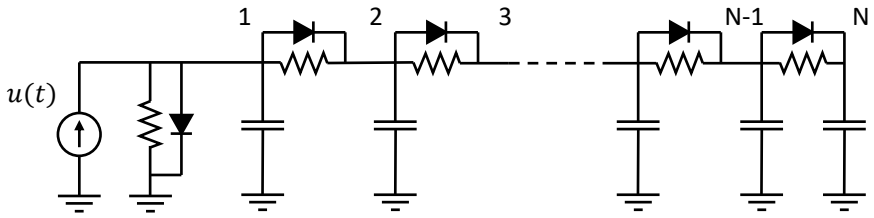

Figure 5.10: *Test case 2*: scheme of the nonlinear transmission line electric circuit considered in Sec. 5.4.2.

the first column of Fig. 5.8 (i.e. $u_1 = \sin(t)\cos(1.3\,t)$, $u_2 = \cos(1.8\,t)\sin(t)$) and we compare the trajectories of the HF model (gray background in Fig. 5.9) with those of four different ROMs (white background in Fig. 5.9), obtained with four different random initializations of the ANN. In the first line of Fig. 5.9 we show the time evolution of the two state variables of the systems. By looking at the the figure it is apparent how different the obtained ANN models can be. However, by observing – in the second row of Fig. 5.9 – the trajectories in the phase space (x_1, x_2), one can see that all the trajectories are approximatively homotopic to the trajectory of the HF model in its phase space $(\vartheta, \dot{\vartheta})$. Finally, in order to better visualize the role of the second variable, we decouple it from x_1 in the following way. First, we collect the values of the two variables at the discrete times $t_0, t_1, \ldots$ in two vectors, which we denote by $\mathbf{z}_1$ and $\mathbf{z}_2$, respectively. Next, we centre the vectors ($\mathbf{z}'_j = \mathbf{z}_j - \bar{\mathbf{z}}_j$, for $j = 1, 2$, where $\bar{\mathbf{z}}$ denotes the mean value of $\mathbf{z}$). Next, we subtract to $\mathbf{z}'_2$ the component parallel to $\mathbf{z}'_1$ (that is to say $\mathbf{z}''_2 = \mathbf{z}'_2 - (\mathbf{z}'_2 \cdot \mathbf{z}'_1)/\,|\mathbf{z}'_1\,|^2\,\mathbf{z}'_1$). Finally, we normalize $\mathbf{z}''_2$ (that is to say $\mathbf{z}'''_2 = \mathbf{z}''_2/\,|\mathbf{z}''_2\,|$). The third row of Fig. 5.9 shows the trajectories in the plane (x_1, x'''_2). For the original model, we show the trajectory in the plane $(\vartheta, \dot{\vartheta}''')$, where the coordinate $\dot{\vartheta}'''$ is computed by the same procedure as x'''_2.

5.4.2 *Test case 2*: Nonlinear transmission line circuit

In order to assess the capability of the proposed reduction approach to reduce the complexity of large-scale nonlinear systems, we consider a popular benchmark in MOR, namely the nonlinear transmission line circuit represented in Fig. 5.10 (see e.g. [CW00; RW01]). It is an electrical network comprising a current source, $N = 1000$ unitary resistors, N unitary capacitors and N nonlinear diods with law $i = e^{40\,v} - 1$. The input of the model is the current source $u(t)$, taking values in $U = [0, 1]$, and the output is the tension at the first node $v_1(t)$. By denoting by v_i the voltage at the i-th node, the HF model reads as follows:

$$\begin{cases} \dot{v}_1(t) = -2\,v_1(t) + v_2(t) + 2 - e^{40\,v_1(t)} - e^{40(v_1(t)-v_2(t))} + u(t) \\ \dot{v}_i(t) = -2\,v_i(t) + v_{i-1}(t) + v_{i+1}(t) + e^{40(v_{i-1}(t)-v_i(t))} - e^{40(v_i(t)-v_{i+1}(t))}, \\ \qquad\qquad\qquad\qquad\qquad\qquad\qquad\qquad\qquad\qquad \text{for } i = 2, \ldots, N-1 \\ \dot{v}_N(t) = -v_N(t) + v_{N-1}(t) - 1 + e^{40(v_{N-1}(t)-v_N(t))}, \end{cases} \tag{5.32}$$

supported by the initial condition $v_1(0) = v_2(0) = \cdots = v_N(0) = 0$. Notice that the HF model is written in the form of Eq. (5.1), for $\mathbf{X} = (v_1, \ldots, v_N)^T$ and $\mathbf{F}\colon \mathbb{R}^N \times [0, 1] \to \mathbb{R}^N$.

We consider the training set represented in Fig. 5.11, comprising 5 step inputs and 20 randomly generated input signals, each of 1 s duration. In this test case we

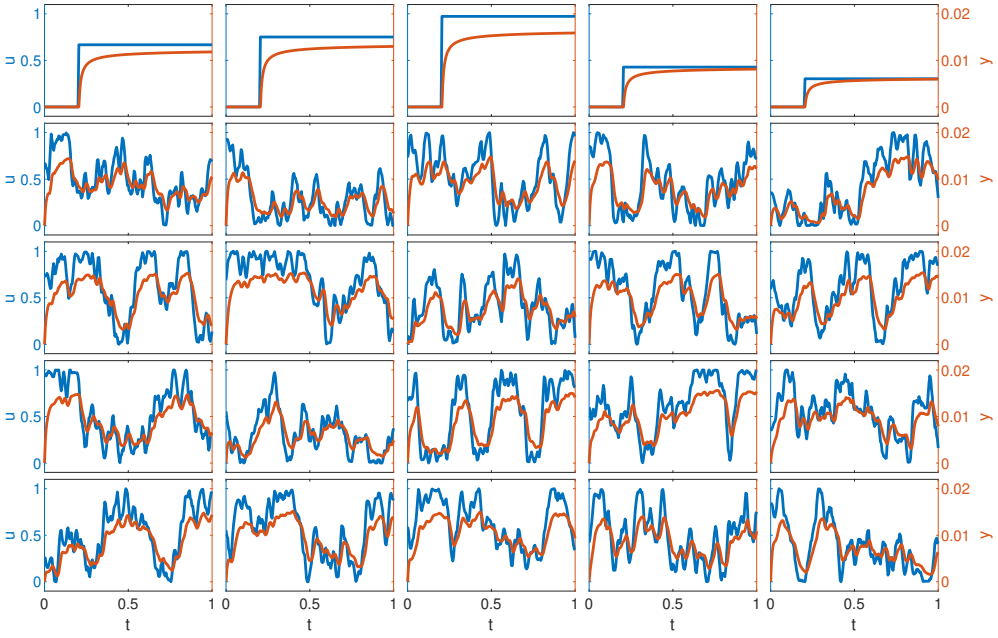

Figure 5.11: *Test case 2*: training set. Blue lines (axis on the left) represent the time evolution of the input, red lines (axis on the right) represent the time evolution of the output.

consider both the output-inside-the-state and the output-outside-the-state cases, for $n = 1, 2, 3$ and we compare the results. In all the cases we employ ANNs with a single hidden layer, with respectively 8 and 3 neurons in the ANN for $\mathbf{f}$ and $\mathbf{g}$. For the time discretization, we employ a time step of $\Delta t = 5 \cdot 10^{-3}$.

As mentioned in Sec. 5.2.4, in the case $n \geq N_y$, models in the form (5.2) can be possibly rewritten in the form (5.17). Even if this is not always valid, we may expect that with the constraint $\mathbf{g} = \boldsymbol{\pi}^{N_y}$ the capacity of the class of models to approximate the HF model is not substantially reduced. Therefore we expect the output-inside-the-state case to provide similar results to the ones obtained with the output-outside-the-state approach.

In Fig. 5.12a we show $\mathcal{E}_{\text{test}}$, the relative L^2 error on the test set (which comprises 25 step responses and 80 randomly generated inputs), for the different cases considered. We notice that, as expected, the two approaches provide, for a given value of n, very similar results. The output-inside-the-state case is thus preferable since it is more efficient both in the offline phase (since the number of design variables is lower) and in the online phase (since $\mathbf{g}$ does not need to be evaluated at each time step). We also notice that, coherently with Prop. 5.2, the error $\mathcal{E}_{\text{test}}$ decreases as n increases, reaching, for $n = 3$, a remarkably good approximation level (nearly $2.5 \cdot 10^{-3}$). In Fig. 5.12b we compare the response of the HF model with that of the three ROMs obtained with the output-inside-the-state case in the time-domain.

5.4.3 *Test case 3*: Heat equation (parabolic PDE)

We consider now the application of the proposed reduction approach to the MOR of a parabolic PDE problem, which extends the benchmark problem considered in

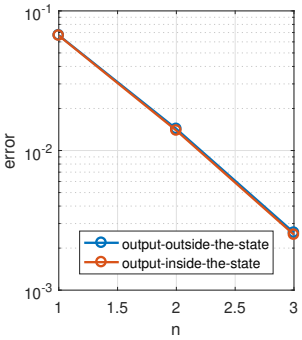

(a) $\mathcal{E}_{\text{test}}$ vs n

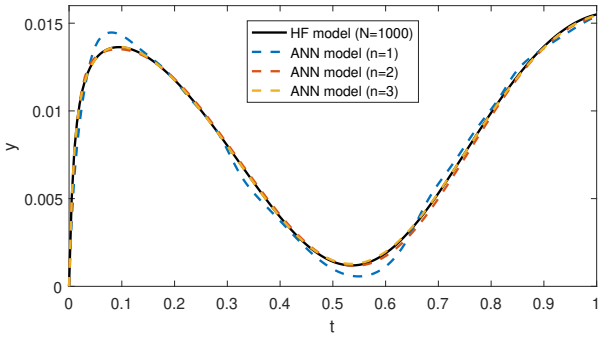

(b) Time domain responses to the input $\mathbf{u}(t) = \frac{1}{2}(1 + \cos(2\pi t))$: comparison between the HF model and three ANN models.

Figure 5.12: *Test case 2*: model errors for $n = 1, 2, 3$ with both output-inside-the-state and output-outside-the-state cases (a) and time-domain model responses (b).

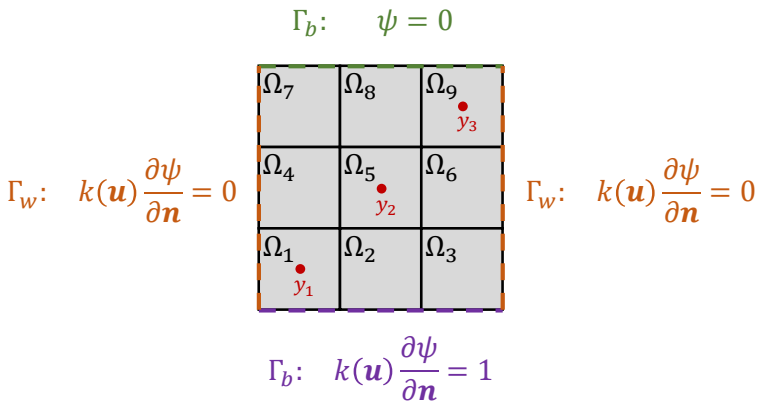

Figure 5.13: *Test case 3*: domain and boundary conditions.

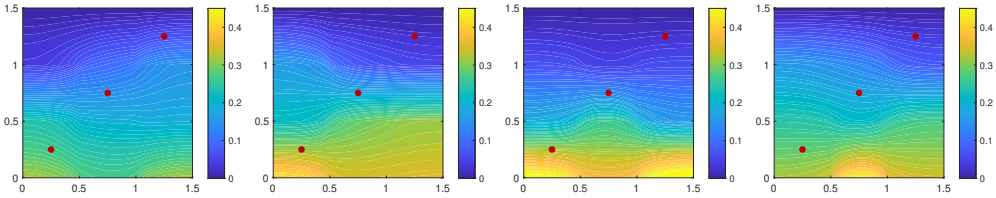

Figure 5.14: *Test case 3*: four examples of snapshots obtained at different times with different inputs.

[MPL16], where its Reduced Basis (RB) reduction has been considered. Consider the spatial domain $\Omega = (0,\, 1.5)^2$, whose boundary $\partial\Omega$ is partitioned into the top border Γ_t, in contact with a heat reservoir with zero temperature, the bottom border Γ_b, with a constant inward heat flux $\varphi = 1$, and the wall borders Γ_w, characterized by no-flux boundary conditions (see Fig, 5.13). The time evolution of the spatially distributed temperature $\psi(\mathbf{x}, t)$ in the domain Ω is thus described by the heat equation:

$$\begin{cases} \dfrac{\partial}{\partial t}\psi(\mathbf{x},t) - \nabla \cdot (k(\mathbf{x},\mathbf{u}(t))\,\nabla\psi(\mathbf{x},t)) = 0 & \text{in } \Omega, \text{ for } t > 0, \\ k(\mathbf{x},\mathbf{u}(t))\,\nabla\psi(\mathbf{x},t)\cdot\mathbf{n} = 0 & \text{on } \Gamma_w, \text{ for } t > 0, \\ k(\mathbf{x},\mathbf{u}(t))\,\nabla\psi(\mathbf{x},t)\cdot\mathbf{n} = \varphi & \text{on } \Gamma_b, \text{ for } t > 0, \\ \psi(\mathbf{x},t) = 0 & \text{on } \Gamma_t, \text{ for } t > 0, \\ \psi(\mathbf{x},0) = 0 & \text{on } \Omega. \end{cases} \tag{5.33}$$

Let us partition the domain Ω into 9 subdomains Ω_i of equal size, for $i = 1, \ldots, 9$, as in Fig. 5.13. Let us consider the piecewise constant thermal conductivity coefficient k, parametrized by the 9-dimensional input $\mathbf{u}(t) \in [10, 100]^9$, defined as follows:

$$k(\mathbf{x}, \mathbf{u}) = \sum_{i=1}^{9} u_i \, \mathbb{1}_{\Omega_i}(\mathbf{x}),$$

where $\mathbb{1}_{\Omega_i}$ is the indicator function of Ω_i. Consider then three probes, located at the centre of the subdomains Ω_1, Ω_5 and Ω_9, measuring the time evolution of the temperature in such points. The output $\mathbf{y}(t) \in \mathbb{R}^3$ is the vector collecting the three temperature values.

For the HF solution of (5.33), we consider the P2 Finite Element approximation on a 30 by 30 uniform square elements grid and we employ the backward Euler scheme, with $\Delta t = 10^{-2}$, for the time discretization, implemented in the MATLAB finite element library `feamat` [Peg19]. The HF model has dimension $N = 3721$.

In this test case we compare the results obtained with the proposed reduction approach with those obtained with a popular MOR method in the field of PDEs, namely the RB method, which exploits the linearity of Eq. (5.33) and the affine dependence on $\mathbf{u}$ [QMN15]. For the ANN-based reduction method we consider n ranging between 1 and 5, by employing both the output-outside-the-state approach and, for $n \geq N_y = 3$, also the output-inside-the-state approach. In each case we use single hidden layer ANNs, with 12 to 16 hidden neurons for $\mathbf{f}$ and 3 or 4 hidden neurons for $\mathbf{g}$, by increasing the number of neurons as n increases. Figure 5.15 reports a subset of the training set, comprising steady-state responses lasting for 0.4 s, obtained by sampling the input space $U = [10, 100]^9$ by means of Latin Hypercube Sampling (see [MBC00]), and twice as much random transients of duration 1 s. This choice aims at covering different working regimes of the HF model, including steady-state and transient regimes. We increase the number of training samples from 150 to 480 while increasing n to reflect the increased capacity of the ANN due to the increased number of neurons. As of the RB method, we build the basis by POD of the snapshot matrix obtained by sampling every 0.1 s the biggest set used to train the ANNs. In both the cases we employ the same time step used for the HF model, i.e. $\Delta t = 10^{-2}$.

In Fig. 5.17 we compare the results obtained by the two methods, by evaluating the error on a test set composed by 20 steady-state inputs, 50 random input signals of duration 1 s (two examples are reported in Fig. 5.16) and 10 random input signals of duration 10 s. The purpose of the latter choice is to assess the capability of the

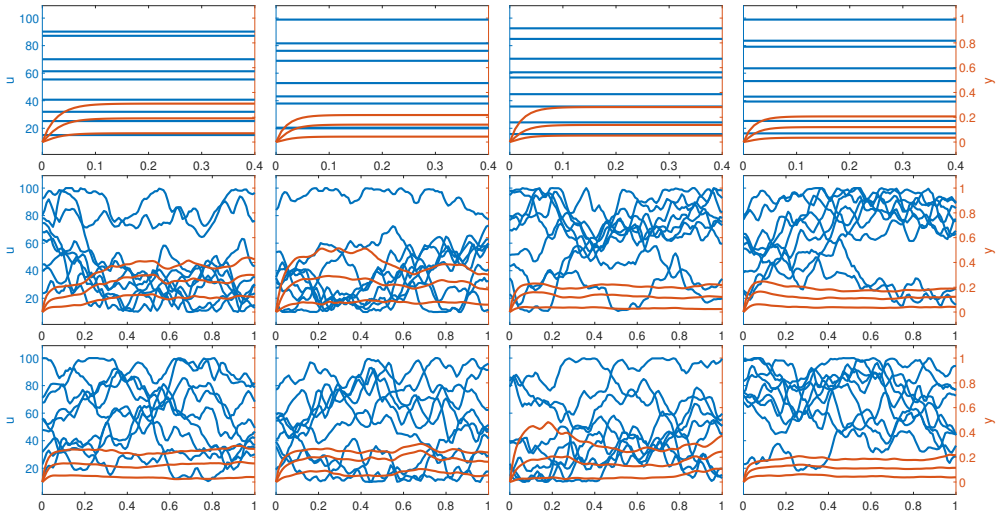

Figure 5.15: *Test case 3*: a subset of the training set. Blue lines (axis on the left) show the time evolution of the 9 inputs (i.e. the thermal conductivities of the 9 subdomains), red lines (axis on the right) show the time evolution of the three outputs (i.e. the temperature at the three probes).

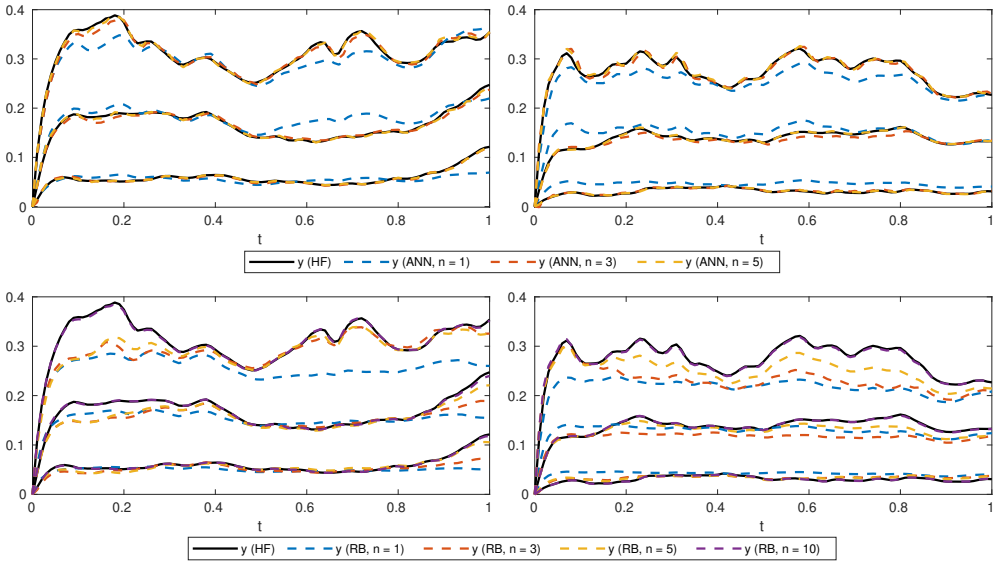

Figure 5.16: *Test case 3*: time-domain comparison of the result of the HF model with those of the different ROMs for two random tests. Top: ANN models vs HF model; bottom: RB models vs HF model.

proposed reduction approach to approximate the evolution of the HF model also for longer time horizons than the ones used in the training phase. As shown in Fig. 5.17a, for a given model size n, the ANN based ROM performs better than the RB one: for $n = 3$, e.g., the corresponding error is almost one order of magnitude smaller than the RB error and to reach the same approximation level with the RB method we need at least $n = 8$. Moreover, the reduction in terms of online computational time is larger with the proposed approach too.

In Fig. 5.17a we plot, together with the errors, the quantity ε_n, defined as

$$\varepsilon_n = \sqrt{\frac{\sum_{i=n+1}^{S} \sigma_i^2}{\sum_{i=1}^{S} \sigma_i^2}},$$

where $\sigma_1, \ldots, \sigma_S$ are the singular values of the snapshots matrix. The quantity ε_n represents the fraction of energy of the snapshots that is not captured by the first n modes and can be used to estimate the "reducibility" of the state space in terms of an n-dimensional subspace (see [QMN15]).

The major drawback of the proposed reduction approach lies in the offline phase, which requires the training of one or two ANNs (for $\mathbf{f}$ and $\mathbf{g}$), while for the RB method we just need to compute the SVD decomposition of the snapshot matrix and to project both the model matrices and right-hand side. Moreover, the computational complexity of the training rapidly grows with n and, for high n, large training sets are needed to avoid overfitting, thus preventing the applicability of the proposed approach to large n. For this reason, we limit ourselves to the cases $n \leq 5$. However, from the presented results it seems that with the proposed approach it is possible to get a good approximation of complex models (like the PDE model considered in this section) just with a few variables, so we do not actually need to increase n if the approximation level is satisfactory for the application. We also notice that in this thesis we employed very basic tools to train the ANNs, while the offline phase may be considerably speeded up with the application of more advanced techniques (see Sec. 5.5) which, besides decreasing the training time also minimize overfitting, thus reducing the number of samples needed to train the ANN, hence making it possible to train ANN models with larger values of n.

Finally, we notice that this comparison has been carried out in the most favourable case for RB, namely linear models with affine input dependence and with linear state-output dependence, while the proposed ANN-based reduction approach does not exploit any of those structural characteristic of the HF model. Therefore, in the nonlinear case or with non affine input dependence, while the RB method requires techniques such as EIM and DEIM (see Sec. 5.1.1), which reduce the performances of the method, the proposed reduction approach can be applied without modifications (see e.g. the *Test case 2*).

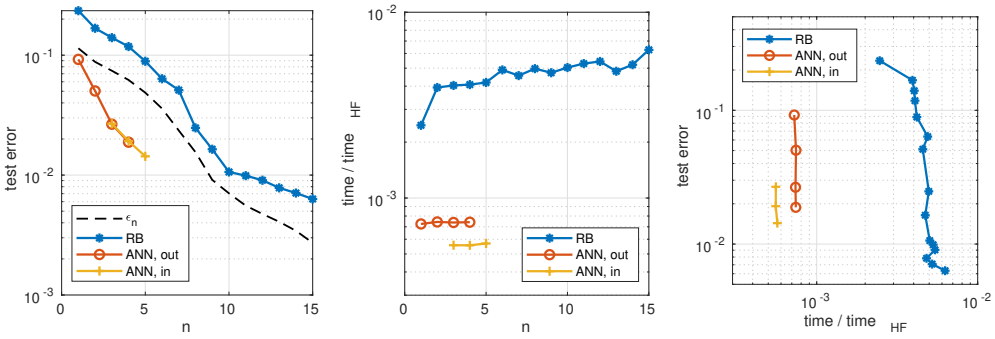

(a) $\mathcal{E}_{\text{test}}$ vs n.

(b) Online computational time reduction vs n.

(c) $\mathcal{E}_{\text{test}}$ vs online computational time reduction.

Figure 5.17: *Test case 3*: comparison between the proposed reduction approach and the RB method. (a) Relative L^2 error versus number of variables of the ROM n; (b) Mean computational time required by the ROM, normalized w.r.t. that required by the HF model to simulate the same amount of physical time, versus n; (c) Relative L^2 error versus normalized computational time. In the legend, "in" refers to output-inside-the-state, while "out" refers to output-outside-the-state

5.4.4 *Test case 4*: Wave equation (hyperbolic PDE)

We now consider an hyperbolic PDE, namely the wave equation in the one-dimensional domain $(0, L)$, with $L = 1$:

$$\begin{cases} \dfrac{\partial^2}{\partial t^2}\psi(x,t) - c^2 \dfrac{\partial^2}{\partial x^2}\psi(x,t) = 0 & \text{for } x \in (0,L),\ t > 0, \\ \psi(0,t) = u_1(t) & \text{for } t > 0, \\ \psi(L,t) = u_2(t) & \text{for } t > 0, \\ \psi(x,0) = 0 & \text{for } x \in (0,L), \\ \dfrac{\partial}{\partial t}\psi(x,0) = 0 & \text{for } x \in (0,L), \end{cases} \tag{5.34}$$

where we set $c = 2$. The 2-dimensional input of the model consists in the Dirichlet boundary conditions at the two ends of the domain, while the output is defined as the value of the solution in the mid-point of the domain $y(t) = \psi(L/2, t)$. For the HF solution we use implicit second order BDF in time and centered second order finite differences in space, with a space discretization step of $h = 10^{-2}$ and a time discretization step of $\Delta t = 10^{-2}$. In Fig. 5.18 we show a solution of the HF model for a random input at different time-steps.

In order to apply the proposed method, we rewrite Eq. (5.34) as a first order (in time) system of PDEs. To train the ANN we consider a training set consisting of 200 random inputs and we employ the same time step used to generate data. In Fig. 5.20 we compare the HF output with the output of the different learned models for 4 different tests. Figure 5.19 shows the test error of the learned models for different values of n, by using the output-inside-the-state approach and by using a single hidden layer with $N_{\text{neurons}} = n + 2$. Also in this test case, the error decreases with n and, noticeably, it decreases faster than ε_n.

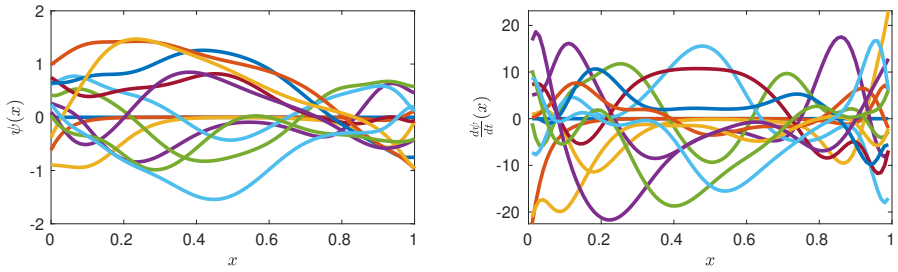

Figure 5.18: *Test case 4*: example of snapshots of the state $\psi(t)$ and its time derivative $\frac{\partial \psi}{\partial t}(x)$ at different time steps for a sample belonging to the training set.

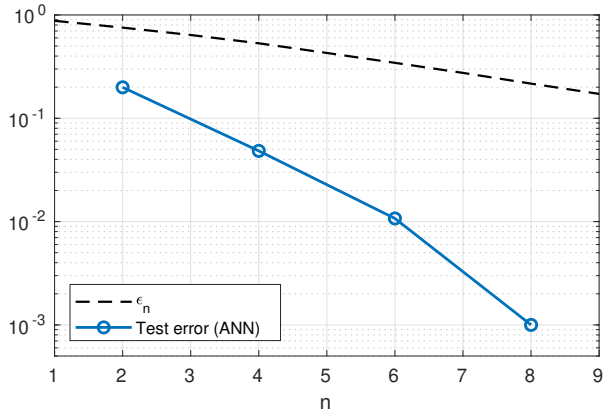

Figure 5.19: *Test case 4*: $\mathcal{E}_{\text{test}}$ vs. number of variables of the ROM n (solid line) and ε_n vs. number of modes (dashed line).

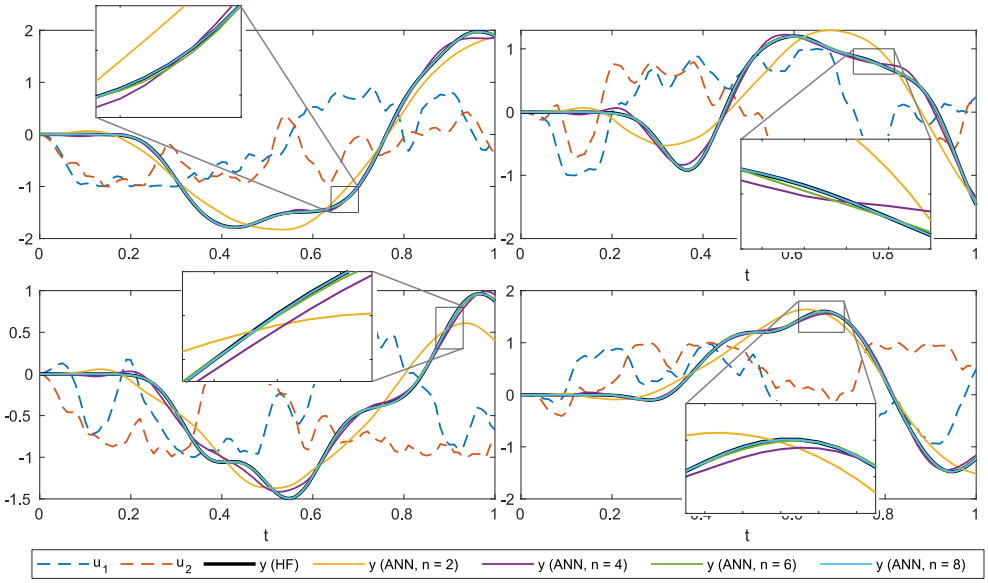

Figure 5.20: *Test case 4*: comparison between the HF solution and the solution with the 4 trained ANN models in 4 different test cases.

5.5 Final remarks and perspectives

We have proposed a data-driven nonlinear MOR technique, based on ANNs. We formulated the model reduction problem as a best-approximation or maximum-likelihood problem, where we look for the most suitable representation of the HF (high-fidelity) dynamical model into a class of simpler models. The latter consists in a class of ODE models described by means of an ANN (or by two of them, in the output-outside-the-state case), which is fed by input-output pairs originated from the HF system. Thanks to this formulation, it is possible to compute the sensitivity of the model error with respect to the parameters of the ANNs, and to exploit standard optimization techniques to make the ANN learn the underlying physics of the system. The proposed reduction approach can be applied to a wide class of dynamical models with time dependent inputs, subject to some minimal requirements (see Sec. 5.2.1).

We have shown that the class of ANN models used in this chapter can approximate within any desired accuracy any model described by a system of ODEs. Moreover, the same result holds by replacing the class of ANNs with any class of functions that can approximate continuous functions on compact sets with arbitrarily small error.

The proposed technique can be flexibly applied for different purposes: (*i*) building a surrogate of a computationally expensive model, which allows for fast evaluations and which can be used for multi-query purposes; (*ii*) reducing the state dimension of a time-dependent model; (*iii*) learning a mathematical model starting from input-output pairs (see Fig. 5.1).

We have assessed the effectiveness of the proposed approach on a simple case study (namely the nonlinear pendulum) and by investigating the reduction of two large-scale problems (a nonlinear system of ODEs and a parabolic PDE), featuring thousands of degrees of freedom, and an hyperbolic PDE. In all the cases we derived ROMs capable of approximating the HF models with an error of order $10^{-2} \div 10^{-3}$, with just a few state variables. We have also compared the performance of the proposed reduction approach with that of the RB method, one of the most popular MOR methods in the field of PDEs. For a given ROM size, despite a more expensive offline phase, the proposed reduction approach yielded much more accurate ROMs than the RB method, also featuring a lower online cost in terms of computational time.

Some crucial aspects, where there is possibility for improvement of the proposed reduction approach, have not been fully explored in the present study. In particular, we have not dealt with the issue of the training set design, where it is possible to employ automatic procedures to select an optimized training set, in a similar manner to the selection of snapshots in the RB framework (see e.g. [QMN15]). Moreover, globalization techniques can be taken into account to deal with the problem of local minima in the optimization process. Furthermore, different optimization algorithms can be considered in place of the Levenberg-Marquardt algorithm (whose computational cost becomes prohibitive when the number of parameters to be trained becomes large), such as Stochastic Gradient Descent [Bot10], AdaGrad [DHS11] or Adam [KB14], which are widely used in Machine Learning. The offline phase may be considerably speeded up also with the application of more advanced learning techniques than the one considered in this thesis, such as stochastic selection of the training set (or mini-batch training, see e.g. [Bot10]), dropout [Sri+14], batch normalization [IS15] and progressive layers freezing [Bro+17]. This would allow to speed up the training phase, thus allowing to further investigate the potential of the proposed method by considering larger values of n.

In this chapter we have performed hyperparameters tuning by a trial-and-error

approach. In future developments we will consider ad-hoc algorithms, such as evolutionary optimization, bayesian optimization, grid search and k-means.

Finally, we notice that the formulation of the MOR problem in terms of minimization problem potentially allows to easily incorporate into the learning stage some a priori knowledge on the HF model, by suitably accounting for a penalization term (we show an example Chap. 6).

Chapter 6

Reduced order models of sarcomere dynamics

High fidelity (HF) mathematical models describing the generation of active force in the cardiac muscle tissue typically feature a large number of state variables to capture the intrinsically complex underlying subcellular mechanisms (see Part I). In this chapter, in order to drastically reduce the computational burden associated with the numerical approximation of these models, we apply the data-driven MOR technique presented in Chap. 5 to models that we proposed in Part I (specifically, to the activation-MH, SE-ODE and MF-ODE models). With this aim, we enrich the fully black-box method of Chap. 5 by feeding the learning process with some a priori information on the HF model, thus moving towards a gray-box (or semi-physical) approach. Part of the results presented in this chapter are taken from the submitted paper [RDQ19c].

Contents

6.1 Model reduction strategy

The goal of this chapter is that of deriving reduced order models for the cardiac mechanical activation models proposed in Part I, by applying the ANN-based MOR strategy proposed in Chap. 5. Specifically, we will consider the model for calcium-driven tissue activation presented in Chap. 2 (the activation-MH model) and the SE-ODE and MF-ODE full-sarcomere models, presented in Chap. 4.

6.1.1 The HF models for sarcomere dynamics

We notice that all the above mentioned models can be written in the form of the HF model of Eq. (5.1), that we recall here for the reader's convenience:

$$\begin{aligned} &\begin{cases} \dot{\mathbf{X}}(t) &= \mathbf{F}(\mathbf{X}(t), \mathbf{u}(t)) \qquad t \in (0,T], \\ \mathbf{X}(0) &= \mathbf{X}_0, \end{cases} \\ &\mathbf{y}(t) = \mathbf{G}(\mathbf{X}(t)) \qquad t \in (0,T], \end{aligned} \tag{6.1}$$

where $\mathbf{X}(t) \in \mathbb{R}^N$ is the vector collecting all the states of the model. Specifically, the vector $\mathbf{X}(t)$ takes the following forms, for the three models considered in this chapter.

- **Activation-MH model**. We have $N = (N_M - 2)4^3 = 2176$ and $\mathbf{X}(t)$ is the vector collecting all the terms in the form:

$$\left\{ \mathbb{P}((\alpha, \overset{i}{\beta}, \delta)^t) \colon i = 2, \dots, N_M - 1, \quad \alpha, \beta, \delta \in \{\mathcal{UN}, \mathcal{BN}, \mathcal{UP}, \mathcal{BP}\} \right\}.$$

- **SE-ODE model**. We have $N = (N_A - 2)2^6 + 4\,N_A = 1408$ and $\mathbf{X}(t)$ collects all the terms in the form:

$$\left\{ \pi_i^{\alpha\beta\delta,\vartheta\eta\lambda}(t) \colon i = 2, \dots, N_A - 1, \quad \vartheta, \eta, \lambda \in \{\mathcal{U}, \mathcal{B}\}, \quad \alpha, \beta, \delta \in \{\mathcal{N}, \mathcal{P}\} \right\};$$

  and in the form:

$$\left\{ \mu_{i,\alpha}^p(t) \colon i = 1, \dots, N_A, \quad \alpha \in \{\mathcal{N}, \mathcal{P}\}, \quad p \in \{0,1\} \right\}.$$

- **MF-ODE model**. We have $N = 2^4 + 4 = 20$ and $\mathbf{X}(t)$ collects all the terms in the form:

$$\left\{ \pi^{\alpha\beta\delta,\eta}(t) \colon \eta \in \{\mathcal{U}, \mathcal{B}\}, \quad \alpha, \beta, \delta \in \{\mathcal{N}, \mathcal{P}\} \right\};$$

  and in the form:

$$\left\{ \mu_\alpha^p(t) \colon \alpha \in \{\mathcal{N}, \mathcal{P}\}, \quad p \in \{0,1\} \right\}.$$

The vector $\mathbf{u}(t)$ represents the input of the model. For the activation-MH model, the input is given by the intracellular calcium concentration ad the sarcomere length. Therefore, we set $\mathbf{u}(t) = ([\mathrm{Ca}^{2+}]_\mathrm{i}(t), SL(t))^T$. Conversely, the two full-sarcomere models have as additional input the rate of shortening of sarcomeres. Therefore, we set $\mathbf{u}(t) = ([\mathrm{Ca}^{2+}]_\mathrm{i}(t), SL(t), \frac{d}{dt}SL(t))^T$.

Finally, the output vector $\mathbf{y}(t)$ collects the quantities of interest that can be computed from the state $\mathbf{X}$. Thus, its definition possibly depends on the application. In this thesis, the final goal is that of employing such models to perform electromechanical numerical simulations. Hence, the quantities of interest are the ones needed to couple

the microscopical force generation model with the other physics. For the activation-MH model, to compute the generated tension we just need the permissivity. Thus, we set $\mathbf{y}(t) = P(t)$ and the observation function $\mathbf{G}$ is given by Eq. (2.7). Concerning the full-sarcomere models SE-ODE and MF-ODE, we will see in Part III that, besides the active tension $T_\mathrm{a}(t)$, in order to perform electromechanical numerical simulations, we also need the active stiffness $K_\mathrm{a}(t)$. Thus, in those cases we set $\mathbf{y}(t) = (T_\mathrm{a}(t), K_\mathrm{a}(t))^T$ and the observation function $\mathbf{G}$ is given by Eq. (4.33) (for the SE-ODE model) or by Eq. (4.47) (for the MF-ODE model). Since the three models here considered can be written in the form of Eq. (6.1), in the following we will refer to Eq. (6.1) as the HF model, and we will give details specific to each model only when necessary.

6.1.2 Black-box model reduction

Within a data-driven framework, we carry out N_s experiments (i.e. numerical simulations) with the HF model and we collect a set of N_s outputs $\mathbf{y}(t)$, each one obtained with a different input $\mathbf{u}(t)$. Hence, for $j = 1, \dots, N_s$, we consider a time interval $[0, T_j]$ and an input function $\widehat{\mathbf{u}}_j \colon [0, T_j] \to U$ and we define $\widehat{\mathbf{y}}_j \colon [0, T_j] \to Y$ as the solution of the HF model (6.1) associated to the input $\widehat{\mathbf{u}}_j$. The j-th training experiment (where $j = 1, \dots, N_s$) consists of the pair $(\widehat{\mathbf{u}}_j, \widehat{\mathbf{y}}_j)$.

The solution of the HF model (6.1) also depends on the initial condition $\mathbf{X}_0$. Because of the non-intrusive nature of our approach, a unique initial condition must be used in each experiment, otherwise the input-output map that we aim to learn would not be well-defined (see Sec. 5.2). Specifically, we set as initial condition for each training experiment the steady-state of the cell in pre-systolic conditions, that is when calcium concentration is $c_0 = 0.1\,\mu\mathrm{M}$ and the sarcomere length is $SL_0 = 2.2\,\mu\mathrm{m}$. The corresponding state can be numerically computed by solving the HF model until a steady-state is reached with input $\mathbf{u}(t) \equiv \mathbf{u}_0$, where $\mathbf{u}_0 := (c_0, SL_0)^T$, for the activation-MH model, or $\mathbf{u}_0 := (c_0, SL_0, 0)^T$, for the full-sarcomere models.

By following the strategy proposed in Chap. 5, we look for a ROM written in the following form:

$$\begin{aligned} &\begin{cases} \dot{\mathbf{x}}(t) &= \mathbf{f}(\mathbf{x}(t), \mathbf{u}(t)) \qquad t \in (0, T], \\ \mathbf{x}(0) &= \mathbf{x}_0, \end{cases} \\ &\mathbf{y}(t) = \mathbf{g}(\mathbf{x}(t)) \qquad t \in (0, T], \end{aligned} \tag{6.2}$$

where the reduced state $\mathbf{x}(t)$ belongs to a low dimensional space $\mathbb{R}^n$, such that $n \ll N$.

6.1.3 Feeding the learning process with a priori knowledge

The approach presented in Chap. 5 is fully black-box, that is it does not require any knowledge about the HF model but for a collection of input-output pairs generated by the HF model itself. However, as for the application considered in this chapter, we may actually have some insight into the HF model that we aim to reduce. Such a priori knowledge can be exploited in the learning process by adding to the cost functional of problem (5.18) suitable penalization terms.

The cycle condition

As explained in Sec. 5.2.4, with the proposed black-box approach it is not possible to give a physical meaning to all the entries of the reduced state $\mathbf{x}(t)$ (apart, in the

output-inside-the-sate approach, from the first N_y entries, which coincides with the output itself). Nonetheless, the reduced state $\mathbf{x}$ is a compact representation of the full-order state $\mathbf{X}$: we may suppose that there exists a map between the full-order and the reduced state. Hence, the initial state $\mathbf{X}_0$ is mapped, by construction, into the reduced initial state $\mathbf{x}_0$.

This implies that, whenever for some input $\widehat{\mathbf{u}}_j(t)$ the HF model returns, at the final time T_j, to the initial state (that is $\mathbf{X}(T_j) = \mathbf{X}_0$), also the ROM should satisfy $\mathbf{x}(T_j) = \mathbf{x}_0$. To enforce this condition, which we call *cycle condition*, we insert in the training set some experiments, labelled by the indexes $j \in J_c$, such that at final time T_j the full-order state coincides with the initial state $\mathbf{X}_0$. Then, we add to the cost functional of problem (5.18) the following term:

$$E_{\mathrm{c}}^2 = a_{\mathrm{c}}^{-1} \sum_{j \in J_c} \sum_{i \in I_c} \frac{\left(\mathbf{x}_j(T_j) \cdot \mathbf{e}_i\right)^2}{\frac{1}{T_j} \int_0^{T_j} \left(\mathbf{x}_j(t) \cdot \mathbf{e}_i\right)^2 \, \mathrm{d}t}, \tag{6.3}$$

where $a_{\mathrm{c}} = |J_c||I_c|$ is a normalization factor, whose role will be discussed later. The set I_c is defined as $I_c = \{1, \ldots, n\}$ in the output-outside-the-state case, or as $I_c = \{N_y + 1, \ldots, n\}$, in the output-inside-the-state case. The reason is that, in the latter case, the first N_y entries of the state are already accounted for in the cost functional of problem (5.18). We also notice that in (6.3) we normalize with respect to the L^2 norm of the history of $\mathbf{x}(t)$, otherwise the introduction of the penalization term (6.3) would be useless. Indeed, if we perform a change of variable for the internal state (by multiplying its entries, but for the first one, by a small constant $\alpha \ll 1$), the quantity $\sum_{j=1}^{N_s} \sum_{i=2}^{n} \left(\mathbf{x}_j(T_j) \cdot \mathbf{e}_i\right)^2$ can be made arbitrary small, without changing the input-output map represented by the model (see Sec. 5.2.4).

The equilibrium condition

In Sec. 6.1.1 we have defined the initial full-order state $\mathbf{X}_0$ as the steady-state associated to the input $\mathbf{u}_0$. Therefore, such state is by definition an equilibrium solution for the input $\mathbf{u}_0$ (i.e. $\mathbf{F}(\mathbf{X}_0, \mathbf{u}_0) = \mathbf{0}$), a condition that should be satisfied also by the ROM (i.e. $\mathbf{f}(\mathbf{x}_0, \mathbf{u}_0) = \mathbf{0}$). To enforce this condition (which we call *equilibrium condition*), we envisage two alternative strategies. The first one, which we call *weak imposition*, consists in adding to the cost functional the following further penalization term:

$$E_{\mathrm{e}}^2 = a_{\mathrm{e}}^{-1} |\mathbf{f}(\mathbf{x}_0, \mathbf{u}_0)|^2, \tag{6.4}$$

where the normalization factor is defined as $a_{\mathrm{e}} = n$. The second one consists in manipulating the ANN architecture in such a way that the equilibrium condition is exactly satisfied. Specifically, we redefine $\mathbf{f}$ as $\mathbf{f}(\mathbf{x}, \mathbf{u}) = \bar{\mathbf{f}}(\mathbf{x}, \mathbf{u}) - \bar{\mathbf{f}}(\mathbf{x}_0, \mathbf{u}_0)$, where $\bar{\mathbf{f}}$ represents the ANN to be trained (from which we remove the last layer of biases since it is canceled by the subtraction). We call this second approach *strong imposition* of the equilibrium condition as the latter is satisfied by construction. In other words, we train the ANN weights and biases, but for the biases of the output layer, which are defined in such a way that the equilibrium condition is satisfied. The reduction of the number of the unknowns is a consequence of the reduction of the space of candidate solutions (we have excluded the functions not satisfying the equilibrium condition).

6.1.4 Gray-box model reduction

The introduction of the cycle condition and of the equilibrium condition, made in Sec. 6.1.3, would not be possible in a strict black-box framework since the internal

state would not be observable. We have thus moved towards a gray-box approach since we have mixed a black-box technique with some insight on the HF model. Before stating the formulation of the gray-box model reduction problem, we introduce the following notation to denote the cost-functional of the black-box formulation (5.18), which penalizes the error between the output of the HF model and that of the ROM:

$$E_{\mathrm{b}}^2 = a_{\mathrm{b}}^{-1} \sum_{j=1}^{N_s} \int_0^{T_j} |\widehat{\mathbf{y}}_j(t) - \mathbf{y}_j(t)|^2 dt, \tag{6.5}$$

where $a_{\mathrm{b}} = \sum_{j=1}^{N_s} \int_0^{T_j} |\widehat{\mathbf{y}}_j(t)|^2 dt$. Then, the gray-box MOR problem reads:

$$\begin{cases} \min\limits_{\mathbf{f}\in\widehat{\mathcal{F}},\mathbf{g}\in\widehat{\mathcal{G}}} & \frac{1}{2}w_{\mathrm{b}}^2 E_{\mathrm{b}}^2 + \frac{1}{2}w_{\mathrm{c}}^2 E_{\mathrm{c}}^2 + \frac{1}{2}w_{\mathrm{e}}^2 E_{\mathrm{e}}^2 \\ \text{s.t.} & \dot{\mathbf{x}}_j(t) = \mathbf{f}(\mathbf{x}_j(t), \widehat{\mathbf{u}}_j(t)), \quad t \in (0, T_j], \quad j = 1, \dots, N_s, \\ & \mathbf{x}_j(0) = \mathbf{x}_0, \quad j = 1, \dots, N_s, \\ & \mathbf{y}_j(t) = \mathbf{g}(\mathbf{x}_j(t)), \quad t \in (0, T_j], \quad j = 1, \dots, N_s. \end{cases} \tag{6.6}$$

The weight factors $w_{\mathrm{b}}, w_{\mathrm{c}}, w_{\mathrm{e}} \in \mathbb{R}^+$ allow to tune the contribution of the different terms. The normalization factors a_{b}, a_{c} and a_{e} allow to keep the relative weight of the different terms unaffected by changes in the number of training samples, in J_c or in n. When the strong imposition of the equilibrium condition is employed, we set $w_{\mathrm{e}} = 0$ and we modify the architecture of $\mathbf{f}$ accordingly.

6.1.5 Discrete version of the MOR problem

As is Chap. 5, we choose as space of candidate functions $\widehat{\mathcal{F}}$ the space of ANNs with $n + N_u$ input variables and n output variables. Moreover, in the output-outside-the-state approach, we choose as space $\widehat{\mathcal{G}}$ the space of ANNs with n input variables and N_y output variables. We denote by $\boldsymbol{\mu}$ and, respectively, $\boldsymbol{\nu}$ the vectors collecting the weights and biases of the two ANNs.

We discretize problem (6.6) both for the state equation and the objective functional. As in Chap. 5, we consider uniform subdivisions of the time intervals $[0, T_j]$ with time step size Δt; then, we discretize the state equation by a Forward Euler scheme and the objective functional in (6.6) by the composite trapezoidal rule.

We notice that all the terms of the objective functional of problem (6.6) can be written as sums of squares. The optimization problem retains a least-squares structure and the Levenberg-Marquardt algorithm can thus be applied. The unique change with respect to the solution of the fully black-box problem (5.18) is that it requires the calculation of the gradient of the terms E_{c} and E_{e} with respect to the design variables $\boldsymbol{\mu}$ and $\boldsymbol{\nu}$, which can be performed by means of the Lagrange Multiplier method (as in Chap. 5) and by differentiation with respect to $\boldsymbol{\mu}$ and $\boldsymbol{\nu}$, respectively.

6.2 Reduced RUs model (activation-MH)

In this section, we consider the activation-MH model (proposed in Chap. 2), and we show the results of the application of the MOR methods presented above. As our goal is to obtain a ROM to be exploited in multiscale cardiac simulations, our inputs will span the range of values possibly covered during the cardiac activity. In particular, since calcium concentration during each heartbeat varies between 0.1 µM and 1 µM and

the working range of sarcomeres spans a length from 1.7µm to 2.3µm [Ber01; Kat10], our input takes values in $U = [c_{\min}, c_{\max}] \times [SL_{\min}, SL_{\max}]$, where we prudentially set $c_{\min} = 0\,\mu\text{M}$, $c_{\max} = 1.5\,\mu\text{M}$, $SL_{\min} = 1.6\,\mu\text{M}$, $SL_{\max} = 2.4\,\mu\text{M}$. Since the output of the model represents the fraction of units in permissive state, we define the space of output values as $Y = [0, 1]$.

To train the ANN we generate a training set by means of the HF model, i.e. a collection of input-output pairs $(\widehat{\mathbf{u}}_j, \widehat{\mathbf{y}}_j)$, for $j = 1, \dots, N_s$. In such training set we insert three kind of input functions:

- 50 step responses of duration $T = 3\,\text{s}$, in the form of $\mathbf{u}(t) = \mathbf{u}_0 + (\bar{\mathbf{u}} - \mathbf{u}_0)\mathbb{1}_{[t_1,t_2)}(t)$, where $t_1 = 0.2\,\text{s}$, $t_2 = 2\,\text{s}$ and where $\bar{\mathbf{u}}$ is randomly selected. Specifically, we put into the train set 40 inputs where the values $\bar{\mathbf{u}}$ are selected by Latin Hypercube Sampling (LHS) of the input set U and 10 additional inputs obtained by LHS of the subset $[0.3, 0.6]\mu\text{M} \times [2.15, 2.25]\mu\text{m} \subset U$, a region where the steady-state force-length relationship has a non regular shape and thus requires a better resolution to be appreciated. The samples belonging to this set are such that the final full state $\mathbf{X}(T)$ virtually coincides (with a relative error lower than 10^{-4}) with $\mathbf{X}_0$. Therefore, we insert the corresponding indexes into the set J_c.

- 45 oscillating inputs of duration $T = 1\,\text{s}$, in the form of:

$$\mathbf{u}(t) = \left(c_{\min} + A \sin\left(\frac{2\pi}{T_1} t\right)^2, B + C \sin\left(\frac{2\pi}{T_2} t\right) \right)^T,$$

  where the periods T_1 and T_2 are randomly selected in the range $0.1 - 0.8\,\text{s}$ and the constants A, B and C are randomly selected, with the constrain that the function values belong to the set U.

- 60 randomly generated inputs of duration $T = 1\,\text{s}$.

In order to select the hyperparameters, we proceed by a trial-and-error approach. Aiming at a drastic reduction of dimensionality of the HF model, we set $n = 2$ internal variables for the ROM. For this choice we found that two hidden layers of 6 neurons each yield accurate results without a significant overfitting, as we will show later (Table 6.1). Finally, we set $w_{\text{b}} = 1$, $w_{\text{c}} = 10^{-1}$ and, for the weak imposition of the equilibrium condition, $w_{\text{e}} = 10^{-1}$. Concerning the time discretization, we employ a time step of $\Delta t = 1 \cdot 10^{-2}\,\text{s}$. In order to lower the computational cost of the training stage, we evaluate the loss functional (6.5) of the step responses every two time steps, as the samples belonging to the latter class do not feature a fast dynamics.

To evaluate the accuracy of the ROM, we build a testing set with a collection of step inputs, randomly generated inputs and the physiological and pathological inputs described in Sec. 6.2.1. Moreover, in order to evaluate the reliability of the ROM over time intervals longer than the one used for the training, we also test the ROM with random inputs of duration $T = 10\,\text{s}$.

Therefore, the ANN is trained based on the input-output pairs generated by the HF model under fundamental regimes (step responses, frequency responses) and random inputs. Then, the learned model is tested on different test cases, including physiological samples. If the ANN model, which has been exposed during the training stage only to fundamental inputs, is able to reproduce the results of the HF model also for physiological inputs, we can conclude that the ANN has really *learned* the dynamics of the system, and it is not simply interpolating among a database of precomputed solutions.

Equilibrium condition	**Cycle condition**	**Relative errors**	
		Training	Test
-	-	$1.62 \cdot 10^{-2}$	$2.66 \cdot 10^{-2}$
weak ($w_e = 10^{-1}$)	-	$1.52 \cdot 10^{-2}$	$2.10 \cdot 10^{-2}$
strong	-	$1.70 \cdot 10^{-2}$	$3.10 \cdot 10^{-2}$
weak ($w_e = 10^{-1}$)	$w_c = 10^{-1}$	$1.48 \cdot 10^{-2}$	$2.35 \cdot 10^{-2}$
strong	$w_c = 10^{-1}$	$1.44 \cdot 10^{-2}$	$1.97 \cdot 10^{-2}$

Table 6.1: Training and test relative errors obtained by training the ANN model with or without imposition of the equilibrium condition (in either weak or strong form) and with or without imposition of the cycle condition.

To make a comparison, this approach is similar to learning a language by studying its rules and the grammar: if the student, after having studied the rules, shows to be able to apply them in practice, we can say that he truly learned the language; if, on the contrary, he studies directly the sentences he needs, we cannot be sure whether he truly learned the language or he is simply repeating sentences learnt by heart.

In Table 6.1 we compare the training and test errors obtained with and without imposition of the equilibrium condition (in weak or strong form) and with or without imposition of the cycle condition. We conclude that the best strategy consists in introducing in the learning process both the cycle condition and the equilibrium condition (the latter with strong imposition).

6.2.1 Validation of the reduced model

We perform with the HF and the ANN model some of the test cases typically employed to validate microscopic cardiac force generation models and we check that the ANN model did not lose the capability of the HF model to reproduce the experimentally observed features of cardiac force generation. The results, reported in Fig. 6.1 and briefly commented in what follows, show a remarkably good match.

Steady-state force-calcium-length relationships

Figures 6.1a and 6.1b show the steady-state force-calcium and force-length relationship (see Sec. 1.3.2).

Isometric twitches

We perform simulations of isometric twitches, i.e. force transients in response to the calcium wave occurring at each heartbeat, at constant SL (see Sec. 1.3.3), by imposing the calcium transient of Eq. (2.23), with $c_0 = 0.1\,\mu M$, $t_0 = 0.1\,s$, $\tau_1 = 0.02\,s$, $\tau_2 = 0.11\,s$. In Fig. 6.1c, we set $c_{max} = 1.2\,\mu M$ and we consider different values of SL. Conversely, in Fig. 6.1d, we set $SL = 2\,\mu m$ and we let c_{max} vary.

Sudden development of tension

Figure 6.1e shows the responses to a step change in calcium at different levels, with $SL = 2.2\,\mu m$, showing that the rate of tension development following a sudden rise of $[Ca^{2+}]_i$ increases with the calcium level.

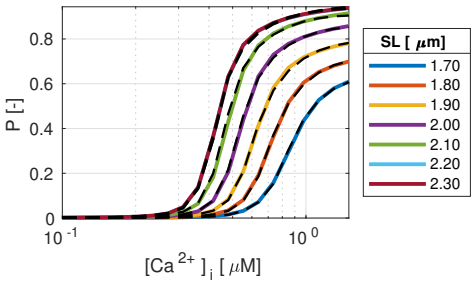

(a) Steady-state force-calcium relationship at different SL.

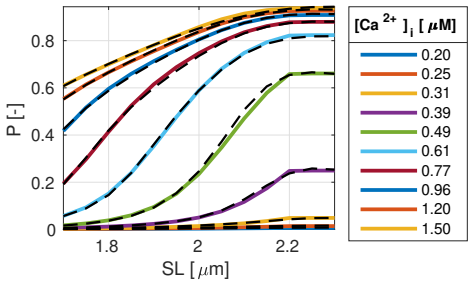

(b) Steady-state force-length relationship at different $[Ca^{2+}]_i$.

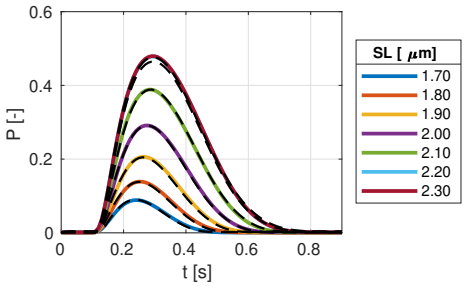

(c) Isometric twitches at different SL.

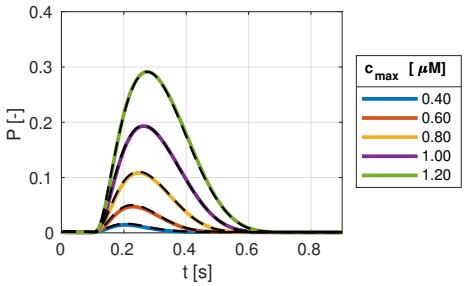

(d) Isometric twitches with different $[Ca^{2+}]_i$ peaks.

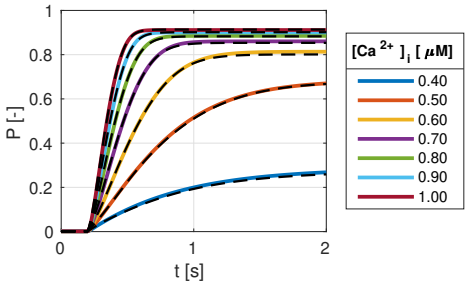

(e) Tesion development for different $[Ca^{2+}]_i$ steps.

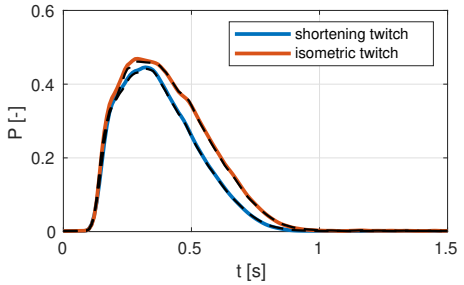

(f) Experimentally measured twitches (from [JT97]).

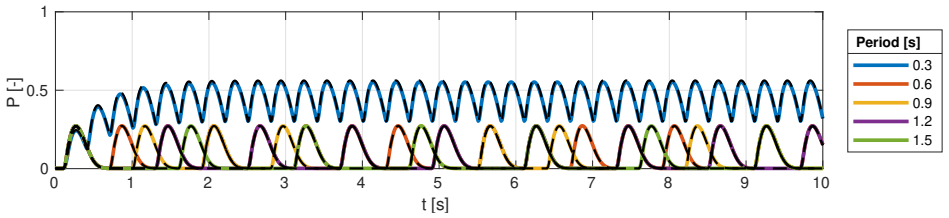

(g) Long-term response to periodic twitches at different frequencies.

Figure 6.1: Comparison between the results of the HF model activation-MH (colored solid lines) and the corresponding ANN-based ROM (black dashed lines) for different test cases, discussed in Sec. 6.2.1.

Isometric versus shortening twitches

The systolic contraction of the myocardium leads to a shortening of the muscle fibers and, as a consequence, to a decrease of SL. Therefore, in the normal cardiac activity, shortening twitches, rather than isometric twitches, are observed. To investigate the difference between the two settings, we consider the experimentally measured $[\mathrm{Ca}^{2+}]_\mathrm{i}$ and SL transients reported in [JT97]. The results of the simulations, shown in Fig. 6.1f, show that the decrease of SL leads to a decrease of force peak and to a slight decrease of duration of activation (see e.g. [Kat10; Ber01]).

Long-term twitches

The normal cardiac activity features a nearly periodic behavior. To test the capability of our model to sustain a periodic input after several cycles, we perform 10 s long simulations by applying the calcium transient (2.23), with $c_{\max} = 1.1\,\mu\mathrm{M}$ and $SL = 2\,\mu\mathrm{m}$, with different periods, ranging from 0.3 to 1.5 s (see Fig. 6.1g). We notice that for the highest frequency the *wave summation* phenomenon occurs, by which the effect of consecutive twitches sum up in a sustained contraction state (see e.g. [Kat10; Ber01]).

6.3 Reduced full-sarcomere models (SE-ODE and MF-ODE)

In this section we consider the SE-ODE and the MF-ODE models of full-sarcomere dynamics (proposed in Chap. 4). We recall that, with respect to the activation-MH model considered in Sec. 6.2, in this case we have a further input, namely the time derivative of SL. Hence, we define the space of the inputs

$$\mathbf{u}(t) = ([\mathrm{Ca}^{2+}]_\mathrm{i}(t), SL(t), \frac{d}{dt}SL(t))^T$$

as:

$$U = [c_{\min}, c_{\max}] \times [SL_{\min}, SL_{\max}] \times [v^{SL}_{\min}, v^{SL}_{\max}],$$

where we prudentially set $c_{\min} = 0\,\mu\mathrm{M}$, $c_{\max} = 1.2\,\mu\mathrm{M}$, $SL_{\min} = 1.6\,\mu\mathrm{M}$, $SL_{\max} = 2.4\,\mu\mathrm{M}$, $v^{SL}_{\max} = -v^{SL}_{\min} = 12\,\mu\mathrm{m\,s}^{-1}$.

Clearly, the input functions used in the training set must be consistent with the fact that the third input variable is the time derivative of the second one. Hence, unlike for the activation-MH model, in this case we cannot employ sharp step responses (corresponding to $\frac{d}{dt}SL(t) \to \pm\infty$). We insert in the training set the following functions.

- 20 *smoothed* step responses, where we randomly select a pair $\overline{c} \in [c_{\min}, c_{\max}]$ and $\overline{SL} \in [SL_{\min}, SL_{\max}]$ and we define:

$$[\mathrm{Ca}^{2+}]_\mathrm{i}(t) = c_0 + (\overline{c} - c_0)\mathbb{1}_{[t_1,t_3)}(t),$$

$$SL(t) = \begin{cases} SL_0 & t \in [0, t_1), \\ SL_0 + \frac{\overline{SL}-SL_0}{2}\left(1 + \cos\left(\pi\frac{t_2-t}{t_2-t_1}\right)\right) & t \in [t_1, t_2), \\ \overline{SL} & t \in [t_2, t_3), \\ \overline{SL} + \frac{SL_0-\overline{SL}}{2}\left(1 + \cos\left(\pi\frac{t_4-t}{t_4-t_3}\right)\right) & t \in [t_3, t_4), \\ SL_0 & t \in [t_4, T], \end{cases}$$

where the amplitude of the time intervals $[t_1, t_2]$ and $[t_3, t_4]$ is chosen so that the time derivative of SL is always contained in the range $[v_{\min}^{SL}, v_{\max}^{SL}]$. Specifically, we set $t_1 = 0.05\,\mathrm{s}$, $t_2 = 0.12\,\mathrm{s}$, $t_3 = 1.18\,\mathrm{s}$, $t_4 = 1.25\,\mathrm{s}$ and $T = 2\,\mathrm{s}$. Moreover, during the time interval $[t_4, T]$ the model state $\mathbf{X}$ goes back (up to an error lower than 10^{-4}) to $\mathbf{X}_0$. Hence, we insert the indexes corresponding to the samples of this first class into the set J_c.

- 50 randomly generated inputs of duration $T = 0.5\,\mathrm{s}$.

In order to better capture the velocity-related effects (that are more relevant than for the activation-MH model, which neglects the dependence on the shortening velocity), we adopt a higher temporal resolution than in Sec. 6.2, by setting $\Delta t = 2 \cdot 10^{-3}\,\mathrm{s}$. However, to lower the computational cost associated with the ANN training, we evaluate the loss functional (6.5) with a time step of $\Delta t = 1 \cdot 10^{-2}\,\mathrm{s}$. On the basis of the results obtained in Sec. 6.2, we adopt a strong imposition of the equilibrium condition and we set $w_{\mathrm{c}} = 10^{-1}$.

We notice that, unlike the activation-MH model, the SE-ODE and the MF-ODE models feature two distinct outputs, namely $T_{\mathrm{a}}(t)$ and $K_{\mathrm{a}}(t)$. However, the results of numerical simulations show that the values of the two outputs feature a very high correlation (data not shown). Hence, we believe that, in the case of the SE-ODE and MF-ODE models, the output-outside-the-state approach is more convenient than the input-inside-the-state approach, as the latter would "lost resources", by making two state variables coincide with the highly correlated variables $T_{\mathrm{a}}(t)$ and $K_{\mathrm{a}}(t)$.

As in Sec. 6.2, we adopt a trial-and-error approach to select the hyperparameters. For brevity reasons, we only report the final setup. For both the SE-ODE and the MF-ODE model, we train an ANN model with $n = 3$ internal variables. The ANN representing the observation function $\mathbf{g}$ has a single hidden layer with 4 neurons, while the ANN representing the right-hand side $\mathbf{f}$ has two hidden layers with 6 (for the SE-ODE model) or 7 neurons (for the MF-ODE model) in both layers. The ANN model trained from the results of the SE-ODE model features a training error of $1.29 \cdot 10^{-2}$ and a test error of $2.46 \cdot 10^{-2}$, while the ANN model trained from the MF-ODE model has a training and a test error of $0.85 \cdot 10^{-2}$ and $1.50 \cdot 10^{-2}$ respectively. Similarly to Sec. 6.2, we insert in the testing set a collection of smoothed step inputs, randomly generated inputs, the inputs described in Sec. 6.3.1 and long-term inputs.

6.3.1 Validation of the reduced models

In this section we validate the two reduced ANN-based models, whose derivation is described above in Sec. 6.3, with respect to the HF models SE-ODE and MF-ODE. With this aim, similarly to what done in Sec. 6.2.1, we consider some of test cases typically employed to validate cardiac force generation models. Specifically, we consider:

- The steady-state force-calcium and force-length relationships.
- Isometric twitches for different values of SL and of calcium peak, where we apply the calcium transient predicted by the TTP06 model for human cardiomyocytes (suitably rescaled to obtain different calcium peak values).
- Shortening twitches for different values of calcium peak, by adopting the calcium transient of the TTP06 model and the SL transient of Eq. (2.24).
- Responses to steps in calcium concentration.

- Long-term periodic twitches, in order to test the capability of the ROM to sustain a long simulation, obtained by applying the calcium transient of the TTP06 model with period $T = 0.8\,\mathrm{s}$.

The results obtained for the SE-ODE and the MF-ODE models are respectively shown in Figs. 6.2 and 6.3. In both cases, the results show a good agreement between the HF and the ROMs, under both steady-state and dynamic conditions.

6.4 Discussion

The ANN models described in this chapter are built from data generated by the corresponding HF models. This is somehow similar to the way the so-called phenomenological models, i.e. models built by fitting the experimental observations with a few number of variables (see e.g. [HMTK98; NHS06; Ric+08; Lan+17]), are built. A natural question is how those models compare with the ANN models.

Building a model consists in the solution of an inverse problem: starting from experimental observations, one looks for a law, written in mathematical terms, and a set of parameters describing the phenomenon that generated the observations themselves. However, experimental data are typically noisy and defective (this is particularly evident in the case considered in this work, due to the microscopic scale at which force is generated and to the intrinsic difficulties in measuring the internal properties of myofilaments without damaging them [Ken+86; DKT02; TK+08]). In the context of inverse problems and statistical learning, the action of compensating for noise and deficiency of data is known as *regularization* (see e.g. [Hay09; LBH15]). Regularization is typically performed either by suitable penalization of the unknown variables, or by restricting the set of candidate solutions [KS06].

Phenomenological models are derived by finding the best fit of experimental data with a simple law chosen a priori. Such a priori assumptions allow for a lumped description of the phenomenon with a small number of parameters to be tuned from experimental data. This is crucial, due to the noisy and defective nature of data. In fact, such a priori assumptions are a way of performing regularization. For instance, to reproduce the nonlinear response of activation to calcium concentration – consequence of the nearest-neighborhood interaction within units – without explicitly representing the units themselves, a power law dependence on $[\mathrm{Ca}^{2+}]_\mathrm{i}$ is typically assumed, and the exponent is estimated by fitting experimental data. However, this law has a phenomenological basis and it is not derived by first principles [Ric+08].

With our approach, instead, regularization is performed during the construction of the HF model thanks to the introduction of physics first principles and to a detailed description of the microscopic arrangement of the contractile system. In such a way, indeed, the set of possible relationships among the variables is restricted to those satisfying some physical principles. Clearly, a detailed physics-based description leads to complex models (in the previous example, a physics-based description of nearest-neighborhood interactions within units is not possible without a spatially-explicit description of the filament). On the other hand, establishing a model on physics principles clearly enhances its predictive power. Then, in a second stage, the ROM is learned from the HF model, which does not suffer from the problems affecting experimental data: training data can be generated from the HF model without noise and without limitations in their quantity. This allows to fit data within a much wider class of candidate solutions (specifically, we fit training data with ANN-based models,

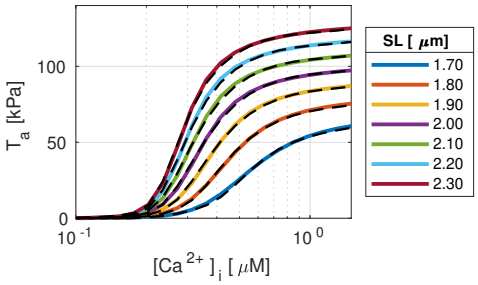

(a) Steady-state force-calcium relationship at different SL.

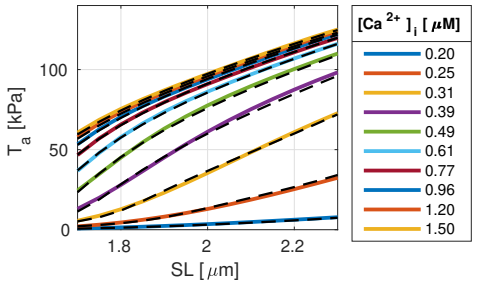

(b) Steady-state force-length relationship at different $[Ca^{2+}]_i$.

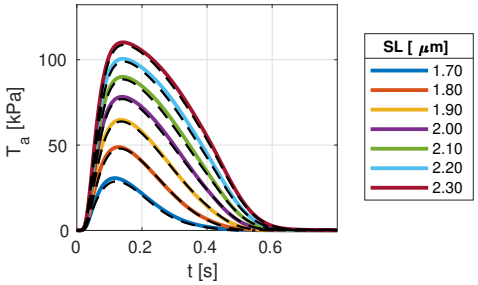

(c) Isometric twitches at different SL.

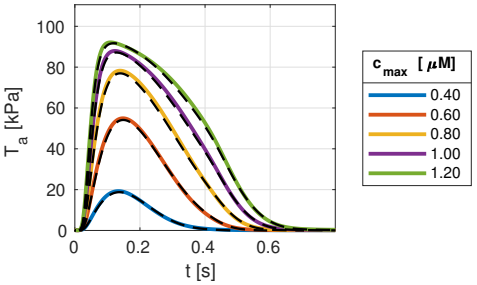

(d) Isometric twitches with different $[Ca^{2+}]_i$ peaks.

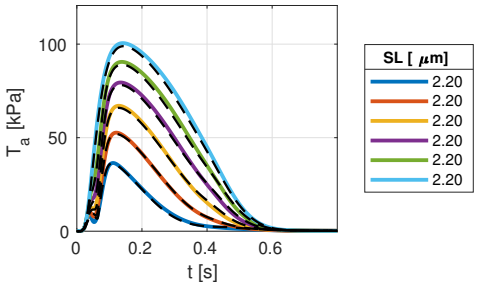

(e) Shortening twitches with different $[Ca^{2+}]_i$ peaks.

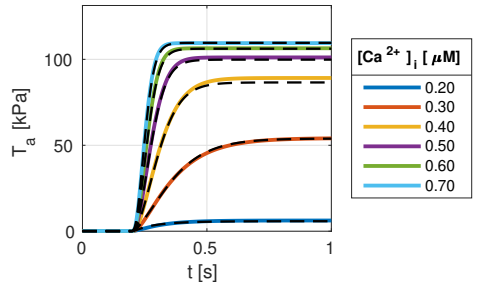

(f) Tesion development for different $[Ca^{2+}]_i$ steps.

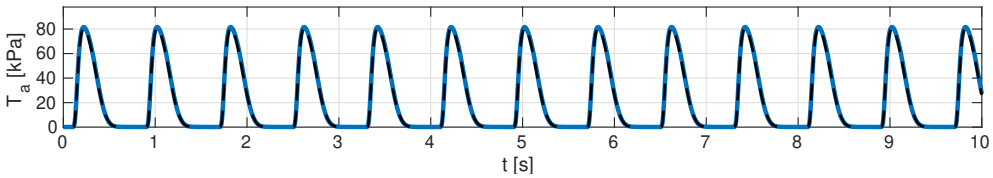

(g) Long-term response to periodic twitches.

Figure 6.2: Comparison between the results of the HF model SE-ODE (colored solid lines) and the corresponding ANN-based ROM (black dashed lines) for different test cases, discussed in Sec. 6.3.1.

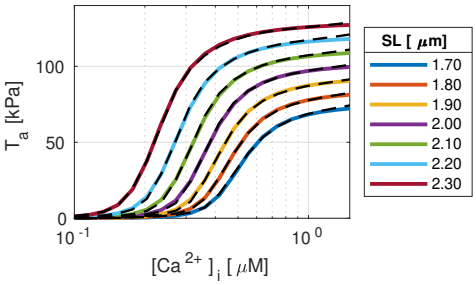

(a) Steady-state force-calcium relationship at different SL.

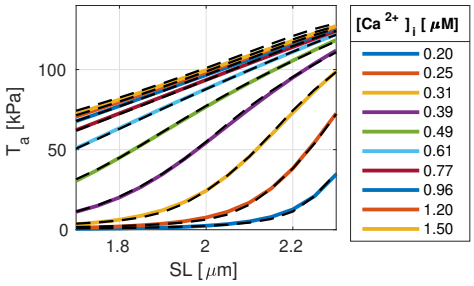

(b) Steady-state force-length relationship at different $[Ca^{2+}]_i$.

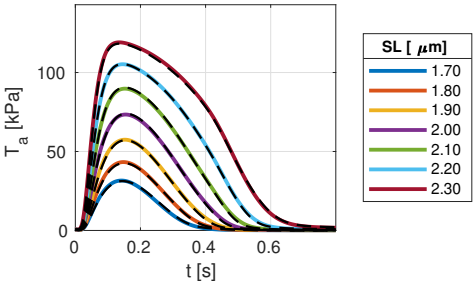

(c) Isometric twitches at different SL.

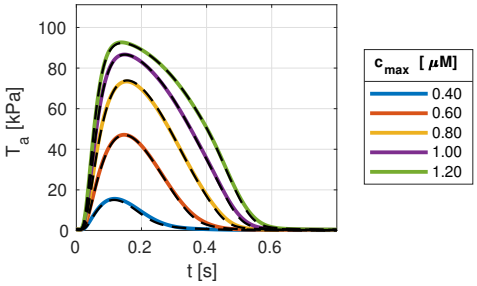

(d) Isometric twitches with different $[Ca^{2+}]_i$ peaks.

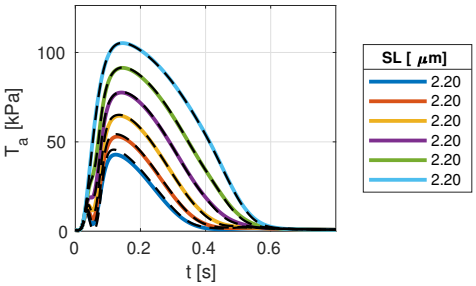

(e) Shortening twitches with different $[Ca^{2+}]_i$ peaks.

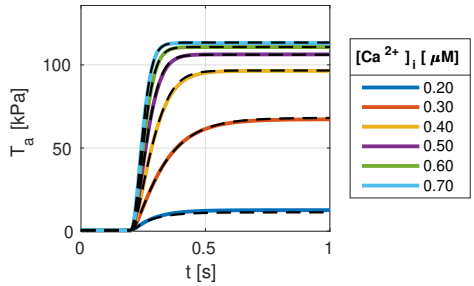

(f) Tesion development for different $[Ca^{2+}]_i$ steps.

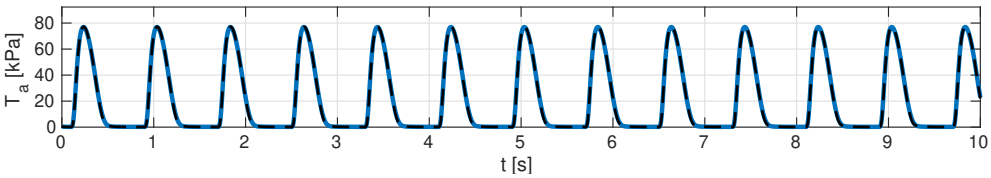

(g) Long-term response to periodic twitches.

Figure 6.3: Comparison between the results of the HF model MF-ODE (colored solid lines) and the corresponding ANN-based ROM (black dashed lines) for different test cases, discussed in Sec. 6.3.1.

which are able to virtually represent all ODE models, if a sufficient number of neurons is used, as proved in Chap. 5).

To summarize, whereas phenomenological models are directly derived from experimental observations, with our approach the process is splitted into two stages. First, we build an HF model, by compensating for the deficiency and bad quality of experimental data thanks to physics. Then, in a second stage, we build a ROM, by fitting data (no more noisy nor defective) generated by HF model. Thus, the ROM should be seen merely as a way of efficiently solving the physics-based model itself.

A further advantage of building a model on the ground of a microscopical description is that this allows to investigate the effects of microscopical properties on the macro-level tissue features (e.g. study the effect of drugs affecting the binding rate of myofilament proteins), whereas the parameters of phenomenological models may not have a clear physical interpretation.

6.5 Final remarks

In this chapter, we have extended the purely black-box MOR approach technique proposed in Chap. 5 by informing the learning machine about some a priori knowledge on the HF model to be reduced. In this way we have obtained a semi-physical, or gray-box, MOR technique.

Successively, we have applied such technique to the activation-MH model, proposed in Chap. 2, and to the SE-ODE and MF-ODE models, proposed in Chap. 4. In this manner, we have derived an ANN-based ROM for each of the above mentioned HF models. These ROMs approximate the results of the corresponding HF models within a relative error of the order of 10^{-2} and with a drastic reduction of the computational cost associated to their numerical approximation. Indeed, the ANN-based ROMs feature as few as two or three state variables, and allow to simulate 1 s of physical time in less than 1 ms of computational time, thus reducing by a factor 10^4 the computational time needed by the corresponding HF models.

At a first sight, the derivation of the models proposed in Part I, which allow to simulate the force generation phenomenon with a significantly reduced computational complexity than with MC (Monte Carlo) models, might appear useless, in light of the MOR technique presented in this chapter. Indeed, the latter technique could in principle be applied directly to the computationally expensive MC models, thus providing ROMs capable of reproducing their results with a very small computational effort. However, the models proposed in Part I (such as the activation-MH model, the SE-ODE and the MF-ODE model) find application in several contexts. Indeed, we recall that the ANN-based ROMs derived in this chapter are associated to a specific set of parameters. Hence, if different values of the parameters are considered, the training phase needs to be re-executed. Conversely, the models proposed in Part I allow to directly investigate the effects on the macroscale of the parameters describing the microscopic force generation apparatus and are suitable for patient-specific personalization of the models. Moreover, the accurate calibration performed in Sec. 4.3 has been possible thanks to the reduced computational cost of the models proposed in Part I. Finally, we remark that the training of the ANN-based ROMs requires order of 10^2 simulations generated with the HF model. Therefore, the generation of an adequate number of simulations with, e.g., the W12 model (that requires nearly 72 hours to simulate 1 s of physical sime, see Chap. 2), would demand nearly one year of computational time.

Part III

Multiscale integrated cardiac electromechanics

Chapter 7

Upscaling active force subcellular models

In Part I we derived models describing the generation of active force in the cardiac muscle at the subcellular level. Then, in Part II, we proposed a strategy to reduce the computational cost associated with the numerical approximation of such models, in order to make them suitable for organ-level simulations. In this last part (Part III) the goal is that of coupling the microscale models proposed in Part I with models of cardiac electrophysiology and tissue mechanics to build a multiscale integrated EM model.

Cardiac EM is in fact a multiscale problem, with spatial scales ranging from tens of nanometers (XB dynamics) to centimeters (ventricle mechanics) and temporal scales ranging from microseconds (XB dynamics) to seconds (heartbeat) [Kat10; Ber01]. As the direct numerical approximation of the EM problem with a resolution corresponding to the smallest involved spatial scale (i.e. by explicitly representing all the cardiomyocytes composing the myocardium) would clearly lead to unbearable computational costs, a multiscale formulation in mandatory in this setting. Hence, in this chapter we derive some relationships linking the microscopic quantities associated with the force generation phenomenon (such as the sarcomere elongation and the sarcomere-level active tension) with quantities referred to the macroscale (such as the tissue strain and stress tensors).

Moreover, the active force at the myofilament level is largely stochastic and it features significant stochastic fluctuations. In this chapter, thus, we also study the effect of stochasticity when a large number of interacting myofilaments are arranged in the series-parallel manner they are arranged in the cardiac tissue.

Contents

7.1 Continuum mechanics

We start by recalling the basic notion of continuum mechanics that are needed to describe the tissue strains and stresses at the macroscopic scale. Detailed derivations of the results here shown can be found, e.g., in [Ant95; Ogd97].

7.1.1 Kinematics

Let $\Omega_0 \subset \mathbb{R}^d$, where $d = 3$, be an open connected set, that we denote as the *reference (or undeformed) configuration*, designating the region of space occupied by an elastic body at rest. We consider a time-dependent *deformation map* $\varphi : \Omega_0 \times [0, T] \to \mathbb{R}^d$ and the associated *deformation gradient* $\mathbf{F}(\mathbf{X}, t) = \nabla_0 \varphi(\mathbf{X}, t)$, where ∇_0 denotes the nabla differential operator in the reference (material) coordinate. Hence, we denote by $\mathbf{X}$ the material coordinate and by $\mathbf{x} = \varphi(\mathbf{X})$ the spatial coordinate. The deformation map is assumed to be smooth enough (twice continuously differentiable is enough, but weaker regularity is admissible), injective and orientation preserving (i.e. its Jacobian $J = \det \mathbf{F}$ satisfies $J > 0$ for any $\mathbf{X} \in \Omega_0$). We denote by $\mathbf{N}$ the outward unit vector normal to the boundary of Ω_0 and by $\mathbf{n}$ the outward unit vector normal to the boundary of the deformed configuration $\Omega(t)$ (i.e. the image of φ at time t). Oriented infinitesimal surfaces in the reference and current configurations are related by the Nanson's formula [Ant95; Ogd97]:

$$\mathbf{n}\, dA = J\, \mathbf{F}^{-T} \mathbf{N}\, dA_0, \qquad \mathbf{N}\, dA_0 = J^{-1}\, \mathbf{F}^T \mathbf{n}\, dA, \tag{7.1}$$

where dA_0 and dA denote the infinitesimal areas in the reference and current configuration, respectively.

We define the *displacement field* $\mathbf{d}(\mathbf{X}) := \varphi(\mathbf{X}) - \mathbf{X}$. We notice that we have $\mathbf{F} = \mathbf{I} + \nabla_0 \mathbf{d}$, where $\mathbf{I}$ denotes the identity tensor. We also introduce the *left Cauchy-Green tensor*, the *right Cauchy-Green tensor* and the *Green-Saint Venant tensor*, defined respectively as:

$$\mathbf{B} = \mathbf{F}\mathbf{F}^T, \qquad \mathbf{C} = \mathbf{F}^T\mathbf{F}, \qquad \mathbf{E} = \frac{1}{2}\left(\mathbf{C} - \mathbf{I}\right). \tag{7.2}$$

We define the invariants of $\mathbf{C}$, which coincide with those of $\mathbf{B}$, as:

$$\mathcal{I}_1 = \mathrm{tr}(\mathbf{C}), \qquad \mathcal{I}_2 = \frac{1}{2}\left(\mathrm{tr}(\mathbf{C})^2 - \mathrm{tr}(\mathbf{C}^2)\right), \qquad \mathcal{I}_3 = \det \mathbf{C} = J^2.$$

By denoting by Lin the vector space of the linear transformations from $\mathbb{R}^d$ into itself, we introduce the following subsets:

$$\begin{aligned} \mathrm{Lin}^+ &:= \{\mathbf{A} \in \mathrm{Lin} \text{ s.t. } \det \mathbf{A} > 0\}, \\ \mathrm{Sym}^+ &:= \{\mathbf{A} \in \mathrm{Lin}^+ \text{ s.t. } \mathbf{A}^T = \mathbf{A}\}, \\ \mathrm{Orth}^+ &:= \{\mathbf{A} \in \mathrm{Lin}^+ \text{ s.t. } \mathbf{A}^T = \mathbf{A}^{-1}\}. \end{aligned} \tag{7.3}$$

By these definitions, we clearly have $\mathbf{F} \in \mathrm{Lin}^+$. Moreover, thanks to the assumption $J > 0$, by the polar decomposition theorem [Ant95; Ogd97], there exists a unique $\mathbf{R} \in \mathrm{Orth}^+$ and $\mathbf{U}, \mathbf{V} \in \mathrm{Sym}^+$ such that:

$$\mathbf{F} = \mathbf{R}\mathbf{U} = \mathbf{V}\mathbf{R}.$$

Moreover, $\mathbf{C} = \mathbf{U}^2$, $\mathbf{B} = \mathbf{V}^2$.

7.1.2 Stress tensors

The state of stress at a given material point $\mathbf{X}$ is defined by the collection of the stress vectors per unit area associated with each plane passing through $\mathbf{X}$, that we denote by $\mathbf{t}^{\mathbf{m}}(\mathbf{X})$, where $\mathbf{m}$ is the unit vector orthogonal to the plane. By the Cauchy stress theorem [Ant95; Ogd97], there exists a second-order symmetric tensor (more precisely, a tensor field), the *Cauchy stress tensor* $\mathbf{T}$, independent of the direction $\mathbf{m}$, such that $\mathbf{t}^{\mathbf{m}}(\mathbf{X}) = \mathbf{T}(\mathbf{X})\mathbf{m}$. The physical interpretation of the Cauchy tensor is thus given through its application to a unit vector. Indeed, if we consider a surface A intersecting the body in the current configuration (possibly belonging to its boundary), the total stress acting on the body through the surface is given by:

$$\mathbf{t} = \int_A \mathbf{T}\mathbf{n}\, dA, \tag{7.4}$$

where $\mathbf{n}$ denotes the unit vector normal to the surface. By the Nanson's formula, the same quantity can be written as an integral referred to the reference configuration:

$$\mathbf{t} = \int_{A_0} J\mathbf{T}\mathbf{F}^{-T}\mathbf{N}\, dA_0 = \int_{A_0} \mathbf{P}\mathbf{N}\, dA_0, \tag{7.5}$$

where $\mathbf{P} := J\mathbf{T}\mathbf{F}^{-T}$ is called the *first Piola-Kirchhoff stress tensor* (or simply Piola stress tensor).

The balance of momentum equation for the continuum body Ω_0 reads as follows:

$$\rho\frac{\partial^2 \mathbf{d}}{\partial t^2} - \nabla_0 \cdot \mathbf{P} = \mathbf{h} \qquad \text{in } \Omega_0 \times (0, T], \tag{7.6}$$

where $\nabla_0 \cdot$ denotes the divergence differential operator in reference coordinates, ρ denotes the density of the material and $\mathbf{h}$ denotes an external load (force per unit volume).

7.1.3 Hyperelasticity

For the sake of model closure, Eq. (7.6) must be supplemented with a material constitutive law, that is to say a relationship linking the state of strain of the body with its state of stress. The constitutive law can possibly depend on the rate of strain (e.g. in the case of visco-elastic materials), but in this work we focus on elastic materials, thus assuming that the stress tensors can be written as functions of the strain tensor (i.e. $\mathbf{T} = \mathbf{T}_{\mathbf{F}}(\mathbf{F})$ and $\mathbf{P} = \mathbf{P}_{\mathbf{F}}(\mathbf{F})$).

In particular, we focus on *hyperelastic materials*, characterized by a *strain energy density* $\mathcal{W}$, such that $\int_{\Omega_0} \mathcal{W}(\mathbf{X})dV_0$ gives the total elastic energy stored by the body as a consequence of the deformation. The strain energy density is uniquely determined by the deformation gradient, that is to say there exists a functional $\mathcal{W}_{\mathbf{F}} : \mathrm{Lin}^+ \to \mathbb{R} \cup \{+\infty\}$ such that $\mathcal{W}(\mathbf{X}) = \mathcal{W}_{\mathbf{F}}(\mathbf{F}(\mathbf{X}))$. Hyperelastic materials are such that the Piola stress tensor is obtained by differentiating the strain energy density with respect to $\mathbf{F}$:

$$\mathbf{P} = \frac{\partial \mathcal{W}}{\partial \mathbf{F}}. \tag{7.7}$$

7.1.4 Frame-indifference

Consider a given deformation with gradient $\mathbf{F}$. Suppose to further deform the body by a rigid rotation $\mathbf{Q}$. The new deformation gradient is given by $\mathbf{Q}\mathbf{F}$. Then, we expect

that the body is characterized by the same state of stress. This is a requirement, called *frame-indifference*, that needs to be satisfied by the material constitutive relation to be physically meaningful.

By the frame-indifference principle, if the stress vector in direction $\mathbf{m}$ before the rotation is $\mathbf{t}$, the force in direction $\mathbf{Qm}$, after the rotation, must be $\mathbf{Qt}$. This entails $\mathbf{T_F}(\mathbf{QF})\mathbf{Qm} = \mathbf{Qt} = \mathbf{QT_F}(\mathbf{F})\mathbf{m}$ for any direction $\mathbf{m}$, or, equivalently, $\mathbf{T_F}(\mathbf{QF}) = \mathbf{QT_F}(\mathbf{F})\mathbf{Q}^T$. By taking $\mathbf{Q} = \mathbf{R}^T$, we have $\mathbf{QF} = \mathbf{U} = \mathbf{C}^2$, and thus $\mathbf{T_F}(\mathbf{F}) = \mathbf{R}^T\mathbf{T_F}\sqrt{\mathbf{C}}\mathbf{R}$, so the function $\mathbf{T_F}$ is determined by its restriction to Sym^+. By similar considerations, the frame-indifference principle can be equivalently stated in one of the following ways. For any $\mathbf{Q} \in \mathrm{Orth}^+, \mathbf{F} \in \mathrm{Lin}^+$, we have:

$$\mathbf{T_F}(\mathbf{QF}) = \mathbf{Q}\,\mathbf{T_F}(\mathbf{F})\,\mathbf{Q}^T, \qquad \mathbf{P_F}(\mathbf{QF}) = \mathbf{Q}\,\mathbf{P_F}(\mathbf{F}), \qquad \mathcal{W}_\mathbf{F}(\mathbf{QF}) = \mathcal{W}_\mathbf{F}(\mathbf{F}).$$

Equivalently, it is possible to write the following quantities as functions of $\mathbf{C}$:

$$\mathbf{T} = \mathbf{T_C}(\mathbf{C}), \qquad \mathbf{P} = \mathbf{P_C}(\mathbf{C}), \qquad \mathcal{W} = \mathcal{W}_\mathbf{C}(\mathbf{C}).$$

7.1.5 Material symmetries

If we imagine to rotate a body by $\mathbf{Q} \in \mathrm{Orth}^+$ and then to apply a deformation with gradient $\mathbf{F}$, we expect the material response to be in general different than the response of the non-rotated body (that is, in general $\mathbf{T_F}(\mathbf{FQ}) \neq \mathbf{T_F}(\mathbf{F})$. However, some materials are such that their response in not affected by a precise class of rotations. This is linked to the symmetry properties of the material. This leads to the definition of the material-symmetry group as:

$$\begin{aligned}\mathcal{G} &:= \{\mathbf{Q} \in \mathrm{Orth}^+ : \mathbf{T_F}(\mathbf{FQ}) = \mathbf{T_F}(\mathbf{F}) \qquad \forall\, \mathbf{F} \in \mathrm{Lin}^+\} \\ &= \{\mathbf{Q} \in \mathrm{Orth}^+ : \mathbf{P_F}(\mathbf{FQ}) = \mathbf{P_F}(\mathbf{F})\,\mathbf{Q} \qquad \forall\, \mathbf{F} \in \mathrm{Lin}^+\} \\ &= \{\mathbf{Q} \in \mathrm{Orth}^+ : \mathcal{W}_\mathbf{F}(\mathbf{FQ}) = \mathcal{W}_\mathbf{F}(\mathbf{F}) \qquad \forall\, \mathbf{F} \in \mathrm{Lin}^+\}.\end{aligned}$$

Isotropic materials

Isotropic materials are such that $\mathcal{G} = \mathrm{Orth}^+$. In this case, taking $\mathbf{Q} = \mathbf{R}^T$, since $\mathbf{FQ} = \mathbf{V} = \sqrt{\mathbf{B}}$, all the quantities in the above definitions can be written as a function of $\mathbf{B}$:

$$\mathbf{T} = \mathbf{T_B}(\mathbf{B}), \qquad \mathbf{P} = \mathbf{P_B}(\mathbf{B}), \qquad \mathcal{W} = \mathcal{W}_\mathbf{B}(\mathbf{B}).$$

By combining this with frame-indifference, we get that $\mathcal{W}$ must be a function of the invariants of $\mathbf{B}$, that coincide with the invariants of $\mathbf{C}$, i.e. $\mathcal{W} = \mathcal{W}_\mathbb{I}(\mathcal{I}_1, \mathcal{I}_2, \mathcal{I}_3)$.

Transversely isotropic materials

Transversely isotropic materials are endowed with a preferential direction $\mathbf{a}$ and feature an isotropic behavior in the plane transverse to $\mathbf{a}$. More precisely, we have:

$$\mathcal{G} = \{\mathbf{Q} \in \mathrm{Orth}^+ : \mathbf{Qa} = \mathbf{a}\}.$$

This, combined with frame-indifference, is equivalent to writing the strain energy density as $\mathcal{W} = \mathcal{W}_\mathbb{I}(\mathcal{I}_1, \mathcal{I}_2, \mathcal{I}_3, \mathcal{I}_{4,a}, \mathcal{I}_{5,a})$, where:

$$\mathcal{I}_{4,a} = \mathbf{a}^T\mathbf{Ca} = |\mathbf{Fa}|^2, \qquad \mathcal{I}_{5,a} = \mathbf{a}^T\mathbf{C}^2\mathbf{a} = |\mathbf{Ca}|^2. \tag{7.8}$$

Orthotropic materials

Orthotropic materials have three mutually orthogonal preferential directions $\mathbf{a}$, $\mathbf{b}$ and $\mathbf{c}$:

$$\mathcal{G} = \{\mathbf{Q} \in \mathrm{Orth}^+ : \mathbf{Qa} = \mathbf{a}, \mathbf{Qb} = \mathbf{b}, \mathbf{Qc} = \mathbf{c}\}.$$

In this case the strain energy density can be written as

$$\mathcal{W} = \mathcal{W}_{\mathbb{I}}(\mathcal{I}_1, \mathcal{I}_2, \mathcal{I}_3, \mathcal{I}_{4,a}, \mathcal{I}_{5,a}, \mathcal{I}_{4,b}, \mathcal{I}_{5,b}),$$

or equivalentely, as

$$\mathcal{W} = \mathcal{W}_{\mathbb{I}}(\mathcal{I}_1, \mathcal{I}_2, \mathcal{I}_3, \mathcal{I}_{4,a}, \mathcal{I}_{4,b}, \mathcal{I}_{5,a}, \mathcal{I}_{8,ab}),$$

where we have defined the invariant $\mathcal{I}_{8,ab} = \mathbf{a}^T\mathbf{Cb} = \mathbf{Fa} \cdot \mathbf{Fb}$.

7.2 Linking the microscale with the macroscale

The heart muscle tissue is characterized by the presence of muscle fibers, organized in sheets (see Sec. 1.2.1), that endow the material with anisotropic properties. Indeed, the heart passive mechanical response is characterized by three mutually orthogonal preferential directions, namely $\mathbf{f}_0$, the direction of fibers, $\mathbf{s}_0$, the direction of sheets and $\mathbf{n}_0$, the fibers-sheets normal direction. The triplet $(\mathbf{f}_0, \mathbf{s}_0, \mathbf{n}_0)$ forms a local orthogonal frame of reference spanning the continuum Ω_0. In this thesis we do not consider the visco-elastic properties of the heart [GSH16] and we assume that the cardiac muscle tissue is described by an hyperelastic material constitutive relation.

In this section, we derive the relationships linking the microscale, where the generation of active force takes place, with the macroscale, thus allowing to couple the microscopic force generation models considered in the first two parts of this thesis with the mathematical models describing the muscle tissue.

We remark that the models presented in Part I have a stochastic nature, as they are based on CTMCs (continuous-time Markov Chains). Therefore, their solution is never a deterministic quantity, but rather a probability distribution (or some function of the probability distribution, such as an expected value or a distribution-moment). Cleary, the effect of the stochastic fluctuations characterizing the results of such models must be taken into account when the microscopic variables are coupled with other models. In this section we neglect, for the moment, the stochastic nature of the considered models, by identifying the model output with its expected value. Then, in Sec. 7.3 we will study the role of stochastic fluctuations when the microscopic models are coupled in a multiscale setting.

7.2.1 From the macroscale to the microscale

To link the tissue deformation at the macroscopic level with the microscopical stretch of sarcomeres, we compute the change of SL associated with a body deformation $\mathbf{d}$. Let us consider a sarcomere located at the material point $\mathbf{X} \in \Omega_0$. Let $\mathbf{X}_1, \mathbf{X}_2 \in \Omega_0$ denote the two ends of the sarcomere in the reference configuration. Being SL_0 the length of a sarcomere when the tissue is at rest, since sarcomeres are aligned with the fibers direction $\mathbf{f}_0$, we have:

$$\mathbf{X}_1 = \mathbf{X} - \frac{1}{2} SL_0\, \mathbf{f}_0(\mathbf{X}), \qquad \mathbf{X}_2 = \mathbf{X} + \frac{1}{2} SL_0\, \mathbf{f}_0(\mathbf{X}).$$

The sarcomere length at time t corresponds to the distance between the images of the two points through the deformation map. Thanks to the scale separation between the sarcomere level and the tissue level, the distance between the two close points $\varphi(\mathbf{X}_1, t)$ and $\varphi(\mathbf{X}_2, t)$ is well approximated by a first-order Taylor expansion:

$$\begin{aligned} SL(\mathbf{X}, t) &= |\varphi(\mathbf{X}_2, t) - \varphi(\mathbf{X}_1, t)| \\ &\simeq |\nabla_0 \varphi(\mathbf{X}, t)\ (\mathbf{X}_2 - \mathbf{X}_1)\,| \\ &= SL_0 |\mathbf{F}(\mathbf{X}, t)\, \mathbf{f}_0(\mathbf{X})| \\ &= SL_0 \sqrt{\mathcal{I}_{4,f}(\mathbf{X}, t)}, \end{aligned} \tag{7.9}$$

where $\mathcal{I}_{4,f} = \mathbf{F}\mathbf{f}_0 \cdot \mathbf{F}\mathbf{f}_0$ denotes the fourth invariant in the fibers direction (see Eq. (7.8)). Equation (7.9) provides a bridge from the macroscale to the microscale, as it allows to compute the microscopic quantity SL from the macroscopic tissue deformation $\mathbf{d}$.

7.2.2 From the microscale to the macroscale

The active force models proposed in Part I describe a pair of interacting AF and half MF. The force predicted by the models, thus, corresponds to the force generated by half MF and is denoted by F_{hf}. In order to link this scalar quantity, defined at the microscale, to the macroscopic momentum balance Eq. (7.6), we consider an infinitesimal surface A_0 in the reference configuration, orthogonal to $\mathbf{f}_0$. The active tension exerted through the surface has the same direction of fibers in the current configuration (i.e. $\mathbf{f} = \mathbf{F}\mathbf{f}_0 / |\mathbf{F}\mathbf{f}_0\,|$). Moreover, the intensity of the active stress vector corresponds to the force exerted by a half MF, times the number of crossed half filaments, given by $|A_0|\sigma_{\text{hf}}$, where σ_{hf} is the surface density of interacting AFs and MFs. Therefore, by Eq. (7.5), the active part of the Piola Stress tensor (that we denote by $\mathbf{P}^{\text{act}}$) satisfies:

$$\int_{A_0} \mathbf{P}^{\text{act}} \mathbf{f}_0 \, dA_0 = |A_0| \sigma_{\text{hf}} F_{\text{hf}} \frac{\mathbf{F}\mathbf{f}_0}{|\mathbf{F}\mathbf{f}_0\,|}.$$

By dividing both sides by $|A_0|$ and letting $|A_0| \to 0$, we get:

$$\mathbf{P}^{\text{act}} \mathbf{f}_0 = \sigma_{\text{hf}} F_{\text{hf}} \frac{\mathbf{F}\mathbf{f}_0}{|\mathbf{F}\mathbf{f}_0|}. \tag{7.10}$$

On the other hand, the active force through surfaces orthogonal to the directions $\mathbf{s}_0$ and $\mathbf{n}_0$ is null. By proceeding as above, we get:

$$\mathbf{P}^{\text{act}} \mathbf{s}_0 = \mathbf{0}, \quad \mathbf{P}^{\text{act}} \mathbf{n}_0 = \mathbf{0}. \tag{7.11}$$

Equations (7.10) and (7.11) give the outcome of the application of $\mathbf{P}^{\text{act}}$ to three independent vectors and thus allow to uniquely identify it as:

$$\mathbf{P}^{\text{act}} = \sigma_{\text{hf}} F_{\text{hf}} \frac{\mathbf{F}\mathbf{f}_0 \otimes \mathbf{f}_0}{|\mathbf{F}\mathbf{f}_0|}. \tag{7.12}$$

We obtain in this way an expression for the active Piola stress tensor also used in other works available in literature (see e.g. [Was+15; Aug+16; GMR19]).

Due to the additive nature of force, the total Piola stress tensor is given by $\mathbf{P} = \mathbf{P}^{\text{pass}} + \mathbf{P}^{\text{act}}$, where the passive part of the Piola stress tensor is obtained as $\mathbf{P}^{\text{pass}} =$

$\frac{\partial \mathcal{W}}{\partial \mathbf{F}}$. Similarly, the Cauchy stress tensor can be written as $\mathbf{T} = \mathbf{T}^{\text{pass}} + \mathbf{T}^{\text{act}}$, where:

$$\begin{aligned} \mathbf{T}^{\text{pass}} &= J^{-1}\mathbf{P}^{\text{pass}}\mathbf{F}^T = J^{-1}\frac{\partial \mathcal{W}}{\partial \mathbf{F}}\mathbf{F}^T, \\ \mathbf{T}^{\text{act}} &= J^{-1}\mathbf{P}^{\text{act}}\mathbf{F}^T = J^{-1}\sigma_{\text{hf}}F_{\text{hf}}\frac{\mathbf{F}\mathbf{f}_0 \otimes \mathbf{F}\mathbf{f}_0}{|\mathbf{F}\mathbf{f}_0|}. \end{aligned} \tag{7.13}$$

Models without XB description

We consider now the case of models not incorporating an explicit description of XBs, such as the activation-MH, presented in Chap. 2. The underlying assumption of such models is that the fraction of cycling XBs is given by the permissivity and that each cycling XB exerts a fixed amount of force, so that the total active tension is proportional to the permissivity. Thus, by denoting by $F_{\text{hf}}^{\max}$ the force exerted by the half filament in condition of full activation (i.e. $P = 1$), Eq. (7.12) reads:

$$\mathbf{P}^{\text{act}} = \sigma_{\text{hf}}F_{\text{hf}}^{\max}P\frac{\mathbf{F}\mathbf{f}_0 \otimes \mathbf{f}_0}{|\mathbf{F}\mathbf{f}_0|} = T_{\text{a}}^{\max}P\frac{\mathbf{F}\mathbf{f}_0 \otimes \mathbf{f}_0}{|\mathbf{F}\mathbf{f}_0|}, \tag{7.14}$$

where $T_{\text{a}}^{\max} = \sigma_{\text{hf}}F_{\text{hf}}^{\max}$ is the maximum tissue-level active tension (see Eq. (2.5)).

Models with XB description

We consider now the models proposed in Chap. 4 (such as the SE-ODE and the MF-ODE models) and we show the specific form assumed by Eq. (7.12) in the case that an explicit representation of XBs is available. We recall that the force generated by half MF is given by (see Eq. (4.31)):

$$F_{\text{hf}} = k_{\text{XB}}\frac{SL_0}{2}N_A\mu^1, \tag{7.15}$$

where μ^1 denotes the mean distortion of attached XBs times the fraction of attached XBs. By combining Eq. (4.31) with Eq. (7.12), we get:

$$\mathbf{P}^{\text{act}} = \frac{1}{2}\sigma_{\text{hf}}\,k_{\text{XB}}\,SL_0\,N_A\frac{\mathbf{F}\mathbf{f}_0 \otimes \mathbf{f}_0}{|\mathbf{F}\mathbf{f}_0\,|}\mu^1 = a_{\text{XB}}\frac{\mathbf{F}\mathbf{f}_0 \otimes \mathbf{f}_0}{|\mathbf{F}\mathbf{f}_0\,|}\mu^1, \tag{7.16}$$

where we have defined the active elastic modulus $a_{\text{XB}} := \frac{1}{2}\sigma_{\text{hf}}\,k_{\text{XB}}\,SL_0\,N_A$. Even if in Chap. 4 we have directly calibrated the value of a_{XB} from experimental measurements, this equation provides a link between the macroscopic parameter a_{XB} and microscopic quantities.

The same result can be derived by energetic considerations. Indeed, if we define the energy associated to a single XB as:

$$\mathcal{W}^{\text{XB}}(x) = \frac{1}{2}k_{\text{XB}}x^2,$$

the energy stored by the pair of interacting AF and half MF is:

$$\mathcal{W}^{\text{hf}} = \sum_{i \text{ s.t. } Z_i \neq \emptyset} \mathcal{W}^{\text{XB}}(Z_i).$$

Thus, the energy density, at the tissue level, stored by XBs is given by:

$$\mathcal{W}^{\text{act}} = \rho_{\text{hf}}\mathcal{W}^{\text{hf}} = \frac{2\,\sigma_{\text{hf}}}{SL_0}\mathcal{W}^{\text{hf}},$$

where $\rho_{\rm hf} = 2\,\sigma_{\rm hf}/SL_0$ is the volume density of interacting AFs and half MFs. Therefore, by identifying the active part of the strain energy density with its expected value, we have:

$$\begin{aligned}
\mathcal{W}^{\rm act}(t) &= \frac{\sigma_{\rm hf}\,k_{\rm XB}}{SL_0}\sum_{i=1}^{N_A}\int_{-\infty}^{+\infty} x^2 \mathbb{f}\left[Z_i^t = x\right]dx \\
&= \frac{\sigma_{\rm hf}\,k_{\rm XB}}{SL_0}\sum_{i=1}^{N_A}\int_{-\infty}^{+\infty} x^2 \left(\mathbb{f}\left[Z_i^t = x, T_i^t = \mathcal{P}\right] + \mathbb{f}\left[Z_i^t = x, T_i^t = \mathcal{N}\right]\right)dx \\
&= \frac{\sigma_{\rm hf}\,k_{\rm XB}}{SL_0}\sum_{i=1}^{N_A}\int_{-\infty}^{+\infty} x^2 \left(n_{i,\mathcal{P}}(x,t) + n_{i,\mathcal{N}}(x,t)\right)dx \\
&= \frac{\sigma_{\rm hf}\,k_{\rm XB}\,SL_0\,N_A}{4}\mu^2(t) \\
&= \frac{1}{2}a_{\rm XB}\,\mu^2(t),
\end{aligned} \tag{7.17}$$

where we have used the definitions of Eqs. (4.21), (4.28) and (4.32).

The active part of the Piola stress tensor can be obtained by differentiating the energy density stored by XBs, $\mathcal{W}^{\rm act}$, with respect to the strain tensor $\mathbf{F}$. However, to compute the differential of $\mathcal{W}^{\rm act}$ with respect to $\mathbf{F}$, one should take into account that the microscopic strain x is related to the macroscopic one by Eq. (7.9). With this aim, we observe that, denoting by $\hat{x}$ the XB elongation in reference (Lagrangian) coordinates, we have:

$$x = \hat{x} + \frac{SL - SL_0}{2}\,.$$

To simplify the notation, we define $\lambda = \sqrt{\mathcal{I}_{4,f}} - 1$, so that the elongation of fibers in direction $\mathbf{f}_0$ is $1+\lambda$ (see Eq. (7.9)). We have $SL = SL_0(1+\lambda)$, which entails $x = \hat{x} + \frac{SL_0}{2}\lambda$. We thus define as $\hat{\mu}^p$ the moments of the displacements in Lagrangian coordinates, for $p \in \mathbb{N}$:

$$\begin{aligned}
\hat{\mu}^p(t) &= \frac{1}{N_A}\sum_{i=1}^{N_A}\int_{-\infty}^{+\infty}\left(\frac{\hat{x}}{SL_0/2}\right)^p\left(n_{i,\mathcal{N}}\left(\hat{x}+\frac{SL_0}{2}\lambda, t\right) + n_{i,\mathcal{P}}\left(\hat{x}+\frac{SL_0}{2}\lambda, t\right)\right)d\hat{x} \\
&= \frac{1}{N_A}\sum_{i=1}^{N_A}\int_{-\infty}^{+\infty}\left(\frac{x}{SL_0/2} - \lambda\right)^p\left(n_{i,\mathcal{N}}(x,t) + n_{i,\mathcal{P}}(x,t)\right)dx.
\end{aligned}$$

Therefore, we have:

$$\mu^0 = \hat{\mu}^0, \qquad \mu^1 = \lambda\hat{\mu}^0 + \hat{\mu}^1, \qquad \mu^2 = \lambda^2\hat{\mu}^0 + 2\lambda\hat{\mu}^1 + \hat{\mu}^2. \tag{7.18}$$

This entails:

$$\mathcal{W}^{\rm act} = \frac{1}{2}a_{\rm XB}\left(\hat{\mu}^0\lambda^2 + 2\hat{\mu}^1\lambda + \hat{\mu}^2\right). \tag{7.19}$$

Thanks to the fact that we have written the XBs coordinate in the reference configuration, the unique term depending on $\mathbf{F}$ in Eq. (7.19) is $\lambda = \lambda(\mathbf{F})$. Therefore, the active part of the Piola stress tensor can be obtained by the chain rule as:

$$\mathbf{P}^{\rm act} = \frac{\partial\mathcal{W}^{\rm act}}{\partial\mathbf{F}} = \frac{\partial\mathcal{W}^{\rm act}}{\partial\lambda}\frac{\partial\lambda}{\partial\mathbf{F}},$$

where:

$$\frac{\partial \mathcal{W}^{\text{act}}}{\partial \lambda} = a_{\text{XB}} \left(\hat{\mu}^0 \lambda + \hat{\mu}^1 \right), \qquad \frac{\partial \lambda}{\partial \mathbf{F}} = \frac{\mathbf{F}\mathbf{f}_0 \otimes \mathbf{f}_0}{1+\lambda}.$$

Finally, we obtain the same result of Eq. (7.16):

$$\mathbf{P}^{\text{act}} = a_{\text{XB}} \left(\hat{\mu}^0 \lambda + \hat{\mu}^1 \right) \frac{\mathbf{F}\mathbf{f}_0 \otimes \mathbf{f}_0}{1+\lambda}. \tag{7.20}$$

From Eq. (7.20) it follows that the active stress vanishes whenever $\mu^1 = \left(\hat{\mu}^0 \lambda + \hat{\mu}^1 \right)$ vanishes, that is to say when the average elongation of attached XBs is zero. Moreover, the active stress tends to compress the fibers when $\mu^1 > 0$ (i.e. when the XBs are attached in average with positive displacement) and to stretch them when $\mu^1 < 0$ (negative average displacement).

Notice that the condition $\mu_1 = 0$, giving zero active force, is equivalent to the condition $\lambda = \lambda^* := -\hat{\mu}^1/\hat{\mu}^0$, corresponding to the mean XB strain in reference coordinates. With this notation, when $\hat{\mu}^0 > 0$, the active tensor can be written as:

$$\mathbf{P}^{\text{act}} = \hat{\mu}^0 a_{\text{XB}} \left(\lambda - \lambda^* \right) \frac{\mathbf{F}\mathbf{f}_0 \otimes \mathbf{f}_0}{1+\lambda}. \tag{7.21}$$

Equation (7.21) can be interpreted as follows: the attached XBs produce a restore force around the equilibrium $\lambda = \lambda^*$ with a stiffness equals to $\hat{\mu}^0 a_{\text{XB}}$, i.e. the stiffness associated to the full activated state times the fraction of attached XBs.

7.2.3 Order preserving properties of the active stress Piola tensor

In both the cases considered in Sec. 7.2.2, the active part of the Piola stress tensor can be written in the form:

$$\mathbf{P}^{\text{act}} = \psi(\lambda) \frac{\mathbf{F}\mathbf{f}_0 \otimes \mathbf{f}_0}{1+\lambda}, \tag{7.22}$$

where $\lambda = \sqrt{\mathcal{I}_{4,f}} - 1$. Specifically, we have $\psi(\lambda) = a_{\text{XB}} \left(\hat{\mu}^0 \lambda + \hat{\mu}^1 \right)$ for models with explicit description of XBs and $\varphi(\lambda) = T_{\text{a}}^{\max} P$ when XBs are not explicitly modeled.

We notice that any tensor in the form of Eq. (7.22) is compliant with the frame-indifference principle. Indeed, λ, being a function of $\mathbf{C}$, is not affected by a left multiplication of the strain tensor by a rotation matrix. Thus, we have, for any $\mathbf{Q} \in \text{Orth}^+$:

$$\mathbf{P}_{\mathbf{F}}^{\text{act}}(\mathbf{Q}\mathbf{F}) = \psi(\lambda) \frac{\mathbf{Q}\mathbf{F}\mathbf{f}_0 \otimes \mathbf{f}_0}{1+\lambda} = \mathbf{Q}\mathbf{P}_{\mathbf{F}}^{\text{act}}(\mathbf{F}). \tag{7.23}$$

Besides the frame-indifference principle, the stress tensor of an elastic body needs to satisfy other properties in order to be physically meaningful. A reasonable assumption is that an increase in a component of strain should be followed by an increase in the corresponding component of stress (see e.g. [Ant95]). Such order-preserve property can be stated in different forms, the simplest one being the strong order-preserving property:

$$\mathbf{H}\colon \frac{\partial \mathbf{P}}{\partial \mathbf{F}} \mathbf{H} > 0 \qquad \forall\, \mathbf{F} \in \text{Lin}^+, \mathbf{H} \in \text{Lin}. \tag{7.24}$$

In the case of hyperelastic materials whose strain energy density is twice differentiable, this condition is equivalent to the convexity of the strain energy density itself.

However, the strong order-preserving condition is too strong to develop a physically meaningful theory of elasticity, as it features some drawbacks. First, it is incompatible with frame-indifference [Ant95]. Moreover, it entails uniqueness of the equilibrium under any given load, but this is not coherent with the experience (for instance, a body with a strongly order-preserving constitutive law does not admit buckling). A different notion, weaker than condition (7.24), is the rank-1 order-preserving property:

$$\mathbf{H}\colon \frac{\partial \mathbf{P}}{\partial \mathbf{F}}\mathbf{H} > 0 \qquad \forall\, \mathbf{F} \in \mathrm{Lin}^{+}, \mathbf{H} \text{ of rank 1.} \tag{7.25}$$

We recall that a second order tensor $\mathbf{H}$ is of rank-1 whenever it can be written as $\mathbf{H} = \mathbf{a} \otimes \mathbf{b}$. For hyperlastic materials, condition (7.25) corresponds to the rank-1 convexity of the strain energy density [Dac07; Ant95]. This condition does not feature the above mentioned drawbacks. Moreover, a body whose stress tensor satisfies such condition is characterized by traveling waves with real velocity [Ant95].

Other intermediate notions have been proposed in the literature, besides conditions (7.24) and (7.25), such as the notion of quasi-convexity of the strain energy density, that, together with suitable growth conditions, allows to prove the existence of equilibria [Dac07]. We notice that such condition is stronger than (7.25) and weaker than (7.24).

Because of the additive decomposition of the Piola stress tensor in passive and active components ($\mathbf{P} = \mathbf{P}^{\mathrm{pass}} + \mathbf{P}^{\mathrm{act}}$), if the passive constitutive behavior of the material is compliant with one of the above mentioned order-preserving notions, it is sufficient, for the total Piola stress tensor to fulfill the same notion, that the active part satisfies its non-strict counterparts (that is to say, the strict inequality can be replaced by the nonstrict one):

$$\mathbf{H}\colon \frac{\partial \mathbf{P}^{\mathrm{act}}}{\partial \mathbf{F}}\mathbf{H} \geq 0 \qquad \forall\, \mathbf{F} \in \mathrm{Lin}^{+}, \mathbf{H} \in \mathrm{Lin}, \tag{7.26}$$

$$\mathbf{H}\colon \frac{\partial \mathbf{P}^{\mathrm{act}}}{\partial \mathbf{F}}\mathbf{H} \geq 0 \qquad \forall\, \mathbf{F} \in \mathrm{Lin}^{+}, \mathbf{H} \text{ of rank 1.} \tag{7.27}$$

Motivated by the above observations, we study the order-preserving properties of the active Piola stress tensors belonging to the family of Eq. (7.22). Such properties are fully characterized by the following result, giving a condition that is necessary for the weaker notion and sufficient for the stronger one.

Proposition 7.1. *Let us consider the Piola stress tensor of Eq.* (7.22)*, where ψ is a differentiable function. If* (7.27) *holds true, than the following two inequalities are satisfied:*

$$\psi(\lambda) \geq 0, \quad \psi'(\lambda) \geq 0 \qquad \forall\, \lambda \in (-1, +\infty). \tag{7.28}$$

Conversely, if the inequalities of (7.28) *are satisfied, the property* (7.26) *holds true.*

Proof. First, we notice that:

$$\mathbf{H}\colon \frac{\partial \mathbf{P}^{\mathrm{act}}}{\partial \mathbf{F}}\mathbf{H} = \frac{\psi(\lambda)}{1+\lambda}\,|\mathbf{H}\mathbf{f}_0\,|^2 + \frac{\psi'(\lambda)(1+\lambda) - \psi(\lambda)}{(1+\lambda)^3}\,(\mathbf{F}\mathbf{f}_0 \cdot \mathbf{H}\mathbf{f}_0)^2\,, \tag{7.29}$$

where we have used the equality $|\mathbf{F}\mathbf{f}_0| = 1 + \lambda$.

Let us suppose that property (7.27) holds. Let us first consider $\mathbf{H} = \mathbf{a} \otimes \mathbf{b}$, where $\mathbf{b} = \mathbf{f}_0$ and $\mathbf{a}$ is a unit vector orthogonal to $\mathbf{F}\mathbf{f}_0$. Then, $|\mathbf{H}\mathbf{f}_0\,|^2 = |\mathbf{a}\,|^2 = 1$ and

$\mathbf{F}\mathbf{f}_0 \cdot \mathbf{H}\mathbf{f}_0 = \mathbf{F}\mathbf{f}_0 \cdot \mathbf{a} = 0$ and the sign of the result is that of $\psi(\lambda)$. Thus $\psi(\lambda) \geq 0$ is a necessary condition for (7.27).

On the other hand, let us take $\mathbf{b} = \mathbf{f}_0$ and $\mathbf{a} = \mathbf{F}\mathbf{f}_0$. In this case $\mathbf{H}\mathbf{f}_0 = \mathbf{F}\mathbf{f}_0$ and the result is $\psi'(\lambda)(1+\lambda)^2$, whose sign is that of $\psi'(\lambda)$. Thus $\psi'(\lambda) \geq 0$ is a necessary condition for (7.27) too.

To show the other implication, we suppose that the inequalities of (7.28) are satisfied and we consider two cases. First, if $\psi'(\lambda)(1+\lambda) - \psi(\lambda) \geq 0$, under the hypothesis $\psi(\lambda) \geq 0$ all the terms are nonnegative, giving the thesis. On the other hand, if the $\psi'(\lambda)(1+\lambda) - \psi(\lambda) < 0$, since $(\mathbf{F}\mathbf{f}_0 \cdot \mathbf{H}\mathbf{f}_0)^2 \leq |\mathbf{F}\mathbf{f}_0|^2 |\mathbf{H}\mathbf{f}_0|^2$, we have:

$$\begin{aligned} \mathbf{H} \colon \frac{\partial \mathbf{P}^{\mathrm{act}}}{\partial \mathbf{F}} \mathbf{H} &\geq \frac{\psi(\lambda)}{1+\lambda} |\mathbf{H}\mathbf{f}_0|^2 + \frac{\psi'(\lambda)(1+\lambda) - \psi(\lambda)}{(1+\lambda)^3} |\mathbf{F}\mathbf{f}_0|^2 |\mathbf{H}\mathbf{f}_0|^2 \\ &= \psi'(\lambda) |\mathbf{H}\mathbf{f}_0|^2 \geq 0, \end{aligned} \tag{7.30}$$

whence the thesis. □

Remark 7.1. The necessity of $\psi(\lambda) > 0$ holds even if we restrict ourselves to incompressible materials, that is if we consider the manifold $\det \mathbf{F} = 1$ (i.e. considering those $\mathbf{H}$ such that $\mathbf{F}^{-T} \colon \mathbf{H} = 0$, which is equivalent in case rank-1 convexity is addressed to $\mathbf{a} \cdot \mathbf{F}^{-1}\mathbf{b} = 0$). Indeed, it is sufficient to take $\mathbf{a}$ orthogonal not only to $\mathbf{F}\mathbf{f}_0$ but also to $\mathbf{F}^{-1}\mathbf{f}_0$, which is always possible.

We notice that, in the case of hyperelastic materials, since the inequalities (7.28) are necessary for the rank-1 order preserving property (weaker than quasi-convexity) and sufficient for the strong order-preserving property (stronger than quasi-convexity), they are also necessary and sufficient conditions for quasi-convexity, that allows to prove existence of equilibria [Dac07].

As simple corollaries of Prop. 7.1, we can derive under which conditions the Piola stress tensors given by the models proposed in this thesis are compliant with the order-preserving property.

Models without XB description

In this case, the active Piola tensor always satisfies property (7.26). Indeed, we have $\varphi(\lambda) = T_{\mathrm{a}}^{\max} P$, which is nonegative and constant.

Models with XB description

Conversely, the active Piola tensor given by models with an explicit XB description satisfies the order-preserving property just on the set of deformation $\mathbf{F} \in \mathrm{Lin}^+$ such that $\mu^1 = \hat{\mu}^0 \lambda + \hat{\mu}^1 \geq 0$. Indeed, in this case we have $\psi(\lambda) = a_{\mathrm{XB}} \left(\hat{\mu}^0 \lambda + \hat{\mu}^1 \right)$, and $\psi'(\lambda) = a_{\mathrm{XB}} \hat{\mu}_0 \geq 0$. As we mentioned before, μ^1/μ^0 corresponds to the mean stretch of attached XBs. Therefore, $\mu^1 < 0$ corresponds to a condition where XBs are attached in average with a negative stretch. This is only possible when the tissue is compressed by an external agent. Indeed, when the XB stretch switches from a positive to a negative value, the active tension is not compressive any more and the tissue stops its spontaneous compression. Incidentally, this is the microscopical basis of the phenomenon by which, when the shortening velocity reaches a given positive value $v^{\max}$, the active force reaches zero. In conclusion, under the normal activity of the muscle tissue (when the tissue is not compressed by external agents and, thus, the shortening velocity is lower than $v^{\max}$), the condition $\mu^1 > 0$ is always satisfied.

7.3 Dealing with stochasticity

The models presented in Part I have a stochastic nature, because of the probabilistic formalism employed to describe the transitions of the RUs and the attachment-detachment process. Therefore, the output quantities of the models are not deterministic values, but rather random variables, with their probability distribution. In fact, the stochastic fluctuations featured by the models are not negligible. The MC simulations performed in Chap. 2 show that, during the activation peak, the standard deviation of the active tension can be up to 25% of its expected value:

$$\frac{\sqrt{\mathrm{Var}\left[F_{\mathrm{hf}}(t)\right]}}{\mathbb{E}\left[F_{\mathrm{hf}}(t)\right]} \simeq 0.25.$$

Such significant stochastic fluctuations must be taken into account when the force generation models are coupled in a multiscale setting.

7.3.1 From the microscale to the macroscale

As we mentioned before, the force generated by half MF features large stochastic fluctuations. However, by looking at the same phenomenon at the macroscale, the active tension in a given region of space is the result of the sum of the force generated by many MFs. If we consider a small region of space (let us consider, to fix ideas, a volume of $V = 1\,\mathrm{mm}^3$), the active force associated to this region of space is given by the sum of the force generated by $N_{\mathrm{hf}} = \rho_{\mathrm{hf}} V \simeq 10^{12}$ interacting AF and half MF (where we have estimated $\rho_{\mathrm{hf}} = 2\sigma_{\mathrm{hf}}/SL_0$ by using the data reported in [Was+15]). If we denote by F^i_{hf} the force exerted by the i-th half filament of the volume, the total force generated in the small volume is thus given by:

$$F_V(t) = \sum_{i=1}^{N_{\mathrm{hf}}} F^i_{\mathrm{hf}}(t). \tag{7.31}$$

Since the two inputs of the model (the calcium concentration and the local stretch of the tissue) vary with a characteristic spatial scale that is that of the macroscale (of the order of 1 mm), the force generated by the filaments belonging to the same small region of space can be considered identically distributed. Moreover, thanks to the independence of the different filaments, we have:

$$\frac{\sqrt{\mathrm{Var}\left[F_V(t)\right]}}{\mathbb{E}\left[F_V(t)\right]} = \frac{\sqrt{N_{\mathrm{hf}}\,\mathrm{Var}\left[F^1_{\mathrm{hf}}(t)\right]}}{N_{\mathrm{hf}}\mathbb{E}\left[F^1_{\mathrm{hf}}(t)\right]} = (N_{\mathrm{hf}})^{-\frac{1}{2}} \frac{\sqrt{\mathrm{Var}\left[F^1_{\mathrm{hf}}(t)\right]}}{\exp\left[F^1_{\mathrm{hf}}(t)\right]} \simeq 10^{-6} \frac{\sqrt{\mathrm{Var}\left[F^1_{\mathrm{hf}}(t)\right]}}{\exp\left[F^1_{\mathrm{hf}}(t)\right]}.$$

Thus, even if the stochastic fluctuations at the level of the single filament are large (more than 0.25), at the tissue level their value is negligible (order of $2.5 \cdot 10^{-7}$). Indeed, due to the scale separation between the microscopic level and the macroscopic one, stochastic fluctuations are homogenized, so that the active force at the tissue level can, in practice, be replaced by its expected value. In other terms, even if the tissue-level active force is a random variable, its variance is so small that it can be considered, in practice, as a deterministic value.

7.3.2 From the macroscale to the microscale

Equation (7.9) allows to relate the macroscopic tissue stretch with the microscopic sarcomere deformation as $SL = SL_0\sqrt{\mathcal{I}_{4,f}}$. However, due to the scale separation

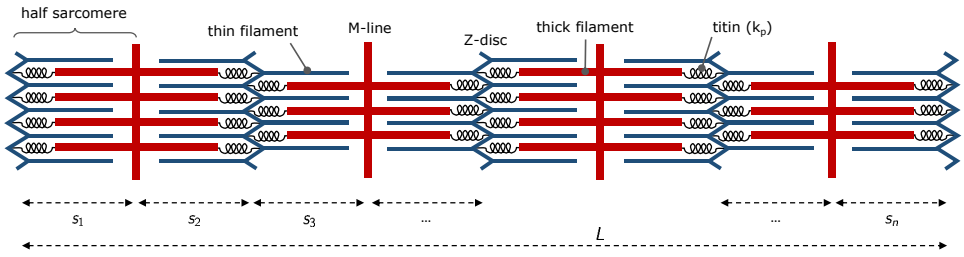

Figure 7.1: Representation of a chain of n half sarcomeres.

between the two levels, $\mathcal{I}_{4,f}$ should be regarded as an average deformation, as it can be the result of nonhomogeneous deformations of the different sarcomeres belonging to the same region of space, in the same manner as the total active force at the tissue level is the result of the sum of many half-filaments forces, each one with a different value. Therefore, to support the validity of Eq. (7.9), we need to investigate the following question: can we assume that sarcomeres close to each others feature similar elongations, or, conversely, nonhomogeneous elongations are possible? We will see that the answer to this question depends on which range of the force-length curve the muscle is working in.

With this aim, we consider the following mesoscale model describing the arrangement of myofilaments and sarcomeres (see Fig. 7.1). Let L denote the length of a chain of n half sarcomeres and let s_j denote the length of the j-th half sarcomere (so that we have $L = \sum_{j=1}^{n} s_j$). Each half sarcomere consists of a parallel arrangement of $N \sim 10^4$ pairs of interacting AFs and half MFs, each one pulling the same Z-disc towards the M-line of the sarcomere [Ber01; Kat10]. Besides the active force, we assume that the sarcomeres are also characterized by a passive stiffness k_{p}, due to the presence of structural proteins such as titin (see Sec. 1.2.3).

We define the mean half sarcomere length as $\overline{s} := L/n$ and the deviation of the j-th half sarcomere as $d_j := s_j - \overline{s}$. We notice that we have $\sum_{j=1}^{n} d_j = 0$. The balance of momentum written at each node connecting two adjacent half sarcomeres (i.e. at each Z-disc and M-line) reads as follows, for $j = 1, \dots, n-1$:

$$-k_{\mathrm{p}}(s_j - s_0) - F_{\mathrm{hs}}^{j} = -k_{\mathrm{p}}(s_{j+1} - s_0) - F_{\mathrm{hs}}^{j+1}, \tag{7.32}$$

where s_0 is the rest length of half sarcomere. It follows that the quantity $C := d_j + F_{\mathrm{hs}}^{j}/k_{\mathrm{p}}$ is constant for each j. To find the value of the constant, we sum over j, obtaining $C = \overline{F}_{\mathrm{hs}}/k_{\mathrm{p}}$, where $\overline{F}_{\mathrm{hs}} = n^{-1} \sum_{j=1}^{n} F_{\mathrm{hs}}^{j}$ denotes the mean active force. Finally, the deviation of the j-th sarcomere from the mean elongation is given by:

$$d_j = \frac{1}{k_{\mathrm{p}}} \left(\overline{F}_{\mathrm{hs}} - F_{\mathrm{hs}}^{j} \right). \tag{7.33}$$

In conclusion, whenever, due to stochastic fluctuations of the different terms F_{hs}^{j}, they differ from their mean value, half sarcomeres close to each others would feature nonhomogeneous deformations. However, thanks to the parallel arrangement of filaments in each sarcomere, the same homogenization phenomenon of Sec. (7.3.1) occurs. Indeed, the active force of half sarcomere is given by $F_{\mathrm{hs}}^{j} = \sum_{i=1}^{N} F_{\mathrm{hf}}^{j,i}$, where $F_{\mathrm{hf}}^{j,i}$ denotes the force generated by the i-th pair of interacting AF and half MH of the j-th half sarcomere. Thus, by proceeding as in Sec. (7.3.1), the stochastic fluctuations at the

level of half sarcomere are given by:

$$\frac{\sqrt{\mathrm{Var}[F_{\mathrm{hs}}^j(t)]}}{\mathbb{E}[F_{\mathrm{hs}}^j(t)]} = N^{-\frac{1}{2}} \frac{\sqrt{\mathrm{Var}[F_{\mathrm{hf}}^{j,1}(t)]}}{\exp[F_{\mathrm{hf}}^{j,1}(t)]} \simeq 10^{-2} \frac{\sqrt{\mathrm{Var}[F_{\mathrm{hf}}^{j,1}(t)]}}{\exp[F_{\mathrm{hf}}^{j,1}(t)]} \leq 2.5 \cdot 10^{-3}.$$

Moreover, in this simple model we are not considering the interactions between sarcomeres belonging to the same plane, that enhances the homogenizing effect due to the parallel arrangement of filaments. In conclusion, the fluctuations at the level of half sarcomere are much smaller than those taking place at the level of filament.

At a first sight, we can thus assume, with a little approximation, that in Eq. (7.33) we have $F_{\mathrm{hs}}^j = \overline{F}_{\mathrm{hs}}$ for any j, so that $d_j = 0$ for any j and all the sarcomeres have the same elongation. However, we need to check that the solution in which $d_j = 0$ for any j is stable, otherwise any little discrepancy from the state of homogeneous sarcomere elongations, caused by the stochastic fluctuations, would lead the system far from such state. This is precisely the goal of the next sections.

Stability of a single half sarcomere

We start by considering a single half sarcomere contracting while loaded by an external force. By denoting by $F_{\mathrm{hs}}(t)$ the force of the sarcomere, the length of the half sarcomere is clearly a decreasing function of the force (the more the half sarcomere pulls, the more it shortens). We have thus $s(t) = h(F_{\mathrm{hs}}(t))$ for some decreasing function h. An example is given by a half sarcomere acting against an external force E. The balance of momentum reads $k_{\mathrm{p}}(s - s_0) + F_{\mathrm{hs}} = E$, which gives $s = h(F_{\mathrm{hs}}) = s_0 + (E - F_{\mathrm{hs}})/k_{\mathrm{p}}$.

We consider for the moment a very simple dynamical model, that however provides a good insight into the phenomenon, namely:

$$\frac{dF_{\mathrm{hs}}}{dt}(t) = f(F_{\mathrm{hs}}(t), s(t)), \qquad t \geq 0. \tag{7.34}$$

We notice that we do not include the dependence on $[\mathrm{Ca}^{2+}]_{\mathrm{i}}$ as we are working under a condition of constant calcium concentration. We denote by $F_{\mathrm{iso}}(s)$ the steady-state force associated to the length s. The function F_{iso} encodes the well-known force-length relationship (see Sec. (1.3.2)). Experiments show that such steady-state condition is a condition of stable equilibrium for the force generation machinery. We have thus, for any s:

$$f(F_{\mathrm{iso}}(s), s) = 0, \qquad \partial_F f(F_{\mathrm{iso}}(s), s) < 0, \tag{7.35}$$

where we denote $\partial_F f := \frac{\partial f}{\partial F_{\mathrm{hs}}}$.

Conditions (7.35) imply that the equilibrium configuration $F_{\mathrm{hs}} = F_{\mathrm{iso}}(s)$ is stable for a fixed s (i.e. under isometric conditions). The goal of this section is that of studying under which conditions the configuration $F_{\mathrm{hs}} = F_{\mathrm{iso}}(s)$, where $s = h(F_{\mathrm{hs}})$, is stable when the half sarcomeres is not kept in isometric conditions, but rather the length is determined by $s = h(F_{\mathrm{hs}})$. In other terms, we are interested in studying the effect, in terms of stability, of the feedback of force on elongation. We thus consider the following dynamical model:

$$\frac{dF_{\mathrm{hs}}}{dt}(t) = f(F_{\mathrm{hs}}(t), h(F_{\mathrm{hs}}(t))), \qquad t \geq 0. \tag{7.36}$$

To study the stability of the equilibrium solution, we study the sign of the derivative of the right-hand side of Eq. (7.36) with respect to the unknown F_{hs}:

$$\frac{d}{dF_{\mathrm{hs}}} f(F_{\mathrm{hs}}, h(F_{\mathrm{hs}})) = \partial_F f(F_{\mathrm{hs}}, s) + \partial_s f(F_{\mathrm{hs}}, s) h'(F_{\mathrm{hs}}). \tag{7.37}$$

In order to compute the term $\partial_s f(F_{\text{hs}}, s)$, we notice that, since for any s have the equality $f(F_{\text{iso}}(s), s) = 0$, it follows:

$$0 = \frac{d}{ds} f(F_{\text{iso}}(s), s) = \partial_F f(F_{\text{iso}}(s), s)\, F'_{\text{iso}}(s) + \partial_s f(F_{\text{iso}}(s), s). \tag{7.38}$$

Therefore, we have:

$$\frac{d}{dF_{\text{hs}}} f(F_{\text{hs}}, h(F_{\text{hs}})) = \partial_F f(F_{\text{hs}}, s)\,(1 - F'_{\text{iso}}(s) h'(F_{\text{hs}}))\,. \tag{7.39}$$

The steady-state solution is thus stable if and only if $F'_{\text{iso}}(s) > 1/h'(F_{\text{hs}})$. In the case of constant external force, the condition reads $F'_{\text{iso}}(s) > -k_{\text{p}}$. Being $h'(F_{\text{hs}}) < 0$, it follows that all the equilibria belonging to the ascending limb of the force-length relationship (i.e. for s such that $F'_{\text{iso}}(s) > 0$) are stable. Conversely, in the descending limb ($F'_{\text{iso}}(s) < 0$), the equilibrium may become unstable.

Fig. 7.2 shows a visual representation of the solution in the case of half sarcomere acting against a fixed load (i.e. $k_{\text{p}}(s - s_0) + F_{\text{hs}} = E$). The solution s is found at the intersection of the curve $F_{\text{hs}} = F_{\text{iso}}(s)$ with $F_{\text{hs}} = E - k_{\text{p}}(s - s_0)$. Depending on the value of E and on the slope of k_{p}, the curves can have one or three distinct intersections, corresponding to as many solutions. Close to the ascending limb, the solution is always unique (Fig. 7.2a). On the descending limb, conversely, the solution can be either unique (if k_{p} is large enough, like in Fig. 7.2b), or multiple (for small k_{p}, like in Fig. 7.2c). In such case, the solution corresponding to the intermediate value of s is unstable (since $F'_{\text{iso}}(s) < -k_{\text{p}}$), while the other two are stable (since $F'_{\text{iso}}(s) > -k_{\text{p}}$). The single equilibrium bifurcates, by effect of a pitchfork bifurcation [Str18], into three equilibria (two stable, one unstable).

We now show that the same result can be obtained for a wide class of force generation models, similar to the models considered in this thesis. We consider indeed a model with an internal state $\mathbf{z} \in \mathbb{R}^{n_z}$, written in the following form:

$$\begin{cases} \dfrac{d\mathbf{z}}{dt}(t) = \mathbf{f}(\mathbf{z}(t), s(t)) & t \geq 0, \\ F_{\text{hs}}(t) = g(\mathbf{z}(t)) & t \geq 0, \end{cases} \tag{7.40}$$

where we do not include for simplicity velocity-related effects. We denote by $\mathbf{z} = \mathbf{z}_{\text{iso}}(s)$ the steady-state solution corresponding to the length s, so that $F_{\text{iso}}(s) = g(\mathbf{z}_{\text{iso}}(s))$. We make the following assumptions, that ensures that the steady-state solution is a stable equilibrium for the force generation dynamics:

$$\mathbf{f}(\mathbf{z}_{\text{iso}}(s), s) = 0, \qquad \partial_{\mathbf{z}} \mathbf{f}(\mathbf{z}_{\text{iso}}(s), s) \text{ is negative definite}, \tag{7.41}$$

where we denote by $\partial_{\mathbf{z}} \mathbf{f}$ the partial derivative of the right-hand side with respect to the state variables. Then, we study the stability of the steady-state solution $\mathbf{z} = \mathbf{z}_{\text{iso}}(s)$, where $s = h(g(\mathbf{z}))$. With this aim we study the spectrum of the Jacobian matrix of the right-hand side of the following dynamical system:

$$\frac{d\mathbf{z}}{dt}(t) = \mathbf{f}(\mathbf{z}(t), h(g(\mathbf{z}(t)))), \qquad t \geq 0. \tag{7.42}$$

We have:

$$\nabla_{\mathbf{z}} \mathbf{f}(\mathbf{z}, h(g(\mathbf{z}))) = \partial_{\mathbf{z}} \mathbf{f}(\mathbf{z}, h(g(\mathbf{z}))) + \partial_s \mathbf{f}(\mathbf{z}, h(g(\mathbf{z})))h'(g(\mathbf{z}))\nabla g^T(\mathbf{z}). \tag{7.43}$$

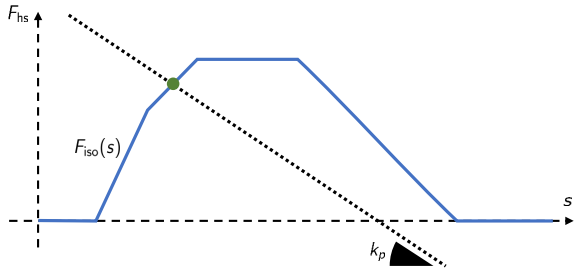

(a) Ascending limb.

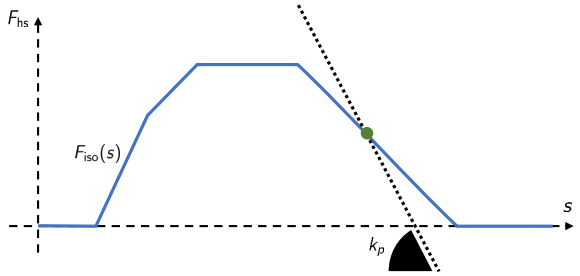

(b) Descending limb (large k_{p}).

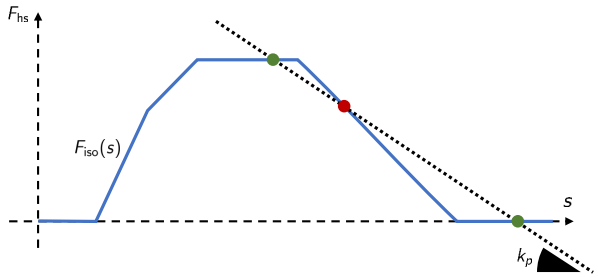

(c) Descending limb (low k_{p}).

Figure 7.2: Equilibrium configurations of a half sarcomere acting against an external load. The blue solid line represents the curve $F_{\mathrm{hs}} = F_{\mathrm{iso}}(s)$, while the black dotted line represents the curve $F_{\mathrm{hs}} = E - k_{\mathrm{p}}(s - s_0)$, for different values of E and k_{p}. Green (respectively, red) dots denote stable (respectively, unstable) equilibria.

Since we have

$$\mathbf{0} = \frac{d}{ds}\mathbf{f}(\mathbf{z}_{\text{iso}}(s), s) = \partial_{\mathbf{z}}\mathbf{f}(\mathbf{z}_{\text{iso}}(s), s)\frac{d}{ds}\mathbf{z}_{\text{iso}}(s) + \partial_s \mathbf{f}(\mathbf{z}_{\text{iso}}(s), s), \tag{7.44}$$

it follows:

$$\nabla_{\mathbf{z}}\mathbf{f}(\mathbf{z}, h(g(\mathbf{z}))) = \partial_{\mathbf{z}}\mathbf{f}(\mathbf{z}, s)\left(\mathbf{I} - h'(F_{\text{hs}})\frac{d}{ds}\mathbf{z}_{\text{iso}}(s)\nabla g^T(\mathbf{z})\right), \tag{7.45}$$

where we write, to ease the notation, $s = h(g(\mathbf{z}))$. Moreover, we notice that:

$$F'_{\text{iso}}(s) = \frac{d}{ds}(g(\mathbf{z}_{\text{iso}}(s))) = \nabla g(\mathbf{z}) \cdot \frac{d}{ds}\mathbf{z}_{\text{iso}}(s). \tag{7.46}$$

To asses the stability of the equilibrium, we study the sign of the eigenvalues of $\nabla_{\mathbf{z}}\mathbf{f}$ in the ascending and descending limb of the force-length relationship (i.e. when $F'_{\text{iso}}(s) > 0$ and $F'_{\text{iso}}(s) < 0$ respectively).

Let $\mathbf{c}_i$ for $i = 1, \ldots, n_z - 1$ be a basis of the subspace orthogonal to the subspace generated by the vector $\nabla g(\mathbf{z})$ (that is nonzero as we are not considering the case $F'_{\text{iso}}(s) = 0$). We have then:

$$\mathbf{c}_i^T \nabla_{\mathbf{z}}\mathbf{f}(\mathbf{z}, s)\mathbf{c}_i = \mathbf{c}_i^T \partial_{\mathbf{z}}\mathbf{f}(\mathbf{z}, s)\mathbf{c}_i < 0, \tag{7.47}$$

where the last inequality is due to the negative definiteness of $\partial_{\mathbf{z}}\mathbf{f}$ at the equilibrium point. Moreover, we have:

$$\begin{aligned}&\left(\frac{d}{ds}\mathbf{z}_{\text{iso}}(s)\right)^T \nabla_{\mathbf{z}}\mathbf{f}\left(\frac{d}{ds}\mathbf{z}_{\text{iso}}(s)\right)\\ &\quad = \left(\frac{d}{ds}\mathbf{z}_{\text{iso}}(s)\right)\partial_{\mathbf{z}}\mathbf{f}(\mathbf{z}, s)\left(\frac{d}{ds}\mathbf{z}_{\text{iso}}(s)\right)\left(1 - h'(F_{\text{hs}})\nabla g(\mathbf{z}) \cdot \frac{d}{ds}\mathbf{z}_{\text{iso}}(s)\right).\end{aligned} \tag{7.48}$$

Because of the negative definiteness of $\partial_{\mathbf{z}}\mathbf{f}$, the above expression is negative if and only if $1 - h'(F_{\text{hs}})\nabla g(\mathbf{z}) \cdot \frac{d}{ds}\mathbf{z}_{\text{iso}}(s) = 1 - h'(F_{\text{hs}})F'_{\text{iso}}(s) > 0$, that is equivalent to $F'_{\text{iso}}(s) > 1/h'(F_{\text{hs}})$. Therefore, since the set $\{\mathbf{c}_1, \ldots, \mathbf{c}_{n_z}, \frac{d}{ds}\mathbf{z}_{\text{iso}}(s)\}$ is a basis of $\mathbb{R}^{n_z}$, the steady-state solution is stable if and only if $F'_{\text{iso}}(s) > 1/h'(F_{\text{hs}})$. We have thus shown the same result obtained for the simpler model of Eq. (7.34).

Stability of a pair of half sarcomeres

In this section we show that, when two half sarcomeres interact, similar instabilities as the one featured by a single sarcomere may occur in the descending limb of the force-length relationship. We consider Eq. (7.33) for $N = 2$. By denoting $d = d_1$, we have:

$$\begin{aligned} s_1 &= \overline{s} + d, \quad F^1_{\text{hs}} = F_{\text{iso}}(s_1),\\ s_2 &= \overline{s} - d, \quad F^2_{\text{hs}} = F_{\text{iso}}(s_2),\\ d &= \frac{1}{2\,k_{\text{p}}}\left(F^2_{\text{hs}} - F^1_{\text{hs}}\right).\end{aligned}$$

The equilibria of the pair of interacting half sarcomeres are thus given by the solutions of the following equation:

$$2\,k_{\text{p}}\,d = F_{\text{iso}}(\overline{s} - d) - F_{\text{iso}}(\overline{s} + d). \tag{7.49}$$

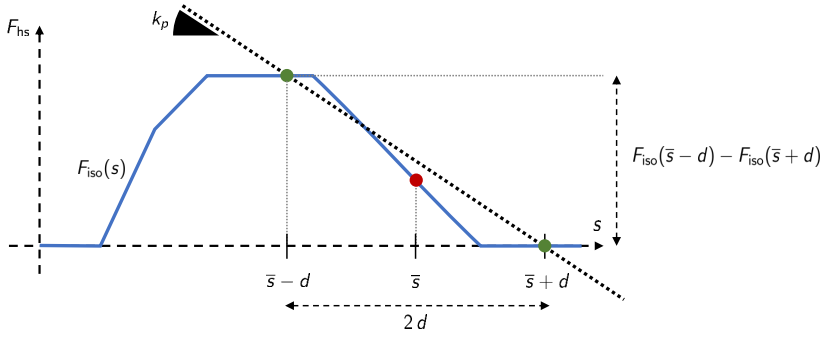

(a)

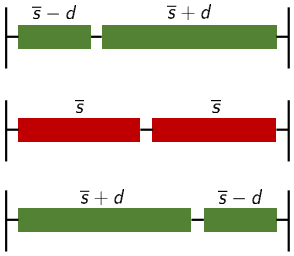

(b)

Figure 7.3: Pair of interacting half sarcomeres. Equilibrium solutions can be found by intersecting the curve $F_{\text{iso}}(s)$ (blue solid line) with lines of slope $-k_{\text{p}}$ (dotted black line). In the case of multiple intersections, such as in (a), the three solutions represented in (b) are possible. The homogeneous solution $s_1 = s_2 = \bar{s}$ is unstable (shown in red), while the two solutions $s_1, s_2 = \bar{s} \pm d$ are stable (shown in green).

Such solutions can be graphically found as the intersections of the F_{iso} curve with lines of slope $-k_{\text{p}}$ (see Fig. 7.3). When the curves feature more than one intersection, the corresponding coordinates (s_1, F^1_{hs}) of (s_2, F^2_{hs}) form an equilibrium configuration for the pair of interacting half sarcomeres. Indeed, the distance $s_2 - s_1$ is by definition $2\,d$, while the distance $F^2_{\text{hs}} - F^1_{\text{hs}}$ is given by $F_{\text{iso}}(\overline{s} - d) - F_{\text{iso}}(\overline{s} + d)$. Since the two points (s_1, F^1_{hs}) and (s_2, F^2_{hs}) lay on a line with slope $-k_{\text{p}}$, Eq. (7.49) is satisfied.

On the ascending limb, only a single intersection is possible, and thus the solution $d = 0$ is the only possible solution. Conversely, on the descending limb, if k_{p} is large enough, we still have only the solution $d = 0$, but if k_{p} is small, multiple intersections are possible. In such case, the pair of half sarcomeres features different equilibrium configurations (see Fig. 7.3b): the trivial one, corresponding to $s_1 = s_2 = \overline{s}$ (homogeneous sarcomeres deformation) and the two nonhomogeneous solutions $s_1, s_2 = \overline{s} \pm d$. We now study the stability of the different solutions. Due to the stochastic fluctuations of the force generation dynamics, indeed, the only solutions that can be observed in reality are those corresponding to stable configurations.

Let us consider, for simplicity, the model of Eq. (7.34), as we have shown above that considering more complex models with internal variables do not affect the essential features of the equilibria. The dynamics of the pair of interacting half sarcomeres is described by the following equation:

$$\begin{cases} \dfrac{dF^1_{\text{hs}}}{dt} = f\left(F^1_{\text{hs}}, \overline{s} + \dfrac{1}{2\,k_{\text{p}}}\left(F^2_{\text{hs}} - F^1_{\text{hs}}\right)\right) & t \geq 0, \\ \dfrac{dF^2_{\text{hs}}}{dt} = f\left(F^2_{\text{hs}}, \overline{s} + \dfrac{1}{2\,k_{\text{p}}}\left(F^1_{\text{hs}} - F^2_{\text{hs}}\right)\right) & t \geq 0. \end{cases} \tag{7.50}$$

We notice that such dynamical system can be written in the following form:

$$\frac{d\mathbf{F}}{dt} = \mathbf{f}(\mathbf{F}), \qquad t \geq 0, \tag{7.51}$$

where we denote by $\mathbf{F} := (F^1_{\text{hs}}, F^2_{\text{hs}})^T$ the state of the system. To investigate the stability properties of equilibria, we study the spectrum of the Jacobian matrix $\nabla\mathbf{f}$, that reads:

$$\nabla\mathbf{f} = \begin{pmatrix} \partial_F f(F^1_{\text{hs}}, s_1) - \frac{1}{2\,k_{\text{p}}}\partial_s f(F^1_{\text{hs}}, s_1) & \frac{1}{2\,k_{\text{p}}}\partial_s f(F^1_{\text{hs}}, s_1) \\ \frac{1}{2\,k_{\text{p}}}\partial_s f(F^2_{\text{hs}}, s_2) & \partial_F f(F^2_{\text{hs}}, s_2) - \frac{1}{2\,k_{\text{p}}}\partial_s f(F^2_{\text{hs}}, s_2) \end{pmatrix}.$$

Thanks to Eq. (7.38), by which $\partial_s f(F^j_{\text{hs}}, s_j) = -\partial_F f(F^j_{\text{hs}}, s_j) F'_{\text{iso}}(s_j)$, the Jacobian matrix can be written as:

$$\nabla\mathbf{f} = \begin{pmatrix} \partial_F f(F^1_{\text{hs}}, s_1)\left(1 + \frac{1}{2\,k_{\text{p}}}F'_{\text{iso}}(s_1)\right) & -\frac{1}{2\,k_{\text{p}}}\partial_F f(F^1_{\text{hs}}, s_1)F'_{\text{iso}}(s_1) \\ -\frac{1}{2\,k_{\text{p}}}\partial_F f(F^2_{\text{hs}}, s_2)F'_{\text{iso}}(s_2) & \partial_F f(F^2_{\text{hs}}, s_2)\left(1 + \frac{1}{2\,k_{\text{p}}}F'_{\text{iso}}(s_2)\right) \end{pmatrix}.$$

The stability of equilibria can be assessed by the sign of the real part of the eigenvalues of the Jacobian matrix. With this aim, we compute trace and determinant of such matrix:

$$\begin{aligned} \operatorname{tr}(\nabla\mathbf{f}) &= \partial_F f(F^1_{\text{hs}}, s_1)\left(1 + \frac{F'_{\text{iso}}(s_1)}{2\,k_{\text{p}}}\right) + \partial_F f(F^2_{\text{hs}}, s_2)\left(1 + \frac{F'_{\text{iso}}(s_2)}{2\,k_{\text{p}}}\right), \\ \det(\nabla\mathbf{f}) &= \partial_F f(F^1_{\text{hs}}, s_1)\partial_F f(F^2_{\text{hs}}, s_2)\left(1 + \frac{F'_{\text{iso}}(s_1) + F'_{\text{iso}}(s_2)}{2\,k_{\text{p}}}\right). \end{aligned}$$

First, we consider the stability of the homogeneous solution $d = 0$. In this case, we have $s_1 = s_2 = \overline{s}$ and $F^1_{\text{hs}} = F^2_{\text{hs}} = \overline{F}_{\text{hs}}$. Hence, trace and determinant of the Jacobian matrix can be written as follows:

$$\operatorname{tr}(\nabla \mathbf{f}) = 2\,\partial_F f(\overline{F}_{\text{hs}}, \overline{s}) \left(1 + \frac{F'_{\text{iso}}(\overline{s})}{2\,k_{\text{p}}}\right),$$
$$\det(\nabla \mathbf{f}) = \partial_F f(\overline{F}_{\text{hs}}, \overline{s})^2 \left(1 + \frac{F'_{\text{iso}}(\overline{s})}{k_{\text{p}}}\right).$$

Clearly, when $F'_{\text{iso}}(\overline{s}) > -k_{\text{p}}$, the homogeneous configuration $d = 0$ is the only possible solution (since only a single intersection can be possible, see Fig. 7.3). In this case, we have:

$$\operatorname{tr}(\nabla \mathbf{f}) < 2\,\partial_F f(\overline{F}_{\text{hs}}, \overline{s}) \left(1 + \frac{-k_{\text{p}}}{2\,k_{\text{p}}}\right) = \partial_F f(\overline{F}_{\text{hs}}, \overline{s}) < 0,$$
$$\det(\nabla \mathbf{f}) > \partial_F f(\overline{F}_{\text{hs}}, \overline{s})^2 \left(1 + \frac{-k_{\text{p}}}{k_{\text{p}}}\right) = 0.$$

Therefore, both eigenvalues have strictly negative real part and, by the Routh–Hurwitz stability criterion [Gop02], the solution is stable.

Conversely, in the case of multiple equilibria (i.e. $F'_{\text{iso}}(\overline{s}) < -k_{\text{p}}$), we have:

$$\det(\nabla \mathbf{f}) < \partial_F f(\overline{F}_{\text{hs}}, \overline{s})^2 \left(1 + \frac{-k_{\text{p}}}{k_{\text{p}}}\right) = 0.$$

Hence, one eigenvalue has strictly positive real part and the configuration is thus unstable.

Let us now study, in the case of multiple equilibria, the stability of the solution $s_1 = \overline{s} + d$, $s_1 = \overline{s} - d$. In this case, we have $F'_{\text{iso}}(s_1) > -k_{\text{p}}$, $F'_{\text{iso}}(s_2) > -k_{\text{p}}$ (otherwise the two curves cannot intersect). Therefore, trace and determinant of the Jacobian matrix satisfy:

$$\begin{aligned}\operatorname{tr}(\nabla \mathbf{f}) &< \partial_F f(F^1_{\text{hs}}, s_1) \left(1 + \frac{-k_{\text{p}}}{2\,k_{\text{p}}}\right) + \partial_F f(F^2_{\text{hs}}, s_2) \left(1 + \frac{-k_{\text{p}}}{2\,k_{\text{p}}}\right) \\ &= \frac{\partial_F f(F^1_{\text{hs}}, s_1) + \partial_F f(F^2_{\text{hs}}, s_2)}{2} < 0, \\ \det(\nabla \mathbf{f}) &> \partial_F f(F^1_{\text{hs}}, s_1) \partial_F f(F^2_{\text{hs}}, s_2) \left(1 + \frac{-k_{\text{p}} - k_{\text{p}}}{2\,k_{\text{p}}}\right) = 0.\end{aligned}$$

The two configurations corresponding to a nonhomogeneous sarcomeres stretch (represented in green in Fig. 7.3b) are thus stable.

In conclusion, on the ascending limb of the force-length relationship, the unique solution is the one where the sarcomeres are homogeneously stretched and such solution is stable. Conversely, on the descending limb, we have two possible scenarios. For large values of the passive stiffness k_{p}, the homogeneous stretch is the unique solution and it is stable, while, for sufficiently mall k_{p}, a pitchfork bifurcation occurs: the homogeneous solution becomes unstable, and two nonhomogenous stable solutions appear.

Stability of a chain of half sarcomeres

We consider then a chain of n half sarcomeres. In this case multiple pitchfork bifurcations can occur on the descending limb of the force-length relationship. However, we

show that, on the ascending limb, the solution with homogeneous sarcomeres elongation is stable.

As we have seen at the beginning of Sec. 7.3.2, equilibrium configurations are such that $s_j = \overline{s} + \frac{1}{k_\mathrm{p}}(\overline{F}_\mathrm{hs} - F^j_\mathrm{hs})$. The dynamics of the chain of half sarcomeres is then described by the following system of equations:

$$\begin{cases} \dfrac{dF^1_\mathrm{hs}}{dt} = f\left(F^1_\mathrm{hs}, \overline{s} + \dfrac{1}{k_\mathrm{p}}\left(\dfrac{1}{n}\displaystyle\sum_{k=1}^{n} F^k_\mathrm{hs} - F^1_\mathrm{hs}\right)\right) & t \geq 0, \\ \dfrac{dF^2_\mathrm{hs}}{dt} = f\left(F^2_\mathrm{hs}, \overline{s} + \dfrac{1}{k_\mathrm{p}}\left(\dfrac{1}{n}\displaystyle\sum_{k=1}^{n} F^k_\mathrm{hs} - F^2_\mathrm{hs}\right)\right) & t \geq 0, \\ \quad\vdots & \\ \dfrac{dF^n_\mathrm{hs}}{dt} = f\left(F^n_\mathrm{hs}, \overline{s} + \dfrac{1}{k_\mathrm{p}}\left(\dfrac{1}{n}\displaystyle\sum_{k=1}^{n} F^k_\mathrm{hs} - F^n_\mathrm{hs}\right)\right) & t \geq 0. \end{cases} \tag{7.52}$$

Such dynamical system can be written in the form of Eq. (7.51), where the state of system is given by $\mathbf{F} := (F^1_\mathrm{hs}, \dots, F^n_\mathrm{hs})^T$. As in the case of a pair of sarcomeres, we study the spectrum of the Jacobian matrix $\nabla\mathbf{f}$. In the following we will use again the result of Eq. (7.38). For $k \neq j$, we have:

$$[\nabla\mathbf{f}]_{j,k} = (k_\mathrm{p} n)^{-1}\partial_s f(F^j_\mathrm{hs}, s_j) = -(k_\mathrm{p} n)^{-1}\partial_F f(F^j_\mathrm{hs}, s_j)F'_\mathrm{iso}(s_j), \tag{7.53}$$

Conversely, the diagonal entries of the Jacobian matrix can be obtained as:

$$[\nabla\mathbf{f}]_{j,j} = \partial_F f(F^j_\mathrm{hs}, s_j) - \frac{n-1}{k_\mathrm{p} n}\partial_s f(F^j_\mathrm{hs}, s_j) = \partial_F f(F^j_\mathrm{hs}, s_j)\left(1 + \frac{n-1}{k_\mathrm{p} n}F'_\mathrm{iso}(s_j)\right). \tag{7.54}$$

By hypothesis (7.35), $\partial_F f(F^j_\mathrm{hs}, s_j) < 0$. Therefore, on the ascending limb of the force-length relationship, where $F'_\mathrm{iso}(s_j) \geq 0$, the real part of any eigenvalue λ of the Jacobian matrix $\nabla\mathbf{f}$ can be bounded, thanks to Gershgorin circle theorem [GL99], as follows:

$$\begin{aligned} \mathrm{Re}(\lambda) &\leq \mathrm{Re}\left([\nabla\mathbf{f}]_{j,j}\right) + \sum_{k\neq j}\left|[\nabla\mathbf{f}]_{j,k}\right| \\ &= \partial_F f(F^j_\mathrm{hs}, s_j)\left(1 + \frac{n-1}{k_\mathrm{p} n}F'_\mathrm{iso}(s_j)\right) - \sum_{k\neq j}\partial_F f(F^j_\mathrm{hs}, s_j)(k_\mathrm{p} n)^{-1}F'_\mathrm{iso}(s_j) \\ &= \partial_F f(F^j_\mathrm{hs}, s_j) < 0. \end{aligned} \tag{7.55}$$

In conclusion, thanks to the Routh–Hurwitz stability criterion [Gop02], the equilibrium configuration in which $s_j = \overline{s}$ for any j, when $\overline{s}$ is on the ascending limb of the force-length relationship, is stable.

On the validity of Eq. (7.9)

To summarize, even if instabilities may occur on the descending limb of the force-length relationship, when the heart works on the ascending limb the assumption that all the sarcomeres belonging to the same region of space feature the same elongation is legitimate. Indeed, the normal working regime of sarcomeres in the heart (approximately 1.7-2.3µm, see Sec. 1.3.2) lies within the ascending limb, thanks to the stiffening of the

parallel elastic component in proximity of $SL \simeq 2.3\,\mu m$ (see Sec. 1.3.1). This prevents the heart tissue to enter in the regime of the force-length relationship with negative apparent stiffness (i.e. the descending limb).

The above considerations provide a justification for Eq. (7.9), that assumes that the sarcomeres close to each other have similar elongations. Nonetheless, one should be aware of the limitations of such relationship and should always check a posteriori that the value of SL does not enter in the descending limb of the force-length relationship.

7.4 Final remarks

In this chapter we have laid the groundwork for a multiscale formulation of cardiac EM, by deriving relationships linking the microscopic variables describing the input and the output of the force generation models derived in Part I with the microscopic variables describing the strains and the stresses at the organ scale. Moreover, we have analyzed how the random fluctuations that characterize the intrinsically stochastic microscopical processes reflect on the macroscale.

Specifically, the local sarcomere elongation can be obtained as shown in Eq. (7.9). Nonetheless, one should be aware that such relationship is based on the assumption that sarcomeres close to each other are elongated in a similar manner. We have shown that under the working regime of cardiac sarcomeres this assumption is valid and thus Eq. (7.9) can be employed to link the two spatial scales. Incidentally, this is not true when sarcomeres are over-elongated, which however never happens when sarcomeres are embedded in the cardiac tissue, thanks to stiff parallel elastic components.

Concerning the upscaling from the microscopic to the macroscopic level, we have derived Eq. (7.12), linking the force generated at the level of myofilmaents with the stress state of the cardiac tissue. Thanks to the additive nature of force, the stochastic fluctuations are homogenized in the transition from the microscale to the macroscale, so that the active tension at the tissue level can be identified with its expected value. In conclusion, while the models at the microscale need to account for stochasticity, the models at the macroscale can be written with a deterministic formalism.

Finally, we have shown the physically meaningfulness of the active Piola stress tensor deriving from the models proposed in Part I, under the normal working regime of sarcomeres during an heartbeat. More precisely, the active Piola stress tensor satisfies the frame-indifference principle. Moreover, we have investigated under which conditions the above-mentioned tensor satisfies the order-preserving property between strain and stress [Ant95; Ogd97]. We have proven that, in the case the underlying model does not incorporate an explicit description of XBs (and thus the active force is assumed to be proportional to permissivity, such as in the activation-MH model), the order-preserving property is satisfied in its strongest form (7.26). Conversely, in the case of microscopic models with an explicit description of XBs (such as the SE-ODE and the MF-ODE models), a condition that is sufficient for the rank-1 order preserving property (7.27) and necessary for the strong order-preserving property (7.26) is that $\mu^1(t) > 0$. Since this condition is always satisfied, unless the tissue is quickly shortened by an external agent, we conclude that, during the normal activity of the cardiac muscle tissue, the Piola stress tensor satisfies the order-preserving properties.

Chapter 8

Cardiac electromechanics

The main motivation of this thesis is the construction of an accurate and efficient computational model of cardiac EM, that drove the development of the mathematical models proposed in Part I and the MOR techniques proposed in Part II. Hence, in this chapter, after having presented the core mathematical models describing the different building blocks of the EM system, we describe our strategy to reduce the computational burden of cardiac multiscale EM simulations. Specifically, the intrinsically complex model describing the microscale generation of active force is replaced by a previously trained ANN-based model, that reproduces, within a little approximation, the results of the corresponding HF model at a significantly lower computational cost. We achieve, in this manner, a strikingly good balance between biophysical detail of description and computational cost. Part of the results presented in this chapter are taken from the submitted paper [RDQ19c].

Contents

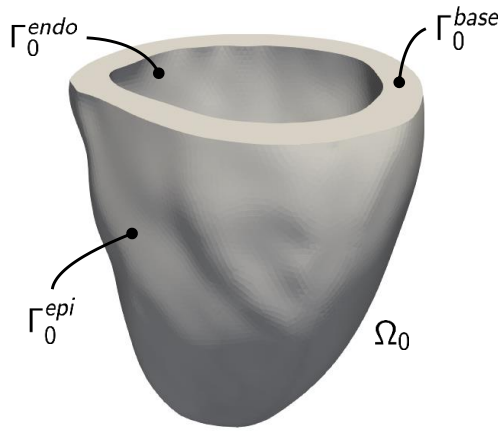

Figure 8.1: Domain and boundaries of the EM problem. The domain shown in the picture is derived from the CAD of [Zyg].

8.1 The electromechanical problem

In this section, we present the models used in this thesis to describe the single building blocks of cardiac EM, represented in Fig. 1. The different physical phenomena involved in the cardiac EM function are typically described by means of ODE or PDE systems, coupled together to account for the intricate interactions among the different building blocks [NS09; Nor+11; Was+13; Was+15; Cha+16; Qua+17; GDQ18a; GDQ18b; Qua+19].

We consider a reference computational domain Ω_0, representing the region of space represented by the cardiac muscle tissue at rest (reference configuration) and a time interval $(0, T]$. Specifically, we focus on the EM of the left ventricle (LV), the most studied of the four cardiac chambers (since it is responsible for the systemic circulation and it is characterized by the largest pressures and strains [TD08; JKT07]). We subdivide the boundary of the domain Ω_0 into three parts, namely the endocardial surface Γ_0^{endo}, the epicardial surface Γ_0^{epi} and the base Γ_0^{base}, an imaginary surface orthogonal to the LV centerline and cutting the ventricle wall. An example of LV domain Ω_0 with the corresponding boundaries is shown in Fig. 8.1. In order to account for the anisotropic mechano-electrical properties of the cardiac tissue, we define a local frame of reference by means of the mutually orthogonal vector fields $\mathbf{f}_0$, $\mathbf{s}_0$ and $\mathbf{n}_0$, denoting respectively the fibers direction, the sheets directions the fibers-sheets normal direction [Qua+17; GDQ18a].

8.1.1 Electrophysiology

The contraction of the heart is driven by an electrical signal, generated in the heart natural pacemaker, the sinoatrial node (see Sec. 1.1.1). Such signal propagates through the atria, reaches the atrioventricular node and, through the Purkinje network, the ventricles. The electrical stimulus triggers the activity of the excitable cardiomyocytes, known as action potential, consisting in a coordinate opening and closing of voltage-gated ion channels and in the consequent ionic fluxes through the cell membrane.

The mathematical description of these phenomena consists in two building blocks: a ionic model, describing the cellular-level activity, and an equation describing the

propagation of the action potential through the cardiac tissue (in this thesis, we consider the *monodomain model* [CFPS06; CFPS14]).

Ionic models

The mathematical formalism used to describe the dynamics of the ionic fluxes and the voltage-gated ion channels is that of the Hodgkin-Huxley model [HH52a; HH52b]. The cell membrane is assumed to behave as a capacitor with capacitance C_m, subject to two electric currents: $\mathcal{I}^{\text{app}}$, the externally applied current, and $\mathcal{I}^{\text{ion}}$ the net current resulting by the ion fluxes across the membrane. A large number of models have been proposed in the literature to model the term $\mathcal{I}^{\text{ion}}$. Such models include variables tracking the concentration of different ionic species and the so-called gating variables, describing the opening state of the voltage-gated channels (such as the O'Hara-Rudy model [O'H+11], the ten Tusscher-Noble-Noble-Panfilov model [TT+04], the ten Tusscher-Panfilov 18-variables model [TTP06a] (TTP06 model) and the ten Tusscher-Panfilov 8-variables model [TTP06b]). Due to the large number of variables needed to accurately describe the dynamics of the ion fluxes across the membrane, simplified models, built on the basis of phenomenological considerations, have been proposed (such as the FitzHugh–Nagumo model [Fit61; NAY62], the Aliev-Panfilov model [AP96] and the Bueno-Orovio minimal model [BOCF08]). In general, each of the above mentioned models can be written in the following form, where $\mathbf{w}$ denotes the vector collecting all the ionic variables (ionic concentrations, gating variables, or phenomenological variables):

$$\begin{cases} C_m \dfrac{\partial v(t)}{\partial t} + \mathcal{I}^{\text{ion}}(v(t), \mathbf{w}(t)) = \mathcal{I}^{\text{app}}(t) & t \in (0, T], \\ \dfrac{d\mathbf{w}(t)}{dt} = \mathbf{h}(v(t), \mathbf{w}(t)) & t \in (0, T], \\ v(0) = v_0, \quad \mathbf{w}(0) = \mathbf{w}_0. \end{cases} \tag{8.1}$$

In this thesis, we consider the ten Tusscher-Panfilov 18-variables model (that we denote as TTP06 model), calibrated for human ventricular myocardial cells [TTP06a], as it provides a detailed description of the calcium dynamics, one of the inputs of the mechanical activation models that we proposed in Part. I.

The monodomain model

The monodomain model provides a description for the propagation of the action potential through the heart tissue (see e.g. [CFPS06; CFPS14]). In this model, the cells are not considered as discrete but rather as a continuum. The transmembrane potential is thus described by a scalar field $v : \Omega_0 \times (0, T] \to \mathbb{R}$ (in the following the dependence on $(\mathbf{x}, T)$ will be implicit). We also define, over the domain Ω_0, the vector field of the ionic variables, that we denote by $\mathbf{w}$. By introducing the membrane surface-to-volume-ratio χ_m (corresponding the the total membrane surface per unit volume), that allows to relate the electical current at the level of the cell membrane with the currents at the level of the continuum, the evolution of the variables v and

$\mathbf{w}$ is described by the monodomain equation (see e.g. [CFPS06; CFPS14]):

$$\begin{cases} \chi_m \left(C_m \dfrac{\partial v}{\partial t} + \mathcal{I}^{\text{ion}}(v, \mathbf{w}) \right) = \nabla_0 \cdot \left(J\, \mathbf{F}^{-1} \mathbf{D} \mathbf{F}^{-T} \nabla_0 v \right) + \mathcal{I}^{\text{app}} & \text{in } \Omega_0 \times (0, T], \\ \dfrac{\partial \mathbf{w}}{\partial t} = \mathbf{h}(v, \mathbf{w}) & \text{in } \Omega_0 \times (0, T], \\ \left(J\, \mathbf{F}^{-1} \mathbf{D} \mathbf{F}^{-T} \nabla_0 v \right) \cdot \mathbf{N} = 0 & \text{on } \partial\Omega_0 \times (0, T], \\ v = v_0, \quad \mathbf{w} = \mathbf{w}_0 & \text{in } \Omega_0 \times \{0\}, \end{cases} \tag{8.2}$$

where $\mathbf{D}$ denotes the electrical conductivity tensor in the current configuration. The tensor $\mathbf{D}_0 = J\, \mathbf{F}^{-1} \mathbf{D} \mathbf{F}^{-T}$ represents the pull-back of such tensor in the reference configuration, by accounting for the tissue deformation encoded into $\mathbf{F}$ [Qua+17; CFPS06]. We notice that, while in Eq. (8.1) the term $\mathcal{I}^{\text{app}}$ denotes the applied electric current per unit area (of membrane surface), in Eq. (8.2) $\mathcal{I}^{\text{app}}$ denotes the applied current per unit volume (of heart tissue).

To reduce the number of parameters, we divide the first equation by the membrane surface-to-volume-ratio χ_m and by the membrane capacitance C_m, obtaining:

$$\frac{\partial v}{\partial t} + \widetilde{\mathcal{I}}^{\text{ion}}(v, \mathbf{w}) = \nabla_0 \cdot \left(J\, \mathbf{F}^{-1} \widetilde{\mathbf{D}} \mathbf{F}^{-T} \nabla_0 v \right) + \widetilde{\mathcal{I}}^{\text{app}},$$

where $\widetilde{\mathcal{I}}^{\text{ion}} = C_m^{-1} \mathcal{I}^{\text{ion}}$, $\widetilde{\mathcal{I}}^{\text{app}} = C_m^{-1} \chi_m^{-1} \mathcal{I}^{\text{app}}$ and $\widetilde{\mathbf{D}} = C_m^{-1} \chi_m^{-1} \mathbf{D}$. To account for the anisotropic properties of the tissue, the diffusion tensor is written as:

$$\widetilde{\mathbf{D}} = \sigma_{\text{iso}} \mathbf{I} + (\sigma_{\text{f}} - \sigma_{\text{iso}})\, \mathbf{f}_0 \otimes \mathbf{f}_0, \tag{8.3}$$

where σ_{f} denotes the conductivity coefficient in the fibers direction and σ_{f} the conductivity coefficient in the transverse direction [Qua+17; GDQ18a].

The electric current $\mathcal{I}^{\text{app}}$, stimulating the heart tissue, originates from the Purkinje network. In this thesis, we do not explicitly model the Purkinje network (such as, for instance, in [Lan+18]), but we consider instead a collection of points $\mathbf{X}_1, \ldots, \mathbf{X}_{N_p}$ where the electrical stimulus is applied, representing the terminations of the network itself. Therefore, we set:

$$\widetilde{\mathcal{I}}^{\text{app}}(\mathbf{X}, t) = \mathcal{I}^{\max} \sum_{j=1}^{N_p} \exp\left(\frac{|\mathbf{X} - \mathbf{X}_j|^2}{\delta^2} \right) \mathbb{1}_{[0, t_{\text{app}}]}(t),$$

where δ is the spatial amplitude of the stimulus, $\mathcal{I}^{\max}$ is the current peak and t_{app} is the stimulus duration.

8.1.2 Mechanical activation

Among the ionic species involved in the action potential dynamics, calcium ions enter inside the cell a few instants after the beginning of the cell excitation. The increase of intracellular calcium ions concentrations triggers the calcium-induced calcium release of the ions stored in the sarcoplasmic reticulum, causing a further increase of $[\text{Ca}^{2+}]_{\text{i}}$ (see Sec. 1.2.4). The increase of calcium concentration, in turn, triggers the activation of the thin filaments inside the sarcomeres and the generation of active force.

A generic force generation model can be written in the following form (see Chap. 6):

$$\begin{cases} \dfrac{\partial \mathbf{z}}{\partial t} = \mathbf{r}\left(\mathbf{z}, [\text{Ca}^{2+}]_{\text{i}}, SL, \dfrac{\partial SL}{\partial t} \right) & \text{in } \Omega_0 \times (0, T], \\ \mathbf{z} = \mathbf{z}_0 & \text{in } \Omega_0 \times \{0\}, \end{cases} \tag{8.4}$$

where $\mathbf{z}(t)$ denotes a vector field, defined over Ω_0, collecting the state variables of the force generation model.

The models of the form of Eq. (8.4) have three inputs. The first is the scalar field $[Ca^{2+}]_i$, denoting the intracellular calcium ions concentration over the domain Ω_0. The most detailed ionic models, including the TTP06 model, provide a description of the intracellular calcium dynamics, so that the field $[Ca^{2+}]_i$ can be obtained directly from the ionic variables $\mathbf{w}$. The other inputs are the scalar field SL, denoting the elongation of the sarcomeres belonging to each region of the domain Ω_0 (that, thanks to the considerations of Sec. 7.3.2, is well-defined), and its partial derivative with respect to time. By Eq. (7.9), the local sarcomere length is obtained by multiplying the rest sarcomere length SL_0 by the local deformation of fibers aligned with the direction $\mathbf{f}_0$ (i.e., $SL = SL_0\sqrt{\mathcal{I}_{4,f}}$). However, it is convenient (mainly for numerical reasons) to regularize the $\mathcal{I}_{4,f}$ field (when a low-order FEM discretization is considered, for instance, $\mathcal{I}_{4,f}$ may be discontinuous); hence, we define SL as the solution of the following differential problem:

$$\begin{cases} \left(SL - SL_0\sqrt{\mathcal{I}_{4,f}}\right) - \delta_{SL}^2 \Delta SL = 0 & \text{in } \Omega_0 \times (0,T], \\ \delta_{SL}^2 \nabla_0 SL \cdot \mathbf{N} = 0 & \text{on } \partial\Omega_0 \times (0,T], \end{cases} \tag{8.5}$$

where δ_{SL} is the regularization radius.

8.1.3 Mechanics

As we mentioned before, we model the heart muscle as an hyperelastic medium. The passive mechanical response of the heart is significantly anisotropic, due to the presence of fibers (see Sec. 1.2.1). Many transversely isotropic or, more in general, orthotropic constitutive laws have been proposed in the literature (see e.g. [GMW91; GCM95; ULM02; HO09]), accounting for the different elastic response along the directions $\mathbf{f}_0$, $\mathbf{s}_0$ and $\mathbf{n}_0$. In this thesis we consider the quasi-incompressible exponential material model of [ULM02], with the hyperelastic strain energy density defined as:

$$\begin{aligned} \mathcal{W} &= \frac{C}{2}\left(e^Q - 1\right) + \frac{B}{2}(J-1)\log J, \\ Q &= b_{ff}E_{ff}^2 + b_{ss}E_{ss}^2 + b_{nn}E_{nn}^2 \\ &\quad + b_{fs}\left(E_{fs}^2 + E_{sf}^2\right) + b_{fn}\left(E_{fn}^2 + E_{nf}^2\right) + b_{sn}\left(E_{sn}^2 + E_{ns}^2\right), \end{aligned} \tag{8.6}$$

where $E_{ab} = \mathbf{E}\,\mathbf{a}_0 \cdot \mathbf{b}_0$, for $a, b \in \{f, s, n\}$, are the entries of the Green-Lagrange strain tensor $\mathbf{E}$ in the $(\mathbf{f}_0, \mathbf{s}_0, \mathbf{n}_0)$ frame of reference. The parameter B is called bulk modulus and it weights the volumetric term $\frac{1}{2}(J-1)\log J$, penalizing the deformations that would lead to a change of the volume occupied by the tissue ($J \neq 1$).

Following the derivation of Sec. 7.2.2, we write the Piola stress tensor as $\mathbf{P} = \mathbf{P}^{\text{pass}} + \mathbf{P}^{\text{act}}$, namely as the sum of a passive term and an active term, given respectively by:

$$\mathbf{P}^{\text{pass}} = \frac{\partial \mathcal{W}}{\partial \mathbf{F}}, \qquad \mathbf{P}^{\text{act}} = T_a \frac{\mathbf{F}\mathbf{f}_0 \otimes \mathbf{f}_0}{|\mathbf{F}\mathbf{f}_0|}, \tag{8.7}$$

where the scalar field T_a denotes the active tension generated in the domain Ω_0 and it is obtained as a function of the activation variables $\mathbf{z}$.

For model closure, the balance of momentum equation (see Eq. (7.6)) needs to be supplemented with suitable boundary conditions, that model the interaction of the LV with the surrounding environment. In the next sections, we present the different boundary conditions imposed on the different parts of the boundary $\partial\Omega_0$.

Boundary conditions on Γ_0^{epi}

The heart is surrounded by the *pericardium*, a double layered sac, with the function of protecting the heart from external shocks. The pericardial cavity is filled with a lubricating serous fluid, that minimizes the friction of the heart wall when the myocardium contracts [TD08; JKT07; Pfa+19].

To model the effect of the pericardium of the epicardial surface of the LV, we consider the following generalized Robin boundary conditions on Γ_0^{epi} (see [GDQ18a]):

$$\mathbf{PN} + (\mathbf{N} \otimes \mathbf{N}) \left(K_{\perp}^{\text{epi}} \mathbf{d} + C_{\perp}^{\text{epi}} \frac{\partial \mathbf{d}}{\partial t} \right) + (\mathbf{I} - \mathbf{N} \otimes \mathbf{N}) \left(K_{\parallel}^{\text{epi}} \mathbf{d} + C_{\parallel}^{\text{epi}} \frac{\partial \mathbf{d}}{\partial t} \right) = \mathbf{0}. \quad (8.8)$$

The tissues surrounding the heart wall are modeled as a system of springs (elastic effects) and dashpots (viscous effects). The coefficient $K_{\perp}^{\text{epi}}$ (respectively, $K_{\parallel}^{\text{epi}}$) represents the spring stiffness per unit area in the normal (respectively, tangent) direction, while $C_{\perp}^{\text{epi}}$ (respectively, $C_{\parallel}^{\text{epi}}$) represents the dashpot viscosity per unit area in the normal (respectively, tangent) direction. For simplicity, we use a unique set of parameters for the region of the LV epicardium in contact with the pericardium and for the region confining with the RV.

Boundary conditions on Γ_0^{endo}

The inner surface of the LV, the endocardium, is in contact with the blood, with which it exchange forces: during systole, the active force generated inside the cardiomyocytes quickly pushes the blood from the LV to the aorta, while, during diastole, the pressure exercised by the blood on the cardiac wall causes the dilation of the LV cavity. To accurately model the coupling between the heart muscle and the blood, fluid-structure interaction (FSI) models can be adopted. In this framework, the blood motion inside the LV cavity is modeled by adopting suitable rheological models for the blood (e.g. by the Navier-Stokes equation), and the coupling between the fluid and the solid is obtained by imposing the continuity of displacement and moment across the interface [Qua+19; TDQ17b; TDQ17a].

Since the focus of this thesis is on cardiac EM, we rather adopt a lumped description of the fluid, similarly to [GDQ18a]. Specifically, by neglecting the shear stress exercised by the fluid on the cardiac wall, we only consider the effect of the fluid pressure, which we assume to be constant in the whole LV cavity (we denote such pressure by the scalar $p(t)$). Then, the force exerted by the fluid on the heart muscle across a surface $A \in \Gamma^{\text{endo}}(t)$, is given by:

$$\int_A \mathbf{T}\mathbf{n}\, dA = -p \int_A \mathbf{n}\, dA. \quad (8.9)$$

By Eq. (7.5) and thanks to the Nanson's formulae, we get:

$$\int_{A_0} \mathbf{PN}\, dA_0 = -p \int_{A_0} J\mathbf{F}^{-T}\mathbf{N}\, dA_0. \quad (8.10)$$

Finally, by the arbitrary of the surface, we get:

$$\mathbf{PN} = -pJ\mathbf{F}^{-T}\mathbf{N} \qquad \text{on } \Gamma_0^{\text{endo}}. \quad (8.11)$$

Boundary conditions on Γ_0^{base}

The base Γ_0^{base} is an artificial boundary and, as such, it must be provided with boundary conditions that account for the effect of the neglected part of the domain on the considered part. We respectively denote by $\widetilde{\Omega}(t)$ and $\widetilde{\Omega}^{\text{fluid}}(t)$ the solid and fluid domains located above the base, and by $\widetilde{\Gamma}^{\text{endo}}(t)$ and $\widetilde{\Gamma}^{\text{epi}}(t)$ the endocardial end epicardial surfaces located above the base. By considering a quasistatic approximation, the momentum equation in the current configuration entails:

$$\begin{aligned}\mathbf{0} &= \int_{\widetilde{\Omega}(t)} \nabla \cdot \mathbf{T}\, dV \\ &= \int_{\partial\widetilde{\Omega}(t)} \mathbf{T}\mathbf{n}\, dA \\ &= \int_{\widetilde{\Gamma}^{\text{epi}}(t)} \mathbf{T}\mathbf{n}\, dA + \int_{\widetilde{\Gamma}^{\text{endo}}(t)} \mathbf{T}\mathbf{n}\, dA + \int_{\widetilde{\Gamma}^{\text{base}}(t)} \mathbf{T}\mathbf{n}\, dA.\end{aligned}$$

We assume that the epicardial surface located above the base is unloaded [Pfa+19], that is $\mathbf{T}\mathbf{n} = \mathbf{0}$ on $\widetilde{\Gamma}^{\text{epi}}(t)$. On $\widetilde{\Gamma}^{\text{endo}}(t)$, which is in contact with the fluid, we have $\mathbf{T}\mathbf{n} = -p\mathbf{n}$. Moreover, we have the following identity:

$$\mathbf{0} = \int_{\Omega^{\text{fluid}}(t)\cup\widetilde{\Omega}^{\text{fluid}}(t)} \nabla p\, dV = \int_{\Gamma^{\text{endo}}(t)} p\mathbf{n}\, dA + \int_{\widetilde{\Gamma}^{\text{endo}}(t)} p\mathbf{n}\, dA,$$

which entails:

$$\int_{\Gamma^{\text{base}}(t)} \mathbf{T}\mathbf{n}\, dA = -\int_{\widetilde{\Gamma}^{\text{base}}(t)} \mathbf{T}\mathbf{n}\, dA = \int_{\Gamma^{\text{endo}}(t)} p\mathbf{n}\, dA = \int_{\Gamma_0^{\text{endo}}} p\, J\mathbf{F}^{-T}\mathbf{N}\, dA_0. \quad (8.12)$$

Equation (8.12) allows to derive the total stress applied on the boundary $\Gamma^{\text{base}}(t)$, but not its pointwise distribution. This is the price to pay as we do not explicitly include the domain $\widetilde{\Omega}(t)$ into the EM model. Nonetheless, if we assume that the stress is uniformly distributed, we get:

$$\mathbf{T}\mathbf{n} = |\Gamma^{\text{base}}(t)|^{-1} \int_{\Gamma_0^{\text{endo}}} p\, J\mathbf{F}^{-T}\mathbf{n}\, dA_0 \qquad \text{on } \Gamma^{\text{base}}(t), \quad (8.13)$$

which reads, in the reference configuration:

$$\mathbf{P}\mathbf{N} = \frac{|J\mathbf{F}^{-T}\mathbf{N}|}{\int_{\Gamma_0^{\text{base}}} |J\mathbf{F}^{-T}\mathbf{N}|\, dA_0} \int_{\Gamma_0^{\text{endo}}} pJ\mathbf{F}^{-T}\mathbf{N} dA_0 \qquad \text{on } \Gamma_0^{\text{base}}. \quad (8.14)$$

We notice that thanks to Eq. (8.14) the net force exerted by the fluid on the solid is null since the stress on Γ_0^{base} perfectly balances the stress exerted on Γ_0^{endo}. This is coherent with the hydrostatic nature of the pressure force, which contributes to the energy of the system, but not to its momentum.

Moreover, we notice that, if we assume that the stress is uniformly distributed in the reference configuration (rather than in the current one), we get the following alternative boundary condition:

$$\mathbf{P}\mathbf{N} = |\Gamma_0^{\text{base}}|^{-1} \int_{\Gamma_0^{\text{endo}}} pJ\mathbf{F}^{-T}\mathbf{N} dA_0 \qquad \text{on } \Gamma_0^{\text{base}}. \quad (8.15)$$

However, even if the boundary condition (8.15) allows for simpler implementations, we will employ the boundary condition (8.14), as it is more natural to assume a uniform distribution in the current configuration.

Balance of momentum equation

To sum up, the balance of momentum written in the reference domain, endowed with boundary and initial conditions, reads as follows :

$$\begin{cases} \rho \dfrac{\partial^2 \mathbf{d}}{\partial t^2} - \nabla_0 \cdot \mathbf{P} = \mathbf{0} & \text{in } \Omega_0 \times (0,T], \\ \mathbf{P}\mathbf{N} + (\mathbf{N}\otimes\mathbf{N}) \left(K_\perp^{\text{epi}} \mathbf{d} + C_\perp^{\text{epi}} \dfrac{\partial \mathbf{d}}{\partial t} \right) & \\ \qquad + (\mathbf{I} - \mathbf{N}\otimes\mathbf{N}) \left(K_\parallel^{\text{epi}} \mathbf{d} + C_\parallel^{\text{epi}} \dfrac{\partial \mathbf{d}}{\partial t} \right) = \mathbf{0} & \text{on } \Gamma_0^{\text{epi}} \times (0,T], \\ \mathbf{P}\mathbf{N} = \dfrac{|J\mathbf{F}^{-T}\mathbf{N}|}{\int_{\Gamma_0^{\text{base}}} |J\mathbf{F}^{-T}\mathbf{N}| dA_0} \displaystyle\int_{\Gamma_0^{\text{endo}}} pJ\mathbf{F}^{-T}\mathbf{N} dA_0 & \text{on } \Gamma_0^{\text{base}} \times (0,T], \\ \mathbf{P}\mathbf{N} = -pJ\mathbf{F}^{-T}\mathbf{N} & \text{on } \Gamma_0^{\text{endo}} \times (0,T], \\ \mathbf{d} = \mathbf{d}_0, \quad \dfrac{\partial \mathbf{d}}{\partial t} = \mathbf{0} & \text{in } \Omega_0 \times \{0\}. \end{cases} \tag{8.16}$$

Recovering the reference configuration

The stress-strain relationship defined by (7.7) is referred to the natural configuration Ω_0. However, the geometry recovered from images taken in vivo (that we denote by $\overline{\Omega}$) does not correspond to the natural stress-free configuration since an internal pressure p is always present in each phase of the heartbeat. Therefore, in the preprocessing stage, we need to recover the reference configuration Ω_0 from $\overline{\Omega}$.

We assume that the configuration Ω_0 is taken during diastole, when the ventricle is loaded by a pressure $p = \overline{p}$ and a residual active tension T_{a} is present. By adopting a static assumption, the displacement observed under such conditions is given by the solution of the following differential problem:

$$\begin{cases} -\nabla_0 \cdot \mathbf{P} = \mathbf{0} & \text{in } \Omega_0, \\ \mathbf{P}\mathbf{N} + K_\parallel^{\text{epi}} \mathbf{d} + (K_\perp^{\text{epi}} - K_\parallel^{\text{epi}}) (\mathbf{N}\otimes\mathbf{N}) \mathbf{d} = \mathbf{0} & \text{on } \Gamma_0^{\text{epi}}, \\ \mathbf{P}\mathbf{N} = \dfrac{|J\mathbf{F}^{-T}\mathbf{N}|}{\int_{\Gamma_0^{\text{base}}} |J\mathbf{F}^{-T}\mathbf{N}| dA_0} \displaystyle\int_{\Gamma_0^{\text{endo}}} pJ\mathbf{F}^{-T}\mathbf{N} dA_0 & \text{on } \Gamma_0^{\text{base}}, \\ \mathbf{P}\mathbf{N} = -pJ\mathbf{F}^{-T}\mathbf{N} & \text{on } \Gamma_0^{\text{endo}}. \end{cases} \tag{8.17}$$

Thus, in order to recover the coordinate $\mathbf{x}_0$ of the configuration Ω_0 we need to solve the following inverse problem: find the domain Ω_0 such that, if we move $\mathbf{x}_0$ by the solution $\mathbf{d}$ of Eq. (8.17) for $p = \overline{p}$, we get the coordinate $\overline{\mathbf{x}}$ of the domain $\overline{\Omega}$ (i.e. $\overline{\mathbf{x}} = \mathbf{x}_0 + \mathbf{d}$). We notice that, however, the displacement $\mathbf{d}$ depends on the Ω_0 itself (i.e. $\mathbf{d} = \mathbf{d}(\mathbf{x}_0)$).

To accomplish this goal, we adopt a strategy similar to that of [Qua+17], where we initially set $\mathbf{x}_0 = \overline{\mathbf{x}}$ and then we iteratively proceed by solving Eq. (8.17) for $p = \overline{p}$ and setting $\mathbf{x}_0 = \overline{\mathbf{x}} - \mathbf{d}(\mathbf{x}_0)$, until the distance between the target coordinate $\overline{\mathbf{x}}$ and the deformed configuration $\mathbf{x}_0 + \mathbf{d}(\mathbf{x}_0)$ is lower than a prescribed tolerance. The fixed-point of the above iterative strategy is clearly a solution of the inverse problem.

After the recovery of the reference configuration, in order to find the initial condition for Eq. (8.16), we set $p = \overline{p}_{\text{ED}}$ and we solve again Eq. (8.17).

8.1.4 Blood external circulation

To close the EM problem, the LV activity must be coupled with equations describing the external circulation. With this aim, we consider a lumped description of the blood

circulation, as done in [GDQ18a], consisting of four phases, where we conventionally start with systole (see Sec. 1.1.2):

1. In the isochoric contraction phase, the pressure $p(t)$ starts from its end-diastolic value ($\overline{p}_{\text{ED}}$) and then raises in such a way that the ventricular volume V is kept constant.

2. When $p(t)$ reaches the aortic valve opening pressure value $\overline{p}_{\text{AVO}}$ (we define such time instant as $t = T^{\text{AVO}}$), the ejection phase starts. In this phase, we describe the evolution of $p(t)$ by means of the following two-elements Windkessel model [WLW09]:
$$\begin{cases} C_{\text{circ}} \dfrac{dp}{dt} = -\dfrac{p}{R_{\text{circ}}} - \dfrac{dV}{dt} & t \in (T^{\text{AVO}}, T^{\text{AVC}}], \\ p(T^{\text{AVO}}) = \overline{p}_{\text{AVO}}, \end{cases} \tag{8.18}$$
where T^{AVC} (aortic valve closing time) is the first time, after T^{AVO}, when the negative flux $\frac{dV}{dt}$ changes its sign.

3. At this stage, another isochoric phase begins. This phase ends when $p(t)$ reaches $\overline{p}_{\text{MVO}}$, the value of the mitral valve opening pressure.

4. In the filling phase, we linearly increase $p(t)$ so that it reaches $\overline{p}_{\text{ED}}$ at the final time T.

In order to compute the ventricular volume V (i.e. the volume of the ventricular cavity), we proceed as follows. First, we identify the center point of the base as:

$$\mathbf{b}(t) = \frac{1}{\left|\Gamma_0^{\text{base}}\right|} \int_{\Gamma_0^{\text{base}}} (\mathbf{X} + \mathbf{d}(t)) dA_0,$$

where $\mathbf{X}$ denotes the material coordinate. Then, we define the surface $\Gamma^{\text{cap}}(t)$ as the surface connecting the point $\mathbf{b}(t)$ with the orifice ring. The ventricular volume is thus defined as the measure of the volume $\Omega^{\text{fluid}}(t)$, delimited by $\Gamma^{\text{endo}}(t)$ and $\Gamma^{\text{cap}}(t)$. By exploiting the identity $\nabla \cdot (\mathbf{x} - \mathbf{b}(t)) = 3$, where $\mathbf{x}$ denotes the spatial coordinate, we have:

$$\begin{aligned} 3V(t) &= \int_{\Omega^{\text{fluid}}(t)} 3\, dV = \int_{\Omega^{\text{fluid}}(t)} \nabla \cdot (\mathbf{x} - \mathbf{b}(t))\, dV \\ &= \int_{\Gamma^{\text{endo}}(t)} (\mathbf{x} - \mathbf{b}(t)) \cdot \mathbf{n}(t)\, dA + \int_{\Gamma^{\text{cap}}(t)} (\mathbf{x} - \mathbf{b}(t)) \cdot \mathbf{n}(t)\, dA, \end{aligned}$$

where $\mathbf{n}(t)$ and $\mathbf{N}$ denote the outward unit vector normal at the surface in the actual and reference domains, respectively. Since, by construction, $(\mathbf{x} - \mathbf{b}(t)) \perp \mathbf{n}(t)$ on $\Gamma^{\text{cap}}(t)$, the second term vanishes, leading to the formula:

$$V(t) = \frac{1}{3} \int_{\Gamma_0^{\text{endo}}} J(t)\, (\mathbf{X} + \mathbf{d}(t) - \mathbf{b}(t)) \cdot \mathbf{F}^{-T}(t) \mathbf{N}\, dA_0.$$

8.1.5 The coupled EM problem

A recap of the different physics involved in the EM problem is shown in Fig. 1, with the quantities that couple the different building blocks. The electrical activity, for which we consider the monodomain model, is tightly coupled with the model describing the

ionic activity. The ionic model provides the calcium concentration, the main input to the model describing the mechanical activation, that in turn feeds the mechanics model with the active component of the stress tensor. The mechanical model, thanks to the presence of an active stress, allows to compute the displacement associated to the contraction of the tissue. Finally, the movement of the computational domain has a feedback both on the electrical activity, as the tissue strain affects the electrical conductivity tensor, and on the mechanical activation, because of the influence of the sarcomere length on the machinery of force generation.

Coupling together the four building blocks of the electrical and ionic activity, mechanical activation and mechanics, we get the EM problem, a system of coupled PDEs and ODEs that reads as follows:

$$
\begin{cases}
\dfrac{\partial v}{\partial t} + \widetilde{\mathcal{I}}^{\text{ion}}(v, \mathbf{w}) = \nabla_0 \cdot \left(J\, \mathbf{F}^{-1} \widetilde{\mathbf{D}} \mathbf{F}^{-T} \nabla_0 v \right) + \widetilde{\mathcal{I}}^{\text{app}} & \text{in } \Omega_0 \times (0,T], \\
\dfrac{\partial \mathbf{w}}{\partial t} = \mathbf{h}(v, \mathbf{w}) & \text{in } \Omega_0 \times (0,T], \\
SL - SL_0 \sqrt{\mathcal{I}_{4,f}} - \delta_{SL}^2 \Delta SL = 0 & \text{in } \Omega_0 \times (0,T], \\
\dfrac{\partial \mathbf{z}}{\partial t} = \mathbf{r} \left(\mathbf{z}, [\mathrm{Ca}^{2+}]_{\mathrm{i}}, SL, \dfrac{\partial SL}{\partial t} \right) & \text{in } \Omega_0 \times (0,T], \\
\rho \dfrac{\partial^2 \mathbf{d}}{\partial t^2} - \nabla_0 \cdot \mathbf{P} = \mathbf{0} & \text{in } \Omega_0 \times (0,T], \\
\left(J\, \mathbf{F}^{-1} \mathbf{D} \mathbf{F}^{-T} \nabla_0 v \right) \cdot \mathbf{N} = 0 & \text{on } \partial\Omega_0 \times (0,T], \\
\delta_{SL}^2 \nabla_0 SL \cdot \mathbf{N} = 0 & \text{on } \partial\Omega_0 \times (0,T], \\
\mathbf{P}\mathbf{N} + (\mathbf{N} \otimes \mathbf{N}) \left(K_{\perp}^{\text{epi}} \mathbf{d} + C_{\perp}^{\text{epi}} \dfrac{\partial \mathbf{d}}{\partial t} \right) & \\
\qquad + (\mathbf{I} - \mathbf{N} \otimes \mathbf{N}) \left(K_{\parallel}^{\text{epi}} \mathbf{d} + C_{\parallel}^{\text{epi}} \dfrac{\partial \mathbf{d}}{\partial t} \right) = \mathbf{0} & \text{on } \Gamma_0^{\text{epi}} \times (0,T], \\
\mathbf{P}\mathbf{N} = \dfrac{|J\mathbf{F}^{-T}\mathbf{N}|}{\int_{\Gamma_0^{\text{base}}} |J\mathbf{F}^{-T}\mathbf{N}| dA_0} \int_{\Gamma_0^{\text{endo}}} p J \mathbf{F}^{-T} \mathbf{N} dA_0 & \text{on } \Gamma_0^{\text{base}} \times (0,T], \\
\mathbf{P}\mathbf{N} = -p J \mathbf{F}^{-T} \mathbf{N} & \text{on } \Gamma_0^{\text{endo}} \times (0,T], \\
v = v_0, \quad \mathbf{w} = \mathbf{w}_0, \quad \mathbf{z} = \mathbf{z}_0, \quad \mathbf{d} = \mathbf{d}_0, \quad \dfrac{\partial \mathbf{d}}{\partial t} = \mathbf{0} & \text{in } \Omega_0 \times \{0\},
\end{cases}
\tag{8.19}
$$

where the endocardial pressure p has to be determined, depending on the cardiac cycle phase, either as Lagrange multiplier for the isovolumetric phases, or as solution of the circulation model (8.18). In Tab. 8.1 we report the full list of parameters of the EM model, with the values used in this thesis.

8.2 Numerical approximation of the EM problem

In order to numerically approximate the solution of the EM problem of Eq. (8.19), we consider a FEM spatial discretization in space and we discretize the time derivatives by means of first-order finite difference schemes [QSS10].

Specifically, we consider a Finite Element space $V_h \subset H^1(\Omega_0^h)$, defined over a tetrahedral computational mesh built upon a suitable discretization Ω_0^h of the reference domain Ω_0. Then, we discretize the problem unknowns as $v_h \in V_h$, $\mathbf{d}_h \in \mathbf{V}_h := [V_h]^d$ and we also discretize each ionic variable and each activation variable as an element of

Variable	Value	Unit	Description
Electrophysiology			
σ_{f}	$1.204 \cdot 10^3$	$\mathrm{mm^2\,s^{-1}}$	Electrical conductivity in fiber direction
σ_{iso}	$0.1761 \cdot 10^3$	$\mathrm{mm^2\,s^{-1}}$	Electrical conductivity in tangential direction
$\mathcal{I}^{\max}$	100	$\mathrm{V\,s^{-1}}$	Applied current value
δ	14	mm	Applied current radius
t_{app}	$2 \cdot 10^{-3}$	s	Applied current duration
Activation			
SL_0	2.0	µm	Reference sarcomere length
δ_{SL}	5	mm	SL regularization radius
Mechanics			
ρ	10^3	$\mathrm{kg\,m^{-3}}$	Tissue density
B	50	kPa	Bulk modulus
C	2	kPa	Material stiffness
b_{ff}	8	-	Hyperelastic parameter
b_{ss}	6	-	Hyperelastic parameter
b_{nn}	3	-	Hyperelastic parameter
b_{fs}	12	-	Hyperelastic parameter
b_{fn}	3	-	Hyperelastic parameter
b_{sn}	3	-	Hyperelastic parameter
$K_{\perp}^{\mathrm{epi}}$	$2 \cdot 10^{-1}$	$\mathrm{kPa\,mm^{-1}}$	Robin boundary condition
$C_{\perp}^{\mathrm{epi}}$	$2 \cdot 10^{-2}$	$\mathrm{kPa\,s\,mm^{-1}}$	Robin boundary condition
$K_{\parallel}^{\mathrm{epi}}$	$2 \cdot 10^{-2}$	$\mathrm{kPa\,mm^{-1}}$	Robin boundary condition
$C_{\parallel}^{\mathrm{epi}}$	$2 \cdot 10^{-3}$	$\mathrm{kPa\,s\,mm^{-1}}$	Robin boundary condition
Circulation			
R_{circ}	$3.5 \cdot 10^{-2}$	$\mathrm{Pa\,s\,mm^{-3}}$	Windkessel model parameters
C_{circ}	4.5	$\mathrm{mm^3\,Pa^{-1}}$	Windkessel model parameters
$\overline{p}_{\mathrm{ED}}$	1.333	kPa	End-diastolic pressure
$\overline{p}_{\mathrm{AVO}}$	9.333	kPa	Aortic valve opening pressure
$\overline{p}_{\mathrm{MVO}}$	0.667	kPa	Mitral valve opening pressure

Table 8.1: Parameters of the EM problem.

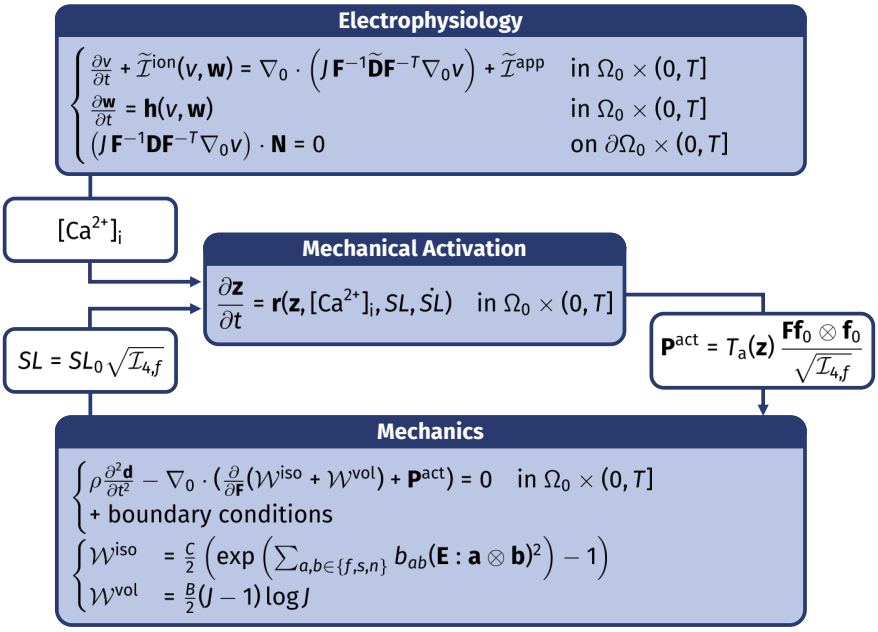

Figure 8.2: The equations describing the building blocks of cardiac EM and the corresponding coupling quantities.

V_h (we denote the discretized ionic and activation variables as $\mathbf{w}_h$ and $\mathbf{z}_h$, respectively). As for the time discretization, we consider a uniform subdivision $0 = t_0 < t_1 < \cdots < t_M = T$ of the time interval $[0, T]$ with time step size Δt. To denote the unknown at the k-th time step, we use a superscript (e.g. $v_h^{(k)} \approx v(t_k)$).

To couple the different core models, different approaches can be adopted. The coupled EM system of Eq. (8.19) can be solved as a monolithic set of equations in a unique mesh [WBG07; GDQ18a]. Alternatively, by an operator splitting approach, the different core models can be sequentially solved in a segregated manner [Was+13; Was+15; Qua+17; GDQ18b]. The advantage of the latter approach is that it allows to employ different meshes with different spatial resolutions to discretize cardiac electrophysiology (that requires a very fine mesh to capture the correct propagation velocity of the electrical signal) and mechanics (that can be solved on a coarser computational mesh) and possibly also different time step sizes [Nor+11; Qua+17; GDQ18b].

In this thesis, we employ the segregated strategy presented in [GDQ18b]. Specifically, at each time step t_k, we sequentially perform the following steps.

I) We update the ionic variables by solving the ionic model (8.1), thus obtaining $\mathbf{w}_h^{(k)}$.

II) We update the potential field $v_h^{(k)}$ by solving the monodomain equation (that is Eq. (8.2)).

III) We recover the local sarcomere length by solving Eq. (8.5) and we update the activation variables $\mathbf{z}_h^{(k)}$ by solving Eq. (8.4).

IV) We update the displacement and the ventricular pressure. In the isochoric phases of the heartbeat, we update $\mathbf{d}_h^{(k)}$ and $p^{(k)}$ simultaneously, by solving Eq. (8.16) together with the equation $V^{(k)} = V^{(k-1)}$. On the other hand, during the ejection and the filling phases, the pressure $p^{(k)}$ is updated before solving the mechanical problem.

At each step, we approximate the quantities that are required to couple the different physics and that have not been updated yet by an extrapolation coherent with the order of the scheme used for the time discretization. For instance, in Step I, we employ the extrapolated value of the electric potential $v^{(*)}$ to update the ionic variables. Since in this thesis we consider a first order time-stepping scheme, the extrapolated values coincide with the values at the previous iteration (i.e. $v^{(*)} = v^{(k-1)}$), but the approach can be easily generalized to higher order schemes.

In the following, we give more details on the different steps.

8.2.1 Step I: Ionic equation

Since the ionic model (8.1) is written as a system of ODEs, we update each degree of freedom of the FEM discretization of the ionic variables independently of the others. To deal with the stiff nature of the TTP06 model, we adopt an implicit-explicit (IMEX) scheme. More precisely, the 18 ionic variables of the TTP06 model can be split into 6 ionic concentrations (featuring a nonlinear but non-stiff dynamics) and 12 gating variables (linear but highly stiff dynamics). This suggests to adopt an explicit handling of the former to avoid the solution of a nonlinear system (such choice does not compromise the stability of the scheme, thanks to the non-stiff dynamics of concentrations), and an implicit handling of the latter, because of the severe CFL condition on the time step that an explicit scheme would bring. However, thanks to the linear dynamics of the gating variables, such implicit handling does not require the solution of a system of linear or nonlinear equations. During the update of both the ionic concentrations and the gating variables, we employ the solution of the potential at the previous time step $v_h^{(k-1)}$. In conclusion, with the considered IMEX scheme, the ionic variables can be updated without the solution of any system of equations.

8.2.2 Step II: Monodomain equation

We update the potential field $v_h^{(k)}$ by solving the FEM discretization of the monodomain equation (Eq. (8.2)), with implicit treatment of the diffusive term and explicit treatment of the $\widetilde{\mathcal{I}}^{\text{ion}}$ term, by employing the updated value of the ionic variables $\mathbf{w}_h^{(k)}$ and the displacement of the previous time step $\mathbf{d}_h^{(k-1)}$. Hence, the solution $v_h^{(k)} \in \mathbf{V}_h$ is obtained as the solution of the following linear variational problem:

$$\begin{aligned}
&\int_{\Omega_0^h} \left(\frac{v_h^{(k)} - v_h^{(k-1)}}{\Delta t} + \widetilde{\mathcal{I}}^{\text{ion}}(v_h^{(k-1)}, \mathbf{w}_h^{(k)}) \right) \xi_h \, dV_0 \\
&+ \int_{\Omega_0^h} \left(J^{(k-1)} \, (\mathbf{F}^{(k-1)})^{-1} \widetilde{\mathbf{D}} (\mathbf{F}^{(k-1)})^{-T} \nabla_0 v_h^{(k)} \right) \cdot \nabla_0 \xi_h \, dV_0 \qquad (8.20) \\
&= \int_{\Omega_0^h} \widetilde{\mathcal{I}}^{\text{app}} \xi_h \, dV_0 \qquad \forall \, \xi_h \in V_h.
\end{aligned}$$

8.2.3 Step III: Activation equation

We discretize the SL field by means of Finite Element too and we find the value of $SL_h \in V_h$ by solving the FEM discretization of Eq. (8.5). Then, as for the ionic variables, we update each degree of freedom of the FEM discretization of $\mathbf{z}_h$ independently of the others, by employing the updated value of the calcium concentration and the sarcomere length field obtained above. Since the solution of the activation model requires a small time step, at this step we perform an inner iteration loop.

8.2.4 Step IV: Mechanics equation

Finally, we solve the FEM discretization of the mechanics problem of Eq. (8.16), with implicit treatment of the unknown $\mathbf{d}^{(k)}$. The discretized version of Eq. (8.16) reads as the following nonlinear variational problem:

$$
\begin{aligned}
&\int_{\Omega_0^h} \rho \frac{\mathbf{d}_h^{(k)} - 2\mathbf{d}_h^{(k-1)} + \mathbf{d}_h^{(k-2)}}{\Delta t^2} \cdot \boldsymbol{\xi}_h \, dV_0 \\
&+ \int_{\Omega_0^h} \left[\frac{\partial \mathcal{W}_{\mathbf{F}}}{\partial \mathbf{F}} \left(\mathbf{F}^{(k)} \right) + T_{\mathrm{a}}^{(k)} \frac{\mathbf{F}^{(k)} \mathbf{f}_0 \otimes \mathbf{f}_0}{|\mathbf{F}^{(k)} \mathbf{f}_0|} \right] : \nabla_0 \boldsymbol{\xi}_h \, dV_0 \\
&+ \int_{\Gamma_0^{\mathrm{epi}}} \left[(\mathbf{N} \otimes \mathbf{N}) \left(K_{\perp}^{\mathrm{epi}} \mathbf{d}_h^{(k)} + C_{\perp}^{\mathrm{epi}} \frac{\mathbf{d}_h^{(k)} - \mathbf{d}_h^{(k-1)}}{\Delta t} \right) \right. \\
&\qquad \left. + (\mathbf{I} - \mathbf{N} \otimes \mathbf{N}) \left(K_{\parallel}^{\mathrm{epi}} \mathbf{d}_h^{(k)} + C_{\parallel}^{\mathrm{epi}} \frac{\mathbf{d}_h^{(k)} - \mathbf{d}_h^{(k-1)}}{\Delta t} \right) \right] \cdot \boldsymbol{\xi}_h \, dA_0 \\
&- \int_{\Gamma_0^{\mathrm{base}}} \left[\frac{|J^{(k)} (\mathbf{F}^{(k)})^{-T} \mathbf{N}|}{\int_{\Gamma_0^{\mathrm{base}}} |J^{(k)} (\mathbf{F}^{(k)})^{-T} \mathbf{N}| dA_0} \int_{\Gamma_0^{\mathrm{endo}}} p^{(k)} J^{(k)} (\mathbf{F}^{(k)})^{-T} \mathbf{N} dA_0 \right] \cdot \boldsymbol{\xi}_h \, dA_0 \\
&+ \int_{\Gamma_0^{\mathrm{endo}}} p^{(k)} J^{(k)} (\mathbf{F}^{(k)})^{-T} \mathbf{N} \cdot \boldsymbol{\xi}_h \, dA_0 = 0 \qquad \forall \, \boldsymbol{\xi}_h \in \mathbf{V}_h.
\end{aligned}
\tag{8.21}
$$

To solve the nonlinear system of equations arising from the variational problem of Eq. (8.21), we employ a Newton-Raphson strategy [QSS10]. More precisely, in order to deal with the nonlocal nature of the boundary condition on Γ_0^{base}, we adopt a quasi-Newton strategy, by computing the Jacobian matrix only with respect to the local terms.

During the two isochoric phases, at the k-th step Eq. (8.21) is solved together with the constraint $V^{(k)} = V^{(k-1)}$. The resulting system of equations is solved for $\mathbf{d}_h^{(k)}$ and $p^{(k)}$, that acts in this setting as a Lagrange multiplier. We solve the saddle-point problem arising from each iteration of the quasi-Newton method by a Schur complement reduction [BGL05]. During the ejection phase, instead, we update $p^{(k)}$ by solving the finite difference discretization of Eq. (8.18) with an implicit treatment of p, before solving Eq. (8.21).

In Sec. 8.4.1, devoted to the SE-ODE and the MF-ODE models, we will propose a modification of Eq. (8.21), in order to avoid numerical instabilities that can occur for large shortening velocities with the latter models.

8.2.5 ANN-based efficient EM simulations

The computational cost associated with the numerical approximation of the EM problem is strongly affected by the solution of the activation model (8.4), both in terms

of memory storage and computational time (we provide quantitative indications in Secs. 8.3). To lower such computational burden, we replace the HF activation models of Eq. (6.1) (activation-MH, SE-ODE or MF-ODE models) with the ROMs given by the ANN-based model of Eq. (6.2). This can be easily done thanks to the fact that the HF models and the corresponding ROMs share the same structure in terms of inputs and outputs.

In Secs. 8.3 and 8.4, we compare the results of EM simulations obtained by employing the HF activation models and by employing the ANN-based models, which we will respectively denote by HF-EM and ANN-EM. All the results presented in the following are obtained with piecewise linear $P1$ Finite Elements and with a time step of $\Delta t = 2 \cdot 10^{-4}$ s.

Error estimation of ANN-EM vs HF-EM in 1D

The zero-dimensional simulations obtained with the reduced ANN-based model (see Secs. 6.2.1 and 6.3.1) are accurate with respect to the ones obtained with the corresponding HF models (relative error of order 10^{-2}). Nevertheless, when the activation model is embedded in the EM coupled system, the model output (i.e. active force) has a feedback on its inputs (mostly on SL, as it causes the tissue contraction, but also on $[Ca^{2+}]_i$, due to the mechano-electrical feedback). Therefore, one should check whether such feedback has the effect of amplifying the error introduced by the ANN reduced model, or not.

To gain some insight on the effect of the feedback of mechanics on activation, we consider a one-dimensional steady-state version of equation (8.16), which can be regarded as a simple model for the tissue deformation along the direction of the active force (i.e. the fibers direction). By denoting by d the one-dimensional displacement and by $e = \frac{d}{dx}d$ the one-dimensional strain, we consider an elastic energy $\mathcal{W}(e)$ and we define the passive stress as $P^{\text{pass}}(e) := \mathcal{W}'(e)$, while we denote by P^{act} the active stress. The mechanical equilibrium equation in the domain $(0, L)$ reads as follows:

$$\begin{cases} -\dfrac{d}{dx}\left(P^{\text{pass}}\left(\dfrac{d}{dx}d(x)\right) + P^{\text{act}}(x)\right) = 0 \qquad \text{for } x \in (0, L), \\ d(0) = 0, \\ P(\frac{d}{dx}d(L)) + P^{\text{act}}(L) = p, \end{cases} \tag{8.22}$$

where we set a symmetry boundary condition at one side and a load p at the other side. Coherently with the activation models considered in this thesis, the active tension is a function of calcium concentration and sarcomere length: $P^{\text{act}}(x) = T_a^{\text{iso}}([Ca^{2+}]_i(x), SL(x))$, where $SL(x) = SL_0(1 + e(x))$. The solution of Eq. (8.22) satisfies:

$$P^{\text{pass}}(e(x)) + T_a^{\text{iso}}([Ca^{2+}]_i(x), SL_0(1 + e(x))) = p \qquad \forall x \in (0, L).$$

Consider now a perturbed version of Eq. (8.22), where the function T_a^{iso} is replaced by a surrogate $\widetilde{T}_a^{\text{iso}} = T_a^{\text{iso}} + \eta$, affected by the error η (in our case, η can be regarded as the approximation error associated with the reduced ANN model). By asymptotic analysis, the perturbed solution $\tilde{d}$ satisfies:

$$\frac{d}{dx}\tilde{d} - \frac{d}{dx}d \sim \eta\left(\frac{\partial T_a^{\text{iso}}}{\partial SL}SL_0 + \mathcal{W}''(e)\right)^{-1}.$$

Hence, the active stress in the perturbed problem is linked with the HF one by:

$$\widetilde{T}_{\mathrm{a}}^{\mathrm{iso}}([\mathrm{Ca}^{2+}]_{\mathrm{i}}, SL_0(1+\tilde{e}(x))) - T_{\mathrm{a}}^{\mathrm{iso}}([\mathrm{Ca}^{2+}]_{\mathrm{i}}, SL_0(1+e(x))) \sim \eta \left(1 + \frac{\frac{\partial T_{\mathrm{a}}^{\mathrm{iso}}}{\partial SL} SL_0}{\mathcal{W}''(e)}\right)^{-1}.$$

Being the elastic energy convex, the term $\mathcal{W}''(e)$ is positive. Thus, on the ascending limb of the force-length relationship ($\frac{\partial T_{\mathrm{a}}^{\mathrm{iso}}}{\partial SL} > 0$), the error η is attenuated; conversely, on the descending limb ($\frac{\partial T_{\mathrm{a}}^{\mathrm{iso}}}{\partial SL} < 0$) it is amplified.

The above results suggest that in the normal working-range of sarcomeres (that lays is the ascending limb of the force-length relationship) the feedback of mechanics on activation has a favourable effect when the HF activation models are replaced by ROMs: a positive deviation of active tension leads to a more pronounced shortening of the tissue (i.e. lower SL), which in turns, makes the active tension decrease, compensating the initial error in T_{a}. This will find a confirmation in the numerical results shown in Sec. 8.3 and 8.4.

8.3 Numerical results: the activation-MH model

In this section we consider the EM problem (8.19) where we employ, to model the mechanical activation, the activation-MH model. In Sec. 8.3.1 we show the results obtained with a benchmark problem, consisting in the contraction of a slab of cardiac tissue. Then, in Sec. 8.3.2, we show the results of the numerical simulation of the contraction of LV.

8.3.1 Test Case 1: cardiac slab

We consider a slab of cardiac tissue, defined by the computational domain $\Omega_0 = (0, 40\,\mathrm{mm}) \times (0, 20\,\mathrm{mm}) \times (0, 8\,\mathrm{mm})$. We consider a fibers field $\mathbf{f}_0 = \mathbf{e}_1$ aligned as the x-axis and a sheets field $\mathbf{s}_0 = \mathbf{e}_3$ aligned as the z-axis. We consider a unique stimulus location $\mathbf{x}_1 = (0, 0, 0)^T$ (point A of Fig. 8.4). Due to the simple domain employed, in this Test Case the three boundaries (Γ_0^{base}, Γ_0^{epi} and Γ_0^{endo}) are not defined. Thus, we change the boundary conditions of the mechanical problem (8.16), by imposing $\mathbf{d} \cdot \mathbf{N} = 0$ and a no-stress condition in tangential direction on the three faces passing through the origin (i.e. $\{\mathbf{x} \colon \mathbf{x} \cdot \mathbf{e}_j = 0\}$, for $j = 1, 2, 3$). In the remaining subset of the boundary, we impose a generalized boundary condition with $K_\perp = 5 \cdot 10^{-1}\,\mathrm{kPa\,mm^{-1}}$, $C_\perp = 1 \cdot 10^{-1}\,\mathrm{kPa\,s\,mm^{-1}}$ and $K_\parallel = C_\parallel = 0$. Finally, we set $T_{\mathrm{a}}^{\max} = 700\,\mathrm{kPa}$.

We consider a structured computational mesh with a uniform subdivision in 16, 8 and 3 elements along the cartesian directions x,y, and z, respectively, for a total of 2304 tetrahedra and 612 dofs. In Figs. 8.3 and 8.4 we show a comparison between the HF-EM and the ANN-EM results. The computational costs are compared in Tab. 8.3.

8.3.2 Test Cases 2 and 3: idealized and realistic left ventricle

We consider an idealized LV (Test Case 2) and a realistic LV derived from the CAD of [Zyg] (Test Case 3). The idealized computational mesh consists of 6500 tetrahedra and 1827 degrees of freedom, whereas the realistic one accounts for $354 \cdot 10^3$ tetrahedra and $65 \cdot 10^3$ degrees of freedom (Fig. 8.5). The electrical stimulus $\mathcal{I}^{\mathrm{app}}$ is applied at three points, located on the endocardial surface close to the apex. We generate the fibers and sheets distribution according to the rule-based algorithm proposed in [Bay+12], by

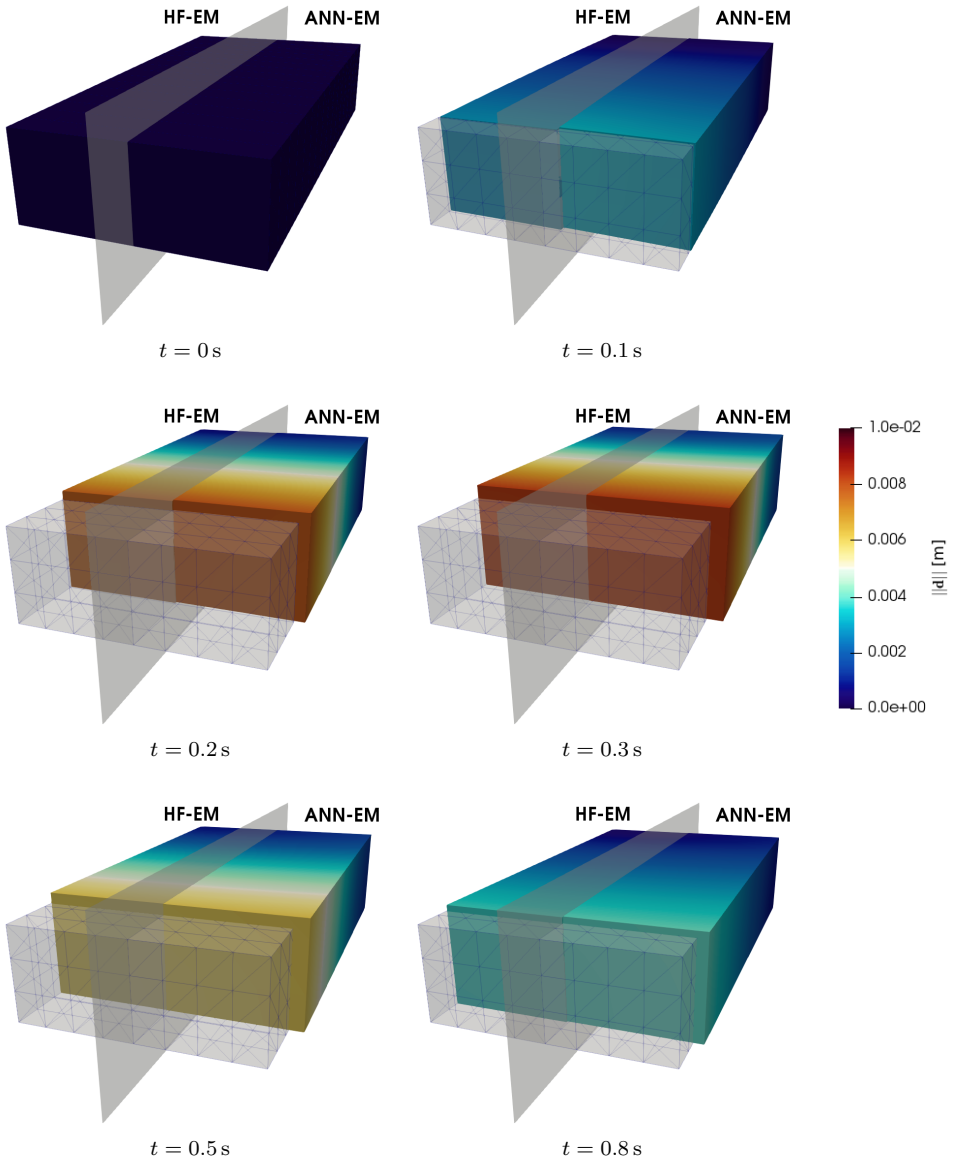

Figure 8.3: Test Case 1: comparison of the displacement field (at different time steps) between the simulations performed with the HF activation-MH model and with the corresponding ANN-based ROM. For visualization purposes, the domain is splitted into two identical subregions: in the left subregion, the solution obtained with the HF model is shown; in the right subregion, the solution obtained with the ANN-based model.

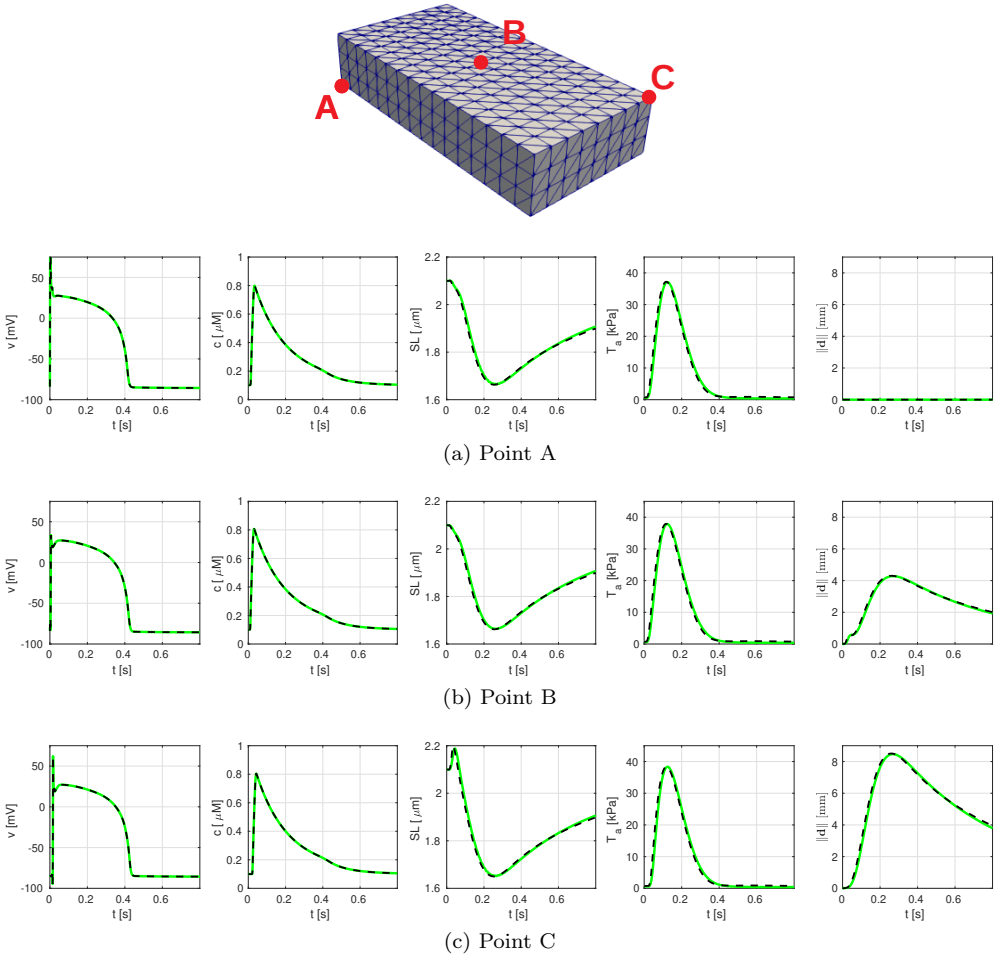

(a) Point A

(b) Point B

(c) Point C

Figure 8.4: Test Case 1: comparison of the time course of quantities of interest in three points (indicated in the top image) obtained with the simulations performed with HF-EM (solid colored lines) and with ANN-EM (black dashed lines).

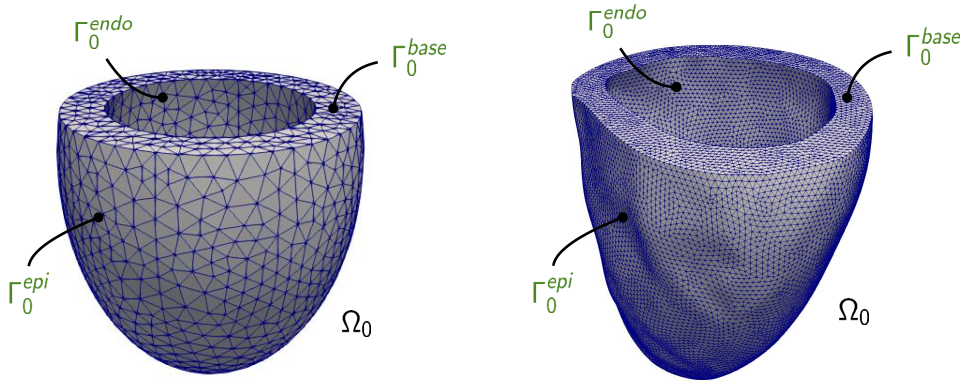

(a) Test Case 2 (b) Test Case 3

Figure 8.5: LV computational meshes of Test Cases 2 and 3.

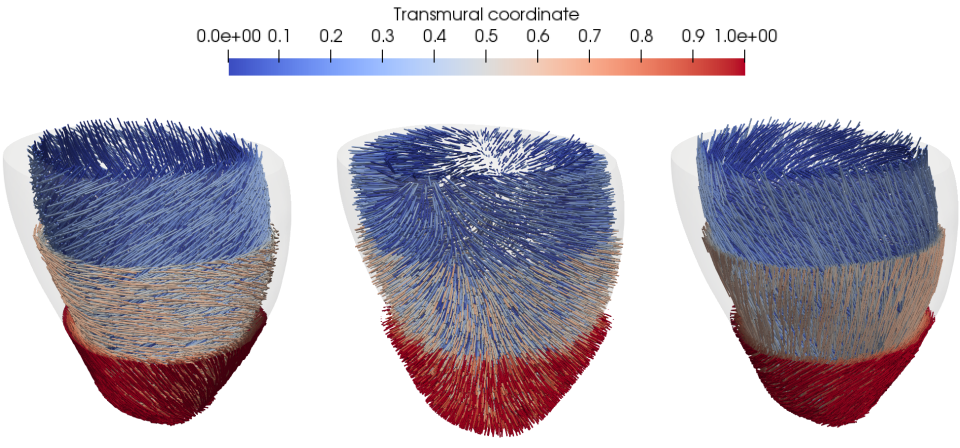

(a) Field $\mathbf{f}_0$ (b) Field $\mathbf{s}_0$ (c) Field $\mathbf{n}_0$

Figure 8.6: Test Case 3: representation of fibers, sheets and normal fields. Three sections in the apico-basal direction allow to appreciate the transmural variation of fibers orientation.

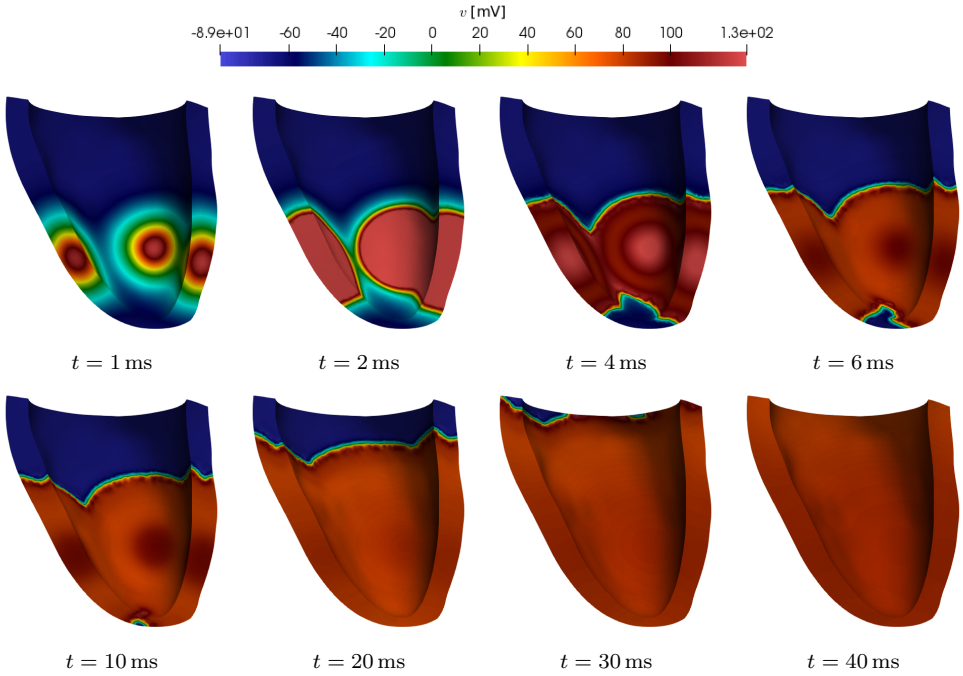

Figure 8.7: Test Case 3 (activation-MH model): transmembrane potential at different times.

setting $\alpha_{\text{endo}} = -60°$, $\alpha_{\text{epi}} = +60°$. The fibers, sheets and normal fields are displayed (just for the realistic geometry) in Fig. 8.6. In Test Case 3, to lower the computational burden due to the fine mesh, we employ a first-order time splitting scheme by solving the mechanical subproblem every five time steps (see [GDQ18b; Ger18]). In order to obtain realistic pressure values, in Test Case 2 we set $T_{\text{a}}^{\max} = 480\,\text{kPa}$, while in Test Case 3 we set $T_{\text{a}}^{\max} = 700\,\text{kPa}$.

In the preprocessing stage, in order to recover the reference configuration associated with the domains shown in Fig. 8.5, we adopt the fixed-point algorithm presented in Sec. 8.1.3. In Test Case 2, we assume that the computational domain of Fig. 8.5a is associated to the end dyastolic phase. Therefore, we recover the natural configuration by setting $\overline{p} = \overline{p}_{\text{ED}}$. On the other hand, as the computational domain of Test Case 3 is associated to a phase of the heart cycle such that the diastolic filling is not fully completed (more precisely, the beginning of the atrial kick), we recover the natural configuration by assuming that the computational domain is at equilibrium with an intermediate pressure between $\overline{p}_{\text{ED}}$ and $\overline{p}_{\text{MVO}}$ (specifically we take $\overline{p} = 5.6\,\text{mmHg}$).

In Figs. 8.7 and 8.8 we show the propagation of the v and the $[\text{Ca}^{2+}]_{\text{i}}$ fields, respectively, for Test Case 3. The active tension field T_{a} is visualized, at different time steps, in Fig. 8.10, where three sections at different quotes along the apex-base coordinate allow to appreciate the distribution of active stress across the transmural coordinate. Finally, in Fig. 8.9 (Test Case 2) and in Fig. 8.11 (Test Case 3), we show the displacement field and the contraction of the LV. The top and frontal sections highlight the torsion that the LV undergoes during the heartbeat and the consequent wall thickening.

Then, in Fig. 8.12 (Test Case 2) and Fig. 8.13 (Test Case 3), we compare the

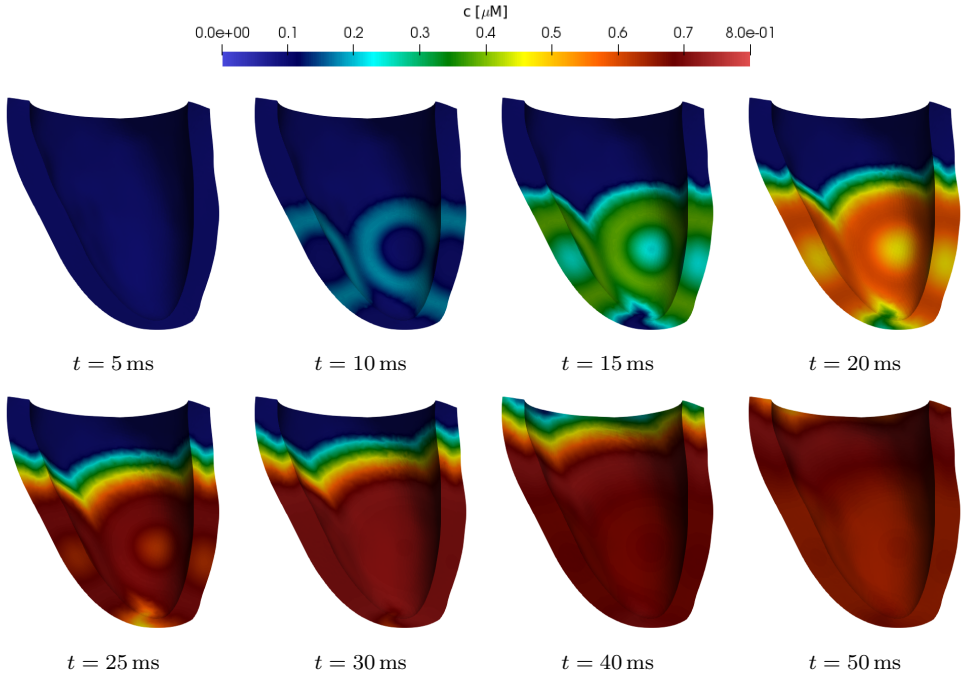

Figure 8.8: Test Case 3 (activation-MH model): intracellular calcium concentration at different times.

results obtained within the HF-EM and the ANN-EM frameworks. In the top row, we show the time evolution, of the average, minimum and maximum value over the domain of $[Ca^{2+}]_i$, SL and T_a. In the bottom row we show the time evolution of the macroscopic quantities p and V and the LV pressure-volume loop. All the curves show a good match between the results obtained in the HF-EM and the ANN-EM frameworks.

The main cardiac indicators, some of them clinically meaningful, computed in the HF-EM and ANN-EM frameworks, are reported in Tab. 8.2. For all the indicators, the error between HF-EM and ANN-EM is even smaller than the train and of the test error associated with the ANN model. This is a consequence of the feedback of active force on SL (see Sec. 8.2.5).

Finally, in Tab. 8.3, we report the computational times associated with the numerical approximation of the EM problem in the HF-EM and in the ANN-EM frameworks. For Test Case 2, a single core was employed, whereas for Test Case 3 simulations were run in parallel on 20 cores.

8.3.3 Reduction of computational cost

The ANN-EM framework accomplishes a significant reduction of computational cost compared to the HF-EM framework. The solution of the activation models, which accounts for most of the computational time of the whole simulation, highlights a gain nearly of a factor 300 in all test cases, reducing the overall computational times by one order of magnitude. The computational speedup is slightly smaller for finer grids, for which the relative weight of the mechanical subproblem is more pronounced. However,

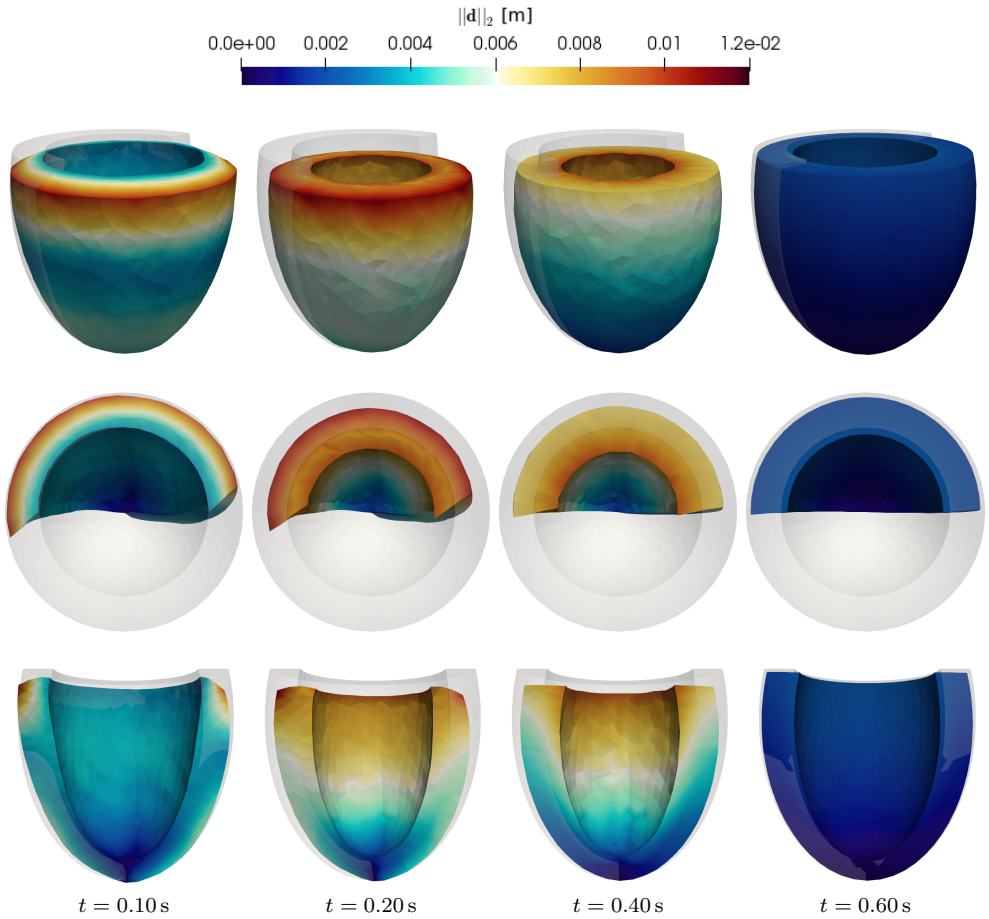

Figure 8.9: Test Case 2 (activation-MH model): deformed geometry and magnitude of displacement at different times. Top row: full geometry. Middle row: half domain (top view). Bottom row: half domain (frontal view).

Indicator	HF-EM	ANN-EM	Relative error
Test Case 2 (idealized LV, 1827 dof)			
Stroke volume (mL)	63.33	63.57	$3.71 \cdot 10^{-3}$
Ejection fraction (%)	46.63	46.80	$3.71 \cdot 10^{-3}$
Systolic pressure (mmHg)	112.96	113.91	$8.38 \cdot 10^{-3}$
Work (mJ)	766	773	$9.08 \cdot 10^{-3}$
Test Case 3 (patient-specific LV, 65476 dof)			
Stroke volume (mL)	56.64	56.39	$4.33 \cdot 10^{-3}$
Ejection fraction (%)	44.48	44.29	$4.33 \cdot 10^{-3}$
Systolic pressure (mmHg)	108.94	109.10	$1.51 \cdot 10^{-3}$
Work (mJ)	662	659	$4.85 \cdot 10^{-3}$

Table 8.2: Test Cases 2 and 3 (activation-MH model): main cardiac indicators. Comparison between the HF-EM and the ANN-EM frameworks and corresponding relative errors.

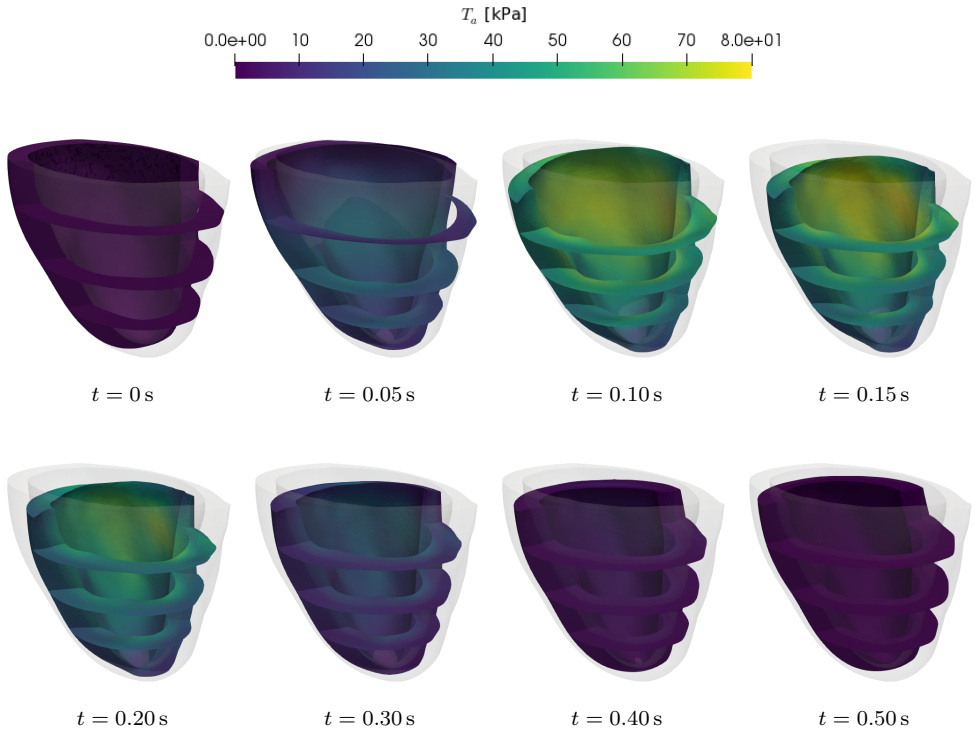

Figure 8.10: Test Case 3 (activation-MH model): active tension at different times.

Simulation type	Ionic	Potential	Activation	Mechanics	Wall time
Test Case 1 (cardiac slab, 612 dof, 1 core)					
HF-EM	6.3%	0.3%	89.0%	4.5%	3h 16’
ANN-EM	53.0%	2.7%	3.3%	41.1%	22’
Test Case 2 (idealized LV, 1827 dof, 1 core)					
HF-EM	4.27%	0.29%	91.94%	3.40 %	9h 31’
ANN-EM	53.38%	3.31%	3.74%	39.57%	46’
Test Case 3 (patient-specific LV, 65476 dof, 20 cores)					
HF-EM	3.14%	0.47 %	83.07%	13.33%	20h 18’
ANN-EM	41.21%	4.80%	2.54%	51.46%	2h 04’

Table 8.3: Comparison of the computational times associated to the four physics and the total wall time between HF-EM and ANN-EM, for both Test Cases.

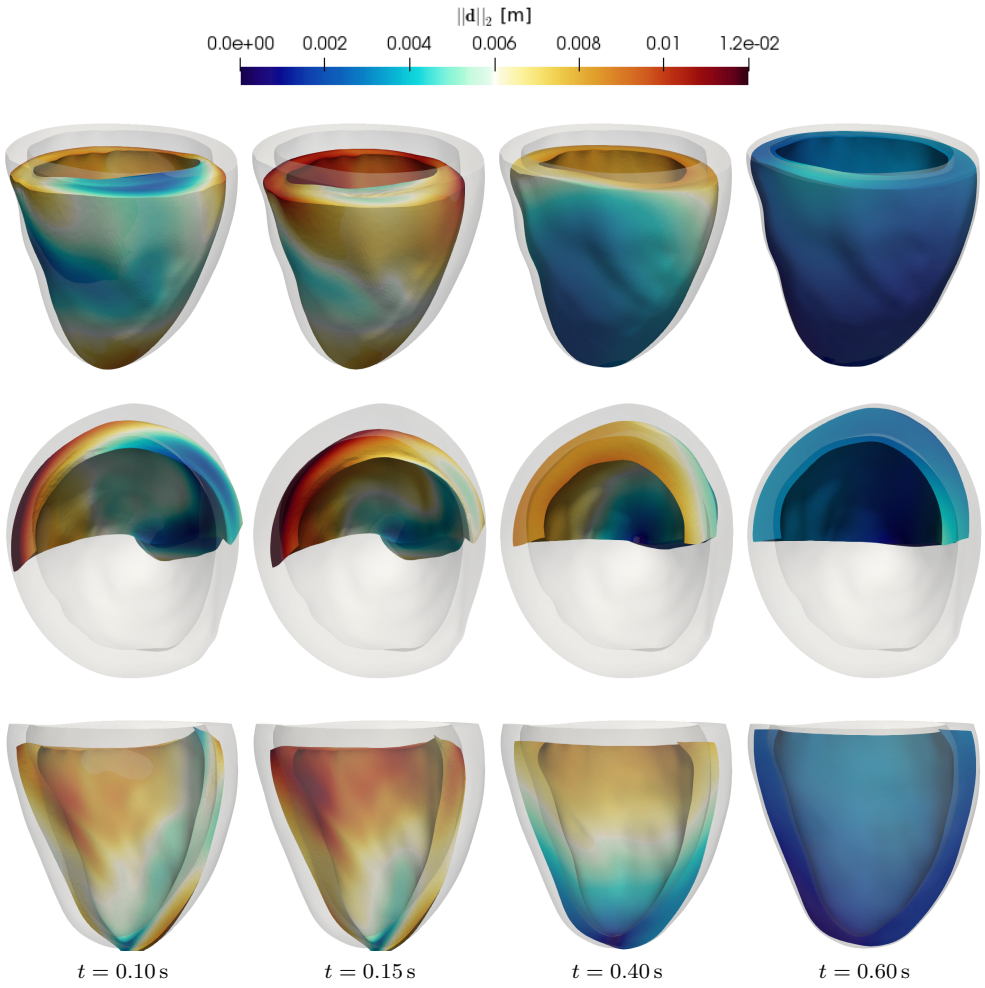

Figure 8.11: Test Case 3 (activation-MH model): deformed geometry and magnitude of displacement at different times. Top row: full geometry. Middle row: half domain (top view). Bottom row: half domain (frontal view).

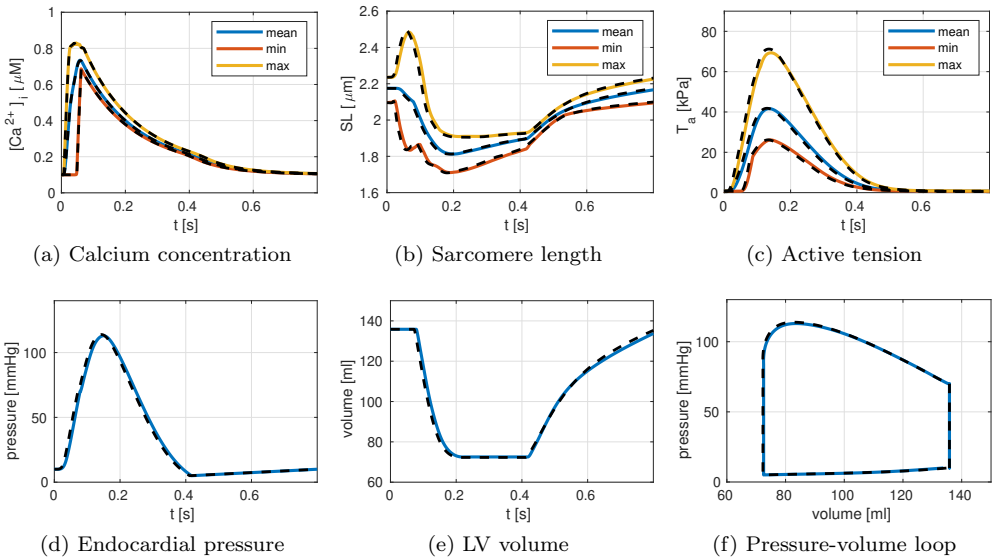

(a) Calcium concentration (b) Sarcomere length (c) Active tension

(d) Endocardial pressure (e) LV volume (f) Pressure-volume loop

Figure 8.12: Test Case 2 (activation-MH model): comparison of the time evolution of quantities of interest and of the pressure-volume loop obtained with the simulations performed with HF-EM (solid colored lines) and with ANN-EM (black dashed lines). In (a)-(b)-(c) the three lines refer to the minimum, maximum and mean value over the computational domain.

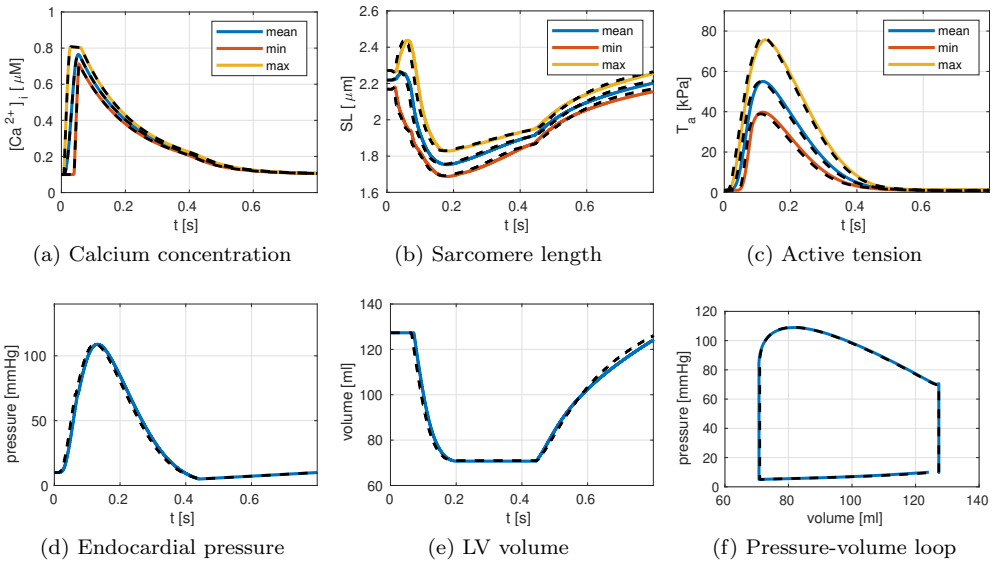

(a) Calcium concentration (b) Sarcomere length (c) Active tension

(d) Endocardial pressure (e) LV volume (f) Pressure-volume loop

Figure 8.13: Test Case 3 (activation-MH model): comparison of the time evolution of quantities of interest and of the pressure-volume loop obtained with the simulations performed with HF-EM (solid colored lines) and with ANN-EM (black dashed lines). In (a)-(b)-(c) the three lines refer to the minimum, maximum and mean value over the computational domain.

whereas the approximation of the electrophysiology subproblem (8.2) requires a finer grid for the convergence of the solution [Qua+19], the computational mesh used in Test Case 3 features a large enough number of elements to get accurate results for the mechanics subproblem (8.16) and to capture the complexity of patient-specific domains [Qua+19; LN15]. Therefore, since when different meshes are employed for the different physics the activation subproblem (8.4) is typically solved on the mesh used for the mechanics [Qua+19], we expect that the speedup obtained in Test Case 3 is representative for the computational gain one can obtain for HF simulations of patient-specific EM.

With the ANN-EM approach, the number of variables for each degree of freedom of the domain is 24 (18 ionic variables, the transmembrane potential, 2 activation variables, 3 components of the displacement), significantly lower than the number of variables with the HF-EM approach (18+1+2176+3 = 2198).

8.4 Numerical results: the SE-ODE and MF-ODE models

In this section we consider the cardiac EM problem of Eq. (8.19), with the mechanical activation subproblem modeled by means of the full-sarcomere models MF-ODE and SE-ODE. First, in Sec. 8.4.1, we deal with numerical instabilities arising from the feedback of the generated force on the shortening velocity of the tissue. Then, in Sec. 8.4.2 we present the results obtained for idealized and realistic LV test cases.

8.4.1 Avoiding velocity-related instabilities

When the SE-ODE or the MF-ODE model are employed, numerical simulations of cardiac EM obtained with the numerical scheme presented in Sec. 8.2 may feature spurious oscillations, even for time step sizes for which the simulations obtained with the activation-MH model are not characterized by oscillations. For instance, by adopting a time step of $\Delta t = 4 \cdot 10^{-4}$ s for the mechanical subproblem and of $\Delta t = 2 \cdot 10^{-4}$ s for the remaining physics, we obtain the results shown by the red lines of Fig. 8.14. Moreover, for slightly larger time steps, the oscillations lead to the divergence of the solution.

The observed oscillations are the effect of numerical instabilities linked to the feedback of the generated force on the tissue shortening velocity (indeed, they are not exhibited by the activation-MH model, that neglects the dependence of velocity on force). The mechanisms underlying the velocity-related instabilities is rooted in the following feedback loop: during the ejection phase, when the active tension rapidly increases, the tissue undergoes a quick shortening; hence, in the next time step, the increase of velocity causes a drop of active force and, consequently, of shortening velocity; in the following time step the active force raises again thanks to the reduced velocity and the cycle is repeated. If the time step Δt is not sufficiently small in relation to the shortening velocity, such loop leads to spurious oscillations in the active force and in the tissue displacement.

Similar numerical instabilities related to the feedback of mechanics of the force generation apparatus have been considered in [NS08], where they are addressed by updating the active force at each Newton iteration of the mechanics problem, thus resulting in a strong coupling between the mechanics and the force generation core models. Conversely, in this section, we propose to introduce a stabilization term

in the variational problem of Eq. (8.21), that allows to tackle such velocity-related instabilities while preserving the fully staggered structure of the scheme presented in Sec. 8.2.

With the aim of deriving a stable discretization scheme for the mechanical subproblem, we take inspiration from the microscale energetic considerations of Sec. 7.2.2 (that lead to the derivation of the active stress tensor $\mathbf{P}^{\text{act}}$, responsible for the observed instabilities). We recall that the active part of the Piola stress tensor can be written in the following alternative forms:

(F1) $\mathbf{P}^{\text{act}} = a_{\text{XB}}\,\mu^1\,\frac{\mathbf{F}\mathbf{f}_0\otimes\mathbf{f}_0}{|\mathbf{F}\mathbf{f}_0|}$;

(F2) $\mathbf{P}^{\text{act}} = a_{\text{XB}}\left(\hat{\mu}^0\lambda+\hat{\mu}^1\right)\frac{\mathbf{F}\mathbf{f}_0\otimes\mathbf{f}_0}{|\mathbf{F}\mathbf{f}_0|}$.

The two formulations are clearly equivalent, as we have $\mu^1 = \hat{\mu}^0\lambda+\hat{\mu}^1$ (see Eq. (7.18)). The difference lays in the coordinate system (Lagrangian or Eulerian, see e.g. [Ant95]), used to describe the microscopic elongation of the myosin arms. Indeed, the formulation (F1) is written with a hybrid Lagrangian-Eulerian formalism: while the macroscale strain $\mathbf{F}$ is written in Lagrangian coordinates, the variable μ^1 is defined as the first-order distribution-moment of the microscopic Eulerian coordinate x. On the other hand, the formulation (F2) is fully Lagrangian.

Hence, even if the variational formulation of Eq. (8.21) (based on the hybrid Eulerian-Lagrangian formulation (F1)) is formally derived as a fully implicit scheme (that is known to be unconditionally stable for the momentum balance equation, if the elastic energy is convex [QV08]), if rewritten in the more coherent fully Lagrangian formalism of (F2), it appears rather as an implicit-explicit scheme. Indeed, the value of $\lambda = |\mathbf{F}\mathbf{f}_0| - 1$ (that depends on the displacement $\mathbf{d}$) is referred to the previous time step, because of the time splitting scheme of Sec. 8.2. Therefore, to derive a fully-implicit numerical scheme in a fully Lagrangian coordinates system, we employ the formulation (F2) as starting point.

As the activation models proposed in Chap. 4 are written with respect to the Eulerian coordinates, we need to relate the Lagrangian quantities ($\hat{\mu}^0$ and $\hat{\mu}^1$) with the Eulerian ones ($T_{\text{a}} = a_{\text{XB}}\mu^1$ and $K_{\text{a}} = a_{\text{XB}}\mu^0$). From Eq. (7.18), it follows that:

$$\begin{aligned} a_{\text{XB}}\hat{\mu}^0 &= K_{\text{a}}, \\ a_{\text{XB}}\hat{\mu}^1 &= T_{\text{a}} - \lambda K_{\text{a}}. \end{aligned}$$

At the discrete-in-time level, the values of $T_{\text{a}}^{(k)} \simeq T_{\text{a}}(t_k)$ and $K_{\text{a}}^{(k)} \simeq K_{\text{a}}(t_k)$ are obtained at Step III for $\lambda(t_k) \simeq \sqrt{\mathcal{I}_{4,f}^*} - 1$, where $\mathcal{I}_{4,f}^*$ denotes the extrapolation of $\mathcal{I}_{4,f}$ from the previous time steps. Hence, we have:

$$\begin{aligned} a_{\text{XB}}\left(\hat{\mu}^0\right)^{(k)} &= K_{\text{a}}^{(k)}, \\ a_{\text{XB}}\left(\hat{\mu}^1\right)^{(k)} &= T_{\text{a}}^{(k)} - \left(\sqrt{\mathcal{I}_{4,f}^*} - 1\right) K_{\text{a}}^{(k)}. \end{aligned}$$

Therefore, the fully Lagrangian formulation (F2) at the discrete-in-time level reads:

$$\begin{aligned} \left(\mathbf{P}^{\text{act}}\right)^{(k)} &= a_{\text{XB}}\left[\left(\hat{\mu}^1\right)^{(k)} + \lambda^{(k)}\left(\hat{\mu}^0\right)^{(k)}\right]\frac{\mathbf{F}^{(k)}\mathbf{f}_0\otimes\mathbf{f}_0}{|\mathbf{F}^{(k)}\mathbf{f}_0|} \\ &= \left[a_{\text{XB}}\left(\hat{\mu}^1\right)^{(k)} + a_{\text{XB}}\left(\hat{\mu}^0\right)^{(k)}\left(\sqrt{\mathcal{I}_{4,f}^{(k)}} - 1\right)\right]\frac{\mathbf{F}^{(k)}\mathbf{f}_0\otimes\mathbf{f}_0}{|\mathbf{F}^{(k)}\mathbf{f}_0|} \\ &= \left[T_{\text{a}}^{(k)} + K_{\text{a}}^{(k)}\left(\sqrt{\mathcal{I}_{4,f}^{(k)}} - \sqrt{\mathcal{I}_{4,f}^{(*)}}\right)\right]\frac{\mathbf{F}^{(k)}\mathbf{f}_0\otimes\mathbf{f}_0}{|\mathbf{F}^{(k)}\mathbf{f}_0|}, \end{aligned}$$

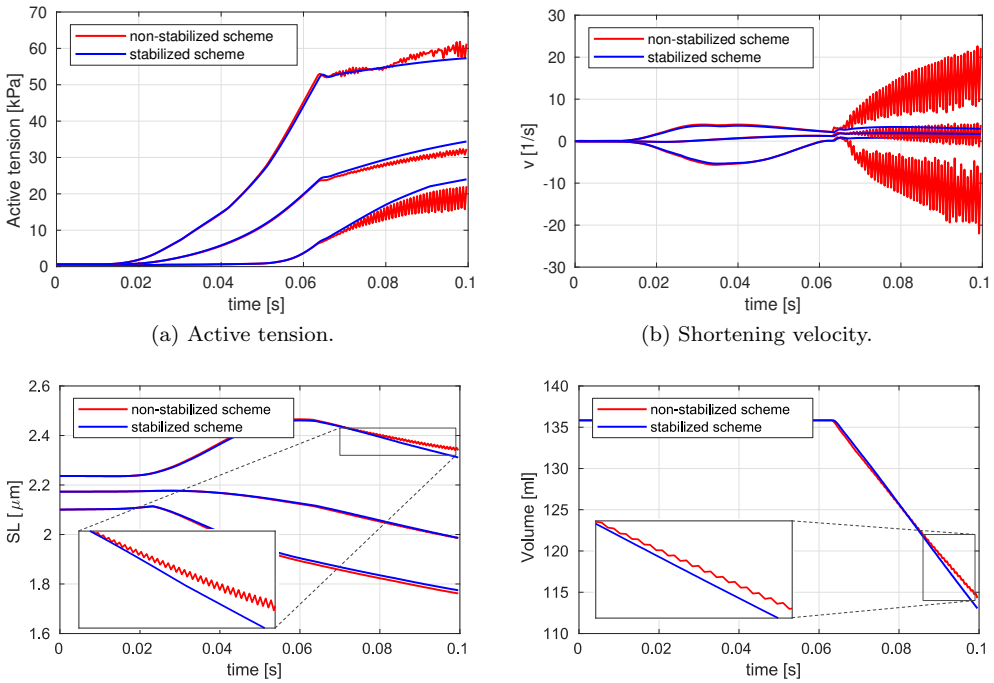

(a) Active tension.

(b) Shortening velocity.

(c) Sarcomere length.

(d) Endocardial volume.

Figure 8.14: Results of numerical simulations of Test Case 2 with the MF-ODE model, obtained with the numerical scheme of Eq. (8.23) (red lines) and of Eq. (8.24) (blue lines). In (a)-(b)-(c) the three lines refer to the minimum, average and maximum value over the computational domain.

where, since we consider in this thesis a first-order time discretization, we have $\mathcal{I}_{4,f}^{(*)} = \mathcal{I}_{4,f}^{(k-1)}$. In conclusion we replace, in the variational formulation (8.21), the term:

$$\int_{\Omega_0^h} T_{\mathrm{a}}^{(k)} \frac{\mathbf{F}^{(k)}\mathbf{f}_0 \otimes \mathbf{f}_0}{|\mathbf{F}^{(k)}\mathbf{f}_0|} : \nabla_0 \boldsymbol{\xi}_h \, dV_0, \tag{8.23}$$

by the term:

$$\int_{\Omega_0^h} \left[T_{\mathrm{a}}^{(k)} + K_{\mathrm{a}}^{(k)} \left(\sqrt{\mathcal{I}_{4,f}^{(k)}} - \sqrt{\mathcal{I}_{4,f}^{(k-1)}} \right) \right] \frac{\mathbf{F}^{(k)}\mathbf{f}_0 \otimes \mathbf{f}_0}{|\mathbf{F}^{(k)}\mathbf{f}_0|} : \nabla_0 \boldsymbol{\xi}_h \, dV_0. \tag{8.24}$$

We notice that the proposed numerical scheme is consistent (in the sense of [QSS10]). Indeed, by setting the discretized variables equal to the exact solution (i.e. $\mathbf{d}_h^{(k)} = \mathbf{d}(t_k)$, $T_{\mathrm{a}}^{(k)} = T_{\mathrm{a}}(t_k)$ and $K_{\mathrm{a}}^{(k)} = K_{\mathrm{a}}(t_k)$) and by letting $\Delta t \to 0$, we get:

$$\left[T_{\mathrm{a}}^{(k)} + K_{\mathrm{a}}^{(k)} \left(\sqrt{\mathcal{I}_{4,f}^{(k)}} - \sqrt{\mathcal{I}_{4,f}^{(k-1)}} \right) \right] \frac{\mathbf{F}^{(k)}\mathbf{f}_0 \otimes \mathbf{f}_0}{|\mathbf{F}^{(k)}\mathbf{f}_0|} \xrightarrow{\Delta t \to 0} T_{\mathrm{a}}(t_k) \frac{\mathbf{F}(t_k)\mathbf{f}_0 \otimes \mathbf{f}_0}{|\mathbf{F}(t_k)\mathbf{f}_0|}.$$

The newly introduced term can thus be interpreted as a consistent stabilization term.

In Fig. 8.14 (blue lines), we show the solution obtained by applying the scheme of Eq. (8.24) to the same test case considered with the scheme of Eq. (8.23). The

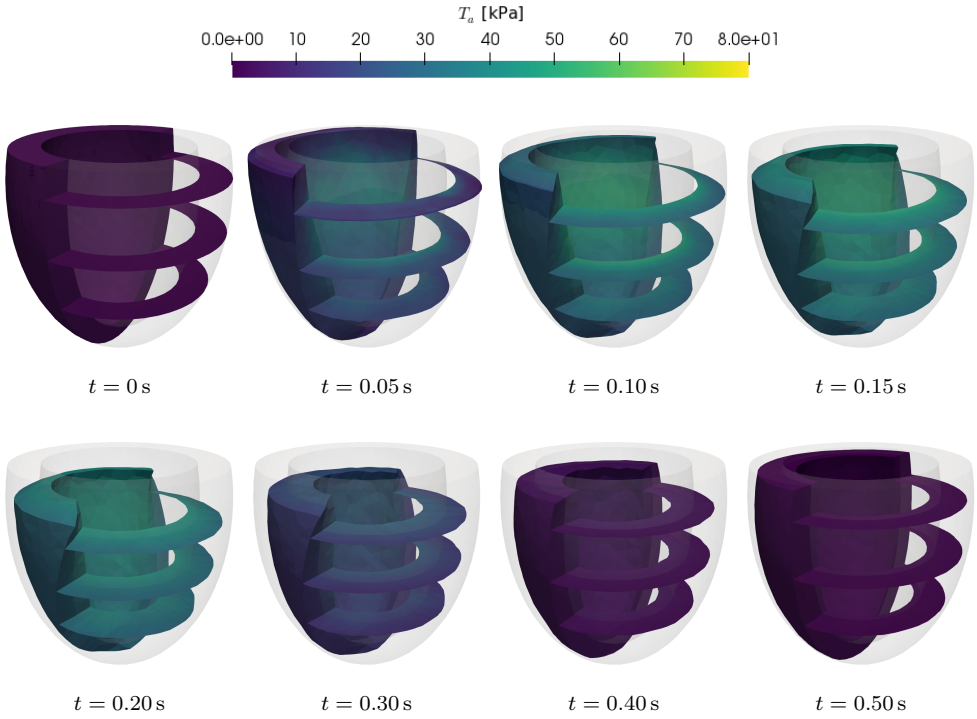

Figure 8.15: Test Case 2 (MF-ODE model): active tension at different times.

results show that the proposed method successfully accomplishes a stabilization of the observed spurious oscillations.

8.4.2 Test Cases 2 and 3: idealized and realistic left ventricle

In this section we show the results obtained by applying the stabilized scheme of Eq. (8.24) to the cardiac EM problem where the mechanical activation is described by means of the SE-ODE or the MF-ODE model. For the latter model, we show the results obtained in Test Cases 2 and 3, while for the former, due to its higher computational cost, we only consider Test Case 2.

In Figs. 8.15, 8.17 and 8.19 we show the active tension obtained with the MF-ODE model in Test Cases 2 and 3, and for the SE-ODE model, in Test Case 2, respectively. In Figs. 8.16, 8.18 and 8.20, we show the displacement field obtained in the same cases listed above.

Then, in Figs. 8.21 and 8.23 (MF-ODE model, Test Cases 2 and 3) and Fig. 8.22 (SE-ODE model, Test Case 2), we show a comparison of the results obtained in the HF-EM and ANN-EM settings, by considering the time evolution of $[\mathrm{Ca}^{2+}]_\mathrm{i}$, SL, T_a, p and V.

Finally, in Tabs. 8.4 and 8.5 we compare the main cardiac indicators obtained with the MF-ODE and SE-ODE models and we report the errors that we obtain with the ANN-EM framework, with respect to the reference values obtained in the HF-EM framework. Similarly to the activation-MH model, thanks to the effect of active force on SL (see Sec. 8.2.5), the error between HF-EM and ANN-EM is smaller than the error between the ANN-based models and the corresponding HF models obtained

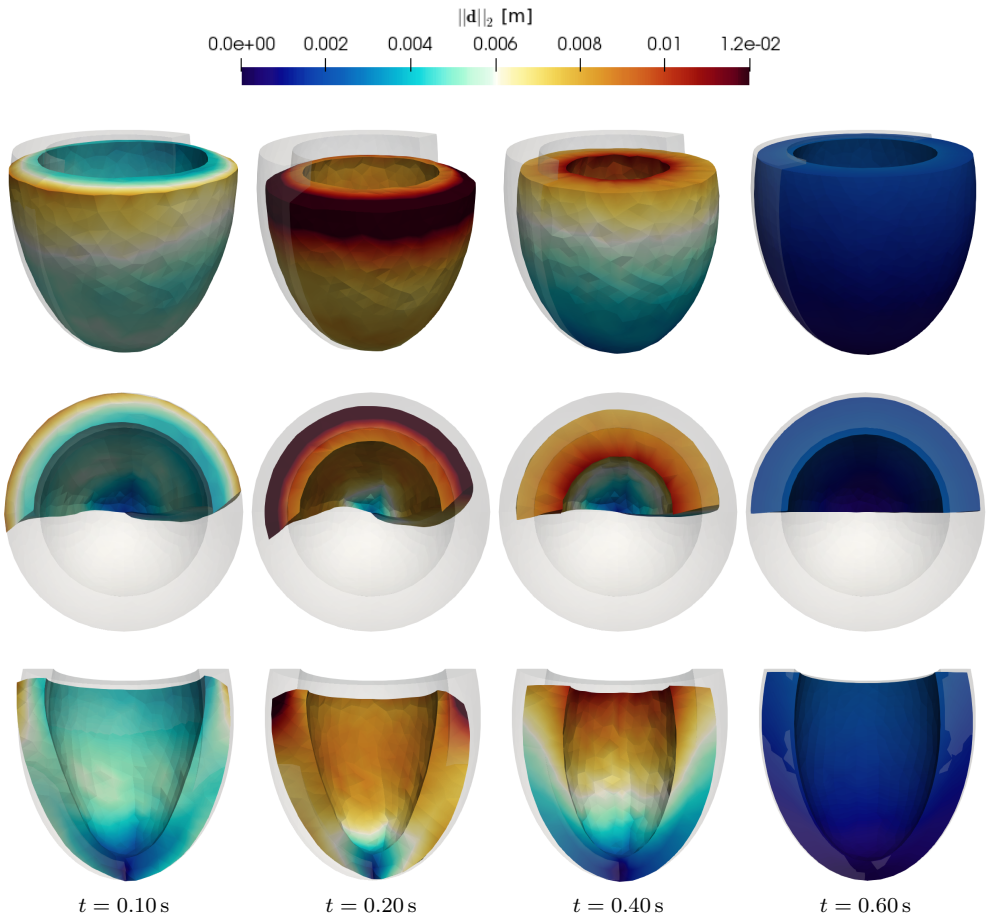

Figure 8.16: Test Case 2 (MF-ODE model): deformed geometry and magnitude of displacement at different times. Top row: full geometry. Middle row: half domain (top view). Bottom row: half domain (frontal view).

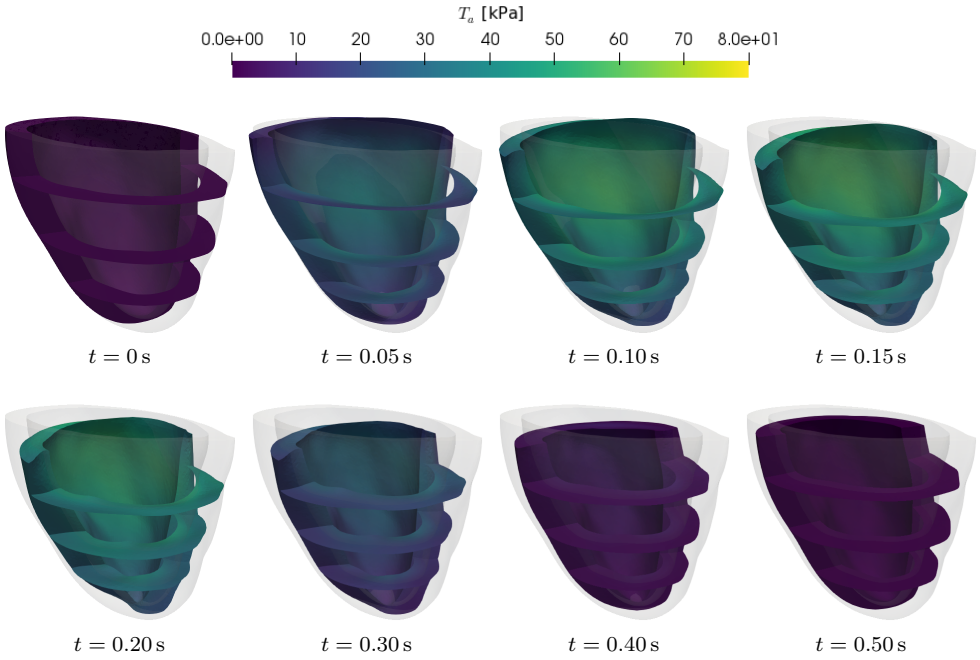

Figure 8.17: Test Case 3 (MF-ODE model): active tension at different times.

when such models are considered alone.

8.5 Final remarks

In this chapter we have presented the EM problem and its numerical approximation by means of FEM discretization in space and a finite difference discretization in time. To couple the different building blocks of the EM system we have considered a first order time splitting scheme, similar to that proposed in [GDQ18b].

We have proposed a novel BC formulation for the boundary Γ_0^{base}, in order to account for the effect of the part of the domain that is not explicitly included into the computational model.

We have then proposed the introduction of a stabilization term, aimed at avoiding velocity-related numerical instabilities, whose effectiveness has been numerically assessed.

Finally, we have shown the results of numerical simulation of EM in a LV, both for idealized and realistic geometries. We have shown that our proposed ANN-based framework for cardiac EM, wherein the computationally expensive HF models of force generation are replaced by the ANN-based ROMs derived in part II, accomplishes a very good balance between accuracy (the main cardiac indicators are computed with an approximation of the order of nearly 10^{-3}) and computational cost. Indeed, the computational time associated with the numerical approximation of the mechanical activation models is reduced by more that 2 orders of magnitude, with an overall speedup of nearly one order of magnitude.

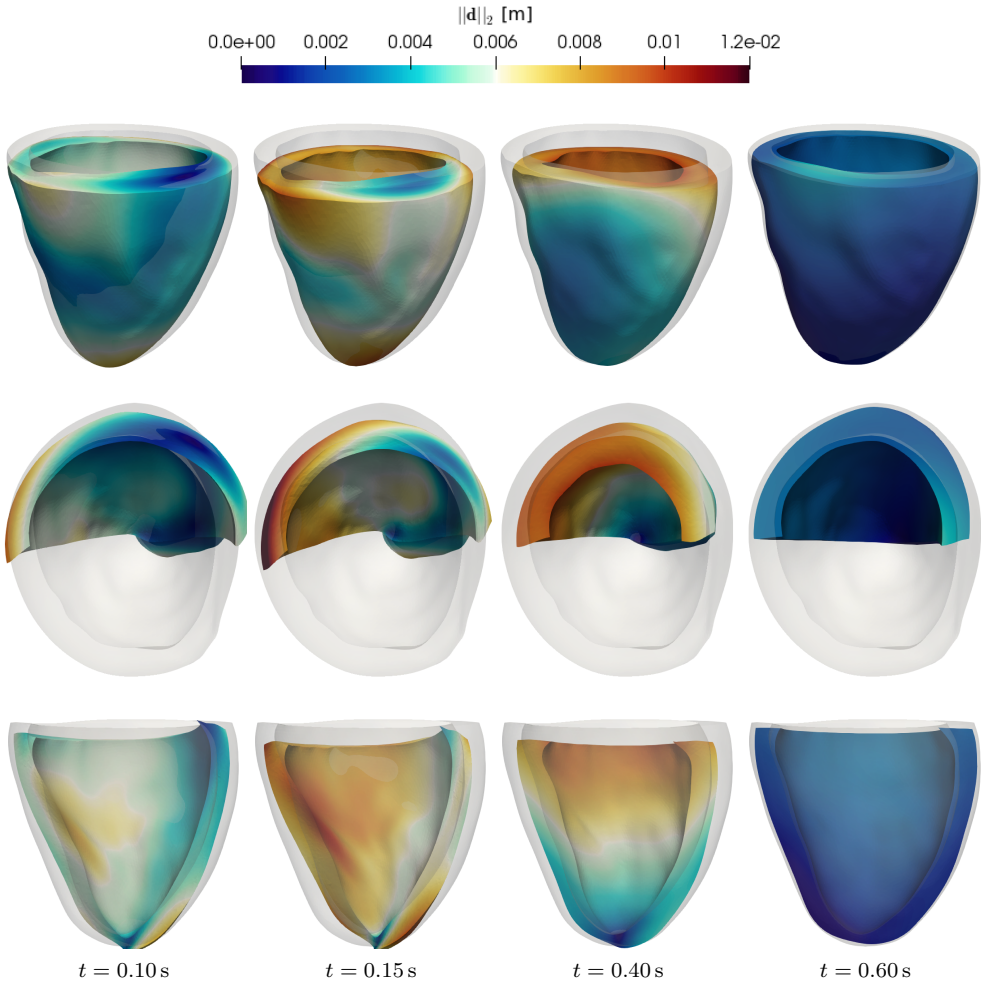

Figure 8.18: Test Case 3 (MF-ODE model): deformed geometry and magnitude of displacement at different times. Top row: full geometry. Middle row: half domain (top view). Bottom row: half domain (frontal view).

Indicator	HF-EM	ANN-EM	Relative error
Test Case 2 (idealized LV, 1827 dof)			
Stroke volume (mL)	76.24	75.56	$8.93 \cdot 10^{-3}$
Ejection fraction (%)	56.13	55.63	$8.93 \cdot 10^{-3}$
Systolic pressure (mmHg)	104.19	103.38	$7.81 \cdot 10^{-3}$
Work (mJ)	882	869	$1.49 \cdot 10^{-2}$
Test Case 3 (patient-specific LV, 65476 dof)			
Stroke volume (mL)	58.53	58.13	$6.92 \cdot 10^{-3}$
Ejection fraction (%)	47.00	46.68	$6.92 \cdot 10^{-3}$
Systolic pressure (mmHg)	87.18	85.93	$1.44 \cdot 10^{-2}$
Work (mJ)	582	568	$2.31 \cdot 10^{-2}$

Table 8.4: Test Cases 2 and 3 (MF-ODE model): main cardiac indicators. Comparison between the HF-EM and the ANN-EM frameworks and corresponding relative errors.

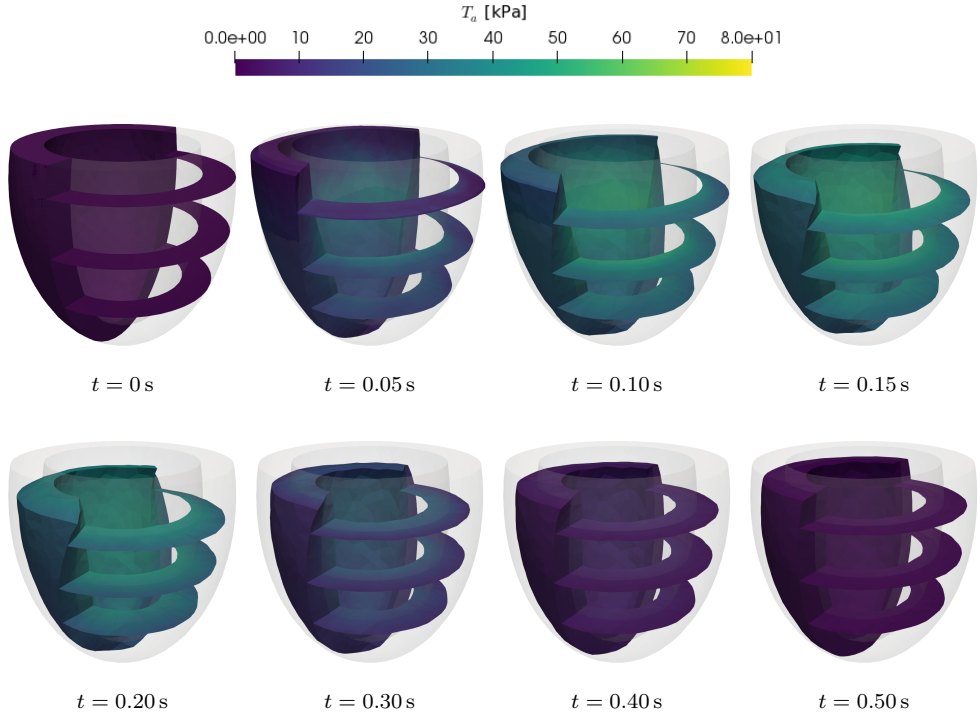

Figure 8.19: Test Case 2 (SE-ODE model): active tension at different times.

Indicator	HF-EM	ANN-EM	Relative error
Test Case 2 (idealized LV, 1827 dof)			
Stroke volume (mL)	73.89	73.79	$1.38 \cdot 10^{-3}$
Ejection fraction (%)	54.40	54.32	$1.38 \cdot 10^{-3}$
Systolic pressure (mmHg)	105.32	105.65	$3.07 \cdot 10^{-3}$
Work (mJ)	857	855	$2.46 \cdot 10^{-3}$

Table 8.5: Test Case 2 (SE-ODE model): main cardiac indicators. Comparison between the HF-EM and the ANN-EM frameworks and corresponding relative errors.

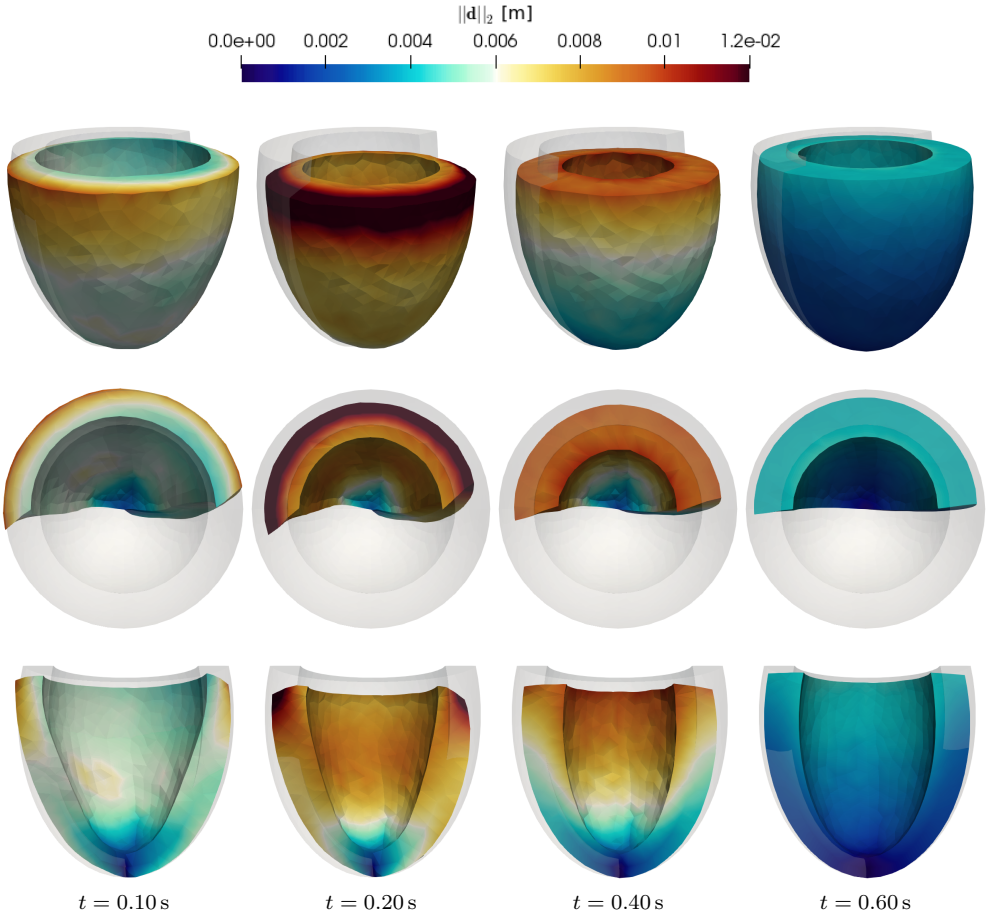

Figure 8.20: Test Case 2 (SE-ODE model): deformed geometry and magnitude of displacement at different times. Top row: full geometry. Middle row: half domain (top view). Bottom row: half domain (frontal view).

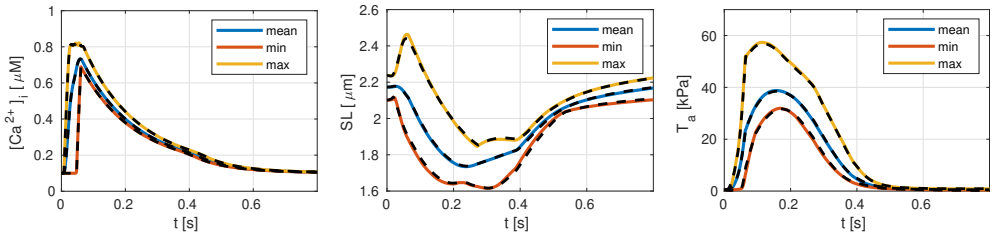

(a) Calcium concentration (b) Sarcomere length (c) Active tension

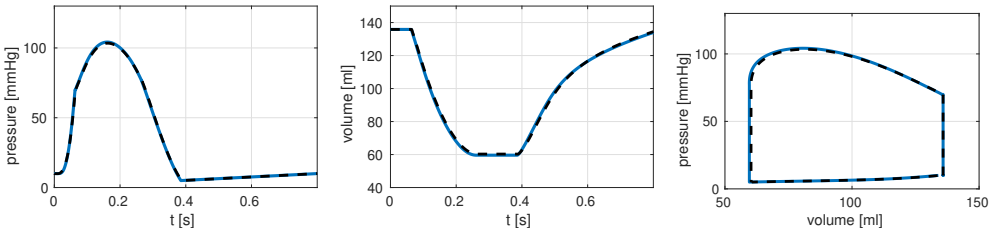

(d) Endocardial pressure (e) LV volume (f) Pressure-volume loop

Figure 8.21: Test Case 2 (MF-ODE model): comparison of the time evolution of quantities of interest and of the pressure-volume loop obtained with the simulations performed with HF-EM (solid colored lines) and with ANN-EM (black dashed lines). In (a)-(b)-(c) the three lines refer to the minimum, maximum and mean value over the computational domain.

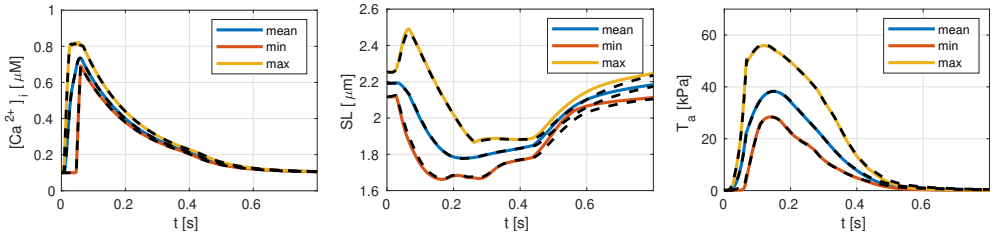

(a) Calcium concentration (b) Sarcomere length (c) Active tension

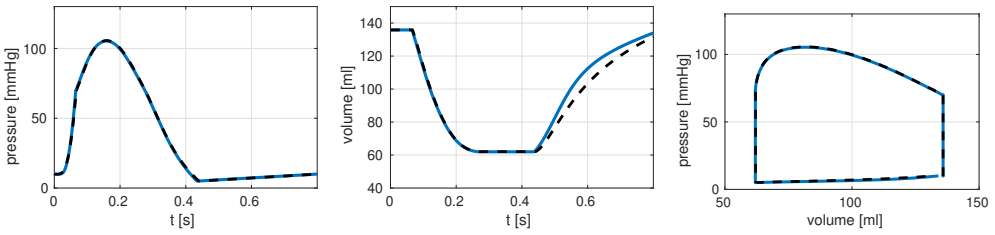

(d) Endocardial pressure (e) LV volume (f) Pressure-volume loop

Figure 8.22: Test Case 2 (SE-ODE model): comparison of the time evolution of quantities of interest and of the pressure-volume loop obtained with the simulations performed with HF-EM (solid colored lines) and with ANN-EM (black dashed lines). In (a)-(b)-(c) the three lines refer to the minimum, maximum and mean value over the computational domain.

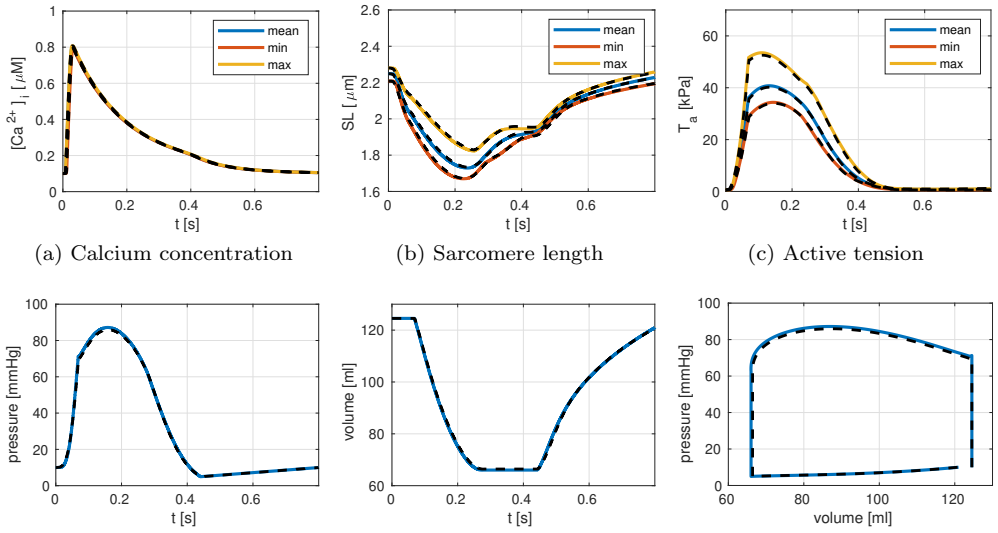

(a) Calcium concentration (b) Sarcomere length (c) Active tension

(d) Endocardial pressure (e) LV volume (f) Pressure-volume loop

Figure 8.23: Test Case 3 (MF-ODE model): comparison of the time evolution of quantities of interest and of the pressure-volume loop obtained with the simulations performed with HF-EM (solid colored lines) and with ANN-EM (black dashed lines). In (a)-(b)-(c) the three lines refer to the minimum, maximum and mean value over the computational domain.

Conclusions

In this thesis, we developed a multiscale mathematical and numerical model for cardiac EM, wherein the microscale phenomenon of active force generation is described by newly developed subcellular models. These latter models are based on a biophysically detailed description of the regulatory and contractile proteins composing the sarcomeres and of their interactions. Thanks to the introduction of physically motivated assumptions on the joint probability distribution of the stochastic variables describing the states of the different proteins, we derived some models describing the complex interactions among the above mentioned proteins with a drastically reduced number of equations, if compared to the full-order FKE (forward Kolmogorov equation). In this manner, the phenomenon of force generation can be simulated by means of systems of ODEs, thus overcoming the computational inefficiency of the MC method, typically employed to approximate the solution of the biophysically detailed force generation models available in literature [Was+13; Was+15; HTR06].

Moreover, we have reduced the computational cost associated with the numerical approximation of the solution of the biophysically detailed force generation models by means of a newly developed MOR technique based on Machine Learning. Within a gray-box (or semi-physical) approach, an ANN learns the dynamics of the HF model from a collection of input-output pairs, generated by the HF model itself, combined with some a priori knowledge, enforced during the learning process. In such a way we derived ROMs with just two or three state variables, capable of reproducing the results of the our proposed HF models of force generation with a relative error of about 10^{-2}.

We thus proposed a novel strategy to reduce the computational burden of cardiac multiscale EM simulations, wherein the intrinsically complex subcellular mechanisms leading to the activation of the muscular tissue make it difficult to trade off the detail of description of activation models (and thus their reliability) with computational efficiency. Specifically, we replace the biophysically detailed HF models of force generation with ANN-based ROMs derived by means of our proposed MOR technique. This operation, because of the scale separation between the organ and the myofilaments, can be performed offline, without any dependence on the three-dimensional setting where we later embed the ROM. Remarkably, thanks to the stabilizing effect of the SL feedback on the activation dynamics, the relative error introduced by employing the ANN-based ROMs in the context of EM is just of about 10^{-3}. We conclude that, in virtue of the offline ANN learning of the complex force generation models, a very favorable balance between modeling accuracy and computational efficiency is achieved,

without any compromise with the detail of description of the microscopic phenomena pertaining the generation of force.

Besides the above mentioned achievements, in this thesis we obtained the following results. In Chap. 2 we proposed a general strategy to describe the dynamics of spatially-explicit mathematical models for the calcium-driven activation of the thin filament with a reduced number of equations. This strategy, based on a conditionally independence assumption that allows to neglect second-order interaction among the proteins, allows to derive equations with a number of variables that is linear in the number of RUs, instead of exponential, as in the FKE.

In Chap. 4 we showed that also a CTMC (continuous-time Markov Chain) model for the full-sarcomere dynamics can be described with a reduced number of equations, if compared to the associated FKE. Such achievement is obtained by undertaking assumptions of conditional independence (similar to the one mentioned above) and by switching from the traditional MF-centered description of XBs [Hux57a; HS71; Smi+08; CMC19] to an AF-centered one. The latter choice allows to decouple the description of the two filaments, without the introduction of new approximations. We then proposed a pipeline to calibrate our SE-ODE and MF-ODE models starting from values coming from experimental measurements available in literature, based on the partial decoupling among the model parameters involved by the different experimental settings. In this manner, we calibrated the two above mentioned models for room-temperature rat and body-temperature human intact cardiomyocytes.

By analyzing the results and the properties of the SE-ODE model, we proposed a possible explanation for the LDA phenomenon, by which a decrease of SL induces a decrease in the apparent calcium sensitivity. Such phenomenon, for which a commonly agreed explanation is still missing [TK16; AM+16; NCC19], is indeed correctly reproduced by our SE-ODE model, without the need of phenomenologically tune the calcium sensitivity as a function of SL, as in most of the existing models [NHS06; Was+12; Was+13; Was+15]. Our proposed microscopic basis for LDA is linked to the low probability of being in the $\mathcal{P}$ state of the RUs located at the end-points of the single-overlap zone. Such bias towards the $\mathcal{N}$ state is propagated towards the center of the AF by the cooperative nearest-neighbor interactions so that, when the muscle shortens, it is enhanced by the reduced extension of the single-overlap zone, thus reducing the apparent sensitivity to calcium.

In Chaps. 7 and 8 we proposed a multiscale EM formulation, by linking in a theoretically sound manner the microscopic scale, where the force generation phenomenon takes place, with the macroscopic scale, associated to the organ deformation. In this regard, we analyzed the effect of the stochastic fluctuations characterizing the dynamics of the proteins involved in the force generation machinery. We justified, through the construction of a mesoscale model, the fact that, when the stochastic microscopic models of force generation are coupled with macroscopic models of tissue mechanics, the random variables associated with the former class of models can be identified with their expected value. This is related to the fact that, thanks to the parallel-series arrangement of myofilaments inside sarcomeres, all the filaments belonging to the same region of space feature homogeneous elongations. Indeed, despite nonhomogeneous deformations are possible when the sarcomeres are over-elongated (so that their length belongs to the descending limb of the force-length relationship), thanks to the presence of stiff parallel elastic components this situation cannot occur when sarcomeres are embedded in the cardiac tissue. Then, we showed that the active Piola stress tensor is compliant with the basic theoretical requirements for its physical meaningfulness, including the frame-indifference principle and the order-preserving property between

strain and stress [Ant95; Ogd97].

Finally, we proposed, in Chap. 8, a stabilized numerical scheme aimed at avoiding spurious oscillations related to the feedback of the tissue shortening velocity on the force generation model in cardiac EM.

Future developments

Several perspectives arise from the work carried out in this thesis.

- The models proposed in this thesis are developed under the hypothesis that ATP is always available when needed by the myosin motors. Despite under physiological conditions such hypothesis is legitimate [TD08], this is not the case when pathological events such as ischemia occur. Hence, the sarcomere models proposed in this thesis can be extended with the inclusion of the role of metabolite concentrations and of their consumption rates (see e.g. [Was+15]) and successively coupled with models of cardiac perfusion [Cha+10; DG+19] and metabolism [MD17].

- The applicability of the black-box MOR strategy proposed in Chap. 5 and its gray-box extension proposed in Chap. 6 overlooks the specific application to cardiac force generation models. Indeed, they can be generally applied to HF models written as ODE or PDE systems (we showed some examples in Chap. 5). Hence, we plan to further develop the proposed MOR strategies, in particular by investigating other manners (besides the two considered in Chap. 6) of informing the learning machine about a priori knowledge from the HF model.

- In each of the test cases for which we applied the proposed MOR technique (such as the ones shown in Chap. 5), we numerically observed a very fast convergence (specifically, exponential convergence) of the approximation error with respect to the number of reduced states. Noticeably, the type of convergence is also shown in the case of hyperbolic PDEs (see Sec. 5.4.4), one of the most complicated class of problems to be reduced by means of the traditional projection-based methods [QMN15]. The development of a theoretical framework in which to derive estimates for the approximation error of the proposed MOR techniques would provide a fruitful insight into the functioning of the method itself, perhaps helping to better its performances.

- Due to its non-intrusive nature, the black-box MOR method of Chap. 5 only needs a collection of input-output pairs, from which it infers a mathematical model written as an ODE system. Therefore, besides for *model reduction* purposes, it can be employed for *model learning* purposes. Indeed, the always increasing availability of data and computational resources could bring to a paradigm shift in the Big Data era by which mathematical models are automatically learned from experimental measurements of the phenomenon to be modeled [BL07; SL09; Sch+11].

- We envision a possible application of the proposed framework (applied in this thesis to reduce the computational burden associated to the usage of biophysically detailed force generation models in EM simulations) to ionic models, whose intrinsic complexity leaves room for offline MOR.

Appendix A

Conservation of probability and self-consistency in RU models

In this appendix we report the proof of Prop. 2.4 and of some preliminary results instrumental for its derivation, including Props. 2.1, 2.2 and 2.3. First, we provide the proofs of Props. 2.1 and 2.2.

Proof of Prop. 2.1. We have:

$$\begin{aligned}
&\sum_{\alpha\in\mathcal{S}}\sum_{\eta\in\mathcal{S}\setminus\{\alpha\}}\left[\Phi_L^i(\eta,\beta,\delta;\alpha;t)-\Phi_L^i(\alpha,\beta,\delta;\eta;t)\right]=0,\\
&\sum_{\beta\in\mathcal{S}}\sum_{\eta\in\mathcal{S}\setminus\{\beta\}}\left[\Phi_C^i(\alpha,\eta,\delta;\beta;t)-\Phi_C^i(\alpha,\beta,\delta;\eta;t)\right]=0,\\
&\sum_{\delta\in\mathcal{S}}\sum_{\eta\in\mathcal{S}\setminus\{\delta\}}\left[\Phi_R^i(\alpha,\beta,\eta;\delta;t)-\Phi_R^i(\alpha,\beta,\delta;\eta;t)\right]=0.
\end{aligned}\tag{A.1}$$

Therefore, for any $\mathbf{z}\in\mathbb{R}^N$, $\mathbf{U}\mathbf{\Phi}(\mathbf{z},t)=\mathbf{0}$.

Moreover, whenever the state $\mathbf{z}(t)$ satisfies condition (c), we have, for $\alpha,\beta\in\mathcal{S}$ and for $i=3,\dots,N_M-1$:

$$\begin{aligned}
&\sum_{\delta\in\mathcal{S}}\sum_{\eta\in\mathcal{S}\setminus\{\alpha\}}\left[\Phi_L^i(\eta,\beta,\delta;\alpha;t)-\Phi_L^i(\alpha,\beta,\delta;\eta;t)\right]\\
&=\sum_{\delta\in\mathcal{S}}\sum_{\eta\in\mathcal{S}\setminus\{\alpha\}}\left[\frac{\sum_{\xi\in\mathcal{S}}k_{i-1}^{\eta\alpha|\xi\beta}\mathbb{P}((\xi,\overset{i-1}{\eta},\beta)^t)\mathbb{P}((\eta,\overset{i}{\beta},\delta)^t)}{\sum_{\xi\in\mathcal{S}}\mathbb{P}((\xi,\overset{i-1}{\eta},\beta)^t)}-\frac{\sum_{\xi\in\mathcal{S}}k_{i-1}^{\alpha\eta|\xi\beta}\mathbb{P}((\xi,\overset{i-1}{\alpha},\beta)^t)\mathbb{P}((\alpha,\overset{i}{\beta},\delta)^t)}{\sum_{\xi\in\mathcal{S}}\mathbb{P}((\xi,\overset{i-1}{\alpha},\beta)^t)}\right]\\
&=\sum_{\eta\in\mathcal{S}\setminus\{\alpha\}}\left[\sum_{\xi\in\mathcal{S}}\Phi_C^{i-1}(\xi,\eta,\beta;\alpha;t)\underbrace{\frac{\sum_{\delta\in\mathcal{S}}\mathbb{P}((\eta,\overset{i}{\beta},\delta)^t)}{\sum_{\xi\in\mathcal{S}}\mathbb{P}((\xi,\overset{i-1}{\eta},\beta)^t)}}_{=1}-\sum_{\xi\in\mathcal{S}}\Phi_C^{i-1}(\xi,\alpha,\beta;\eta;t)\underbrace{\frac{\sum_{\delta\in\mathcal{S}}\mathbb{P}((\alpha,\overset{i}{\beta},\delta)^t)}{\sum_{\xi\in\mathcal{S}}\mathbb{P}((\xi,\overset{i-1}{\alpha},\beta)^t)}}_{=1}\right]\\
&=\sum_{\eta\in\mathcal{S}\setminus\{\alpha\}}\sum_{\xi\in\mathcal{S}}\left[\Phi_C^{i-1}(\xi,\eta,\beta;\alpha;t)-\Phi_C^{i-1}(\xi,\alpha,\beta;\eta;t)\right].
\end{aligned}\tag{A.2}$$

Similarly, we have for $i = 2, \ldots, N_M - 2$:

$$\begin{aligned}&\sum_{\alpha\in\mathcal{S}}\sum_{\eta\in\mathcal{S}\setminus\{\delta\}}\left[\Phi_R^i(\alpha,\beta,\eta;\delta;t) - \Phi_R^i(\alpha,\beta,\delta;\eta;t)\right]\\ &= \sum_{\eta\in\mathcal{S}\setminus\{\delta\}}\sum_{\xi\in\mathcal{S}}\left[\Phi_C^{i+1}(\beta,\eta,\xi;\delta;t) - \Phi_C^{i+1}(\beta,\delta,\xi;\eta;t)\right].\end{aligned} \tag{A.3}$$

Thus, under the hypothesis that the state $\mathbf{z}(t)$ satisfies condition (c), the computation of the time derivative of both sides of (a) leads to the same result, i.e.:

$$\frac{d}{dt}\sum_{\xi,\beta\in\mathcal{S}}\mathbb{P}((\xi,\overset{i-1}{\alpha},\beta)^t) = \sum_{\eta\in\mathcal{S}\setminus\{\alpha\}}\sum_{\xi,\beta\in\mathcal{S}}\left[\Phi_C^{i-1}(\xi,\eta,\beta;\alpha;t) - \Phi_C^{i-1}(\xi,\alpha,\beta;\eta;t)\right],$$

$$\begin{aligned}\frac{d}{dt}\sum_{\beta,\delta\in\mathcal{S}}\mathbb{P}((\alpha,\overset{i}{\beta},\delta)^t) &= \sum_{\eta\in\mathcal{S}\setminus\{\alpha\}}\sum_{\beta,\delta\in\mathcal{S}}\left[\Phi_L^i(\eta,\beta,\delta;\alpha;t) - \Phi_L^i(\alpha,\beta,\delta;\eta;t)\right]\\ &= \sum_{\eta\in\mathcal{S}\setminus\{\alpha\}}\sum_{\xi,\beta\in\mathcal{S}}\left[\Phi_C^{i-1}(\xi,\eta,\beta;\alpha;t) - \Phi_C^{i-1}(\xi,\alpha,\beta;\eta;t)\right].\end{aligned}$$

By using the same argument, a similar result can be shown for (b). Finally, if condition (c) hold for $\mathbf{z}(t)$, the time derivatives of both sides of (c) coincide. Indeed,

$$\begin{aligned}\frac{d}{dt}\sum_{\delta\in\mathcal{S}}\mathbb{P}((\alpha,\overset{i}{\beta},\delta)^t) &= \sum_{\eta\in\mathcal{S}\setminus\{\alpha\}}\sum_{\delta\in\mathcal{S}}\left[\Phi_L^i(\eta,\beta,\delta;\alpha;t) - \Phi_L^i(\alpha,\beta,\delta;\eta;t)\right]\\ &+ \sum_{\eta\in\mathcal{S}\setminus\{\beta\}}\sum_{\delta\in\mathcal{S}}\left[\Phi_C^i(\alpha,\eta,\delta;\beta;t) - \Phi_C^i(\alpha,\beta,\delta;\eta;t)\right]\\ &= \sum_{\eta\in\mathcal{S}\setminus\{\alpha\}}\sum_{\xi\in\mathcal{S}}\left[\Phi_C^{i-1}(\xi,\eta,\beta;\alpha;t) - \Phi_C^{i-1}(\xi,\alpha,\beta;\eta;t)\right]\\ &+ \sum_{\eta\in\mathcal{S}\setminus\{\beta\}}\sum_{\delta\in\mathcal{S}}\left[\Phi_C^i(\alpha,\eta,\delta;\beta;t) - \Phi_C^i(\alpha,\beta,\delta;\eta;t)\right],\end{aligned}$$

$$\begin{aligned}\frac{d}{dt}\sum_{\xi\in\mathcal{S}}\mathbb{P}((\xi,\overset{i-1}{\alpha},\beta)^t) &= \sum_{\eta\in\mathcal{S}\setminus\{\alpha\}}\sum_{\xi\in\mathcal{S}}\left[\Phi_C^{i-1}(\xi,\eta,\beta;\alpha;t) - \Phi_C^{i-1}(\xi,\alpha,\beta;\eta;t)\right]\\ &+ \sum_{\eta\in\mathcal{S}\setminus\{\beta\}}\sum_{\xi\in\mathcal{S}}\left[\Phi_R^{i-1}(\xi,\eta,\alpha;\beta;t) - \Phi_R^{i-1}(\xi,\alpha,\beta;\eta;t)\right]\\ &= \sum_{\eta\in\mathcal{S}\setminus\{\alpha\}}\sum_{\xi\in\mathcal{S}}\left[\Phi_C^{i-1}(\xi,\eta,\beta;\alpha;t) - \Phi_C^{i-1}(\xi,\alpha,\beta;\eta;t)\right]\\ &+ \sum_{\eta\in\mathcal{S}\setminus\{\beta\}}\sum_{\delta\in\mathcal{S}}\left[\Phi_C^i(\alpha,\eta,\delta;\beta;t) - \Phi_C^i(\alpha,\beta,\delta;\eta;t)\right].\end{aligned}$$

Thus, we conclude that $\mathbf{\Phi}(\mathbf{z},t) \in \mathrm{Ker}(\mathbf{W})$. □

Proof of Prop. 2.2. We notice that Eq. (A.1) holds also for $\widetilde{\Phi}_L$ and $\widetilde{\Phi}_R$. Hence, we have $\mathbf{U}\boldsymbol{\Phi}(\mathbf{z},t) = \mathbf{0}$ for any $\mathbf{z} \in \mathbb{R}^N$.

Moreover, when the right-hand side defined in Eq. (2.10) is considered, properties equivalent to Eqs. (A.3) and (A.2) holds true even without the assumptions that the state $\mathbf{z}(t)$ satisfies condition (c). Indeed, we have, for $\alpha, \beta \in \mathcal{S}$ and for $i = 3, \ldots, N_M - 1$:

$$
\begin{aligned}
&\sum_{\delta\in\mathcal{S}}\sum_{\eta\in\mathcal{S}\setminus\{\alpha\}}\left[\widetilde{\Phi}_L^i(\eta,\beta,\delta;\alpha;t) - \widetilde{\Phi}_L^i(\alpha,\beta,\delta;\eta;t)\right] \\
&= \sum_{\delta\in\mathcal{S}}\sum_{\eta\in\mathcal{S}\setminus\{\alpha\}}\left[\frac{\sum_{\xi\in\mathcal{S}} k_{i-1}^{\eta\alpha|\xi\beta}\mathbb{P}((\xi,\overset{i-1}{\eta},\beta)^t)\mathbb{P}((\eta,\overset{i}{\beta},\delta)^t)}{\sum_{\xi\in\mathcal{S}}\mathbb{P}((\eta,\overset{i}{\beta},\xi)^t)} - \frac{\sum_{\xi\in\mathcal{S}} k_{i-1}^{\alpha\eta|\xi\beta}\mathbb{P}((\xi,\overset{i-1}{\alpha},\beta)^t)\mathbb{P}((\alpha,\overset{i}{\beta},\delta)^t)}{\sum_{\xi\in\mathcal{S}}\mathbb{P}((\alpha,\overset{i}{\beta},\xi)^t)}\right] \\
&= \sum_{\eta\in\mathcal{S}\setminus\{\alpha\}}\left[\sum_{\xi\in\mathcal{S}}\Phi_C^{i-1}(\xi,\eta,\beta;\alpha;t)\underbrace{\frac{\sum_{\delta\in\mathcal{S}}\mathbb{P}((\eta,\overset{i}{\beta},\delta)^t)}{\sum_{\xi\in\mathcal{S}}\mathbb{P}((\eta,\overset{i}{\beta},\xi)^t)}}_{=1} - \sum_{\xi\in\mathcal{S}}\Phi_C^{i-1}(\xi,\alpha,\beta;\eta;t)\underbrace{\frac{\sum_{\delta\in\mathcal{S}}\mathbb{P}((\alpha,\overset{i}{\beta},\delta)^t)}{\sum_{\xi\in\mathcal{S}}\mathbb{P}((\alpha,\overset{i}{\beta},\xi)^t)}}_{=1}\right] \\
&= \sum_{\eta\in\mathcal{S}\setminus\{\alpha\}}\sum_{\xi\in\mathcal{S}}\left[\Phi_C^{i-1}(\xi,\eta,\beta;\alpha;t) - \Phi_C^{i-1}(\xi,\alpha,\beta;\eta;t)\right].
\end{aligned}
\tag{A.4}
$$

Similarly, we have for $i = 2, \ldots, N_M - 2$:

$$
\begin{aligned}
&\sum_{\alpha\in\mathcal{S}}\sum_{\eta\in\mathcal{S}\setminus\{\delta\}}\left[\widetilde{\Phi}_R^i(\alpha,\beta,\eta;\delta;t) - \widetilde{\Phi}_R^i(\alpha,\beta,\delta;\eta;t)\right] \\
&= \sum_{\eta\in\mathcal{S}\setminus\{\delta\}}\sum_{\xi\in\mathcal{S}}\left[\Phi_C^{i+1}(\beta,\eta,\xi;\delta;t) - \Phi_C^{i+1}(\beta,\delta,\xi;\eta;t)\right].
\end{aligned}
$$

Hence, by proceeding as in the proof of Prop. 2.1, we get the thesis. □

In the following we report the proof of Prop. 2.3.

Proof of Prop. 2.3. First, we notice that the transition rates are bounded in $[0,T]$, being continuous functions of the bounded variables $[\mathrm{Ca}^{2+}]_{\mathrm{i}}(t)$ and $SL(t)$. That is, there exists some constant $K > 0$ such that we have:

$$
k_i^{\beta\eta|\alpha\delta} \le K \qquad \forall\, \alpha,\beta,\delta,\eta \in \mathcal{S}, \quad \forall\, i = 1, \ldots, N_M. \tag{A.5}
$$

Since the functions $\boldsymbol{\Phi}$ are differentiable with respect to their arguments, to prove that they are Lipschitz continuous it is enough to show that their first partial derivatives with respect to each of their arguments are bounded. Moreover, as Eqs. (2.10) and (2.13) are written as the sum of many terms, we just need to consider the nonlinear ones (the coefficients multiplying the linear terms are indeed bounded, thanks to Eq. (A.5)).

In the following, we consider the terms $\Phi_L^i(\alpha,\beta,\delta;\eta;t)$ and $\widetilde{\Phi}_L^i(\alpha,\beta,\delta;\eta;t)$ for $i = 3, \ldots, N_M - 1$, since the other nonlinear terms can be treated in a similar manner. Concerning the term Φ_L, whose definition we recall here for the reader's convenience:

$$
\Phi_L^i(\alpha,\beta,\delta;\eta;t) = \frac{\sum_{\xi\in\mathcal{S}} k_{i-1}^{\alpha\eta|\xi\beta}\mathbb{P}((\xi,\overset{i-1}{\alpha},\beta)^t)\,\mathbb{P}((\alpha,\overset{i}{\beta},\delta)^t)}{\sum_{\xi\in\mathcal{S}}\mathbb{P}((\xi,\overset{i-1}{\alpha},\beta)^t)},
$$

we have, thanks to the fact that the terms $\mathbb{P}((\xi, \overset{i-1}{\alpha}, \beta)^t)$ are nonnegative:

$$\left| \frac{\partial \Phi_L^i(\alpha,\beta,\delta;\eta;t)}{\partial \mathbb{P}((\alpha,\overset{i}{\beta},\delta)^t)} \right| = \left| \frac{\sum_{\xi\in\mathcal{S}} k_{i-1}^{\alpha\eta|\xi\beta} \mathbb{P}((\xi,\overset{i-1}{\alpha},\beta)^t)}{\sum_{\xi\in\mathcal{S}} \mathbb{P}((\xi,\overset{i-1}{\alpha},\beta)^t)} \right| \leq \max_{\psi\in\mathcal{S}} k_{i-1}^{\alpha\eta|\psi\beta} \leq K.$$

Moreover, we have, for $\varphi \in \mathcal{S}$:

$$\frac{\partial \Phi_L^i(\alpha,\beta,\delta;\eta;t)}{\partial \mathbb{P}((\varphi,\overset{i-1}{\alpha},\beta)^t)} = \frac{\sum_{\xi\in\mathcal{S}} \left[k_{i-1}^{\alpha\eta|\varphi\beta} - k_{i-1}^{\alpha\eta|\xi\beta} \right] \mathbb{P}((\xi,\overset{i-1}{\alpha},\beta)^t)}{\left[\sum_{\xi\in\mathcal{S}} \mathbb{P}((\xi,\overset{i-1}{\alpha},\beta)^t)\right]^2} \mathbb{P}((\alpha,\overset{i}{\beta},\delta)^t).$$

Since $\mathbf{z} \in \mathrm{Ker}(\mathbf{W})$, by condition (c) we have:

$$\mathbb{P}((\alpha,\overset{i}{\beta},\delta)^t) \leq \sum_{\xi\in\mathcal{S}} \mathbb{P}((\alpha,\overset{i}{\beta},\xi)^t) = \sum_{\xi\in\mathcal{S}} \mathbb{P}((\xi,\overset{i-1}{\alpha},\beta)^t).$$

Hence:

$$\begin{aligned} \left| \frac{\partial \Phi_L^i(\alpha,\beta,\delta;\eta;t)}{\partial \mathbb{P}((\varphi,\overset{i-1}{\alpha},\beta)^t)} \right| &\leq \frac{\sum_{\xi\in\mathcal{S}} \left| k_{i-1}^{\alpha\eta|\varphi\beta} - k_{i-1}^{\alpha\eta|\xi\beta} \right| \mathbb{P}((\xi,\overset{i-1}{\alpha},\beta)^t)}{\sum_{\xi\in\mathcal{S}} \mathbb{P}((\xi,\overset{i-1}{\alpha},\beta)^t)} \\ &\leq \max_{\psi\in\mathcal{S}} \left| k_{i-1}^{\alpha\eta|\varphi\beta} - k_{i-1}^{\alpha\eta|\xi\beta} \right| \leq 2\,K. \end{aligned}$$

Therefore, on the set $\mathbf{z} \in \mathrm{Ker}(\mathbf{W})$, the right-hand side defined in Eqs. (2.10) has bounded first partial derivative with respect to all of its arguments and thus it is Lipschitz continuous $\mathbf{z}$, uniformly in t.

Concerning the right-hand side of Eqs. (2.13), defined as:

$$\widetilde{\Phi}_L^i(\alpha,\beta,\delta;\eta;t) = \frac{\sum_{\xi\in\mathcal{S}} k_{i-1}^{\alpha\eta|\xi\beta} \mathbb{P}((\xi,\overset{i-1}{\alpha},\beta)^t)\, \mathbb{P}((\alpha,\overset{i}{\beta},\delta)^t)}{\sum_{\xi\in\mathcal{S}} \mathbb{P}((\alpha,\overset{i}{\beta},\xi)^t)},$$

we have, for any $\varphi \in \mathcal{S}$:

$$\left| \frac{\partial \widetilde{\Phi}_L^i(\alpha,\beta,\delta;\eta;t)}{\partial \mathbb{P}((\varphi,\overset{i-1}{\alpha},\beta)^t)} \right| = \left| \frac{k_{i-1}^{\alpha\eta|\varphi\beta} \mathbb{P}((\alpha,\overset{i}{\beta},\delta)^t)}{\sum_{\xi\in\mathcal{S}} \mathbb{P}((\alpha,\overset{i}{\beta},\xi)^t)} \right| \leq K.$$

Moreover, for $\varphi \in \mathcal{S} \setminus \{\delta\}$, we have:

$$\frac{\partial \widetilde{\Phi}_L^i(\alpha,\beta,\delta;\eta;t)}{\partial \mathbb{P}((\alpha,\overset{i}{\beta},\varphi)^t)} = -\frac{\sum_{\xi\in\mathcal{S}} k_{i-1}^{\alpha\eta|\xi\beta} \mathbb{P}((\xi,\overset{i-1}{\alpha},\beta)^t)\, \mathbb{P}((\alpha,\overset{i}{\beta},\delta)^t)}{\left[\sum_{\xi\in\mathcal{S}} \mathbb{P}((\alpha,\overset{i}{\beta},\xi)^t)\right]^2}.$$

Hence, since $\mathbb{P}((\alpha,\overset{i}{\beta},\delta)^t) \le \sum_{\xi\in\mathcal{S}} \mathbb{P}((\alpha,\overset{i}{\beta},\xi)^t)$, we have:

$$\begin{aligned}\left|\frac{\partial\,\widetilde{\Phi}^i_L(\alpha,\beta,\delta;\eta;t)}{\partial\,\mathbb{P}((\alpha,\overset{i}{\beta},\varphi)^t)}\right| &\le \frac{\sum_{\xi\in\mathcal{S}} k_{i-1}^{\alpha\eta|\xi\beta}\mathbb{P}((\xi,\overset{i-1}{\alpha},\beta)^t)}{\sum_{\xi\in\mathcal{S}}\mathbb{P}((\alpha,\overset{i}{\beta},\xi)^t)}\\ &\le \max_{\psi\in\mathcal{S}} k_{i-1}^{\alpha\eta|\psi\beta}\frac{\sum_{\xi\in\mathcal{S}}\mathbb{P}((\xi,\overset{i-1}{\alpha},\beta)^t)}{\sum_{\xi\in\mathcal{S}}\mathbb{P}((\alpha,\overset{i}{\beta},\xi)^t)}\\ &= \max_{\psi\in\mathcal{S}} k_{i-1}^{\alpha\eta|\psi\beta} \le K,\end{aligned}$$

where we have used by condition (c), since $\mathbf{z}\in\mathrm{Ker}(\mathbf{W})$. Finally, we have:

$$\begin{aligned}\frac{\partial\,\widetilde{\Phi}^i_L(\alpha,\beta,\delta;\eta;t)}{\partial\,\mathbb{P}((\alpha,\overset{i}{\beta},\delta)^t} &= \frac{\sum_{\xi\in\mathcal{S}} k_{i-1}^{\alpha\eta|\xi\beta}\mathbb{P}((\xi,\overset{i-1}{\alpha},\beta)^t)\,\sum_{\xi\in\mathcal{S}\setminus\{\delta\}}\mathbb{P}((\alpha,\overset{i}{\beta},\xi)^t)}{\left[\sum_{\xi\in\mathcal{S}}\mathbb{P}((\alpha,\overset{i}{\beta},\xi)^t)\right]^2}\\ &\le \frac{\sum_{\xi\in\mathcal{S}} k_{i-1}^{\alpha\eta|\xi\beta}\mathbb{P}((\xi,\overset{i-1}{\alpha},\beta)^t)}{\sum_{\xi\in\mathcal{S}}\mathbb{P}((\alpha,\overset{i}{\beta},\xi)^t)}\\ &\le \max_{\psi\in\mathcal{S}} k_{i-1}^{\alpha\eta|\psi\beta}\frac{\sum_{\xi\in\mathcal{S}}\mathbb{P}((\xi,\overset{i-1}{\alpha},\beta)^t)}{\sum_{\xi\in\mathcal{S}}\mathbb{P}((\alpha,\overset{i}{\beta},\xi)^t)}\\ &= \max_{\psi\in\mathcal{S}} k_{i-1}^{\alpha\eta|\psi\beta} \le K,\end{aligned}$$

where we have used again condition (c). □

In order to prove Prop. 2.4, we show the following lemma.

Lemma A.1. *Let us consider the closed convex set $\Sigma\subset\mathbb{R}^N$, defined as:*

$$\Sigma := \left\{\mathbf{x}\in\mathbb{R}^N\colon \mathbf{a}_j\cdot\mathbf{x}\le b_j,\ \text{for } j=1,\dots,q\right\} \tag{A.6}$$

where $\mathbf{a}_j\in\mathbb{R}^N$ and $b_j\in\mathbb{R}$ for $j=1,\dots,q$. Let us then consider a function $\mathbf{\Phi}\colon\mathbb{R}^N\times[0,T]\to\mathbb{R}^N$, satisfying, for some constant $L>0$:

$$|\mathbf{\Phi}(\mathbf{x}_1,t)-\mathbf{\Phi}(\mathbf{x}_2,t)|\le L\,|\mathbf{x}_1-\mathbf{x}_2| \qquad \forall\,\mathbf{x}_1,\mathbf{x}_2\in\Sigma,\quad t\in[0,T]. \tag{A.7}$$

Let us the suppose that, for $j=1,\dots,q$ and for any $\mathbf{x}\in\Sigma$ and $t\in[0,T]$:

$$\mathbf{a}_j\cdot\mathbf{x}=b_j \quad\Longrightarrow\quad \mathbf{\Phi}(\mathbf{x},t)\cdot\mathbf{a}_j\le 0. \tag{A.8}$$

Let us consider the following ODE system:

$$\begin{cases}\dot{\mathbf{x}}(t)=\mathbf{\Phi}(\mathbf{x}(t),t) & t\in[0,T],\\ \mathbf{x}(0)=\mathbf{x}_0.\end{cases} \tag{A.9}$$

such that $\mathbf{x}_0\in\Sigma$. Then, there exists a unique solution of Eq. (A.9) *such that $\mathbf{x}(t)\in\Sigma$ for any $t\in[0,T]$.*

Proof. Let us consider the following ODE system:

$$\begin{cases} \dot{\mathbf{x}}(t) = \boldsymbol{\Phi}(\Pi_\Sigma(\mathbf{x}(t)), t) & t \in [0,T], \\ \mathbf{x}(0) = \mathbf{x}_0, \end{cases} \tag{A.10}$$

where we denote by $\Pi_\Sigma : \mathbb{R}^N \to \Sigma$ the projection operator onto the convex set Σ. By the Picard-Lindelöf theorem [Tes12], since the function $\boldsymbol{\Phi} \circ \Pi_\Sigma$ is globally Lipschitz continuous in its first argument, uniformly w.r.t. the second, in the domain $\mathbb{R}^N \times [0,T]$ (being the composition of Lipschitz continuous functions), there exists a unique function $\widehat{\mathbf{x}}\colon [0,T] \to \mathbb{R}^N$ solution of Eq. (A.10).

Let us suppose, by contradiction, that for some $t \in [0,T]$ we have $\widehat{\mathbf{x}}(t) \notin \Sigma$. Due to the continuity of $\widehat{\mathbf{x}}$, it follows that there exist two time instants $0 \le t_1 < t_2 \le T$ and an index $j \in \{1,\dots,q\}$ such that the quantity $z_j(t) := \mathbf{a}_j \cdot \widehat{\mathbf{x}}(t)$ satisfies:

$$z_j(t_1) = b_j, \qquad z_j(t) > b_j \text{ for } t \in (t_1, t_2].$$

By the mean value theorem [JJS99], there exists a time instant $t^* \in (t_1,t_2)$ such that:

$$\dot{z}_j(t^*) = \frac{z_j(t_2) - z_j(t_1)}{t_2 - t_1} > 0. \tag{A.11}$$

However, since for $t \in (t_1,t_2]$ we have $\mathbf{a}_j \cdot \widehat{\mathbf{x}}(t) = z_j(t) > b_j$, the projection $\Pi_\Sigma(\mathbf{x}(t))$ satisfies $\mathbf{a}_j \cdot \Pi_\Sigma(\widehat{\mathbf{x}}(t)) = b_j$ and then, by Eq. (A.8), we have:

$$\dot{z}_j(t) = \mathbf{a}_j \cdot \boldsymbol{\Phi}(\Pi_\Sigma(\widehat{\mathbf{x}}(t)), t) \le 0 \qquad \forall t \in (t_1,t_2],$$

that is in contradiction with Eq. (A.11). Hence, $\widehat{\mathbf{x}}(t) \in \Sigma$ for any $t \in [0,T]$.

In order to show the uniqueness of the solution, we suppose, by contradiction, the existence of another solution of Eq. (A.9) (that we denote by $\widetilde{\mathbf{x}}(t)$), such that $\widetilde{\mathbf{x}}(t) \in \Sigma$ for any $t \in [0,T]$. Then, $\widetilde{\mathbf{x}}(t)$ is also a solution of Eq. (A.10). By the uniqueness of solutions of Eq. (A.10), we get the thesis. □

Finally, we provide the proof of Prop. 2.4.

Proof of Prop. 2.4. This proof is based on Lemma A.1. Indeed, the set $\mathbf{z}_0 \in \mathrm{Ker}(\mathbf{W}) \cap [0,+\infty)^N$ can be written in the form of (A.6), where the vectors $\mathbf{a}_j$ are given by the collection of the unit vectors $-\mathbf{e}_j$, for $j = 1,\dots,N$, the rows of the matrix $\mathbf{W}$ and their negative and $b_j = 0$ for any $j = 1,\dots,r$.

The hypothesis of Eq. (A.7) is a direct consequence of Prop. 2.3. Moreover, Eq. (A.8) follows from Props. 2.1 and 2.2 and by the fact that, in case $\mathbf{e}_j \cdot \mathbf{z} = 0$, the negative terms in Eqs. (2.10) and (2.13) vanish and $\mathbf{e}_j \cdot \boldsymbol{\Phi}(\mathbf{z},t) \ge 0$.

Hence, in virtue of Lemma A.1, both Eqs. (2.10) and (2.13) admit a unique solution satisfying $\mathbf{z}(t) \in \mathrm{Ker}(\mathbf{W}) \cap [0,+\infty)^N$ for any $t \in [0,T]$. Since the right-hand sides of Eqs. (2.10) and (2.13) coincide on the set $\mathrm{Ker}(\mathbf{W})$, the two solutions coincide.

Moreover, we have, thanks to Props. 2.1 and 2.2:

$$\frac{d}{dt}(\mathbf{U}\mathbf{z}(t)) = \mathbf{U}\boldsymbol{\Phi}(\mathbf{z}(t),t) = \mathbf{0},$$

which entails $\mathbf{U}\mathbf{z}(t) = \mathbf{U}\mathbf{z}_0 = \mathbf{b}$ for any $t \in [0,T]$.

Finally, the positivity of the solution combined with $\mathbf{U}\mathbf{z}(t) = \mathbf{b}$ entails $\mathbf{e}_j \cdot \mathbf{z}(t) \le 1$ for any $j = 1,\dots,N$ and for any $t \in [0,T]$. □

Bibliography

[AGI16] A. C. Antoulas, I. V. Gosea, and A. C. Ionita. "Model reduction of bilinear systems in the Loewner framework". In: *SIAM Journal on Scientific Computing* 38.5 (2016), B889–B916.

[AJM74] D. Allen, B. Jewell, and J. Murray. "The contribution of activation processes to the length–tension relation of cardiac muscle". In: *Nature* 248.5449 (1974), p. 606.

[AK82] D. G. Allen and S. Kurihara. "The effects of muscle length on intracellular calcium transients in mammalian cardiac muscle." In: *The Journal of Physiology* 327.1 (1982), pp. 79–94.

[Ale+01] N. M. Alexandrov, R. M. Lewis, C. R. Gumbert, L. L. Green, and P. A. Newman. "Approximation and model management in aerodynamic optimization with variable-fidelity models". In: *Journal of Aircraft* 38.6 (2001), pp. 1093–1101.

[Aln+15] M. S. Alnæs, J. Blechta, J. Hake, A. Johansson, B. Kehlet, A. Logg, C. Richardson, J. Ring, M. E. Rognes, and G. N. Wells. "The FEniCS Project Version 1.5". In: *Archive of Numerical Software* 3.100 (2015).

[AM+16] Y. Ait-Mou, K. Hsu, G. P. Farman, M. Kumar, M. L. Greaser, T. C. Irving, and P. P. de Tombe. "Titin strain contributes to the Frank–Starling law of the heart by structural rearrangements of both thin- and thick-filament proteins". In: *Proceedings of the National Academy of Sciences* 113.8 (2016), pp. 2306–2311.

[Ant05] A. C. Antoulas. *Approximation of large-scale dynamical systems*. Vol. 6. Siam, 2005.

[Ant95] S. S. Antman. *Nonlinear Problems of Elasticity*. Springer, 1995.

[AP96] R. R. Aliev and A. V. Panfilov. "A simple two-variable model of cardiac excitation". In: *Chaos, Solitons & Fractals* 7.3 (1996), pp. 293–301.

[ASG00] A. C. Antoulas, D. C. Sorensen, and S. Gugercin. *A survey of model reduction methods for large-scale systems*. Tech. rep. 2000.

[Aug+16] C. M. Augustin, A. Neic, M. Liebmann, A. J. Prassl, S. A. Niederer, G. Haase, and G. Plank. "Anatomically accurate high resolution modeling of human whole heart electromechanics: a strongly scalable algebraic multigrid solver method for nonlinear deformation". In: *Journal of Computational Physics* 305 (2016), pp. 622–646.

[AW94] A. Araujo and J. Walker. “Kinetics of tension development in skinned cardiac myocytes measured by photorelease of Ca2+”. In: *American Journal of Physiology-Heart and Circulatory Physiology* 267.5 (1994), H1643–H1653.

[Bac+95] P. Backx, W. Gao, M. Azan-Backx, and E. Marbán. “The relationship between contractile force and intracellular [Ca2+] in intact rat cardiac trabeculae.” In: *The Journal of General Physiology* 105.1 (1995), pp. 1–19.

[Bai02] Z. Bai. “Krylov subspace techniques for reduced-order modeling of large-scale dynamical systems”. In: *Applied Numerical Mathematics* 43.1-2 (2002), pp. 9–44.

[Bar+04] M. Barrault, Y. Maday, N. C. Nguyen, and A. T. Patera. “An ’empirical interpolation’ method: application to efficient reduced-basis discretization of partial differential equations”. In: *Comptes Rendus Mathematique* 339.9 (2004), pp. 667–672.

[Bau+11] U. Baur, C. Beattie, P. Benner, and S. Gugercin. “Interpolatory projection methods for parameterized model reduction”. In: *SIAM Journal on Scientific Computing* 33.5 (2011), pp. 2489–2518.

[Bay+12] J. D. Bayer, R. C. Blake, G. Plank, and N. A. Trayanova. “A novel rule-based algorithm for assigning myocardial fiber orientation to computational heart models”. In: *Annals of Biomedical Engineering* 40.10 (2012), pp. 2243–2254.

[BCS01] J. Bestel, F. Clément, and M. Sorine. “A biomechanical model of muscle contraction”. In: *International Conference on Medical Image Computing and Computer-Assisted Intervention*. Springer. 2001, pp. 1159–1161.

[Ber01] D. Bers. *Excitation-contraction coupling and cardiac contractile force*. Vol. 237. Springer Science & Business Media, 2001.

[BGL05] M. Benzi, G. H. Golub, and J. Liesen. “Numerical solution of saddle point problems”. In: *Acta Numerica* 14 (2005), pp. 1–137.

[BGW15] P. Benner, S. Gugercin, and K. Willcox. “A survey of projection-based model reduction methods for parametric dynamical systems”. In: *SIAM Review* 57.4 (2015), pp. 483–531.

[BL07] J. Bongard and H. Lipson. “Automated reverse engineering of nonlinear dynamical systems”. In: *Proceedings of the National Academy of Sciences* 104.24 (2007), pp. 9943–9948.

[BMS05] P. Benner, V. Mehrmann, and D. C. Sorensen. *Dimension reduction of large-scale systems*. Vol. 35. Springer, 2005.

[BOCF08] A. Bueno-Orovio, E. M. Cherry, and F. H. Fenton. “Minimal model for human ventricular action potentials in tissue”. In: *Journal of Theoretical Biology* 253.3 (2008), pp. 544–560.

[Bot10] L. Bottou. “Large-scale machine learning with stochastic gradient descent”. In: *Proceedings of COMPSTAT’2010*. Springer, 2010, pp. 177–186.

[BPK16] S. L. Brunton, J. L. Proctor, and J. N. Kutz. “Discovering governing equations from data by sparse identification of nonlinear dynamical systems”. In: *Proceedings of the National Academy of Sciences* (2016), p. 201517384.

[Bra+87] P. Brandt, M. Diamond, J. Rutchik, and F. Schachat. “Co-operative interactions between troponin-tropomyosin units extend the length of the thin filament in skeletal muscle”. In: *Journal of Molecular Biology* 195.4 (1987), pp. 885–896.

[Bro+17] A. Brock, T. Lim, J. M. Ritchie, and N. Weston. “FreezeOut: Accelerate Training by Progressively Freezing Layers”. In: *arXiv preprint arXiv:1706.04983* (2017).

[Bro76] C. Brokaw. “Computer simulation of flagellar movement. IV. Properties of an oscillatory two-state cross-bridge model”. In: *Biophysical Journal* 16.9 (1976), pp. 1029–1041.

[Bru+14] E. Brunello, M. Caremani, L. Melli, M. Linari, M. Fernandez-Martinez, T. Narayanan, M. Irving, G. Piazzesi, V. Lombardi, and M. Reconditi. “The contributions of filaments and cross-bridges to sarcomere compliance in skeletal muscle”. In: *The Journal of Physiology* 592.17 (2014), pp. 3881–3899.

[Cam+10] S. Campbell, F. Lionetti, K. Campbell, and A. McCulloch. “Coupling of adjacent tropomyosins enhances cross-bridge-mediated cooperative activation in a Markov model of the cardiac thin filament”. In: *Biophysical Journal* 98.10 (2010), pp. 2254–2264.

[Car+14] M. Caruel, R. Chabiniok, P. Moireau, Y. Lecarpentier, and D. Chapelle. “Dimensional reductions of a cardiac model for effective validation and calibration”. In: *Biomechanics and Modeling in Mechanobiology* 13.4 (2014), pp. 897–914.

[Car+16] M. Caremani, F. Pinzauti, M. Reconditi, G. Piazzesi, G. J. Stienen, V. Lombardi, and M. Linari. “Size and speed of the working stroke of cardiac myosin in situ”. In: *Proceedings of the National Academy of Sciences* 113.13 (2016), pp. 3675–3680.

[Car11] M. Caruel. “Mechanics of Fast Force Recovery in striated muscles”. PhD thesis. Ecole Polytechnique, 2011.

[CB02] G. Casella and R. L. Berger. *Statistical inference*. Vol. 2. Duxbury Pacific Grove, CA, 2002.

[CFPS06] P Colli Franzone, L. F. Pavarino, and G. Savaré. “Computational electrocardiology: mathematical and numerical modeling”. In: *Complex Systems in Biomedicine*. Springer, 2006, pp. 187–241.

[CFPS14] P. Colli Franzone, L. F. Pavarino, and S. Scacchi. *Mathematical cardiac electrophysiology*. Vol. 13. Springer, 2014.

[Cha+10] D. Chapelle, J.-F. Gerbeau, J Sainte-Marie, and I. Vignon-Clementel. “A poroelastic model valid in large strains with applications to perfusion in cardiac modeling”. In: *Computational Mechanics* 46.1 (2010), pp. 91–101.

[Cha+12] D. Chapelle, P. Le Tallec, P. Moireau, and M. Sorine. “Energy-preserving muscle tissue model: formulation and compatible discretizations”. In: *International Journal for Multiscale Computational Engineering* 10.2 (2012).

[Cha+16] R. Chabiniok, V. Wang, M. Hadjicharalambous, L. Asner, J. Lee, M. Sermesant, E. Kuhl, A. Young, P. Moireau, M. Nash, D. Chapelle, and D. Nordsletten. “Multiphysics and multiscale modelling, data–model fusion and integration of organ physiology in the clinic: ventricular cardiac mechanics”. In: *Interface Focus* 6.2 (2016), p. 20150083.

[Cip87] B. Cipra. “An introduction to the Ising model”. In: *American Mathematical Monthly* 94.10 (1987), pp. 937–959.

[CL01] R. Craig and W. Lehman. “Crossbridge and tropomyosin positions observed in native, interacting thick and thin filaments”. In: *Journal of Molecular Biology* 311.5 (2001), pp. 1027–1036.

[CMA94] J. T. Connor, R. D. Martin, and L. E. Atlas. “Recurrent neural networks and robust time series prediction”. In: *IEEE Transactions on Neural Networks* 5.2 (1994), pp. 240–254.

[CMC19] M. Caruel, P. Moireau, and D. Chapelle. “Stochastic modeling of chemical–mechanical coupling in striated muscles”. In: *Biomechanics and Modeling in Mechanobiology* 18.3 (2019), pp. 563–587.

[Cra+04] E. J. Crampin, M. Halstead, P. Hunter, P. Nielsen, D. Noble, N. Smith, and M. Tawhai. “Computational physiology and the physiome project”. In: *Experimental Physiology* 89.1 (2004), pp. 1–26.

[CS10] S. Chaturantabut and D. C. Sorensen. “Nonlinear model reduction via discrete empirical interpolation”. In: *SIAM Journal on Scientific Computing* 32.5 (2010), pp. 2737–2764.

[CT18] M. Caruel and L. Truskinovsky. “Physics of muscle contraction”. In: *Reports on Progress in Physics* 81.3 (2018), p. 036602.

[CW00] Y. Chen and J. White. “A quadratic method for nonlinear model order reduction”. In: (2000).

[Cyb89] G. Cybenko. “Approximation by superpositions of a sigmoidal function”. In: *Mathematics of Control, Signals and Systems* 2.4 (1989), pp. 303–314.

[Dac07] B. Dacorogna. *Direct methods in the calculus of variations*. Vol. 78. Springer Science & Business Media, 2007.

[Daw79] A. Dawid. “Conditional independence in statistical theory”. In: *Journal of the Royal Statistical Society. Series B (Methodological)* (1979), pp. 1–31.

[DBY95] L. Dobrunz, P. Backx, and D. Yue. “Steady-state [Ca2+] i-force relationship in intact twitching cardiac muscle: direct evidence for modulation by isoproterenol and EMD 53998”. In: *Biophysical Journal* 69.1 (1995), pp. 189–201.

[DD05] D. Deschrijver and T. Dhaene. “Rational modeling of spectral data using orthonormal vector fitting”. In: *9th IEEE Workshop on Signal Propagation on Interconnects*. 2005, pp. 111–114.

[DG+19] S. Di Gregorio, M. Fedele, G. Pontone, A. F. Corno, P. Zunino, C. Vergara, and A. Quarteroni. “A multiscale computational model of myocardial perfusion in the human heart”. In: *MOX Report 2019/48, Politecnico di Milano* (2019).

[DHD07] D. Deschrijver, B. Haegeman, and T. Dhaene. “Orthonormal vector fitting: A robust macromodeling tool for rational approximation of frequency domain responses”. In: *IEEE Transactions on Advanced Packaging* 30.2 (2007), pp. 216–225.

[DHO12] M. Drohmann, B. Haasdonk, and M. Ohlberger. “Reduced basis approximation for nonlinear parametrized evolution equations based on empirical operator interpolation”. In: *SIAM Journal on Scientific Computing* 34.2 (2012), A937–A969.

[DHS11] J. Duchi, E. Hazan, and Y. Singer. “Adaptive subgradient methods for online learning and stochastic optimization”. In: *Journal of Machine Learning Research* 12.Jul (2011), pp. 2121–2159.

[DKT02] D. Dobesh, J. Konhilas, and P. de Tombe. “Cooperative activation in cardiac muscle: impact of sarcomere length”. In: *American Journal of Physiology-Heart and Circulatory Physiology* 51.3 (2002), H1055.

[Dup+16] L. Dupuis, J. Lumens, T. Arts, and T. Delhaas. “Mechano-chemical Interactions in Cardiac Sarcomere Contraction: A Computational Modeling Study”. In: *PLoS Computational Biology* 12.10 (2016), e1005126.

[ES95] R. Everson and L. Sirovich. “Karhunen–Loeve procedure for gappy data”. In: *Journal of the Optical Society of America A* 12.8 (1995), pp. 1657–1664.

[Far+10] G. P. Farman, E. J. Allen, K. Q. Schoenfelt, P. H. Backx, and P. P. De Tombe. “The role of thin filament cooperativity in cardiac length-dependent calcium activation”. In: *Biophysical Journal* 99.9 (2010), pp. 2978–2986.

[FC18] B. A. Freno and K. T. Carlberg. “Machine-learning error models for approximate solutions to parameterized systems of nonlinear equations”. In: *arXiv preprint arXiv:1808.02097* (2018).

[FHS77] L. Ford, A. Huxley, and R. Simmons. “Tension responses to sudden length change in stimulated frog muscle fibres near slack length”. In: *The Journal of Physiology* 269.2 (1977), pp. 441–515.

[Fin+11] M. Fink, S. Niederer, E. Cherry, F. Fenton, J. Koivumäki, G. Seemann, R. Thul, H. Zhang, F. Sachse, D. Beard, E. Crampin, and N. Smith. “Cardiac cell modelling: observations from the heart of the cardiac physiome project”. In: *Progress in Biophysics and Molecular Biology* 104.1 (2011), pp. 2–21.

[Fit61] R. FitzHugh. “Impulses and physiological states in theoretical models of nerve membrane”. In: *Biophysical Journal* 1.6 (1961), pp. 445–466.

[FM98] D. P. Fitzsimons and R. L. Moss. “Strong binding of myosin modulates length-dependent Ca2+ activation of rat ventricular myocytes”. In: *Circulation Research* 83.6 (1998), pp. 602–607.

[FPM01] D. Fitzsimons, J. Patel, and R. Moss. “Cross-bridge interaction kinetics in rat myocardium are accelerated by strong binding of myosin to the thin filament”. In: *The Journal of Physiology* 530.2 (2001), pp. 263–272.

[FPM98] D. P. Fitzsimons, J. R. Patel, and R. L. Moss. "Role of myosin heavy chain composition in kinetics of force development and relaxation in rat myocardium". In: *The Journal of Physiology* 513.1 (1998), pp. 171–183.

[FR83] J. P. Fink and W. Rheinboldt. "On the error behavior of the reduced basis technique for nonlinear finite element approximations". In: *ZAMM-Journal of Applied Mathematics and Mechanics/Zeitschrift für Angewandte Mathematik und Mechanik* 63.1 (1983), pp. 21–28.

[Fre03] R. W. Freund. "Model reduction methods based on Krylov subspaces". In: *Acta Numerica* 12 (2003), pp. 267–319.

[GA15] I. V. Gosea and A. C. Antoulas. "Model reduction of linear and nonlinear systems in the Loewner framework: A summary". In: *Control Conference (ECC), 2015 European*. IEEE. 2015, pp. 345–349.

[Gao+94] W. Gao, P. Backx, M. Azan-Backx, and E. Marban. "Myofilament Ca2+ sensitivity in intact versus skinned rat ventricular muscle." In: *Circulation Research* 74.3 (1994), pp. 408–415.

[GCM95] J. M. Guccione, K. D. Costa, and A. D. McCulloch. "Finite element stress analysis of left ventricular mechanics in the beating dog heart". In: *Journal of Biomechanics* 28.10 (1995), pp. 1167–1177.

[GDQ18a] A. Gerbi, L. Dedè, and A. Quarteroni. "A monolithic algorithm for the simulation of cardiac electromechanics in the human left ventricle". In: *Mathematics in Engineering* 1.1 (2018), pp. 1–37.

[GDQ18b] A. Gerbi, L. Dedè, and A. Quarteroni. "Segregated algorithms for the numerical simulation of cardiac electromechanics in the left human ventricle". In: *MOX Report 2018/28, Politecnico di Milano* (2018).

[Ger18] A. Gerbi. "Numerical Approximation of Cardiac Electro-fluid-mechanical Models: Coupling Strategies for Large-scale Simulation". PhD thesis. Ecole Polytechnique Fédérale de Lausanne, 2018.

[GH19] M. Guo and J. S. Hesthaven. "Data-driven reduced order modeling for time-dependent problems". In: *Computer Methods in Applied Mechanics and Engineering* 345 (2019), pp. 75–99.

[GHJ66] A. Gordon, A. F. Huxley, and F. Julian. "The variation in isometric tension with sarcomere length in vertebrate muscle fibres". In: *The Journal of Physiology* 184.1 (1966), pp. 170–192.

[GJGGJ03] H. G. Gauch Jr, H. G. Gauch, and H. G. Gauch Jr. *Scientific method in practice*. Cambridge University Press, 2003.

[GL99] G. Golub and C. V. Loan. *Matrix computations*. Johns Hopkins University Press, 1999.

[GMR19] G. Giantesio, A. Musesti, and D. Riccobelli. "A comparison between active strain and active stress in transversely isotropic hyperelastic materials". In: *Journal of Elasticity* (2019), pp. 1–20.

[GMW91] J. M. Guccione, A. D. McCulloch, and L. Waldman. "Passive material properties of intact ventricular myocardium determined from a cylindrical model". In: *Journal of Biomechanical Engineering* 113.1 (1991), pp. 42–55.

[Gop02] M. Gopal. *Control systems: principles and design*. Tata McGraw-Hill Education, 2002.

[Gra13] A. Graves. “Generating sequences with recurrent neural networks”. In: *arXiv preprint arXiv:1308.0850* (2013).

[GRH01] A. Gordon, M Regnier, and E Homsher. “Skeletal and cardiac muscle contractile activation: tropomyosin “rocks and rolls””. In: *Physiology* 16.2 (2001), pp. 49–55.

[GS11] L. Grippo and M. Sciandrone. *Metodi di ottimizzazione non vincolata*. Springer Science & Business Media, 2011.

[GSH16] O. Gültekin, G. Sommer, and G. A. Holzapfel. “An orthotropic viscoelastic model for the passive myocardium: continuum basis and numerical treatment”. In: *Computer Methods in Biomechanics and Biomedical Engineering* 19.15 (2016), pp. 1647–1664.

[Gu11] C. Gu. “QLMOR: A projection-based nonlinear model order reduction approach using quadratic-linear representation of nonlinear systems”. In: *IEEE Transactions on Computer-Aided Design of Integrated Circuits and Systems* 30.9 (2011), pp. 1307–1320.

[Hac79] W. Hackbusch. “On the fast solving of parabolic boundary control problems”. In: *SIAM Journal on Control and Optimization* 17.2 (1979), pp. 231–244.

[Hay09] S. S. Haykin. *Neural networks and learning machines*. Vol. 3. Pearson Upper Saddle River, 2009.

[HB89] S. M. Harrison and D. M. Bers. “Influence of temperature on the calcium sensitivity of the myofilaments of skinned ventricular muscle from the rabbit.” In: *The Journal of General Physiology* 93.3 (1989), pp. 411–428.

[He+18] J. He, L. Li, J. Xu, and C. Zheng. “Relu deep neural networks and linear finite elements”. In: *arXiv preprint arXiv:1807.03973* (2018).

[HG08] A. F. Hernandez and M. G. Gallivan. “An exploratory study of discrete time state-space models using kriging”. In: *Proceedings of American Control Conference, 2008*. IEEE. 2008, pp. 3993–3998.

[HH52a] A. L. Hodgkin and A. F. Huxley. “A quantitative description of membrane current and its application to conduction and excitation in nerve”. In: *The Journal of Physiology* 117.4 (1952), pp. 500–544.

[HH52b] A. L. Hodgkin and A. F. Huxley. “Propagation of electrical signals along giant nerve fibres”. In: *Proceedings of the Royal Society of London. Series B-Biological Sciences* 140.899 (1952), pp. 177–183.

[HH54] H. Huxley and J. Hanson. “Changes in the Cross-Striations of Muscle during Contraction and Stretch and their Structural Interpretation”. In: *Nature* 173.4412 (1954), pp. 973–976.

[Hil10] A. V. Hill. “The possible effects of the aggregation of the molecules of haemoglobin on its dissociation curves”. In: *The Journal of Physiology* 40 (1910), pp. 4–7.

[Hil38] A. Hill. “The heat of shortening and the dynamic constants of muscle”. In: *Proceedings of the Royal Society of London B: Biological Sciences* 126.843 (1938), pp. 136–195.

[Hin+12] G. Hinton, L. Deng, D. Yu, G. E. Dahl, A. Mohamed, N. Jaitly, A. Senior, V. Vanhoucke, P. Nguyen, and T. N. Sainath. "Deep neural networks for acoustic modeling in speech recognition: The shared views of four research groups". In: *IEEE Signal Processing Magazine* 29.6 (2012), pp. 82–97.

[HMTK98] P. Hunter, A. McCulloch, and H. Ter Keurs. "Modelling the mechanical properties of cardiac muscle". In: *Progress in Biophysics and Molecular Biology* 69.2 (1998), pp. 289–331.

[HN54] A. F. Huxley and R. Niedergerke. "Structural Changes in Muscle During Contraction: Interference Microscopy of Living Muscle Fibres". In: *Nature* 173.4412 (1954), pp. 971–973.

[HO09] G. A. Holzapfel and R. W. Ogden. "Constitutive modelling of passive myocardium: a structurally based framework for material characterization". In: *Philosophical Transactions of the Royal Society A: Mathematical, Physical and Engineering Sciences* 367.1902 (2009), pp. 3445–3475.

[HO10] M. Hochbruck and A. Ostermann. "Exponential integrators". In: *Acta Numerica* 19 (2010), pp. 209–286.

[Hot33] H. Hotelling. "Analysis of a complex of statistical variables into principal components." In: *Journal of Educational Psychology* 24.6 (1933), p. 417.

[HRS16] J. S. Hesthaven, G. Rozza, and B. Stamm. *Certified reduced basis methods for parametrized partial differential equations*. Springer, 2016.

[HS71] A. Huxley and R. Simmons. "Proposed mechanism of force generation in striated muscle". In: *Nature* 233.5321 (1971), pp. 533–538.

[HSLV89] D. Heeley, L. Smillie, and E. Lohmeier-Vogel. "Effects of deletion of tropomyosin overlap on regulated actomyosin subfragment 1 ATPase". In: *Biochemical Journal* 258.3 (1989), pp. 831–836.

[HTR06] J. Hussan, P. de Tombe, and J. Rice. "A spatially detailed myofilament model as a basis for large-scale biological simulations". In: *IBM Journal of Research and Development* 50.6 (2006), pp. 583–600.

[Hux57a] A. F. Huxely. "Muscle structure and theories of contraction". In: *Prog Biophys Biophys Chem* (1957), pp. 255–318.

[Hux57b] A. F. Huxley. "Muscle structure and theories of contraction". In: *Progress in Biophysics and Biophysical Chemistry* 7 (1957), pp. 255–318.

[Irv+00] T. C. Irving, J. Konhilas, D. Perry, R. Fischetti, and P. P. De Tombe. "Myofilament lattice spacing as a function of sarcomere length in isolated rat myocardium". In: *American Journal of Physiology-Heart and Circulatory Physiology* 279.5 (2000), H2568–H2573.

[IS15] S. Ioffe and C. Szegedy. "Batch normalization: Accelerating deep network training by reducing internal covariate shift". In: *arXiv preprint arXiv:1502.03167* (2015).

[JG91] L. A. Jelicks and R. K. Gupta. "Intracellular Free Magnesium and High Energy Phosphates in the Perfused Normotensive and Spontaneously Hypertensive Rat Heart A 31P NMR Study". In: *American Journal of Hypertension* 4.2_Pt_1 (1991), pp. 131–136.

[JH95] P. Janssen and W. Hunter. “Force, not sarcomere length, correlates with prolongation of isosarcometric contraction”. In: *American Journal of Physiology - Heart and Circulatory Physiology* 269.2 (1995), H676–H685.

[JJS99] H. Jeffreys, B. Jeffreys, and B. Swirles. *Methods of mathematical physics*. Cambridge University Press, 1999.

[JKT07] G. W. Jenkins, C. P. Kemnitz, and G. J. Tortora. *Anatomy and physiology: from science to life*. Wiley Hoboken, 2007.

[JSM02] P. Janssen, L. Stull, and E. Marbán. “Myofilament properties comprise the rate-limiting step for cardiac relaxation at body temperature in the rat”. In: *American Journal of Physiology-Heart and Circulatory Physiology* 282.2 (2002), H499–H507.

[JT97] P. Janssen and P. de Tombe. “Uncontrolled sarcomere shortening increases intracellular Ca2+ transient in rat cardiac trabeculae”. In: *American Journal of Physiology - Heart and Circulatory Physiology* 272.4 (1997), H1892–H1897.

[Kat10] A. M. Katz. *Physiology of the Heart*. Lippincott Williams & Wilkins, 2010.

[KB14] D. P. Kingma and J. Ba. “Adam: A method for stochastic optimization”. In: *arXiv preprint arXiv:1412.6980* (2014).

[Kee11] K. J. Keesman. *System identification: an introduction*. Springer Science & Business Media, 2011.

[Ken+86] J. Kentish, H. ter Keurs, L. Ricciardi, J. Bucx, and M. Noble. “Comparison between the sarcomere length-force relations of intact and skinned trabeculae from rat right ventricle. Influence of calcium concentrations on these relations.” In: *Circulation Research* 58.6 (1986), pp. 755–768.

[Kim+19] F. Kimmig, M. Caruel, P. Moireau, and D. Chapelle. “Activation-contraction coupling in a multiscale heart model”. In: *Proceedings of CMBE 2019 (volume 1)*. 2019, pp. 96–99.

[Kim19] F. Kimmig. “Multi-scale modeling of muscle contraction - From stochastic dynamics of molecular motors to continuum mechanics”. PhD thesis. Université Paris-Saclay, 2019.

[KN12] H. Keurs and M. I. Noble. *Starling’s law of the heart revisited*. Vol. 89. Springer Science & Business Media, 2012.

[Kno90] D. Knowles. *Explanation and its Limits*. Vol. 27. Cambridge University Press, 1990.

[Kri51] D. G. Krige. “A statistical approach to some basic mine valuation problems on the Witwatersrand”. In: *Journal of the Southern African Institute of Mining and Metallurgy* 52.6 (1951), pp. 119–139.

[KS06] J. Kaipio and E. Somersalo. *Statistical and computational inverse problems*. Vol. 160. Springer Science & Business Media, 2006.

[KS09] J. Keener and J. Sneyd. *Mathematical Physiology*. Vol. 1. Springer, 2009.

[KS98] I. Karatzas and S. E. Shreve. *Brownian Motion and Stochastic Calculus*. Springer, 1998.

[KTKA88] J. Kentish, H. Ter Keurs, and D. Allen. “The contribution of myofibrillar properties to the sarcomere length-force relationship of cardiac muscle”. In: *Starling’s Law of The Heart Revisited*. Springer, 1988, pp. 1–17.

[LA10] S. Lefteriu and A. C. Antoulas. “A new approach to modeling multiport systems from frequency-domain data”. In: *IEEE Transactions on Computer-Aided Design of Integrated Circuits and Systems* 29.1 (2010), pp. 14–27.

[Lan+12] S. Land, S. A. Niederer, J. M. Aronsen, E. K. Espe, L. Zhang, W. E. Louch, I. Sjaastad, O. M. Sejersted, and N. P. Smith. “An analysis of deformation-dependent electromechanical coupling in the mouse heart”. In: *The Journal of Physiology* 590.18 (2012), pp. 4553–4569.

[Lan+17] S. Land, S. Park-Holohan, N. Smith, C. dos Remedios, J. Kentish, and S. Niederer. “A model of cardiac contraction based on novel measurements of tension development in human cardiomyocytes”. In: *Journal of Molecular and Cellular Cardiology* 106 (2017), pp. 68–83.

[Lan+18] M. Landajuela, C. Vergara, A. Gerbi, L. Dedè, L. Formaggia, and A. Quarteroni. “Numerical approximation of the electromechanical coupling in the left ventricle with inclusion of the Purkinje network”. In: *International journal for numerical methods in biomedical engineering* 34.7 (2018), e2984.

[LBH15] Y. LeCun, Y. Bengio, and G. Hinton. “Deep Learning”. In: *Nature* 521.7553 (2015), p. 436.

[LC18] K. Lee and K. Carlberg. “Model reduction of dynamical systems on nonlinear manifolds using deep convolutional autoencoders”. In: *arXiv preprint arXiv:1812.08373* (2018).

[Lju98] L. Ljung. “System identification”. In: *Signal Analysis and Prediction*. Springer, 1998, pp. 163–173.

[LN15] S. Land and S. Niederer. “A spatially detailed model of isometric contraction based on competitive binding of troponin I explains cooperative interactions between tropomyosin and crossbridges”. In: *PLoS Computational Biology* 11.8 (2015), e1004376.

[Loe78] M. Loeve. “Probability theory, vol. ii”. In: *Graduate Texts in Mathematics* 46 (1978), pp. 0–387.

[LS94] A. Landesberg and S. Sideman. “Coupling calcium binding to troponin C and cross-bridge cycling in skinned cardiac cells”. In: *American Journal of Physiology-Heart and Circulatory Physiology* 266.3 (1994), H1260–H1271.

[LT71] R. Lymn and E. W. Taylor. “Mechanism of adenosine triphosphate hydrolysis by actomyosin”. In: *Biochemistry* 10.25 (1971), pp. 4617–4624.

[Löw34] K. Löwner. “Über monotone matrixfunktionen”. In: *Mathematische Zeitschrift* 38.1 (1934), pp. 177–216.

[MA07] A. Mayo and A. Antoulas. “A framework for the solution of the generalized realization problem”. In: *Linear Algebra and its Applications* 425.2-3 (2007), pp. 634–662.

[Mad+07] Y. Maday, N. C. Nguyen, A. T. Patera, and G. S. Pau. “A general, multipurpose interpolation procedure: the magic points”. In: (2007).

[Mat] *MATLAB Documentation*. 2019. URL: `https://www.mathworks.com/help/matlab/`.

[MBC00] M. D. McKay, R. J. Beckman, and W. J. Conover. "A comparison of three methods for selecting values of input variables in the analysis of output from a computer code". In: *Technometrics* 42.1 (2000), pp. 55–61.

[MD17] A. D. McDougal and C. F. Dewey. "Modeling oxygen requirements in ischemic cardiomyocytes". In: *Journal of Biological Chemistry* 292.28 (2017), pp. 11760–11776.

[MH06] D. E. Mohrman and L. J. Heller. *Cardiovascular physiology*. Lange Medical Books/McGraw-Hill New York, 2006.

[MMK03] D. J. MacKay and D. J. Mac Kay. *Information theory, inference and learning algorithms*. Cambridge Iniversity Press, 2003.

[Moo81] B. Moore. "Principal component analysis in linear systems: Controllability, observability, and model reduction". In: *IEEE Transactions on Automatic Control* 26.1 (1981), pp. 17–32.

[MPL16] A. Manzoni, S. Pagani, and T. Lassila. "Accurate solution of Bayesian inverse uncertainty quantification problems combining reduced basis methods and reduction error models". In: *SIAM/ASA Journal on Uncertainty Quantification* 4.1 (2016), pp. 380–412.

[MSDR13] A. Menafoglio, P. Secchi, and M. Dalla Rosa. "A Universal Kriging predictor for spatially dependent functional data of a Hilbert Space". In: *Electronic Journal of Statistics* 7 (2013), pp. 2209–2240.

[MT10a] L. Marcucci and L. Truskinovsky. "Mechanics of the power stroke in myosin II". In: *Physical Review E* 81.5 (2010), p. 051915.

[MT10b] L. Marcucci and L. Truskinovsky. "Muscle contraction: A mechanical perspective". In: *The European Physical Journal E* 32.4 (2010), pp. 411–418.

[NAY62] J. Nagumo, S. Arimoto, and S. Yoshizawa. "An active pulse transmission line simulating nerve axon". In: *Proceedings of the IRE* 50.10 (1962), pp. 2061–2070.

[NCC19] S. A. Niederer, K. S. Campbell, and S. G. Campbell. "A short history of the development of mathematical models of cardiac mechanics". In: *Journal of molecular and cellular cardiology* 127 (2019), pp. 11–19.

[Nel13] O. Nelles. *Nonlinear system identification: from classical approaches to neural networks and fuzzy models*. Springer Science & Business Media, 2013.

[NHS06] S. A. Niederer, P. J. Hunter, and N. P. Smith. "A quantitative analysis of cardiac myocyte relaxation: a simulation study". In: *Biophysical Journal* 90.5 (2006), pp. 1697–1722.

[NMA15] F. Negri, A. Manzoni, and D. Amsallem. "Efficient model reduction of parametrized systems by matrix discrete empirical interpolation". In: *Journal of Computational Physics* 303 (2015), pp. 431–454.

[Nor+11] D. Nordsletten, S. Niederer, M. Nash, P. Hunter, and N. Smith. "Coupling multi-physics models to cardiac mechanics". In: *Progress in Biophysics and Molecular Biology* 104.1-3 (2011), pp. 77–88.

[Nor98] J. Norris. *Markov chains*. 2. Cambridge University Press, 1998.

[NP90] K. S. Narendra and K. Parthasarathy. "Identification and control of dynamical systems using neural networks". In: *IEEE Transactions on Neural Networks* 1.1 (1990), pp. 4–27.

[NP92] K. S. Narendra and K. Parthasarathy. "Neural networks and dynamical systems". In: *International Journal of Approximate Reasoning* 6.2 (1992), pp. 109–131.

[NS08] S. A. Niederer and N. P. Smith. "An improved numerical method for strong coupling of excitation and contraction models in the heart". In: *Progress in biophysics and molecular biology* 96.1-3 (2008), pp. 90–111.

[NS09] S. A. Niederer and N. P. Smith. "The role of the Frank–Starling law in the transduction of cellular work to whole organ pump function: a computational modeling analysis". In: *PLoS computational biology* 5.4 (2009), e1000371.

[NW06] J. Nocedal and S. Wright. *Numerical optimization*. second. New York, NY, USA: Springer Science & Business Media, 2006.

[O'H+11] T. O'Hara, L. Virág, A. Varró, and Y. Rudy. "Simulation of the undiseased human cardiac ventricular action potential: model formulation and experimental validation". In: *PLoS computational biology* 7.5 (2011), e1002061.

[Ogd97] R. W. Ogden. *Non-linear Elastic Deformations*. Courier Corporation, 1997.

[Pat+17] A. S. Patelli, L. Dedè, T. Lassila, A. Bartezzaghi, and A. Quarteroni. "Isogeometric approximation of cardiac electrophysiology models on surfaces: An accuracy study with application to the human left atrium". In: *Computer Methods in Applied Mechanics and Engineering* 317 (2017), pp. 248–273.

[PDQ19] L. Pegolotti, L. Dedè, and A. Quarteroni. "Isogeometric Analysis of the electrophysiology in the human heart: Numerical simulation of the bidomain equations on the atria". In: *Computer Methods in Applied Mechanics and Engineering* 343 (2019), pp. 52–73.

[Pea+07] J. T. Pearson, M. Shirai, H. Tsuchimochi, D. O. Schwenke, T. Ishida, K. Kangawa, H. Suga, and N. Yagi. "Effects of sustained length-dependent activation on in situ cross-bridge dynamics in rat hearts". In: *Biophysical Journal* 93.12 (2007), pp. 4319–4329.

[Pea01] K. Pearson. "LIII. On lines and planes of closest fit to systems of points in space". In: *The London, Edinburgh, and Dublin Philosophical Magazine and Journal of Science* 2.11 (1901), pp. 559–572.

[Peg19] L. Pegolotti. *Feamat*. 2019. URL: `https://github.com/lucapegolotti/feamat`.

[Pet89] J. S. Peterson. "The reduced basis method for incompressible viscous flow calculations". In: *SIAM Journal on Scientific and Statistical Computing* 10.4 (1989), pp. 777–786.

[Pfa+19] M. R. Pfaller, J. M. Hörmann, M. Weigl, A. Nagler, R. Chabiniok, C. Bertoglio, and W. A. Wall. "The importance of the pericardium for cardiac biomechanics: From physiology to computational modeling". In: *Biomechanics and Modeling in Mechanobiology* 18.2 (2019), pp. 503–529.

[PGL89] B. Pan, A. Gordon, and Z. Luo. "Removal of tropomyosin overlap modifies cooperative binding of myosin S-1 to reconstituted thin filaments of rabbit striated muscle." In: *Journal of Biological Chemistry* 264.15 (1989), pp. 8495–8498.

[PGW17] B. Peherstorfer, S. Gugercin, and K. Willcox. "Data-Driven Reduced Model Construction with Time-Domain Loewner Models". In: *SIAM Journal on Scientific Computing* 39.5 (2017), A2152–A2178.

[Pia+07] G. Piazzesi, M. Reconditi, M. Linari, L. Lucii, P. Bianco, E. Brunello, V. Decostre, A. Stewart, D. B. Gore, T. C. Irving, et al. "Skeletal muscle performance determined by modulation of number of myosin motors rather than motor force or stroke size". In: *Cell* 131.4 (2007), pp. 784–795.

[Pir+07] N. Piroddi, A. Belus, B. Scellini, C. Tesi, G. Giunti, E. Cerbai, A. Mugelli, and C. Poggesi. "Tension generation and relaxation in single myofibrils from human atrial and ventricular myocardium". In: *Pflügers Archiv-European Journal of Physiology* 454.1 (2007), pp. 63–73.

[Pre+86] W. H. Press, B. P. Flannery, S. A. Teukolsky, and W. T. Vetterling. *Numerical recipes: the art of scientific computing*. Cambridge Univ. Press, New York, 1986.

[Pru+02] C. Prud'Homme, D. V. Rovas, K. Veroy, L. Machiels, Y. Maday, A. T. Patera, and G. Turinici. "Reliable real-time solution of parametrized partial differential equations: Reduced-basis output bound methods". In: *Journal of Fluids Engineering* 124.1 (2002), pp. 70–80.

[PTS05] C. Poggesi, C. Tesi, and R. Stehle. "Sarcomeric determinants of striated muscle relaxation kinetics". In: *Pflügers Archiv* 449.6 (2005), pp. 505–517.

[PW15a] B. Peherstorfer and K. Willcox. "Dynamic data-driven reduced-order models". In: *Computer Methods in Applied Mechanics and Engineering* 291 (2015), pp. 21–41.

[PW15b] B. Peherstorfer and K. Willcox. "Online adaptive model reduction for nonlinear systems via low-rank updates". In: *SIAM Journal on Scientific Computing* 37.4 (2015), A2123–A2150.

[Pyt] *The Python Language Reference*. 2019. URL: `https://docs.python.org/3.8/reference/`.

[QMN15] A. Quarteroni, A. Manzoni, and F. Negri. *Reduced basis methods for partial differential equations: an introduction*. Vol. 92. Springer, 2015.

[QMV17] A. Quarteroni, A. Manzoni, and C. Vergara. "The cardiovascular system: mathematical modelling, numerical algorithms and clinical applications". In: *Acta Numerica* 26 (2017), pp. 365–590.

[QR14] A. Quarteroni and G. Rozza. *Reduced order methods for modeling and computational reduction*. Vol. 9. Springer, 2014.

[QSS10] A. Quarteroni, R. Sacco, and F. Saleri. *Numerical Mathematics*. Vol. 37. Springer Science & Business Media, 2010.

[Qua+17] A. Quarteroni, T. Lassila, S. Rossi, and R. Ruiz-Baier. "Integrated Heart–Coupling multiscale and multiphysics models for the simulation of the cardiac function". In: *Computer Methods in Applied Mechanics and Engineering* 314 (2017), pp. 345–407.

[Qua+19] A. Quarteroni, L. Dedè, A. Manzoni, and C. Vergara. *Mathematical Modelling of the Human Cardiovascular System: Data, Numerical Approximation, Clinical Applications*. Cambridge Monographs on Applied and Computational Mathematics. Cambridge University Press, 2019.

[QV03] A. Quarteroni and A. Veneziani. "Analysis of a geometrical multiscale model based on the coupling of ODE and PDE for blood flow simulations". In: *Multiscale Modeling & Simulation* 1.2 (2003), pp. 173–195.

[QV08] A. Quarteroni and A. Valli. *Numerical approximation of partial differential equations*. Vol. 23. Springer Science & Business Media, 2008.

[Ras04] C. E. Rasmussen. "Gaussian processes in machine learning". In: *Advanced lectures on machine learning*. Springer, 2004, pp. 63–71.

[RB+14] R. Ruiz-Baier, A. Gizzi, S. Rossi, C. Cherubini, A. Laadhari, S. Filippi, and A. Quarteroni. "Mathematical modelling of active contraction in isolated cardiomyocytes". In: *Mathematical Medicine and Biology* 31.3 (2014), pp. 259–283.

[RBC99] M. Razumova, A. Bukatina, and K. Campbell. "Stiffness-distortion sarcomere model for muscle simulation". In: *Journal of Applied Physiology* 87.5 (1999), pp. 1861–1876.

[RDQ18] F. Regazzoni, L. Dedè, and A. Quarteroni. "Active contraction of cardiac cells: a reduced model for sarcomere dynamics with cooperative interactions". In: *Biomechanics and Modeling in Mechanobiology* (2018), pp. 1–24.

[RDQ19a] F. Regazzoni, L. Dedè, and A. Quarteroni. "Active force generation in cardiac muscle cells: mathematical modeling and numerical simulation of the actin-myosin interaction". In: *MOX Report 2019/45, Politecnico di Milano* (2019).

[RDQ19b] F. Regazzoni, L. Dedè, and A. Quarteroni. "Machine learning for fast and reliable solution of time-dependent differential equations". In: *Journal of Computational Physics* 397 (2019), p. 108852.

[RDQ19c] F. Regazzoni, L. Dedè, and A. Quarteroni. "Machine learning of multiscale active force generation models for the efficient simulation of cardiac electromechanics". In: *MOX Report 2019/33, Politecnico di Milano* (2019).

[Rec06] M. Reconditi. "Recent improvements in small angle x-ray diffraction for the study of muscle physiology". In: *Reports on Progress in Physics* 69.10 (2006), p. 2709.

[Reg19] F. Regazzoni. *model-learning*. 2019. URL: `https://github.com/FrancescoRegazzoni/model-learning`.

[RG01] C. E. Rasmussen and Z. Ghahramani. "Occam's razor". In: *Advances in neural information processing systems*. 2001, pp. 294–300.

[Ric+03] J. Rice, G. Stolovitzky, Y. Tu, and P. de Tombe. “Ising model of cardiac thin filament activation with nearest-neighbor cooperative interactions”. In: *Biophysical Journal* 84.2 (2003), pp. 897–909.

[Ric+08] J. Rice, F. Wang, D. Bers, and P. de Tombe. “Approximate model of cooperative activation and crossbridge cycling in cardiac muscle using ordinary differential equations”. In: *Biophysical Journal* 95.5 (2008), pp. 2368–2390.

[RK18] M. Raissi and G. E. Karniadakis. “Hidden physics models: Machine learning of nonlinear partial differential equations”. In: *Journal of Computational Physics* 357 (2018), pp. 125–141.

[Ros+14] S. Rossi, T. Lassila, R. Ruiz-Baier, A. Sequeira, and A. Quarteroni. “Thermodynamically consistent orthotropic activation model capturing ventricular systolic wall thickening in cardiac electromechanics”. In: *European Journal of Mechanics-A/Solids* 48 (2014), pp. 129–142.

[RPK17a] M. Raissi, P. Perdikaris, and G. E. Karniadakis. “Machine learning of linear differential equations using Gaussian processes”. In: *Journal of Computational Physics* 348 (2017), pp. 683–693.

[RPK17b] M. Raissi, P. Perdikaris, and G. E. Karniadakis. “Physics Informed Deep Learning (Part I): Data-driven solutions of nonlinear partial differential equations”. In: *arXiv preprint arXiv:1711.10561* (2017).

[RPK17c] M. Raissi, P. Perdikaris, and G. E. Karniadakis. “Physics informed deep learning (Part II): data-driven discovery of nonlinear partial differential equations”. In: *arXiv preprint arXiv:1711.10566* (2017).

[RPK18] M. Raissi, P. Perdikaris, and G. E. Karniadakis. “Multistep Neural Networks for Data-driven Discovery of Nonlinear Dynamical Systems”. In: *arXiv preprint arXiv:1801.01236* (2018).

[RPK19] M. Raissi, P. Perdikaris, and G. E. Karniadakis. “Physics-informed neural networks: A deep learning framework for solving forward and inverse problems involving nonlinear partial differential equations”. In: *Journal of Computational Physics* 378 (2019), pp. 686–707.

[RT04] J. Rice and P. de Tombe. “Approaches to modeling crossbridges and calcium-dependent activation in cardiac muscle”. In: *Progress in Biophysics and Molecular Biology* 85.2 (2004), pp. 179–195.

[RW01] M. Rewieński and J. White. “A trajectory piecewise-linear approach to model order reduction and fast simulation of nonlinear circuits and micromachined devices”. In: *Proceedings of the 2001 IEEE/ACM international conference on Computer-aided design*. IEEE Press. 2001, pp. 252–257.

[RW77] T. F. Robinson and S. Winegrad. “Variation of thin filament length in heart muscle”. In: *Nature* 267.5606 (1977), p. 74.

[RWH99] J. Rice, R. Winslow, and W. Hunter. “Comparison of putative cooperative mechanisms in cardiac muscle: length dependence and dynamic responses”. In: *American Journal of Physiology-Heart and Circulatory Physiology* 276.5 (1999), H1734–H1754.

[Sac04] F. Sachse. *Computational Cardiology: Modeling Of Anatomy, Electrophysiology, And Mechanics (Lecture Notes In Computer Science)*. Secaucus, NJ, USA: Springer-Verlag New York, Inc., 2004.

[Sae+01] Y. Saeki, K. Takigiku, H. Iwamoto, S. Yasuda, H. Yamashita, S. Sugiura, and H. Sugi. "Protein kinase A increases the rate of relaxation but not the rate of tension development in skinned rat cardiac muscle". In: *The Japanese Journal of Physiology* 51.4 (2001), pp. 427–433.

[Sae+04] Y. Saeki, T. Kobayashi, S.-i. Yasuda, S. Nishimura, S. Sugiura, H. Yamashita, and H. Sugi. "Role of Ca2+ in determining the rate of tension development and relaxation in rat skinned myocardium". In: *Journal of Molecular and Cellular Cardiology* 36.3 (2004), pp. 371–380.

[Sch+11] M. D. Schmidt, R. R. Vallabhajosyula, J. W. Jenkins, J. E. Hood, A. S. Soni, J. P. Wikswo, and H. Lipson. "Automated refinement and inference of analytical models for metabolic networks". In: *Physical biology* 8.5 (2011), p. 055011.

[SGS03] F. Sachse, K. Glänzel, and G. Seemann. "Modeling of protein interactions involved in cardiac tension development". In: *International Journal of Bifurcation and Chaos* 13.12 (2003), pp. 3561–3578.

[Sir87] L. Sirovich. "Turbulence and the dynamics of coherent structures. I. Coherent structures". In: *Quarterly of Applied Mathematics* 45.3 (1987), pp. 561–571.

[SL09] M. Schmidt and H. Lipson. "Distilling free-form natural laws from experimental data". In: *science* 324.5923 (2009), pp. 81–85.

[SLI09] Y.-B. Sun, F. Lou, and M. Irving. "Calcium-and myosin-dependent changes in troponin structure during activation of heart muscle". In: *The Journal of Physiology* 587.1 (2009), pp. 155–163.

[SM18] O. San and R. Maulik. "Neural network closures for nonlinear model order reduction". In: *Advances in Computational Mathematics* (2018), pp. 1–34.

[SM92] D. Swartz and R. L. Moss. "Influence of a strong-binding myosin analogue on calcium-sensitive mechanical properties of skinned skeletal muscle fibers." In: *Journal of Biological Chemistry* 267.28 (1992), pp. 20497–20506.

[Smi+04] N. Smith, D. Nickerson, E. Crampin, and P. Hunter. "Multiscale computational modelling of the heart". In: *Acta Numerica* 13 (2004), pp. 371–431.

[Smi+08] D. Smith, M. A. Geeves, J Sleep, and S. M. Mijailovich. "Towards a unified theory of muscle contraction. I: foundations". In: *Annals of Biomedical Engineering* 36.10 (2008), pp. 1624–1640.

[Sri+14] N. Srivastava, G. Hinton, A. Krizhevsky, I. Sutskever, and R. Salakhutdinov. "Dropout: a simple way to prevent neural networks from overfitting". In: *The Journal of Machine Learning Research* 15.1 (2014), pp. 1929–1958.

[Str18] S. H. Strogatz. *Nonlinear dynamics and chaos: with applications to physics, biology, chemistry, and engineering*. CRC Press, 2018.

[Sug+12] S. Sugiura, T. Washio, A. Hatano, J. Okada, H. Watanabe, and T. Hisada. "Multi-scale simulations of cardiac electrophysiology and mechanics using the University of Tokyo heart simulator". In: *Progress in Biophysics and Molecular Biology* 110.2 (2012), pp. 380–389.

[SV17] V. Sequeira and J. van der Velden. “The Frank–Starling Law: a jigsaw of titin proportions”. In: *Biophysical Reviews* 9.3 (2017), pp. 259–267.

[SX19] J. W. Siegel and J. Xu. “On the approximation properties of neural networks”. In: *arXiv preprint arXiv:1904.02311* (2019).

[TCD17] S. Trehan, K. T. Carlberg, and L. J. Durlofsky. “Error modeling for surrogates of dynamical systems using machine learning”. In: *International Journal for Numerical Methods in Engineering* 112.12 (2017), pp. 1801–1827.

[TD08] G. J. Tortora and B. H. Derrickson. *Principles of anatomy and physiology*. John Wiley & Sons, 2008.

[TDQ17a] A. Tagliabue, L. Dedè, and A. Quarteroni. “Complex blood flow patterns in an idealized left ventricle: a numerical study”. In: *Chaos: an Interdisciplinary Journal of Nonlinear Science* 27.9 (2017), p. 093939.

[TDQ17b] A. Tagliabue, L. Dedè, and A. Quarteroni. “Fluid dynamics of an idealized left ventricle: the extended Nitsche’s method for the treatment of heart valves as mixed time varying boundary conditions”. In: *International Journal for Numerical Methods in Fluids* 85.3 (2017), pp. 135–164.

[Tes12] G. Teschl. *Ordinary differential equations and dynamical systems*. Vol. 140. American Mathematical Society, 2012.

[TK+08] H. Ter Keurs, T. Shinozaki, Y. Zhang, M. Zhang, Y. Wakayama, Y. Sugai, Y. Kagaya, M. Miura, P. Boyden, B. Stuyvers, et al. “Sarcomere mechanics in uniform and non-uniform cardiac muscle: a link between pump function and arrhythmias”. In: *Progress in biophysics and molecular biology* 97.2-3 (2008), pp. 312–331.

[TK+80] H. Ter Keurs, W. H. Rijnsburger, R. Van Heuningen, and M. J. Nagelsmit. “Tension development and sarcomere length in rat cardiac trabeculae. Evidence of length-dependent activation.” In: *Circulation Research* 46.5 (1980), pp. 703–714.

[TK16] P. P. de Tombe and H. E. ter Keurs. “Cardiac muscle mechanics: sarcomere length matters”. In: *Journal of Molecular and Cellular Cardiology* 91 (2016), pp. 148–150.

[TKHK00] H. Ter Keurs, E. Hollander, and M. ter Keurs. “The effect of sarcomere length on the force–cytosolic [Ca2+] relationship in intact rat cardiac trabeculae”. In: *Skeletal muscle mechanics: from mechanics to function. Wiley, New York* (2000), pp. 53–70.

[Top] *The TOP500 Project*. 2019. URL: `https://www.top500.org`.

[TR11] N. Trayanova and J. Rice. “Cardiac electromechanical models: from cell to organ”. In: *Frontiers in Physiology* 2 (2011), p. 43.

[TS07] P. de Tombe and G. Stienen. “Impact of temperature on cross-bridge cycling kinetics in rat myocardium”. In: *The Journal of Physiology* 584.2 (2007), pp. 591–600.

[TS97] P. de Tombe and G. Stienen. “The rate of tension redevelopment in rat cardiac muscle: Influence of temperature and contractile activation level”. In: *Circulation*. Vol. 96. 8. 1997, pp. 2900–2900.

[TT+04] K. Ten Tusscher, D. Noble, P.-J. Noble, and A. V. Panfilov. "A model for human ventricular tissue". In: *American Journal of Physiology-Heart and Circulatory Physiology* 286.4 (2004), H1573–H1589.

[TTP06a] K. H. Ten Tusscher and A. V. Panfilov. "Alternans and spiral breakup in a human ventricular tissue model". In: *American Journal of Physiology-Heart and Circulatory Physiology* 291.3 (2006), H1088–H1100.

[TTP06b] K. H. Ten Tusscher and A. V. Panfilov. "Cell model for efficient simulation of wave propagation in human ventricular tissue under normal and pathological conditions". In: *Physics in Medicine & Biology* 51.23 (2006), p. 6141.

[Tøn+15] K. Tøndel, S. Land, S. A. Niederer, and N. P. Smith. "Quantifying inter-species differences in contractile function through biophysical modelling". In: *The Journal of Physiology* 593.5 (2015), pp. 1083–1111.

[ULM02] T. P. Usyk, I. J. LeGrice, and A. D. McCulloch. "Computational model of three-dimensional cardiac electromechanics". In: *Computing and Visualization in Science* 4.4 (2002), pp. 249–257.

[Was+12] T. Washio, J. Okada, S. Sugiura, and T. Hisada. "Approximation for cooperative interactions of a spatially-detailed cardiac sarcomere model". In: *Cellular and Molecular Bioengineering* 5.1 (2012), pp. 113–126.

[Was+13] T. Washio, J. Okada, A. Takahashi, K. Yoneda, Y. Kadooka, S. Sugiura, and T. Hisada. "Multiscale heart simulation with cooperative stochastic cross-bridge dynamics and cellular structures". In: *Multiscale Modeling & Simulation* 11.4 (2013), pp. 965–999.

[Was+15] T. Washio, K. Yoneda, J. Okada, T. Kariya, S. Sugiura, and T. Hisada. "Ventricular fiber optimization utilizing the branching structure". In: *International Journal for Numerical Methods in Biomedical Engineering* (2015).

[WBG07] J. P. Whiteley, M. J. Bishop, and D. J. Gavaghan. "Soft tissue modelling of cardiac fibres for use in coupled mechano-electric simulations". In: *Bulletin of mathematical biology* 69.7 (2007), pp. 2199–2225.

[WLW09] N. Westerhof, J.-W. Lankhaar, and B. E. Westerhof. "The arterial Windkessel". In: *Medical & Biological Engineering & Computing* 47.2 (2009), pp. 131–141.

[WMM95] M. Wolff, K. McDonald, and R. Moss. "Rate of tension development in cardiac muscle varies with level of activator calcium". In: *Circulation Research* 76.1 (1995), pp. 154–160.

[Yeg09] B. Yegnanarayana. *Artificial neural networks*. PHI Learning Pvt. Ltd., 2009.

[Zah81] G. I. Zahalak. "A distribution-moment approximation for kinetic theories of muscular contraction". In: *Mathematical Biosciences* 55.1-2 (1981), pp. 89–114.

[Zha+19] W. Zhang, A. Capilnasiu, G. Sommer, G. Holzapfel, and D. Nordsletten. "An Efficient and Accurate Method for Modeling Nonlinear Fractional Viscoelastic Biomaterials". In: *arXiv preprint arXiv:1910.02141* (2019).

[ZPJ94] G. Zou and G. N. Phillips Jr. “A cellular automaton model for the regulatory behavior of muscle thin filaments”. In: *Biophysical Journal* 67.1 (1994), pp. 11–28.

[Zyg] *Zygote 3D models*. 2019. URL: `https://www.zygote.com/`.